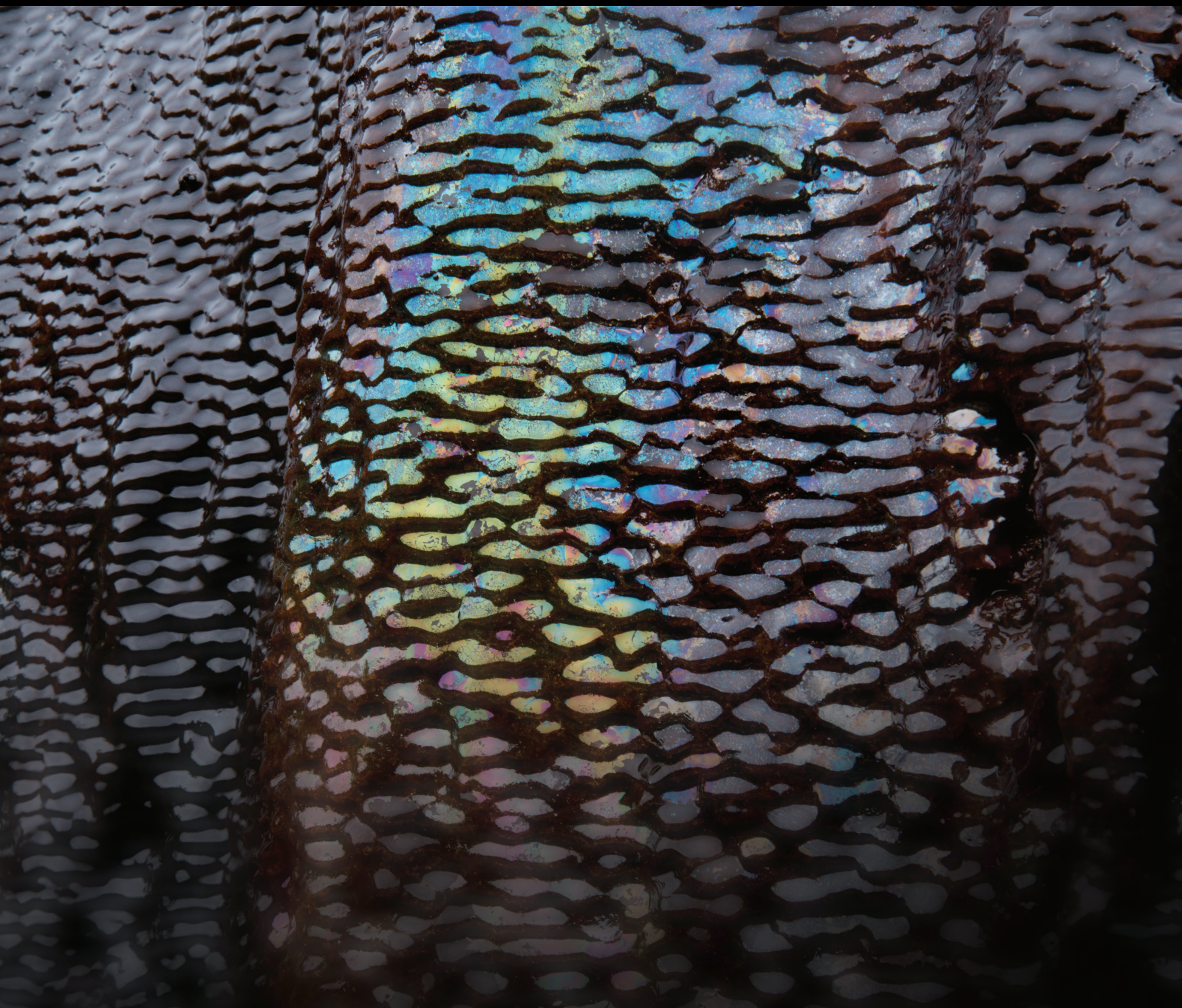# The Role and Impact of Geofluids in Geohazards

Lead Guest Editor: Ching Hung
Guest Editors: Xueyu Pang, Guan-Wei Lin, Kuo-Hsin Yang, and Ryosuke Uzuoka

The Role and Impact of Geofluids in Geohazards

The Role and Impact of Geofluids in Geohazards

Lead Guest Editor: Ching Hung
Guest Editors: Xueyu Pang, Guan-Wei Lin, Kuo-Hsin Yang, and Ryosuke Uzuoka

Editorial Board

Contents

Editorial

The Role and Impact of Geofluids in Geohazards

Ching Hung ⓘ,[1] Xueyu Pang,[2] Guan-Wei Lin ⓘ,[3] Kuo-Hsin Yang,[4] and Ryosuke Uzuoka ⓘ[5]

[1]Department of Civil Engineering, National Cheng Kung University, Tainan, Taiwan
[2]College of Petroleum Engineering, China University of Petroleum, China
[3]Department of Earth Sciences, National Cheng Kung University, Tainan, Taiwan
[4]Department of Civil Engineering, National Taiwan University, Taipei, Taiwan
[5]Disaster Prevention Research Institute, Kyoto University, Uji, Kyoto, Japan

Correspondence should be addressed to Ching Hung; chinghung@mail.ncku.edu.tw

1. Motivation and Background

Geohazard events over recent decades are demanding state-of-the-art, real-time, scientific, and practical strategies to mitigate their social and environmental impacts. Principally, geofluids play a significant role in geohazards in many aspects, such as water infiltration, precipitation, seepage, unsaturated behavior, freezing/thawing, weathering, strength softening, liquefaction, landslide, erosion, and sediment discharge.

Geohazard activities have become more frequent and disruptive in recent decades with changing climates becoming the new normal. To properly disclose the role of geofluids in geohazards and for the purpose of forecasting, emergency response, disaster mitigation, and protecting inhabitants affected by geohazards, a thorough understanding of the scientific background and driving force is essential. At present, combined approaches, integrating state-of-the-art methods numerically, experimentally, or technologically, should be applied to stress on the scientific issues associated with geohazard activities concerning the mechanisms, interplay of geofluid scientific strategies, driving force, dynamics processes, and progress in geohazards.

2. Contents of the Special Issue

In the paper "Impact of an Extreme Typhoon Event on Subsequent Sediment Discharges and Rainfall-Driven Landslides in Affected Mountainous Regions of Taiwan" by C. Hung et al., the research focused on the role of extreme rainfall event on subsequent rainfall-driven landslides and sediment discharges. The extreme rainfall event caused by the 2009 Typhoon Morakot in Taiwan was selected as a case study, and three catchments were chosen as the study areas. Through the rating curve method and landslide mapping, the results indicate that the sediment supply in these catchments was greatly affected by the extreme rainfall. It is further revealed that a significant increase in the number of landslide was attributed to the impact of extreme typhoon event, and the critical rainfall condition triggering landslides declined for 4-5 years.

In the paper "Geohazard Caused by Groundwater in Urban Underground Excavation" by B.-C. B. Hsiung et al., the research addresses how water plays its role in urban underground excavation disaster. Underground water-related hazards, i.e., leakage of the tunnel eye due to launching and docking of the shield, failure of the cross-seepage excavation, and failure of the retaining wall caused by water ingress during deep excavation, would lead to georelated catastrophe. By using finite element simulation to analyze leakage of the tunnel eye during shield launching resulting in failure, the authors find out that flush-in water on the other side of the tunnel and gravity are the main factors causing failure. Failure prevention can be achieved through reduction of soil permeability and increase of cohesion force.

In the paper "Numerical Investigation of Rainfall-Induced Landslide in Mudstone Using Coupled Finite and Discrete Element Analysis" by C. Hung et al., the authors studied the role of water infiltration on a rainfall-induced landslide in mudstone. The prefailure and postfailure characteristics of the landslide were simulated by finite element analysis (FEA) and discrete element analysis (DEA), respectively. Based on FEA results, the onset of landslide initiation was captured through assessing the rapid change of source displacement (RCSD) within the slope. In addition, according to the DEA result, the study indicated that water infiltration and transition in steepness played significant roles in the behavior of runout process. The results of this study demonstrated that a combination of FEA and DEA can be a useful approach to better understand the process of rainfall-induced landslides.

In the paper "Consolidated and Undrained Ring Shear Tests on the Sliding Surface of the Hsien-du-shan Landslide in Taiwan" by H.-M. Lin et al., the authors developed a new consolidated undrained ring shear test capable of measuring the pore pressures to investigate the initiation mechanism of the Hsien-du-shan rock avalanche. The research discusses the postpeak behavior to address the unstable geomorphological precursors observed before the landslide occurred. Experimental results show that the shear contractions of the sliding surface generated excess pore pressure. In addition, when the sliding surface is sheared under large normal stress, the low hydraulic conductivity of a landslide gouge would result in continuous pore pressure increase during long shear displacement. The excess pore pressure feedback at the sliding surface may have accelerated the landslide.

In the paper "Preferential Water Infiltration Path in a Slow-Moving Clayey Earthslide Evidenced by Cross-Correlation of Hydrometeorological Time Series (Charlaix Landslide, French Western Alps)" by G. Bièvre et al., the authors studied the role of water infiltration on a slow-moving clayey landslide. The landslide characteristics, such as seasonal rainfall, deformation displacement, and variation of the groundwater table, were documented through a multidisciplinary monitoring from 2010 to 2017, and a conceptual hydrogeological model of the site was built. The study demonstrated that the behaviors of the phreatic water table and the water table near the shear surface agreed with the landslide kinematics in different seasons. In addition, the fissures connected to the shear surface are the preferential infiltration paths within the clayey landslide.

In the paper "Effects of the Grain Size on Dynamic Capillary Pressure and the Modified Green–Ampt Model for Infiltration" by Y.-Z. Tsai et al., the authors performed downward infiltration experiments to investigate the cumulative infiltration, wetting front depth, and wetting front velocity in sand columns with various grain sizes. They found that the sand column with a smaller grain size exhibited a lower infiltration rate and a lower wetting front velocity, resulting in increased infiltration time. The modified Green–Ampt (MGAM) model was used to estimate the equilibrium capillary head and suction head from the experiment data. The effects of grain size of sand and porosity on the model parameters were also discussed in the study.

In the paper "Modeling of Transient Flow in Unsaturated Geomaterials for Rainfall-Induced Landslides Using a Novel Spacetime Collocation Method" by C.-Y. Ku et al., the research presents a new spacetime collocation method for transient flow in unsaturated soils of rainfall-induced landslides. The numerical solution is obtained by superpositioning Trefftz basis function that satisfies linearized the Richards equation and Gardner exponential model to describe the soil-water characteristic curve in unsaturated soils. The infinite slope stability analysis with the proposed meshless method is developed to deal with the rainfall-induced landslides. Through conducting several test problems, the method is proved to be accurate to deal with the transient flow in unsaturated soils for rainfall-induced landslides. This method can also be applied to different soil textures for future studies.

In the paper "Numerical Analysis of Damaged River Embankment during the 2011 Tohoku Earthquake Using a Multiphase-Coupled FEM Analysis Method" by L. Chen and S. Kimoto, the authors use a three-phase coupled finite element program, COMVI2D-DY, a program for analyzing large deformation of partially saturated soils, to simulate not only a damaged river embankment on the Naruse River but also the embankment reconsolidation process. In order to do so, a cyclic elastoplastic constitutive model based on nonlinear kinematical hardening rule modified by considering stiffness recovery is applied. The result shows that numerical methods enable the key damage pattern, and the embankment is destroyed and collapsed towards the landside for most of the cases, and the settlement is 2.5 m above the embankment. The reconsolidation analysis can also be obtained through simulation results.

In the paper "Soil-Water Characteristic Curve of Residual Soil from a Flysch Rock Mass" by J. Peranić et al., the research presents the soil-water characteristic curves (SWCCs) of residual soil formed by the weathering process of a flysch rock mass. Six different devices were used to perform experiments on intact specimens to cover different stress conditions and from saturated to air-dried conditions. An improved understanding of the soil-water characteristic of residual soil from flysch rock mass is valuable for future studies on assessing the rainfall-induced landslide in flysch slopes.

In the paper "Seepage Behavior of an Inclined Wall Earth Dam under Fluctuating Drought and Flood Conditions" by W. Ye et al., the authors studied the seepage characteristic of an inclined wall dam under fluctuating drought-flood condition using a large-scale physical model. According to the results, the permeability coefficients were much smaller than those of the saturated permeability in the area with low crack development and were much larger than those of the saturated permeability in crack area after drought. As the water level rose, cracks could heal themselves, but the integrity of the dam slope was much less than its original state. In addition, the formation of cracks permanently weakened the antiseepage performance of the clay soil. Monitoring and protecting the weak parts of seepage dams could be benefited by the results.

In the paper "Towards Automated Real-time Detection and Location of Large-Scale Landslides through Seismic

Waveform Back Projection," E.-J. Lee et al. present a semiautomatic algorithm for detecting and locating landslide events using both broadband and short-period recordings and have successfully applied to landslides in Taiwan. The results show that the landslide detection and spatial-temporal location system could benefit the establishment of rainfall-triggered landslide forecast models and provide more reliable constraints for physics-based landslide modeling. The accumulating seismic recording of landslide events could be used as a training dataset for machine learning.

Conflicts of Interest

The editors declare that they have no conflicts of interest regarding the publication of this special issue.

Acknowledgments

Ching Hung
Xueyu Peng
Guan-Wei Lin
Kuo-Hsin Yang
Ryosuke Uzuoka

Research Article

Structural Response of the Metro Tunnel under Local Dynamic Water Environment in Loess Strata

Junling Qiu [ID],[1] **Yiwen Qin,**[1] **Jinxing Lai** [ID],[1] **Ke Wang** [ID],[2] **Fangyuan Niu,**[3] **Hao Wang** [ID],[4] **and Guanglong Zhang**[5]

[1]*School of Highway, Chang'an University, Xi'an 710064, China*
[2]*State Key Laboratory of Rail Transit Engineering Informatization, China Railway First Survey and Design Institute Group Co. Ltd., Xi'an, Shaanxi 710043, China*
[3]*China State Construction Silkroad Construction Investment Group Co., Ltd., Xi'an, Shaanxi 710068, China*
[4]*School of Civil & Construction Engineering, Oregon State University, 101 Kearney Hall, Corvallis, OR 97331, USA*
[5]*Shandong Academy of Building Research, Ji'nan 250031, China*

Correspondence should be addressed to Jinxing Lai; laijinxing@chd.edu.cn

The reasons, prevention, and control of loess disaster are of great concern in practice. In recent years, Xi'an city, China, has taken the leadership in large-scale construction of subway lines in the loess strata. To study the structural response of the tunnel in loess region under local hydrodynamic environment, an experimental testing in 1g as well as a numerical simulation were performed, in which the achieved results were verified and were found to be in good agreement. Furthermore, the results showed that when the water outlet point is above the lining, the overall stress of the lining is "peanut shell," as the water pressure of the outlet point decreases, the tensile stress of the top and bottom of the lining increases, while the compressive stress on both sides decreases; the channel form of the flow to the lining changes with the variation of the position of the water outlet point. It is worth mentioning that in the process of water gushing, the closer to the water source, the greater surface subsidence is, and there is a positive correlation between water pressure and surface subsidence. This study is of significant benchmark for the construction, maintenance, and prevention of tunnel in loess strata under the influence of water environment.

1. Introduction

In the 1840s, Lyell studied sediment deposits along the Mississippi River in the middle of the United States and initially proposed the academic term "Loess" [1]. Compared with other soil, the loess has special structural and water sensitivity: (1) the joint fissure is developed, the mesoscopic structure is porous, and the difference of dry and wet strength is remarkable; (2) most of them have strong collapsibility, softening, and deforming in water [2–6]. Therefore, the change of water environment is very easy to induce engineering geological hazard, and the effect of humankind engineering activity can easily increase the disaster of loess [7–13]. In the past 10 years, Xi'an city, as a main developing city in Western China, has taken the leadership in large-scale construction of subway in the loess strata [14, 15]. On the one hand, according to the situation of Xi'an subway planning, most of the upper layers of subway construction are new loess which have physical features such as high void ratio, incomplete consolidation, and low strength [16–22]. On the other hand, there are lots of ground fissures in Xi'an, so the disturbance of tunnel construction will inevitably lead to large strata deformation [23–27]. During the deformation process, the leakage of urban pipelines will easily lead to large-scale collapsibility of loess strata.

In recent years, on the one hand, scholars in related fields took soak infiltration as the main condition of the experiment and analyzed the mechanism of the catastrophe of subway tunnel project in the groundwater depression cone area and the effect of leakage range of pipeline on the deformation
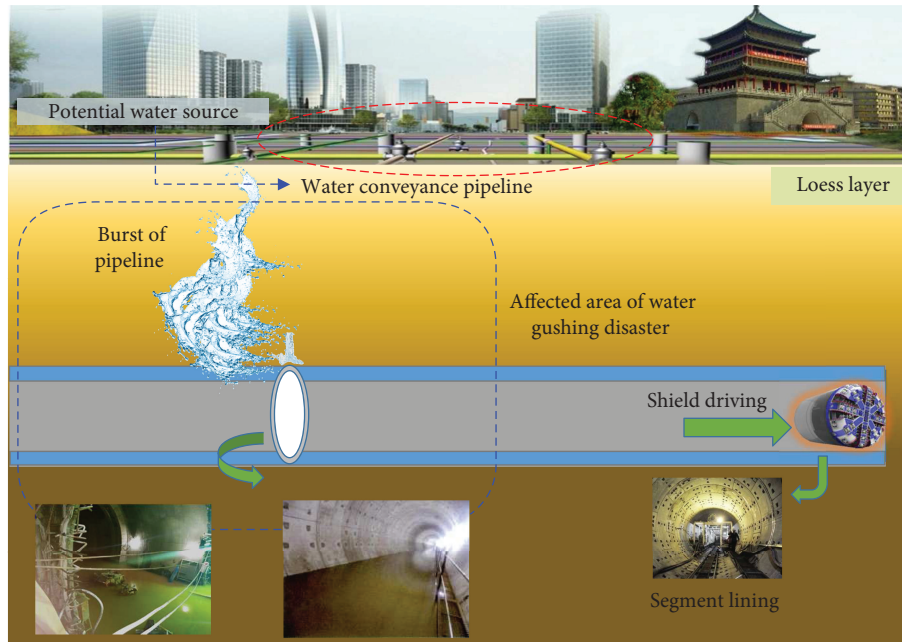
FIGURE 1: Sketch map of water gushing at site.

and failure of tunnel surrounding rock [28–32]. According to the influence of water leakage at different parts of the tunnel on the surrounding soil and the parallel tunnel, the critical gap width of disaster caused by soil loss was proposed [33–38]. On the other hand, in view of the engineering properties of different rocks and soil under the influence of water, different analytical methods have been used to carry out research: in the clay stratum, the researchers used the homogeneous permeation theory to analyze the effect of long-term seepage of subway tunnel in soft soil area on tunnel and surface subsidence [39–43]; in karst tunnel, researchers carried out model experiments to reveal the catastrophic characteristics of water inrush in the filling karst pipeline and summarized the general characters of the water inrush structure of the rock tunnels [44–48]; in the loess stratum, the researchers through on-site monitoring, radar detection, numerical analysis, and other methods analyzed the damage to the segment structure of the subway water gushing and got the deformation characteristics of the segment structure in the process of water gushing and the distribution laws of the crack and the dislocation of the pipe [49–55].

The mentioned research is mostly concerned with the clay and sandy stratum, and the main condition of the experiment is soak infiltration. Research on water gushing mechanism of subway tunnel in collapsible loess strata involves less, such as the temporal and spatial law of structural damage of the subway tunnel under local dynamic water and mechanical formation mechanism of the water gushing channel in the loess stratum. To study the structural response and damage evolution of tunnel in loess region under local hydrodynamic environment, the water gushing disaster of a section tunnel on Xi'an Metro Line 4 is taken into account as a case study, using experimental testing in 1g and numerical simulation to verify each other, the key analyzed the variation law of pore water pressure, vertical stress of surrounding rock,

the strain of lining, and surface settlement, providing a theoretical reference for the construction, maintenance, and prevention of tunnel in loess strata under the influence of water environment.

2. Experiment

2.1. General Situation of Engineering. The preliminary investigation of Xi'an Metro Line 4 showed that there was a large-area collapse loess with large thickness at the southern section of the line, which the maximum thickness of collapse loess layer was within 25 m; the maximum collapsibility was around 1000 mm, and the length of the affected subway line was about 6 km. Simultaneously, the gushing water section of Xi'an Metro Line 4 was located in a busy urban area, and the underground pipeline was dense as well.

The water gushing occurred in a section of Xi'an Metro Line 4. The tunnel is located in the collapsible loess stratum, and scene investigation shows that the water rich in the tunnel site is weak. It is concluded that the groundwater is not developed, and the water content in the stratum is low. The site of water gushing disaster was initially discovered when the top of ring beam of segment appeared with a sudden water leakage in which the content continued to increase and accompanied by a large number of sediment emission. The assessment demonstrated that the water mainly derived from the water pipe (see Figure 1). Furthermore, the ground appeared subsidence, and the subsidence area was with the length, width, and depth of 20, 12, and 6.5 m, respectively.

2.2. Similar Materials. An experiment was carried out on the basis of water gushing from a tunnel in Xi'an Metro Line 4. Based on the actual engineering geological condition, it is assumed that the tunnel is completely located in the collapsible loess stratum in the model test, and the model test does

TABLE 1: Similarity ratios of physical quantities.

Physical quantity	Dimension	Similarity relation	Similarity ratio
l	L	$C_l = 25$	25
γ	$MT^{-2}L^{-2}$	$C_\gamma = 1$	1
σ	$MT^{-2}L^{-1}$	$C_\sigma = C_l C_\gamma$	25
ε	$M^0 T^0 L^0 = 1$	$C_\varepsilon = 1$	1
μ	$T^0 M^0 L^0 = 1$	$C_\mu = 1$	1
E	$MT^{-2}L^{-1}$	$C_E = C_\sigma$	25
k	$T^{-1}L$	$C_k = 1$	1
Q	$T^{-1}L^3$	$C_Q = C_k C_l^2$	625
u	$MT^{-2}L^{-1}$	$C_u = C_\sigma$	25
t	T	$C_t = \dfrac{C_l}{C_k}$	25
v	$T^{-1}L$	$C_v = C_k$	1

TABLE 2: Physical parameters of loess.

Parameter	Prototype	Model
Water content ω (%)	20	20
Bulk density γ (kN/m³)	18.7	18.7
Void ratio e	0.757	0.757
Cohesion C (kPa)	30	30
Internal friction angle Φ (°)	20	20
Permeability coefficient k (m/d)	7	7
Elastic modulus E (kPa)	9.0×10^3	360
Poisson ratio μ	0.32	0.32

not take into account the influence of groundwater. The experimental testing has used dimensional analysis which is based on Buckingham's π theorem [56]. The theorem appropriately describes a relationship between physical variables and fundamental dimensions. It is pointed out that any physical equations can be transformed into equations of dimensionless quantities [57]. The model is a double-field coupled model under the combined action of stress field and seepage field [58–61]. The physical quantities to be considered in a stress field include geometrical dimension (l), bulk density (γ), stress (σ), strain (ε), Poisson's ratio (μ), and elastic modulus (E); the physical quantities to be considered in a seepage field include permeability coefficient (k), seepage velocity (v), seepage discharge (Q), and pore water pressure (u). All physical variables can be represented by fundamental dimensions which include time (T), quality (M), and length (L). The similarity ratios of various physical quantities are calculated, as shown in Table 1.

The actual parameters of loess are converted into theoretical similar parameters of the model according to similarity ratio, which is summarized in Table 2. According to the relevant literature and experimental results [27, 62–67], loess on the spot is used in this model test, and some barite powder, river sand, and industrial salt are added as surrounding

rock materials. Barite powder can improve the cohesiveness of soil; river sand can improve the permeability of soil, and industrial salt can improve the collapsibility of soil. In the model test, bulk density is selected as the major controlling index. The elastic modulus of samples with different proportioning is measured by a universal press, and their internal friction angle and cohesive force are measured by direct shear tests. The test process and results of collapsibility of loess are shown in Figure 2. The proportioning basically meets the requirements of the model experiment. The proportioning of similar materials in the test is summed up in Table 3.

2.3. Model Equipment. The model test apparatus consists of three parts: test-bed, water injection control system, and measurement system. The test-bed is made of a tempered glass, and the sides are fixed with wooden boards. Its dimension is 1.5 m in length, 0.6 m in breadth, and 1.5 m in depth. Water injection control system includes a water storage system, water inlet pip, and pipe head. The pipe head was buried in the soil and connected with the inlet pipe. The other end of the inlet pipe was connected with a reservoir in which a water pump was placed there as well. The type of the water pump is YLJ-750; the pump head is 0 to 2 m, and the diameter of the water pipe is 16 mm, which accords with *China's Structural design code for pipelines of water supply and waste water engineering* (GB50332-2002). Sketch map of model test apparatus is shown in Figure 3. During the experiment, the measured physical quantities include pore water pressure, vertical stress of surrounding rock, and the strain of lining and surface settlement. Measurement of the lining strain used BE120-5AA type resistance strain gauge, and the data acquisition system employed JM3813 type static strain gauge. Measurement of the pore water pressure utilized YB-strain gauge. Measurement of the surface settlement used displacement meter. Measurement of the vertical stress of the surrounding rock employed pressure cell as well. The measuring device is shown in Figure 4.

2.4. Experiment Design and Procedures. In the experiment, four measurement sections are set up, including three longitudinal sections (denoted by A, B, and C) and one cross section (D). The measuring points of vertical stress of surrounding rock are arranged on the A, B, and C section. The measuring points of pore water pressure are arranged on the B and D sections. Since the experiment does not involve lining excavation, the strain measuring points are arranged along the circumferential direction of the lining. The measuring points of strain of lining are arranged on the A and B sections. The layout of each section and measuring point is shown in Figure 5. The measurement of surface settlement is arranged with 3 measuring lines, in which each measuring line has 4 measuring points (see Figure 6). The experiment procedure is shown in Figure 7.

2.5. Results and Analysis. In order to better analyze the real characteristics of water gushing, all the experimental data are converted to prototype by similarity ratio. From starting water injection to water gushing in the lining, experiment lasted for 4800 s. Experimental results showed that the tunnel
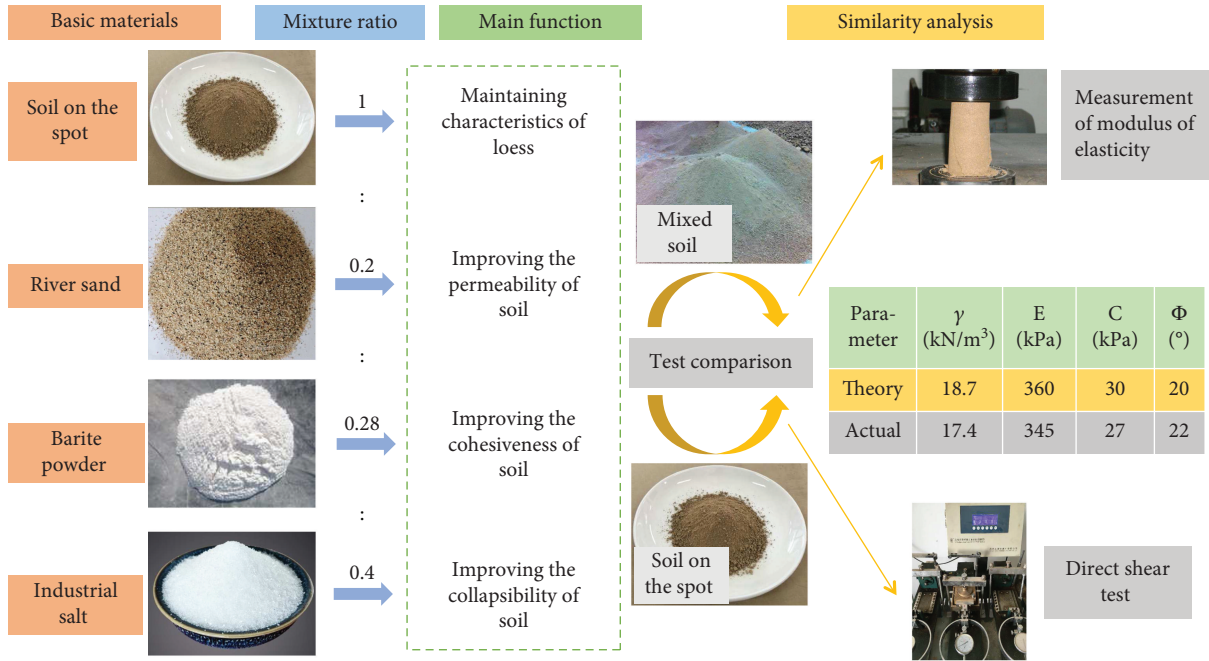
Figure 2: The test process and results of collapsibility of loess.

Table 3: The proportioning of similar material.

Structure	Proportioning
Surrounding rock	Soil on the spot : barite powder : river sand : industrial salt = 1 : 0.28 : 0.2 : 0.4
Lining	Water : barite powder : plaster = 1.7 : 0.1 : 1
	Thickness: 120 mm; diameter: 250 mm

face appears to have water gushing, and a subsidence area with several cracks formed on the surface (see Figure 8). According to the data obtained during the experiment, the variation law of pore water pressure, vertical stress of surrounding rock, and the strain of lining and surface settlement were analyzed.

2.5.1. Pore Water Pressure.
The time-history curve of pore water pressure of three measured points on the D section, as shown in Figure 9, demonstrated that the curves of the three measuring points are similar, and their numerical values are pretty close. From 100 to 2400 s, the pore water pressure of three points was gradually increasing, and the growth rate was faster. It illustrated that the water inflow channel in this direction was gradually formed and continued to expand. When the pore water pressure reached the peak, the water flowed along the channel to the circumference, and the pore water pressure of three points gradually decreased and tended to 0.

The time-history curve of pore water pressure of three measured points on the B section (see Figure 10) showed that the trends of the curves are approximately similar; however, the values of pore water pressure are different. S1 was located below the water gushing point, and from 100 to 3200, the pore water pressure of S1 gradually increased, and the growth rate was faster, while after 3600 s, the pore water pressure gradually tended to be stable. S2 was located at the 45 degrees' direction of the lining, and from 2400 to 3300 s, the pore water pressure of S2 gradually increased; however, after 3600 s, the pore water pressure gradually tended to be stable. The variation of the pore water pressure between S3 and S2 is similar; however, the pore water pressure of S3 is smaller than that of S2.

In conclusion, in the process of formation of water inflow channel, the main channel of water gushing is a channel beginning from the water gushing point to S1, while there is no large water inflow channel between S2 and S3. Three measuring points S4, S5, and S6 were located in the horizontal direction of the water gushing point, in which along these directions, the water gushing channel rapidly formed. However, with the formation of the main channel of water gushing, the water flow gradually decreased through these channels. The experimental results illustrated that the tunnel began to appear to have water gushing from the position of the arch crown of the tunnel face (see Figure 8(a)). It shows that the water will flow from the water source to the nearest surrounding of tunnel face, causing tunnel water gushing disaster.

2.5.2. Vertical Stress of the Surrounding Rock.
Figure 11 represents the time-history curve of vertical stress of the surrounding rock of four measured points on the B section which was below the water gushing point. As depicted in Figure 11, the vertical stress variations of the three measuring points of Y4, Y5, and Y7 are similar. First, it was gradually increased, reached its peak value, and then gradually decreased after the period of stabilization. It reflected that the water inflow channel was smaller at the first and the stress of the surrounding rock gradually increased; however, with the continuous increasing of the water inflow, more water

(a) Main view of test-bed

(b) Left view of test-bed
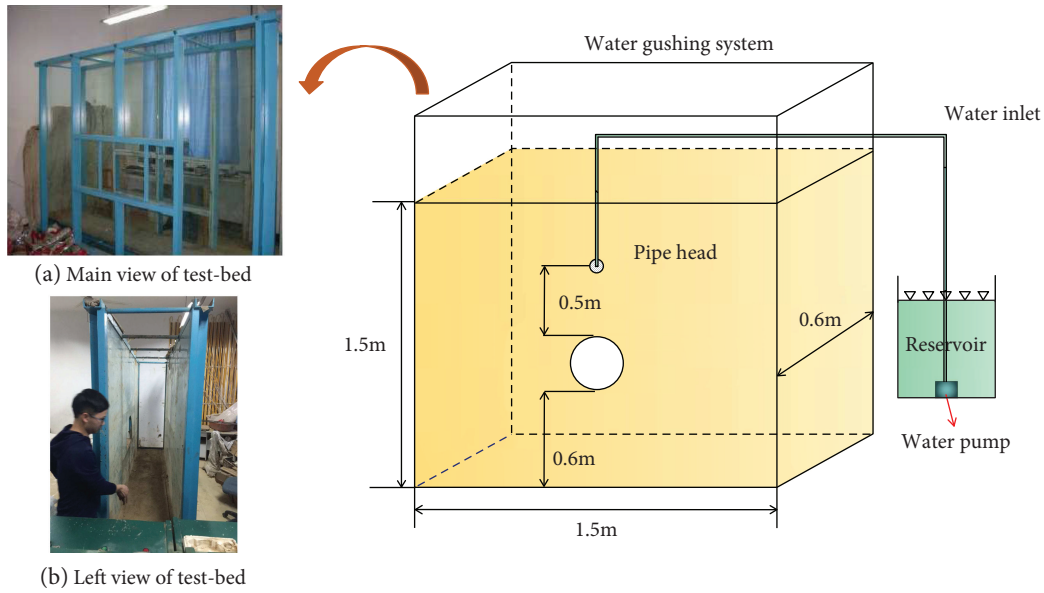
FIGURE 3: Sketch map of the model test apparatus.
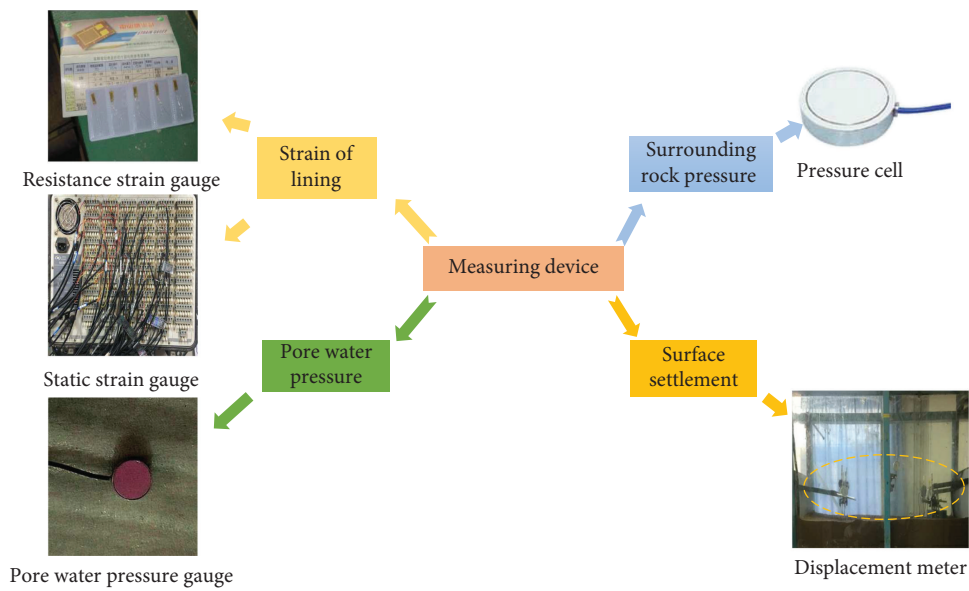
FIGURE 4: Measuring devices.

passages were formed, and the stress gradually decreased. The three differences are that the peak value of the stress of Y4 was the maximum; it rapidly decreased after the peak value, while the stress variation of Y7 gradually decreased after reaching the peak value and ran through the whole test process; the stress at the Y5 had a steady phase after the peak and then decreased gradually. It was indicated that the main channel of water gushing was the channel starting from the direction of Y4 to Y7, and it did not reach the tunnel bottom; the direction of Y4 to Y5 was the secondary channel.

Figure 12 shows the time-history curve of vertical stress of surrounding rock of three measured points on the A section, and Figure 13 displays the time-history curve of vertical stress of the surrounding rock of three measured points on

the C section. It can be seen that the variation of the surrounding rock of three measuring points on the A and C sections are similar to the variation of Y4, Y5, and Y6 on the B section; however, their stress values are smaller. It was indicated that the direction of Y1 to Y3 and the direction of Y8 to Y10 were the secondary channels of water gushing, while they did not reach at the bottom of the tunnel; the direction of Y1 to Y2 and the direction of Y8 to Y9 were permeable channels, which had trivial impact on the surrounding rock.

According to the formation of the mentioned water gushing channels, it can be concluded that in the experimental model, the range of water gushing was within 20 cm around the water gushing point and 50 cm below the water gushing point. In addition, it can be concluded that the stress
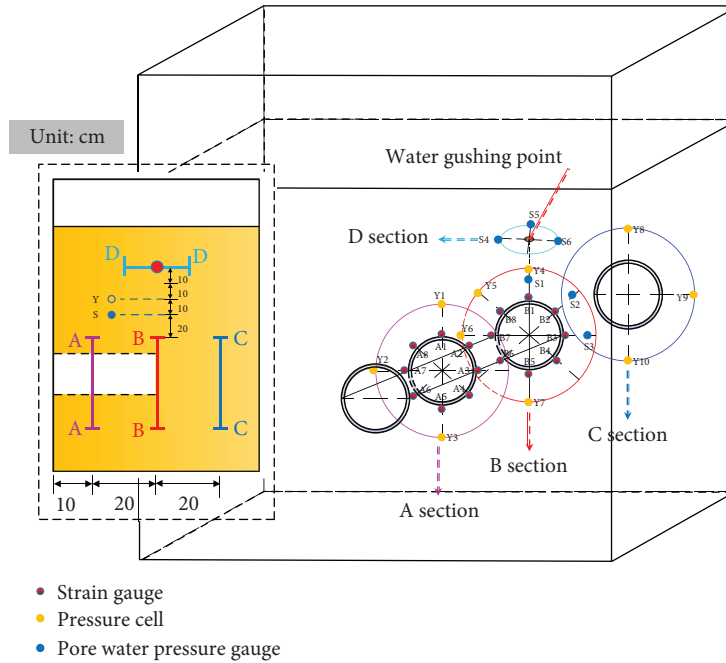
Figure 5: Monitoring section and measuring points' layout.
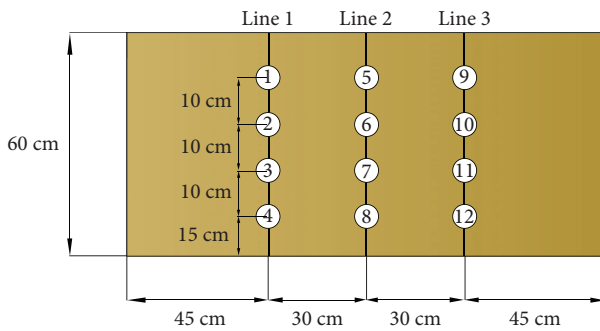
Figure 6: Layout of monitoring points for surface settlement.

distribution of the surrounding rock gradually decreased from the arch crown to the two sides when the water gushing point is located above the lining. The reason may be attributed to the mechanical properties of the soil above the arch crown, which were changed due to the combination of soil and water. When the loess encountered with water, its collapsibility gradually revealed, its fluidity enhanced, and the stress of the surrounding rock above the tunnel gradually increased. With the increasing of water content, the water flow caused the soil to move to the four sides, which aggravated the soil erosion and led to gradually increase the stress of the surrounding rock on both sides of the lining. When the water gushing channels gradually formed and the water flow was dispersed and formed more channels, the vertical stress of the surrounding rock gradually decreased. Moreover, based on the results of the experiment, it can be seen that the surrounding rock above the tunnel collapsed, so it can be inferred that the arching effect of the surrounding rock above the lining vault is lost due to soil erosion, resulting in surface subsidence.

2.5.3. The Strain of the Lining. Figure 14 depicts the time-history curve of the strain of the lining for eight measured points on the A section, and Figure 15 is the time-history curve of the strain of lining for eight measured points on the C section. As shown in Figure 14, the strain of the lining of the eight points on the A section slightly varied before 4000 s, in which after 4000 s, it notably changed. Among them, the stresses of A1, A2, A5, and A6 were positive (tensile stresses), and from 4000 to 4300 s, they gradually increased, in which the growth rate was faster, and they gradually stabilized after 4300 s. Additionally, the stresses of A3, A4, A7, and A8 were negative (compressive stresses), and from 4000 to 4300 s, they gradually increased, in which the growth rate was faster and gradually stabilized after 4300 s. It can be seen from Figure 15 that the strain variation of the measurement points on the B section was basically the same as that of the A section.

It has been indicated that the lining in the longitudinal direction made tensile deformation, and both sides of the lining made inward contraction; the overall stress of the lining is "peanut shell" shape. When gushing water formed a main water channel with vertical direction and an auxiliary water channel with horizontal direction, the soil above the tunnel was squeezed to the sides of the lining, resulting in the deformation of the lining. Since the lining had a certain distance from the water source, the stress of the lining gradually increased, which occurred in the second half of the experiment. This is consistent with the conclusions drawn from the vertical stress of the surrounding rock.

2.5.4. Surface Settlement. Figure 16 displays the surface subsidence curve of three measuring lines. It can be seen that the settlement values of the three measuring lines increased with the increase of axis distance, in which among them, the
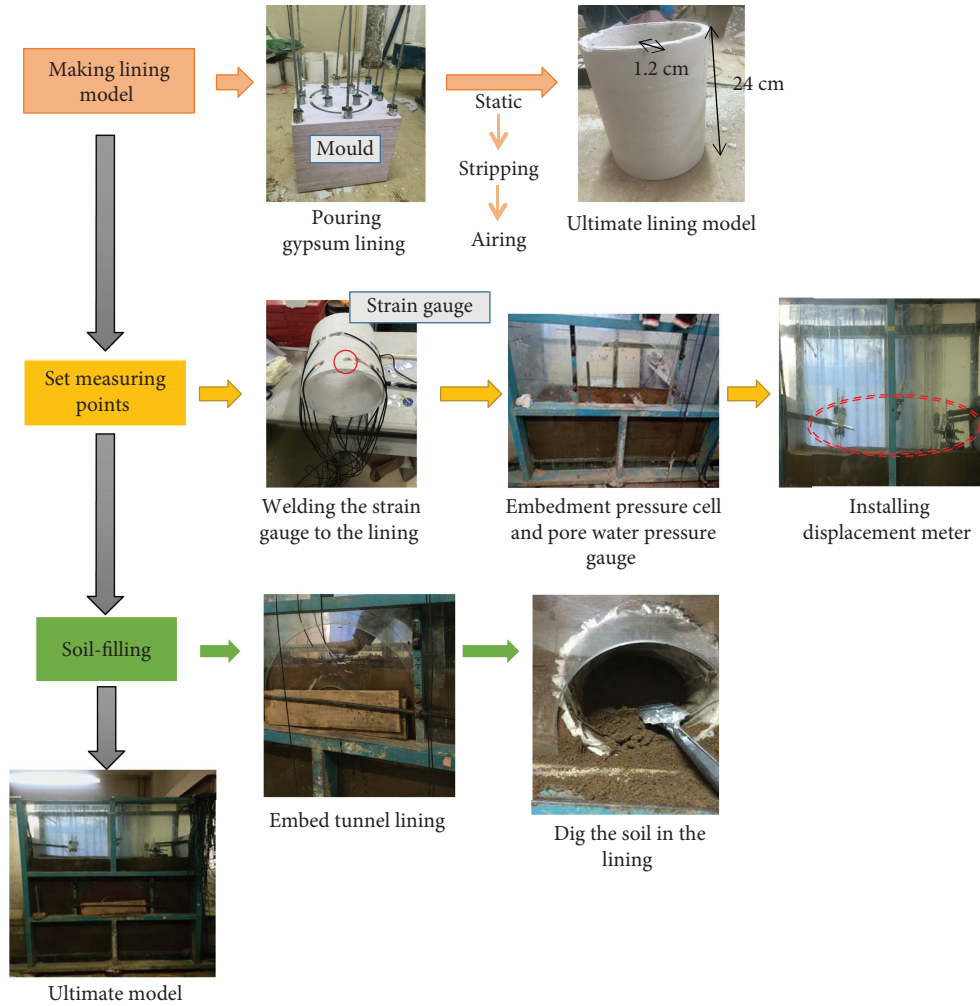
FIGURE 7: Experiment procedure.

(a)

(b)
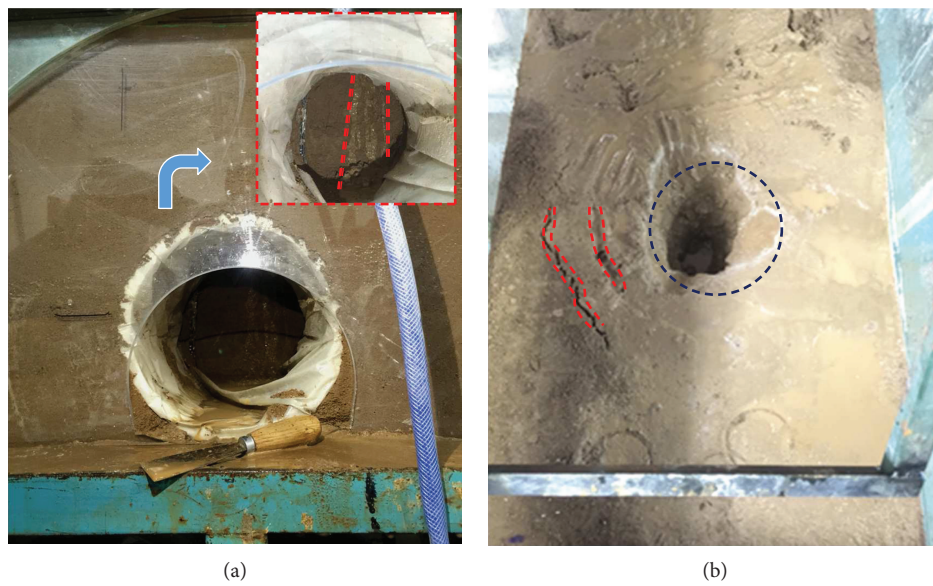
FIGURE 8: Experiment results. (a) Water gushing in lining; (b) subsidence area.
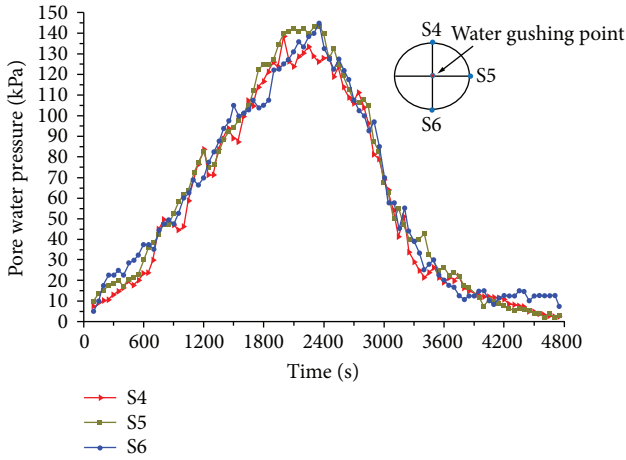
Figure 9: Pore water pressure–time curves of S4, S5, and S6.
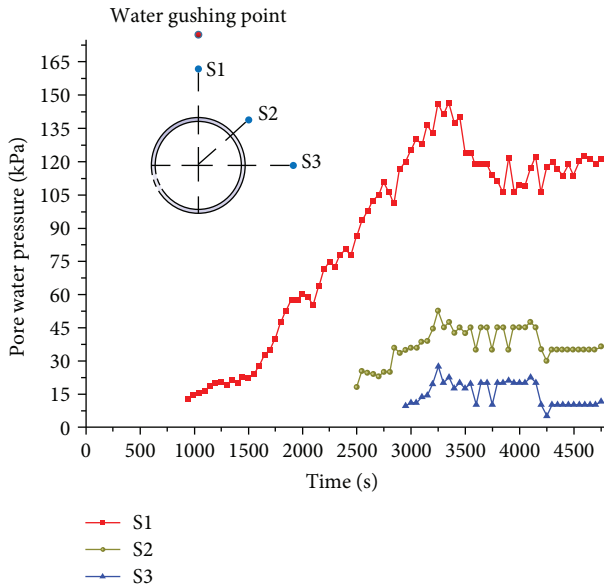
Figure 10: Pore water pressure–time curves of S1, S2, and S3.

Figure 11: Surrounding rock pressure–time curves of Y4, Y5, Y6, and Y7.
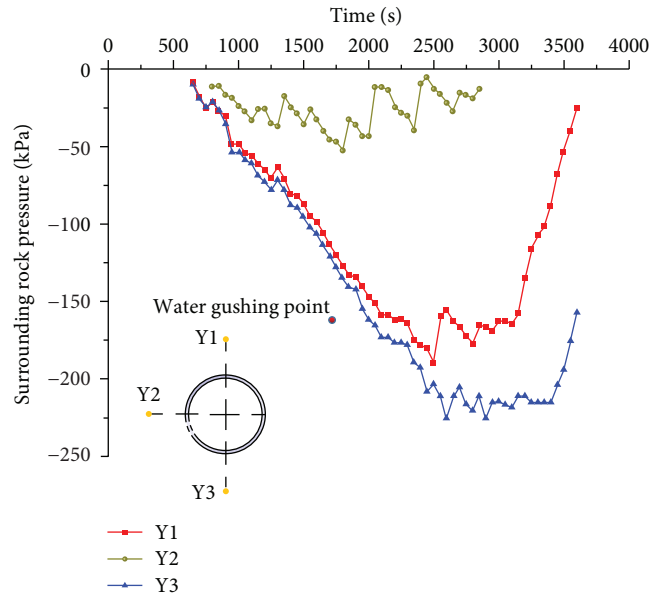
Figure 12: Surrounding rock pressure–time curves of Y1, Y2, and Y3.

settlement values of lines 1 and 3 were smaller, while the settlement value of line 2 was larger, indicating that the main water gushing channel was along the direction of line 2, and there were no main water gushing channels in the soil layers of lines 1 and 3. This is because the measuring line 2 was located above the tunnel, in which during the process of water gushing, the tunnel would not significantly deform due to the action of water flow. However, the surrounding soil would settle; thus, the farther distance from the tunnel lining, the greater settlement of the soil layer.

3. Modeling Analysis

The main objective of this study is investigating the characteristic of gushing water near the tunnel face, which the influence of tunnel excavation is not considered. In the modeling process, in order to highlight the main objective, the problem is simplified as a plane strain problem. Therefore, a two-dimensional tunnel water-inflow model was developed using the ABAQUS [68] finite element software to simulate the flow state of water flow in a saturated loess layer.

3.1. Modeling Introduction. Module of coupling of seepage and stress in the ABAQUS was used for analysis. In the modeling process, the porous loess layer was regarded as multiphase materials, and the unit type was four-node plane strain element (CPE4). The lining was regarded as an elastic element, and the stiffness of element was calculated according to the elastic modulus and Poisson's ratio of the steel and concrete. Model of seepage and stress coupling, which is based on large deformation of clay, was developed by using the updated Lagrangian method. The soil model followed the Mohr-Coulomb failure criterion [69], and the pore water pressure obeyed Darcy's law in order to appropriately
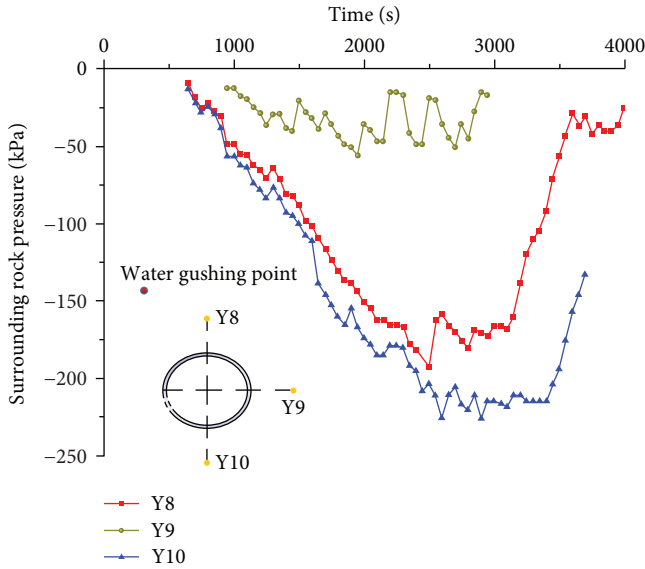
Figure 13: Surrounding rock pressure–time curves of Y8, Y9, and Y10.
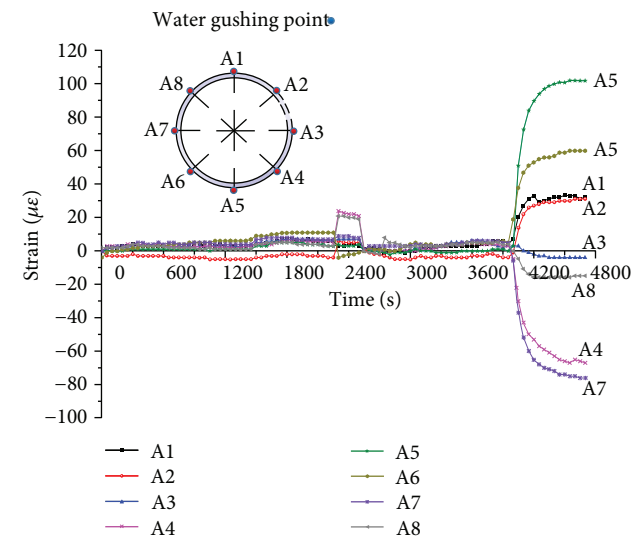
Figure 14: Strain-time curves of A1–A8 on the A section.

Figure 15: Strain-time curves of B1–B8 on the B section.
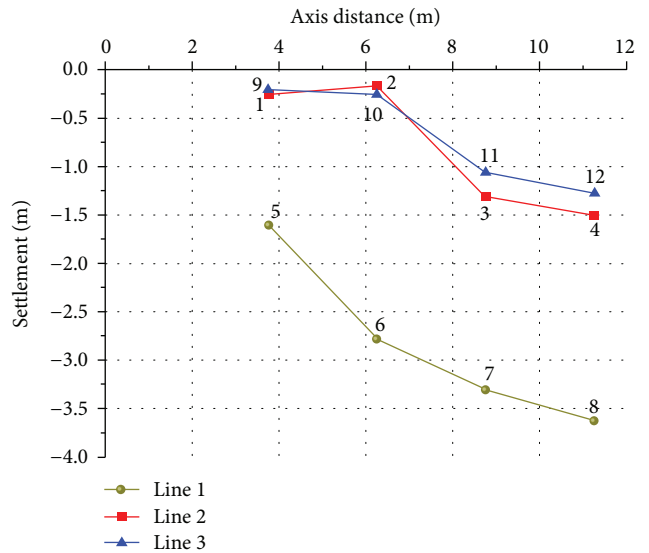
Figure 16: Surface subsidence curve.

simulate the seepage of saturated loess. In the modeling, the lower boundary of the model restricted displacement in the X and Y directions, in which two sides of the model restricted displacement in the X direction. Applying the corresponding node pore pressure function to the node of the pipe to simulate the water out state of the pipeline, the boundary pore pressure under the stratum was set to 0, and using the pressure head and gravity action, the water seepage in the soil layer was realized. In the computation, the analysis of the stability of crustal stress was initially performed, and then, the transient analysis of fluid-structure interaction was conducted. In the process of transient analysis, the pipe outlet time was set to 3600 s. The model consists of 6 operating conditions, as listed in Table 4. The Saint Venant principle showed that the model size is generally 3~5 times of the hole diameter, in which due to the limitations of the test box, the

boundary of the test model was not fully selected according to the actual size. However, in numerical modeling, in order to more accurately simulate the actual situation, the size of the model was taken into account as length of 50 m, width of 50 m, the lining diameter was 6 m, and thickness and burial depth of tunnel were 30 cm and 15 m, respectively, as shown in Figure 17. The physical and mechanical properties of the lining are listed in Table 5 as well.

3.2. Analysis of Calculation Results

3.2.1. Comparison and Analysis of Working Condition 1 and Model Experiment. The simulation process of operating condition 1 is similar to the experimental model. The measurement points in the same positions of the B section, as shown in Figure 5, are selected in the finite element modeling, and the variation of the relevant results with the time was analyzed in order to verify the correctness of the law obtaining based on experimental model.

TABLE 4: Model operating condition.

Operating condition	Effluent point	Water pressure (MPa)	Lining patterns
Condition 1	1	0.25 MPa	Segment lining
Condition 2	2	0.25 MPa	Segment lining
Condition 3	3	0.25 MPa	Segment lining
Condition 4	1	0.2 MPa	Segment lining
Condition 5	1	0.15 MPa	Segment lining
Condition 6	1	0.25 MPa	Composite lining

TABLE 5: Physical and mechanical properties of the lining.

Parameter	Bulk density γ (kN/m^3)	Elastic modulus E (kPa)	Poisson ratio μ	Thickness h (m)
Lining	24	3.45×10^7	0.3	0.3
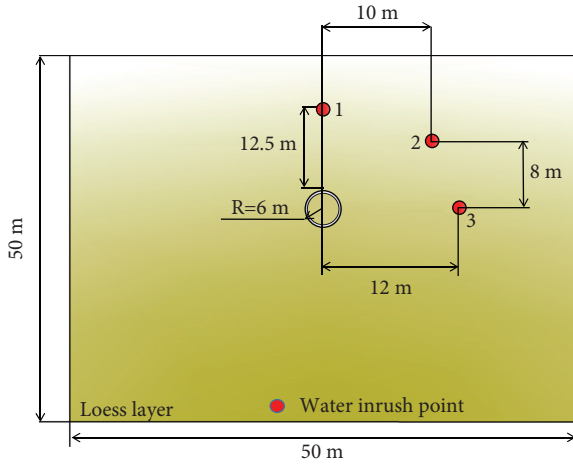
FIGURE 17: Model schematic diagram.

FIGURE 18: Pore water pressure–time curves of S1, S2, and S3.

(1) Pore Water Pressure. The law of pore water pressure regarding the variation of three points computed by finite element analysis is depicted in Figure 18. The analysis results showed that the pore water pressure of the three points gradually increased with the passing of time and gradually decreased at within 1500s. This law is partially consistent with the law derived from the experimental model, and the reason for the difference is that the process simulated by the finite element method was longer than the experimental model. When the flow time was longer, more loess would contact with the water flow, which would lead to the reduction of water flow in the same location, and the pore water pressure around the lining was gradually decreased.

Figure 19 displays the path of water flow in different time periods for condition 1, and the blue region indicates the affected area of the water flow. It can be seen that when the direction of effluent was not limited, under the dual actions of water pressure and gravity, the water would mainly flow in the direction of gravity and then formed the flow channel. The position of 1 to 2 m, based on the ground surface, was the highest position of the flow upward, indicating that the soil layer at this height would be affected by water gushing. In addition, the soil layer within the double diameter ranges of the left and right sides of the tunnel was affected by water gushing. A well agreement between the results of finite element analysis and experimental was observed as well.

(2) Vertical Stress of the Surrounding Rock. In ABAQUS, the tensile stress is defined as positive, and the compressive stress

is negative. As shown in Figure 20, the vertical stress of the four points gradually increased with time and then gradually decreased after reaching its peak. This is basically the same in the experimental model, and the difference is described by the curve of Y6. In the experimental model, the vertical stress value of Y6 was very small, and the amplitude of the variation was not very much, while in the finite element analysis, the vertical stress of Y6 was great. This may be attributed to a fact that in the experimental model, the water flow had not been affected by the soil layer at the top of Y6. However, in the finite element analysis, the water pressure was closer to the actual situation, and the water flow formed a passage around the lining as well.

(3) The Stress of the Lining. The cloud picture of the maximum principal stress of the lining is shown in Figure 21. It can be seen that the two sides of the lining were compressed and the top and the bottom were drawn. This is in agreement with analyzing the experimental model. Figure 22 shows the time-history curve of the stress for lining. As illustrated in Figure 21, B1 at the vault and B5 at the bottom, the stress variation was initially increased and then decreased; the stress of B3 was gradually increased, while the stresses of B2 and B4 were slightly changed. It can be concluded that when the tunnel produced water gushing, the top and both sides of the lining are the main force zones, requiring to be considered in the process of monitoring.

(4) Surface Settlement. Selecting 5 measuring points in the range of 10 m on the right side of the ground surface above the center line of the tunnel, the distance between each measuring point is 2 m; point 1 was the closest to the center line,
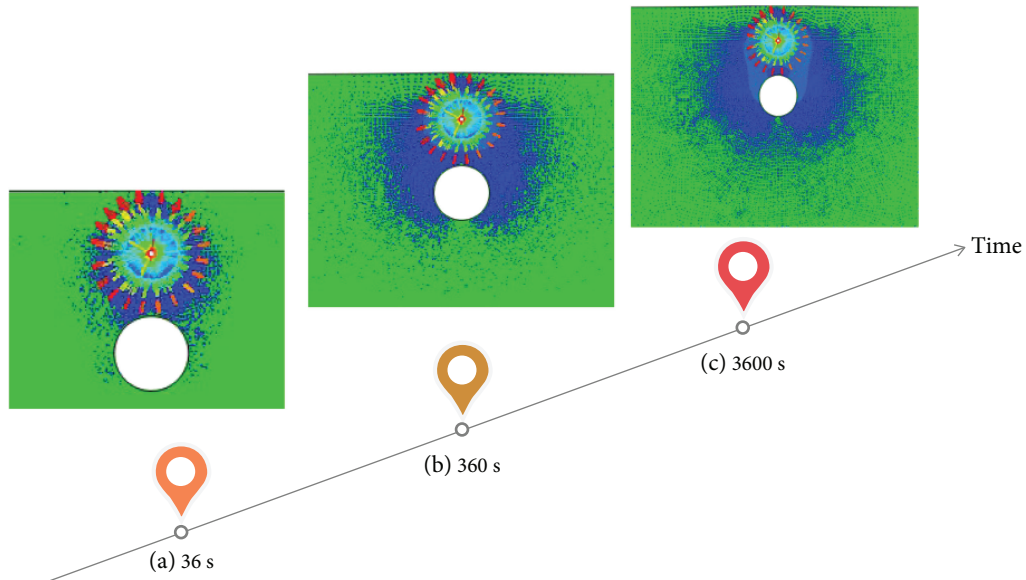
FIGURE 19: The path of water flow in a different time period of condition 1.
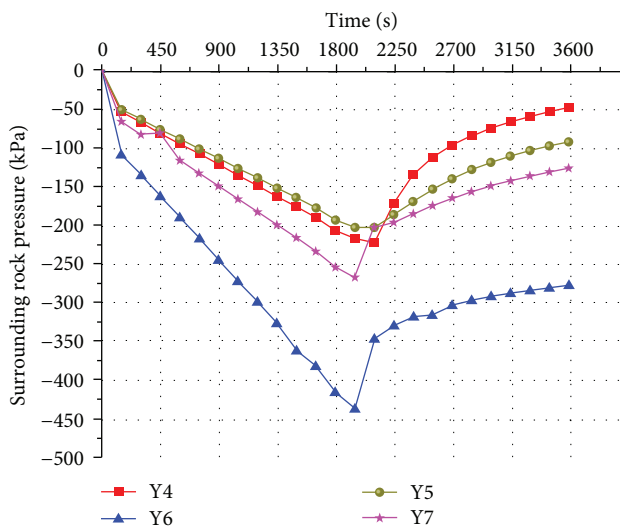
FIGURE 20: Surrounding rock pressure–time curves of Y4, Y5, Y6, and Y7.

FIGURE 21: The cloud picture of the maximum principal stress of the lining (Pa).

while point 5 was the farthest from the center line (see Figure 23). Figure 23 displays the surface subsidence curve of the five measuring points. It can be seen that the closer to the water gushing point, the greater the settlement of the soil layer, which is in agreement with the results of the experimental model.

In summary, the experimental findings were verified by numerical simulation. Combined with other operating conditions, the flow state of water in different water pressures, along with different water gushing points, and various types of tunnel lining in saturated loess stratum should be further analyzed in order to study the pore water pressure field of the surrounding rock, the force condition of the lining, and the distribution law of the displacement of the stratum.

3.2.2. Distribution of Pore Water Pressure Field in the Surrounding Rock.
Figure 24 shows the path of the water flow for four different conditions under the same time and water pressure. As illustrated in Figures 24(a)–24(c), there is a significant variation in the flow path of the water when the water outlet position is different. When the outlet position was above the lining, under the dual actions of water pressure and gravity, a vertical main flow channel was formed, while the top and both sides of the lining were the main areas of water flow; when the outlet point was located in the 45 degrees' direction of the lining, a 45-degree flow channel was formed, which the main areas of water flow were the top of the lining and a side near the water outlet point, and there was no apparent water channel within 5 m below the surface. When the outlet point was in the horizontal
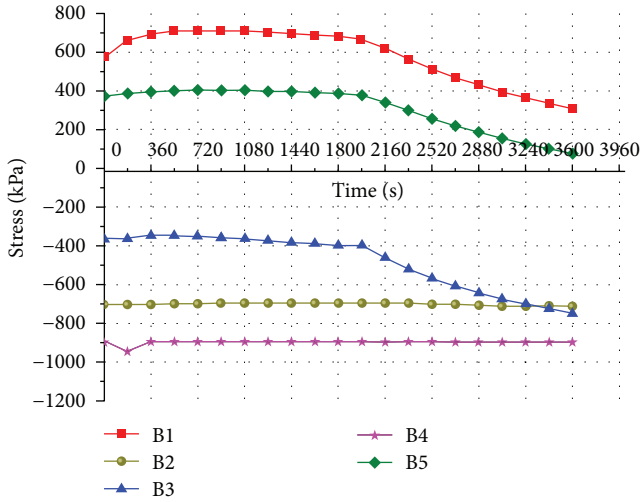
FIGURE 22: Stress-time curves of B1–B5.
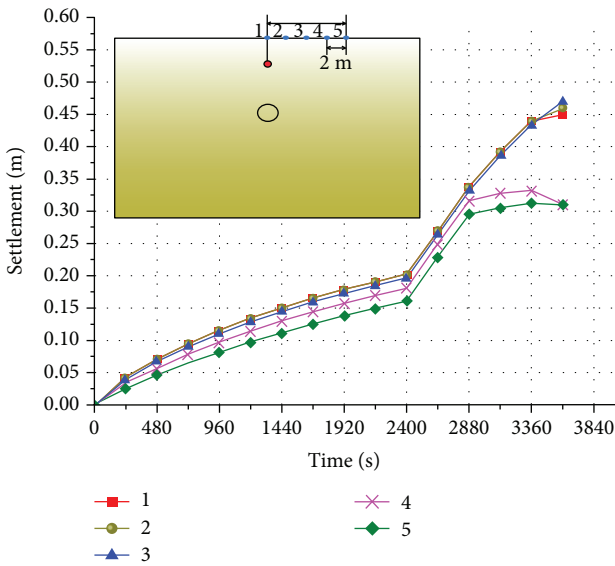
FIGURE 23: Surface subsidence curve.

direction of the lining, the water would still flow to the surrounding of the lining due to the action of water pressure, and the arch bottom and the side near the water outlet point were the main areas of water flow. As shown in Figure 24(a), the flow channels are roughly the same, while there is a difference in the areas of water flow. When the type was composite lining, the flow of water was more uniform around the lining, and when the type was segment lining, the flow of water was less in the part of the arch bottom.

3.2.3. Distribution of Stress Field of the Lining. Figure 25 illustrates the cloud picture of the maximum principal stress of the lining for four different conditions in various water pressures and different forms of lining. As displayed in Figures 25(a)–25(c), with decreasing the water pressure of the outlet point, the tensile stress of the top and bottom of the lining was increased, while the compressive stress on both sides decreased, indicating that during the same time, the

greater the water pressure was, the more complete water flow channel was formed; consequently, more surrounding rocks were moved to both sides of the lining, resulting in the increase of compressive stress on both sides of the lining. As shown in Figures 25(a) and 25(d), the composite lining was fully pressed, which was different from the force of segment lining, indicating that when the soil layer produces gushing water, the whole composite lining is mainly compressed, in which the stress on both sides of the arch foot and shoulder part is the largest.

3.2.4. Distribution of Displacement Field of the Surrounding Rock. Under the same time and outlet location, the effect of different water pressures on the settlement of the stratum is basically the same, and the only difference is related to the settlement value. Figure 26 shows surface subsidence under different water pressures. As depicted in Figure 26, when the water pressure is 0.25 MPa, the maximum settlement is 0.48 m; when the water pressure is 0.20 MPa, the maximum settlement is 0.44 m; when the water pressure is 0.15 MPa, the maximum settlement is 0.41 m. It is concluded that the water pressure directly affects the surface subsidence, the larger the water pressure, the greater surface settlement is obtained.

4. Conclusions

Based on the water gushing disaster of a section tunnel on Xi'an Metro Line 4, the structural response and damage evolution of the tunnel in loess region under local hydrodynamic environment are systematically studied by model test and numerical simulation. The main conclusions:

(1) The experimental model and the numerical simulation in the condition 1 verified each other. When the water outlet point is above the lining, the stress distribution of the surrounding rock is gradually reduced from the arch crown to both sides, and the overall stress of the lining is "peanut shell"; the gushing water forms a main water channel with vertical direction and an auxiliary water channel with horizontal direction. In the process of water gushing, the closer to the water source, the greater pore water pressure is; the closer to the water source, the greater surface subsidence is, while in the direction of the tunnel axis, the settlement of the stratum which has the lining is smaller than that of the stratum without lining

(2) When the position of the water outlet changes, the channel form of the flow to the lining is also varied; when the outlet point is located in the 45 degrees' direction of the lining, a 45-degree flow channel is formed. In addition, when the outlet point is in the horizontal direction of the lining, the main channel of the water flow does not pass through the lining; however, there will be a small amount of water flowing into the lining near the water outlet point. Under the same water outlet position, the flow of water
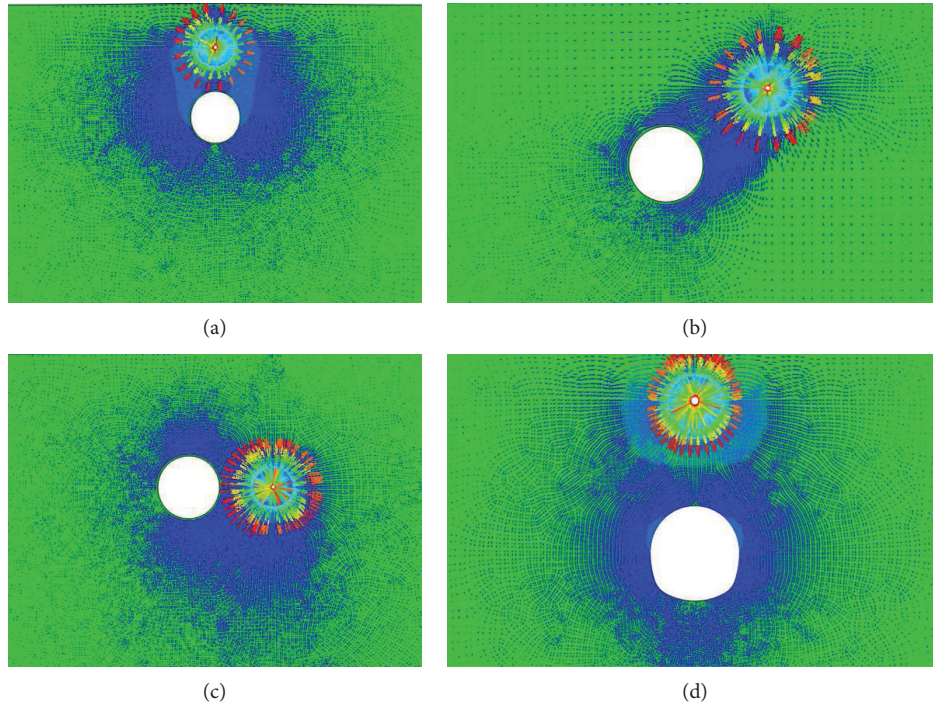
FIGURE 24: The path of the water flow of four conditions. (a) Condition 1; (b) condition 2; (c) condition 3; and (d) condition 6.
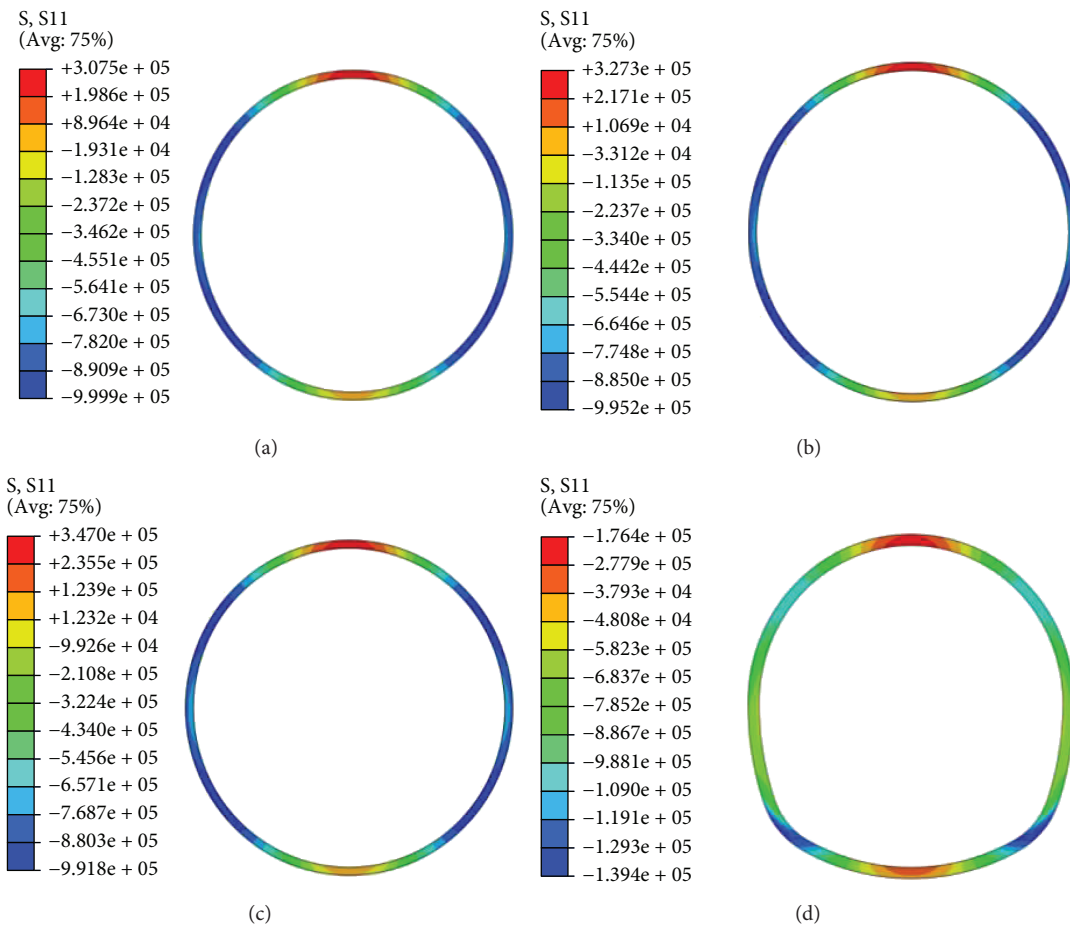
FIGURE 25: The maximum principal stress of the lining of four conditions (unit: Pa). (a) Condition 1; (b) condition 4; (c) condition 5; and (d) condition 6.
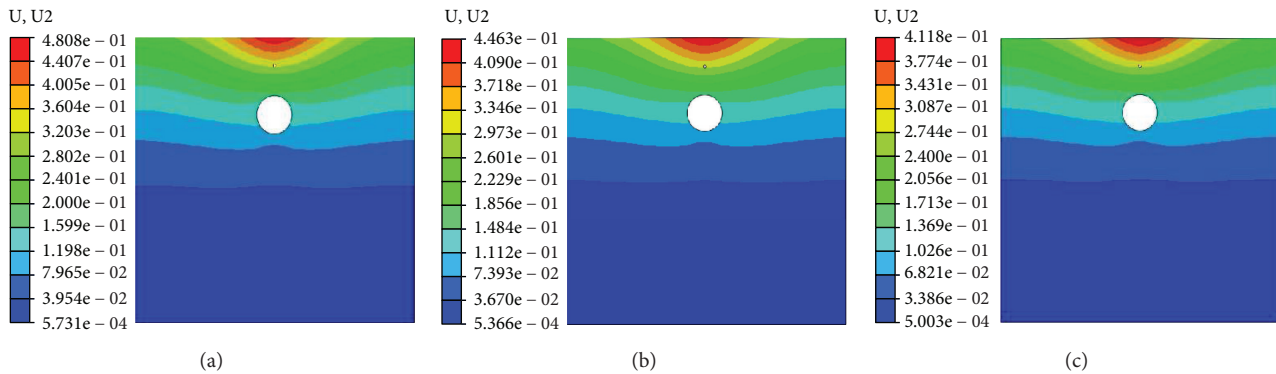
FIGURE 26: Surface subsidence under different water pressure (unit: m). (a) Condition 1; (b) condition 4; and (c) condition 5.

around composite lining is more uniform, while there is less flow at the bottom of segment lining

(3) As the water pressure of the outlet point decreases, the tensile stress of the top and bottom of the lining increases, while the compressive stress on both sides decreases; segment lining is subjected to pressure on both sides and the vault and arch bottom are pulled, while composite lining is mainly subjected to compression, and the compressive stress at both ends of the arch foot is the largest

(4) The water pressure directly affects the surface subsidence; the larger the water pressure, the greater surface settlement is; however, the settlement range is mainly affected by time, that is, the longer the time of water gushing, the greater scope of the surface subsidence is obtained

Data Availability

The data used to support the findings of this study are available from the corresponding author upon request.

Conflicts of Interest

The authors declare that there is no conflict of interests regarding the publication of this paper.

Acknowledgments

References

[1] J. O. Snowden, R. R. Priddy, and C. D. Caplenor, *Loess Investigations in Mississippi: Geology of Mississippi Loess*, Mississippi Geological, Economic and Topographical Survey, 1968.

[2] G. Gao, "The distribution and geotechnical properties of loess soils, lateritic soils and clayey soils in China," *Engineering Geology*, vol. 42, no. 1, pp. 95–104, 1996.

[3] Q. Liang, J. Li, X. Wu, and A. Zhou, "Anisotropy of Q_2 loess in the Baijiapo Tunnel on the Lanyu Railway, China," *Bulletin of Engineering Geology and the Environment*, vol. 75, no. 1, pp. 109–124, 2016.

[4] M. Zhang and J. Liu, "Controlling factors of loess landslides in western China," *Environmental Earth Sciences*, vol. 59, no. 8, pp. 1671–1680, 2010.

[5] Q. Wang and H. Sun, "Traffic structure optimization in historic districts based on green transportation and sustainable development concept," *Advances in Civil Engineering*, vol. 2019, Article ID 9196263, 15 pages, 2019.

[6] P. Li, F. Wang, and Q. Fang, "Undrained analysis of ground reaction curves for deep tunnels in saturated ground considering the effect of ground reinforcement," *Tunnelling and Underground Space Technology*, vol. 71, pp. 579–590, 2018.

[7] T. X. Zhu, "Gully and tunnel erosion in the hilly Loess Plateau region, China," *Geomorphology*, vol. 153-154, pp. 144–155, 2012.

[8] Y. Bai, Z. Dai, and W. Zhu, "Multiphase risk-management method and its application in tunnel engineering," *Natural Hazards Review*, vol. 15, no. 2, pp. 140–149, 2014.

[9] S. Rezaeimalek, A. Nasouri, J. Huang, S. Bin-Shafique, and S. T. Gilazghi, "Comparison of short-term and long-term performances for polymer-stabilized sand and clay," *Journal of Traffic and Transportation Engineering (English Edition)*, vol. 4, no. 2, pp. 145–155, 2017.

[10] R. Qiao, Z. Shao, W. Wei, and Y. Zhang, "Theoretical Investigation into the Thermo-Mechanical Behaviours of Tunnel Lining During RABT Fire Development," *Arabian Journal for Science and Engineering*, 2018, in press.

[11] C. Liu, Z. Fan, X. Chen, C. Zhu, and G. Bai, "Experimental study on bond behavior between section steel and RAC under full replacement ratio," *KSCE Journal of Civil Engineering*, vol. 23, no. 2, pp. 1–12, 2019.

[12] Z.-F. Wang, W.-C. Cheng, and Y.-Q. Wang, "Investigation into geohazards during urbanization process of Xi'an, China," *Natural Hazards*, vol. 92, no. 3, pp. 1937–1953, 2018.

[13] X. Pang, J. Singh, and W. Cuello Jimenez, "Characterizing gas bubble size distribution of laboratory foamed cement using X-ray micro-CT," *Construction and Building Materials*, vol. 167, pp. 243–252, 2018.

[14] J. Lai, K. Wang, J. Qiu, F. Niu, J. Wang, and J. Chen, "Vibration response characteristics of the cross tunnel structure," *Shock and Vibration*, vol. 2016, Article ID 9524206, 16 pages, 2016.

[15] Y. Wei, S. Liang, W. Guo, and W. Hansen, "Stress prediction in very early-age concrete subject to restraint under varying

temperature histories," *Cement and Concrete Composites*, vol. 83, pp. 45–56, 2017.

[16] P. F. Li, F. Wang, L. F. Fan, H. D. Wang, and G. W. Ma, "Analytical scrutiny of loosening pressure on deep twin-tunnels in rock formations," *Tunnelling and Underground Space Technology*, vol. 83, pp. 373–380, 2019.

[17] J. Wang, Q. Huo, Z. Song, and Y. Zhang, "Study on adaptability of primary support arch cover method for large-span embedded tunnels in the upper-soft lower-hard stratum," *Advances in Mechanical Engineering*, vol. 11, no. 1, pp. 1–15, 2019, in press.

[18] Y. Luo, J. Chen, P. Huang, M. Tang, X. Qiao, and Q. Liu, "Deformation and mechanical model of temporary support sidewall in tunnel cutting partial section," *Tunnelling and Underground Space Technology*, vol. 61, pp. 40–49, 2017.

[19] Z. Wang, Y. Xie, and H. Liu, "Analysis on deformation and structural safety of a novel concrete-filled steel tube support system in loess tunnel," *European Journal of Environmental and Civil Engineering*, 2018, in press.

[20] H. Yu, Y. Yuan, G. Xu, Q. Su, X. Yan, and C. Li, "Multi-point shaking table test for long tunnels subjected to non-uniform seismic loadings - Part II: application to the HZM immersed tunnel," *Soil Dynamics and Earthquake Engineering*, vol. 108, pp. 187–195, 2018.

[21] Q. Yan, H. Chen, W. Chen, J. Zhang, S. Ma, and X. Huang, "Dynamic characteristic and fatigue accumulative damage of a cross shield tunnel structure under vibration load," *Shock and Vibration*, vol. 2018, Article ID 9525680, 14 pages, 2018.

[22] Q. Yan, W. Zhang, C. Zhang, H. Chen, Y. Dai, and H. Zhou, "Back Analysis of Water and Earth Loads on Shield Tunnel and Structure Ultimate Limit State Assessment: A Case Study," *Arabian Journal for Science and Engineering*, 2018, in press.

[23] Z.-F. Wang, S.-L. Shen, W.-C. Cheng, and Y.-S. Xu, "Ground fissures in Xi'an and measures to prevent damage to the Metro tunnel system due to geohazards," *Environmental Earth Sciences*, vol. 75, no. 6, p. 511, 2016.

[24] S. He, L. Su, H. Fan, and R. Ren, "Methane Explosion Accidents of Tunnels in SW China," *Geomatics, Natural Hazards and Risk*, vol. 10, no. 1, pp. 1–15, 2019, in press.

[25] Y. Fang, J. Guo, J. Grasmick, and M. Mooney, "The effect of external water pressure on the liner behavior of large cross-section tunnels," *Tunnelling and Underground Space Technology*, vol. 60, pp. 80–95, 2016.

[26] Y. Fang, C. He, A. Nazem, Z. Yao, and J. Grasmick, "Surface settlement prediction for EPB shield tunneling in sandy ground," *KSCE Journal of Civil Engineering*, vol. 21, no. 7, pp. 2908–2918, 2017.

[27] R. Ren, H. Zhou, Z. Hu, S. He, and X. Wang, "Statistical Analysis of Fire Accidents in Chinese Highway Tunnels 2000-2016," *Tunnelling and Underground Space Technology*, vol. 83, pp. 452–460, 2019.

[28] L. Tong, L. Liu, G. Cai, and G. du, "Assessing the coefficient of the earth pressure at rest from shear wave velocity and electrical resistivity measurements," *Engineering Geology*, vol. 163, no. 16, pp. 122–131, 2013.

[29] Z. Q. Zhang, H. Zhang, Y. T. Tan, and H. Y. Yang, "Natural wind utilization in the vertical shaft of a super-long highway tunnel and its energy saving effect," *Building and Environment*, vol. 145, pp. 140–152, 2018.

[30] C. P. Zhang, Y. J. Yue, and Y. Cai, "Influence of pipeline leakage range on ground deformation and failure during shallow

[31] W. C. Cheng, J. C. Ni, and Y. H. Cheng, "Alternative shoring for mitigation of pier-foundation excavation disturbance to an existing freeway," *Journal of Performance of Constructed Facilities*, vol. 31, no. 5, 2017.

[32] C. Liu, Z. Lv, C. Zhu, G. Bai, and Y. Zhang, "Study on calculation method of long term deformation of RAC beam based on creep adjustment coefficient," *KSCE Journal of Civil Engineering*, vol. 23, no. 1, pp. 260–267, 2019.

[33] G. Zheng, X. Dai, and Y. Diao, "Parameter analysis of water flow during EPBS tunnelling and an evaluation method of spewing failure based on a simplified model," *Engineering Failure Analysis*, vol. 58, pp. 96–112, 2015.

[34] G. Zheng, X.-s. Zhang, Y. Diao, and H.-y. Lei, "Experimental study on grouting in underconsolidated soil to control excessive settlement," *Natural Hazards*, vol. 83, no. 3, pp. 1683–1701, 2016.

[35] Y. W. Zhang, X. L. Weng, Z. P. Song, and Y. F. Sun, "Modeling of loess soaking induced impacts on metro tunnel using water soaking system in centrifuge," *Geofluids*, vol. 2019, Article ID 5487952, 14 pages, 2019.

[36] R. Qiao, Z. Shao, F. Liu, and W. Wei, "Damage evolution and safety assessment of tunnel lining subjected to long-duration fire," *Tunnelling and Underground Space Technology*, vol. 83, pp. 354–363, 2019.

[37] X. Luo, D. Li, and S. Zhang, "Traffic Flow Prediction in Holidays Based on DFT and SVR," *Journal of Sensors*, vol. 2019, Article ID 6461450, 9 pages, 2019.

[38] Z.-F. Wang, J. S. Shen, and W.-C. Cheng, "Simple method to predict ground displacements caused by installing horizontal jet-grouting columns," *Mathematical Problems in Engineering*, vol. 2018, Article ID 1897394, 11 pages, 2018.

[39] Z. J. Zhou, C. N. Ren, G. J. Xu, H. C. Zhan, and T. Liu, "Dynamic failure mode and dynamic response of high slope using shaking table test," *Shock and vibration*, vol. 2019, Article ID 4802740, 15 pages, 2019.

[40] D. M. Zhang, L. X. Ma, J. Zhang, P. Y. Hicher, and C. H. Juang, "Ground and tunnel responses induced by partial leakage in saturated clay with anisotropic permeability," *Engineering Geology*, vol. 189, pp. 104–115, 2015.

[41] D. M. Zhang, Z. K. Huang, Z. Y. Yin, L. Z. Ran, and H. W. Huang, "Predicting the grouting effect on leakage-induced tunnels and ground response in saturated soils," *Tunnelling and Underground Space Technology*, vol. 65, pp. 76–90, 2017.

[42] Y. Luo, J. Chen, B. Liu, L. Chen, and J. Xie, "Analysis of pipe-roof in tunnel exiting portal by the foundation elastic model," *Mathematical Problems in Engineering*, vol. 2017, Article ID 9387628, 12 pages, 2017.

[43] H. Yu, C. Cai, A. Bobet, X. Zhao, and Y. Yuan, "Analytical solution for longitudinal bending stiffness of shield tunnels," *Tunnelling and Underground Space Technology*, vol. 83, pp. 27–34, 2019.

[44] E. J. Britton and P. J. Naughton, "The arching phenomena observed in experimental trap door model tests," in *Geo-Frontiers 2011*, pp. 788–797, Dallas, TX, USA, 2011.

[45] L. P. Li, S. C. Li, and Q. S. Zhang, "Study of mechanism of water inrush induced by hydraulic fracturing in karst tunnels," *Rock and Soil Mechanics*, vol. 31, no. 2, pp. 523–528, 2010.

[46] S. C. Li, J. Wu, Z. H. Xu, and L. P. Li, "Unascertained measure model of water and mud inrush risk evaluation in karst tunnels

and its engineering application," *KSCE Journal of Civil Engineering*, vol. 21, no. 4, pp. 1170–1182, 2017.

[47] B. Liu, Z. Liu, S. Li, K. Fan, L. Nie, and X. Zhang, "An improved time-lapse resistivity tomography to monitor and estimate the impact on the groundwater system induced by tunnel excavation," *Tunnelling and Underground Space Technology*, vol. 66, pp. 107–120, 2017.

[48] J. Zhang, S. Li, L. Li et al., "Grouting effects evaluation of water-rich faults and its engineering application in Qingdao Jiaozhou Bay Subsea Tunnel, China," *Geomechanics and Engineering*, vol. 12, no. 1, pp. 35–52, 2017.

[49] X. Guo, J. R. Chai, Y. Qin, Z. G. Xu, Y. N. Fan, and X. W. Zhang, "Mechanism and Treatment Technology of Three Water Inrush Events in the Jiaoxi River Tunnel in Shaanxi, China," *Journal of Performance of Constructed Facilities*, vol. 33, no. 1, article 04018098, p. 12, 2019.

[50] Y. Luo, J. Chen, H. Wang, and P. Sun, "Deformation rule and mechanical characteristics of temporary support in soil tunnel constructed by sequential excavation method," *KSCE Journal of Civil Engineering*, vol. 21, no. 6, pp. 2439–2449, 2017.

[51] J. Wang, Z. Ren, Z. Song, R. Huo, and T. Yang, "Study of the effect of micro-pore characteristics and saturation degree on the longitudinal wave velocity of sandstone," *Arabian Journal of Geosciences*, 2019, in press.

[52] J. Qiu, X. Wang, J. Lai, Q. Zhang, and J. Wang, "Response characteristics and preventions for seismic subsidence of loess in Northwest China," *Natural Hazards*, vol. 92, no. 3, pp. 1909–1935, 2018.

[53] X. Luo, L. Niu, and S. Zhang, "An algorithm for traffic flow prediction based on improved SARIMA and GA," *KSCE Journal of Civil Engineering*, vol. 22, no. 10, pp. 4107–4115, 2018.

[54] H. J. Zhang, Z. Z. Wang, F. Lu, G. Y. Xu, and W. G. Qiu, "Analysis of the displacement increment induced by removing temporary linings and corresponding countermeasures," *Tunnelling and Underground Space Technology*, vol. 73, pp. 236–243, 2018.

[55] Z. Zhang, H. Li, H. Yang, and B. Wang, "Failure modes and face instability of shallow tunnels under soft grounds," *International Journal of Damage Mechanics*, 2018, in press.

[56] E. Buckingham, "On physically similar systems; illustrations of the use of dimensional equations," *Physics Review*, vol. 4, no. 4, pp. 345–376, 1914.

[57] L. Russo, M. Sorrentino, P. Polverino, and C. Pianese, "Application of buckingham π theorem for scaling-up oriented fast modelling of proton exchange membrane fuel cell impedance," *Journal of Power Sources*, vol. 353, pp. 277–286, 2017.

[58] X. Li and Z. Shao, "Investigation of Macroscopic Brittle Creep Failure Caused by Microcrack Growth Under Step Loading and Unloading in Rocks," *Rock Mechanics and Rock Engineering*, vol. 49, no. 7, pp. 2581–2593, 2016.

[59] Q. Yan, Y. Xu, W. Zhang, P. Geng, and W. Yang, "Numerical analysis of the cracking and failure behaviors of segmental lining structure of an underwater shield tunnel subjected to a derailed high-speed train impact," *Tunnelling and Underground Space Technology*, vol. 72, pp. 41–54, 2018.

[60] X. Nie, X. Wei, X. Li, and C. Lu, "Heat treatment and ventilation optimization in a deep mine," *Advances in Civil Engineering*, vol. 2018, Article ID 1529490, 12 pages, 2018.

[61] X. Z. Li, X. L. Qu, C. Z. Qi, and Z. S. Shao, "A unified analytical method calculating brittle rocks deformation induced by crack growth," *International Journal of Rock Mechanics and Mining Sciences*, vol. 113, pp. 134–141, 2019.

[62] R. Ren, D. Yu, L. Wang, K. Wang, H. Wang, and S. Y. He, "Typhoon triggered operation tunnel debris flow disaster in coastal areas of SE China," *Geomatics, Natural Hazards and Risk*, vol. 10, no. 1, pp. 562–575, 2019, in press.

[63] Y. J. Zhang, X. Wang, Q. G. Liang, D. J. Jiang, and X. N. Ma, "Development of model test similar material of collapsible loess," *Chinese Journal of Rock Mechanics and Engineering*, vol. 32, no. 2, pp. 4019–4024, 2013.

[64] Z. Zhang, X. Shi, B. Wang, and H. Li, "Stability of NATM tunnel faces in soft surrounding rocks," *Computers and Geotechnics*, vol. 96, pp. 90–102, 2018.

[65] Y. Li, Y. Yang, H.-S. Yu, and G. Roberts, "Principal stress rotation under bidirectional simple shear loadings," *KSCE Journal of Civil Engineering*, vol. 22, no. 5, pp. 1651–1660, 2018.

[66] J. Wang, Z. Song, B. Zhao, X. Liu, J. Liu, and J. Lai, "A study on the mechanical behavior and statistical damage constitutive model of sandstone," *Arabian Journal for Science and Engineering*, vol. 43, no. 10, pp. 5179–5192, 2018.

[67] Y.-Q. Wang, Z.-F. Wang, and W.-C. Cheng, "A review on land subsidence caused by groundwater withdrawal in Xi'an, China," *Bulletin of Engineering Geology and the Environment*, pp. 1–13, 2018.

[68] ABAQUS, *Abaqus Scripting User's Manual, Version 6.10*, ABAQUS, Inc., Johnston, RI, USA, 2010.

[69] Y. Li, S. Xu, H. Liu, E. Ma, and L. Wang, "Displacement and stress characteristics of tunnel foundation in collapsible loess ground reinforced by jet grouting columns," *Advances in Civil Engineering*, vol. 2018, Article ID 2352174, 16 pages, 2018.

Research Article

Towards Automated Real-Time Detection and Location of Large-Scale Landslides through Seismic Waveform Back Projection

En-Jui Lee,[1] Wu-Yu Liao,[1] Guan-Wei Lin [1], Po Chen,[2] Dawei Mu,[3] and Ching-Weei Lin[1]

[1]*Department of Earth Sciences, National Cheng-Kung University, No. 1, University Rd., East Dist., Tainan City 70101, Taiwan*
[2]*Department of Geology and Geophysics, University of Wyoming, Dept. 3006, 1000 E University Ave, Laramie, WY 82071, USA*
[3]*San Diego Supercomputer Center, University of California, San Diego, 10100 Hopkins Drive, La Jolla, CA 92093, USA*

Correspondence should be addressed to Guan-Wei Lin; gwlin@mail.ncku.edu.tw

Rainfall-triggered landslides are one of the most deadly natural hazards in many regions. Seismic recordings have been used to examine source mechanisms and to develop monitoring systems of landslides. We present a semiautomatic algorithm for detecting and locating landslide events using both broadband and short-period recordings and have successfully applied our system to landslides in Taiwan. Compared to local earthquake recordings, the recordings of landslides usually show longer durations and lack distinctive P and S wave arrivals; therefore, the back projection method is adopted for the landslide detection and location. To identify the potential landslide events, the seismic recordings are band-passed from 1 to 3 Hz and the spectrum pattern in the time-frequency domain is used to distinguish landslides from other types of seismic sources based upon carefully selected empirical criteria. Satellite images before and after the detected and located landslide events are used for final confirmation. Our landslide detection and spatial-temporal location system could potentially benefit the establishment of rainfall-triggered landslide forecast models and provide more reliable constraints for physics-based landslide modeling. The accumulating seismic recordings of landslide events could be used as a training dataset for machine learning techniques, which will allow us to fully automate our system in the near future.

1. Introduction

Landslides and debris flows are one of serious hazards in Taiwan. Many events occurred by heavy rainfalls during rainy and typhoon seasons. The constant gravitational pull may cause downslope movement of large volumes of material. These mass movement events occur throughout the world, and under certain circumstances, some of them can produce catastrophic consequences. The general public may sometimes underestimate landslide hazards because many of the landslide events are not reported separately but are included with the descriptions of the events that have triggered them, such as volcanic eruptions, earthquakes, and major rainstorms. Globally, landslides are directly responsible for billions of dollars in damage and thousands of fatalities and injuries each year (e.g., [1]).

Situated at the boundary between the Philippine Sea Plate to the east and the Eurasian Plate to the west, Taiwan is a mountainous and seismically active region (e.g., [2]). About one-third of Taiwan's land area is covered by rugged mountainous topography. Temperature differences between the East Asian continent and the Pacific Ocean drive monsoonal flow that carries warm, moist air from the Indian Ocean and the Pacific Ocean and delivers periodic monsoon rains and several typhoons each year. The combination of rugged mountainous topography, abundant water, and frequent earthquakes makes Taiwan particularly susceptible to landslide hazards. The 2009 Typhoon Morakot produced

an accumulated rainfall of 2777 mm and triggered over 400 large-scale landslides involving over $100,000 \, m^2$ area throughout southern Taiwan, leaving nearly 700 fatalities and over \$4.7 billion USD in damage (e.g., [3]). It is therefore crucial to establish the capability to detect and locate hazardous landslides in (near) real-time in Taiwan for emergency response and hazard mitigation purposes.

For rainfall-induced landslides, surveillance photographs from aircrafts and/or optical remote-sensing satellites are not immediately available often due to extreme weather conditions. Previous studies have shown that the landslide can be represented as an equivalent shallow seismic source with either a nearly horizontal single-force mechanism or a horizontal thrust fault mechanism (e.g., [4–7]). These results suggest that it is possible to adapt seismic techniques for (near) real-time earthquake detection and epicenter location to detect and locate landslides rapidly.

However, such an adaptation is not straightforward. Complications arise from two major differences between the seismograms generated by a landslide and those generated by a typical tectonic earthquake. First, seismograms from landslides often lack clear arrivals of P and S body wave phases, which are key signatures for identifying and locating earthquakes in the majority of (near) real-time earthquake detection/location techniques. Second, seismograms generated by landslides are often highly complex and it is not yet clear what may constitute a robust waveform signature for distinguishing landslides from other seismic events.

It appears that landslides are capable of generating sufficient low-frequency energies that can be detected by broadband seismic stations located at large distances. Inversions of such long-period waveforms (0.02~0.05 Hz) allowed Lin et al. [8] to recover the locations and source mechanisms of 52 landslides and submarine slumps during the 2009 Typhoon Morakot. More recently, the near real-time "landquake" monitoring system of Chao et al. [9] is also based upon the inversion of low-frequency waveforms (0.02~0.05 Hz) in their detection module. However, automated detection and inversion algorithms based purely upon low-frequency waveforms have the risk of misidentifying medium-sized and large earthquakes, which can also generate significant low-frequency energies, such as landslides, and may miss some landslides that do not generate sufficient low-frequency energies.

Our semiautomated landslide detection and location system mainly relies upon seismic waveform data in the frequency range 1~3 Hz. We use low-frequency waveforms (e.g., in the 0.02~0.05 Hz band) mainly for the purpose of rejecting teleseismic events, which may have similar time-frequency spectrum as landslides in the 1~3 Hz band. This choice of the frequency band allows us to utilize waveforms not only from the broadband seismic network but also from the extensive short-period seismic network in Taiwan. The increased station density reduces station gaps and improves azimuthal coverage, which is often a crucial factor in reducing location uncertainties.

Because of the lack of clear P and S arrivals on landslide seismograms, in our automated location algorithm, we have adopted the back projection algorithm, originally developed for locating nonvolcanic tremors and glacial earthquakes, for locating landslides in Taiwan (e.g., [10, 11]). The travel times used in back projection are computed using 3D ray tracing in one of the latest 3D seismic velocity models of Taiwan. To improve the efficiency of our landslide location code, we compute all travel time data in advance and archive them on disk. The code for locating the landslide only needs to read the data from the disk without performing time-consuming ray-tracing calculations.

We have tested our automated system on past continuous seismic recordings from broadband and short-period seismic networks in Taiwan. Our semiautomated system correctly identified the majority of the landslide events and provided the locations with ~2 km uncertainty in less than 5 minutes of the event origin time. When applied to real-time continuous seismic recordings, our semiautomated system may help reduce the emergency response time in disastrous landslide events.

Furthermore, to understand the complex mechanisms of rainfall-triggered landslides, the knowledge from different disciplines, such as geology, hydrology, geomorphology, and soil sciences, need to be considered in the system. The initiation time and location of a landslide event are critical for understanding the threshold conditions of landslide occurrences. The landslide events determined based on seismic recordings provide accurate initiation times and reliable locations, and this type of information could benefit other rainfall-triggered landslide studies. For example, accurate rainfall-triggered landslide catalog and rainfall records could be very helpful in developing a more reliable rainfall-based landslide forecast model for hazard management and mitigation (e.g., [12–14]). In addition, accurate occurrence times of rainfall-triggered landslides could provide more reliable conditions (e.g., rainfall duration, rainfall intensity, and cumulative rainfall) for physics-based landslide modeling (e.g., [15, 16]).

2. Data and Landslide Waveform Characteristics

2.1. Seismic Networks in Taiwan. In Taiwan, the majority of previous seismic studies of landslides (e.g., [1–4]) have been using only waveform recordings from the Broadband Array in Taiwan for Seismology (BATS), which is operated by the Institute of Earth Sciences (IES) of Academia Sinica and the Central Weather Bureau (CWB) [2]. In addition to BATS, the CWB also operates a telemetered, digital, short-period seismic network (Figure 1) composed of 1 Hz Teledyne S13 seismometers [17]. For the frequency band used in this study (i.e., 1~3 Hz), waveforms recorded by the short-period network can also be utilized to improve landslide detection accuracy and to constrain landslide locations. By including the stations from the short-period network, in addition to the stations in the BATS, into our landslide detection/location system, we reduced the average interstation distance from over ~30 km to less than ~20 km (Figure 1).

A subset of the short-period stations is colocated with the broadband stations in the BATS. In Figure 2, we show the high waveform similarities within the frequency band
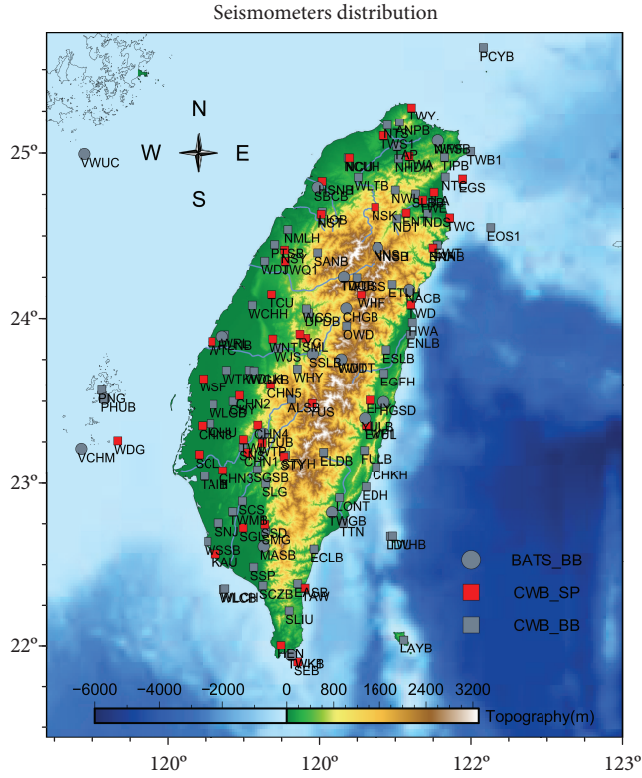
FIGURE 1: Distributions of broadband (gray symbols) and short-period (red squares) stations in Taiwan. The background color shows regional topography and bathymetry.

1~3 Hz of a typical landslide recorded by colocated broadband and short-period stations. Our back projection algorithm uses the envelopes of the 1~3 Hz waveforms. In Figure 2(f), we show that the envelope of the short-period recording within the 1~3 Hz frequency band is practically identical to that of the broadband recording in the same frequency band with a correlation coefficient larger than ~0.9. In our study, waveform recordings from both networks are utilized and, at those locations where broadband and short-period instruments are colocated, the waveform data from the broadband instruments take precedence.

2.2. Waveform Signature of the Landslide in the Time-Frequency Domain. Previous studies have shown that within the 1~3 Hz frequency band, waveforms of the landslide have a distinctive time-frequency domain signature that can be used to distinguish them from local tectonic earthquakes and teleseismic earthquakes (e.g., [9, 18–23]).

Figure 3 shows seismic waveform recordings of a landslide (Figure 3, left), a typical local earthquake (Figure 3, center), and a typical teleseismic event (Figure 3 right) recorded by Taiwan's seismic network. Compared to the local earthquake signal, the landslide signal lacks clear onsets of seismic body wave arrivals (i.e., P and S wave arrivals) and has a longer temporal duration. On the time-frequency spectrum, the landslide event shows a distinctive isosceles triangle or shield pattern (Figure 3 bottom left), which is substantially different from a right-angle triangle pattern (Figure 3, bottom center) typical for local earthquakes. The

comparison of time-frequency domain spectrums suggests that high-frequency energies generated by landslides arrive later and decay earlier within the duration of the signal than those generated by a typical local tectonic earthquake. This observation is consistent with results from previous studies, and we also use this observation to distinguish landslides from local earthquakes in our landslide detection algorithm.

However, the time-frequency domain spectrum patterns are not sufficient to distinguish teleseismic events from landslides. Certain portions of the teleseismic recording (Figure 3, bottom right) can show a similar time-frequency domain spectrum pattern within the 1~3 Hz frequency band as that of a typical landslide (Figure 3 bottom center). In our landslide detection algorithm, we use low-frequency waveforms (0.02~0.05 Hz) to distinguish teleseismic events from landslides. At such low frequencies, teleseismic recordings at different stations tend to have high waveform similarities and the differential travel time at neighboring stations tends to be very small. These low-frequency features of teleseismic events are mainly due to the high incidence angles of the incoming wave and can be used as additional criteria for rejecting teleseismic earthquakes.

3. Methods and Representative Examples

Conceptually, we can organize our landslide detection/location workflow sequentially into 5 different stages (Figure 4):

(i) Stage 1: waveform preprocessing

(ii) Stage 2: landslide event detections

(iii) Stage 3: inspection of preliminary landslide events

(iv) Stage 4: refine location of selected landslide events

(v) Stage 5: confirmation of landslide events based on satellite images

Currently, these 5 stages are carried out iteratively in a semiautomated process. In the following, we will discuss each stage separately.

3.1. Seismic Data Preprocessing. The main purpose of the data preprocessing stage is to enhance the waveform signature of landslides while suppressing contributions from local tectonic earthquakes and other unwanted seismic events. This stage has 5 separate steps, and all the steps were designed to facilitate the detection and location algorithms downstream in our flowchart (Figure 4).

First, we cut all continuous raw waveform recordings from both the broadband and the short-period seismic networks into 70-minute-long segments with 10-minute-long overlaps (Figure 5(a)). The choices of time segment length and overlap length are configurable and can be adjusted manually to optimize the overall performance of the entire system.

Second, we remove the mean and the linear trend of each time segment and then apply a minimal-phase Butterworth bandpass filter with corner frequencies at 1 and 3 Hz (Figure 5(b)).

(a) ELD broadband: raw

(b) ELD short-period: raw

(c) ELD broadband: 1~3 Hz

(d) ELD short-period: 1~3 Hz

--- BB envelope
— SP envelope

(e) ELD broadband: envelope

(f) ELD short-period: envelope
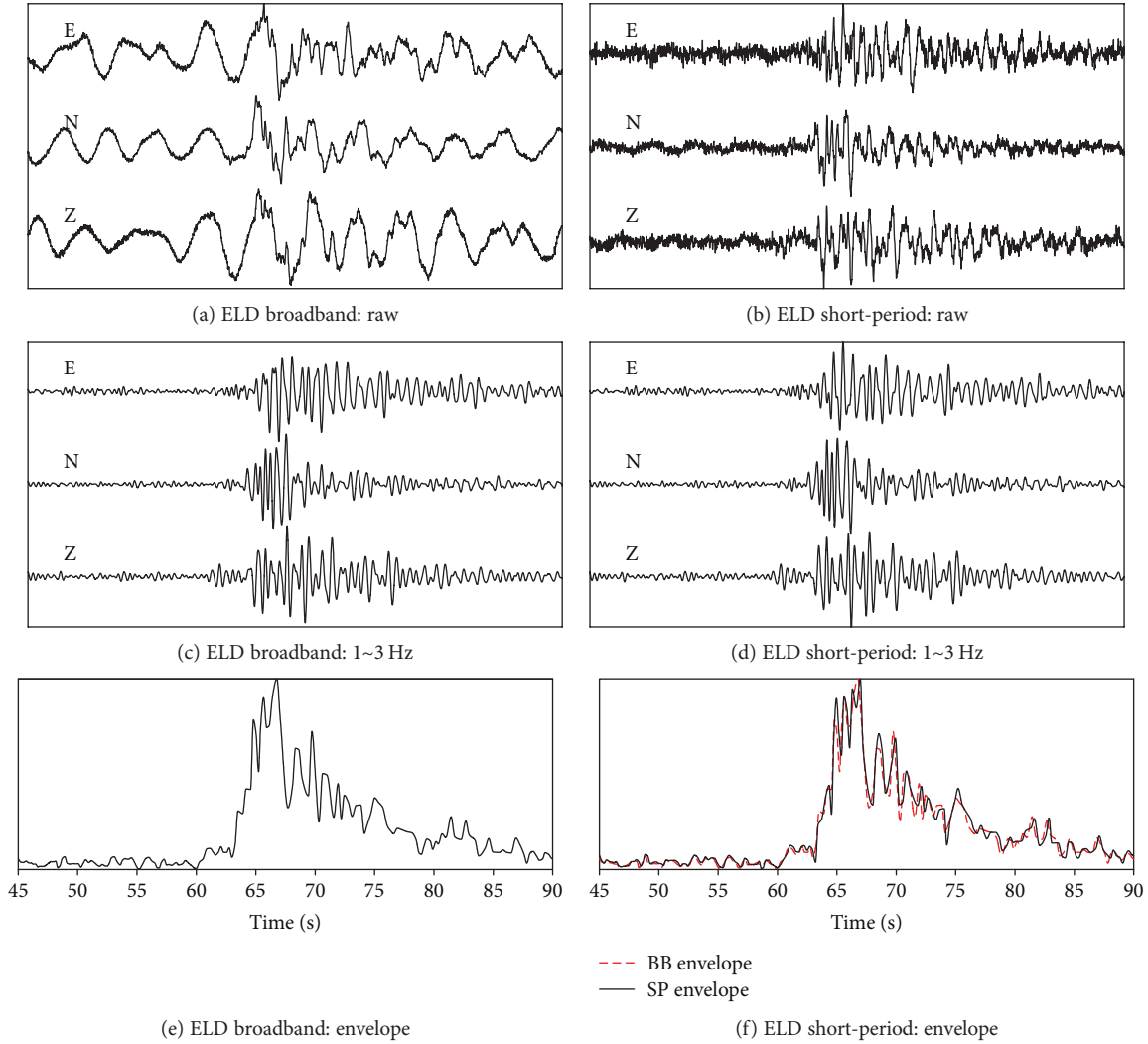
FIGURE 2: The three-component, east, north, vertical (Z), seismic recordings of a landslide event at the station ELD, where broadband (left) and short-period (right) instruments are colocated. (a, b) Raw waveform data and (c, d) bandpass-filtered (1~3 Hz) broadband and short-period waveforms. (e, f) The envelopes of bandpass-filtered broadband and short-period three-component root-mean-square waveforms (section 3.1).

Third, we calculate the root mean square (RMS) of three-component recordings ($\sqrt{u_E^2(t) + u_N^2(t) + u_Z^2(t)}$) for each station (Figure 5(c)). In general, the landslide signal has time durations longer than about 15 seconds. To suppress short-term fluctuations, we smooth the RMS by computing its moving average with a 10-second-long time window (Figure 5(d)).

Fourth, the smoothed RMS is normalized using a threshold value chosen specifically for each individual time segment. An example is shown in Figure 5(d), in which we can see clearly an event with the largest amplitude located at ~12 minutes, which is due to a local M_L 3.6 earthquake, and an event with a smaller amplitude located at ~57 minutes, which is due to a landslide. In this example, the threshold value is set at the 99th percentile of the entire time segment. Values above this threshold are clipped, and values below this threshold are normalized using the threshold value. Figure 5(d) shows the smoothed RMS after the threshold normalization (red line) in comparison with the one

before the threshold normalization (black line). The event associated with the landslide at ~57 minutes is enhanced, while the event associated with the local earthquake at ~12 minutes is suppressed. We have tried different threshold values for the normalization, and generally values between the 99th and 99.5th percentiles of the smoothed RMS amplitudes gave reasonable results for our landslide detection and location stages later on.

Finally, we compute the envelope of the time segment obtained from the fourth step through Hilbert transform and feed the result to the detection algorithm in the next stage.

3.2. Landslide Event Detection. The majority of conventional earthquake-location techniques mainly rely upon picking the onset time of body wave arrivals, such as P and S waves (e.g., [24]). The seismic recordings of landslides usually lack clear onset time of body wave phases (Figure 3), and their waveform characteristics resemble those of seismic tremors
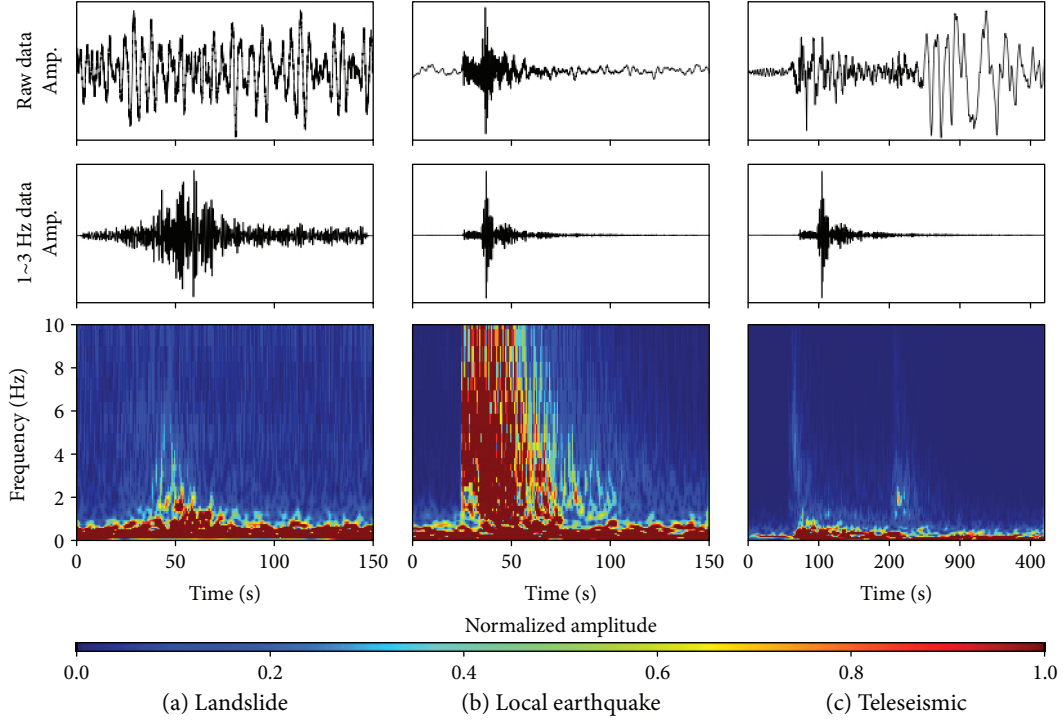
FIGURE 3: The raw recordings (upper row), 1~3 Hz bandpass-filtered waveforms (middle row), and time-frequency spectrum (bottom row) of a landslide (a), a typical local earthquake (b), and a typical teleseismic event (c). The color scale in the bottom row indicates the normalized amplitudes of the raw recordings.

(e.g., [19]). The back projection method for locating seismic sources does not rely upon precise picks of body wave onset times and has been successfully applied to locate tremors, as well as many different types of seismic sources (e.g., [19, 25–27]). In this study, we have adopted the back projection method to detect and locate landslides in Taiwan.

We back project a segment of the envelope function obtained at the end of stage 1 (section 3.1) and perform a weighted stack across multiple stations according to the following equation:

$$S(x, t) = \int_{\tau_0}^{\tau_1} \frac{\sum_{i=1}^{N} (W_i E_i \tau + t_i(x, t))}{\sum_{i=1}^{N} W_i} d\tau, \quad (1)$$

where E_i is the normalized envelop at station i; t_i is the model-predicted travel-time from a source located at x with origin time t to station i; $[\tau_0, \tau_1]$ is the time window containing the normalized and shifted envelopes used for stacking; W_i is the weighting factor for station i; and N is the total number of stations used in the back projection.

The name "back projection" comes from the temporal shift $t_i(x, t)$, which propagates the envelop function backwards in time from the station location to the space-time coordinate (x, t) of the potential source. If the seismic source is in fact located at x and occurred at time t, the normalized and shifted envelopes at different stations E_i will be systemically aligned and stack constructively, which would lead to a local maximum of the stacking function S at the source space-time coordinate (x, t); otherwise, they will

stack incoherently and will not produce a maximum. By detecting the emergence of such maxima, we can detect the occurrences and estimate the locations of landslides and other seismic events.

In the landslide detection stage, we use a spatial grid with 3 km grid spacing that covers the surface topography of Taiwan at elevations higher than 10 m above the sea level. Previous studies have suggested that the dominant seismic energies generated by landslides are primarily Rayleigh waves and/or shear waves (e.g., [9, 18–23]). We therefore calculated and archived the S wave travel times from each spatial grid point to all stations in BATS and the short-period network using one of the latest 3D seismic velocity models of Taiwan [28]. Currently we use the 3D ray tracing software, simulPS12 [29], for travel time calculations. Surface waves usually arrive slightly later than S waves; we therefore multiply the model-predicted S wave travel times by 1.08 to obtain estimates of surface wave travel times for the shifting operation.

Seismic signals generated by landslides usually have longer duration than local tectonic earthquakes. Increasing the length of the time window $[\tau_0, \tau_1]$ used in the stacking operation can potentially suppress contributions from unwanted local tectonic earthquakes. We have tried various time window lengths, and in general, a length of about 20 seconds provides reasonable estimates of landslide sources.

For (near) real-time applications, the processing speed of the detection stage is critically important. To accelerate the process of detection and location and to reduce the computational cost, currently we only use the 10~20
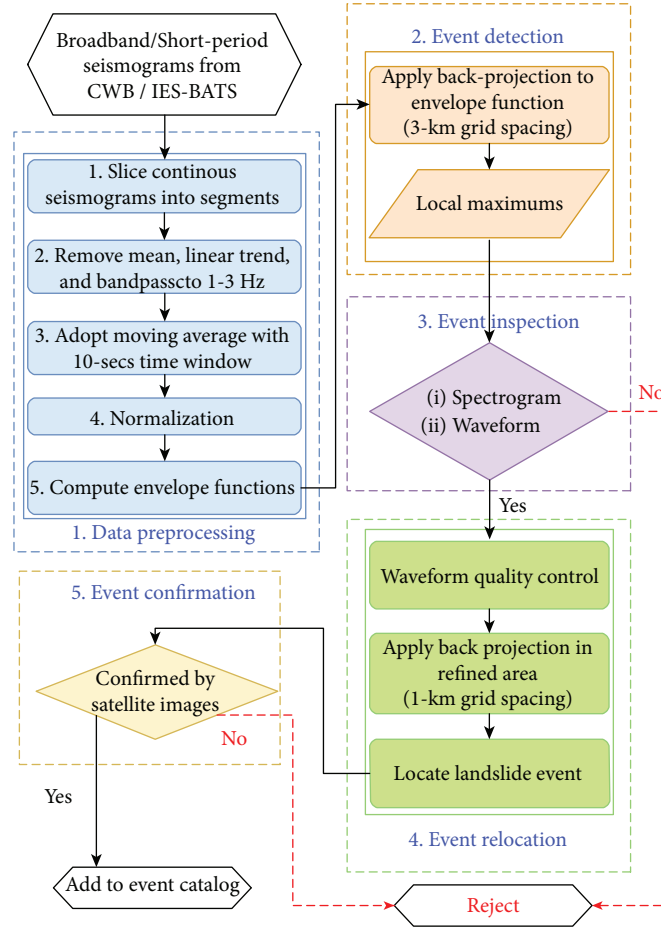
FIGURE 4: A flowchart of our landslide detection/location system. The five major components of the system are marked with colored dash boxes.

stations closest to each potential source grid point for back projection and stacking. Seismic recordings from all available broadband and short-period stations are examined during the landslide inspection and relocation stage (section 3.3 and 3.4).

At the detection stage, we assign the same weighting factor W_i to the envelope function of each selected station. The local maxima in the stacking function S indicate potential landslide events (Figures 5(e) and 5(f)). In this study, we select the local maxima with values larger than 6 times the median absolute deviation (MAD) of the stacking function as the space-time coordinates of potential landslide events. The detection criteria could be adjusted based on the researchers' actual applications.

3.3. Landslide Event Inspection. In general, due to their short temporal durations, we can effectively reject the majority of small local tectonic earthquakes ($M_L < 2.5$) during stage 2. The primary purpose of stage 3 is to reject any local earthquakes that we failed to reject during stage 2 and any teleseismic events with substantial energy in the 1~3 Hz frequency band.

For every event detected in stage 2, we cut the seismic waveform recordings from 30 s before the origin time to 180 s after the origin time at all available broadband and short-period stations. The selected waveform data are then converted into the time-frequency domain through continuous wavelet transform, and we check the patterns of the time-frequency spectrum. As shown in Figure 3, seismograms generated by landslides usually show an isosceles triangle or shield spectrum pattern in the time-frequency domain, while the spectrums of local earthquakes often show a right-angle triangle pattern. We use this criterion to reject any remaining local earthquakes from the set of events detected during stage 2.

Teleseismic events are rejected based upon a different criterion, since their time-frequency spectrum may have similar patterns as those of landslides in the 1~3 Hz frequency band. Seismograms from teleseismic events usually contain significant low-frequency energies, and the waveforms have very high similarities among the stations. We apply a Butterworth bandpass filter with corner frequencies at 0.02 and 0.05 Hz to the broadband recordings. For waveforms with a signal-to-noise ratio larger than 5, we then calculate the waveform correlation coefficients among station pairs and also the differential delay times. If the average of the correlation coefficients is higher than a given threshold (e.g., 0.8 in our current implementation)
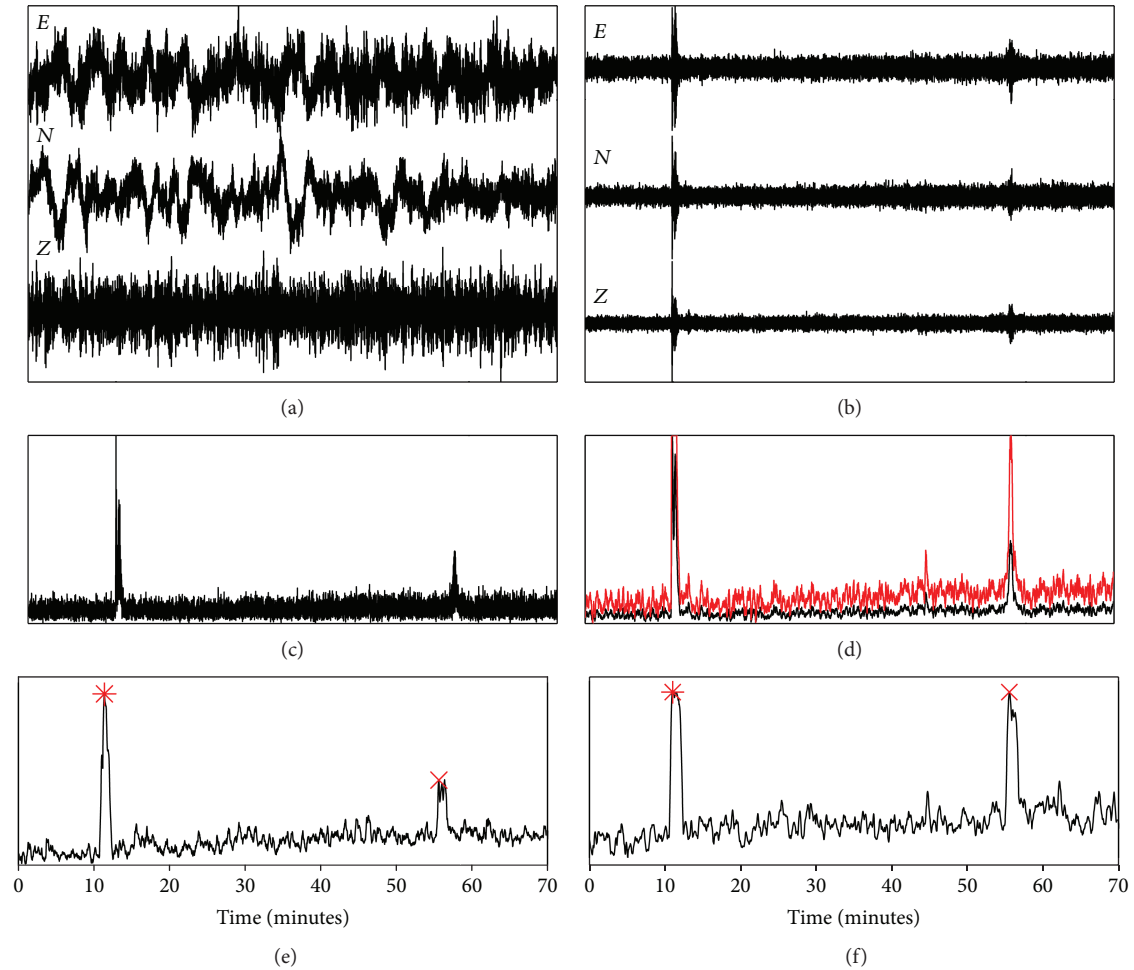
FIGURE 5: An example of the seismic data preprocessing (section 3.1) and the landslide detection (section 3.2) stages. (a) 3-component raw recordings are cut into 70-minute-long segments with 10-minute-long overlaps. (b) Waveforms bandpassed between 1 to 3 Hz. (c) The root mean square (RMS) of three-component bandpass-filtered waveforms. (d) Envelopes obtained by normalizing using the maximum (black line) and by normalizing using the value at the 99th percentile (red line). (e) The stacking function obtained from envelopes normalized by the maximum. (f) The stacking function obtained from envelopes normalized by the value at the 99th percentile. Stars: a local earthquake (M_L 3.6). Crosses: a landslide event detected by our algorithm.

and the differential delay times between station pairs are much smaller than the expected travel times for the S wave, we reject the event.

An example is shown in Figure 6. During the 2015 Typhoon Soudelor, one event detected during stage 2 has landslide-like waveforms at the high-frequency band (1~3 Hz), but it was rejected in stage 3 based upon our teleseismic rejection criteria. The waveforms at the low-frequency band (0.02~0.05 Hz) show very high similarities (Figure 6(b)). The differential delay times between station pairs are much smaller than the corresponding travel times of S arrivals. For example, the model-predicted S travel time differences from the detected source location are 39.88 s for MASB and SSLB, 26.32 s for SSLB and YHNB, and 26.99 s for MASB and YULB. But the differential delay times for the above station pairs are only 3.75 s, 1.25 s, and 0.75 s, respectively. The significant variations in time differences among the station pairs indicate that the low-frequency energies were generated by a teleseismic event,

which was verified by the 1000-second long low-frequency recordings (Figure 6(c)).

3.4. Landslide Event Relocation and Magnitude Estimates. All the events that have survived stage 3 are then relocated at stage 4. At this relocation stage, the seismic recordings are selected based upon a more stringent signal-to-noise ratio (SNR) criterion and the source location search is performed on a refined grid surrounding the preliminary location obtained from stage 2.

Figure 7 shows examples of the relocation stage for landslide events during the 2012 Typhoon Saola and the 2015 Typhoon Soudelor periods. The inputs at this stage are the envelopes of the 3-component RMS of 1~3 Hz bandpass-filtered broadband and short-period recordings (Figures 7(a) and 7(b), right). Different from stage 2, each envelope is normalized by the maximum amplitude at the station. For each envelope, we select a time window from 5 s before the model-predicted S arrival time to 25 s after

(a) 2015-08-10T10:12:00 1~3 Hz

(b) 2015-08-10T10:12:00 0.02~0.05 Hz

(c) 2015-08-10T10:12:00 0.02~0.05 Hz
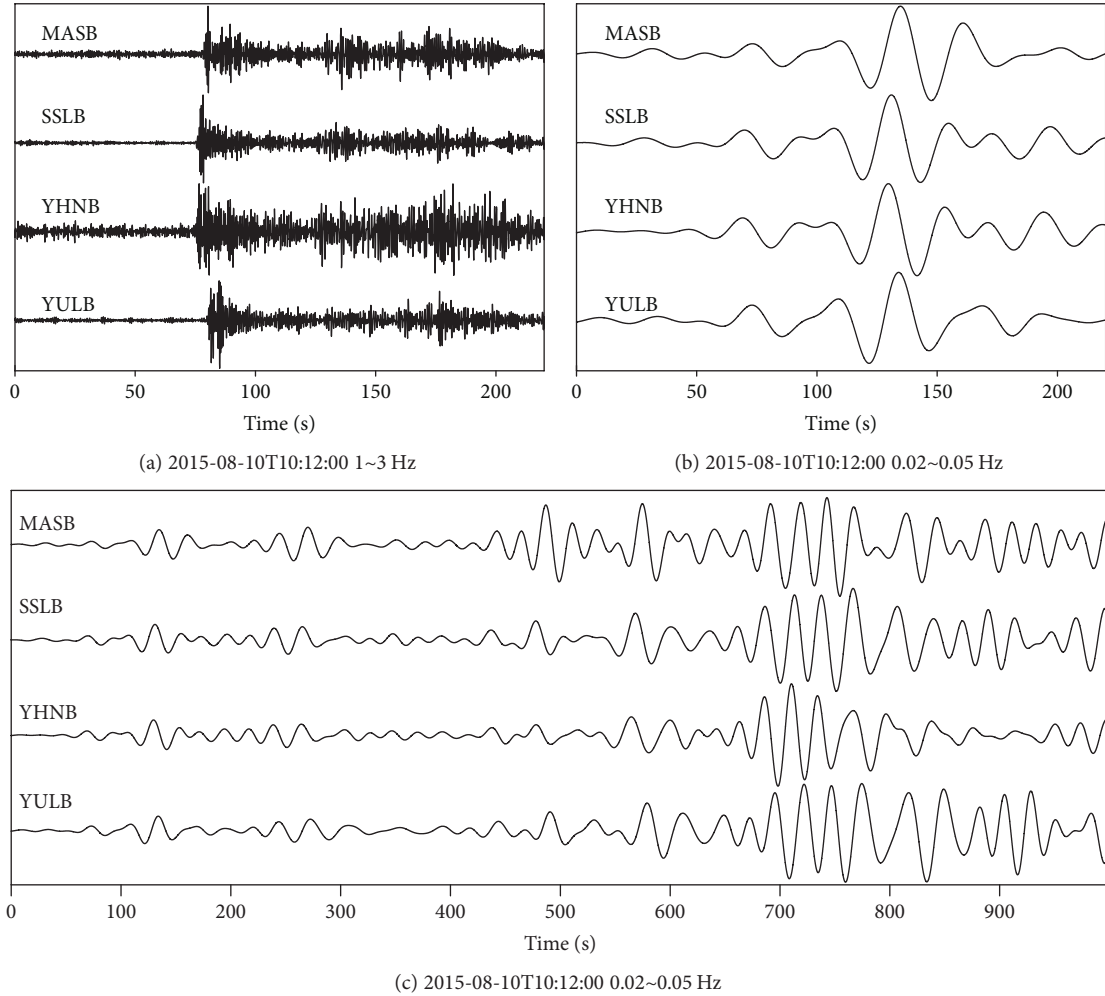
FIGURE 6: The vertical component broadband seismograms of a teleseismic event during the 2015 Typhoon Soudelor period. (a) The 220 s-long waveforms bandpass-filtered between 1 and 3 Hz and (b) the 220 s-long waveforms bandpass-filtered from 0.02 to 0.05 Hz. (c) The extended 1000 s-long waveforms bandpass-filtered from 0.02 to 0.05 Hz, which confirm that these seismograms were generated by a teleseismic event.

the model-predicted S arrival time based upon the preliminary source location obtained from stage 2. The SNR is then computed as the ratio between the mean of the envelope amplitudes within the time window and the mean of the amplitudes of the entire envelope. The envelopes with SNR larger than 1.5 are then used for back projection and for computing the stacking function. Examples of selected qualified envelopes are shown in Figures 7(a) and 7(b) (right).

At this stage, we search for the optimal source location on a 60 km wide square grid with 1 km grid spacing and centered at the location obtained from stage 2 (Figures 7(a) and 7(b), left). We use the SNR of each envelope as the weighting factor, W_i, and the length of stacking time window $[\tau_0, \tau_1]$ is 5 s long. The maximum of the stacking function over the refined grid gives the estimated landslide location of stage 4 (Figures 7(a) and 7(b), left).

The amplitudes of recorded ground motions could be used to quantify the energy released by sources. Similar concepts have been applied to landslide magnitude estimate in previous studies [19, 30]. For example, Lin et al. [30] use

the long-period signals (20–50 s) of large landslides occurred during 2009 Typhoon Morakot to define an empirical equation for landslide magnitudes. Kao et al. [19] used the maximum amplitudes from the recordings for magnitude estimates. In this study, we adopted the definition of local magnitude for earthquakes in Taiwan area [31] to estimate the magnitude of a detected landslide. In the local magnitude formula, the distances from the event are based on our refined landslide location to individual stations. The magnitudes of the landslides which occurred during 2012 Typhoon Saola and 2015 Typhoon Soudelor are $M_L = 1.6$ and $M_L = 2.0$, separately.

3.5. Landslide Event Confirmation. To confirm the landslides detected and located during stages 1–4, we manually check the satellite images before and after each typhoon event. If a significant landslide could be identified within 10 km of our estimated landslide location, we consider our detection and location system to be successful and then catalog the landslide event. If our system did not detect the landslide event
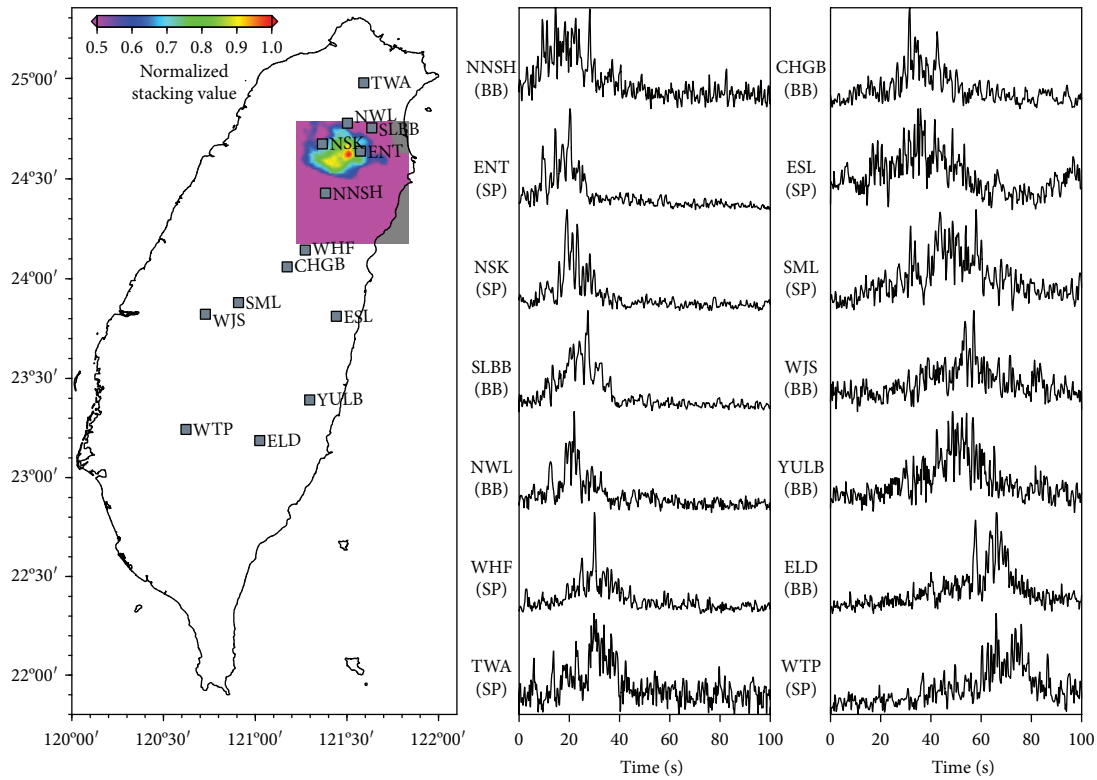
(a) 2012-08-01T18:40:28
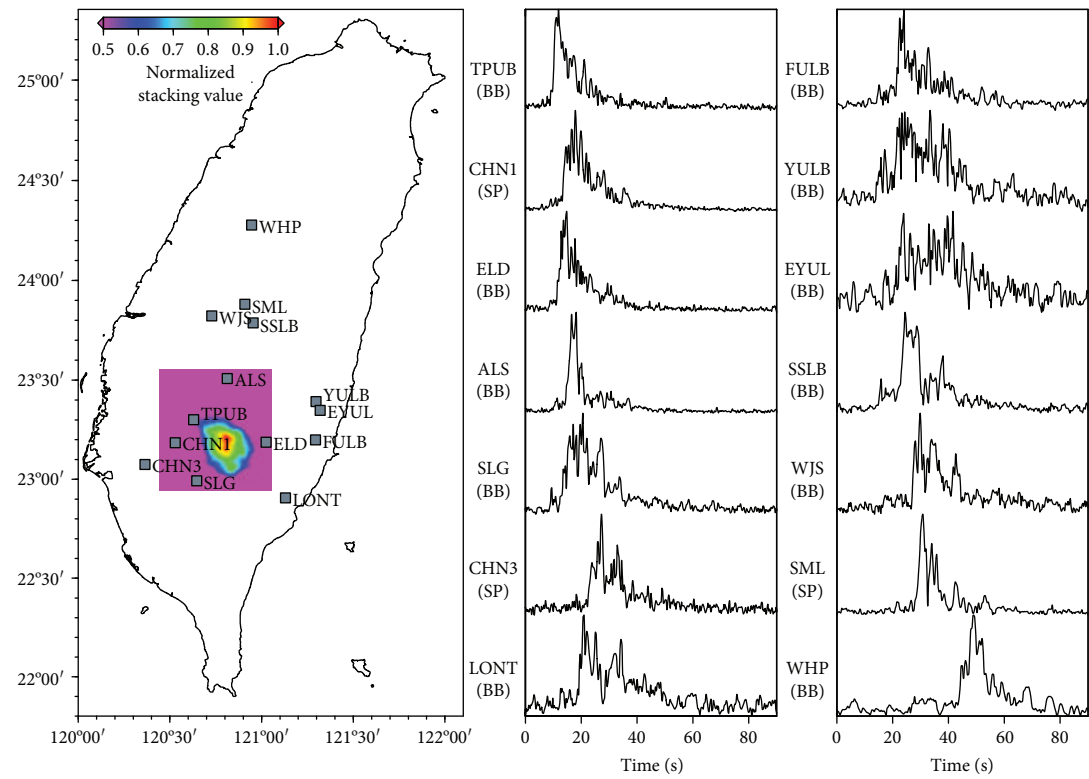
(b) 2015-08-08T19:00:47

FIGURE 7: Two examples of landslide relocation results during the 2012 Typhoon Saola (a) and the 2015 Typhoon Soudelor (b). The maps show the optimal locations determined by the back projection method. The 1~3 Hz RMS envelopes of broadband and short-period recordings used in the back projection are displayed on the right of each map.
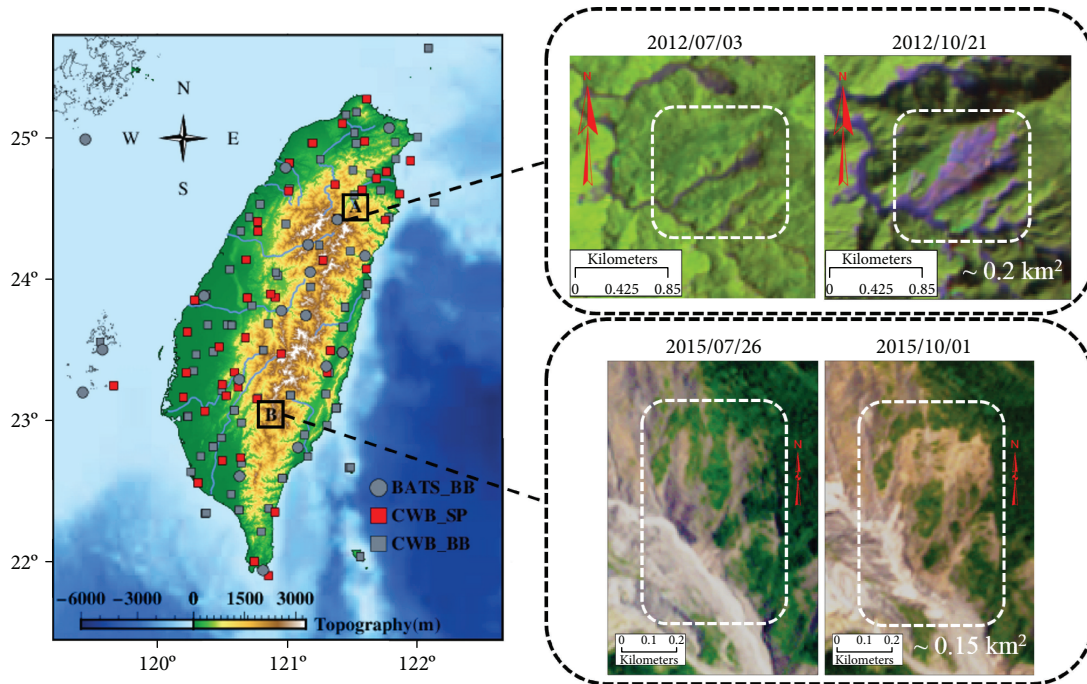
FIGURE 8: Prior/post landslide satellite images of the two landslide events during the 2012 Typhoon Saola and the 2015 Typhoon Soudelor. Locations of these two landslides determined using our seismic system are shown in Figure 7.

or our estimated location is more than 10 km away from the actual location, we consider this case as a failure. Figure 8 shows the satellite images of two landslide events detected and located by our system (Figure 7) during the 2012 Typhoon Saola and the 2015 Typhoon Soudelor periods. The 2012 landslide event is located by our system at 121.51°E, 24.62°N. The location of this landslide identified from the satellite images is around 121.57°E, 24.57°N. The location difference is about 8.6 km. For the 2015 landslide event, the optimal location estimated using our system is at 120.81°E, 23.21°N and the closest event identified from the satellite image is at around 120.78°E, 23.21°N. The location difference is about 3.3 km. Since the SNRs of the seismic waveforms generated by the 2012 landslide event are relatively low (Figure 7(a)), as compared with those from the 2015 event (Figure 7(b)), it is expected that the location error for the 2012 event is larger than that of the 2015 event.

4. Discussion

4.1. Comparison with Landslide Events Determined by Other Methods. We have applied our system to detect and locate landslides during several previous typhoon events, including the 2009 Typhoon Morakot. In previous studies [18, 19], only the broadband seismograms recorded by the BATS were used for landslide locations. We have included all available broadband and short-period seismograms from CWB's networks in our workflow. The landslide events listed in [18, 19] have all been successfully detected and located by our system. In addition to those landslide events, our system also identified a few more landslide events that were missed by previous studies. Figure 9 shows some additional landslide examples

detected by our algorithm and confirmed by satellite images. In general, locations determined by our system are consistent with those obtained from satellite images.

4.2. Other (Near) Real-Time Automated Landslide Detection/ Location Systems in Taiwan. At the current stage, the majority of previous landslide studies in Taiwan have not yet considered real-time automation in detail (e.g., [8, 18, 19]). The latest (near) real-time automated landslide detection/ location system proposed in [9] has a detection module that is based primarily upon low-frequency (0.02~0.05 Hz) seismic signals recorded by broadband instruments only. The landslide events detected by this system have been cataloged and archived at the website http://collab.cv.nctu.edu.tw/ catalog.html. A close examination of this catalog shows that, without human intervention, a considerable number of local earthquakes have been misclassified as landslides (i.e., false positive). Taiwan is a region with high seismicity, and the frequent medium-sized local earthquakes can generate considerable low-frequency energies. If the local earthquake has a shallow hypocenter and a low-angle thrust mechanism, there is a high probability of misidentifying such an earthquake as a landslide.

A second drawback of using only low-frequency signals for landslide detection is that there is a high possibility of missing landslides that do not generate sufficient low-frequency energies (i.e., false negative). In Figure 10, we show broadband recordings of two landslides, one during the 2012 Typhoon Saola (Figure 9, left) and the other during the 2015 Typhoon Soudelor (Figure 9, right). For both events, the waveforms at the 1~3 Hz frequency bands show significant energies and good SNR, but at the 0.02~0.05 Hz band, the
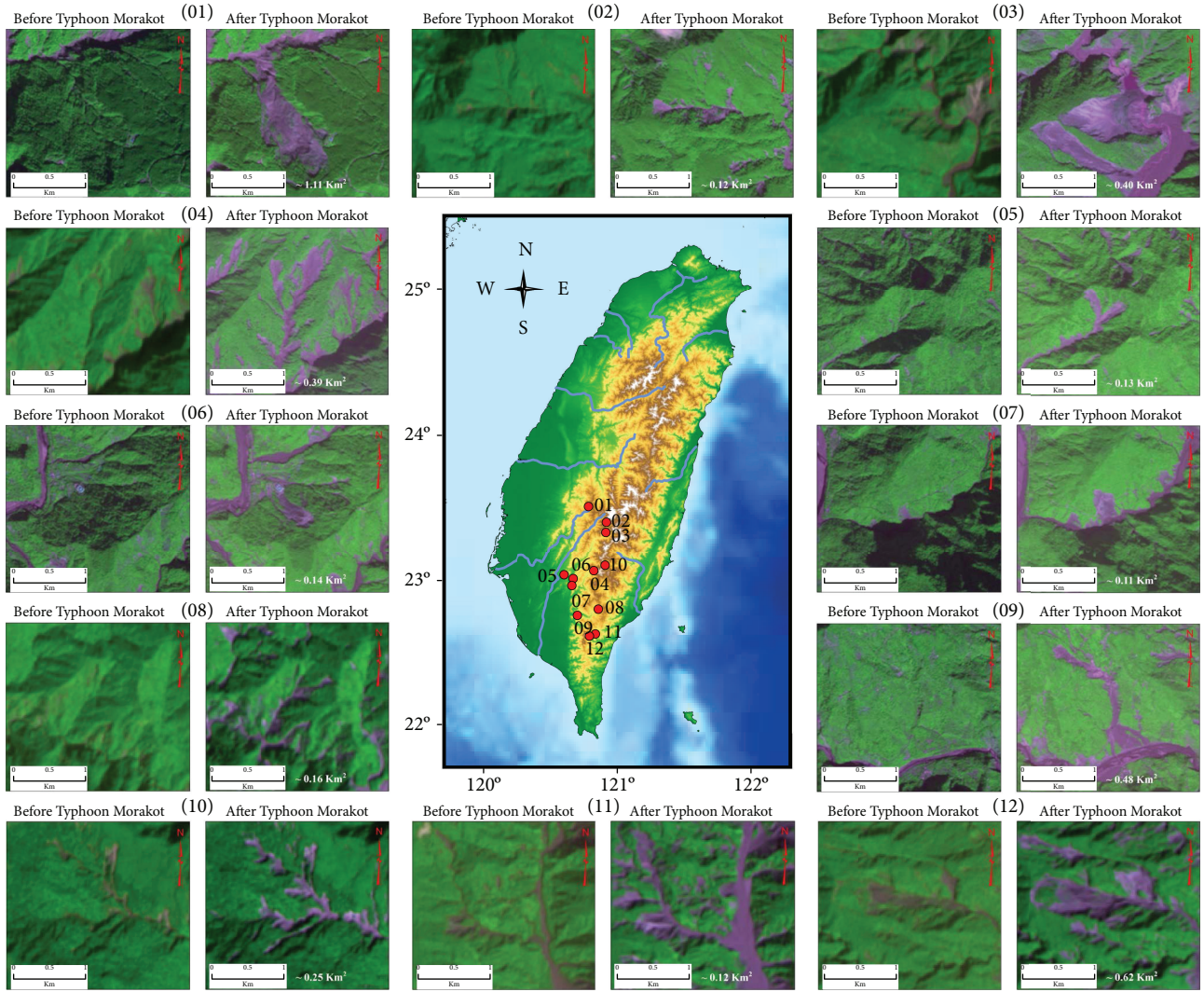
FIGURE 9: Examples of landslides that occurred during the 2009 Typhoon Morakot detected based upon our algorithm and confirmed by satellite images.

2012 landslide shows poor SNR. Our semiautomated landslide detection/location system is based primarily upon the broadband and short-period recordings in the 1~3 Hz brand.

4.3. Landslide Relocation Algorithms. In [9], the landslide relocation algorithm is based upon the cross-correlation of the horizontal envelope function at neighboring stations. Such a cross-correlation-based relocation algorithm has been successfully applied to relocate nonvolcanic tremors [32], whose seismograms usually lack clear body wave onsets just like the seismograms generated by landslides. However, we must point out that there are substantial differences between the source mechanisms of nonvolcanic tremors and those of typical landslides. For nonvolcanic tremors, weak sources with similar mechanisms occur in a short period of time (e.g. a few minutes) and the time intervals between significant energy bursts (e.g., *S* waves) at neighboring stations are almost identical. A direct consequence of such source mechanisms is that the envelope functions at neighboring stations have very high similarities (e.g., Figure 7 in [33]); therefore,

the cross-correlation lag times between stations can be treated as the differential *S* wave travel times for relocating tremors. The source mechanisms of landslides can be very different from those of nonvolcanic tremors, and the similarities of the envelope functions at neighboring stations are not as high, especially when taking into account the relatively larger station gaps of the broadband network in Taiwan. Examples of highly dissimilar envelope functions from a landslide are shown in Figure 7. Those fundamental differences in source mechanisms may increase the errors in the landslide locations obtained from the cross-correlation relocation algorithm.

5. Conclusions and Future Developments

We have developed a semiautomatic system for landslide detection and location using broadband and short-period seismic recordings, and we have successfully applied our system to landslides in Taiwan. The design of our algorithm takes into account the possibility that some landslides

(a) 2012-08-01T18:40:32

(b) 2015-08-08T19:00:00
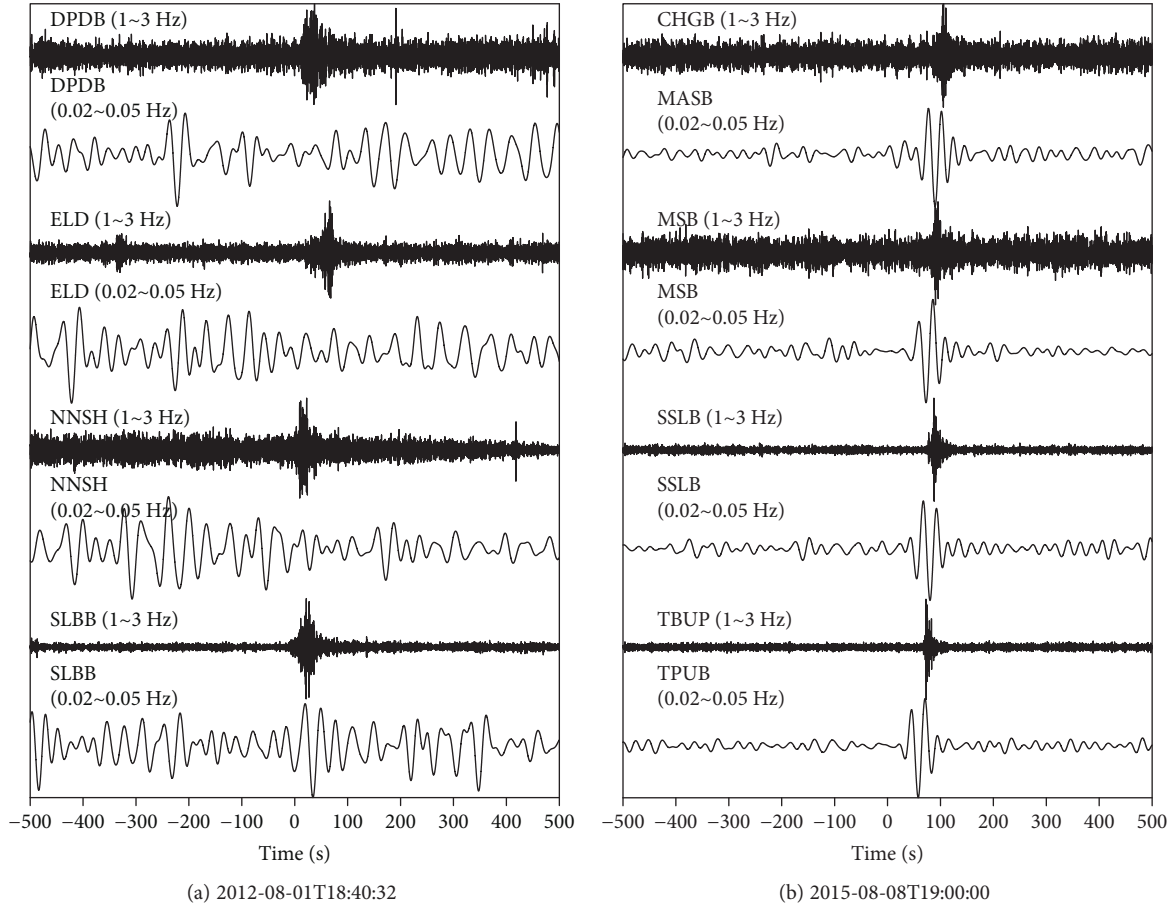
FIGURE 10: The vertical component broadband seismograms of the landslide events analyzed by our system during the 2012 Typhoon Saola (a) and the 2015 Typhoon Soudelor (b). The seismograms bandpass-filtered between 1 and 3 Hz show good SNR for both events, while those filtered between 0.02 and 0.05 Hz show good SNR for the 2015 event (b) and poor SNR for the 2012 event (a).

may not generate significant low-frequency energies, so we mainly use seismic recordings in the high-frequency band (1~3 Hz) for detection and location. To prevent earthquakes (local or teleseismic) from being classified as landslides, we have implemented rejection criteria based upon time-frequency domain spectrum patterns and low-frequency (0.02~0.05 Hz) interstation waveform correlations. The satellite images before and after the detected and located landslide events near the affected regions are used for landslide event confirmation.

Mass-movement hazards, such as landslides, are one of the most dangerous natural disasters in the world (e.g., [34]). Many countries, including Taiwan, suffer significant fatalities and damages from rainfall-triggered landslides each year during monsoon/typhoon seasons. Accurate estimates of occurrence times and locations of landslide events are playing an increasingly important role in improving our understanding of landslide initiation conditions, physics-based modeling, and developing forecast models. We expect our landslide detection/location system to make valuable contributions to the global efforts in landslide hazard analysis and mitigation.

Recent advances in deep neural networks (e.g., [35]) have opened up opportunities to fully automate our landslide detection/location system. Successes in image classification using deep convolutional neural networks (CNN) suggest that we can adopt CNN for distinguishing seismograms generated by landslides from those generated by earthquakes using time-frequency domain spectrograms automatically.

The grid search for finding optimal source locations and origin times can be accelerated, perhaps significantly, by adopting massively parallel coprocessors such as the graphic processing unit (GPU). The use of the GPU for accelerating the detection of small- to medium-sized earthquakes through cross-correlation-based template matching has been successfully implemented and tested [36]. Similar GPU acceleration techniques can also be adopted for landslide detection and location. We will leave those studies for future publications.

Data Availability

The waveform data used for this study are from the Geophysical Database Management System (GDMS) in Taiwan operated by the Central Weather Bureau (CWB) and the Broadband Array in Taiwan for Seismology (BATS) operated by the Institute of Earth Sciences, Academia Sinica (IES). The satellite images are provided by the Center for Space and Remote Sensing Research at the National Central University.

Conflicts of Interest

Acknowledgments

References

[1] International Fedaeration of Red Cross and Red Crescent Societies, *World Disasters Report 2003: Focus on Ethics in Aid*, International Federation of red Cross and red Crescent Societies, London, 1 edition, 2003.

[2] T.-C. Shin, C.-H. Chang, H.-C. Pu, H.-W. Lin, and P.-L. Leu, "The geophysical database management system in Taiwan," *Terrestrial, Atmospheric and Oceanic Sciences*, vol. 24, no. 1, p. 11, 2013.

[3] X. Ge, T. Li, S. Zhang, and M. Peng, "What causes the extremely heavy rainfall in Taiwan during typhoon Morakot (2009)?," *Atmospheric Science Letters*, vol. 11, pp. 46–50, 2010.

[4] H. Kanamori and J. W. Given, "Analysis of long-period seismic waves excited by the May 18, 1980, eruption of Mount St. Helens-a terrestrial monopole?," *Journal of Geophysical Research: Solid Earth*, vol. 87, no. B7, pp. 5422–5432, 1982.

[5] H. K. Eissler and H. Kanamori, "A single-force model for the 1975 Kalapana, Hawaii, earthquake," *Journal of Geophysical Research*, vol. 92, no. B6, pp. 4827–4836, 1987.

[6] F. A. Dahlen, "Single-force representation of shallow landslide sources," *Bulletin of the Seismological Society of America*, vol. 83, no. 1, pp. 130–143, 1993.

[7] E. E. Brodsky, E. Gordeev, and H. Kanamori, "Landslide basal friction as measured by seismic waves," *Geophysical Research Letters*, vol. 30, no. 24, 2003.

[8] C. H. Lin, H. Kumagai, M. Ando, and T. C. Shin, "Detection of landslides and submarine slumps using broadband seismic networks," *Geophysical Research Letters*, vol. 37, no. 22, 2010.

[9] W.-A. Chao, Y. M. Wu, L. Zhao et al., "A first near real-time seismology-based landquake monitoring system," *Scientific Reports*, vol. 7, no. 1, article 43510, 2017.

[10] C. S. Larmat, R. A. Guyer, and P. A. Johnson, "Time-reversal methods in geophysics," *Physics Today*, vol. 63, no. 8, pp. 31–35, 2010.

[11] H. Kao, P. J. Thompson, G. Rogers, H. Dragert, and G. Spence, "Automatic detection and characterization of seismic tremors in northern Cascadia," *Geophysical Research Letters*, vol. 34, no. 16, 2007.

[12] M. J. Crozier, "Prediction of rainfall-triggered landslides: a test of the antecedent water status model," *Earth Surface Processes and Landforms*, vol. 24, no. 9, pp. 825–833, 1999.

[13] F. Guzzetti, S. Peruccacci, M. Rossi, and C. P. Stark, "The rainfall intensity–duration control of shallow landslides and debris flows: an update," *Landslides*, vol. 5, no. 1, pp. 3–17, 2008.

[14] F. Guzzetti, S. Peruccacci, M. Rossi, and C. P. Stark, "Rainfall thresholds for the initiation of landslides in central and southern Europe," *Meteorology and Atmospheric Physics*, vol. 98, no. 3-4, pp. 239–267, 2007.

[15] R. M. Iverson, "Landslide triggering by rain infiltration," *Water Resources Research*, vol. 36, no. 7, pp. 1897–1910, 2000.

[16] T.-L. Tsai and J.-C. Yang, "Modeling of rainfall-triggered shallow landslide," *Environmental Geology*, vol. 50, no. 4, pp. 525–534, 2006.

[17] T. C. Shin, Y. B. Tsai, and Y. M. Wu, "Rapid response of large earthquakes in Taiwan using a real-time telemetered network of digital accelerographs," in *Eleventh World Conference on Earthquake Engineering*, pp. 1–8, Acapulco, Mexico, 1996.

[18] C.-H. Chen, W. A. Chao, Y. M. Wu et al., "A seismological study of landquakes using a real-time broad-band seismic network," *Geophysical Journal International*, vol. 194, no. 2, pp. 885–898, 2013.

[19] H. Kao, C. W. Kan, R. Y. Chen et al., "Locating, monitoring, and characterizing typhoon-linduced landslides with real-time seismic signals," *Landslides*, vol. 9, no. 4, pp. 557–563, 2012.

[20] E. Suriñach, I. Vilajosana, G. Khazaradze, B. Biescas, G. Furdada, and J. M. Vilaplana, "Seismic detection and characterization of landslides and other mass movements," *Natural Hazards and Earth System Science*, vol. 5, no. 6, pp. 791–798, 2005.

[21] A. Helmstetter and S. Garambois, "Seismic monitoring of Séchilienne rockslide (French Alps): analysis of seismic signals and their correlation with rainfalls," *Journal of Geophysical Research*, vol. 115, no. F3, 2010.

[22] F. Dammeier, J. R. Moore, F. Haslinger, and S. Loew, "Characterization of alpine rockslides using statistical analysis of seismic signals," *Journal of Geophysical Research*, vol. 116, no. F4, 2011.

[23] C. Hibert, A. Mangeney, G. Grandjean, and N. M. Shapiro, "Slope instabilities in Dolomieu crater, Réunion Island: from seismic signals to rockfall characteristics," *Journal of Geophysical Research*, vol. 116, no. F4, 2011.

[24] Y.-B. Tsai and H.-H. Wu, "A study of the errors in locating earthquakes due to the geometry of the taiwan seisimc network," *Terrestrial, Atmospheric and Oceanic Sciences*, vol. 8, no. 3, pp. 355–370, 1997.

[25] N. Langet, A. Maggi, A. Michelini, and F. Brenguier, "Continuous kurtosis-based migration for seismic event detection and location, with application to Piton de la Fournaise Volcano, La Reunion," *Bulletin of the Seismological Society of America*, vol. 104, no. 1, pp. 229–246, 2014.

[26] C. Larmat, J.-P. Montagner, M. Fink, Y. Capdeville, A. Tourin, and E. Clévédé, "Time-reversal imaging of seismic sources and application to the great Sumatra earthquake," *Geophysical Research Letters*, vol. 33, no. 19, article L19312, 2006.

[27] E. Kiser and M. Ishii, "Back-projection imaging of earthquakes," *Annual Review of Earth and Planetary Sciences*, vol. 45, no. 1, pp. 271–299, 2017.

[28] H.-H. Huang, Y. M. Wu, X. Song et al., "Joint Vp and Vs tomography of Taiwan: implications for subduction-collision orogeny," *Earth and Planetary Science Letters*, vol. 392, pp. 177–191, 2014.

[29] C. H. Thurber, "Earthquake locations and three-dimensional crustal structure in the Coyote Lake area, central California,"

Journal of Geophysical Research: Solid Earth, vol. 88, no. B10, pp. 8226–8236, 1983.

[30] C. H. Lin, J. C. Jan, H. C. Pu, Y. Tu, C. C. Chen, and Y. M. Wu, "Landslide seismic magnitude," *Earth and Planetary Science Letters*, vol. 429, pp. 122–127, 2015.

[31] T.-C. Shin, "The calculation of local magnitude from the simulated Wood-Anderson seismograms of the short-period seismograms in the Taiwan area," *Terrestrial, Atmospheric and Oceanic Sciences*, vol. 4, no. 2, pp. 155–170, 1993.

[32] A. G. Wech and K. C. Creager, "Automated detection and location of Cascadia tremor," *Geophysical Research Letters*, vol. 35, no. 20, 2008.

[33] S. Y. Schwartz, "4.15 - episodic aseismic slip at plate boundaries," *Treatise on Geophysics*, vol. 4, pp. 445–472, 2007.

[34] P. E. Bryant, *Natural Hazards, Updated Edition*, Cambridge University Press, Cambridge, 2005.

[35] I. Goodfellow, Y. Bengio, A. Courville, and Y. Bengio, *Deep Learning, vol. 1*, MIT Press Cambridge, 2016.

[36] D. Mu, E.-J. Lee, and P. Chen, "Rapid earthquake detection through GPU-based template matching," *Computers & Geosciences*, vol. 109, pp. 305–314, 2017.

Research Article

Impact of an Extreme Typhoon Event on Subsequent Sediment Discharges and Rainfall-Driven Landslides in Affected Mountainous Regions of Taiwan

Ching Hung [iD],[1] Guan-Wei Lin [iD],[2] Hsien-Li Kuo,[2] Jia-Ming Zhang,[2] Chi-Wen Chen,[3] and Hongey Chen[3,4]

[1]Department of Civil Engineering, National Cheng Kung University, No. 1, University Road, Tainan City 70101, Taiwan
[2]Department of Earth Sciences, National Cheng Kung University, No. 1, University Road, Tainan City 70101, Taiwan
[3]National Science and Technology Center for Disaster Reduction, No. 200, Sec. 3, Beixin Road, Xindian District, New Taipei City, Taiwan
[4]Department of Geosciences, National Taiwan University, No. 1, Section 4, Roosevelt Road, Taipei 10617, Taiwan

Correspondence should be addressed to Guan-Wei Lin; gwlin@mail.ncku.edu.tw

Fluctuations in the sediment yielding rate within mountainous areas are found after extreme precipitations. These changes are associated with rainfall-driven landslides and can be evaluated through observations of sediment transported in river water. In this study, we assess the differential impact level and duration of an extreme rainfall event caused by the 2009 Typhoon Morakot in Taiwan. Using a time series of suspended sediment data and landslide inventories within three affected catchments, our results found that the proportion of the typhoon-generated sediment discharges reached 58% of the 2009 annual sediment discharges, and the annual sediment discharges could be 15-fold higher than the average annual sediment discharges prior to the typhoon. The impact of the typhoon on suspended sediment discharge lasted for around four months. It is further revealed that a significant increase in the number of landslides was attributed to the impact of the extreme typhoon event, and the critical rainfall condition triggering landslides, based on the relationship between rainfall and landslide number and the rainfall intensity-duration thresholds, declined for 4–5 years.

1. Introduction

Located in the subtropical monsoon climate area in Asia, Taiwan encounters an average of four typhoons annually and is subjected to an average rainfall of approximately 2500 mm/yr [1]. In the wet seasons, such annual rainfall can induce numerous landslides in mountainous areas [2–4]. Because of generated landslides, fluctuations in the sediment yielding rate within mountainous areas can be perceived in Taiwan, especially after extreme precipitations given that sediments generated by landslides are largely transported to rivers [3, 5–10]. The above studies suggest that to better understand the role of extreme rainfalls on landslides and mitigate their social and environmental impacts, the issues

associated with rainfall-driven landslides and sediment transported in river could be investigated.

In 2009, within a short period of six days (6–11 August), Typhoon Morakot dropped more than 1500 mm of rainfall in the central and southwestern mountainous regions of Taiwan (Figure 1(a)) [11], which resulted in catastrophic landslides and flooding disasters [12]. This extreme event caused more than 700 fatalities, destroyed hundreds of houses, and left thousands of people homeless. It is important to note that a large amount of soil and rock was delivered into the rivers along with heavy rains, producing large amounts of suspended sediment; therefore, this extreme rainfall event provides a good opportunity to evaluate the differential impact level and duration of affected areas that could be

(a)

(b)

(c)
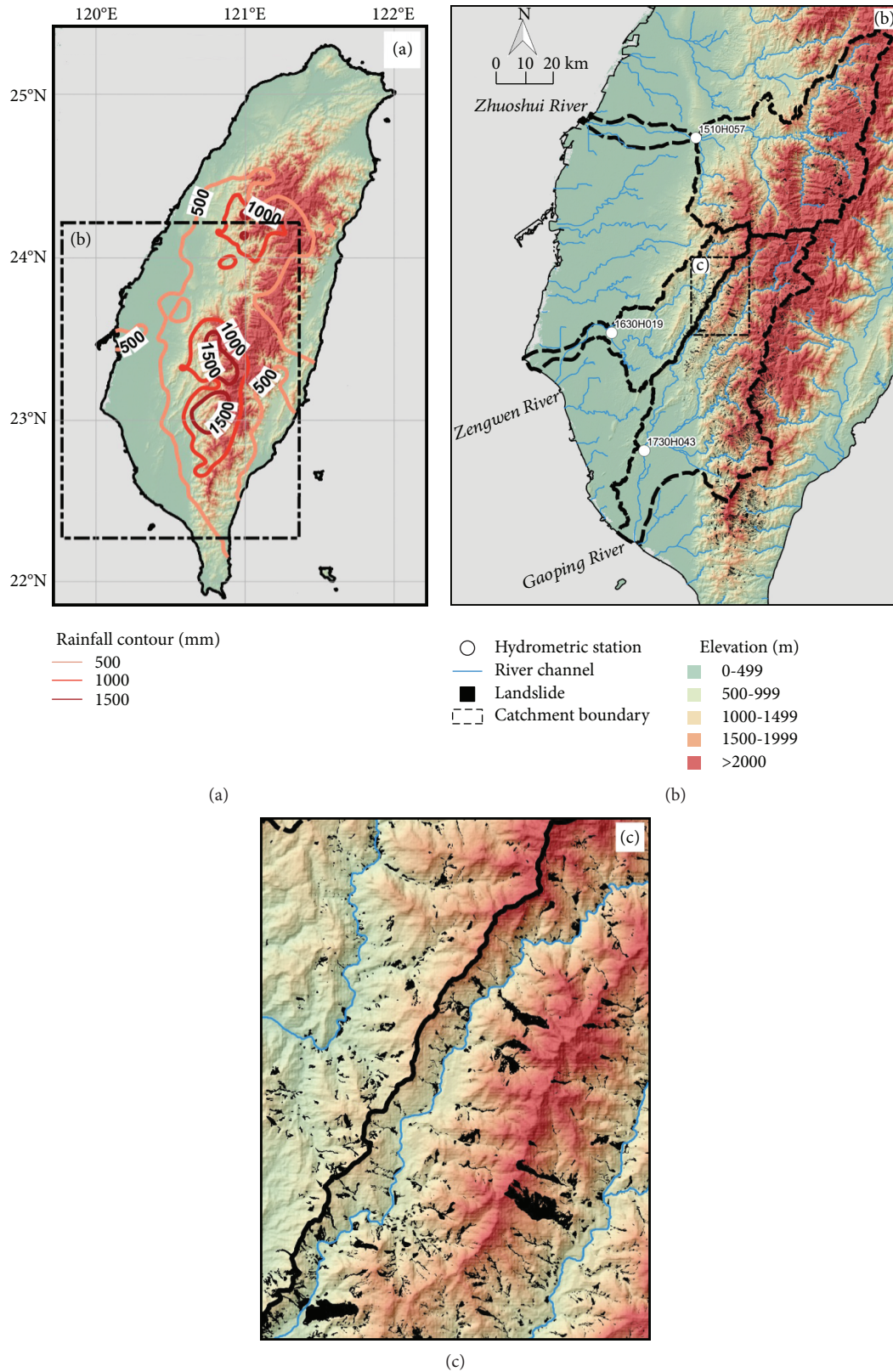
Figure 1: The rainfall and landslide distributions caused by Typhoon Morakot in 2009 and the 2009 annual suspended sediment discharges from the three rivers. (a) The contour lines represent the cumulative rainfall during the period from August 6 to 11, 2009. The numbers along the contour lines are the values of cumulative rainfall in mm. (b) The location of hydrometric stations and the boundaries of the three rivers. (c) Zoom-in view of landslide distribution around the boundary between the Zengwen River and the Gaoping River.

insightful for understanding the role of an extreme rainfall event on subsequent rainfall-driven landslides and sediment discharges.

In this study, we focused on the amount of suspended sediment discharge (SSD) and mapped landslides in three major river catchments in central and southwestern Taiwan, including the Zhuoshui River, the Zengwen River, and the Gaoping River, to assess the impact of an extreme rainfall event on the occurrence of rainfall-driven landslides and sediment discharges transported in rivers (Figure 1(b)). The total area of these three catchments is $7151\,km^2$, covering the major regions affected by heavy rainfall during Typhoon Morakot. The Zhuoshui River is the longest river in Taiwan, with a total length of $187\,km$ and a catchment area of $2906\,km^2$. The Gaoping River, the second longest river in Taiwan, has a total length of $171\,km$ and the largest catchment area in Taiwan, $3257\,km^2$. The Zengwen River is the fourth longest river in Taiwan, with a main stream length of $139\,km$ and a catchment area of $988\,km^2$; furthermore, the largest reservoir in Taiwan is located in the upstream area of this river.

2. Study Methods

2.1. Estimating Suspended Sediment Discharge (SSD). The sediment concentration data used in this study were mainly collected from the Water Resources Agency (WRA) of Taiwan. The WRA staff sampled river water two to three times a month at each river hydrometric station using a DH-48 full-depth sampler and measured sediment concentrations [13]. The measured hydrometric data for this study were selected from the Changyun Bridge (1510H057) on the Zhuoshui River, the Xingchung Bridge (1630H019) on the Zengwen River, and the Liling Bridge (1730H043) on the Gaoping River. The rating curve method was used to estimate the amount of SSD transported during the whole year and during typhoon periods.

The rating curve method is one of the most common estimation methods for SSD [14–18], especially in cases of insufficient hydrometric data. The method is based on a power law regression relationship between the measured water discharge Q (m^3/s) and the daily suspended sediment discharge Q_s (t). Furthermore, a $Q - Q_s$ equation can be used to estimate the amount of SSD through the measured water discharge (Figure 2). The $Q - Q_s$ equation is usually written in the form of $Q_s = \kappa Q^b$, where b is determined by the availability and mobilization of sediment and κ is the suspended sediment discharge at a unit discharge. Therefore, the rating curve method has an advantage in that only a small amount of measured sediment concentration data is required to estimate SSD. In general, the traditional rating curve method is suitable for estimating SSD in rivers within a transport-dominated environment [19], but its shortcomings are that the estimated SSD values are expected values and that there are residuals between the calculated and measured SSD values. Therefore, a modified rating curve method was developed by Kao et al. [17] to reduce the residuals. An error correction parameter used in the modified rating curve method is written as follows:

$$\beta = \frac{\sum_{i=1}^{n} \left(Q_{si} - \kappa Q_i^b \right)}{\sum_{i=1}^{n} \kappa Q_i^b}, \tag{1}$$

where Q_{si} is the ith measured daily SSD (ton) and Q_i is the ith measured water discharge (m^3/sec). In general, twenty to thirty SSD measurements and in situ measurements of daily water discharge are collected per year at each hydrometric station. Hence, a yearly modified rating curve can be written as follows:

$$\widehat{Q}_{sj} = \kappa Q_j^b (1 + \beta), \tag{2}$$

where $\widehat{Q}_{sj}$ is the calculated daily SSD (tons/day) and Q_j is the measured daily water discharge (m^3/sec) on the jth day. In the study, all yearly rating curves were demanded to have a coefficient of determination greater than 0.70. Once a modified rating curve is constructed for a given year, the annual SSD can be calculated by the following equations:

$$TSS = \frac{365}{n} \sum_{j=1}^{n} \left(\widehat{Q}_{sj} \right) \text{ for normal years}, \tag{3}$$

$$TSS = \frac{366}{n} \sum_{j=1}^{n} \left(\widehat{Q}_{sj} \right) \text{ for leap years}, \tag{4}$$

where TSS is the annual SSD (tons) and n is the number of measured daily water discharge data. In addition, the number of measurements of daily water discharge per year at each hydrometric station should be greater than 200 to make sure that the estimation of TSS is statistically convincing.

In this study, the daily water discharges measured at the three hydrometric stations were used to calculate the daily SSD using the modified $Q - Qs$ rating curve method. During the typhoon periods, $\widehat{Q}_{sj}$ accumulates in amount. The κ and b of the yearly rating curves obtained from the $Q - Qs$ equation mentioned earlier and the measured data of the three rivers are summarized in Tables S1, S2, and S3.

Given the fact that the largest reservoir in Taiwan only affects a tributary of the Zengwen River and its influence area is less than 50% of the entire catchment, the reservoir may not play a significant role in the $Q - Qs$ relationships at the downstream channels. In addition, the rapid accumulation of bedload in the reservoir area is mostly associated with the coarse sediment transport in the Zengwen River, suggesting that the influence of dam on the SSD could be minimized if it is based on the fine-grained sediment transport (i.e., suspended sediment discharge) [13, 20].

2.2. Landslide Mapping. To understand the extent and duration of the impact of Typhoon Morakot, catchment-scale landslide inventories across Taiwan were interpreted using SPOT-4 satellite remote sensing images with a spatial resolution of $10\,m$ in multispectral mode. Images with minimal cloud cover were selected from before and after the typhoon and heavy rainfall events. All images were orthorectified to a standard base image and checked manually using fixed visible markers to ensure spatial consistency over time. Given

(a) Zhuoshui River (1510H057)

(b) Zengwen River (1630H019)

(c) Gaoping River (1730H043)
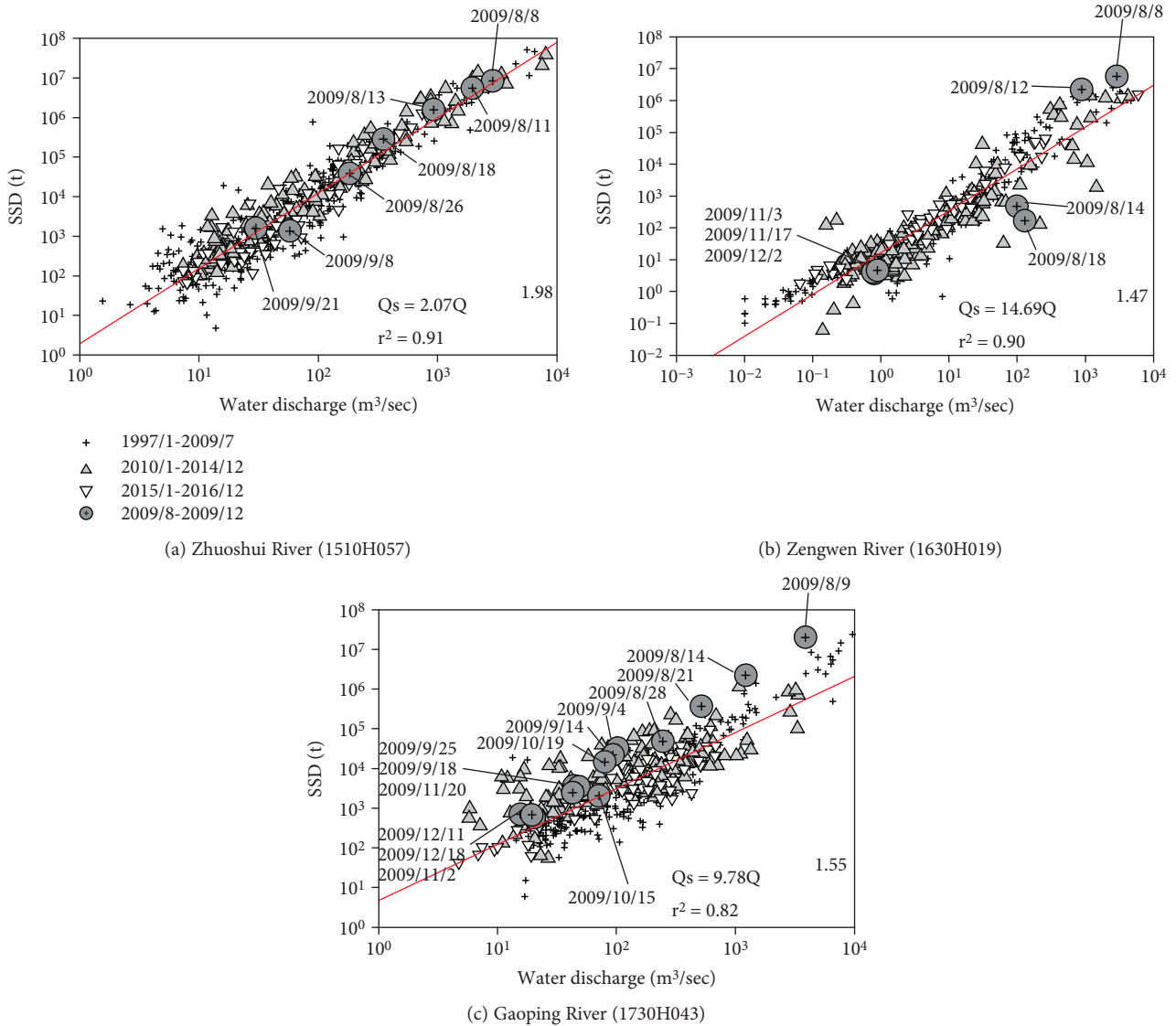
Figure 2: Relationship between suspended sediment discharge (Q_s) and water discharge (Q) for each river: (a) the Zhuoshui River, (b) the Zengwen River, and (c) the Gaoping River. The red lines represent the regression lines of all 1997–2016 data.

that a fully manual interpretation of landslides for wide catchments remains inefficient and impractical, the landslide mapping utilized an automated and preliminary interpretation procedure, which has been validated a priori against a subcatchment of the Zhuoshui River, rendering an accuracy of greater than 90%. Presented herein is a brief description of the procedure to determine the landslide inventory maps to form the basis for the presented results.

The normalized difference vegetation index (NDVI) was adopted to conduct a preliminary and supervised classification of bare areas [21]. The exact NDVI thresholds for bare areas differed from one image to another and were determined by tuning the cutoff value based on visible contrasts. Subsequently, the classified areas were clustered based on slopes using a digital elevation model (DEM) with a resolution of 40 m to identify bare areas not associated with landslides (e.g., slope of the source area less than 10°). The interpretation procedure, facilitated by the NDVI thresholds

and DEM-derived slope map, was implemented on the Arc-GIS software for the automated interpretation. The interpretation results were carefully compared with an official 1 : 5000 topographic map to exclude areas of interpretation misjudgment (e.g., roads and buildings). Compared to a manual landslide identification using aerial photography, the accuracy of the automated interpretation (NDVI and DEM-derived slope map) showed to be greater than 90% (Figure S1). The annual landslide distribution map for each catchment is the result after the erasure of landslides that occurred in the previous year. In this study, the landslide ratios were also quantified to characterize landslides [4, 5]. The landslide ratio is the ratio of the total landslide area to the total catchment area.

3. Results

3.1. Suspended Sediment Discharge before the 2009 Typhoon Morakot. The historical variations of SSD from the three

considered rivers were gained by the modified rating curve method. In the period of 1997–2008, the cumulative SSD transported through the Zhuoshui River was 1152 Mt and the cumulative water flux was $58.5 \times 10^9 \, m^3$ (Figure 3(a)). The Zhuoshui River produced the largest amount of SSD among the three rivers. The average annual SSD before the 2009 Typhoon Morakot in the Zhuoshui River was 96.0 Mt/yr, and the average sediment yield in the unit catchment area was 33,035 t/km^2/yr.

As a result of the extreme Mw 7.3 earthquake of September 21, 1999, which significantly affected the mountainous areas of Taiwan, more than 10,000 landslides occurred. Some studies have reported that SSD obviously increases after a heavy earthquake [6, 22–24], and so accordingly, the 1999 earthquake can be used to divide the long-term average SSDs into pre- and postearthquake SSDs.

The average cumulative rate of SSD in unit water volume in the Zhuoshui River was $4.8 \times 10^{-3} \, t/m^3$ before 1999 and $51.2 \times 10^{-3} \, t/m^3$ in the period of 1999–2001, which was the highest of the increased rate among the three rivers. The result indicates that the yield of sediment in the Zhuoshui River was obviously increased by the earthquake in 1999.

The Zengwen catchment is located a fair distance from the epicenter area of the 1999 earthquake and, consequently, the seismic waves weakened gradually. The annual SSD in the Zengwen River in the period of 1997–2008 ranged between 1.2 Mt/yr and 24.5 Mt/yr, with an average of 7.9 Mt/yr, and the average sediment yield in the unit catchment area per year was 8026 t/km^2/yr. In the period of 1997–2008, the cumulative SSD transported through the Zengwen River was 95 Mt and the cumulative water flux was $15.8 \times 10^9 \, m^3$ (Figure 3(b)). Consequently, in the period of 1997–2008, the average cumulative rate of SSD in unit water volume in the Zengwen River was $3.8 \times 10^{-3} \, t/m^3$.

The average annual SSD in the Gaoping River in the period of 1997–2008 was 38.9 Mt/yr, and the average sediment yield in the unit catchment area per year was 11,956 t/km^2/yr. The cumulative SSD transported through the river before 2009 was 266.3 Mt, and the cumulative water flux was $92 \times 10^9 \, m^3$ (Figure 3(c)). The average cumulative rate of SSD in unit water volume in the Gaoping River was $2.8 \times 10^{-3} \, t/m^3$.

3.2. SSD during Typhoon Morakot and the 2009 Annual Sediment Discharge.
During Typhoon Morakot, the SSD of 136.5 Mt was transported from the mountainous catchment of the Zhuoshui River, which comprised 91.4% of the annual SSD in 2009 and even reached 142.2% of the average annual SSD (Table 1). Furthermore, the cumulative rates of SSD in unit water volume of $42.7 \times 10^{-3} \, t/m^3$ in 2009 were 2.7-fold higher than the average in the period of 2001–2008. In the southwestern region, the Zengwen River produced an SSD of 50.7 Mt during Typhoon Morakot; its SSD value reached 58.3% of the 2009 annual SSD. The cumulative rate of SSD in unit water volume reached $30.3 \times 10^{-3} \, t/m^3$.

In addition, during Typhoon Morakot, the Gaoping River produced SSDs of 570 Mt (97.6% of the 2009 annual SSD), which exceeded the average annual SSDs of the river by 15-fold. Meanwhile, the 2009 cumulative rate of SSD in unit water volume in the river was $102.3 \times 10^{-3} \, t/m^3$. The 2009 cumulative rates of SSD in unit water volume increased 37 times. These facts strongly suggest that abundant sources of sediment significantly increase the SSD in rivers after a heavy typhoon.

The calculation of the 2009 annual SSDs showed that the Gaoping River produced the maximum annual SSD of 584.2 Mt, followed by the Zhuoshui River, with 149.3 Mt. The amount of sediment brought to the rivers due to huge mass movements on slopes after the typhoon raised the 2009 annual SSD to 15 times higher than the past annual averages.

3.3. Catchment-Scale Variations of Landslides.
Considering the differences in the catchment area between the three rivers, the influence of Typhoon Morakot on the different catchments is presented in terms of landslide ratio. The landslide ratio induced by Typhoon Morakot in the Zhuoshui River was not significantly higher than that in the past, and the ratios descended quickly after 2009 (Figure 4). The typhoon caused the largest scale mass movements in the Zengwen and Gaoping Rivers in the past decades. It is clear that landslide ratios in the three catchments were associated with differential impact levels.

The variation in the number of landslides during 2005–2016 in the Zengwen catchment is almost consistent with the changes in landslide ratios (Figure 5(a)). In the past 12 years, these results have indicated that the main types and sizes of mass movements in the Zengwen catchment changed within a narrow range, and it is clear that Typhoon Morakot was the rainstorm event that caused the most landslides. By comparing the amount of cumulative rainfall and landslide numbers during 2005–2008, we found that the number of landslides rose with increasing cumulative rainfall, but this state was changed after the typhoon. The extreme cumulative rainfall during the typhoons caused an abrupt increase in the number of landslides. After Typhoon Morakot, the intensity of rainfall brought by typhoons in the period of 2010–2014 was relatively moderate, but the number of landslides was not significantly reduced. Therefore, before and after Typhoon Morakot, the relationship between cumulative rainfall and landslide number seems to have exhibited different trends (Figure 5(b)). It is noteworthy that, in 2015 and 2016, the relationship between cumulative rainfall caused by typhoons and the number of landslides appeared to have returned to the state prior to Typhoon Morakot.

4. Discussion

The changes in observations of SSD reflected the impact of Typhoon Morakot on the annual SSD from the rivers in central and southwestern Taiwan. The extreme rainstorms during the typhoon not only induced a great deal of event-induced SSD but also affected the amount of SSD. The influences of Typhoon Morakot on sediment yields in each catchment were obviously different. The suspended sediment discharge measured in the period from August 7 to December 31 in 2009 was compared with all SSD data

(a) Zhuoshui River (1510H057)

(b) Zengwen River (1630H019)

(c) Gaoping River (1730H043)
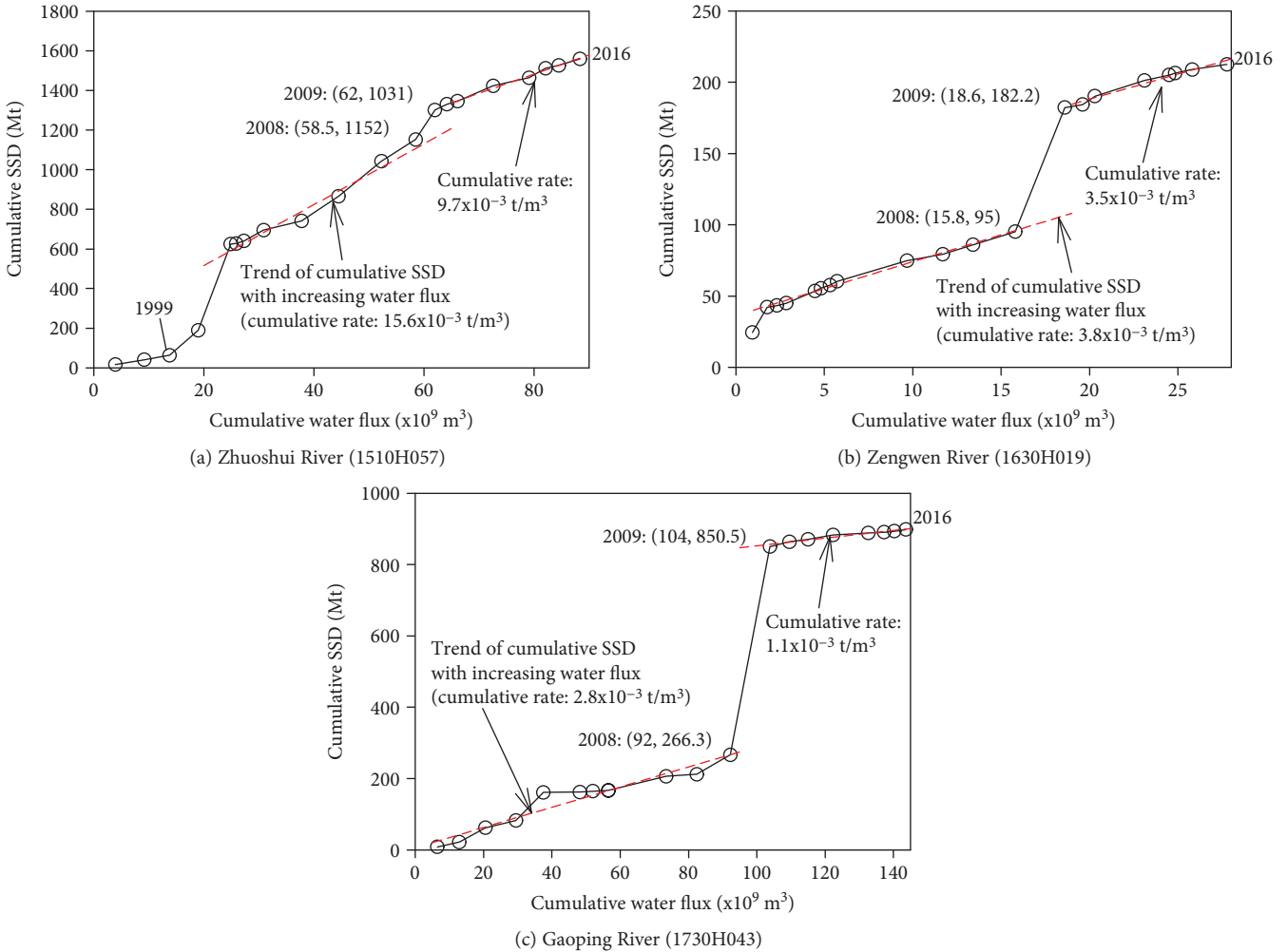
FIGURE 3: Cumulative water flux and SSD in (a) the Zhuoshui River, (b) the Zengwen River, and (c) the Gaoping River in the period from 1997 to 2016.

TABLE 1: Statistics of SSD in the three catchments.

Catchment	Area (km²)	SSD during Typhoon Mindulle (Mt)	2009 SSD (Mt)	Proportion of typhoon SSD to 2009 SSD (%)	1997–2008 average annual SSD (Mt)	2010–2015 average annual SSD (Mt)
Zhuoshui River	2906	136.5	149.3	91.4	96.0 ± 34.8	37.5 ± 9.6
Zengwen River	988	50.7	87.0	58.3	7.9 ± 2.1	4.4 ± 1.5
Gaoping River	3257	570.0	584.2	97.6	38.9 ± 16.3	7.2 ± 2.0

(Figure 2). The SSD in the Gaoping River increased most significantly. The comparison of the relationship between SSD and water discharge after the Typhoon Morakot with the relationship before the typhoon presents a different variation mode in the Zengwen River and Gaoping River. In contrast to the fact that the amount of SSD delivered from the Gaoping River increased significantly after the typhoon, the SSD greater than the historical mean in the Zengwen River was observed only when water discharge was greater than 100 m³/sec, and even measured SSD was greater than the historical maximum at the same water discharge. The maximum cumulative rainfall during Typhoon Morakot in the southwestern region exceeded 1500 mm; however, the maximum cumulative rainfall in the central region did not exceed 1500 mm (Figure 1), indicating that the cumulative rainfall decreased northward. The difference between the SSD after the Typhoon Morakot and historical data of the Zhuoshui River was insignificant, and this is explained by the fact that the influence of the typhoon gradually decreased northward.

The κ value of the $Q_s - Q$ rating curve, corresponding to the twenty-year data collected from the Zengwen River, is larger than that of the Zhuoshui River and the Gaoping River (Figure 2). A large part of the Zengwen River catchment is

(a) Zhuoshui River

(b) Zengwen River

(c) Gaoping River
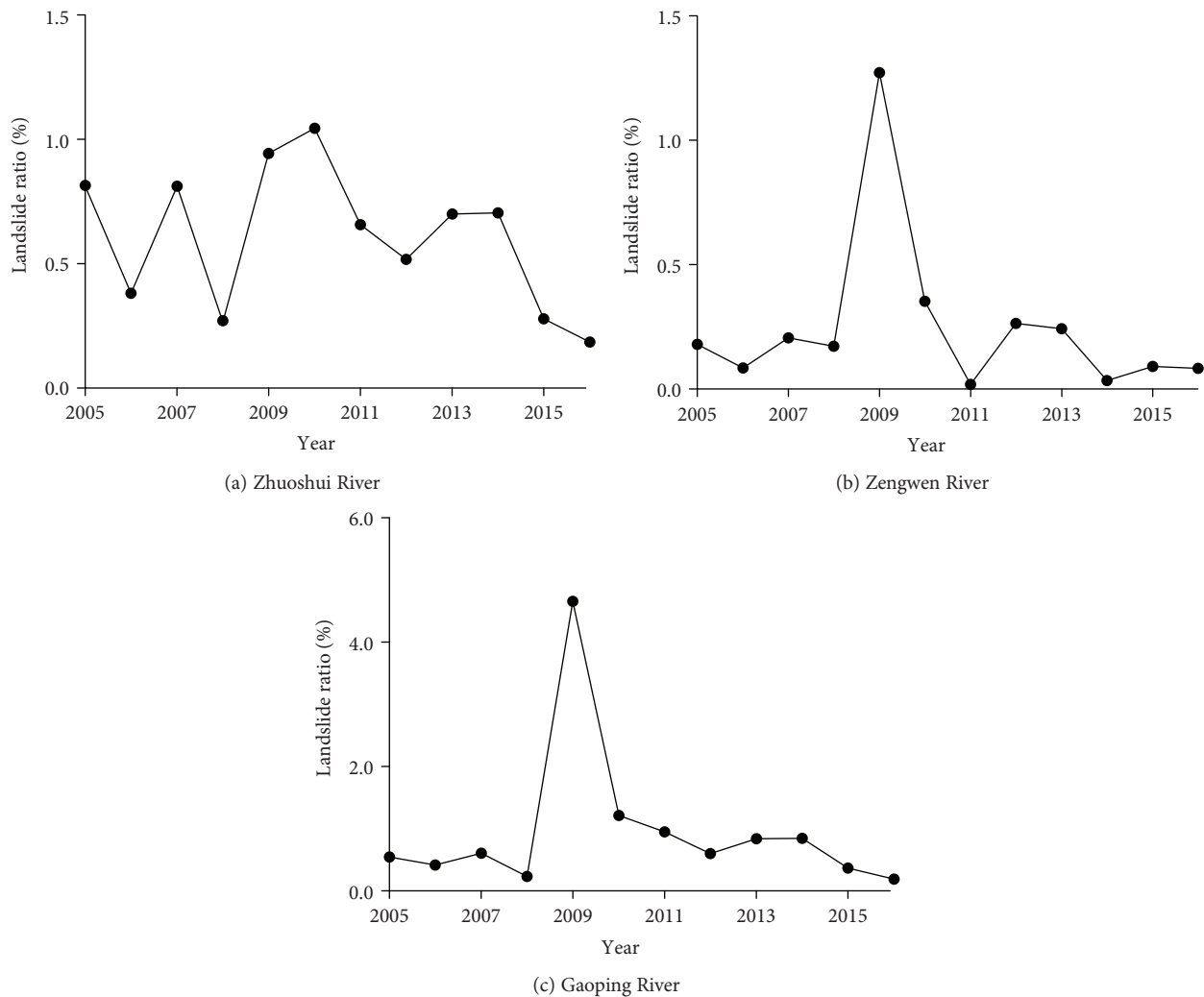
FIGURE 4: The variations of landslide ratios in the three catchments during 2005–2016.

occupied of young and poorly cemented mudstones [25–27]. The natural characteristics of the mudstones are sensitive to weathering and prone to rainfall-induced erosions, bringing abundant fine-grained sediments and relatively greater yielding rates of the SSD [28, 29]. The fine-grained sediments stemming from the mudstones also explained the milder decrements in the cumulative rate of the SSD in the Zengwen River (Figure 3). When water discharge was less than $100 \, \mathrm{m}^3/\mathrm{sec}$, the observed SSDs in the following four months (September to December) after the typhoon had unobvious difference from that SSDs observed prior to the typhoon. In addition, a huge amount of fine-grained sediment would be delivered downstream during the typhoon as well as the subsequent months, alleviating the cumulative rates of the SSD in the following years after the Typhoon Morakot. The variations of the cumulative rates of the SSD during 1997–2016 signify that the impact of an extreme rainstorm on fluvial fine-grain sediment could be violent; nevertheless, such impact may last for only a few months.

Although the landslide ratios appear to have rapidly declined after 2010, it should be noted that Taiwan's mountainous areas had relatively dry climatic conditions during 2010–2014. It is noteworthy that, in 2015 and 2016, the relationship between cumulative rainfall caused by typhoons and the number of landslides in the Zengwen River catchment appeared to have returned to the state prior to Typhoon Morakot. In terms of the changes in relationships between landslide and rainfall, a similar trait was established in catchments of the Gaoping and Zengwen Rivers, both showing that the influence of the typhoon could linger for 4–5 years; however, such trait could not be observed in the Zhuoshui River catchment (Figure 5). According to the results, the influence of the typhoon on landslides and SSD was quite different, in which, the former and the latter lasted 4–5 years and 4 months, respectively. The relatively longer recovery period on landslides could be attributed to the gradual process of landslide materials developing into fine-grained sediments, eventually becoming the sources of SSD.

The slight difference in landslide ratios for the relatively drier periods during 2010–2014 pointed out that rainfall conditions for triggering landslides could have changed after Typhoon Morakot. The Soil and Water Conservation Bureau of Taiwan investigated more than 321 landslides
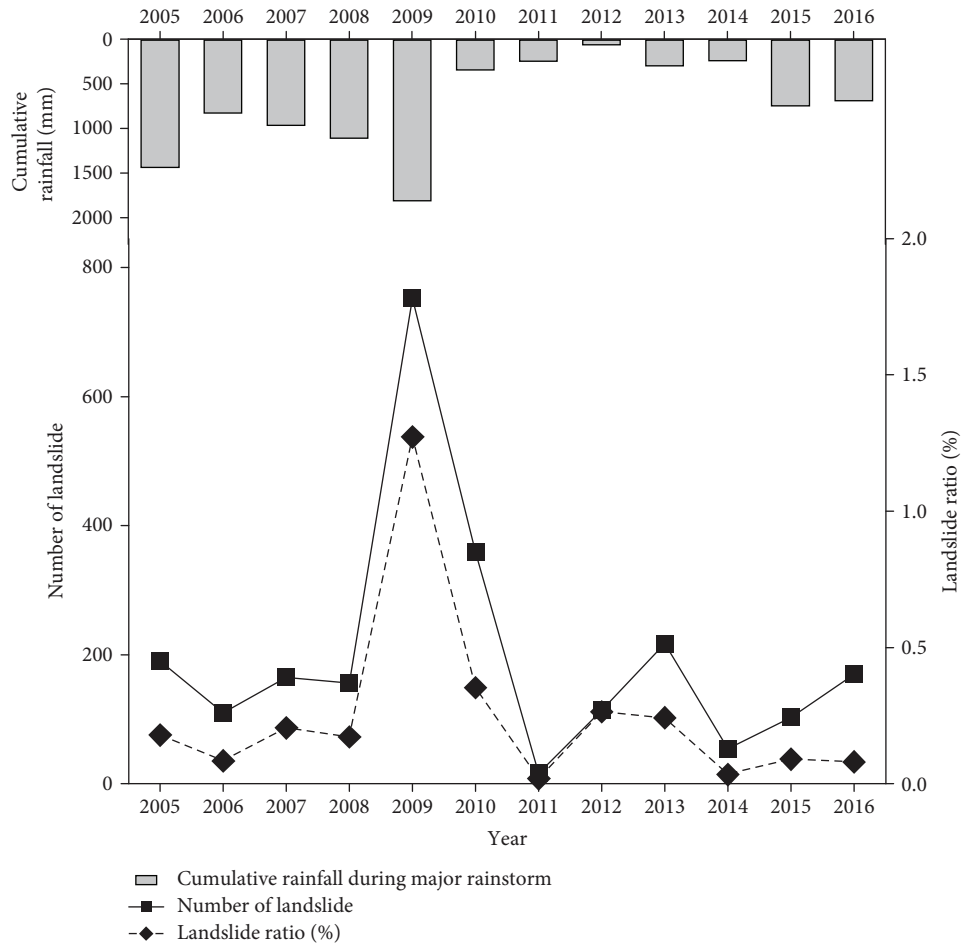
(a) Zengwen
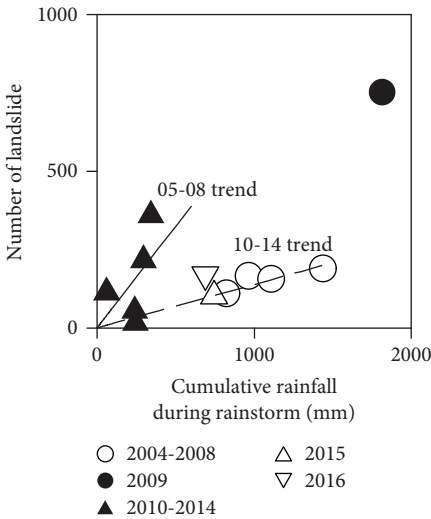
(b) Zengwen
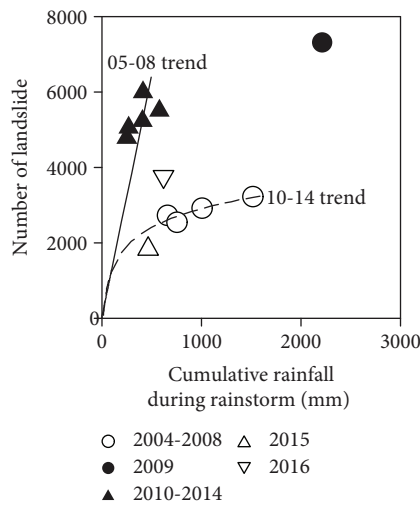
(c) Gaoping
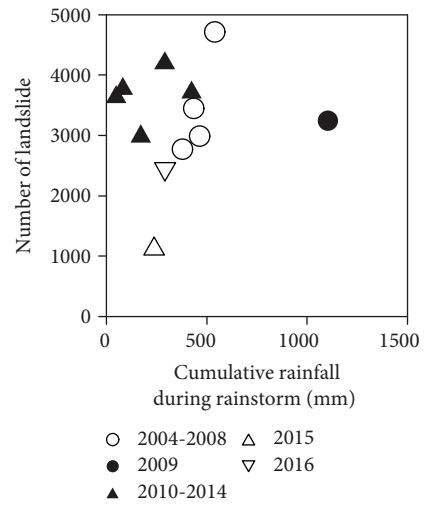
(d) Zhuoshui

FIGURE 5: (a) The variations of landslides during 2005–2016 in the Zengwen River catchment. (b–d) The relationships between the landslide number and cumulative rainfall in the Zengwen River, Gaoping River, and Zhuoshui River catchments.

that occurred in Taiwan during 2006–2014 and collected rainfall data for the areas where they occurred. The numbers of investigated landslides in the southern region barring 2009

data (outlier) were 35 during 2006–2008 and 23 during 2010–2014. The critical rainfall condition for landslides was estimated by the rainfall intensity-duration (I-D) threshold
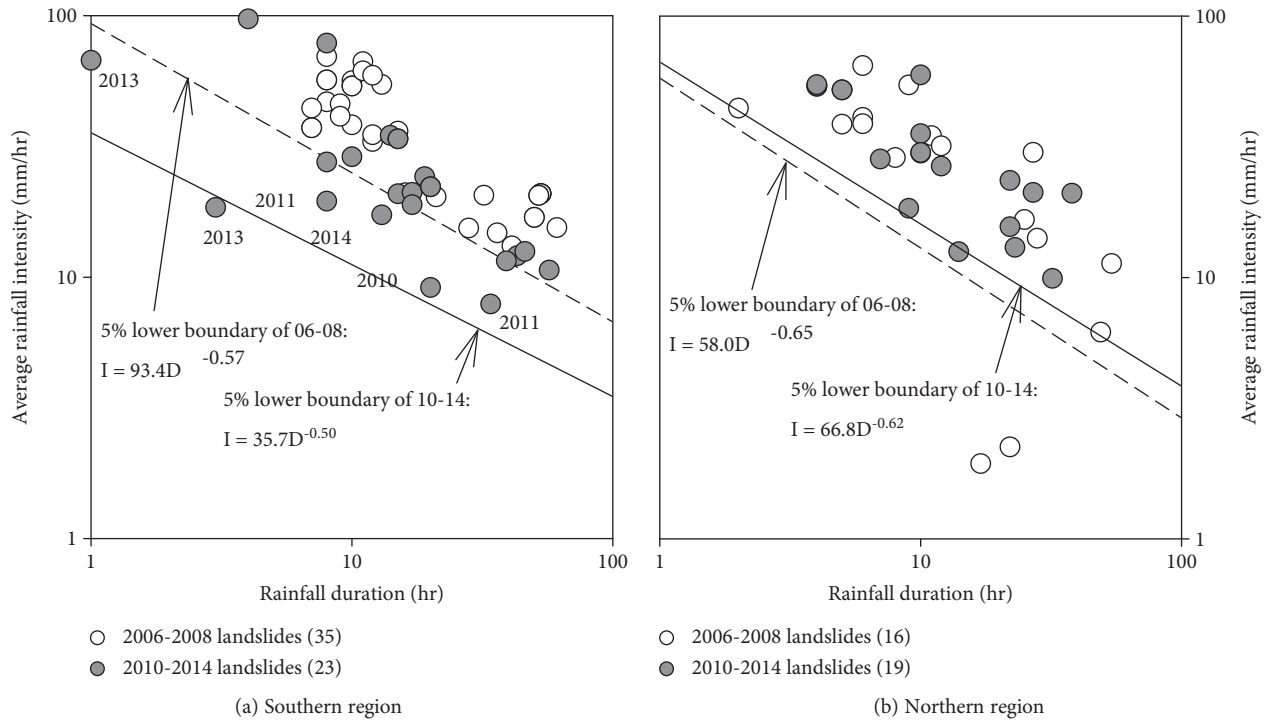
FIGURE 6: The lower boundaries of rainfall condition for triggering landslides in 2006–2008 and 2010–2014. (a) 58 landslides in the southern region. The numbers labeled around the data lower than the lower boundary of 06–08 mean the occurrence year of event. (b) 35 landslides in the northern region.

using the frequentist method proposed by Brunetti et al. [30]. In that study, the critical line was defined as the threshold corresponding to the 5% exceedance probability. Obviously, the 2010–2014 critical line was lower than the 2006–2008 line (Figure 6(a)), indicating that the critical rainfall for initiating landslides in the southern region dropped after Typhoon Morakot. In contrast, the change in the rainfall conditions for triggering landslides in the northern region was rather slight after the typhoon (Figure 6(b)). Furthermore, on a long-term basis, to explore the gradual restoration of the threshold after an extreme typhoon and expound the role of such event in subsequent sediment discharges and rainfall-driven landslides, it is suggested that future observations on the effects of Typhoon Morakot be continued.

5. Conclusions

The maximum cumulative rainfall caused by Typhoon Morakot in 2009 exceeded 1500 mm, leading to catastrophic slope failures and flooding disasters in the central and southwestern regions of Taiwan, as well as large amounts of suspended sediment discharges (SSDs). In this study, the SSDs in the three major rivers in Taiwan, the Zhuoshui River, the Zengwen River, and the Gaoping River, were estimated from the measured data of water discharge and sediment concentration. The estimation of the SSD from each river showed that the sediment yields during Typhoon Morakot comprised at least 58% of the 2009 annual SSD, and the SSD in the

Gaoping River during the typhoon reached 98% of the annual SSD. In addition, during Typhoon Morakot, the total amount of SSD in the catchments in the southwestern region of Taiwan exceeded the average annual sediment discharge for the years before 2008. This finding is a clear indication that the amount of SSD of a single rainstorm can be higher than the average annual SSD. The amount of the 2009 annual SSD in each river was attributed to an extreme event and can lead to SSD 15 times higher than the corresponding average annual SSD. These results indicate that the sediment supply in these catchments was greatly affected by the extreme rainfall during Typhoon Morakot, creating an unusually large sediment discharge for the year. By comparing the SSDs affected by Typhoon Morakot in the three rivers, we found that the Gaoping River was affected most significantly, but the influence gradually decreased northward. The impact of the typhoon on suspended sediment discharge lasted for around four months. The variations of landslide ratios in these three catchments revealed that Typhoon Morakot caused the largest-scale mass movement disaster in the southwestern region of Taiwan in the past decades. The relationship between the landslide number and rainfall in the Zengwen River and Gaoping River catchments during 2005–2016 revealed that the impact of an extreme typhoon on landslides in a given basin could last for 4–5 years. Furthermore, the comparison of the rainfall thresholds before and after the typhoon indicated that the critical rainfall for triggering landslides declined during the years following the extreme event.

Data Availability

The data used to support the findings of this study are available from the corresponding author upon request.

Conflicts of Interest

The authors declare that they have no conflicts of interest.

Acknowledgments

Supplementary Materials

The supplementary material includes one supplementary figure (Figure S1) and three supplementary tables (Tables S1~S3). Figure S1: the comparison of landslide inventory maps of manual and automated identification. Tables S1, S2, and S3: the yearly rating curves and observation days of SSD and water discharge in the Zhuoshui River, Zengwen River, and Gaoping River, respectively. (Supplementary Materials)

References

[1] S. L. Shieh, *Users' Guide for Typhoon Forecasting in the Taiwan Area (VIII)*, Central Weather Bureau, Taipei, 2000.

[2] Y. C. Chen, K. T. Chang, Y. J. Chiu, S. M. Lau, and H. Y. Lee, "Quantifying rainfall controls on catchment-scale landslide erosion in Taiwan," *Earth Surface Processes and Landforms*, vol. 38, no. 4, pp. 372–382, 2013.

[3] C. W. Chen, T. Oguchi, Y. S. Hayakawa et al., "Sediment yield during typhoon events in relation to landslides, rainfall, and catchment areas in Taiwan," *Geomorphology*, vol. 303, pp. 540–548, 2018.

[4] G. W. Lin, H. Chen, Y. H. Chen, and M. J. Horng, "Influence of typhoons and earthquakes on rainfall-induced landslides and suspended sediments discharge," *Engineering Geology*, vol. 97, no. 1-2, pp. 32–41, 2008.

[5] S. C. Chuang, H. Chen, G. W. Lin, C. W. Lin, and C. P. Chang, "Increase in basin sediment yield from landslides in storms following major seismic disturbance," *Engineering Geology*, vol. 103, no. 1-2, pp. 59–65, 2009.

[6] S. J. Dadson, N. Hovius, H. Chen et al., "Links between erosion, runoff variability and seismicity in the Taiwan orogen," *Nature*, vol. 426, no. 6967, pp. 648–651, 2003.

[7] A. C. Gellis, "Factors influencing storm-generated suspended-sediment concentrations and loads in four basins of contrasting land use, humid-tropical Puerto Rico," *Catena*, vol. 104, pp. 39–57, 2013.

[8] T. Y. Lee, J. C. Huang, J. Y. Lee, S. H. Jien, F. Zehetner, and S. J. Kao, "Magnified sediment export of small mountainous rivers in Taiwan: chain reactions from increased rainfall intensity under global warming," *PLoS One*, vol. 10, no. 9, article e0138283, 2015.

[9] G. W. Lin, H. Chen, D. N. Petley, M. J. Horng, S. J. Wu, and B. Chuang, "Impact of rainstorm-triggered landslides on high turbidity in a mountain reservoir," *Engineering Geology*, vol. 117, no. 1-2, pp. 97–103, 2011.

[10] Y. M. Wang, S. S. Tfwala, H. C. Chan, and Y. C. Lin, "The effects of sporadic torrential rainfall events on suspended sediments," *Archives of Sciences*, vol. 66, pp. 211–224, 2013.

[11] CWB, *Climatological Data Annual Report*, Central Weather Bureau, Taipei, Taiwan, 2009.

[12] J. C. Chen and M. R. Chuang, "Discharge of landslide-induced debris flows: case studies of Typhoon Morakot in southern Taiwan," *Natural Hazards and Earth System Sciences*, vol. 14, no. 7, pp. 1719–1730, 2014.

[13] WRA, "Hydrological yearbook of Taiwan," in *Water Resources Agency*, Ministry of Economic Affairs, Taiwan, 2015.

[14] K. H. Ahn and S. Steinschneider, "Time-varying suspended sediment-discharge rating curves to estimate climate impacts on fluvial sediment transport," *Hydrological Processes*, vol. 32, no. 1, pp. 102–117, 2018.

[15] Z. A. Boukhrissa, K. Khanchoul, Y. Le Bissonnais, and M. Tourki, "Prediction of sediment load by sediment rating curve and neural network (ANN) in El Kebir catchment, Algeria," *Journal of Earth System Science*, vol. 122, no. 5, pp. 1303–1312, 2013.

[16] T. A. Cohn, "Recent advances in statistical methods for the estimation of sediment and nutrient transport in rivers," *Reviews of Geophysics*, vol. 33, no. S2, pp. 1117–1123, 1995.

[17] S. J. Kao, S. C. Chan, C. H. Kuo, and K. K. Liu, "Transport-dominated sediment loading in Taiwanese rivers: a case study from the Ma-an Stream," *The Journal of Geology*, vol. 113, no. 2, pp. 217–225, 2005.

[18] S. Tfwala and Y.-M. Wang, "Estimating sediment discharge using sediment rating curves and artificial neural networks in the Shiwen River, Taiwan," *Water*, vol. 8, no. 2, 2016.

[19] N. Hovius, C. P. Stark, C. Hao-Tsu, and L. Jiun-Chuan, "Supply and removal of sediment in a landslide-dominated mountain belt: Central Range, Taiwan," *The Journal of Geology*, vol. 108, no. 1, pp. 73–89, 2000.

[20] J. Xu, "Trends in suspended sediment grain size in the upper Yangtze River and its tributaries, as influenced by human activities," *Hydrological Sciences Journal*, vol. 52, no. 4, pp. 777–792, 2007.

[21] C. W. Lin, C. L. Shieh, B. D. Yuan, Y. C. Shieh, S. H. Liu, and S. Y. Lee, "Impact of Chi-Chi earthquake on the occurrence of landslides and debris flows: example from the Chenyulan River watershed, Nantou, Taiwan," *Engineering Geology*, vol. 71, no. 1-2, pp. 49–61, 2004.

[22] H. Ding, Y. Li, S. Ni et al., "Increased sediment discharge driven by heavy rainfall after Wenchuan earthquake: a case study in the upper reaches of the Min River, Sichuan, China," *Quaternary International*, vol. 333, pp. 122–129, 2014.

[23] N. Hovius, P. Meunier, C. W. Lin et al., "Prolonged seismically induced erosion and the mass balance of a large earthquake," *Earth and Planetary Science Letters*, vol. 304, no. 3-4, pp. 347–355, 2011.

[24] M. Vanmaercke, A. J. Kettner, M. Van Den Eeckhaut et al., "Moderate seismic activity affects contemporary sediment yields," *Progress in Physical Geography*, vol. 38, no. 2, pp. 145–172, 2014.

[25] H. W. Chang, Y. M. Tien, and C. H. Juang, "Formation of south-facing bald mudstone slopes in southwestern Taiwan," *Engineering Geology*, vol. 42, no. 1, pp. 37–49, 1996.

[26] C. S. Ho, *An Introduction to the Geology of Taiwan Explana-tory Text of the Geologic Map of Taiwan*, Central Geological Survey, Taipei, 1994.

[27] D. H. Lee, K. G. Tien, and C. H. Juang, "Full-scale field exper-imentation of a new technique for protecting mudstone slopes, Taiwan," *Engineering Geology*, vol. 42, no. 1, pp. 51–63, 1996.

[28] D. H. Lee, C. S. Tsai, and C. T. Weng, "A study on the failure behaviors of mudstones and the stabilization measures," in *Disaster Prevention Investigation*, National Science Council of Taiwan, Taipei, Taiwan, 1984.

[29] D. H. Lee and Y. M. Tien, "Fundamental engineering behav-iors of mudstone," *Sino-Geotechnics*, vol. 19, pp. 26–34, 1985.

[30] M. T. Brunetti, S. Peruccacci, M. Rossi, S. Luciani, D. Valigi, and F. Guzzetti, "Rainfall thresholds for the possible occur-rence of landslides in Italy," *Natural Hazards and Earth System Sciences*, vol. 10, no. 3, pp. 447–458, 2010.

Research Article

Geohazard Caused by Groundwater in Urban Underground Excavation

Bin-Chen Benson Hsiung (ID)

Department of Civil Engineering, National Kaohsiung University of Sciences and Technology, 415, Chen Kung Road, Kaohsiung 807, Taiwan

Correspondence should be addressed to Bin-Chen Benson Hsiung; benson.hsiung@gmail.com

This paper addresses the important role of water in geohazard and failure in urban underground excavation. These so-called underground water-related hazards, such as leakage of the tunnel eye due to launching and docking of the shield, failure of the cross-passage excavation, and failure of the retaining wall caused by water ingress for deep excavation, often lead to catastrophic disasters. Leakage of the tunnel eye during shield launching that results in failure was selected for further analysis using finite element simulations. According to this work, the flush-in of water mainly leads to the failure of soils located at the invert of the tunnel immediately behind the wall, and gravity is the cause of such failure phenomena; these findings agree with field observations. A significant reduction in the pore pressure of soils behind the wall associated with water relief through the tunnel eye and the quantity of water flow into the excavation is predicted. Piping failure is also suggested to occur during shield launching under the current arrangements. Finally, according to parametric studies, reducing the soil permeability and increasing the cohesion force are recommended to prevent the opportunity for failure.

1. Introduction

Modern underground excavations are frequently utilised to expand the underground space in modern cities, and deep excavations and tunnelling are used as tools for the construction of urban underground spaces. However, such large-scale excavations often lead to accidents that cause the loss of property and human life. These accidents and hazards are frequently connected with groundwater. Despite this fact, studies of such collapse and hazards in the geotechnical aspects of urban underground excavation are mainly focused on observations, mitigation measures, and the possible reasons leading to hazards based on case histories of previous studies. In this paper, in contrast to previous studies, modelling and the mechanism of geohazards due to groundwater in urban underground excavations (mainly deep excavation and tunnelling in highly permeable ground with a high ground water level) are provided and discussed. The roles of water in the failure mechanism, the pore pressure distribution and changes, the groundwater flow direction, and the quantity of water flow caused by launching the shield are included in the simulation. Finally, the impacts of the permeability, strength, and stiffness of improved soils on the failure of soils are also examined.

2. Geohazards Caused by Groundwater in Cases of Urban Underground Excavation

Wagner and Knights [1] highlighted the geohazard and risk management of underground construction and stated that the financial losses from 15 major tunnels within 10 years exceeds USD 500 million. To minimise the risks due to underground construction activities, many professions and organisations, such as the British Tunnel Society [2], Eskeren et al. [3], GEO [4], and The International Tunnelling Insurance Group [5], have proposed a variety of follow-up guidelines or codes of practice. At the same time, using the metro system as an example, Moh and Hwang [6] indicated 23 major accidents during the construction of urban underground infrastructure from 2001 to 2006 in the Asia Pacific

TABLE 1: Significant accidents in construction of underground metro system caused by groundwater in Asia Pacific region from 2001 to 2006.

Locations	Causes	Consequence
Taipei, Taiwan	Leakage of tunnel eye	More than 100 residential houses damaged
Shanghai, China	Failure of cross passage	Collapse or tilting of several buildings
Kaohsiung, Taiwan	Leakage of tunnel eye	Seven buildings damaged and 40 families evacuated
Kaohsiung, Taiwan	Leakage of diaphragm wall	A nearby hospital was endangered
Guangzhou, China	Rupture of water main led to collapse of diaphragm wall	3 persons fell into sinkhole and one person severely injured
Taipei, Taiwan	Rupture of water main	A large sinkhole
Taipei, Taiwan	Leakage of tunnel eye	A large sinkhole
Kaohsiung, Taiwan	Leakage of diaphragm wall	4 buildings collapsed and 3 buildings severely damaged
Kaohsiung, Taiwan	Failure of cross passage	The tunnel, together with the underpass above the tunnel, about 100 m in length were totally damaged
Beijing, China	Rupture of sewer	A large sinkhole
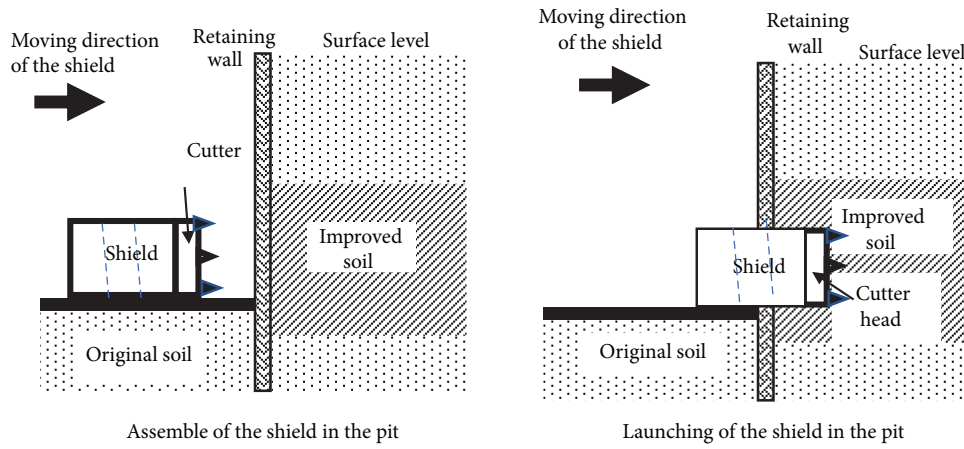
(a) Schematic drawing of launching of a shield

(b) The shield in the pit

(c) Tunnel eye for launching

(d) Launching of shields

FIGURE 1: The launching of a shield.
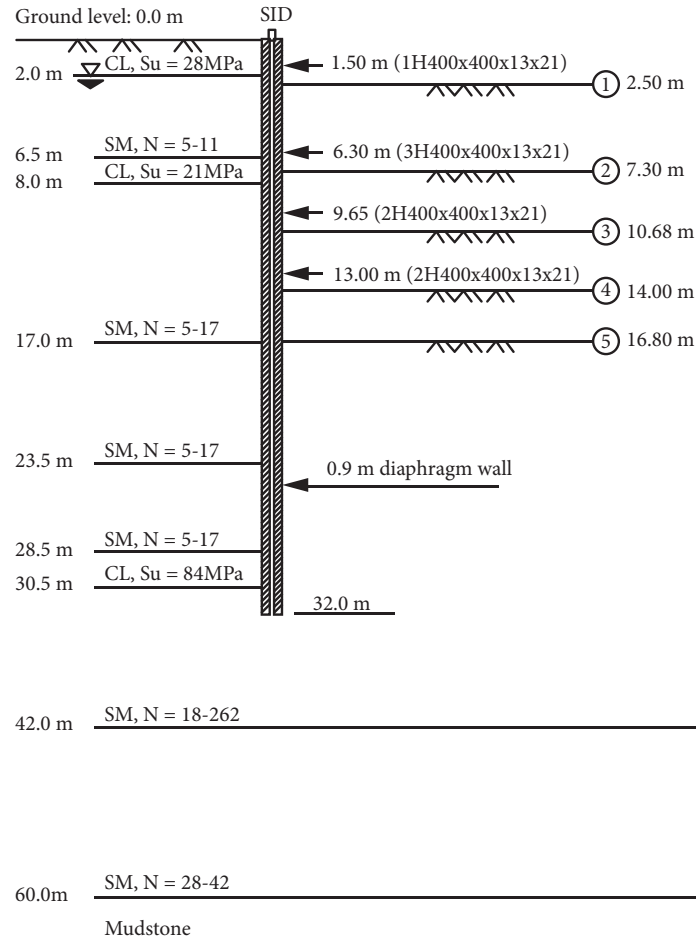
FIGURE 2: Cross section and ground profile of the excavation.
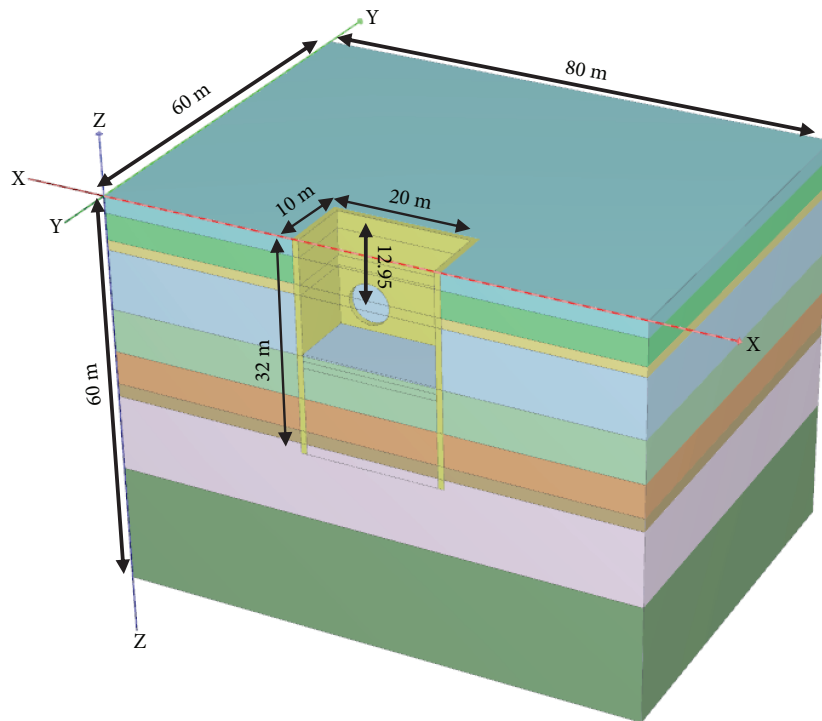
FIGURE 3: 3-dimensional model of simulation of launching of a shield.
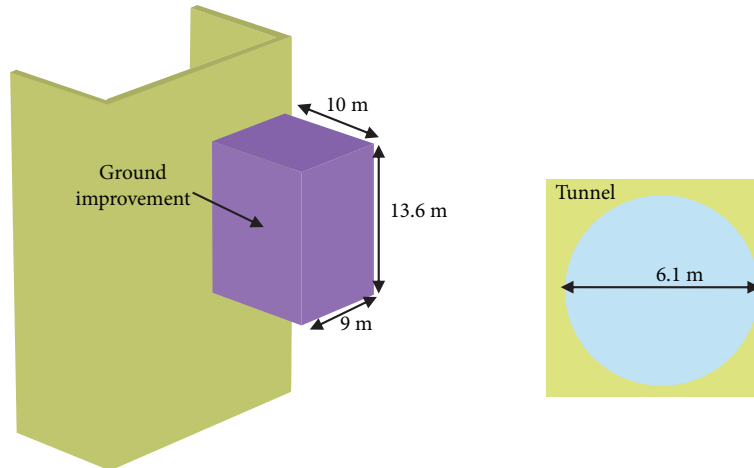
FIGURE 4: Details of tunnel eye and soil improvement zone in the model.

(a)

(b)

(c)

(d)
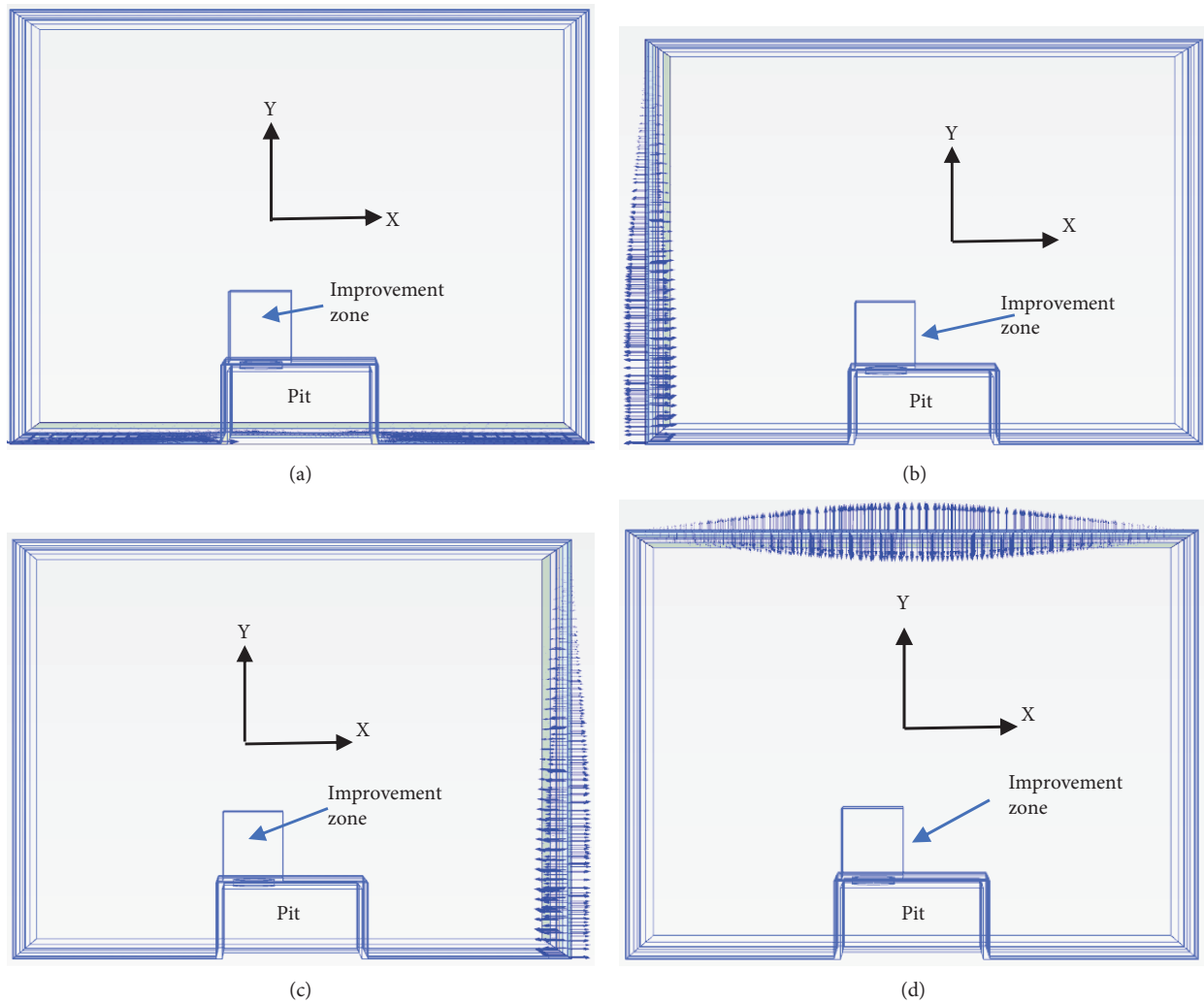
FIGURE 5: Boundaries conditions of water in the model (Plane view). (a) Y_{min} closed; (b) X_{min} opened; (c) X_{max} opened; and (d) Y_{max} opened.

region and, among them, estimated that 10 were directly caused by groundwater, which is a very high proposition, as listed in Table 1. As categorised by Moh and Hwang [6],

the geohazards related to groundwater for urban underground excavations are stated in Table 1 and include leakage at the tunnel eye (via launching or docking of the shield in

TABLE 2: Input parameters of soils and structures.

(a) Sandy soil (hardening soil with small strain)

Layer	Depth (m)	Drainage type	Unit weight (kN/m^3)	ϕ' (°)	E_{50}^{ref} (kPa)	K0	G_0^{ref} (kN/m^2)
2	2.0–6.5	Drained	20.9	32	26.22×10^3	0.4701	1.44×10^5
4	8.0–17.0	Drained	20.6	32	21.9×10^3	0.4701	1.41×10^5
5	17.0–23.5	Drained	18.6	32	24.06×10^3	0.4701	1.41×10^5
6	23.5–28.5	Drained	19.6	33	26.25×10^3	0.4554	1.6×10^5
8	30.5–42	Drained	19.6	34	29.58×10^3	0.4408	1.62×10^5
9	42–60	Drained	19.6	34	33.15×10^3	0.4408	1.77×10^5

Note: $v' = 0.3$; $\gamma_{0.7} = 1 \times 10^{-4}$; $E_{ur}^{ref} = 3E_{50}^{ref}$; $E_{oed}^{ref} = E_{50}^{ref}$; $m = 0.5$; permeability $= 2 \times 10^{-4}$ cm/sec; Rf = 0.9.

(b) Clay (Mohr-Coulomb)

Layer	Depth (m)	Soil type	γ (kN/m^3)	S_u (kPa)	E' (kPa)	v'	K0	Permeability (cm/sec)
1	0.0–2.0	CL	19.3	28	13,060	0.3947	1.0	1×10^{-8}
3	6.5–8.0	CL	19.7	21	9800	0.3953	1.0	1×10^{-8}
7	28.0–30.5	CL	18.6	84	39,200	0.3953	1.0	1×10^{-8}

(c) Improvement soils

Depth (m)	Drainage type	γ (kN/m^3)	c' (kN/m^3)	ϕ' (°)	E' (kPa)	v'	K0	Permeability (cm/sec)
10.0–16.0	Undrained	21	100	34	120,000	0.3	0.44	1×10^{-6}

[#]Using the function of UC test implemented in PLAXIS, an equivalent undrained shear strength (Su) of routed sand is thus defined. Through an empirical approach [15], an assumption of Eu = 500 Su is adopted to determine the undrained Young's modulus (Eu). Effective soil stiffness E' is required to be applied in the analyses so an equation of E'= 2 (1 + v')/3 × Eu is used to determine E' (0.3 of v' is used). [*]In engineering practice, standard requirement of improved soils outside the pit for launching of shield is in the range of 1×10^{-5} to 1×10^{-6} cm/sec but tends to be stricter (1×10^{-6} cm/sec) for highly permeable ground (such as sand) with high ground water level to reduce the risk [16].

(d) Retaining structure

Parameter	Name	Value	Unit
Compressive strength of concrete	f_c'	28	MPa
Thickness	d	0.9	m
Young's modulus	E	24.8×10^6	kPa
Young's modulus x 70%	70%E	17.36×10^6	kPa
Unit weight	w	5.5	kN/m^3
Poisson's ratio	v	0.2	

(e) Steel strut

Strut level	Strut level	Preload (kN)	Section area (m^2)	EA (kN)	60%EA (kN)
Level 1	1H400x400x13x21	450	0.0219	4.59×10^6	2.75×10^6
Level 2	2H400x400x13x21	1000	0.0437	9.18×10^6	5.50×10^6
Level 3	2H400x400x13x21	1400	0.0437	9.18×10^6	5.50×10^6
Level 4	2H400x400x13x21	1400	0.0437	9.18×10^6	5.50×10^6

the shaft), failure of cross-passage excavation in the tunnelling process, and failure of the retaining wall or diaphragm wall caused by water ingress during deep excavations as well as rupture of water mains or sewers caused by the nearby construction activity of deep excavations or tunnelling. Through risk assessment, the geohazards stated above for urban underground excavations are recognised as high-risk activities and could lead to severe damage. However, none

TABLE 3: Construction sequence in simulation.

Phase number	Construction activities
0	Initial stress generation
1	Wall installation
2	Main excavation
3	Ground improvement
4	Launching of the shield
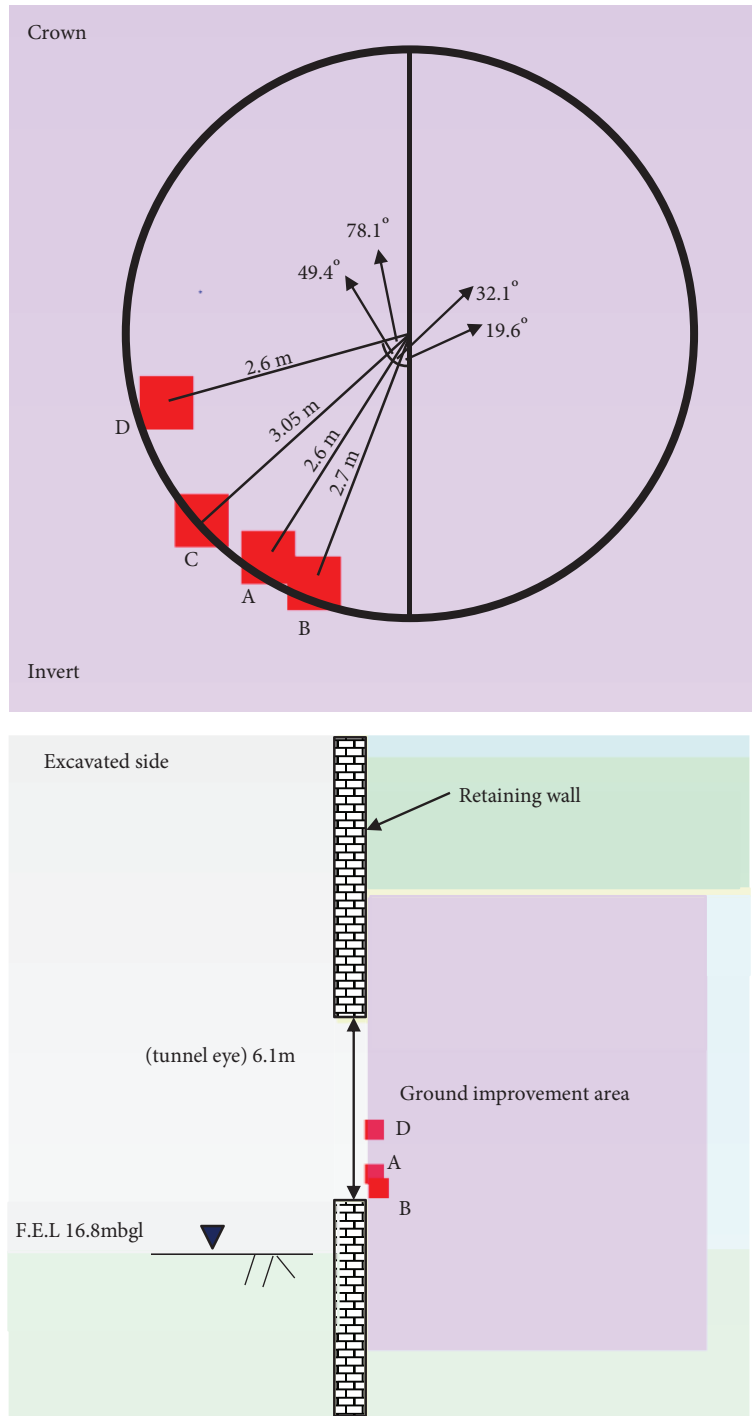
Figure 6: Failure points during the launching of a shield (transverse section immediately behind the wall).

of the literature has previously stated how to access and quantify the impact of groundwater on failure using numerical technologies, especially for highly permeable ground with a high groundwater level.

Considering the statements above, fatal failures caused by the groundwater during urban underground excavation and the launching of the shield in the shaft are further analysed and discussed in this paper. In addition, the impacts of

the permeability, strength, and stiffness of improved soils on failure are examined.

3. Construction Background and Analytical Approaches

The construction background associated with launching of a shield in a working shaft is introduced first. In an
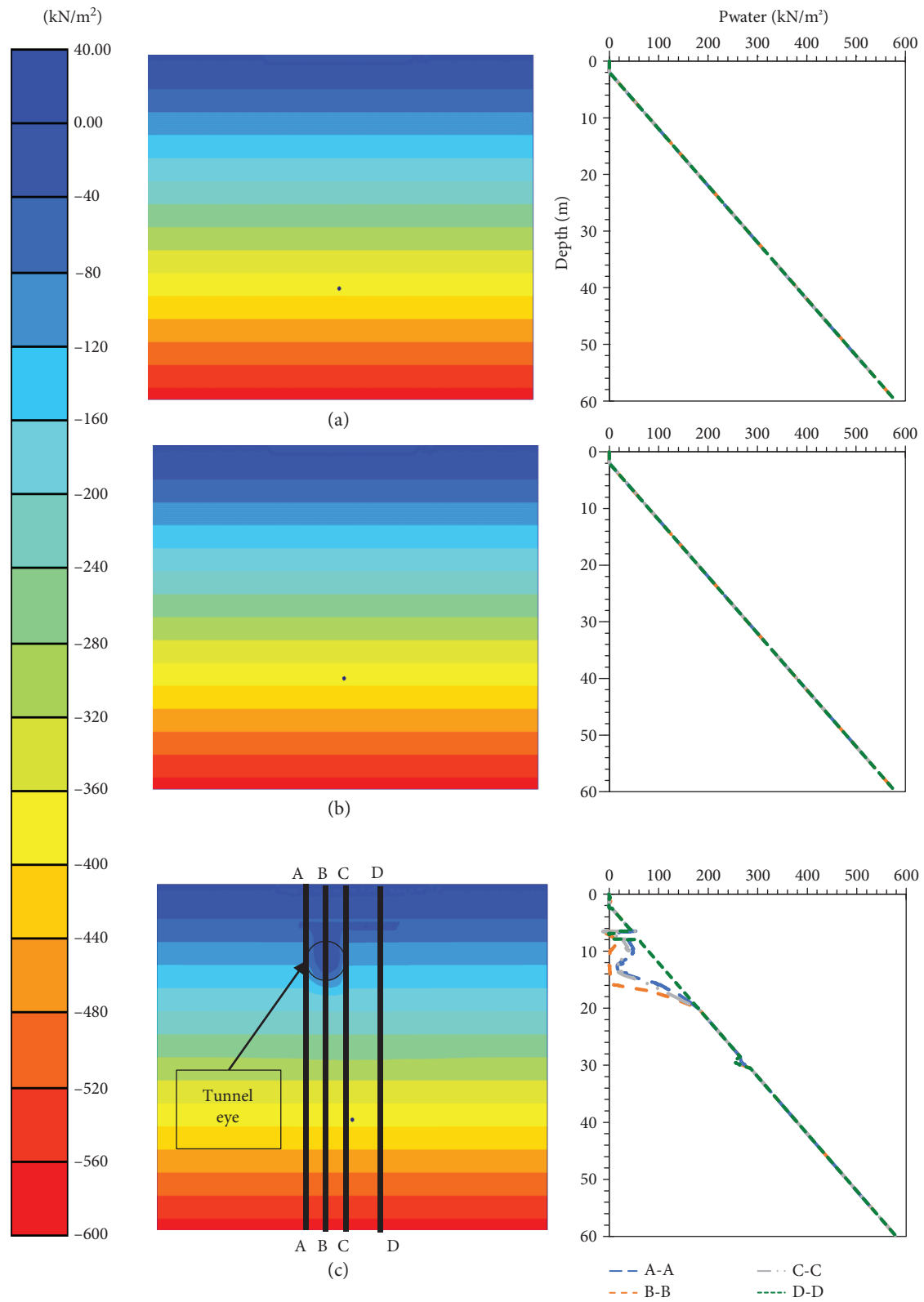
FIGURE 7: Change of pore pressure distribution at various depths and locations at different phases of launching of a shield in transverse direction. (a) Initial phase. (b) Main excavation. (c) Launching of the shield. Note: A-A: left side of tunnel eye; B-B: center of tunnel; C-C: right side of tunnel eye; and D-D: 5 m away from the right side corner. "-"in pore pressure distribution contour is positive pore pressure and "Pwater" means pore pressure.
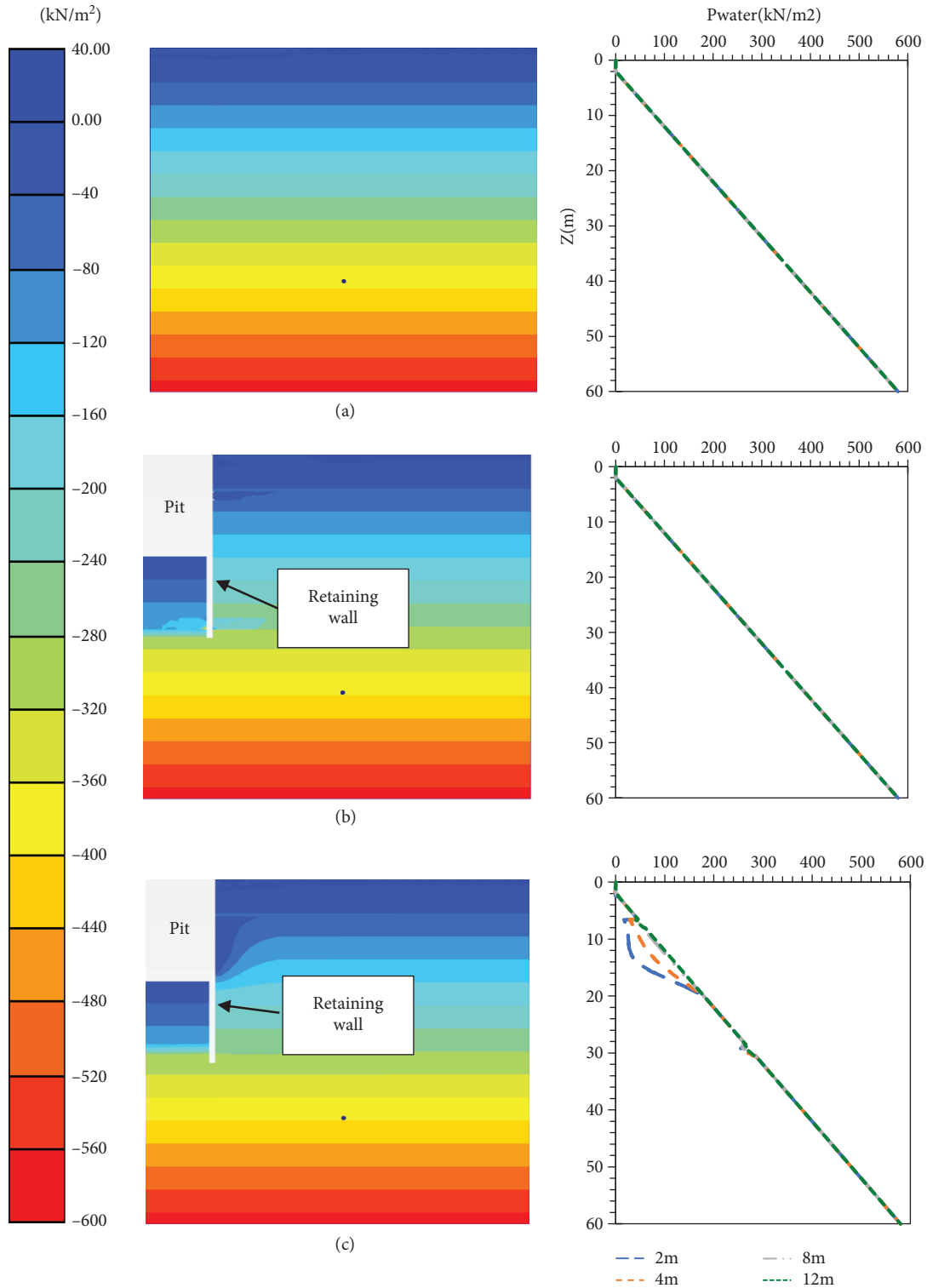
FIGURE 8: Change of pore pressure distribution at various depths and locations at different phases of launching of a shield in longitudinal direction. (a) Initial phase. (b) Main excavation. (c) Launching of the shield. Note: legend means points at various distance from the retaining wall and "-" in pore pressure distribution contour is positive pore pressure. "Pwater" means pore pressure.

urban underground infrastructure system, very often, shield-machine bored tunnels are adopted instead of cut-and-cover tunnels to reduce the interruption of traffic

and daily life of the population on the surface level. To initiate tunnelling, the working shafts must be constructed at two ends of the tunnels to allow the shield to be
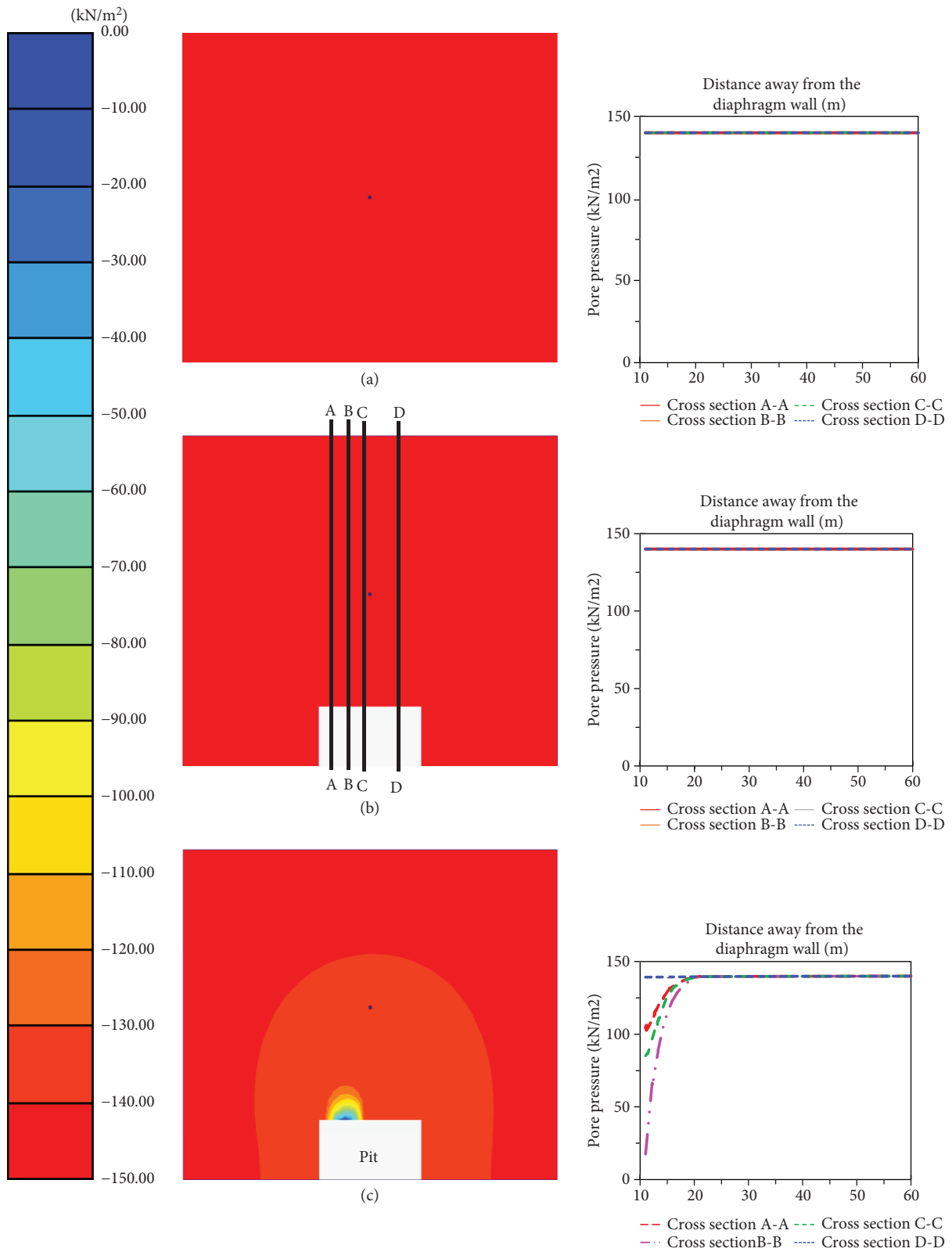
FIGURE 9: Change of pore pressure at various depths and locations at different phases of launching of a shield in plane view at 16 mbgl. (a) Initial phase. (b) Main excavation. (c) Launching of the shield. Note: A-A: left side of tunnel eye; B-B: center of tunnel; C-C: right side of tunnel eye; and D-D: 5 m away from the right side corner and "-" in pore pressure distribution contour is positive pore pressure.
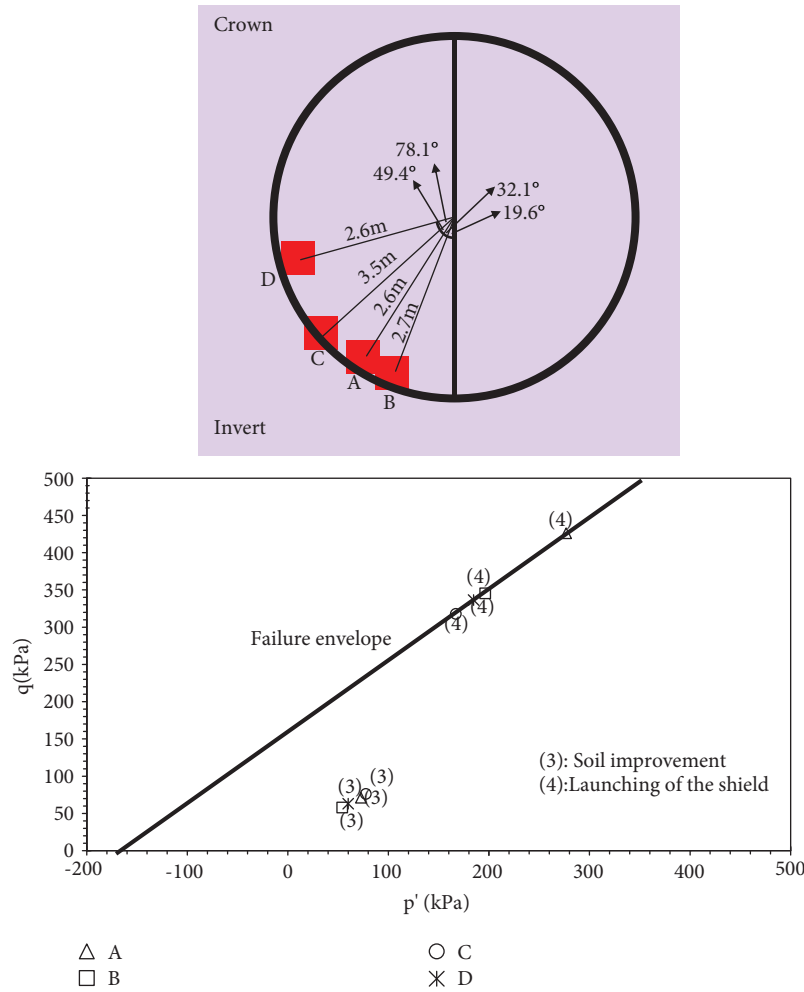
FIGURE 10: Effective stress path and failure envelope for failure caused by launching of a shield for soils immediately behind the wall.

initially assembled and launched at the shaft of one end and then the excavation of the tunnel to gradually continue until reaching the other end of the tunnel. Once the tunnel excavation has been completed, the shield is docked in the shaft at the other end of the tunnel and then disassembled. A schematic drawing of the launching of a shield tunnelling activity is presented in Figure 1. To prevent water ingress leading to failure during launching of the shield, the soil must be grouted to form a grouted box outside the shaft. In this manner, soil strength and stiffness are increased and soil permeability is reduced to allow the break-in of the retaining wall of the shaft to be delivered for shield launching and eliminate the opportunity for failure caused by water ingress.

A simulation of the failure caused by water ingress via launching of the shield is conducted first. Senthilnath [7] has simulated underground docking of a tunnelling boring (shield) machine, which involves a mechanism similar to the mechanism of launching; however, the goal was to simulate docking of the machine in a shaft constructed in low permeable rock bed without failure, which differs from the goals of this paper.

Referring to Hsiung et al. [8], part of the same excavation is assumed as the pit used for launching of the shield. The pit is retained by a 0.9-m-thick and 32-m-deep reinforcement concrete diaphragm wall with additional four-level horizontal struts. The maximum excavation level reaches 16.8 m below ground level. Figure 2 presents the cross section and ground profile of the excavation. A half-symmetric model for the excavation is made, and the size of the model is set as 80 m × 60 m × 60 m. In principle, the boundaries are established at places that are not affected by any construction activity or where the ground is sufficiently stiff. The model consists of 93,847 ten-node tetrahedral elements with a total of 132,018 nodes. The "very fine" mesh is applied for the improved soil zone, and the "normal" mesh setting is chosen for the rest. The 3-dimensional model is presented in Figure 3, and analytical software PLAXIS3D with version 2016 is adopted for the analyses. The diameter of the tunnel eye used for launching of the shield that must fit the outer diameter of the shield on the retaining wall is assumed to be 6.1 m. The depth of the center of the tunnel eye is set at 12.95 m below surface level. As stated above, the soils outside the pit must be improved to reduce their
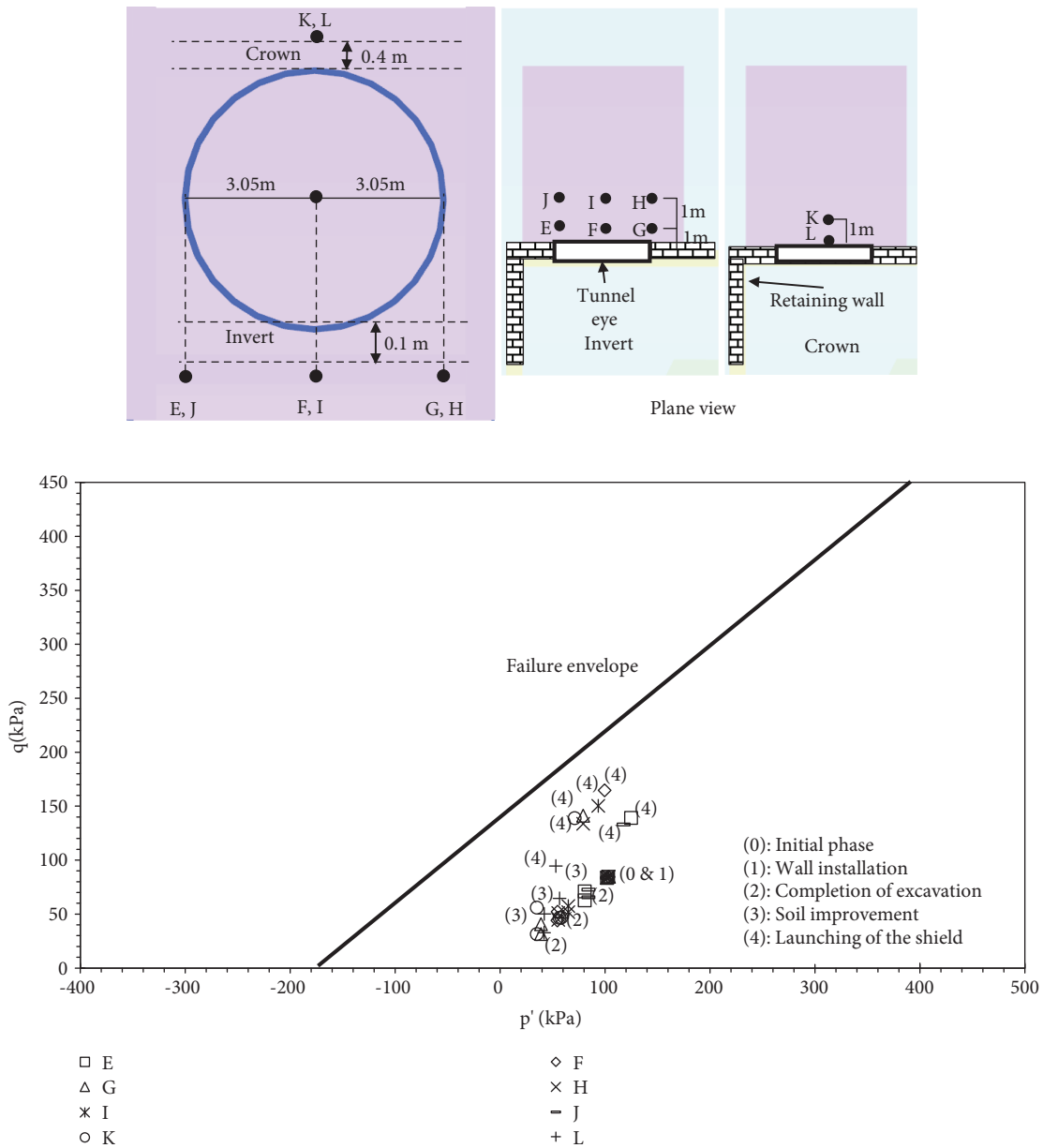
FIGURE 11: Effective stress path and failure mechanism for soils at various locations outside the pit.

permeability and increase their strength; the soil improvement zone outside the pit is assumed to be 10 m long, 9 m wide, and 13.6 m thick. Figure 4 presents the assumed details of the tunnel eye and the soil improved zone in the model.

It is assumed that groundwater is allowed to flow into the model from all directions, except at the surface level and inside the pit. The boundary conditions for the water are shown in Figure 5. The water flow is closed in the Ymin and Zmax planes but not the other planes.

Because the focus is the failure mechanism caused by water ingress due to launching of the shield, the seepage function must be used instead of elastic-plastic analyses. Moreover, the soil profile is the same as that of Hsiung et al. [8], and the constitutive model that gives special

consideration to small strain behaviour, HS-small (HSS), was selected for original sandy soils; however, the elastic-perfect plastic Mohr-Coulomb model was chosen instead for clays and improved soils because of the limits of the available input parameters, the input parameters of improved soils are referred to Dano et al. [9]. The linear-elastic model is chosen for simulation of the reinforcement concrete diaphragm wall. Node-to-node anchor elements and node-to-fixed end anchor elements are used for struts in the transverse direction and the longitudinal direction, respectively. Table 2 presents details on the input parameters of the soil and structures used for the analyses.

In engineering practice, the highly permeable soils outside the pit shall be improved by various methods at various levels, with achieving certain level of undrained shear strength of
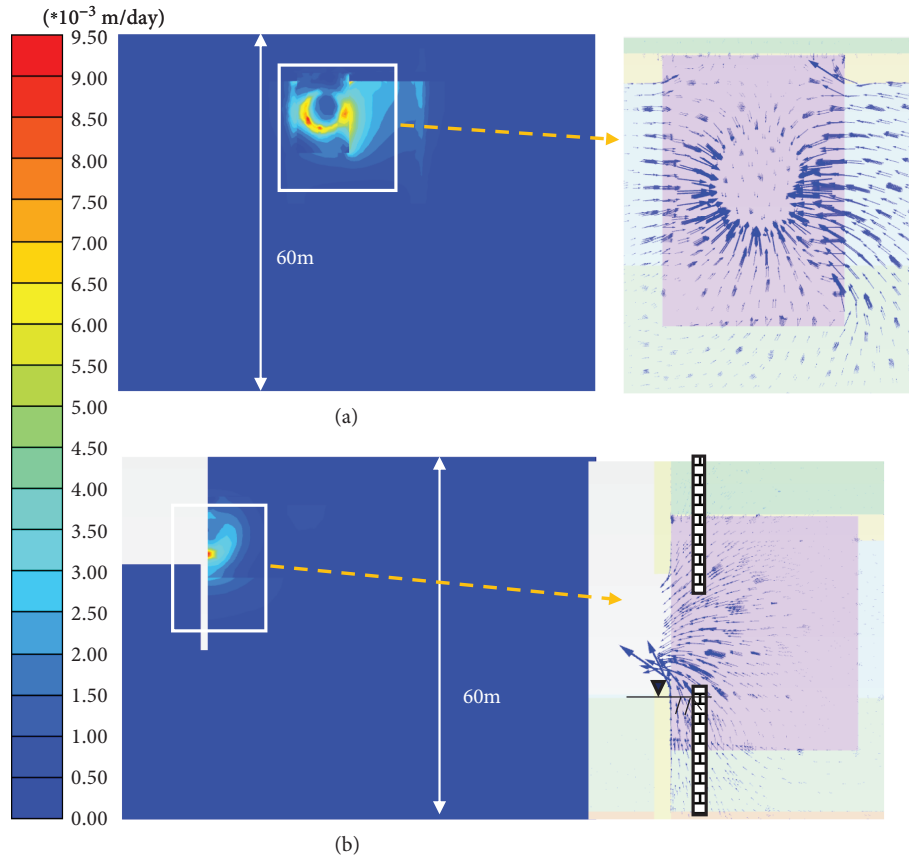
FIGURE 12: Flow line at failure caused by launching of a shield. (a) Transverse direction. (b) Longitudinal direction.

improved soils, in general, as reported in [9–11]. However, to run fully coupled seepage analyses, the effective strength parameters of improved soils must be given; moreover, as noted by Dano et al. [9], for improved soils, the effective friction angle is one to four degrees higher than that of the original soils. By using the "triaxial test" function implemented in PLAXIS3D, it is recommended that 100 kPa of equivalent cohesion force and 34 degrees of equivalent effective friction angle shall be determined for improved soils based on 120 kPa of undrained shear strength.

To further reduce the running time of analyses, the wall installation and main excavation of the pit are assumed to be "wished-in-place (WIP)" analyses, i.e., displacements induced by both stages are ignored. Table 3 presents the construction phases used for simulation of the launching of the shield.

4. Results and Discussion

Figure 6 presents the failure points caused by launching of the shield, and all failure soils are presented in terms of the angle to the six o'clock direction and the distance to the tunnel center. The angle is in the range of 19.6 to 78.1 degrees in the clockwise direction, and the distance remains the same with the radius of the tunnel eye (3.05 m). All failure soils are located immediately behind the wall, mainly at the invert of the tunnel (the points in red, named "A," "B," "C,"

and "D"); further discussion regarding the locations of the failure soils are provided in a later section.

Figure 7 shows the pore pressure distribution at various stages for soils immediately behind the wall in the transverse direction. The pore pressure almost does not change until the completion of the main excavation. It is likely that the size of the excavation is not huge, with cut-off reinforcement concrete retaining walls, and a layer of impermeable clayey material is found at the depth near the wall toe (at 28.5 m to 30. 5 m below ground level); the necessary dewatering inside the excavation could thus lead to very limited impacts on the pore pressure outside the excavation. However, the pore pressure is significantly reduced in the zone in which the wall (tunnel eye) is broken for launching of the shield; although the soil has been improved and the soil permeability, the strength, and the stiffness are all different for the original soils but not for others, such as Section D-D. Improvement most prominently affects the pore pressure at Section B-B, close to the invert of the tunnel, where the maximum difference is as significant as 100 kPa. The flush-in of groundwater into the pit is thus concluded to cause water relief and reduce the pore pressure of the soils at the back of the wall specifically in soils in the zone close to the tunnel eye.

To further demonstrate the impacts of groundwater on launching of the shield, the pore pressure distribution contour at various stages for soils outside the excavation in the longitudinal direction is presented in Figure 8. In the same
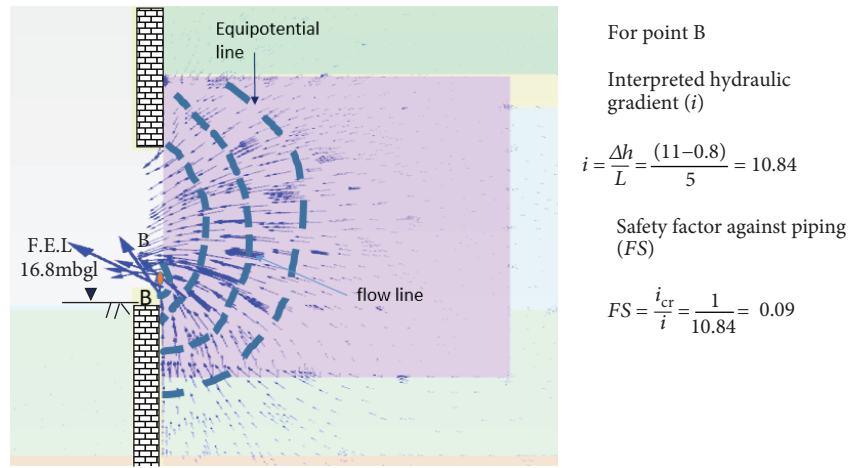
(a) Failure case ($C' = 100$ kPa; $\Phi' = 34°$; $E' = 120,000$ kPa and 1×10^{-6} cm/sec of permeability)

For point B

Interpreted hydraulic gradient (i)

$$i = \frac{\Delta h}{L} = \frac{(11-0.8)}{5} = 10.84$$

Safety factor against piping (FS)

$$FS = \frac{i_{cr}}{i} = \frac{1}{10.84} = 0.09$$
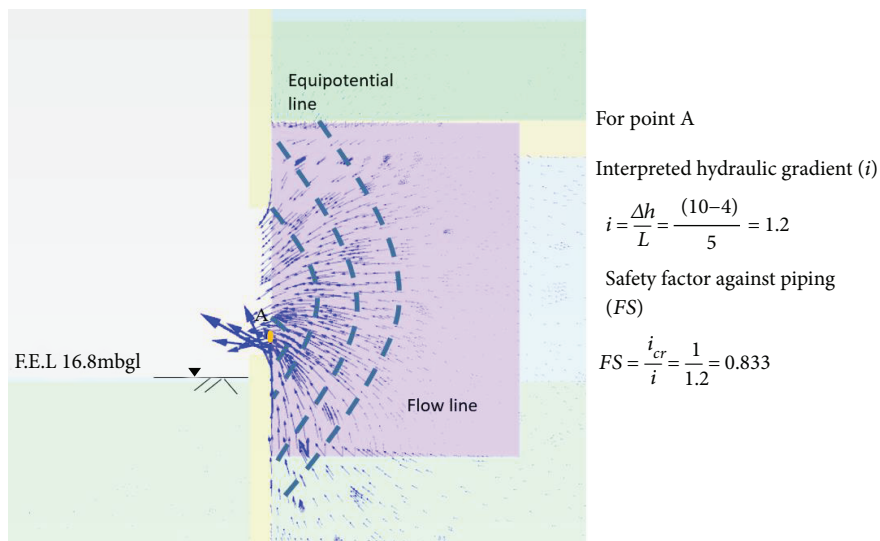
(b) Nonfailure case ($C' = 200$ kPa; $\Phi' = 34°$; $E' = 169,000$ kPa and 1×10^{-6} cm/sec of permeability)

For point A

Interpreted hydraulic gradient (i)

$$i = \frac{\Delta h}{L} = \frac{(10-4)}{5} = 1.2$$

Safety factor against piping (FS)

$$FS = \frac{i_{cr}}{i} = \frac{1}{1.2} = 0.833$$

FIGURE 13: Schematic drawing of flow net and safety factor against piping calculation.

figure, the pore pressure of soils located at 2, 4, 8, and 12 m from the wall along the depth are also plotted; similar to the pore pressure distribution shown in the transverse direction, the pore pressure in this plot remains almost the same during the main excavation stage. Due to the flush-in of groundwater, a decrease in pore pressure as great as 60 kPa is observed at the invert of the tunnel when compared with the stress at the initial stage at the same location for the pore pressure at 2 m away from the wall. Launching of the shield only influences the pore pressure at approximately 7 m to 18 m below the surface level at a degree that is slightly more than the tunnel eye zone, as shown in Figure 8(c). However, once the distance is farther away, the impact is gradually reduced. Until a distance of 12 m from the wall, the launching of the shield does not cause any change in pore pressure.

The major influence on pore pressure distribution is found at a similar depth as the invert of the tunnel, according to the previous discussion; thus, Figure 9 presents the pore

pressure change contour at the said depth of the soils. As shown in Figure 9, regardless of the section, decreases in pore pressure are observed in the locations spanning from immediately next to the wall to 20 m from the wall but remain unchanged for grounds residing at more than 20 m from the wall. It can also be inferred from Figure 9 that Section B-B has the largest change, whereas Section D-D does not exhibit any change at distances greater than 10 m from the wall, because this section is not within the tunnel eye zone.

The effective stress path and the failure mechanism of soils outside the excavation are examined. Figure 10 shows the various soil elements at various locations surrounding the tunnel eye from the view of the transverse direction for soils behind the wall together with the effective stress path of each soil element and its relative locations within the failure envelope. The labels "p'" and "q" indicate the mean effective stress and the deviatoric stress, respectively. Stress relief is observed during the main excavation stage, leading to

(a1)

(a2)

(b1)

(b2)

(c1)

(c2)
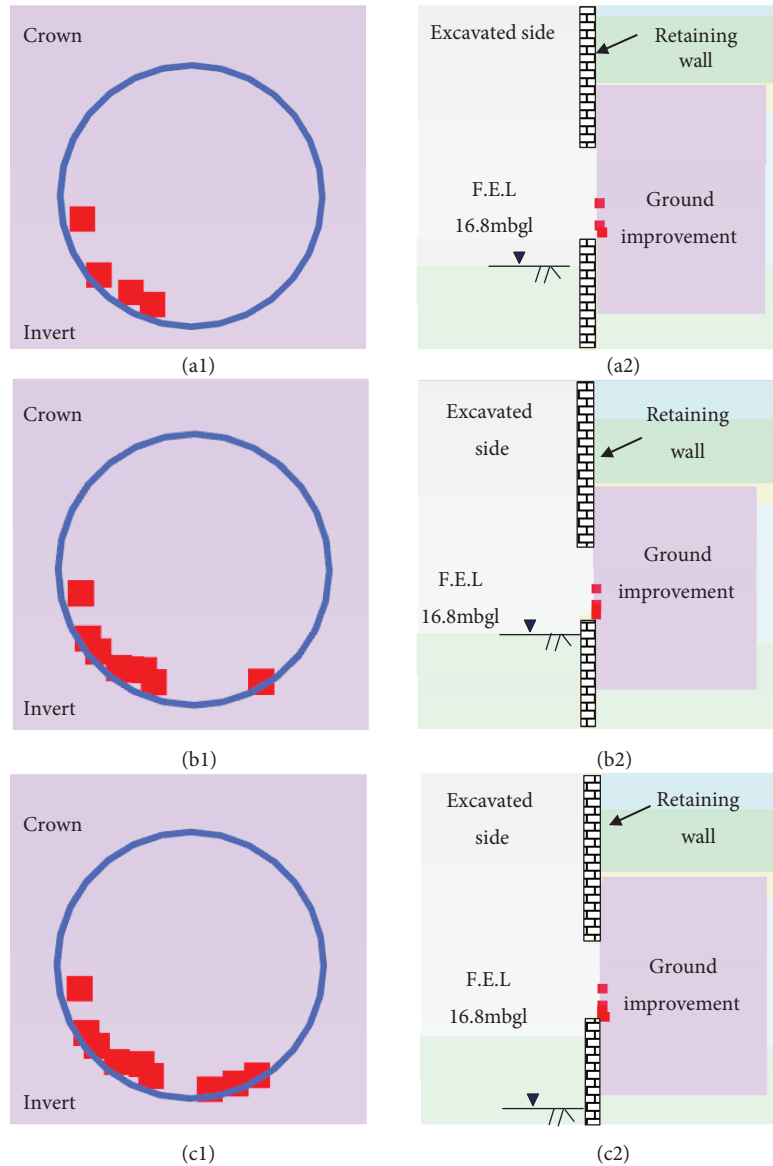
FIGURE 14: Impacts from various soil permeability on failure caused by launching of a shield. Note: "1" means transverse direction and "2" means longitudinal direction. (a) 10^{-6} cm/sec, (b) 10^{-5} cm/sec, and (c) 10^{-4} cm/sec.

reductions of p' and q. The stress status does not change during the soil improvement stage, and it is presumed that soil improvement is conducted in a limited zone and does not change the stress significantly afterwards, even though the soil properties have been fully changed after improvement. Once the shield is launched, the effective stress of the soils at points A to D (refer to Figure 6 for locations) reaches the failure status; therefore, these points lie on the failure envelope, as shown in Figure 10. The flush-in of groundwater significantly increases the vertical stress but causes a very limited increase in the effective stress in the lateral direction and is expected to be the reason for the simultaneous increases in p' and q from phase 3 to phase 4.

The effective stress path and failure mechanism of soils at additional locations are also examined from the views in both the transverse and longitudinal directions, as presented in Figure 11. Similarly, the soil elements closer to the excavation have more significant stress relief at the main excavation stages, such as points E, F, G, and L, rather than points H, I, J, and K. Moreover, because of the flush-in of groundwater, both p' and q increase via a similar trend, where the stress in the soils closer to the wall changes but does not reach failure, as shown in Figure 11.

Figure 12 shows the flow line directly output from the simulation model in both the transverse direction and the longitudinal direction. The size of the arrow implies the quantity of water flow. In either the transverse or longitudinal direction, water flows into the pit mainly in the invert part of the tunnel, consistent with the observations of Moh and Hwang [6] and Ju et al. [12] from accidents caused by the launching and docking of the shield in the pit. This agreement further validates the accuracy of the numerical model
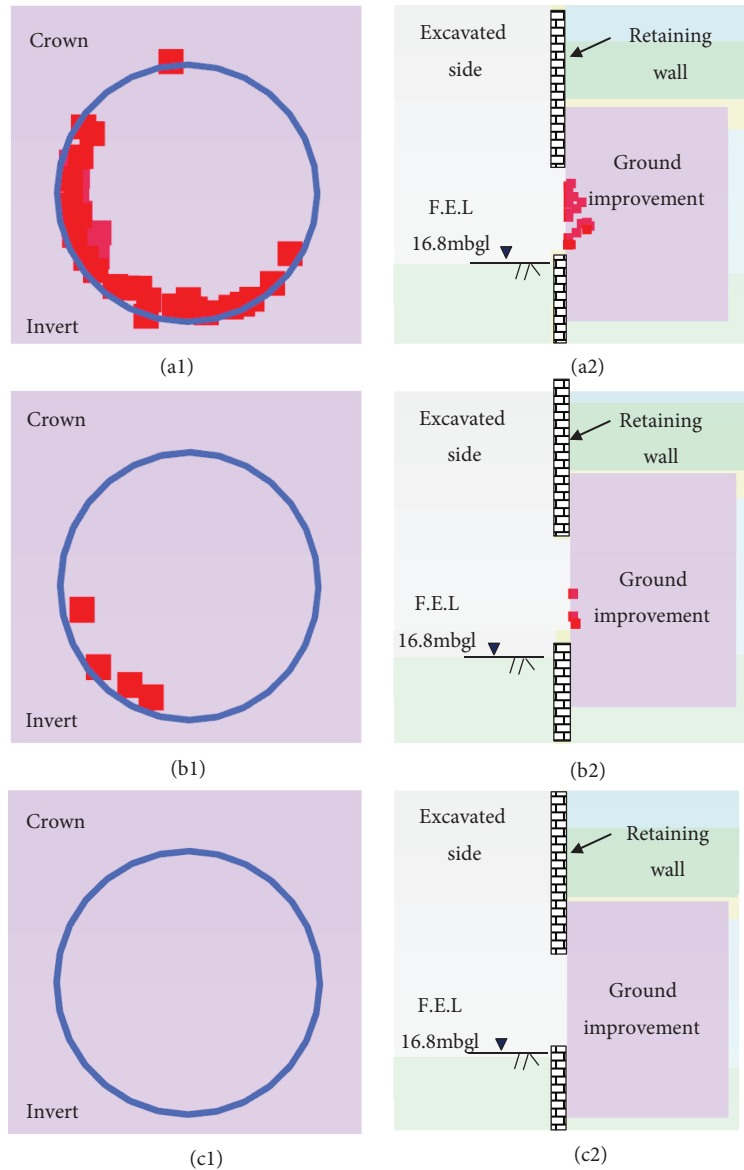
FIGURE 15: Impacts from various soil strength on failure caused by launching of a shield. Note: "1" means transverse direction and "2" means longitudinal direction. (a) 50 kPa (cohesion), (b) 100 kPa (cohesion), and (c) 200 kPa (cohesion).

built in this study. It is anticipated that gravity causes most of the water flow from the invert part of the tunnel into the bottom of the pit. The predicted quantity of water flush into the pit is 0.1225 m^3 per day, which is equivalent to 85 ml per minute.

Ou [13] indicated that the excavation in highly permeable ground may lead to piping failure, which is also closely connected with groundwater, and Pratama and Ou [14] conducted a study using both numerical analyses and an empirical approach to interpret the safety factor against the piping. As indicated previously, the flow line caused by the launching of the shield can be presented, but the software used does not have the function to present the equipotential line and the flow net. Therefore, a personal judgement is required to allow the hydraulic gradient and the safety factor to be interpreted based on the

pressure head and coordinates of the related nodes in the model. A schematic drawing of the flow net and the details of the safety factor against the piping calculation are presented in Figure 13(a). Accordingly, the factor is only 0.09, which should lead to piping failure during the launching of the shield. However, potential of nonfailure case for safety against piping is examined also and it presents the safety factor is much higher but still less than 1, as shown in Figure 13(b). It means potential of piping failure still exists for nonfailure case which is connected to different definitions and mechanism of failure in analyses. It is thus recommended that an additional check for safety factor against piping of any nonfailure case shall be considered.

To further evaluate the impacts from soil permeability, strength, and stiffness, parametric studies were conducted on
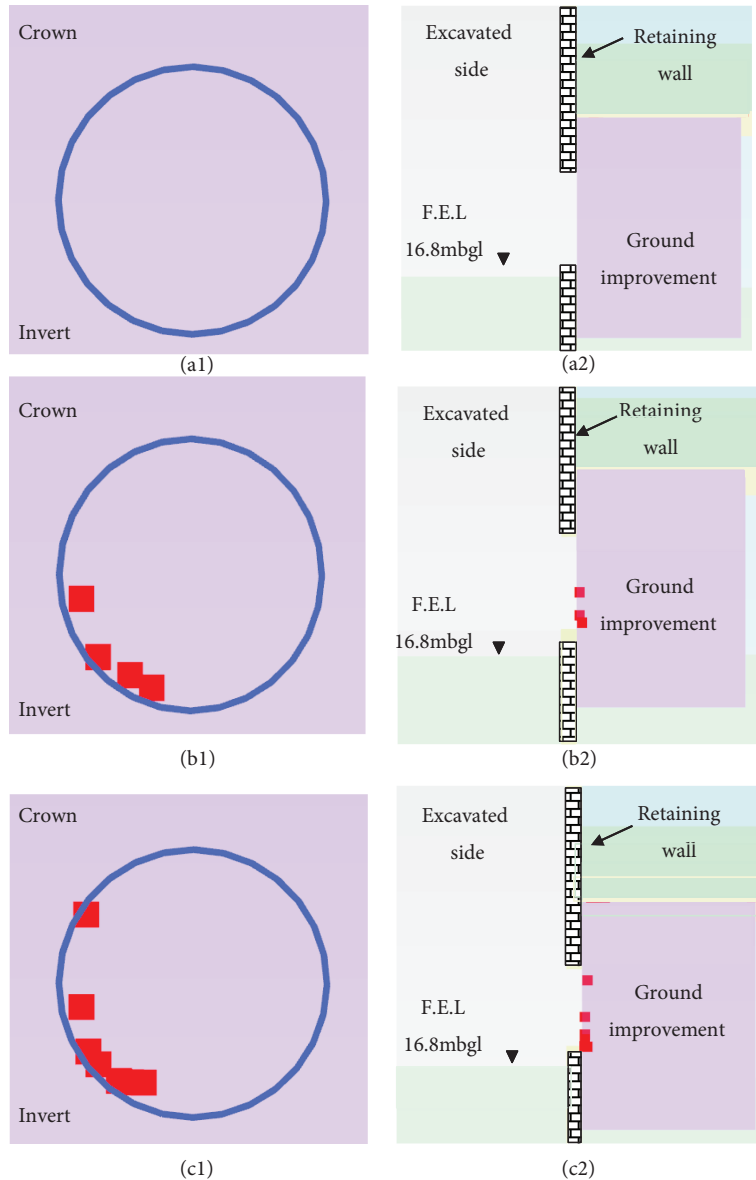
FIGURE 16: Impacts from various soil stiffness (elastic modulus) on failure caused by launching of a shield for (a) 65×10^3 kPa, (b) 130×10^3 kPa, and (c) 260×10^3 kPa. Note: "1" means transverse direction and "2" means longitudinal direction.

geohazards and failure caused by groundwater. Figure 14 presents the failure soils in the model from the views of both transverse and longitudinal directions for the permeability of the improved soils with values of 10^{-6} cm/sec, 10^{-5} cm/sec, and 10^{-4} cm/sec. More failure soils are found to be gradually associated with decreasing permeability, and it is suggested that permeability plays an important role in the control of soil failure. In addition, the failure of soil can be prevented if soil permeability can be reduced through the necessary soil improvement activities.

Figure 15 shows the improved soils with the cohesion force increasing from 50 kPa to 200 kPa. As shown in Figure 15, the soils are likely to fail if only 50 kPa of cohesion exists; however, the status can change to "no failure" for 200 kPa of cohesion. This is consistent with the conclusion of Dano et al. [9]: a higher cohesion force increases the failure strength of the soil and is the basis of such a phenomenon.

Impacts due to the elastic modulus of improved soils are also examined. The elastic modulus of the improved soils is assumed to be 65,000 kPa, 130,000 kPa, and 260,000 kPa. Soils with an elastic modulus of 65,000 kPa can reach the "no failure" status; however, more failure soils were observed once the elastic modulus of the improved soils increases, as shown in Figure 16. Because the failure strength of improved soils remains unchanged, it is likely that a very small strain can easily cause soils to reach failure once the improved soil becomes very stiff. Therefore, one can draw a conclusion that a very high elastic modulus of the improved soil may not be sufficient to prevent the failure of soils due to groundwater during underground excavation.

5. Conclusions

The following conclusions can be drawn based on this study:

(1) It is well recognised that groundwater plays an important role in urban underground excavation and very often leads to catastrophic hazards. Such hazards include geotechnical failure caused by leakage of the tunnel eye via launching and docking of the shield, failure of cross-passage construction for tunnelling, and failure of the retaining wall or diaphragm wall caused by water ingress for deep excavation as well as rupture of a water main or sewer caused by any construction activity of deep excavation or nearby tunnelling, especially for highly permeable ground with a high groundwater level

(2) For geohazards induced by groundwater in urban underground excavation, leakage and failure of the tunnel eye during launching of the shield were selected for further simulation using finite element analyses; this important work had not been previously performed. A three-dimensional model was built to simulate the pore pressure distribution, the quantity of flush-in groundwater, the flow direction, and the failure of soils during launching of the shield. As failure of cross passage and leakage of diaphragm wall related to underground water also often lead to catastrophic accidents, simulations of both matters can be considered to be delivered to understand related behaviours and mechanism in the future

(3) Considering current assumptions and the results of the study, it was concluded that most of the failed soils are located at the invert of the tunnel, immediately behind the wall. According to site observations, it is likely that gravity is the cause of such failure phenomena. However, findings also indicate that all soils located 1 m from the wall remain stable and do not fail

(4) The pore pressure of soils is significantly reduced during launching of the shield as the ingress of water simultaneously releases the pore pressure of the soils behind the wall. The predicted quantity of water through the tunnel eye during launching of the shield is 85 ml per minute. According to the evaluation of the changes in the mean effective stress (p') and the deviator stress (q), both p' and q increase during the process of shield launching

(5) After examining the potential of piping, it is suggested that the current arrangements of improved soils outside the pit would not prevent piping failure during the launching of the shield. However, an additional check for safety factor against piping of any nonfailure case shall be considered due to different definitions and mechanism of failure

(6) The results of a parametric study of the impacts of the permeability, strength, and stiffness of improved soils on the geohazards and soil failures caused by groundwater ingress suggested that the reduction in soil permeability and the increase in cohesion force can successfully prevent the opportunities of failure.

In contrast, a very high elastic modulus may not help to prevent the failure of soils

Data Availability

The data used to support the findings of this study are available from the corresponding author upon request.

Conflicts of Interest

The author declares no conflicts of interest.

References

[1] H. Wanger and M. Knights, "Risk management of tunneling works," in *Workshop on safety in tunnels and underground structure*, pp. 8-9, International Tunnel Association, Riyadh, 2006.

[2] British Tunnel Society, *The Joint Code of Practice for Risk Management of Tunnel Works in UK*, British Tunnel Society, 2003.

[3] S. Degn Eskesen, P. Tengborg, J. Kampmann, and T. H. Veicherts, "Guidelines for tunnelling risk management: international tunnelling association, working group no. 2," *Tunnelling and Underground Space Technology*, vol. 19, no. 3, pp. 217–237, 2004.

[4] GEO, "Geotechnical risk management for tunnel works," in *GEO Technical Guidance Note No. 25 (TGN25)*, Hong Kong, China, 2005.

[5] The International Tunnelling Insurance Group, *A Code of Practice for Risk Management of Tunnel Works*, International Tunnel Association, 2006.

[6] Z. C. Moh and R. N. Hwang, "Lessons learned from recent MRT construction failure in Asia Pacific," *Journal of Southeast Asian Geotechnical Society*, vol. 38, pp. 122–137, 2007.

[7] G. T. Senthilnath, "Mid- tunnel undergound docking of tunnel boring machine in Singapore," in *Challenges and Innovation to Geotechnics. Proceedings of the 8th Asian Young Geotechnical Engineers Conference*, Astana, Kazakhstan, August 2016.

[8] B. C. B. Hsiung, K. H. Yang, W. Aila, and C. Hung, "Three-dimensional effects of a deep excavation on wall deflections in loose to medium dense sands," *Computers and Geotechnics*, vol. 80, pp. 138–151, 2016.

[9] C. Dano, P. Y. Hicher, and S. Tailliez, "Engineering properties of grouted sands," *Journal of Geotechnical and Geoenvironmental Engineering*, vol. 130, no. 3, pp. 328–338, 2004.

[10] Y. S. Fang, C. C. Kao, J. Chou, K. F. Chain, D. R. Wang, and C. T. Lin, "Jet grouting with the superjet-midi method," *Proceedings of the Institution of Civil Engineers - Ground Improvement*, vol. 10, no. 2, pp. 69–76, 2006.

[11] B. C. B. Hsiung, "Field performance of an excavation using sleeve grouting," *Proceedings of the Institution of Civil Engineers-ground improvement*, vol. 162, no. 4, pp. 175–183, 2009.

[12] H. Ju, Y. S. Fang, W. C. Huang, and C. Liu, "Rescue and rehabilitation of damaged subway shield tunnels," *Sino Geotechnics*, vol. 155, pp. 1–14, 2018.

[13] C. Y. Ou, *Deep Excavation: Theory and Practice*, Taylor & Francis, Netherlands, 2006.

[14] I. T. Pratama and C. Y. Ou, "Analysis of sand boiling failure in deep excavation," in *Proceedings of the 2nd International*

Symposium on Asia Urban, Changsha, Hunan, China, November 2017.

[15] S. Y. Dao, *Application of numerical analyses for deep excavations in soft ground, [Ph.D. thesis]*, National Kaohsiung University of Applied Sciences, Kaohsiung, Taiwan, 2015.

[16] H. S. Liao, "Discussion of design and construction of high-pressure jet grouting," in *Presented in 19th workshop of Sino Geotechnics Foundation*, Kaohsiung, Taiwan, August 2006.

Research Article

Numerical Investigation of Rainfall-Induced Landslide in Mudstone Using Coupled Finite and Discrete Element Analysis

Ching Hung [iD],[1,2] Chih-Hsuan Liu,[1] and Chia-Ming Chang[1]

[1]*Department of Civil Engineering, National Cheng Kung University, No. 1 University Road, Tainan City, Taiwan*
[2]*Disaster Prevention Research Institute, Kyoto University, Uji, Kyoto, Japan*

Correspondence should be addressed to Ching Hung; chinghung@mail.ncku.edu.tw

In this study, the role of water infiltration on a rainfall-induced landslide in mudstone is investigated. Finite element analysis (FEA) and discrete element analysis (DEA) were employed to explore the driving mechanism in the prefailure regime and the dynamic runout process in the postfailure regime, respectively. The driving mechanism was revealed in terms of the pore water pressures, saturation, and displacement of the sliding zone. To account for water infiltration associated with the dynamic runout process of the landsliding, the sliding friction coefficient in DEA was examined. Based on the results, satisfactory agreement between the numerical analysis and landslide behavior was realized. In prefailure regime, the onset of landslide initiation was found through assessment of rapid change of source displacement (RCSD). The estimated seepage force was about 0.5 N at landslide initiation. In postfailure regime, the results demonstrate that water infiltration and transition in steepness play significant roles in the behavior of the dynamic runout process. The landsliding exhibited a maximum speed of 4.41 m/s and decelerated as it reached a more gentle slope. Overall, the study indicated that the coupling of FEA and DEA can be used to investigate the role of water infiltration and provide useful insights. The approach can be further applied for studies on many other rainfall-induced geohazards to disclose the role of water infiltration with the prefailure and postfailure characteristics.

1. Introduction

Rainfall-induced landslides are a common geohazard worldwide in tropical and subtropical regions [1–3], and studies have clearly indicated that these hazards are destructive to properties and lives [4–6]. Situated within a mountainous subtropical region with frequent typhoons, rainfall-induced landslides have been a critical issue for Taiwan [7]. To facilitate accurate prediction and provide countermeasures for reducing landslide damage, failure mechanisms of rainfall-induced landslides have been studied in recent years [8–10]. These studies indicate that water infiltration may play a critical role in landslide occurrence through a decrease in suction and increase in saturation and unit weight, making slopes unstable. Furthermore, to predict areas prone to rainfall-induced landslides, the dynamic runout behaviors of rainfall-induced landslides have been investigated [11, 12]. Although the above studies highlighted

the role of water in rainfall-induced landslides, they are rather limited to areas where sandstone and shale prevail. Note that it is also essential that a practical approach towards connecting failure mechanism and runout behavior be established to enhance understanding of landsliding.

On September 28, 2016, typhoon Megi slammed Taiwan and forced more than 14,000 people to evacuate from mountainous regions near the coast to government shelters. Among the damage caused, a mudstone landslide in Yanchao district, Kaohsiung, was induced by the rainfall of typhoon Megi. Of particular note is that, although the affected area is considered small-scale (<10 ha) [13], it damaged a two-story residential building, led to three deaths, and raised public attention to landslides in the region. Despite the fact that mudstone is common in southwestern Taiwan and has a proclivity to fail under heavy rain [14, 15], the failure mechanism and dynamic process in these site conditions have not been extensively studied. Consequently, the 2016 Yanchao

mudstone landslide provides a unique opportunity to examine the driving mechanism and dynamic process of these slope failures.

With rapid advancement in computing capabilities, numerical simulations have become a more prevalent tool to reconstruct and analyze the progress of slope failures, which facilitates better understanding of the driving mechanism and dynamic process of landsliding [16–18]. Of particular utility for the analysis of landslides is finite element analysis (FEA) and discrete element analysis (DEA). FEA has been utilized in investigating the role of water infiltration such as the change of pore water pressure and the strain of geomaterial interacting water. Leshchinsky et al. [19] used coupled transient unsaturated seepage-stress FEA to investigate the complex behaviors of the progressive slope failure in Yumokjeong, Korea. Yang et al. [10] coupled FEA and unsaturated seepage concept to investigate the failure and deformation mechanisms of slopes in Taipei, Taiwan. Both studies demonstrated that FEA is a useful approach for reviewing the role of water infiltration in prefailure regimes. Recent studies have also suggested the FEA can be used to the initiation time of landsliding and defines the initiation time as the time when a rapid change of source displacement (RCSD) surfaced [20, 21].

In addition to FEA, DEA is an effective approach for studying dynamic process of landslides that deaggregate or flow after failure, given that it treats geomaterials as discontinuous bodies [22–26]. The approach was first utilized to simulate problems relating to rock mechanics [22] and other geomaterials [23] and has been applied to simulate landslide problems in recent decades, as it is capable of simulating the kinematic process and runout dynamics that occur after failure [24–26].

In this study, a coupled approach of finite element analysis (FEA) and discrete element analysis (DEA) is employed to analyze the rainfall-induced landslide in Yanchao mudstone, a geomaterial common in the mountainous areas of southwestern Taiwan. Analysis of the landslide was divided into the prefailure and postfailure regimes, involving evaluation of the driving mechanism and dynamic runout process. The influence of partial saturation was considered through coupling of the soil water characteristic curve (SWCC), hydraulic conductivity function (HCF), and unsaturated shear strength for the modeled geomaterials [10, 19, 27–29], used to investigate the onset of failure. The variations of pore water pressure, saturation, and rate of source displacement in the sliding zone are compared and discussed. The dynamic runout process was simulated based on the commercial particle flow code [30], obeying Newton's second law. The seepage forces and reduced sliding friction coefficient were considered within the discrete element method analyses to capture the impacts of water infiltration [11, 12]. The runout behavior of the landslide is characterized by discrete particles and walls, and six phases were presented to enable better understanding of the dynamic process of landslide movements after failure. This study provides new insight into the influence of precipitation on the onset of failure and the runout behavior of landslides that occur in mudstone using coupled numerical modeling.

2. Study Area

The landslide occurred in the Yanchao district of Kaohsiung city, Taiwan, in the early morning of September 28, 2016. The failure occurred as a result of rains brought by the typhoon Megi. The nearest rain station is the Agongdian rain station which is located approximately 3 km northwest of the landslide (Figure 1, 120.3552 long. 22.8041 lat., 56 m asl.), where rainfall totals were measured hourly. The rain data showed that the total accumulated rainfall was 408.5 mm from the period of September 27, 12 a.m., to September 28, 12 p.m. According to the Central Weather Bureau (CWB), the event was classified as an extreme torrential rain event. Interestingly, very few landslides had been observed in the areas comprised of mudstone, resulting in a newfound awareness of a hazard that was not considered previously. This event resulted in the revision of local landslide hazard maps, produced by the government, to include areas of mudstone that were potentially unstable.

In southwestern Taiwan, the mudstone formation was formed in the end of the Tertiary Period to the early Quaternary Period [15]. According to ISRM classification [31], mudstone is classified as very weak to extremely weak rock in a high water content. Based on its characteristic, the behavior of a mudstone landslide would progress like a flow-like landslide. Understanding the interplay of rainfall in a mudstone landsliding would help reveal the prefailure mechanism. Figure 2 shows the photos taken from the site investigation after the landslide, where cracks can be seen on the surface of the surrounding geomaterials. Figure 3 shows the cross section (line A-A′) before and after the landslide, composed of the mudstone (Ku-ting-keng formation) and weathered formations [32]. The resolution of the cross section was 16 cm and was created using a digital elevation model (DEM) with the aid of unmanned aerial vehicle (UAV) photos, in which the source area was depicted. Note that steeper and gentler slope angles of 27 and 15 degrees, respectively, are delineated based on the DEM. The sliding mass occupied an area of about 4350 m^2, and the total estimated volume was about 8700 m^3. The height, length, and width of the sliding zone (source area) are approximately 45, 90, and 30 m, respectively. Of particular interest is the observation that the damaged building at its toe displaced about 12–14 m from its original position. To acquire the permeability of geomaterials, the field test proposed by Hoek and Bray [33] was conducted and a saturated hydraulic conductivity of 8.33×10^{-5} m/s was obtained. Other laboratory tests, including grain size distributions, unit weight tests, and specific gravity tests, were also conducted to get the basic properties of sliding mass.

3. Methodology

The principles that govern FEA and DEA are briefly introduced to provide context to the numerical modeling performed in this study. To address the role of water infiltration, FEA incorporated the flow equation controlling the unsaturated filtration and the coupled stress-pore
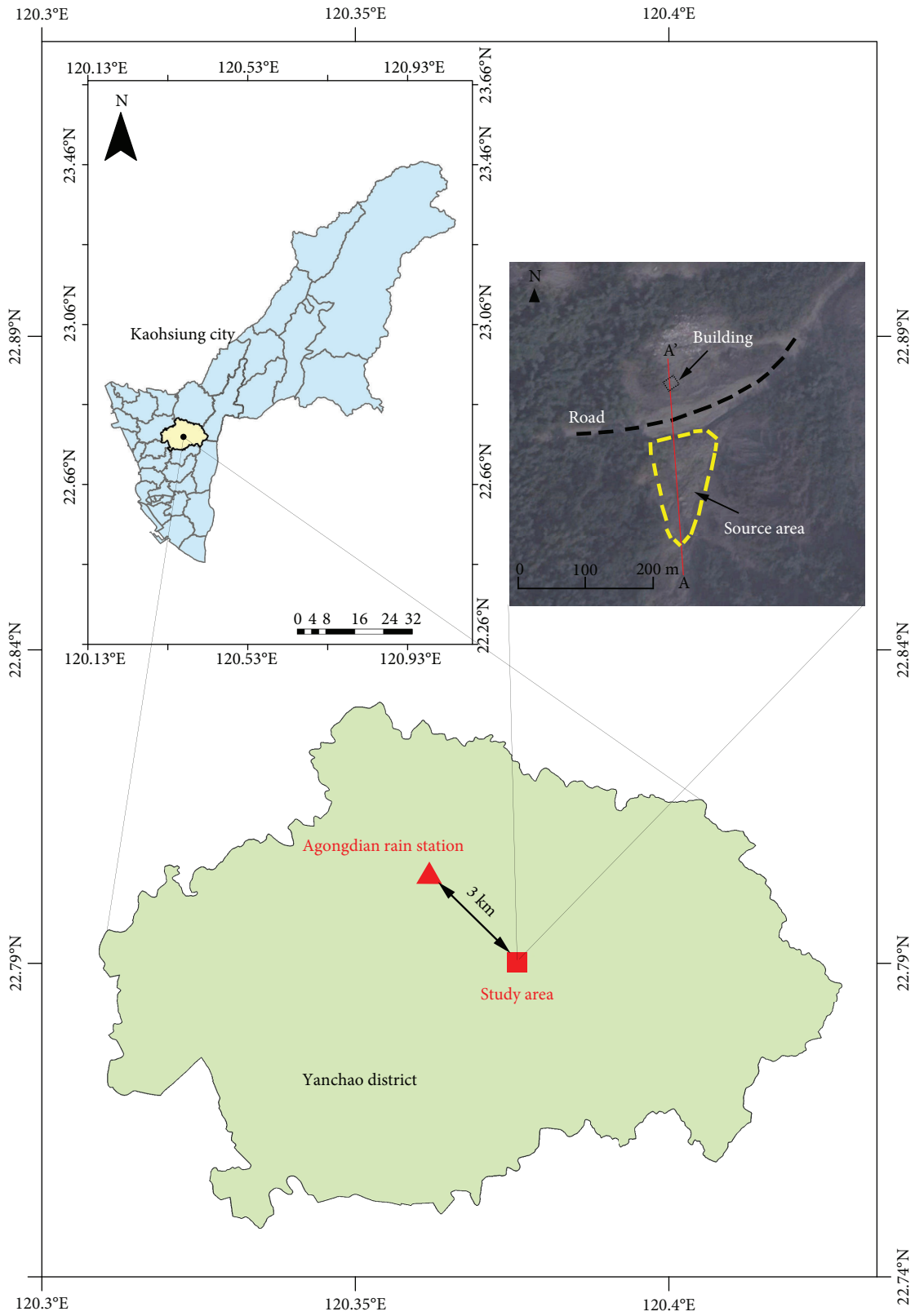
FIGURE 1: Location of the study area and the Agongdian rain station.

pressure formulation, which requires the integration of the concepts including soil water characteristic curve (SWCC), hydraulic conductivity function (HCF), and unsaturated shear strength [10, 19, 27–29]. The algorithm in DEA is based on particle flow code (PFC), seepage force, and sliding friction coefficients [11, 12, 26, 30, 34].
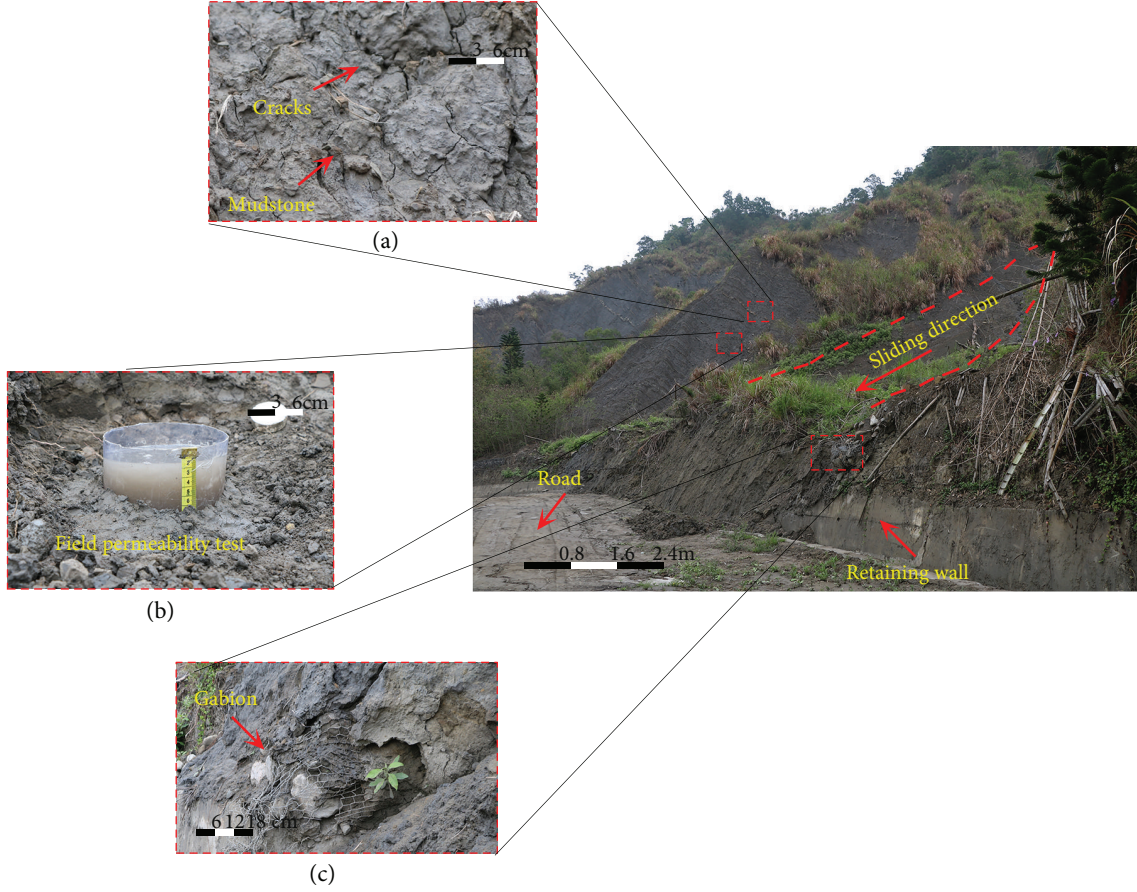
FIGURE 2: (a) The geomaterials of the study area, (b) field permeability test (after Hoek and Bray [33]), and (c) the condition of retaining the structure after the failure.
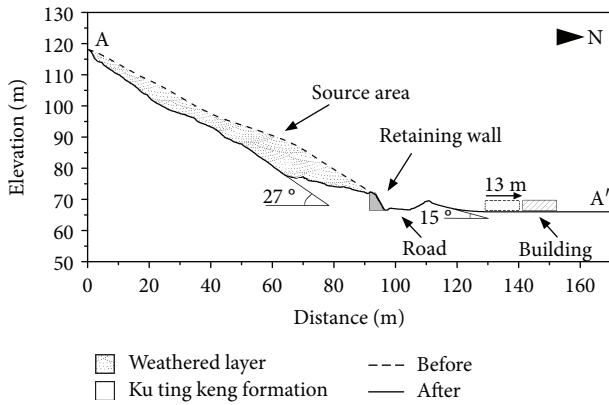
FIGURE 3: Schematic of the terrain and geomaterials of the study area (after Chen [32]).

3.1. Finite Element Analysis (FEA).
In FEA, the failure mass of the landslide can be represented by a large number of small elements, enabling quantitative assessment of the prefailure behavior of the landslide, evaluated through time-dependent iterations of the coupled stress-pore pressure formulation until a convergence is achieved.

The movement of the water in unsaturated soil was derived from Richards equation [35]:

$$k_x \frac{\partial^2 h}{\partial x^2} + k_y \frac{\partial^2 h}{\partial y^2} = \frac{\partial \theta}{\partial t} = m_w \rho_w g \frac{\partial h}{\partial t}, \qquad (1)$$

where k_x and k_y represent the hydraulic conductivities in the x and y directions, respectively, h is the total hydraulic head of flow, θ is water content, m_w is the coefficient of water volume change, ρ_w is the unit weight of water, g is gravity, and t is the time.

The coupled stress-pore pressure formulation is defined as

$$\int_v \sigma : \delta \varepsilon dV = \int_s t \cdot \delta v \, \delta S + \int_v f \cdot \delta v \, dV + \int_v (Sn + n_t) \rho_w g \cdot \delta v dV, \qquad (2)$$

where V is volume, σ is true stress, $\delta \varepsilon$ is the virtual rate of deformation, δv is the virtual velocity field, t is surface tractions per unit area, f is the body force barring the weight of the liquid (water), n is porosity, n_t is the volume of trapped wetting liquid per unit of current volume, S is the degree of saturation, ρ_w is the unit weight of water, and g is gravity [19, 29]. The last term in (1) represents
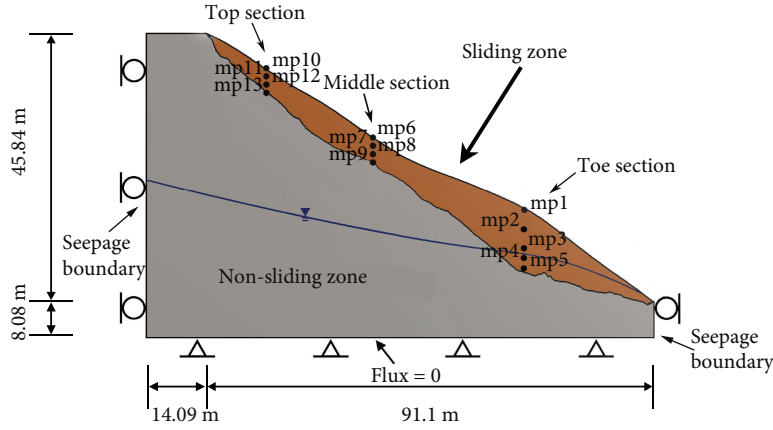
FIGURE 4: The slope geometry and boundary conditions.
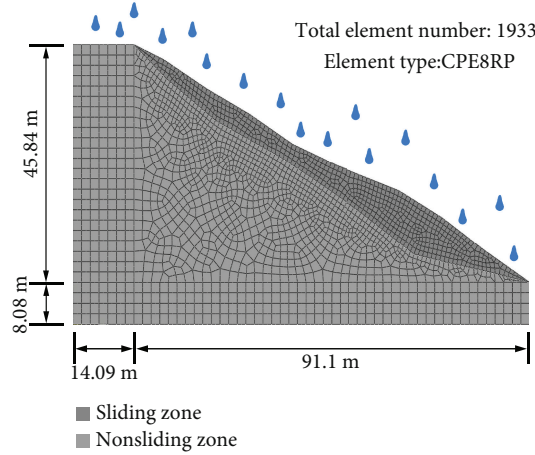
FIGURE 5: The finite element meshes used in FEA.

the body forces of trapped wetting liquid in the voids and the volumetric flow rate of water to capture both the weight of the water and the inertial effects of flow, known as the Forchheimer term [36]. The principle of virtual work represented in (1) is evaluated for equilibrium in the volume under consideration in its current configuration at time t under transient seepage induced by boundary conditions representative of rainfall.

The SWCC describes the relationship between matric suction and the normalized volumetric water content while the HCF evaluates changes in hydraulic conductivity with the normalized volumetric water content. SWCC and HCF were utilized in the study following van Genuchten-Mualem's model [27, 28]. Then, since the normalized degree of saturation is equal to the normalized volumetric water content, the SWCC and the HCF can be expressed as

$$\frac{\theta - \theta_r}{\theta_s - \theta_r} = \left(\frac{1}{1 + [\alpha(u_a - u_w)]^n} \right)^m,$$

$$k_{rel} = \frac{k_{usat}}{k_{sat}} = S_e^{1/2} \left[1 - \left(1 - S_e^{1/m} \right)^m \right]^2, \quad (3)$$

where S_e is the normalized degree of saturation; θ is the water content; θ_s is the saturated water content; θ_r is the residual water content; α, n, and m are constants; $(u_a - u_w)$ is suction (where u_a and u_w are the pore pressure and pore water pressure, respectively); k_{rel} is the relative hydraulic conductivity; k_{usat} is the unsaturated hydraulic conductivity; and k_{sat} is the saturated hydraulic conductivity.

To evaluate the unsaturated shear strength, the study uses the equation proposed by Vanapalli et al. [37], which is defined as

$$\tau = c' + (\sigma - u_a)_f \tan \varnothing' + \frac{\theta - \theta_r}{\theta_s - \theta_r} (u_a - u_w)_f \tan \varnothing', \quad (4)$$

where τ is the soil shear strength, $(\sigma - u_a)_f$ is the normal stress on the failure surface at failure, $(u_a - u_w)_f$ is suction on the failure surface at failure, $\varnothing'$ is the effective friction angle, and c' is effective cohesion.

3.2. Discrete Element Analysis (DEA). The commercial program particle flow code (PFC), based on the concept of DEA, was utilized in this study. The program, featuring
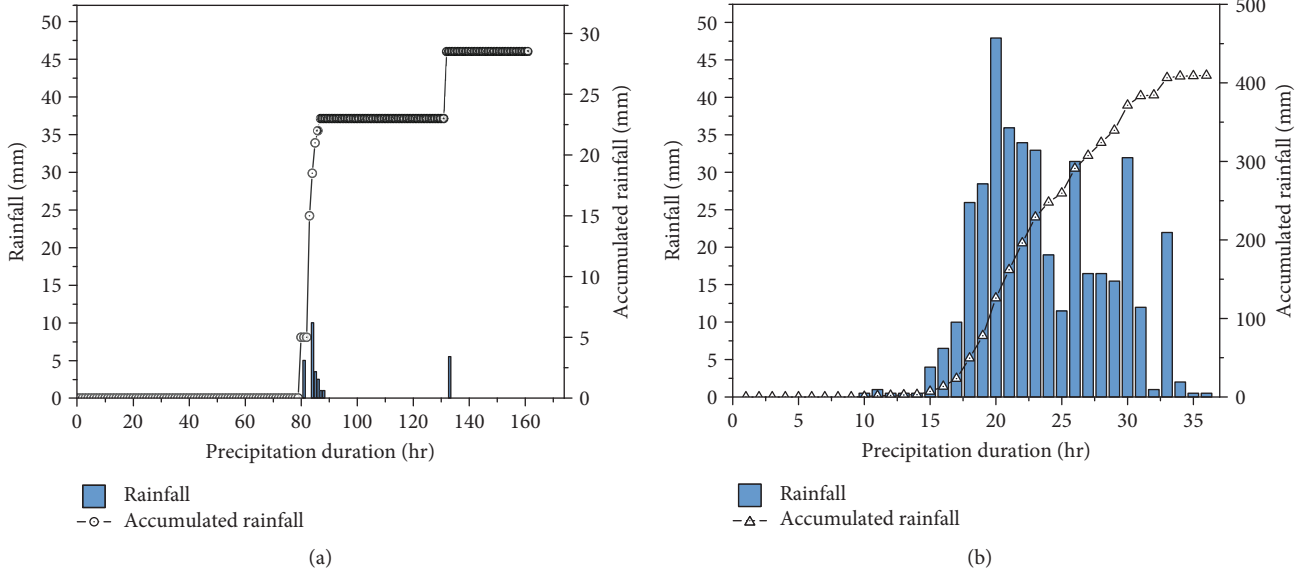
FIGURE 6: (a) The antecedent rainfall data used in FEA and (b) the typhoon rainfall data used in FEA.

TABLE 1: The input geomaterial parameters in FEA.

Geomaterial	Model	Unit weight[a] (kN/m^3)	Poisson's ratio[a]	Cohesion[b] (kPa)	Friction angle[b] (°)	Saturated hydraulic conductivity (m/s)	Young's modulus[a](kPa)
Sliding zone	Mohr-Coulomb	21.58	0.25	16.4	17	5.5×10^{-5}	2×10^4
Nonslide zone	Mohr-Coulomb	21.58	0.25	1530	26.7	5.5×10^{-5}	2.273×10^5

[a][15], [b][43, 44].

particles and boundary conditions, is suitable for analyzing the postfailure kinematic process of landslide runout [24, 34]. Through a continuous calculation cycle, the force-displacement law is obeyed on the contacts between particles and Newton's second law is maintained to compute the new velocity and position of particles.

The effect of water infiltration on landsliding has been addressed, in which the importance of water head difference (seepage force) and the decreased interparticle sliding friction coefficient are determined [11, 12, 26]. To address the effect of water infiltration and realistically simulate the landslide, the study considered seepage forces and the decreased friction coefficient stemming from precipitation. The seepage force is computed by the following equation:

$$F = \gamma_w \times i \times V, \qquad (5)$$

where F is the seepage force, γ_w is the unit weight of water, i is the hydraulic gradient, and V is the volume of each particle [11, 38]. Due to the fact that the damaged building (the reference for runout behavior) moved about 12–14 m in the Yanchao mudstone landsliding, the decreased friction coefficient could be explored through sensitivity analysis to provide insights on the effect of water infiltration [39].

4. Numerical Simulation

The setting of FEA and DEA is introduced in this section. The setting in the FEA includes the modeling, boundary conditions, and material properties, while the setting in DEA includes transformation and calibration of parameters and modeling.

4.1. FEA Model and Boundary Conditions. In FEA modeling, the landslide mass was discretized differently than the area outside the failure plane. The bottom boundary was restrained in the vertical and horizontal directions, and the two lateral boundaries were restrained in the horizontal direction. The two lateral hydraulic boundaries were set to permit change in the ground water level (GWL) accounting for water infiltration while the bottom hydraulic boundary was set as impervious. The slope geometry and boundary conditions are illustrated in Figure 4.

To calculate the change of the pore water pressure and saturation, eight-node pore-stress, reduced-integration quadrilateral elements (CPE8RP) were used to discretize the model. The model is comprised of 1933 elements, as shown in Figure 5. Thirteen monitoring points were prescribed in the sliding zone to measure the change of the pore water pressure, saturation, and displacements throughout the landslide mass and were divided into three sections including the toe, middle, and top (Figure 4).

(a)

(b)

(c)
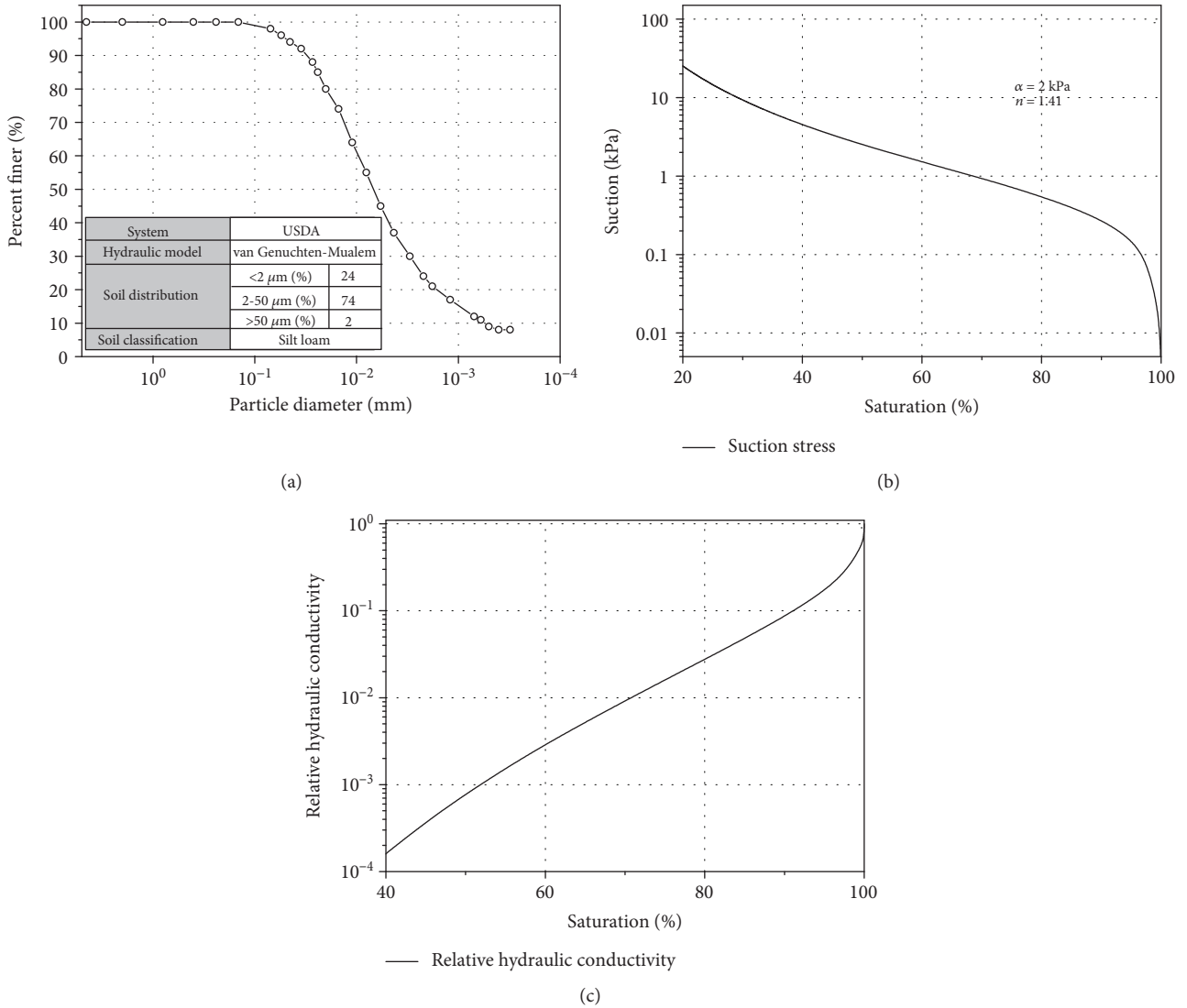
FIGURE 7: (a) Particle distribution curve; (b) soil water characteristic curve (SWCC); (c) relationship between the relative hydraulic conductivity and the saturation based on the hydraulic conductivity function (HCF).

TABLE 2: Comparison between macroparameters of DEA model and laboratory experiment.

	Macroparameters of the DEA model	Macroparameters of laboratory experiment
Young's modulus (kPa)	1.9×10^4	2×10^4
UCS (kPa)	168	169

TABLE 3: Microparameters in the DEA models.

Microparameters of PFC model	Sliding zone	Building[a]
Minimum radius (m)	0.08	0.5
Maximum radius (m)	0.09	0.5
Normal stiffness (GPa)	0.03	36
Stiffness ratio (kn/ks)	1.2	32.72
Friction coefficient	0.05	1
Parallel bond normal stiffness (GPa)	0.03	20
Parallel bond stiffness ratio (kn/ks)	1.2	3.33
Parallel bond tensile strength (kPa)	170	2.8×10^6
Parallel bond cohesion (kPa)	15	2.8×10^6

[a][50].

The FEA model was divided into three steps including the gravity, antecedent rainfall, and typhoon rainfall. In the gravity step, the initial pore stress, based on unit weight of geomaterial, was computed and the distribution of the initial water pressure was established by hydraulic boundaries. The distribution of the initial water pressure was determined by achieving hydraulic equilibrium based on the development feasibility report by China steel [40]. In general, it is difficult

to discern groundwater flow regimes with any great certainty in the field. However, at the assumed domain, the lateral and bottom boundaries were considered to be under "far-field"
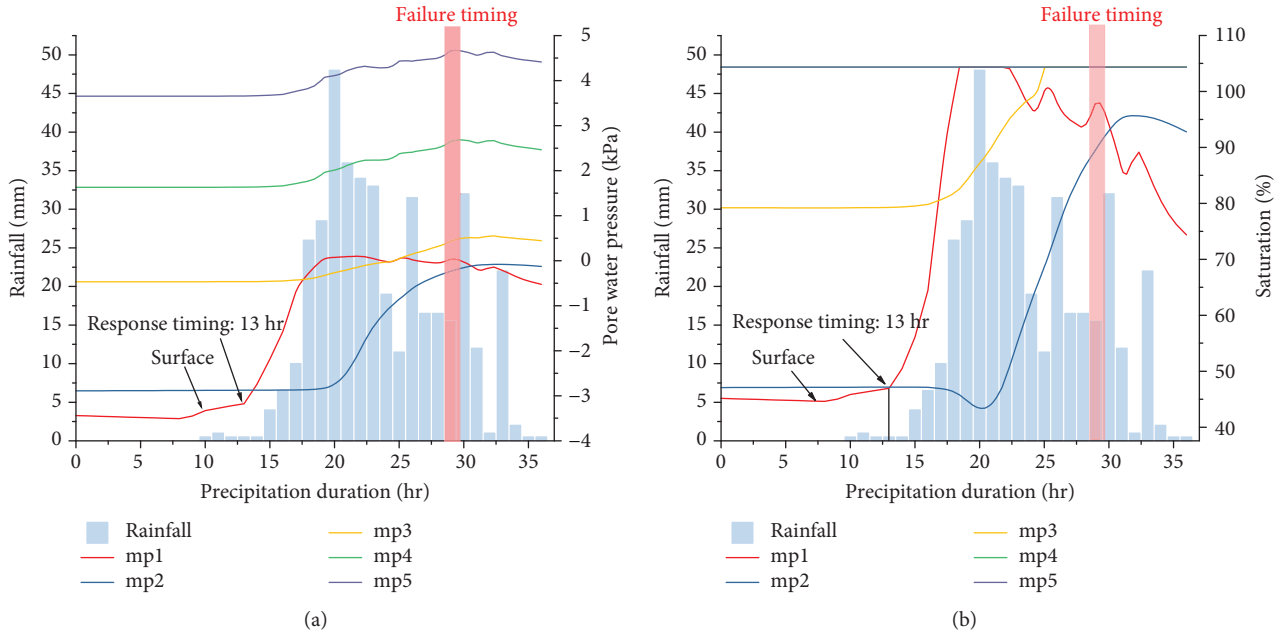
Figure 8: (a) The variation of the pore water pressure for monitoring points: mp1–5. (b) The variation of the saturation for monitoring points: mp1–5.

constant flow conditions (i.e., zero fluid flux), and the regimes were specified at nodes located along these boundaries.

The effect of the antecedent rainfall was considered in the study because previous studies have revealed that antecedent rainfalls have an influence on slope stability [18, 41]. According to Rahardjo et al. [42], cumulative rainfall in the week prior to a landslide event is important in considering susceptibility of slope failures. Recorded rainfall data for the week preceding the Yanchao mudstone landslide is considered for the purpose of establishing realistic initial hydrologic conditions in the study, as shown in Figure 6(a). Finally, the typhoon Megi rainfall data obtained from the Agongdian rain station was applied in the typhoon rainfall step (Figure 6(b)) to incite a slope failure.

4.2. FEA Geomaterial Properties. The geomaterial parameters of the sliding zone and nonsliding zone were established from laboratory tests [15, 43, 44] and were characterized by an elastoplastic Mohr-Coulomb model widely used in the slope analysis [19, 45, 46]. Table 1 summarizes the input parameters of geomaterials used in the present study. The unsaturated hydraulic properties including SWCC and HCF were evaluated by the RETC program combining the grain size distribution and van Genuchten-Mualem's model [27, 28], as shown in Figure 7.

5. Transformation and Calibration of Parameters

In DEA, microparameters such as stiffness and parallel bond stiffness were characterized to represent interactions between particles; however, microparameters cannot be obtained from physical experimentation. Through transformation and calibration, the microparameters can be determined.

The transformation procedure used in this study was suggested by Potyondy and Cundall [47]. The microparameters were calibrated through uniaxial compression test to reproduce macroparameters such as Young's modulus, strain behaviors, and uniaxial compressive strength [24, 25, 48]. The calibrated microparameters and macroparameters are presented in Tables 2 and 3, respectively.

5.1. DEA Model. In the DEA model, the profile of the Yanchao mudstone landslide was created for subsequent release. When simulating runout problems, the stipulated distribution of particle sizes should capture a balance between model resolution and practical computational time [49]. When the particle sizes are adequately small, it sufficiently simulates the flow-like landslide behavior after failure, enabling movement of geomaterials in both vertical and longitudinal directions [26]. To capture this behavior, the sliding mass was constructed using 16,200 particles with radiuses of 0.08–0.09 m, and the nonsliding zone was represented by no displacement boundary condition.

To investigate the effect to water infiltration on landslide runout, a sensitivity analysis was performed against the movement of a building displaced by the landslide at the base of the slope, discretized by rigid particles based on Design Specifications for Concrete Structures Taiwan [50], and the parameters are shown in Table 3. The seepage force could be estimated by coupling the water head difference obtained from the result of FEA and (5).

6. Result and Discussion

6.1. FEA Results and Discussion. Figures 8, 9, and 10 illustrate the variation of saturation and pore water pressure at the monitoring points in three sections during typhoon Megi.
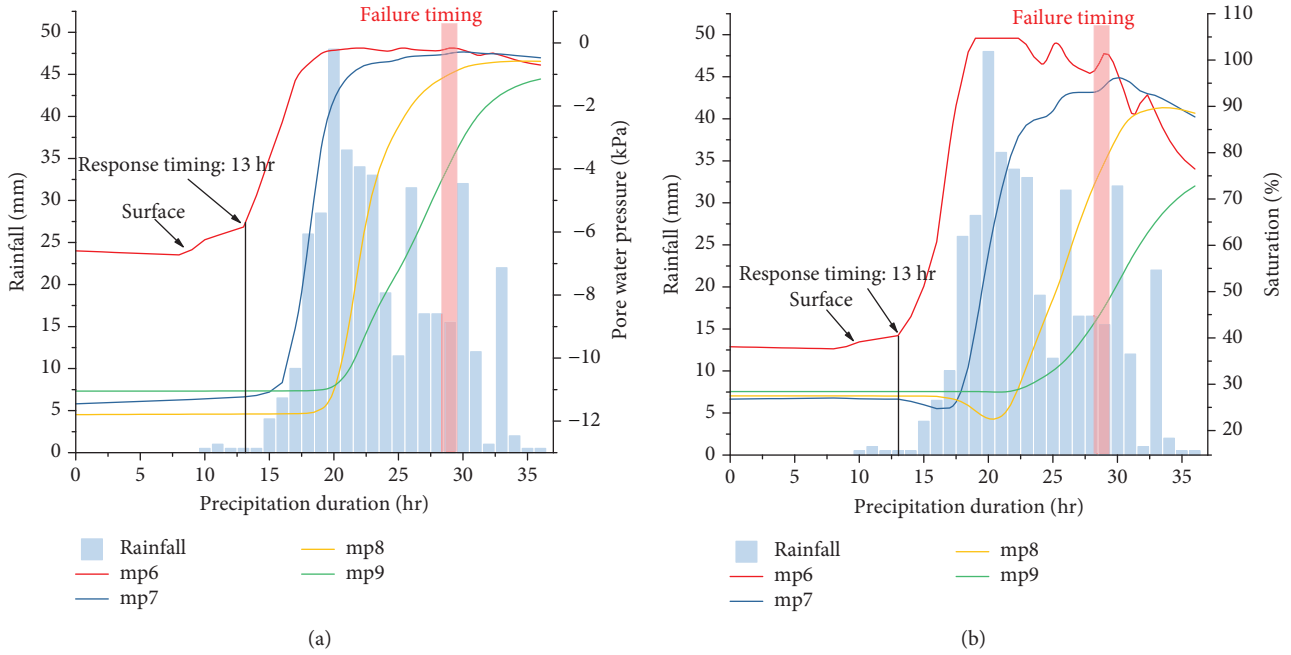
FIGURE 9: (a) The variation of the pore water pressure for monitoring points: mp6–9. (b) The variation of the saturation for monitoring points: mp6–9.
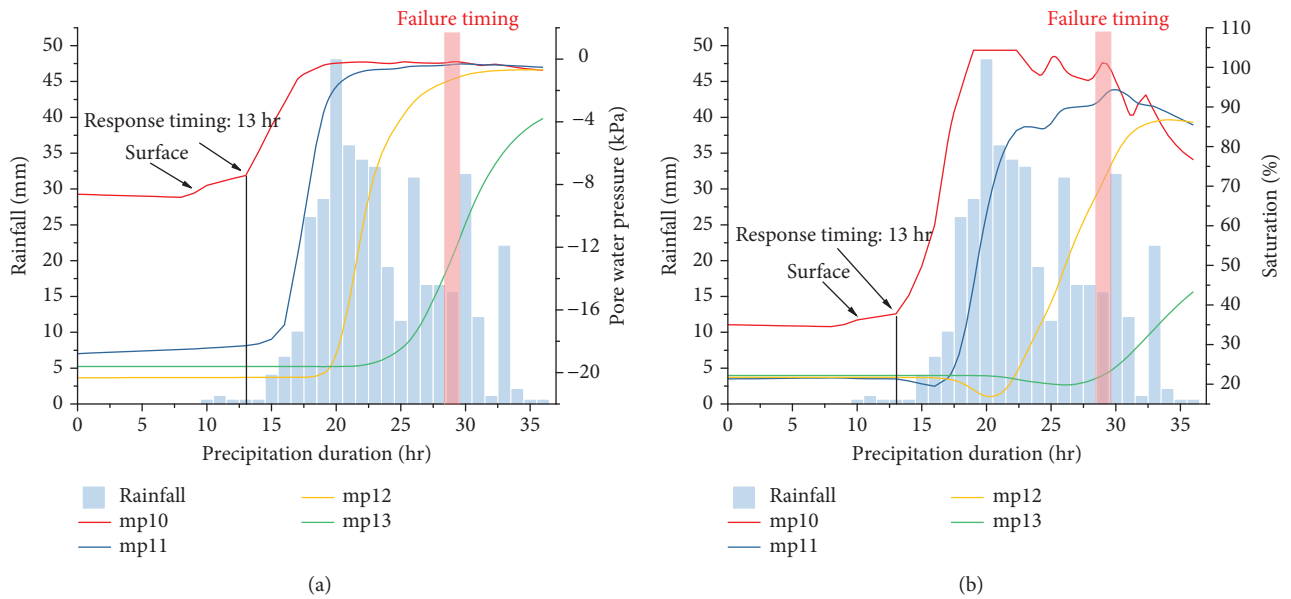
FIGURE 10: (a) The variation of the pore water pressure for monitoring points: mp10–13. (b) The variation of the saturation for monitoring points: mp10–13.

As shown in Figures 8, 9, and 10, when the rainfall intensity is about 0.5 mm/hr at the initial period of precipitation duration (10–12 hr), the variations of saturation and pore water pressure were almost constant in all monitoring points. At $t = 13$ hr, there is a notable increase in saturation and pore water pressures near the surface. This observation is reasonable as rainfall must first pass through the monitoring points near the surface (mp1, mp6, and mp10), called a wetting front. With continuous water infiltration, saturations and pore water pressures increased gradually. At $t = 20$ hr,

the rainfall intensity increased to 48 mm/hr, creating saturations near 100% and positive pore water pressures at the monitoring points near the surface. At $t = 23$ hr, when the water infiltration caused the perceivable increase in the ground water level, pore water pressure near the ground water level (mp3) turned positive. At $t = 28$ hr, the negative pore water pressure (suction) almost dissipates in the toe section and decreased the shear strength and destabilized the slope. In addition, Figure 11 illustrates the displacement for monitoring points near the failure (mp5, mp9, and

(a) Precipitation duration (hr)

(b) Pore water pressure

(c) Deformation

(d) Stress
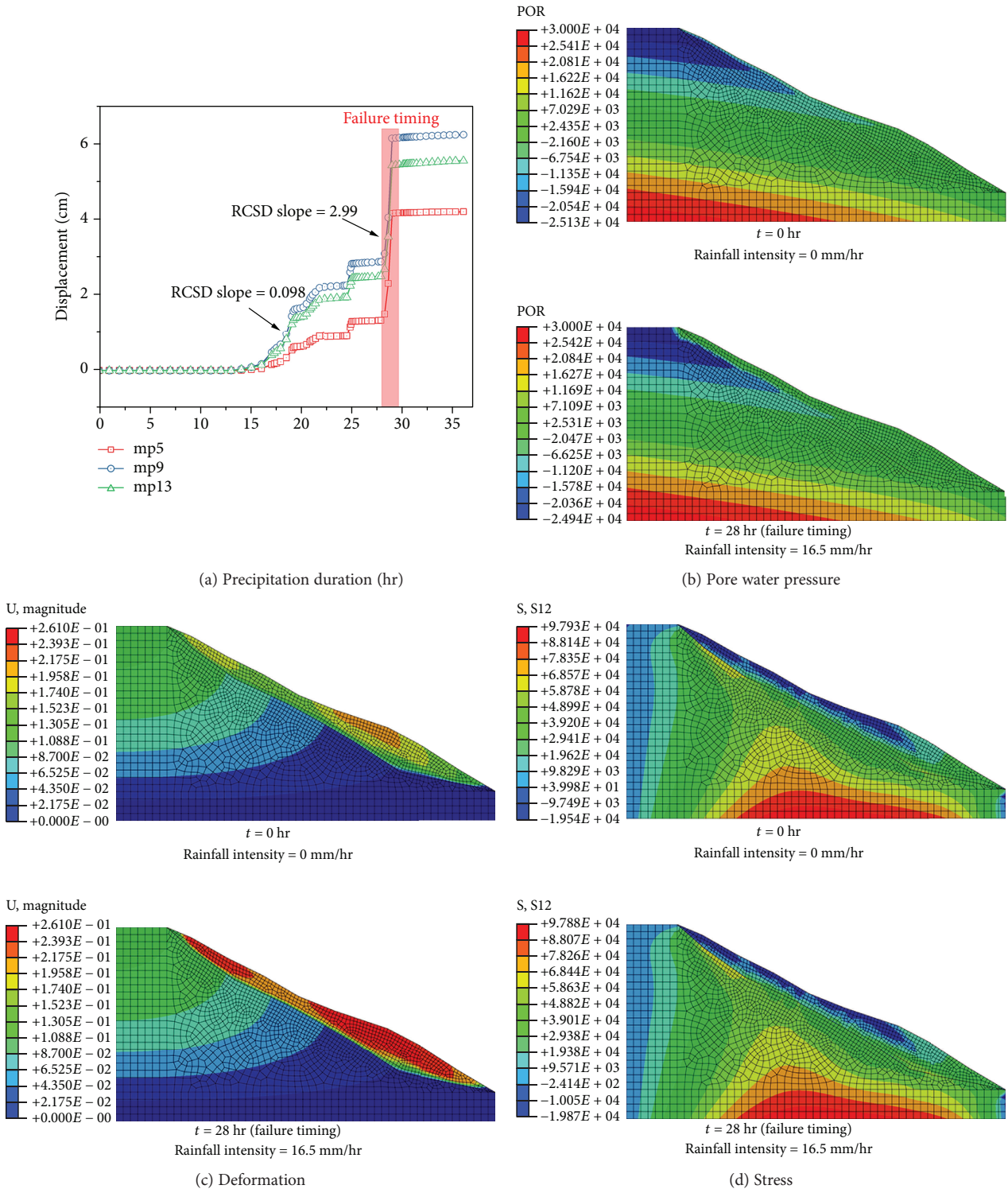
FIGURE 11: The displacement for monitoring points: mp5, 9, and 13.

mp13) of the three sections and the FEA contours during the typhoon rainfall. It is observed that rapid change of source displacement (RCSD) occurred at 28 hr. These results indicate that the likely failure timing was at approximately 28 hr from the beginning of the typhoon rainfall. The results observed in the three monitoring sections also indicated that the effect of the water infiltration resulted in variation

of pore water pressure, saturation, and ground water level, which was consistent with the previous studies [51, 52].

Figure 12 shows the variation of pore water pressure at the monitoring points near the failure of the three sections during the typhoon rainfall. In Figure 12, the response timing of the pore water pressure at mp5, approximately 17 hr, was faster than that at mp9 and mp13, which were
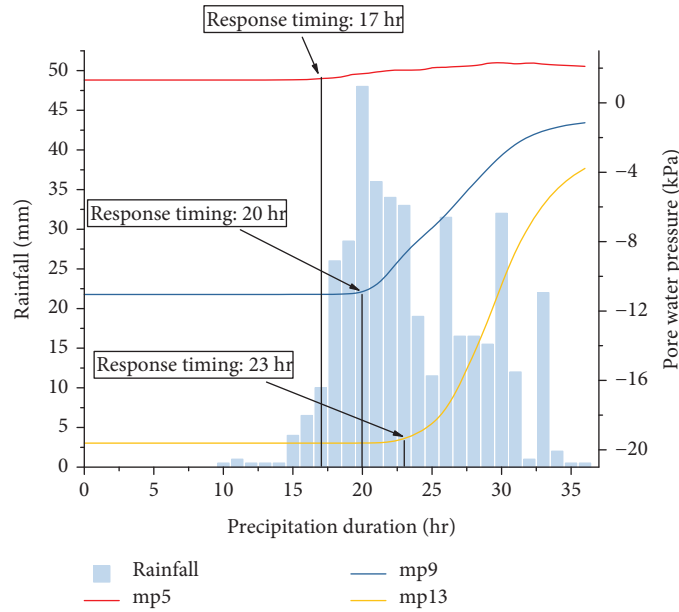
FIGURE 12: The variation of the pore water pressure for monitoring points: mp5, 9, and 13.
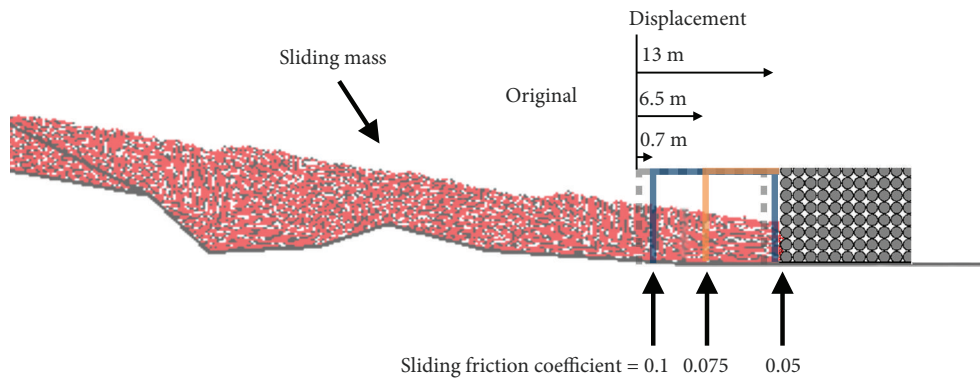
FIGURE 13: The sensitivity analysis for the relationship between the sliding friction coefficient and the displacements.

approximately 20 hr and 23 hr, respectively. Such an observation is reasonable given the monitoring point, as higher permeability causes a shorter response timing, corroborating the lag observed in saturation levels at different monitoring points, each with varying conductivities. The variation of the pore water pressure at mp5 is small because it is located under the ground water level (GWL). The head difference between two hydraulic boundaries at $t = 28$ hr was 9 m. Through coupling the water head difference obtained from the result of FEA and (5), the seepage force was determined to be 0.5 N.

6.2. DEA Results and Discussion. The postfailure behavior of the Yanchao mudstone landslide is considered through DEA modeling that considers the seepage force and reduced friction stemming from precipitation. Through FEA, the failure timing of the landslide was determined to occur at 28 hr after the typhoon started, whereas the seepage force at this time was 0.5 N. The seepage force determined from this

analysis was applied in DEA to account for more realistic initial conditions on landslide runout behavior. Although the friction coefficient required in the DEA cannot be obtained from the physical experimentation, it could be determined through iterative study and comparison of the displacement of the reference building (Figure 13).

Figure 13 shows the relationship between the friction coefficient and the displacement of the building obtained through DEA. A displacement of 13 m was observed with a friction coefficient of 0.05, agreeing to the result observed in the field. It is revealed that a minor difference of the friction coefficient would lead to a significant difference in the displacement of the reference building, as shown in Figure 13. The result also suggested that water infiltration plays a critical role in the kinematic process of the landslide runout as well as the affected areas.

To better understand the kinematic process of the landslide travel, the failure process is divided into six phases (Figure 14). The six phases represented (a) the initial phase,
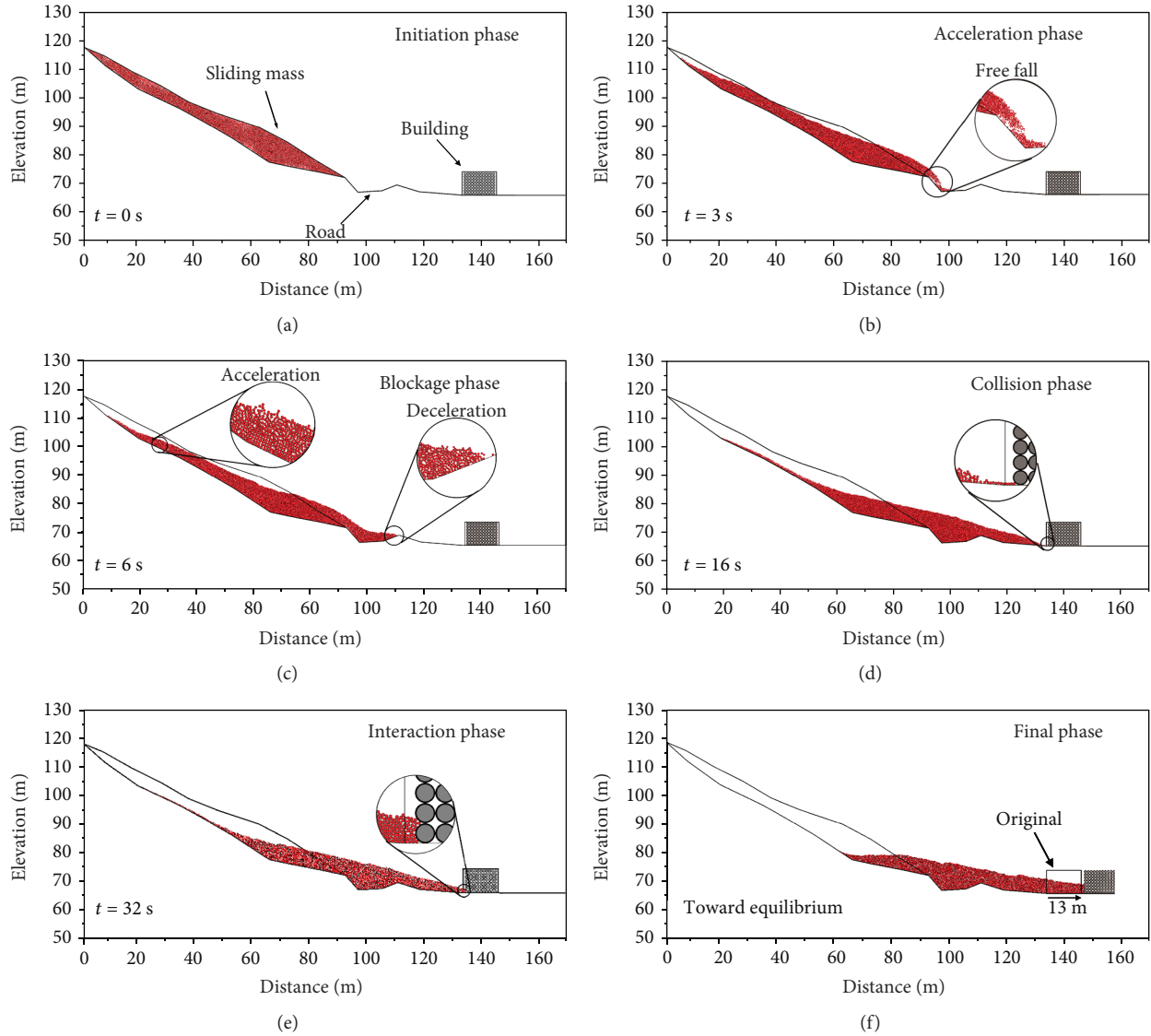
FIGURE 14: The kinematic process of Yanchao mudstone landslide: (a) the initiation phase, (b) the acceleration phase, (c) the blockage phase, (d) the collision phase, (e) the interaction phase, and (f) the final phase.

(b) acceleration phase, (c) blockage phase, (d) collision phase, (e) interaction phase, and (f) the final phase. In general, the results and discussion on each stage are as follows:

(i) Stage (a): at the beginning of the postfailure regime, the seepage force was applied, coupling the result of FEA.

(ii) Stage (b): the sliding mass accelerated along the steeper section of the slope (27°), indicating that the front of the sliding mass was dominated by free falls attributed to the terrain. The maximum average velocity of the sliding mass was reached at this stage, at approximately 4.41 m/s.

(iii) Stage (c): the acceleration of the front of the sliding mass began to drop noticeably as it reached a gentler slope while the back of the sliding mass accelerated

continuously. At this stage, the sliding mass had almost blocked the road.

(iv) Stage (d): the sliding mass moved continuously and began to collide with the reference building. Due to the sliding mass colliding the reference building, the velocity decreased slightly once again.

(v) Stage (e): the interaction between sliding mass and reference building was observed. In this stage, the kinematic process did not yet reach a force balance.

(vi) Stage (f): in the final phase, deposition of the sliding mass was completed. The final displacement of the reference building was 13 m, satisfying the result observed in the field.

Figure 15 presents the relationship between average velocity and time obtained through DEA. As shown in
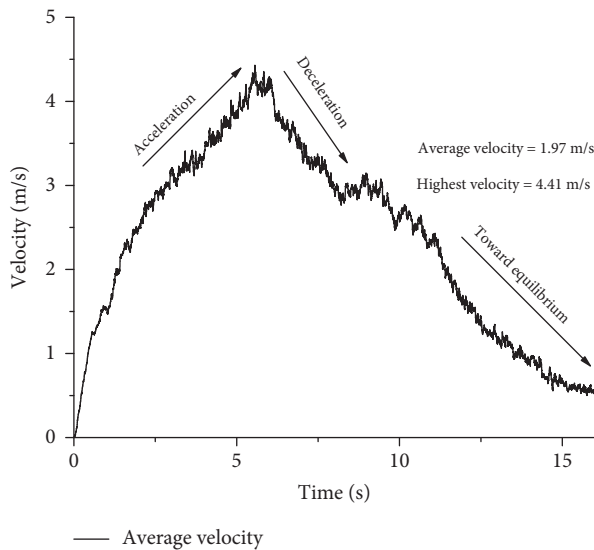
FIGURE 15: The average velocity of the landslide before colliding the reference building.

Figure 15, the average velocity of the landslide before colliding with the reference building was 1.97 m/s ranging from very rapid to extremely rapid velocity classes according to Cruden and Varnes [53], leaving only 16 s to respond from the onset of the landslide. Besides, the velocity fluctuates as a result of particle collisions during the sliding process [54]. Based on the result, it is revealed that the variation of velocity was dominated by the variation of terrain.

6.3. General Discussion. The focus of this paper is on the application of a coupled finite and discrete element on analyzing a rainfall-induced mudstone landslide. The results show that the effects of water infiltration including increases of saturation, pore water pressure, and displacement could be observed during the typhoon rainfall. The variation of saturation and pore water pressure near the surface increased remarkably at $t = 13$ hr, which was earlier than other locations, because rainfall first passes through the monitoring points near the surface.

In general, there are three types of rheology commonly used for simulations of landslides with rapid movements: (i) frictional rheology, (ii) the Voellmy rheology, and (iii) the Pouliquen rheology [55, 56]. Pirulli and Mangeney [56] conducted a comparison between the three rheologies by back analysis on a rock avalanche. They concluded that the three rheologies assumed were capable of producing the runout area and the final deposit with satisfactory accuracy. The main advantage of the frictional rheology is that only one parameter, the dynamic friction angle, needs to be calibrated. This advantage is particularly important for the sensitivity analysis performed in the study. For this reason, the frictional rheology was selected with the expectation that it will provide practical results.

Based on site investigation, the building displaced on its shallow foundation—no basement was present. It is

observed that the present setting would reproduce the in situ condition specifically for the postfailure kinematic process. The study has assumed the building, with properties based on the Design Specifications for Concrete Structures Taiwan [50], standing on the ground without the basement or foundation. Additionally, based on the site investigation, the impact of the lateral dispersion of landslide debris at the toe was not considered critical as it was concentrated within a landslide width similar to that of the zone of rupture [57]; thus, 2D modeling was considered sufficient. By assessing the DEA results obtained in the study, the landslide progressed as a mudflow with an average velocity of 1.97 m/s, ranging from a class of very rapid to an extremely rapid [53]. The result was satisfactory as compared to field observations and case studies by Hungr et al. [58].

7. Conclusions

This study used a combination of FEA and DEA to investigate the process of Yanchao mudstone landslide including prefailure and postfailure regimes. The initiation time of landslide was investigated. The effect of water infiltration, the runout behaviors of mudstone landsliding, and general discussions regarding the numerical setting were also examined and discussed. The following conclusions can be drawn from the following results:

  (i) The initiation time of Yanchao mudstone landslide was revealed by the RCSD, and the likely failure timing was ascertained as 28 hr from the beginning of the typhoon rainfall

 (ii) The landslide hit the residential building within 16 s. During landslide runout, the primary increase in the sliding velocity was attributed to the steepness of the slope, suggesting that the runout behavior is dominated by the terrain

(iii) The frictional rheology for simulating the kinematic process of the Yanchao landslide is reasonable, based on the DEA results. However, further investigations of the landslide kinematic features considering different rheology may also provide additional insights into the interplay of rainfall in the landslide

(iv) The present study demonstrates that a combination of FEA and DEA can be an effective and useful approach to better understand the process of rainfall-induced landslides

The results of the study provided useful information about the role of water in the failure of mudstone slopes. This insight is valuable for formulating disaster prevention and mitigation strategies.

Data Availability

The data that support the findings of this study are available from the corresponding author on request.

Conflicts of Interest

Acknowledgments

References

[1] I. Tsaparas, H. Rahardjo, D. G. Toll, and E. C. Leong, "Controlling parameters for rainfall-induced landslides," *Computers and Geotechnics*, vol. 29, no. 1, pp. 1–27, 2002.

[2] A. Tohari, M. Nishigaki, and M. Komatsu, "Laboratory rainfall induced slope failure with moisture content measurement," *Journal of Geotechnical and Geoenviromental Engineering*, vol. 133, no. 5, pp. 575–587, 2007.

[3] A. Ali, J. Huang, A. V. Lyamin, S. W. Sloan, and M. J. Cassidy, "Boundary effects of rainfall-induced landslides," *Computers and Geotechnics*, vol. 61, pp. 341–354, 2014.

[4] B. D. Collins and D. Znidarcic, "Stability analyses of rainfall induced landslides," *Journal of Geotechnical and Geoenvironmental Engineering*, vol. 130, no. 4, pp. 362–372, 2004.

[5] R. L. Baum and J. W. Godt, "Early warning of rainfall-induced shallow landslides and debris flows in the USA," *Landslides*, vol. 7, no. 3, pp. 259–272, 2010.

[6] C. Melchiorre and P. Frattini, "Modelling probability of rainfall-induced shallow landslides in a changing climate, Otta, Central Norway," *Climatic Change*, vol. 113, no. 2, pp. 413–436, 2012.

[7] Y. F. Lee and Y. Y. Chi, "Rainfall-induced landslide risk at Lushan, Taiwan," *Engineering Geology*, vol. 123, no. 1-2, pp. 113–121, 2011.

[8] C. Chien-Yuan, C. Tien-Chien, Y. Fan-Chieh, and L. Sheng-Chi, "Analysis of time-varying rainfall infiltration induced landslide," *Environmental Geology*, vol. 48, no. 4-5, pp. 466–479, 2005.

[9] S. Friedel, A. Thielen, and S. M. Springman, "Investigation of a slope endangered by rainfall-induced landslides using 3D resistivity tomography and geotechnical testing," *Journal of Applied Geophysics*, vol. 60, no. 2, pp. 100–114, 2006.

[10] K.-H. Yang, R. Uzuoka, J. N.'a.'a. Thuo, G.-L. Lin, and Y. Nakai, "Coupled hydro-mechanical analysis of two unstable unsaturated slopes subject to rainfall infiltration," *Engineering Geology*, vol. 216, pp. 13–30, 2017.

[11] Y. W. Pan, H. K. Su, J. J. Liao, and M. W. Huang, "Reconstruction of rainfall-induced landslide dam by numerical simulation - the Barrier Lake in Taimali River as an example," in *ISRM International Symposium-8th Asian Rock Mechanics Symposium*, pp. 1784–1791, International Society for Rock Mechanics and Rock Engineering, Sapporo, Japan, October 2014.

[12] C. Shi, D. J. Li, K. H. Chen, and J. W. Zhou, "Failure mechanism and stability analysis of the Zhenggang landslide in Yunnan Province of China using 3D particle flow code simulation," *Journal of Mountain Science*, vol. 13, no. 5, pp. 891–905, 2016.

[13] M. Chigira, *The Potential Area of Large-Scale Landslides*, Scientific & Technical Publishing Co., Ltd, Taiwan, 2011.

[14] C. Liu and S. Lu, "Research on mechanism of mudstone degradation and softening in water," *Rock and Soil Mechanics*, vol. 21, no. 1, pp. 28–31, 2000.

[15] D. H. Lee, H. M. Lin, and J. H. Wu, "The basic properties of mudstone slope in southwestern Taiwan," *Journal of GeoEngineering*, vol. 2, no. 3, pp. 81–95, 2007.

[16] A. C. Trandafir, R. C. Sidle, T. Gomi, and T. Kamai, "Monitored and simulated variations in matric suction during rainfall in a residual soil slope," *Environmental Geology*, vol. 55, no. 5, pp. 951–961, 2008.

[17] S. J. Harris, R. P. Orense, and K. Itoh, "Back analyses of rainfall-induced slope failure in Northland Allochthon formation," *Landslides*, vol. 9, no. 3, pp. 349–356, 2012.

[18] A. Rahimi, H. Rahardjo, and E. C. Leong, "Effect of antecedent rainfall patterns on rainfall-induced slope failure," *Journal of Geotechnical and Geoenviromental Engineering*, vol. 137, no. 5, pp. 483–491, 2011.

[19] B. Leshchinsky, F. Vahedifard, H. B. Koo, and S. H. Kim, "Yumokjeong landslide: an investigation of progressive failure of a hillslope using the finite element method," *Landslides*, vol. 12, no. 5, pp. 997–1005, 2015.

[20] J. W. Zhou, P. Cui, and X. G. Yang, "Dynamic process analysis for the initiation and movement of the Donghekou landslide-debris flow triggered by the Wenchuan earthquake," *Journal of Asian Earth Sciences*, vol. 76, pp. 70–84, 2013.

[21] C. Hung, C. H. Liu, B. Leshchinsky, and G. W. Lin, "The Aso-Bridge coseismic landslide: a numerical investigation of failure and runout behavior using finite and discrete element methods," *Bulletin of Engineering Geology and the Environment*, 2018.

[22] P. A. Cundall, "A computer model for simulating progressive large-scale movements in blocky rock systems," in *Proceedings of the International Symposium on Rock Mechanics*, pp. 2–8, Nancy, France, 1971.

[23] P. A. Cundall and O. D. L. Strack, "A discrete numerical model for granular assemblies," *Geotechnique*, vol. 29, no. 1, pp. 47–65, 1979.

[24] C. L. Tang, J. C. Hu, M. L. Lin et al., "The Tsaoling landslide triggered by the Chi-Chi earthquake, Taiwan: insights from a discrete element simulation," *Engineering Geology*, vol. 106, no. 1-2, pp. 1–19, 2009.

[25] C.-M. Lo, M.-L. Lin, C.-L. Tang, and J.-C. Hu, "A kinematic model of the Hsiaolin landslide calibrated to the morphology of the landslide deposit," *Engineering Geology*, vol. 123, no. 1-2, pp. 22–39, 2011.

[26] W. C. Li, H. J. Li, F. C. Dai, and L. M. Lee, "Discrete element modeling of a rainfall-induced flowslide," *Engineering Geology*, vol. 149-150, pp. 22–34, 2012.

[27] Y. Mualem, "A new model for predicting the hydraulic conductivity of unsaturated porous media," *Water Resources Research*, vol. 12, no. 3, pp. 513–522, 1976.

[28] M. T. van Genuchten, "A closed form equation for predicting the hydraulic conductivity of unsaturated soils," *Soil Science Society of America Journal*, vol. 44, no. 5, pp. 892–898, 1980.

[29] C. Yoo, "Effect of rainfall on performance of geosynthetic reinforced soil wall using stress-pore pressure coupled analysis," in *Geo-Congress 2013*, pp. 566–573, San Diego, CA, USA, 2013.

[30] Itasca, *PFC (Particle Flow Code) Version 5.0*, Itasca Consulting Group Inc, Minneapolis, USA, 2014.

[31] E. T. Brown, *Rock Characterization, Testing and Monitoring: ISRM Suggested Methods*, Pergamon Press, Oxford, 1981.

[32] S. T. Chen, "The investigation on erosion characteristics of mudstone slope land in southwestern Taiwan (II)," The Hazard Mitigation Technology Report No. 74-05, National Science Council, 1985.

[33] E. Hoek and J. Bray, *Rock Slope Engineering*, The Institution of Mining and Metallurgy, London, Revised 2nd edition, 1981.

[34] C.-M. Lo, C.-F. Lee, and W.-K. Huang, "Failure mechanism analysis of rainfall-induced landslide at Pingguang stream in Taiwan: mapping, investigation, and numerical simulation," *Environment and Earth Science*, vol. 75, no. 21, pp. 1–20, 2016.

[35] L. A. Richards, "Capillary conduction of liquids through porous mediums," *Physics*, vol. 1, no. 5, pp. 318–333, 1931.

[36] Hibbitt, Karlsson, Sorensen, *ABAQUS/Standard User's Manual, 1*, Hibbitt, Karlsson & Sorensen, 2018.

[37] S. K. Vanapalli, D. G. Fredlund, D. E. Pufahl, and A. W. Clifton, "Model for the prediction of shear strength with respect to soil suction," *Canadian Geotechnical Journal*, vol. 33, no. 3, pp. 379–392, 1996.

[38] R. D. Holtz and W. D. Kovacs, *An Introduction to Geotechnical Engineering*, Pearson, 2nd edition, 2011.

[39] K. J. Chang, A. Taboada, M. L. Lin, and R. F. Chen, "Analysis of landsliding by earthquake shaking using a block-on-slope thermo-mechanical model: example of Jiufengershan landslide, central Taiwan," *Engineering Geology*, vol. 80, no. 1-2, pp. 151–163, 2005.

[40] China Steel structural Co, Ltd, *Feasibility Assessment Report of China Steel in Yanchao*, Urban Development Bureau, Kaohsiung City Government, 2010.

[41] H. Rahardjo, X. W. Li, D. G. Toll, and E. C. Leong, "The effect of antecedent rainfall on slope stability," *Geotechnical and Geological Engineering*, vol. 19, no. 3/4, pp. 371–399, 2001.

[42] H. Rahardjo, E. C. Leong, and R. B. Rezaur, "Effect of antecedent rainfall on pore-water pressure distribution characteristics in residual soil slopes under tropical rainfall," *Hydrological Processes*, vol. 22, no. 4, pp. 506–523, 2008.

[43] T. T. Wang and T. H. Huang, "An experience of tunnelling in mudstone area in southwestern Taiwan," *Tunnelling and Underground Space Technology*, vol. 17, no. 4, pp. 425–436, 2002.

[44] D. H. Lee, Y. Y. Jhin, and K. G. Tien, "Characteristics of mudstone and the methods for slope protection," *Sino-Geotechnics*, vol. 48, pp. 35–47, 1994.

[45] L. Tacher, C. Bonnard, L. Laloui, and A. Parriaux, "Modelling the behaviour of a large landslide with respect to hydrogeological and geomechanical parameter heterogeneity," *Landslides*, vol. 2, no. 1, pp. 3–14, 2005.

[46] C. Hung, G.-W. Lin, H.-S. Syu, C.-W. Chen, and H.-Y. Yen, "Analysis of the Aso-bridge landslide during the 2016 Kumamoto earthquakes in Japan," *Bulletin of Engineering Geology and the Environment*, pp. 1–11, 2017.

[47] D. O. Potyondy and P. A. Cundall, "A bonded-particle model for rock," *International Journal of Rock Mechanics and Mining Sciences*, vol. 41, no. 8, pp. 1329–1364, 2004.

[48] C. M. Lo, C. F. Lee, H. T. Chou, and M. L. Lin, "Landslide at Su-Hua Highway 115.9k triggered by Typhoon Megi in Taiwan," *Landslides*, vol. 11, no. 2, pp. 293–304, 2014.

[49] N. Thompson, M. R. Bennett, and N. Petford, "Analyses on granular mass movement mechanics and deformation with distinct element numerical modeling: implications for large-scale rock and debris avalanches," *Acta Geotechnica*, vol. 4, no. 4, pp. 233–247, 2009.

[50] *Design Specifications for Concrete Structures*, Ministry of the Interior, R.O.C, 2002.

[51] H. Lan, C. Zhou, C. F. Lee, S. Wang, and F. Wu, "Rainfall-induced landslide stability analysis in response to transient pore pressure," *Science in China Series E Technological Sciences*, vol. 46, no. 7, pp. 52–68, 2004.

[52] M. Calvello, L. Cascini, and G. Sorbino, "A numerical procedure for predicting rainfall-induced movements of active landslides along pre-existing slip surfaces," *International Journal for Numerical and Analytical Methods in Geomechanics*, vol. 32, no. 4, pp. 327–351, 2008.

[53] D. M. Cruden and D. J. Varnes, "Landslide types and processes," in *Landslides Investigation and Mitigation*, A. K. Turner and R. L. Schuster, Eds., pp. 36–75, Transportation Research Board, US National Research Council. Special Report 247, Washington, DC, 1996.

[54] C. Y. Lu, C. L. Tang, Y. C. Chan, J. C. Hu, and C. C. Chi, "Forecasting landslide hazard by the 3D discrete element method: a case study of the unstable slope in the Lushan hot spring district, central Taiwan," *Engineering Geology*, vol. 183, pp. 14–30, 2014.

[55] G. B. Crosta, H. Chen, and C. F. Lee, "Replay of the 1987 Val Pola Landslide, Italian Alps," *Geomorphology*, vol. 60, no. 1-2, pp. 127–146, 2004.

[56] M. Pirulli and A. Mangeney, "Results of back-analysis of the propagation of rock avalanches as a function of the assumed rheology," *Rock Mechanics and Rock Engineering*, vol. 41, no. 1, pp. 59–84, 2008.

[57] Y. F. Su, H. H. Fu, Y. C. Lin et al., *The Report of Disasters Induced the Typhoon Megi*, Soil and Water Conservation Bureau, 2016.

[58] O. Hungr, S. Leroueil, and L. Picarelli, "The Varnes classification of landslide types, an update," *Landslides*, vol. 11, no. 2, pp. 167–194, 2014.

Research Article

Consolidated and Undrained Ring Shear Tests on the Sliding Surface of the Hsien-du-shan Landslide in Taiwan

Hung-Ming Lin,[1] Jian-Hong Wu [ID],[2] and Erik Sunarya[2]

[1]*Sustainable Environment Research Laboratories, National Cheng Kung University, Tainan, Taiwan*
[2]*Department of Civil Engineering, National Cheng Kung University, Tainan 701, Taiwan*

Correspondence should be addressed to Jian-Hong Wu; jhwu@mail.ncku.edu.tw

A new consolidated undrained ring shear test capable of measuring the pore pressures is presented to investigate the initiation mechanism of the Hsien-du-shan rock avalanche, triggered by Typhoon Morakot, in southern Taiwan. The postpeak state of the landslide surface between the Tangenshan sandstone and the remolded landslide gouge is discussed to address the unstable geomorphological precursors observed before the landslide occurred. Experimental results show that the internal friction angle of the high water content sliding surface in the total stress state, between 25.3 and 26.1°, clarifies the reason of the stable slope prior to Typhoon Morakot. In addition, during the ring shear tests, it is observed that the excess pore pressure is generated by the shear contractions of the sliding surface. The remolded landslide gouge, sheared under the high normal stress, rendered results associated with high shear strength, small shear contraction, low hydraulic conductivity, and continuous excess pore pressure. The excess pore pressure feedback at the sliding surface may have accelerated the landslide.

1. Introduction

In 2009, the Hsien-du-shan landslide, triggered by Typhoon Morakot [1, 2], killed more than 400 people at the Hsiaolin village, Kaohsiung, Taiwan. Before this landslide mobilized, the authority announced two potential debris flow torrents (Kaohsiung County DF06 and DF07) (http://246.swcb.gov .tw/allfiles/PDF/98%E5%B9%B4%E8%8E%AB%E6%8B%89 %E5%85%8B%E9%A2%B1%E9%A2%A8-%E9%AB%98%E 9%9B%84%E7%94%B2%E4%BB%99-001-(%E9%80%9F).pdf) as major threats to the local residents in the Hsiaolin village. The debris flow damaged the village during the Kalmaegi in 2008. However, the historical record was unavailable to warn the residents that the village is located at a geological site with a large unstable slope.

The Hsien-du-shan landslide had demanded the authorities to respond urgently in developing new technologies for warning the occurrence of a rainfall-induced rock avalanche. In addition to detecting an abnormal geomorphological pattern [3, 4], clarification of the initiation mechanism of a large rock avalanche is another important task to mitigate disasters

(Chen and Wu (2018); Hung et al. (2018); [5]). Figure 1 shows the available mathematical models to describe the mechanical behavior of the sliding surface of the Hsien-du-shan landslide. A conventional constant friction coefficient was applied to different numerical methods to simulate the postfailure behavior (dashed line) (Figure 1) [1, 2, 6]. Kuo et al. [7] discovered experimentally slip weakening by the colluvium on the sliding surface that was within the range of natural water contents using high-speed rotary shear tests with maximum shear speed and shear displacement of up to 1.3 m/s and 90 m, respectively (solid lines). Slip weakening is defined as a significant decrease in the friction angle of a sliding surface under high-speed sliding. However, the friction models in Figure 1 did not explicitly consider the pore pressure changes during the Hsien-du-shan landslide. But, studies [8–10] highlighted the importance of including changes in pore pressure to clarify the triggering process of a sliding surface. Lee and Delaney [9] concluded analytically that the rise in temperature and pore pressure were, respectively, 200 K and 0.2–2 MPa during the movement of the San Andreas Fault zone with an average stress of 10 MPa.
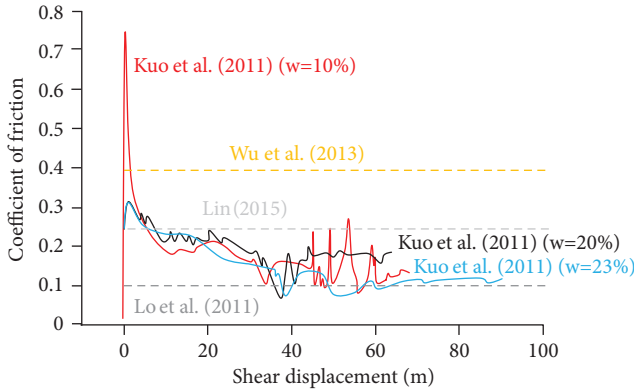
FIGURE 1: Different friction model for the initiation of the Hsien-du-shan landslide.

Miller et al. [10] calculated the excess pore pressure of a fault using the porosity reduction mechanism. Iverson [8] proposed that landslide motion is regulated by α, which depends on the dilatancy angle and the intrinsic timescales for pore pressure generation and dissipation. When $\alpha < 0$, soil in the shear zone contracts during slope failure. Then, the shear zone causes positive pore pressure feedback and runaway acceleration. Conversely, when $\alpha > 0$, slow and steady landslide motion occurs while positive pore pressure is supplied by rain infiltration.

Currently, knowledge of the shear behavior of rock avalanches is rather limited, especially when sliding occurs at a great depth. Fortunately, the ring shear apparatus has two obvious advantages for investigating the initiation of a rock avalanche: (1) there is no change in the cross-sectional area of the shear plane as the test proceeds; and (2) the sample can be sheared through an uninterrupted displacement of any magnitude [11].

Table 1 shows the available ring shear tests. Developing a CU ring shear test apparatus is crucial to clarify the coupling of landslide motion and pore pressure feedback. In addition, ring shear tests have focused on sand [12, 13] and clayey soils [14–18]. Moore and Iverson [18] concluded that although dilation reduces the internal friction angle of dry granular materials, pore expansion in fluid-saturated materials increases friction and strength by reducing pore-fluid pressure and increasing normal stresses at grain contacts. Atterberg limits, particle shapes, and shearing rates strongly govern stress fluctuations [17], although the particle size distribution is an additional factor for controlling the residual shear strength [19] in ring shear tests.

The maximum depth of the Hsien-du-shan rock avalanche was 85.6 m [20] based on the topographic data before and after the sliding event. In this study, the unit weight of the soils is assumed to be $\gamma = 27.1$ kN/m^3. The maximum normal stress may exceed 2000 kPa. In Table 1, although the designed maximum normal stresses of the DPRI-4, DPRI-5, and DPRI-6 exceeded 2000 kPa, a successful case study indicating a maximum normal stress exceeding 2000 kPa was lacking. Although the DPRI-7 achieved a successful maximum normal stress of up to 750 kPa, Sassa et al. [21] raised the issue regarding the poor performance

of a servo-control system. Therefore, only the ring shear test devices proposed by Liao et al. [22], ICL-2 [23], and Wu et al. [24] would fulfill the desired high normal stresses that occurred at the Hsien-du-shan rock avalanche. This study presents an improvement in the ring shear device proposed by Liao et al. [22] and Wu et al. [24] to monitor the pore water pressure and the shear behavior of the soil/rock interface of the Hsien-du-shan rock avalanche.

2. The New Ring Shear Apparatus

The ring shear box consists of the upper ring shear box (Figure 2(a)) and the lower shear box (Figure 2(b)). For the ring shear apparatus only for the soils ([15, 25]; https://www.youtube.com/watch?v=R9vTsrE8bSA), the rough interface or vanes must be installed at the top and the bottom shear boxes to ensure that the shear failure occurs in the soils but not the interface of the shear box and the soils. In this study, the apparatus was designed to investigate the interface of two rock samples or of the rock and the soil. Rock sample is adhered to the upper shear box, and the interface between the rock sample and the top shear box is flat (Figure 2(a)). The soils are installed to the lower ring shear box (Figure 2(c)).

This ring shear system consists of an MTS, ring shear box, ring displacement control system, signal generator, and data acquisition system (Figure 3(a)). The MTS applies the normal stresses and measures the normal displacement and torque in the ring shear tests. The axial force and torque capacities of the MTS are 50 kN and 500 N-m, respectively. The ring shear box (Figure 3(b)) comprises the upper and lower boxes and is capable of functioning a maximum normal loading of 100 kN. When investigating the interface of the two rock samples, an epoxy is used to adhere rock specimens to both the upper and lower shear boxes [26]. However, when a soil-rock interface is investigated, the rock sample is adhered to the upper shear box, and the soils are put in the lower shear box. The ring displacement control system below the lower shear box, with a large displacement and rotational speeds ranging from 0.0018–1.8 mm/min, drives the lower shear box during the shearing tests. In each testing, the Square Teflon O-rings are, respectively, attached on the inner and outer sides of the samples, in the upper and lower shear boxes, to prevent extrusions water and soils.

In this study, the inner and outer diameters of the ring-shaped specimen are 11.0 cm and 14.9 cm, respectively. The inner and outer radius ratio is $n = 0.74$. The designs meet the dimensional requirements for a specimen as suggested by (1) [11] and (2) [27], for obtaining a uniform distribution of stress on the shear plane.

$$n = \frac{R_i}{R_o} = \frac{D_i}{D_o} \geq 0.71, \tag{1}$$

$$n = \frac{R_i}{R_o} = \frac{D_i}{D_o} \geq 0.65, \tag{2}$$

where R_o is the specimen outer radius, R_i is the specimen inner radius, D_o is the specimen outer diameter, D_i is the

TABLE 1: The sample size of ring shear test (modified by [39]).

Author	Inner diameter, D_i (cm)	Outer diameter, D_o (cm)	n (D_i/D_o)	Sample	Max. normal stress (kPa)	Pore pressure monitoring
Bishop et al.	10.16	15.24	0.67	Clay	980	N
Hungr and Morgenstern	22.00	30.00	0.73	Coarse sand, sand-rock flour mixtures, and polystyrene beads	200	N
Tika and Hutchinson [40]	10.16	15.24	0.67	Cohesive soil	980	N
Garga and Sendano	9.20	13.30	0.69	Sand	660	N
Sassa (DPRI-3)	21.0	31.0	0.68	Soils	500	Y
Sassa (DPRI-4)	21.0	29.0	0.72	Coarse grain sandy soil	3000	Y
Sassa (DPRI-5)	12.0	18.0	0.67	Soils	2000	Y
Sassa (DPRI-6)	25.0	35.0	0.71	Sands	3000 (designed) 750 (success)*	Y
Sassa (DPRI-7)	27.0	35.0	0.77	Silica sand	500	Y
Iverson et al. [16]	48.5	60.0	0.81	Tills	400	N
Liao et al. [22]	11.0	14.9	0.74	Sandstone	12,600 (designed) 4000 (success)**	N
Ostric et al. [41] (ICL-1)	10.0	14.0	0.71	Marl	1000	Y
Tomasetta et al. [42]	6.0	12.0	0.50	Fine powders	14.795	N
Hoyos et al. [15]	9.65	15.24	0.63	Soils	732	Y (suction)
Sassa et al. [23] (ICL-2)	10.0	14.2	0.70	Sands	3000	Y
Jeong et al. (2014)	11.0	25.0	0.44	Gravelly sandy soil	100	Y
Wu et al. [24]	11.0	14.9	0.74	Sandstone/remolded shale	4000	N
This study	11.0	14.9	0.74	Sandstone/remolded shear gouge	2710	Y

*Normal stress servo-control system does not function well. Tests were conducted to 750 kPa by changing the normal stress load cell [21]; **successful case study of the Tsaoling landslide during the Chi-Chi earthquake [22].

specimen inner diameter, and n is the ratio of the inner radius to the outer radius.

The normal and shear stresses applied to the shear zone of the specimen are represented by (3), (4), and (5):

$$\sigma_n = \frac{F_n}{\pi \left(R_o^2 - R_i^2 \right)}, \tag{3}$$

$$M = 2\pi \int_{R_i}^{R_o} \tau \cdot r^2 dr = \frac{2\pi\tau \left(R_o^3 - R_i^3 \right)}{3}, \tag{4}$$

$$\tau = \frac{3M}{2\pi \left(R_o^3 - R_i^3 \right)}, \tag{5}$$

where σ_n is normal stress, τ is shear stress, F_n is normal force, M is torque, and R_i and R_o are the inner and outer radii, respectively.

When the ring shear tests start, a stress-controlled normal stress is applied from the upper shear box to consolidate the soil samples, and then the ring displacement control system below the lower shear box drives the lower shear box at a specified shear rate. The shear resistance along the shear plane, the interface of the samples, is measured.

During the ring shear test, the sliding surface must ensure a high water tightness, and the pore pressure cell installation must be adjoining to the sliding surface to accurately measure the changes in sliding-induced pore pressures. In the new ring shear apparatus, a drainage pipeline is drilled in the lower shear box slightly lower than the Teflon square O-ring and is adjoined to the sliding surface (Figure 3(b)). Note that if the pressure cell is directly attached to the drainage pipeline, the rotating ring shear test apparatus under a large shear displacement may tie up the pore pressure cell cable and break the pore pressure cell. To avoid the pressure cell damage, the drainage pipeline is connected to a pore pressure cell by a flexible tube to monitor the pore pressure of the shear plane (Figure 3(c)). The flexible tube is connected to the drainage pipeline after setting rock samples to the ring shear test apparatus, and the infilling water to the hollow acrylic cover should fill up the tube and the pipeline (Figure 3(b)). The pore pressure cell should be connected to the flexible tube below the water table and then is attached to the top of the acrylic cover (Figure 3(c)) before the shear test starts. The water tightness of the new ring shear apparatus was assured by Wu [28], in which the pore pressure reduced from its initial state of 125 to 120 kPa within 20 hours. The dilatancy or contraction at the shear plane during shearing can be obtained from changes in the specimen height.

(a) Upper shear box with rock sample

(b) Lower shear box without soils

(c) Lower shear box with soils
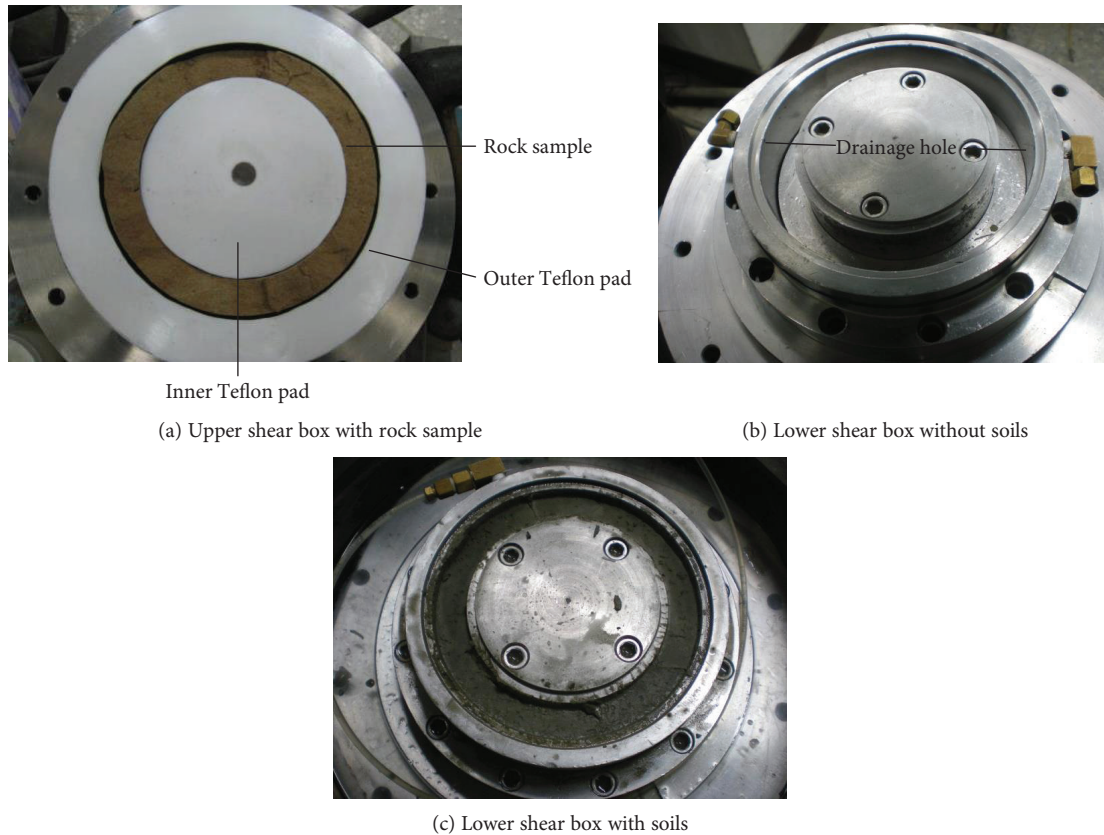
Figure 2: Ring shear box.

3. The Hsien-du-shan Rock Avalanche

Figure 4 shows the rainfall data during Typhoon Morakot in 2009 recorded at the Chiahsien Station, which is the nearest rainfall station to the Hsien-du-shan landslide site in Kaohsiung County, Taiwan. The cumulative rainfall exceeded 2000 mm. The Hsien-du-shan rock avalanche occurred at 6:09 a.m. on August 9 and resulted in compound disasters, comprised of slope failure, landslide dam, and dam breakage, claiming more than 400 local residents of Hsiaolin village near the toe of the slope in Kaohsiung (Figure 5).

The shear strength parameters of the sliding surface are key factors when investigating a failure mechanism. Studies by Kuo et al. [7] indicated that the static friction as the peak coefficient of friction is between 0.3 ($\emptyset = 16.7°$) and 0.75 ($\emptyset = 36.9°$), with a normal stress = 1.0 MPa, when the water content of local colluvium is between 9 and 25% (Figure 1). When the rotary shear speed reaches 1.3 m/s, significant slip weakening occurs, and the coefficient of friction drops to a range between 0.1 ($\emptyset = 5.71°$) and 0.2 ($\emptyset = 11.3°$). The experimental results of the rotary shear test clarify that the shear strength of the sliding surface decreases remarkably when the landslide accelerates. Wu et al. [2] applied conventional direct shear tests to the high water content remolded soil obtained from the sliding slope of the Hsien-du-shan slope and suggested the normal stresses of 0.5, 1.0, 2, and 3.49 MPa for the experimental testing. The shear strength parameters of the high water content remolded soil are $c =$

0 kPa and $\emptyset = 21.4°$. In addition, Lin et al. [29] concluded that the shear strength parameters of the interface between the Tangenshan sandstone and the remolded Yenshuikeng shale, exhibiting high water contents, were $c = 0.0$ and $\emptyset = 24.3°$ as determined by conventional direct shear tests. Then, the studies validated the stability of the Hsien-du-shan slope under the impact of the Chi-Chi earthquake in 1999 and the Heng-Chun earthquake in 2006. In fact, due to the absence of well-installed in situ groundwater monitoring instruments, the pore pressure change of the Hsien-du-shan sliding surface during its initiation is difficult to be obtained. In addition to field monitoring, Kuo et al. [7] and Wu et al. [2] have also difficulties in monitoring the pore pressure changes in experimental shear tests.

3.1. Geological Outline. The Hsien-du-shan slope is located at the east wing of the Hsiaolin syncline. The Hsiaolin syncline axis is located at the toe of the slope near the Hsiaolin Village and is east of the Chishan River [30–32]. A shear zone was discovered at the south boundary of the Hsien-du-shan rock avalanche [32].

The topographic and elevation differences in the source area before and after the occurrence of a landslide can be used to obtain the volume and maximum thickness of the sliding mass, respectively. The obtained values are carefully considered for maximum normal stress during the shear tests. Chen and Wu [20] calculated that the slid volume of the Hsien-du-shan rock avalanche was c.a. $27.118 \times 10^6 \, \text{m}^3$

(a) Ring shear test system

(b) Sketch of the ring shear box

(c) Arrangement of the pore pressure cell
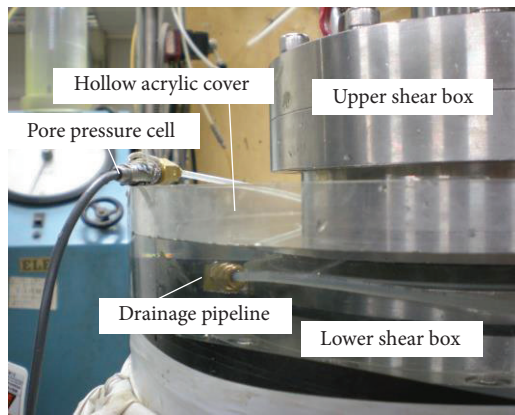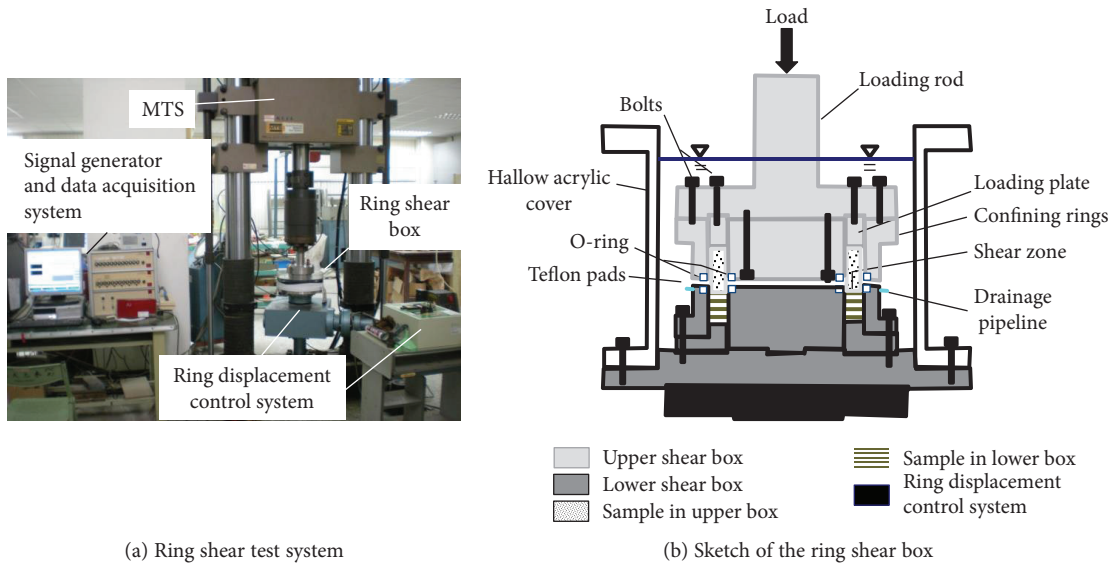
FIGURE 3: New pore pressure monitoring ring shear test apparatus.

Chiahsien station-typhoon Morakot
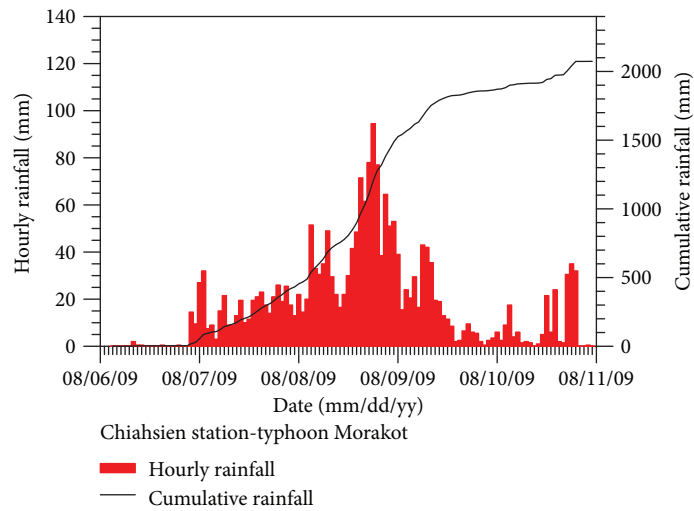
FIGURE 4: Rainfall data at the Chiahsien station.
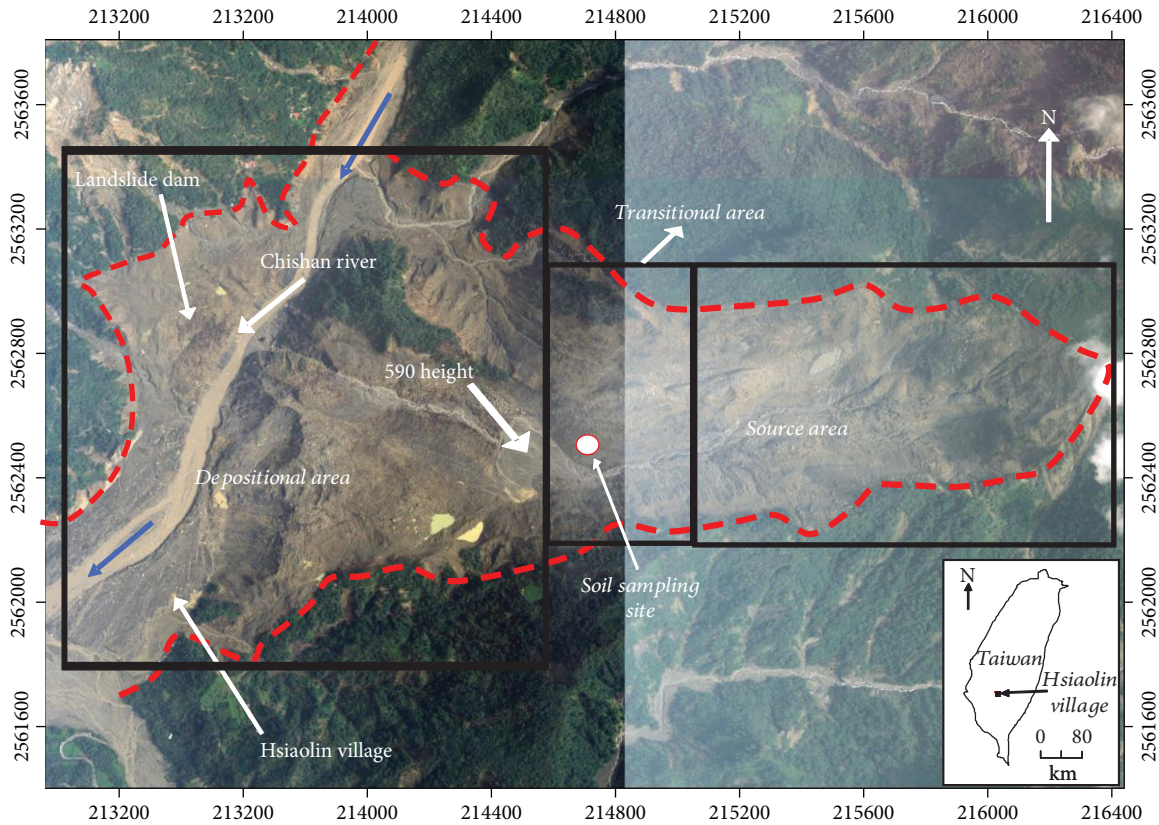
FIGURE 5: Aerial photo of the Hsien-du-shan rock avalanche.

and the maximum sliding thickness was 85.6 m using a 5 m × 5 m Digital Elevation Model before and after the landslide. The sliding surface is located at the interface of the fractured and weathered Yenshuikeng shale at the top and the Tangenshan sandstone at the bottom [30]. The water content of the sliding surface was high because the rock avalanche was triggered by heavy rainfall. Gravitational slope deformations were observed as unstable precursors before slope failure [2, 32].

4. The Consolidated Undrained Ring Shear Tests

4.1. Sample Preparation. In 2009 and 2010, the sliding gouges still covered the Tangenshan sandstone formation near the source area post the landslide event. The yellow sliding gouge implies that the gouge was generated as a filling layer at the interface of the Yenshuiken shale and Tangenshan sandstone prior to the incident of the landslide. In addition, the results of the X-ray diffraction analysis indicated that the minerals in the sliding gouge are very close to those observed in the Yenshuikeng shale [33]. To better understand the shear behavior of the sliding surface of the Hsien-du-shan rock avalanche, the interface between the sliding gouge and the Tangenshan sandstone is also investigated.

4.1.1. The Tangenshan Sandstone Sample. Tangenshan sandstones were obtained at the slope near the east edge of the 590 height (Figure 5), whose elevation is 590 m above the sea

level. The physical and mechanical properties of the obtained Tangenshan sandstone are shown in Table 2. The uniaxial compressive strength and Young's modulus of the sandstone decrease significantly as the water content increases. In addition, the slake-durability index of the sandstone is $Id_1 = 99.03–99.29$ and $Id_2 = 98.39–98.76$. Based on the Gamble classification, sandstone is classified as a very high-durability rock [34].

Hollow cylinder samples with an inner diameter of 11.0 cm and an outer diameter of 14.9 cm are drilled from the retrieved rocks. The cylinders are cut with a height of 5 ± 0.2 cm to satisfy the size requirements of the ring shear box (Figure 6).

4.1.2. The Remolded Landslide Gouge. Due to the precipitous landform, a sufficient number of the gouges at the sliding surface of the source area were unavailable. In this study, the sandstones and the gouge at the sliding surface were taken in the transitional zone (Figures 5 and 7(a)). Therefore, the gouges are remolded to investigate the postpeak shear behavior because of the unstable topographical precursors before the landslide [2, 32]. In addition, Japanese landslide case studies [35] showed good agreement between the residual friction angles determined from undisturbed samples and remolded specimens using ring shear tests.

In Figure 7(a), only the gouges at the depth adjoining to the underlying Tangenshan sandstone were taken to avoid mixing external debris at the ground surface during slope failure (Figure 7(b)). Table 3 shows the physical properties

TABLE 2: Physical and mechanical properties of the Tangenshan sandstone.

Properties	Value
Air-dried unit weight, γ_d (kN/m³)	24.40–25.25
P-wave velocity, V_p (m/s)	2463.24–2692.51
S-wave velocity, V_s (m/s)	1477.94–1549.23
Uniaxial compressive strength, σ_c (MPa)	
Air-dried sample with water content = 0.72%	64.96–73.52
High water content sample with water content = 2.85%	48.44–61.80
Young's modulus, E (MPa)	
Air-dried sample with water content = 0.72%	7885.98–9488.41
High water content sample with water content = 2.85%	3014.21–4962.34
Slake-durability index (%)	
Id_1	99.03–99.29
Id_2	98.39–98.76

FIGURE 6: Hollow cylinder sample of the Tangenshan sandstone.

of the landslide gouge, which are classified to be CL based on the Unified Soil Classification.

The procedures for preparing the remolded local soils for the consolidated undrained (CU) ring shear tests include the following:

Step 1. Soils are passed through a no. 10 sieve to reduce the impacts of large grains on the shear test because the thickness of the sample is 2 cm. The lower shear box is installed in the ring displacement control system (Figure 3). Then, the lower shear box is filled with the dry gouges until the groove for the square Teflon O-ring.

Step 2. At the Hsien-du-shan slope, the landslide gouge is located above the Tangenshan sandstone. However, in the ring shear test, the arrangement of the Tangenshan sandstone sample above the remolded gouges (Figure 8) is opposite to the in situ case on the Hsien-du-shan slope. The upper and the lower shear boxes are integrated into the ring shear apparatus. The specified normal force is applied to the soil sample in dry conditions for 12 hours. Then, the interface of the remolded landslide gouge and sandstone sample is

submerged in water for an additional 36 hours for the CU ring shear tests considering that the Hsien-du-shan landslide was triggered by heavy rainfall.

4.2. Identification of Test Parameters. The area of the ring shear sample, A, is 79.33×10^{-4} m² because the outer and inner diameters of the sample are 14.9 and 11.0 cm, respectively. The normal forces used in the tests are calculated by the equation $F_n = \gamma \times \mathrm{Dep} \times A$. In the CU tests, the normal force, F_n, to consolidate the remolded landslide gouge is 21.5 kN, considering the maximum depth of the Hsien-du-shan rock avalanche was roughly 100 m based on the topographic data before and after the landslide. Then, three normal forces, $N_{50} = 10.75$ kN, $N_{75} = 16.125$ kN, and $N_{100} = 21.5$ kN, corresponding to depths (Dep) of 50 m, 75 m, and 100 m, respectively, covered the normal force calculated from the maximum sliding thickness of 85.6 m [20] and are applied in the ring shear tests.

Vertical displacement of the sample in each test is monitored using the LVDT of the MTS from the beginning of the consolidation. A pore pressure sensor having a full capacity of 500 kPa, manufactured by Kyowa, Japan, is connected to the drainage pipeline beneath the water table at the lower ring shear box (Figure 3(b)) before the ring shear test starts. The ring displacement control system below the lower shear box (Figure 3(a)) controls the shear rate of 1.5 mm/min (1.3 degree/min) for the CU shear test after the normal stress, converging the vertical displacement, is applied. The normal and shear stresses are computed by incorporating the measured axial force and torque to (3) and (5). Subsequently, the curves of the shear stress-shear displacement, normal displacement-shear displacement, and pore water pressure change-shear displacement are plotted.

5. Experimental Results

CU ring shear tests were conducted on the interface of the Tangenshan sandstone and the remolded landslide gouges to clarify the mechanical behavior of this surface under large shear displacement. Figure 9 shows the CU ring shear test results under the three normal forces, $N_{50} = 10.75$ kN, $N_{75} = 16.125$ kN, and $N_{100} = 21.5$ kN. For each ring shear test, the sample was sheared for 3 cycles (rotation angle = 1080°; shear displacement = 1218 mm). The experimental time is approximately 13.5 hours under the shear rate of 1.5 mm/min.

The Mohr-Coulomb failure criterion (Figure 10) is obeyed to interpret the corresponding shear stresses by the three designed normal stresses, N_{50}, N_{75}, and N_{100}, based on the shear stress-shear displacement curves (Figure 9). Figure 10 shows the minimum, average, and maximum residual strengths of the ring shear tests in each shear circle. The total stress failure criteria of each shear circle show that the cohesion of the sliding interface is 0.0 kPa. In addition, the internal friction angles are $\phi = 25.3°$ (coefficient of friction = 0.480), 26.1° (coefficient of friction = 0.491), and 25.3° (coefficient of friction = 0.473) for shear circles 1, 2, and 3, respectively. The total stress failure criteria changed insignificantly when the shear distance is within 1218 mm, which can be considered as a landslide initiation (Figure 10).

(a) Location to get the soils at the sliding surface

(b) Picture to get the landslide gouge
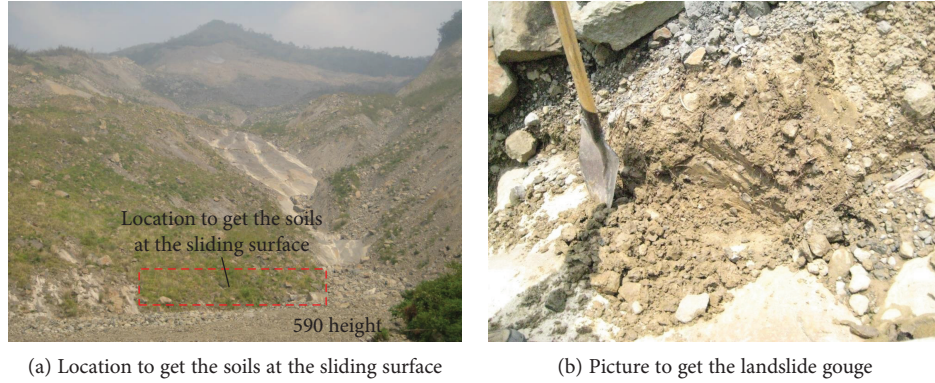
Figure 7: Soil sampling at the sliding slope.

Table 3: Physical properties of local landslide gouge.

Sample number	Sample 1	Sample 2	Sample 3
Specific gravity (G_s)	2.711	2.709	2.696
Liquid limit (LL)	29.39	28.84	29.51
Plastic limit (PL)	14.42	15.90	15.22
Plastic index (PI)	14.97	12.94	14.29
D_{10} (mm)	0.01247	0.00909	0.01097
D_{30} (mm)	0.06612	0.06545	0.05478
D_{60} (mm)	0.07304	0.07254	0.07099
Uniform coefficient, C_u	5.857	7.977	6.469
Coefficient of gradation, C_c	4.798	6.494	3.852
Unified soil classifications	CL	CL	CL

Comparing this experimental data to the available shear strength parameters of the Hsien-du-shan sliding surface (Figure 1), the ring shear test results are close to the data obtained from conventional direct shear tests, $\phi = 21.4°$ [2]. However, this new ring shear test provides higher strengths than the strengths determined by high-speed rotary shear tests with a water content exceeding 20% [7] (coefficient of friction = 0.1 to 0.2), numerical simulations [6] (coefficient of friction = 0.1), or the topographic map [1, 2] (coefficient of friction = 0.23). Studies by Kuo et al. [7] and Lo et al. [6] focused on investigating slip weakening of the sliding surface under high speed and very large shear movements. Rock mass disintegrations and the high sliding speed are key factors in decreasing the friction angle [2, 7] of the postfailure rock mass. However, the objective of this study is to investigate the slope failure initiation. The internal friction angles of the sliding surface investigated by the ring shear test, $\phi = 25.3°$ to 26.1°, are larger than the dip angle of the slope (Figure 5), which clarifies that the Hsien-du-shan slope was stable before Typhoon Morakot.

In addition, in Figure 9, the sliding interface undergoes shear contractions when normal stresses corresponding to depths of 50, 75, and 100 m are applied. The slope of the axial stroke vs. shear displacement curve is defined as $\tan\psi$. The dilatancy angle, ψ, is positive in the case of dilative shearing, but this value is negative in the case of contractive shearing.

The value of ψ evolves as shear displacement proceeds, and $\psi \rightarrow 0$ indicates that these shear displacements are large enough that the deforming soil in the shear zone approaches a constant critical state porosity.

The flexible tube connecting the drainage pipeline and the pore pressure cell (Figure 3(b)) is full of water and is returned to zero before the ring shear test starts. Figure 9 shows the pore pressure variation during the shear test. Shear contraction increases pore pressure during the ring shear tests. However, pore pressures decrease in the first 2 shear cycles in all the ring shear tests. The pore pressure decrease during the initial stage of the ring shear tests may be due to the unsaturated remolded landslide gouge even if it is put in water and is consolidated for 36 hours. When the sample is fully saturated, the shear contraction (Figure 9) increases the pore pressures in an undrained condition. Oppositely, water may flow into the shear face and decrease the pore pressure.

Table 4 shows the water contents of the remolded landslide gouge cross section and rock samples after the ring shear tests. The water contents of the remolded landslide gouge are between 8.82 and 14.49%, varying within 2% in the cross section. The water content is close to the PL of the landslide gouge (Table 3) and is within the range for in situ colluvium, which is between 9 and 25% [7]. The increase in pore pressures caused by the shear contraction implies that the effective normal stress and slope stability both decrease as the shear displacement increases after the onset of the sliding. In addition, an increase in the consolidating pressure increases the density but decreases the hydraulic conductivity of the remolded landslide gouge. Therefore, by considering both the long shear displacement of the rock avalanche and the large normal stress, the pore pressure would increase significantly and continuously (Figure 9).

The new CU ring shear tests provide additional remarks to clarify the initial sliding behavior of the Hsien-du-shan rock avalanche:

(1) The sliding surface is in the postpeak state because of unstable topographical precursors before the landslide [2, 32]

(2) After the landslide starts, the CU ring shear test results indicate that shear contractions would occur

(a) Sample in the ring shear apparatus

(b) Integrated samples

FIGURE 8: Sample arrangement for the ring shear test.
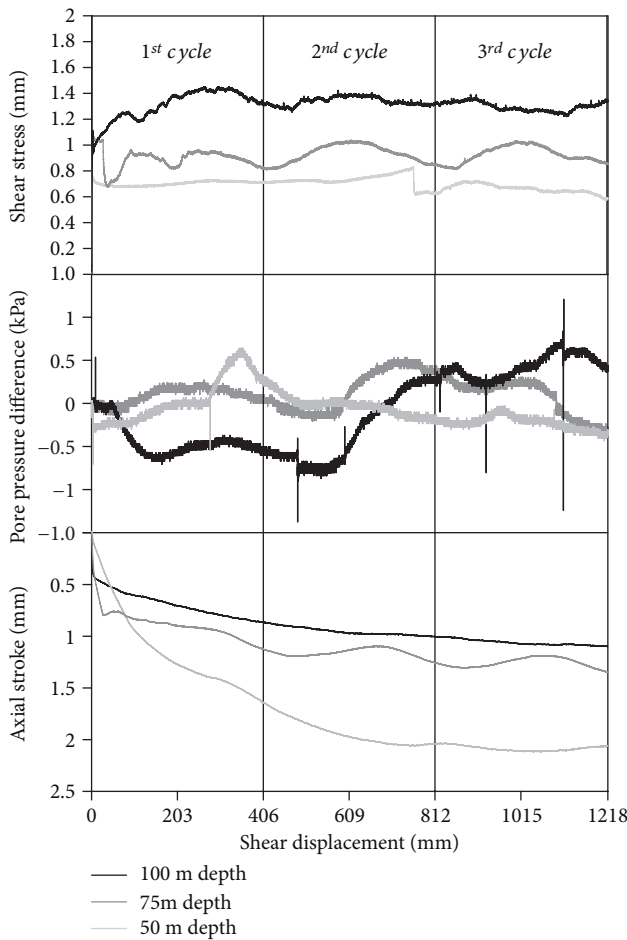
FIGURE 9: Experimental results of CU ring shear test.

at the sliding surface leading to a large increase in the pore pressure. Iverson [8] has also supported that the increasing pore pressure would further accelerate the sliding. In addition, a deep sliding surface with a high normal stress results in a landslide gouge with low hydraulic conductivity, which dissipates the pore pressure later

(3) The ring shear test results with a shearing rate of 1.5 mm/min are close to the data from conventional direct shear tests, $\varnothing = 21.4°$ [2]. Both shear tests got the shear strength parameters when the landslide was initiated with slow shearing rate but not the whole sliding process. The sliding velocity of the Hsien-du-shan landslide is estimated from 20.4 to 33.7 m/s [32]. Yang et al. [36] indicated that the shear rate controls the shear behavior of a sliding surface. When the sliding surface is accelerated to a high speed, the slip weakening [7] governs the mechanical properties of the sliding surface. In addition, Wu [37] showed that the disintegration of the rock mass during a landslide increases the run-out distance of the sediments. Therefore, the slip weakening at the sliding surface and the disintegration of the blocky rock mass are the two main reasons that the internal friction angle of the sliding surface determined by the ring shear test ($\varnothing = 25.3°$ to 26.1°) surpassed the apparent friction angle ($\varnothing = 13°$), which is defined as the ratio of the vertical height and the horizontal travel distance of a landslide, suggested by the topography [2]. Further verifications can be carried out by a discrete element method with the slip weakening algorithm [38] in the future

6. Conclusions

In this study, a new ring shear apparatus capable of conducting a CU shear test was developed. The capacity of the new device is ascertained by the successful modelling of the initiation of the heavy rainfall-induced Hsien-du-shan rock avalanche at the sandstone/landslide gouge interface with a maximum normal stress exceeding 2 MPa. Furthermore, the shear behaviors of the sliding surface under the different normal stresses were explored.

The experimental results indicated that the remolded landslide gouge governs the shear behavior of a high water content sliding surface such as the Hsien-du-shan rock avalanche. The internal friction angle of the sliding surface in the total stress state investigated by the ring shear test falls between 25.3 and 26.1°, which is larger than the dip angle
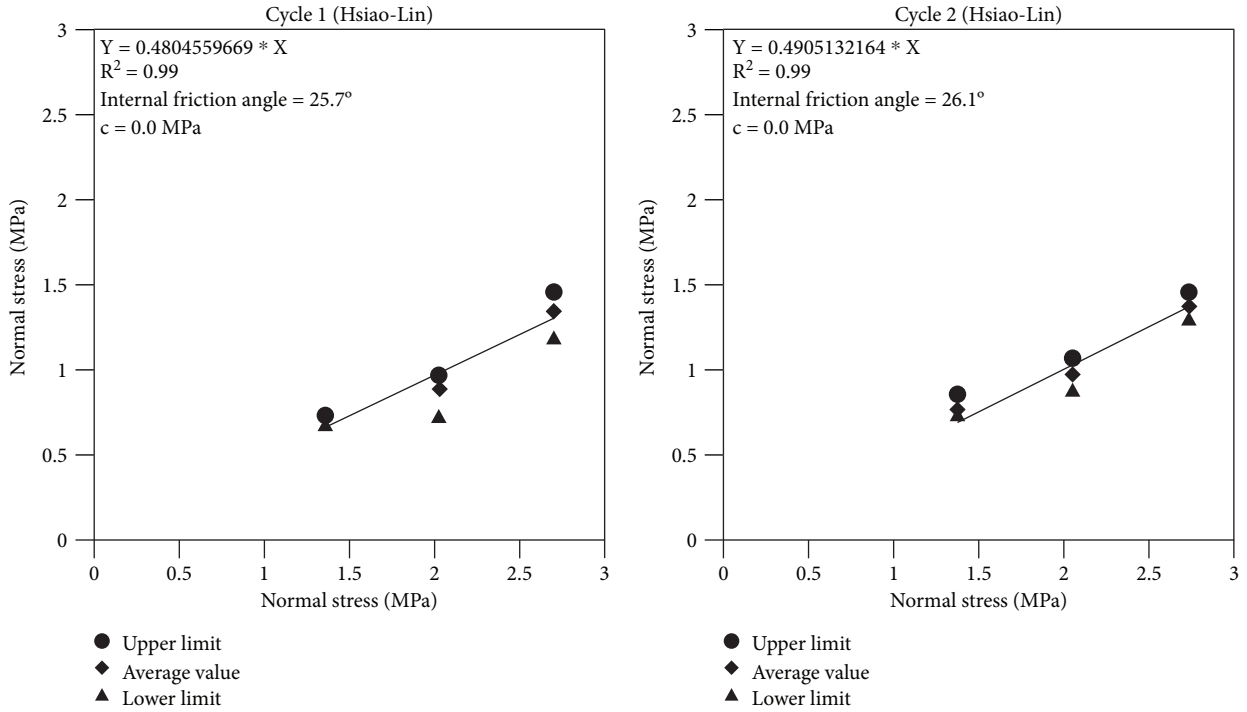
(a) Cycle 1

(b) Cycle 2
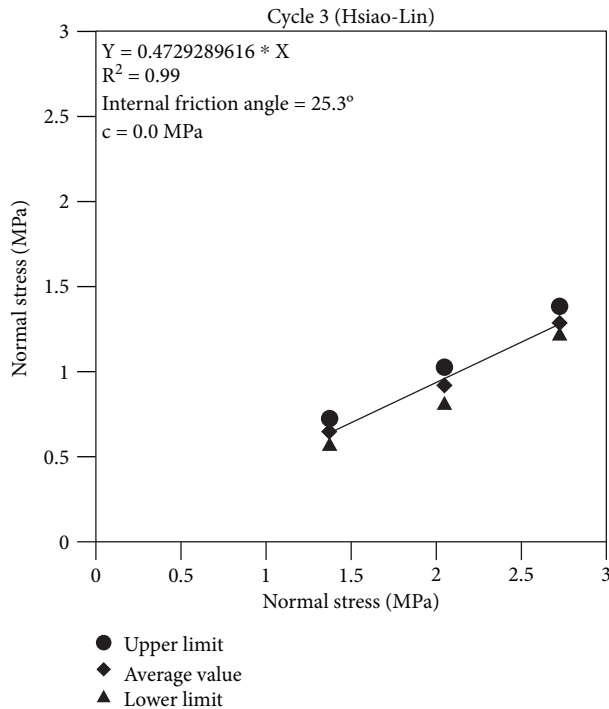
(c) Cycle 3

Figure 10: Failure criteria of the sliding interface.

of the slope and thus clarifies the stability of the slope before Typhoon Morakot.

When the movement of the sliding interface initiated, the shear contraction at the sliding surface generates excessive pore pressure feedback and destabilizes the slope. In addition, the low hydraulic conductivity of the landslide gouge/ sandstone interface would result in the significant and continuous pore pressure increase during the long shear

TABLE 4: Water content of the samples after ring shear test.

Sample		Depth = 100 m	Depth = 75 m	Depth = 50 m
	Upper part	8.82%	14.49%	10.56%
Remolded landslide gouge	Middle part	10.03%	11.83%	10.29%
	Lower part	9.93%	12.00%	9.88%
Tangenshan rock		1.94%	2.13%	—

displacement when the sliding surface is sheared under large normal stresses. The excessive pore pressure can accelerate the rock avalanche.

Data Availability

The data used to support the findings of this study are available from the corresponding author upon request.

Conflicts of Interest

The authors declare that they have no conflicts of interest.

Acknowledgments

References

[1] W. K. Lin, *Simulating the Rock Avalanche by Three Dimensional Distinct Element Method, [M.S. Thesis]*, National Cheng Kung University, Tainan, Taiwan, 2015.

[2] J. H. Wu, J. H. Chen, and C. W. Lu, "Investigation of the Hsien-du-shan rock avalanche caused by typhoon Morakot in 2009 at Kaohsiung county, Taiwan," *International Journal of Rock Mechanics and Mining Sciences*, vol. 60, pp. 148–159, 2013.

[3] M. Chigira, C. Y. Tsou, Y. Matsushi, N. Hiraishi, and M. Matsuzawa, "Topographic precursors and geological structures of deep-seated catastrophic landslides caused by typhoon Talas," *Geomorphology*, vol. 201, pp. 479–493, 2013.

[4] W. H. Schulz, "Landslide susceptibility revealed by LIDAR imagery and historical records, Seattle, Washington," *Engineering Geology*, vol. 89, no. 1-2, pp. 67–87, 2007.

[5] J. H. Wu, W. K. Lin, and H. T. Hu, "Post-failure simulations of a large slope failure using 3DEC: the Hsien-du-shan slope," *Engineering Geology*, vol. 242, pp. 92–107, 2018.

[6] C. M. Lo, M. L. Lin, C. L. Tang, and J. C. Hu, "A kinematic model of the Hsiaolin landslide calibrated to the morphology of the landslide deposit," *Engineering Geology*, vol. 123, no. 1-2, pp. 22–39, 2011.

[7] C. Y. Kuo, Y. C. Tai, C. C. Chen et al., "The landslide stage of the Hsiaolin catastrophe: simulation and validation," *Journal of Geophysical Research*, vol. 116, no. F4, 2011.

[8] R. M. Iverson, "Regulation of landslide motion by dilatancy and pore pressure feedback," *Journal of Geophysical Research*, vol. 110, no. F2, 2005.

[9] T. C. Lee and P. T. Delaney, "Frictional heating and pore pressure rise due to a fault slip," *Geophysical Journal International*, vol. 88, no. 3, pp. 569–591, 1987.

[10] S. A. Miller, A. Nur, and D. L. Olgaard, "Earthquakes as a coupled shear stress-high pore pressure dynamical system," *Geophysical Research Letters*, vol. 23, no. 2, pp. 197–200, 1996.

[11] A. W. Bishop, G. E. Green, V. K. Garga, A. Andresen, and J. D. Brown, "A new ring shear apparatus and its application to the measurement of residual strength," *Geotechnique*, vol. 21, no. 4, pp. 273–328, 1971.

[12] A. C. Trandafir and K. Sassa, "Undrained cyclic shear response evaluation of sand based on undrained monotonic ring shear tests," *Soil Dynamics and Earthquake Engineering*, vol. 24, no. 11, pp. 781–787, 2004.

[13] G. Wang and K. Sassa, "Seismic loading impacts on excess pore-water pressure maintain landslide triggered flowslides," *Earth Surface Processes and Landforms*, vol. 34, no. 2, pp. 232–241, 2009.

[14] J. A. Clausen, R. H. Gabrielsen, E. Johnsen, and J. A. Korstgård, "Fault architecture and clay smear distribution. Examples from field studies and drained ring-shear experiments," *Norwegian Journal of Geology*, vol. 83, no. 2, pp. 131–146, 2003.

[15] L. R. Hoyos, C. L. Velosa, and A. J. Puppala, "Residual shear strength of unsaturated soils via suction-controlled ring shear testing," *Engineering Geology*, vol. 172, pp. 1–11, 2014.

[16] N. R. Iverson, R. W. Baker, and T. S. Hooyer, "A ring-shear device for the study of till deformation: tests on tills with contrasting clay contents," *Quaternary Science Reviews*, vol. 16, no. 9, pp. 1057–1066, 1997.

[17] Y. R. Li and A. Aydin, "Shear zone structures and stress fluctuations in large ring shear tests," *Engineering Geology*, vol. 167, pp. 6–13, 2013.

[18] P. L. Moore and N. R. Iverson, "Slow episodic shear of granular materials regulated by dilatant strengthening," *Geology*, vol. 30, no. 9, pp. 843–846, 2002.

[19] Y. R. Li, B. P. Wen, A. Aydin, and N. P. Ju, "Ring shear tests on slip zone soils of three giant landslides in the Three Gorges Project area," *Engineering Geology*, vol. 154, pp. 106–115, 2013.

[20] S. C. Chen and C. H. Wu, "The geomorphological variation triggered by catastrophic deep landslide in Siaolin village," *Journal of Chinese Soil and Water Conservation*, vol. 40, pp. 359–376, 2009.

[21] K. Sassa, B. He, K. Dang, O. Nagai, and K. Takara, "Plenary: Progress in landslide dynamics," in *Landslide Science for a Safer Geoenvironment*, vol. 1, pp. 37–67, Springer, Cham, Switzerland, 2014.

[22] C. J. Liao, D. H. Lee, J. H. Wu, and C. Z. Lai, "A new ring-shear device for testing rocks under high normal stress and dynamic

conditions," *Engineering Geology*, vol. 122, no. 1-2, pp. 93–105, 2011.

[23] K. Sassa, K. Dang, B. He, K. Takara, K. Inoue, and O. Nagai, "A new high-stress undrained ring-shear apparatus and its application to the 1792 Unzen–Mayuyama megaslide in Japan," *Landslides*, vol. 11, no. 5, pp. 827–842, 2014.

[24] J. H. Wu, C. J. Liao, H. M. Lin, and T. T. Fang, "An experimental study to characterize the initiation of the seismic-induced Tsaoling rock avalanche," *Engineering Geology*, vol. 217, pp. 110–121, 2017.

[25] Y. Hong, G. Yu, Y. Wu, and X. Zheng, "Effect of cyclic loading on the residual strength of over-consolidated silty clay in a ring shear test," *Landslides*, vol. 8, no. 2, pp. 233–240, 2011.

[26] D. H. Lee, C. H. Juang, J. W. Chen, H. M. Lin, and W. H. Shieh, "Stress paths and mechanical behavior of a sandstone in hollow cylinder tests," *International Journal of Rock Mechanics and Mining Sciences*, vol. 36, no. 7, pp. 857–870, 1999.

[27] E. N. Bromhead, "A simple ring shear apparatus," *Ground Engineering*, vol. 12, no. 5, pp. 40–44, 1979.

[28] C. H. Wu, *Investigating the Residual Strength of the Soft Rocks at South Taiwan Using the Ring-Shear Test Apparatus, [M.S. Thesis]*, Department of Civil Engineering, National Cheng Kung University, Tainan, Taiwan, 2005.

[29] H. M. Lin, J. H. Wu, and E. Sunarya, "Stability analysis of Hsien-du-shan rock slope during the earthquakes," *Disaster Advances*, vol. 6, no. 10, pp. 4–10, 2013.

[30] C. T. Lee, J. J. Dong, and M. L. Lin, "Geological investigation on the catastrophic landslide in Siaolin village, southern Taiwan," *Sino-Geotechnics*, vol. 122, pp. 87–94, 2009.

[31] Q. C. Sung, C. W. Lin, W. H. Lin, and W. C. Lin, *Geologic Map and Explanatory Text of Taiwan Scale 1:50,000 51 Chiahsien*, CGS, MOEA, Taipei, Taiwan, 2000.

[32] C. Y. Tsou, Z. Y. Feng, and M. Chigira, "Catastrophic landslide induced by typhoon Morakot, Shiaolin, Taiwan," *Geomorphology*, vol. 127, no. 3-4, pp. 166–178, 2011.

[33] J. H. Wu, J. H. Chen, E. Sunarya, and T. N. Do, "Technical report of investigating and simulating the large landslides under global warming," National Science Council of Taiwan, Taipei, Taiwan, 2013.

[34] J. C. Gamble, *Durability–Plasticity Classification of Shales and other Argillaceous Rocks. [Ph.D. Thesis]*, University of Illinois Urbana Champaign, Urbana Champaign, Urbana, IL, USA, 1971.

[35] B. Tiwari, T. L. Brandon, H. Marui, and G. R. Tuladhar, "Comparison of residual shear strengths from back analysis and ring shear tests on undisturbed and remolded specimens," *Journal of Geotechnical and Geoenvironmental Engineering*, vol. 131, no. 9, pp. 1071–1079, 2005.

[36] C. M. Yang, W. L. Yu, J. J. Dong et al., "Initiation, movement, and run-out of the giant Tsaoling landslide — what can we learn from a simple rigid block model and a velocity–displacement dependent friction law?," *Engineering Geology*, vol. 182, pp. 158–181, 2014.

[37] J. H. Wu, "Applying discontinuous deformation analysis to assess the constrained area of the unstable Chiu-fen-erh-shan landslide slope," *International Journal for Numerical and Analytical Methods in Geomechanics*, vol. 31, no. 5, pp. 649–666, 2007.

[38] L. Z. Wang, H. Y. Jiang, Z. X. Yang, Y. C. Xu, and X. B. Zhu, "Development of discontinuous deformation analysis with displacement-dependent interface shear strength," *Computers and Geotechnics*, vol. 47, pp. 91–101, 2013.

[39] K. Sassa, H. Fukuoka, G. Wang, and N. Ishikawa, "Undrained dynamic-loading ring-shear apparatus and its application to landslide dynamics," *Landslides*, vol. 1, no. 1, pp. 7–19, 2004.

[40] T. E. Tika and J. N. Hutchinson, "Ring shear tests on soil from the Vaiont landslide slip surface," *Geotechnique*, vol. 49, no. 1, pp. 59–74, 1999.

[41] M. Ostric, K. Ljutic, M. Krkac et al., "Portable ring shear apparatus and its application on Croatian landslides," *Annuals of Disaster Prevention Research Institute, Kyoto University*, vol. 55, no. B, pp. 57–65, 2012.

[42] I. Tomasetta, D. Barletta, and M. Poletto, "The high temperature annular shear cell: a modified ring shear tester to measure the flow properties of powders at high temperature," *Advanced Powder Technology*, vol. 24, no. 3, pp. 609–617, 2013.

Research Article

Preferential Water Infiltration Path in a Slow-Moving Clayey Earthslide Evidenced by Cross-Correlation of Hydrometeorological Time Series (Charlaix Landslide, French Western Alps)

Grégory Bièvre [ID],[1] **Agnès Joseph,**[2] **and Catherine Bertrand**[3]

[1]*Université Grenoble Alpes, Université Savoie Mont Blanc, CNRS, IRD, IFSTTAR, and ISTerre, 38000 Grenoble, France*
[2]*CEREMA, Direction Territoriale Centre-Est, 69000 Bron, France*
[3]*Chrono-Environnement, Université de Franche-Comté, 25000 Besançon, France*

Correspondence should be addressed to Grégory Bièvre; gregory.bievre@univ-grenoble-alpes.fr

Slow-moving clayey earthslides frequently exhibit seasonal activity suggesting that deformation processes do not only depend on slope and intrinsic geomechanical parameters. On the contrary, seasonal motion patterns are frequently observed with acceleration during the wet season and deceleration during the dry season. Within landslides, it is mainly the phreatic water table which is monitored. However, in the case of deep-seated landslides made of heterogeneous lithological units and with several slip surfaces, the characterization of the phreatic water table does not allow to relate satisfactorily the activity of the landslide with environmental parameters such as rainfall and subsequent water infiltration at depth. This paper presents a seasonal analysis of water infiltration within a slow-moving clayey landslide. Results of an extensive geotechnical and geophysical prospect are first exposed. Then, rainfall and water table level time series are analysed for two water tables using the cross-correlation technique: the phreatic water table located a few metres deep and a water table located above a shear surface located 12 m deep. Results show that water infiltrates faster down to the deepest water table. Then, time series were split between "dry" and "wet" seasons and the effective rainfall was computed from the original rainfall time series. Cross-correlation results show that the phreatic water table responds identically to rainfall in both seasons. On the contrary, the water table located above the shear surface has a very contrasting behaviour between summer (mainly drainage) and winter (behaviour similar to the phreatic water table with storage of water during a few weeks). This difference in behaviour is in agreement with the landslide kinematics.

1. Introduction

Slow-moving clayey earthslides frequently exhibit seasonal activity suggesting that deformation processes do not only depend on slope and intrinsic geomechanical parameters. On the contrary, seasonal motion patterns are frequently observed with acceleration during the wet season and deceleration during the dry season [1–7]. On the one hand, acceleration phases are classically related to an increase in pore water pressure following water infiltration and an increase in water table level during wet seasons. On the other hand,

deceleration phases are related to water drainage, lowering of the water table level, and subsequent decrease in pore water pressure during dry seasons. This might also be related to potential dilation of fine-grained material in the vicinity of the shear zone [8, 9], or to liquefaction/fluidization of water-saturated sediments close to the rupture zone [10–13]. However, this seasonal dichotomy is not systematic and slow-moving landslides can be reactivated and fail without warning during dry seasons [14]. Water flux is mainly considered vertical from the surface down to depth with infiltration occurring through the matrix [15]. As such, 1D models for

water infiltration are widely used to evaluate and/or predict shallow landslide response to rainfall. This led to an establishment of empirical relationships relating the total amount of rainfall over a period (thus defining a so-called intensity-duration index) to shallow landside activity, at a local, regional, and/or global scale (e.g., [16–21]). Based on rainfall thresholds, these relationships were further applied to the build-up of early-warning systems [22, 23] and/or to landslide forecasting [24, 25]. However, these approaches are devoted to shallow landslides, with disrupted mass a very few metres thick and with a relatively homogeneous motion for water infiltration. They do not take into account possible and rapid infiltration through fissures. Furthermore, they cannot account for complex deep-seated landslides with possibly several shear surfaces located down to several tens of metres. The evolution of ground mechanical characteristics (and the physical processes at stake) close to rupture surfaces which control landslide acceleration and/or fluidization is still an open question, and several works were devoted to this specific task in the past decade [10–13, 26–30]. However, and even if rainfall and subsequent water infiltration are known to be a major driving mechanism for landslide acceleration (e.g., [31]), the experimental observation of water infiltration deeper than a few metres remains poorly reported.

In the Trièves area (French Western Alps), numerous slow-moving clayey earthslides are observed and have been studied for more than 30 years [2, 3, 32, 33]. In this area, conceptual models based on field observations and tests proposed that water infiltrates preferentially through subvertical surface cracks which are further connected to shear surfaces at depth [5, 34]. This model was confirmed both numerically [35] and experimentally [36]. From a numerical point of view, it remains difficult and challenging to integrate dense fissure networks to hydrological models [37]. From an experimental point of view, multidisciplinary approaches are often required to evidence infiltration phenomena. Recently, geophysical (resistivity and seismic) methods along with hydrological and geological prospecting were applied on the Avignonet landslide in the Trièves area [36]. Results showed that fissures served as preferential paths for rapid water infiltration from the surface down to the phreatic water table located a very few metres below the surface. Similar results were obtained by Travelletti et al. [38] during a controlled rain infiltration experiment monitored by electrical resistivity within black shales (Super-Sauze landslide, SE France). However, because of superficial water tables and limited resolution at depth, these observations were limited to very shallow infiltration. Using temperature logging in a borehole naturally filled with water, Bièvre et al. [36] noticed a small positive temperature anomaly at 10 m depth in summer which they related to a fast infiltration of water along a fissure/shear surface. Finally, most of water table datasets within deep-seated landslides of a thickness of several tens of metres concern phreatic (i.e., superficial) water tables (among many others, [6, 39]). All these results indicate that it remains difficult to evidence experimentally in situ fast motions of water infiltration deeper than a very few metres. To overcome this issue, an original experiment was designed in this work. Two piezometers (equipped with pore pressure

sensors) were installed at different depths: the first one to monitor the phreatic water table located at a few metres depth and the second one to monitor a water table located a few metres deeper, immediately above a shear surface located at a depth of 12 m. Water tables and rainfall were monitored for 4 years from late 2012 to late 2016. The first objective of this work is to present the results of a multidisciplinary study to document a slow-moving clayey landslide. The second objective is to expose original results which highlight experimentally the differential water infiltration modality for the two water tables and, more specifically, to evidence the role of fissures as preferential and fast water infiltration paths at depth. The third objective of this work is to evaluate the use of effective rainfall (instead of total rainfall) to establish correlations with water table time series and to test the possible advantage of this dataset corrected from evapotranspiration. Finally, the final objective of this work is to establish seasonal correlations between time series and to evidence a possible variability of water infiltration from the surface and further underground water flow as a function of the period of the year.

2. Study Site

The study site is located in the western Alps in SE France (Figure 1(a)), near the city of La Mure. It is located on the eastern flank of the NNE-orientated valley of La Bonne river, the basement of which is made of marly limestones of Aalenian age. This flank of the valley is the western border of the Beaumont plateau, a more or less flat structure made of quaternary sediments and located at an average elevation of around 850 m above sea level (asl). The physiography of the study area is mainly controlled by its quaternary history. During the Last Glacial Maximum (LGM), the valley was dammed twice by the Bonne glacier coming from the east [40]. These successive phases of advance and retreat led to the deposit and erosion of lithologically contrasted layers, including moraines, glaciolacustrine, and deltaic sediments. Over the Jurassic bedrock and from the base to the top, the stratigraphy is as follows [40]. At the end of the interglacial Würm I sequence, alluvial sediments with a thickness of around 50 m were deposited by the paleo-Bonne river. These sediments are mainly made of sands and gravels but also contain pebbles. They are locally cemented. At the beginning of the next glacial period (Würm II), the valley was dammed by the Bonne glacier and a lake was created. Fine-grained sediments made of alternating layers of clays and silts (so-called laminated clays) settled in the lake over a thickness of around 20 m. These levels are associated to the Trièves clays in terms of age and of lithological content. During the peak of this glacial episode (LGM), the progradation of the glacier towards the west was accompanied by the deposition of 40 m-thick ground moraines with a high clay content. Following an episode of warming, the glacier melted and the lake was established once again. Around 60 m of laminated clays were first deposited. They are overlain by 40 m of lacustrine sands and then deltaic sands and gravels. This sedimentary sequence marks the progressive filling of the lake in the area. These deposits are overlain by a few metres
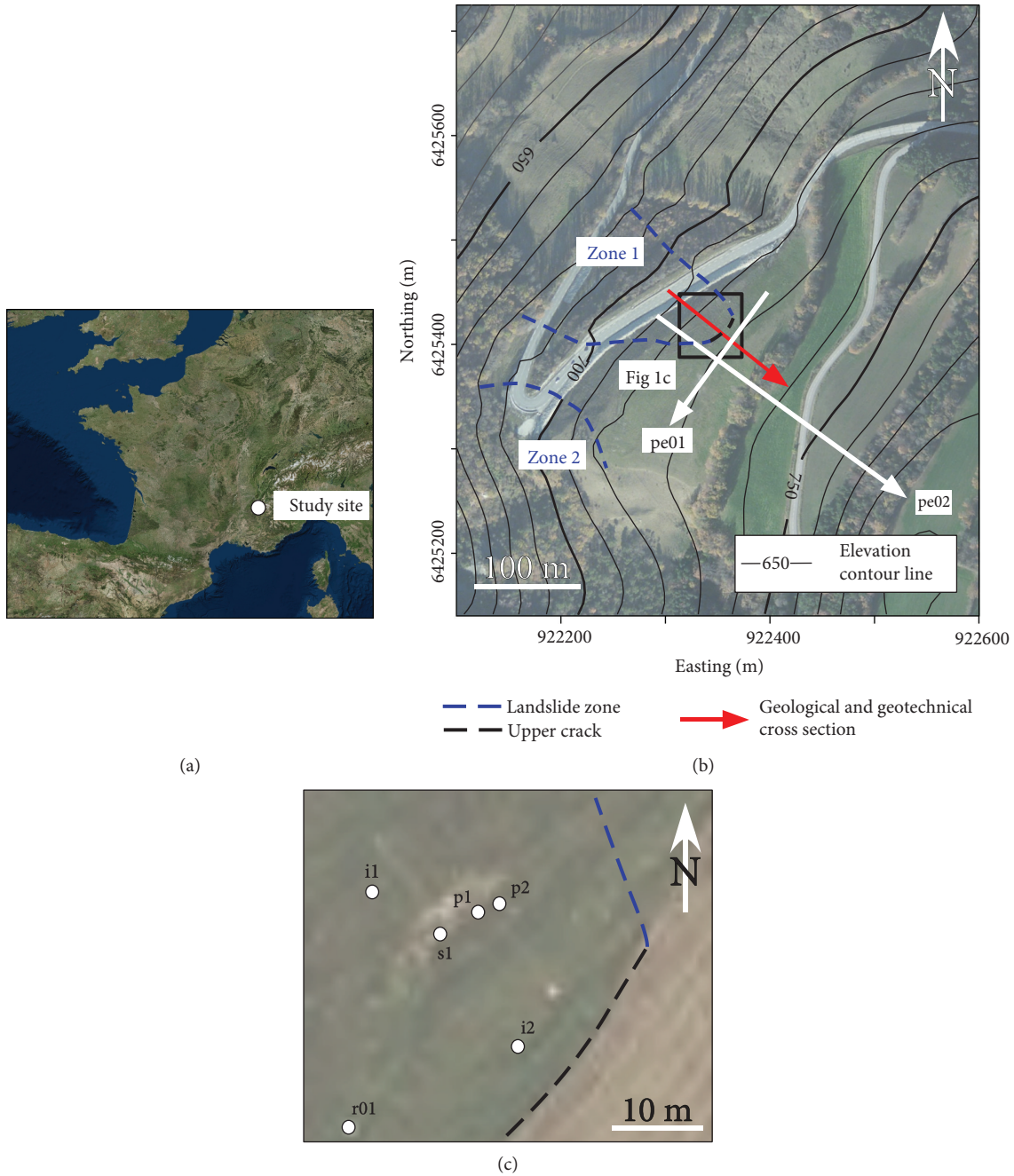
FIGURE 1: Location of the study site and of the tests. (a) General location. (b) Detailed morphology and location of the tests. pe01 and pe02 are electrical resistivity profiles. The red arrow represents the geological and geotechnical cross sections used in Figure 11. The black rectangle represents the location of Figure 1(c). Coordinates are metric and expressed in the French Lambert93 system. (c) Close-up on the location of inclinometers (i1 and i2), piezometers (p1 and p2), coring s1, and geodetic station r01.

of moraines containing big blocks and which are indicative of a further glacial episode (Würm III), with somewhat a more limited extension than the previous one. By analogy with the Trièves area, the definitive melting of the glacier allowed the Bonne river to erode into these soft sediments and to initiate landsliding [33]. Numerous landslides were reported and studied along the Bonne valley since more than 35 years [2–5, 26, 32, 41, 42]. Synthetically, it was shown that these landslides were settled within laminated clays and revealed several shear surfaces at depths ranging from a few metres

to up to 30 m to 40 m. Moreover, it was evidenced that the activity of these landslides was seasonal, with higher deformation occurring during autumn and winter and which originates from snowmelt and heavy rain falls.

Over the study site, the thickness of sediments over the Jurassic basement is estimated to be around 100 m. The vertical lithological heterogeneity induces heterogeneity in terms of hydrogeological and mechanical properties. The average slope of the valley is 18°. Two main landslide zones (labelled 1 and 2 in Figure 1(b)) were observed and

TABLE 1: Dates and characteristics of the experiments.

Experiment	Installation date	Characteristics	Sampling period
Inclinometer i1	September 2010	Borehole equipped with a 25 m deep inclinometer casing. Definitively sheared in late November 2012	1 to 3 months
ERT profile pe01	03 August 2012	62 electrodes, 5 m apart, in a multigradient configuration	X
Coring s1	September 2012	25.2 m deep coring	X
Boreholes p1 and p2	September 2012	8.5 m and 12.5 m deep boreholes equipped with pressure sensors	1 hour
Inclinometer i2	July 2013	Borehole equipped with a 40 m deep inclinometer casing. Definitively sheared after mid-March 2015	1 to 3 months
ERT profile pe02	09 August 2013	76 electrodes, 2 m apart, in a multigradient and dipole-dipole Configuration	X
EM profiling	17 February 2014	EM31 mapping in the SE part of the landslide	X
GNSS monitoring	27 November 2014 10 March 2015 28 July 2015	Real-time kinematic GNSS measurements	1 to 3 months
EM profiling	28 July 2015	EM31 mapping in the NW part of the landslide	X
GNSS monitoring	7 October 2015 17 March 2016	Real-time kinematic GNSS measurements	1 to 3 months
Water infiltration tests w1 and w2	17 March 2016	Beerkan infiltration tests	X
GNSS monitoring	15 June 2016 29 September 2016 8 December 2016 22 June 2017	Real-time kinematic GNSS measurements	1 to 3 months

monitored since the late 1970s. Several shear surfaces were evidenced by geotechnical prospecting, the two most active being located within the first 10–15 m below the surface. The first one is at a depth of around 5 m and is located at the interface between moraines and laminated clays. The second one is at a depth of around 12 m and is located within the laminated clays. These depths are similar to those of the most active shear surfaces affecting landslides in the Trièves area [27, 33, 36]. This landslide corresponds to a clay/silt compound landslide according to Hungr et al. [28].

On the study site, these shear surfaces affect a road with a consequent traffic of 1750 vehicles per day, 7% of which are trucks (http://www.enroute.mediterranee.developpement-durable.gouv.fr). Recent remediation works conducted in 2009 allowed improving traffic conditions and adapting the road to less intense deformation in zone 2. In this area, present-day motions are lower than 2 cm/yr. However, remediation works did not allow to decrease the motion of zone 1 which is still highly active. Remediation works consisted of retaining permeable structure along the uphill flank of the road. The road was also shifted a few metres uphill (towards the east) with the objective of moving it out of the main crack in zone 1 and in zone 2. Drainage structures were dug in the upper part of the slope to reduce and maintain the phreatic water table at a low level for increasing the security factor of the site (by decreasing pore pressure). Geotechnical design of those structures was performed by modelling and calculation (see Section 3.5). The purpose was to get a safety factor close to 1.3. This is lower than the safety factor of 1.5 usually required according to French and/or European standards

[43]. However, the purpose was not to reach a full security factor. This would have led to a designing of huge retaining structures, hard to build on the site with the consequence of a significant increase in the cost of works.

3. Material and Methods

The site was investigated using various ranges of in situ techniques to determine the geological, geophysical, geotechnical, and hydrogeological characteristics of the site. Measurements started in September 2010 and ended in late June 2017. The different techniques used in this work are detailed in the following section, and a synthesis of the experiments is provided in Table 1.

3.1. Geological, Geophysical, and Hydrogeological Prospecting

3.1.1. Coring. A 25.2 m-long borehole, labelled s1 in Figure 1(c), was cored to study the lithological characteristics of the site. The average recovery was 72%. Core samples were visually analysed. This allowed identifying the distinct lithological units. It was also possible to visually identify disrupted levels corresponding to shear surfaces. Finally, samples were analysed in terms of grain size distribution and geotechnical parameters (identification and tests) for further geotechnical modelling.

3.1.2. 2D Electrical Resistivity Tomography. 2 electrical resistivity tomography (ERT) profiles were conducted on the site, namely, pe01 and pe02 (Figure 1). This method is a classical technique for landslide investigation (for a review,

see [44, 45]). Resistivity measurements were conducted with a multichannel ABEM Terrameter LS. pe01 was conducted along a NW-SE direction, with 62 electrodes with a constant spacing of 5 m. The objective of this profile was to gain information on the geological setting. 1105 measurements were acquired in a multigradient configuration [46]. pe02 was conducted at the top of zone 1 along a NNE-SSW direction. It consisted of 64 electrodes with a constant spacing of 2 m. One further roll-along (12 electrodes) allowed gathering a 150 m-long profile. The objective of this profile was to get a high-resolution image of the subsurface at the top of zone 1. Measurements were acquired in a multigradient configuration and also in a dipole-dipole configuration (see [47]). The 2964 experimental measurements were inverted jointly.

Apparent resistivity data were inverted using the boundless electrical resistivity tomography (BERT) algorithm developed by Günther et al. [48]. This code is based on finite element computations with irregularly shaped triangles [49]. The regularization strength (lambda) was manually tuned to get a chi^2 value close to 1, indicating that the data were fitted within a default error of 3%. Inversion provided satisfactory results with relative root mean square (RRMS) errors below 5% after 3 and 2 iterations for pe01 and pe02, respectively.

3.1.3. Electromagnetic Profiling.
Electromagnetic (EM) profiles were acquired using an EM31 conductivity metre (Geonics Ltd., Mississauga, Canada). The fundamentals of the technique are provided in reference books (e.g., [50], and specifics about the device can be found in McNeill [51]). In clayey landslide investigation, this technique is used to map the spatial distribution of apparent resistivity over the first metres below ground, noticeably to detect the presence of electrically conductive materials such as quick clays [52] or to highlight the geology below a weathered and disrupted cover [53]. Measurements were acquired with horizontal coplanar loops. This configuration mainly provides information on ground properties in the very first metres but with sensitivity to EM properties down to a maximum depth of around 5 m to 6 m. The EM device was coupled to a global navigation satellite system (GNSS) to georeference the measurements. A total area of 0.2 km^2 was covered. Experimental data, with an average coverage of 0.5 pt/m^2, were interpolated using a kriging algorithm with a mesh size of 5 m × 5 m. The result is a map depicting the spatial distribution of the apparent resistivity over the first metres below the surface.

3.1.4. Water Infiltration Tests.
Finally, two infiltration tests were conducted at the top of landslide zone 1 with the objective of evaluating the steady-state infiltration rate (SIR) of two contrasted levels. The tests are based on the Beerkan infiltration method developed by Braud et al. [54] and improved by Lassabatère et al. [55]. It consisted in infiltrating known volumes of water with a variable head through a single annular ring of a diameter of 12.5 cm. The ring was set at a depth of 1 to 2 cm and further coated with clay to avoid lateral loss. First, 20 cl of water was poured and the time needed for the complete infiltration was measured. A second volume of water was immediately poured, and, once again, the time needed for the complete infiltration was measured. On the study site, three to five successive infiltrations were needed to achieve the experiments. These were conducted after removing the first 0.3 m of the ground to avoid root effects. For the first volumes, the water is infiltrated through the unsaturated zone in transient regime while, for longer times, the water is infiltrated through the saturated zone in steady-state regime. SIR is derived by computing the slope of the cumulated water height as a function of time, in steady-state regime (last experimental points). This method was successfully applied by Bièvre et al. [56] on the Avignonet landslide, in similar lithological units, to characterize the hydraulic properties of contrasted geological layers, and results by these authors will be compared to those obtained in the present work.

3.2. Landslide Deformation and Kinematics

3.2.1. Surface Kinematics.
Monitoring of surface kinematics is a key point to landslide studies, noticeably to establish relationships between surface motion and the evolution of environmental parameters (such as rainfall and water table [6, 33, 57–59]). 50 to 60 geodetic stations were monitored using a real-time kinematic (RTK) differential GNSS (D-GNSS) which provided measurements with an error of a few mm relative to the base station. For each campaign, the location of the base station, which acquired measurements for at least two hours, was postprocessed using the Trimble Business Center software (geospatial.http://trimble.com). It provided maximum errors of 2.5 cm (highest error on the vertical component). It was difficult to set permanent geodetic stations in the south-eastern part of the site because of farming activity (cattle). In this area, metallic plates connected to a drainage system were used as permanent stations.

The monitoring started with around 50 stations in late November 2014. The number of stations progressively increased, and 60 stations were fully operational starting from mid-March 2016 until late June 2017. Annual average total displacement rates were computed between mid-March 2016 and late June 2017 using the three directional components. Data were interpolated using a kriging algorithm with a mesh size of 2.5 m × 2.5 m to produce a spatially continuous map depicting the average annual displacement rates. This small mesh size was chosen to evidence potential lateral variations where numerous stations were close by. Cumulated displacements were also analysed for three stations (r01 to r03) located in the south-eastern part of the slide, in the vicinity of the upper limit of landslide zone 1. Finally, horizontal displacement rate was also computed at station r01 which is located close to borehole i3. It was compared with the motion deduced from inclinometer data (see below). D-GNSS measurements were also used to build a digital elevation model (DEM) of the study site in late July 2015. Topographic cross sections were extracted from this DEM. Finally, the mapping of some structures, such as cracks, was also achieved using this technique.

3.2.2. Deformation and Kinematics at Depth. Two boreholes were drilled to monitor the evolution of the deformation at depth as a function of time using inclinometer probes. Details about this kind of instrumentation can be found in reference books (e.g., [60]), and recent applications to landslides can be found in Uhlemann et al. [59] and in Gullà et al. [61]. Measurements and processing were conducted periodically (typically between 1 and 3 months) following French standard NFP94-156 [62]. Succinctly, a grooved tube is introduced into a borehole and is further sealed to the ground. The measuring probe is inserted into the tube, and sprung wheels are used to guide the probe along the grooves. The inclination with respect to the vertical axis is measured by accelerometers. Measurements were conducted each 0.5 m, from the base to the top of the tube. Using trigonometric relationships, the inclination at each depth step is turned into a horizontal displacement with reference to the first measurement in time. Displacements are then expressed as the cumulation of individual displacements at each depth step from the base to the top of the tube. The first measurement in time serves as a reference measurement.

3.3. Meteorological and Hydrogeological Time Series. The effective rainfall or groundwater recharge is estimated with a soil-water balance based on characterization of evapotranspiration (ET_c) and parameters characterising the recharge area (soil available water capacity (SAWC), runoff, and vegetation coefficient K_c). The effective rainfall is estimated according to the workflow calculation proposed by Vallet et al. [63]. This workflow requires the records of precipitation, air temperature, relative humidity, solar radiation, and wind speed within or close to the study area. Daily rainfall and average wind velocity data were obtained from a meteorological station operated by the French Office of Meteorology (Météo-France) and which is located around 2.5 km NW of the study site. Daily solar radiation data were measured by a station operated by Météo-France and located 30 km south of the study site. Temperature and atmospheric pressure data were obtained from a station located in the Avignonet landslide in the Trièves area, 12 km WNW of the study site, and at an elevation of 680 m asl (i.e., comparable to the study site). This station is operated by the French National Observatory on Landslides OMIV [64]. Hourly temperatures were turned into average daily data. Daily minimum and maximum temperatures were extracted from the hourly time series.

The estimation of the effective rainfall with the soil-water balance requires the determination of three parameters which are ET_c, K_c, and SAWC. ET_c and K_c are related and are expressed as follows:

$$ET_c = ET_0 \cdot K_c, \tag{1}$$

where ET_0 is the reference evapotranspiration and is determined using the Penman-Monteith method [65]. K_c depends on the stage of development of the vegetation (cattle grass on the study site). It varies from a minimum value during winter (0.85) to a maximum value during summer (1) according to Allen et al. [65]. An average value of 0.94 was used in this

study. SAWC is deduced from the nature of the soil. From field observation and laboratory tests, it was estimated to be 30 mm.

Two pore pressure sensors were installed in late September 2012 in two distinct boreholes (p1 and p2 in Figure 1(c)) and with two distinct recording units. The sensor in p1 was set at a depth of 8.5 m, 0.5 m below the base of the morainic cover, to monitor the phreatic water table. The sensor in p2 was set at a depth of 12.5 m to monitor a water table located above a shear surface at 12 m depth. Both pressure sensors were installed in closed boreholes (see [60]). The monitoring systems were also ventilated to remove the effect of atmospheric pressure variation [66].

3.4. Cross-Correlation of Rainfall and Water Table Time Series. The linear relationships between rainfall and water table were further studied using cross-correlation. This mathematical technique is classically applied in hydrogeology, notably to study the linear dependency between rainfall and aquifer recharge [67–70]. In landslide studies, this technique has however been little applied. Helmstetter and Garambois [71] used it on the Séchilienne rockslide (French Alps) to correlate seismic catalogues and environmental parameters (rainfall). They evidenced very short reaction times (<1 day) between rainfall and the initiation of rockfalls and of micro-earthquakes within the landslide.

Daily values were first standardized (subtraction of the mean and normalization by the standard deviation of the dataset) to get time series with a mean centred on zero and with a variance of 1. The 95% confidence interval r, in this case, depends only on the length of the dataset [72, 73] and is classically of the form

$$r = \frac{2}{\sqrt{n}}, \tag{2}$$

where n is the length of the dataset. It was modified to take into account the decrease in the length of the dataset n as the time series to be correlated is moved apart from the centre of the reference time series. For positive lags, it is expressed by

$$r_i = \frac{2}{\sqrt{n-i}}, \tag{3}$$

where r_i is the 95% confidence interval value at position i along the time series. For negative lags, it is symmetric of r_i for positive lags.

3.5. Stability Calculations. Stability calculations were conducted at the limit equilibria using the global perturbation method of the normal stress along a failure curve [74] with a Mohr-Coulomb criterion. This method was developed in France and is applicable to any shape of slip surface. A classical 2D model has been implemented to illustrate field observations in a simplified way. The model was built from geological observations (lithology, geometry), and geomechanical parameters were derived from laboratory tests. The topographic cross section (red arrow in Figure 1(b)) was derived from a DEM built from D-GNSS measurements.

The geometry of the geomechanical layers was derived from boreholes located close to the cross section (i.e., i1, i2, s1, p1, p2, and other boreholes not presented in this work).

The rock riprap retaining structure was not modelled. This was chosen to compute the actual stability of this particular area of the site from a general point of view and a general stability site study consideration. The riprap structure is made of rock blocks which are not connected to each other. This structure was designed to act as a drainage structure but also as a protection for the road and its users. It has no stabilizing role.

Computations were conducted with the software Geostab 2013 [75]. An initial calculation was conducted with fixed mechanical parameters, especially the cohesion and the internal friction angle of the soil. These parameters were obtained from residual shear tests which provided residual cohesion and friction angle of the upper part of the laminated clays. The failure curve was designed based on inclinometer data and on the location of cracks observed in the field (see Figure 1). Then, two water table levels were taken into account for the calculations. Time series from pressure sensors p1 and p2 indicated a low level corresponding to the lowest measured level (in summer) and a high table level, corresponding to the highest level measured (in winter).

4. Results

4.1. Geological, Geophysical, and Hydrogeological Characterization. The detailed analysis of the samples from coring s1 allowed establishing the lithological characteristics of the site. From the surface down to a depth of 8 m, the lithology is made of a mixture of sands, gravels, and pebbles within a clayey matrix. Endogenous and limestone pebbles suggest that this level is partially made of moraines. These moraines were most probably reworked by surface processes and by the activity of the landslide. From an 8 m depth down to 22.3 m, alternating laminae of clays and silts, with a unitary thickness of the order of the cm, were found. These levels correspond to glaciolacustrine deposits. Distorted strata were observed at depth ranges of 10.7–11.4, 15–16 m, and 18.9–20.4 m. One missing level (no core recovery) between 7.2 m and 7.7 m deep probably corresponds to disrupted soils. Below 22.3 m and down to 25.2 m (end of the coring), another heterogeneous level was observed. It is made of a dark clayey matrix containing sands and gravels. Several pebbles with diameters ranging between 2 cm and 8 cm were observed. These pebbles were made of dark limestone and also endogenous rocks and were marked by scours, which suggests that these levels correspond to morainic deposits.

Figure 2 presents ERT profiles pe01 and pe02. The 315 m-long profile pe01 (Figure 2(a)) shows the presence of layers with a resistivity higher than 100 $\Omega \cdot$m (and up to more than 500 $\Omega \cdot$m) for elevations above 720 m asl. Below this elevation, resistivity is lower than 50 $\Omega \cdot$m, which corresponds to the laminated glaciolacustrine clays identified in s1 (Figure 2(a)). The interface between these low-resistivity levels and the overlying formations appears subhorizontal. The base of the clays seems to be located at an elevation of around 670 m to 680 m, and the underlying formations

exhibit higher resistivity (around 150 $\Omega \cdot$m to 200 $\Omega \cdot$m). The interface between these two units also appears subhorizontal with undulations. However, it must be stressed out that these levels at the bottom of the geophysical images are very poorly investigated and that, consequently, it is difficult to interpret them confidently. Using the log established by Monjuvent [40] on an outcrop located around 700 m NE of the landslide, it was possible to define the stratigraphy of the study site. The upper resistive layers could correspond to a composite unit made of, from the base to the top, lacustrine laminated fine sands, deltaic sands and gravels of Würm II age and, finally, moraines of Würm III age. The underlying laminated clays correspond to glaciolacustrine deposits of Würm II age. These deposits are similar to the prone-to-landsliding Trièves clays, in terms of age and geomechanical properties. The badly resolved more resistive layers located below 670 m to 680 m asl could correspond to the Lower Moraines unit. This interface is located at least 20 m below the morainic levels detected at the base of s1 (Figure 2). However, this interface appears continuous on ERT profile pe01 and, below the base of s1, low resistivity levels are clearly identified. This apparent discrepancy remains difficult to interpret, and further prospecting is required to solve this issue.

ERT profile pe02 was conducted at the top of landslide zone 1 (location in Figure 1(b)), perpendicular to the slide motion. It shows the presence of two main units. The top unit is made of around 2 to 3 m of material with a resistivity of around 150 $\Omega \cdot$m to 200 $\Omega \cdot$m. However, between 70 m and 105 m along the profile, the resistivity is higher (200 $\Omega \cdot$m to up to 500 $\Omega \cdot$m) with a thickness increasing to around 6 m at a distance of 80 m to 90 m along the profile. Below are found lower resistivity levels (30 $\Omega \cdot$m to 100 $\Omega \cdot$m) which could correspond to the glaciolacustrine laminated clays.

The map in Figure 3 presents the spatial distribution of apparent resistivity over the first metres below the surface. Apparent resistivity up to 75 $\Omega \cdot$m is observed in the Northern and Western parts of the site (i.e., downslope). This location and elevation correspond to clayey units as observed on nearby outcrops [40]. Resistivity then increases from around 75 $\Omega \cdot$m to up to 200 $\Omega \cdot$m southward and eastward (upslope). This location corresponds to the morainic cover associated with lacustrine fine sands and deltaic sands and gravels observed on ERT profiles (Figure 2). Apparent resistivity values are slightly higher than those obtained with ERT for both moraines and clays. This probably originates from superficial effects (surface processes, farming activity, landslide activity, etc.) which slightly increase the porosity of the ground and, consequently, its resistivity. More interestingly, the relatively high resistivity zone in the south-eastern and uphill parts of the figure appears to be connected to the upper part of landslide zone 1. This observation is in good agreement with ERT profile pe02 which shows, at the same location, a thickening and an increase in resistivity of the morainic unit at the surface (Figure 2(b)). These higher resistivity levels are interpreted as originating from a higher proportion of coarse elements (and, correlatively, a lower clay content). Consequently, it suggests that a channel of higher permeability could preferentially drive the water flux from the upper moraines, deltaic gravels, and lacustrine sands located above

(a)

(b)
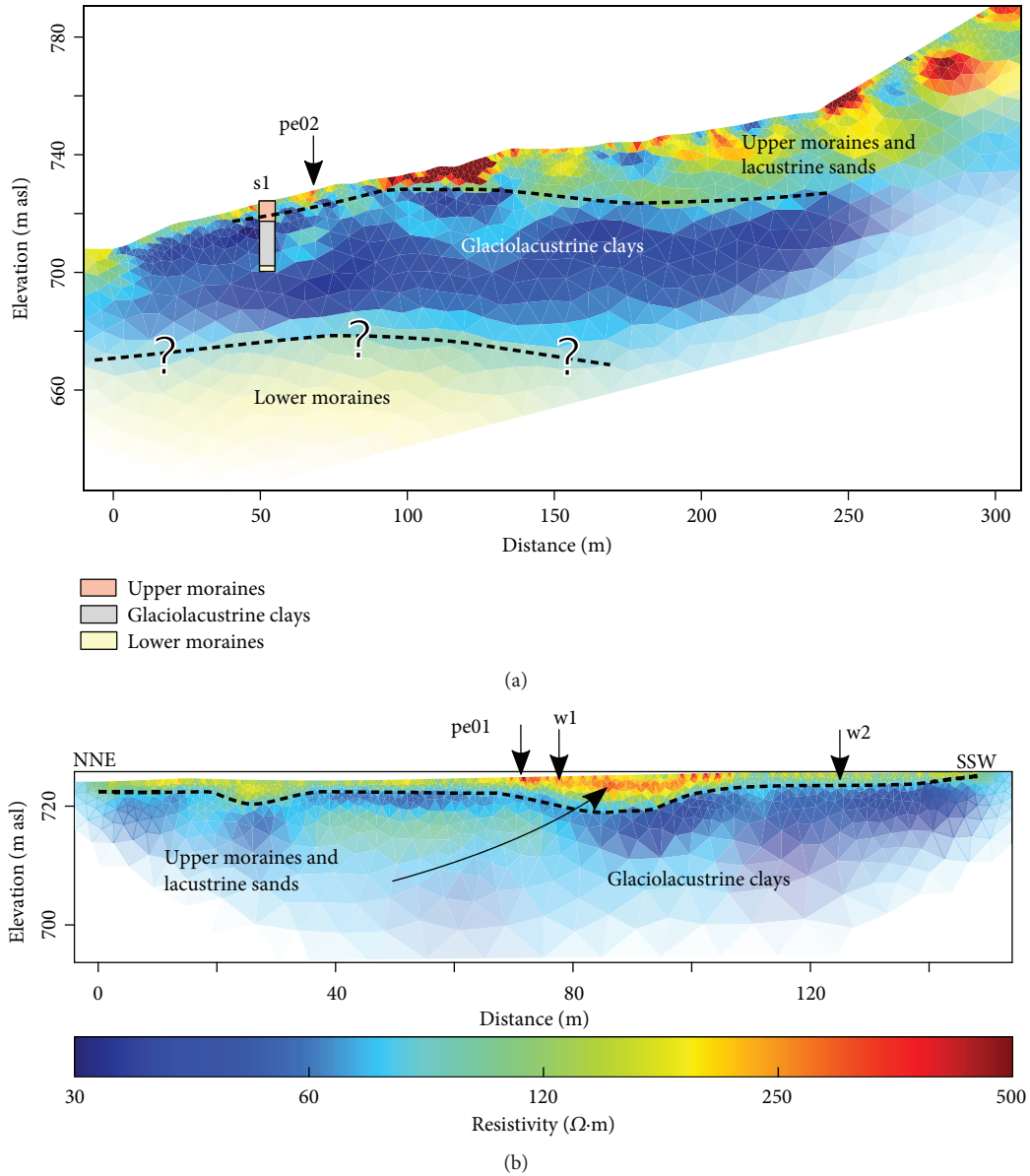
FIGURE 2: ERT profiles (a) pe01 and (b) pe02. Location is indicated in Figure 1. w1 and w2: water infiltration tests.

around 720 m asl (Figure 2(a)) down to the top of landslide zone 1. This is materialized by a blue arrow in Figure 3.

To confirm the hypothesis of a high permeability channel, water infiltration tests w1 and w2 (location in Figure 3) were conducted within high and low resistivity levels (moraines and clays, resp.). Results are presented in Figure 4. The curves depict the cumulated infiltrated water as a function of time. The steady-state regime was established relatively shortly after the experiments started but the last three values were used to compute the saturated infiltration rate (SIR). The obtained SIR values are 0.57×10^{-5} m/s and 1×10^{-5} m/s for w1 in the moraines and for w2 in the laminated clays, respectively. This factor of two confirms the difference in permeability and, hence, in grain size, between the two units. However, it must be stressed out that measurements were conducted at a depth of 0.3 m and that, at this depth, surface processes at stake (weathering, farming,

landslide activity, etc.) prevent from considering these values as representative of the subsurface at depth. Furthermore, measurements were conducted using a ring with a diameter of 0.125 m. As such, measurements are very local. Despite these limitations, the factor of two evidenced from these tests give an order of magnitude of the difference between the two units.

4.2. Surface and Depth Kinematics. Figure 5(a) presents the map of surface displacement rates measured at the 60 geodetic stations between mid-March 2016 and late June 2017. Velocities range between less than 2.5 cm/yr (i.e., within the error bar) in the Western and Northern parts of the slide and up to 15 cm/yr in the south-eastern part of the slide.

Figure 5(b) presents the topographic cross section along with displacement rates measured at experimental geodetic stations. The displacement rate is almost 12 cm/yr at the
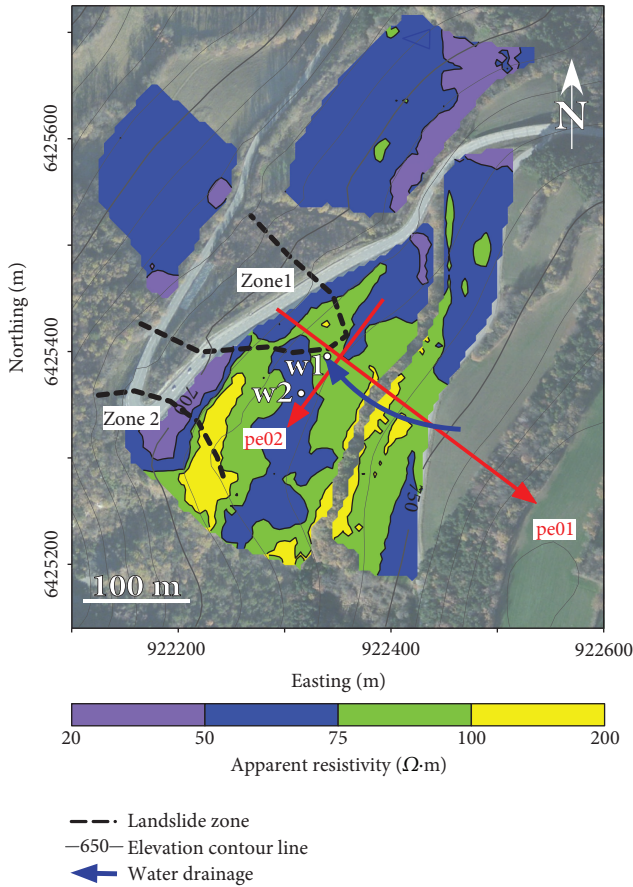
Figure 3: Map of the apparent resistivity over the first 5 m. The blue arrow represents a possible preferential water drainage path. The location of water infiltration tests w1 and w2 is indicated. The location of resistivity profiles pe01 and pe02 is indicated by red arrows.
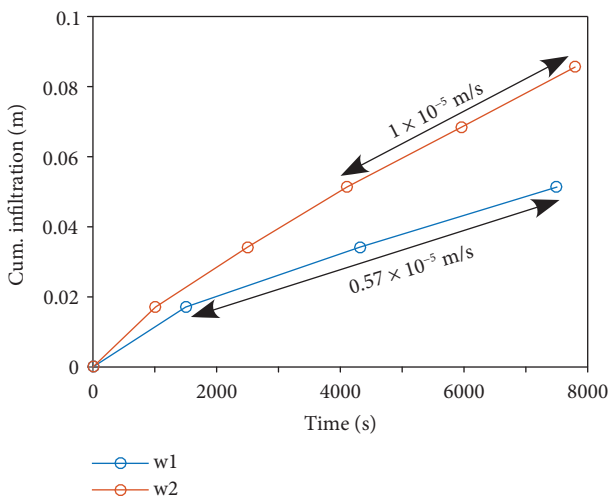
Figure 4: Water infiltration tests w1 and w2 (location in Figures 2(b) and 3) and saturated hydraulic conductivity.

south-east, close to the landslide limit. Then, the rate increases to 15 cm/yr downhill and further decreases to 6.2 cm/yr on top of the rock riprap. On the road close to

the base of the riprap, the displacement rate decreases to 2.5 cm/yr. These results suggest that the high rates observed in the SW part of the slide are presently strongly attenuated by the riprap structure. It also suggests that this structure, made of individual rock blocks, might undergo mid- to long-term irreversible deformation (block falls).

Finally, Figure 5(c) details displacements measured at geodetic stations r01 to r03 (location in Figure 5(a)). r01 and r02 are located in the immediate vicinity of the upper part of landslide zone 1. They exhibit relatively linear trends with displacement rates of 11.3 cm/yr (r01) and 9 cm/yr (r02). Considering the limited number of measurements and the width of the error bars (+/− 2.5 cm), it is not possible to determine if the motions are affected by seasonal changes. Unlike r01 and r02, r03 is located away from landslide zone 1. Except between mid-March and mid-June 2016 where it shows a motion of almost 16 cm/yr, it exhibits no movement since mid-June 2016.

Results from inclinometer monitoring are presented in Figure 6. The first inclinometer (i1, location in Figure 5(c)) was set to a depth of 25 m. It was definitely sheared 25.5 months after it was installed (from mid-October 2010 to late November 2012). Results show the presence of 2 shear surfaces at depths of around 6 m and 12 m. From 13 m to 17 m deep, the curves suggest the presence of one further shear surface. Finally, from 17 m down to the bottom of the inclinometer, the curves are not stable, which suggest that the inclinometer was not set in a stable area with no deformation. Maximum measured displacements are around 15 cm, half of which are accommodated by the first shear surface at 4 m depth.

Inclinometer i2 (location in Figure 5(c)) was set to a depth of 40 m. It was sheared 17 months after its installation (reference measurement in mid-October 2013 and last measurement mid-March 2015). The average horizontal motion close to the surface (at 0.5 m depth) is 7.4 cm/yr. At geodetic station r01, located 10 m W of i2 (Figure 1(c)), the average horizontal motion was 5.6 cm/yr. Considering the error on measurements with GNSS systems (around 2 cm along the horizontal plane) and also that the monitored periods do not match exactly, these motions derived from variable instruments are in good agreement. In the same way as i1, the same deformation mechanisms are observed from the surface down to a depth of around 15 to 17 m. Below, a shear surface is observed at a depth of 29–30 m. Finally, below a depth of 29–30 m, no noticeable movements are observed, which suggests that the base of the landslide is located at this depth. From a quantitative point of view, 52% of the total deformation is accommodated by the shear surface at around 5 m depth, 25% at around 12 m depth, 15% at around 15 m depth, and finally, 8% at 30 m depth.

For both i1 and i2, the maximum deformation was observed at a depth of around 4 m to 5 m. Cumulated displacements at this depth are presented in Figures 6(c) and 6(d) for i1 and i2, respectively, as a function of time. Average motions for i1 and i2 at 4 m depth are 7.2 cm/yr and 7.8 cm/yr, respectively.

The curves for both i1 and i2 exhibit a nonlinear increase of the cumulated displacements. However, separating annual

(a)

(b)

(c)
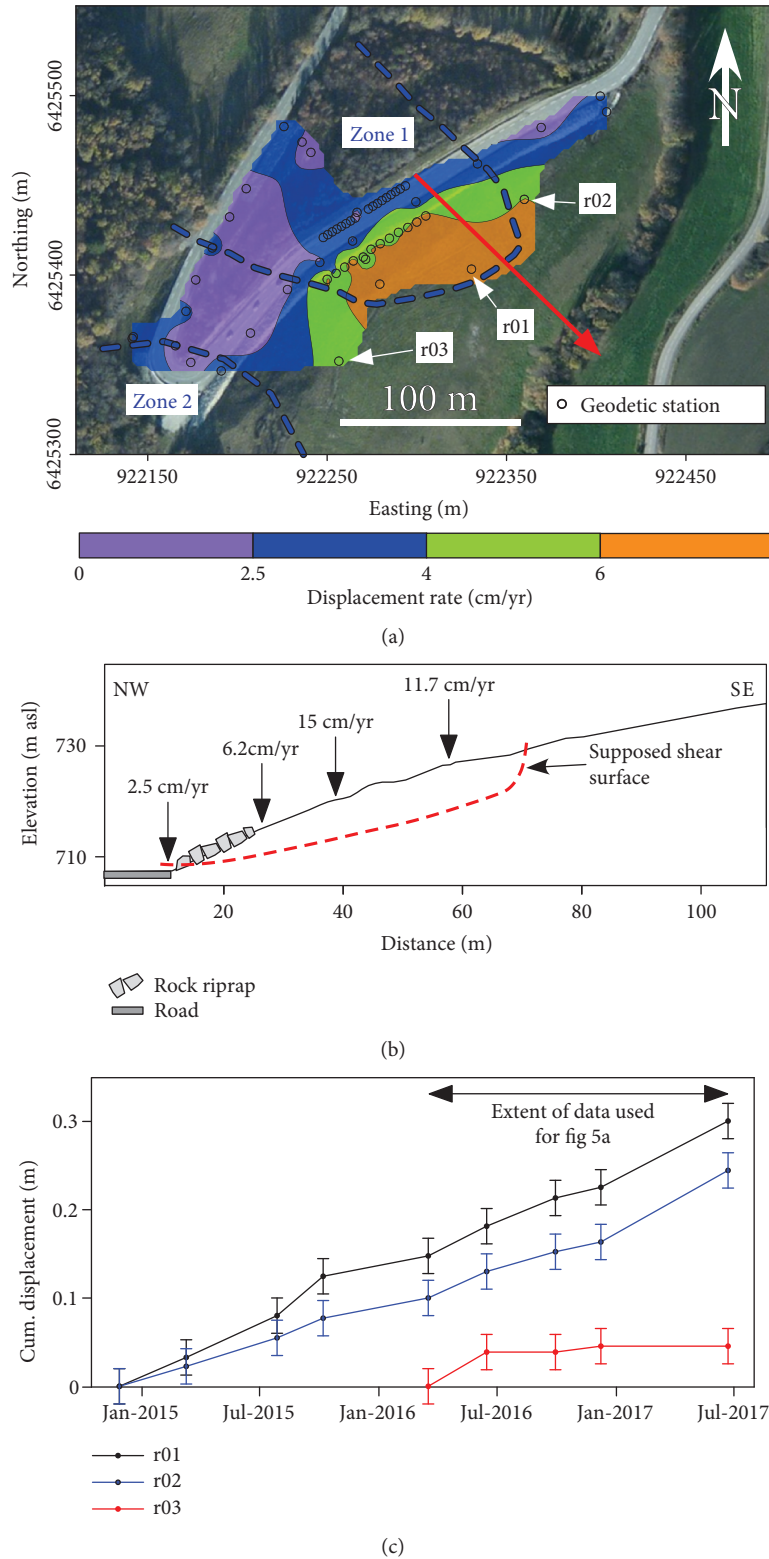
FIGURE 5: Surface deformation. (a) Interpolated map of surface displacement rates between March 2016 and June 2017. The red arrow corresponds to the topographic profile in Figure 5(b). (b) Topographic cross section, surface displacement rates measured at geodetic stations, and supposed location of the shear surface at around 10 m depth. (c) Time series of cumulated total displacements (XYZ) for stations r01 and r02 between late November 2014 and late June 2017 and for station r03 between mid-March 2016 and late June 2017 (location in Figure 5(a)).
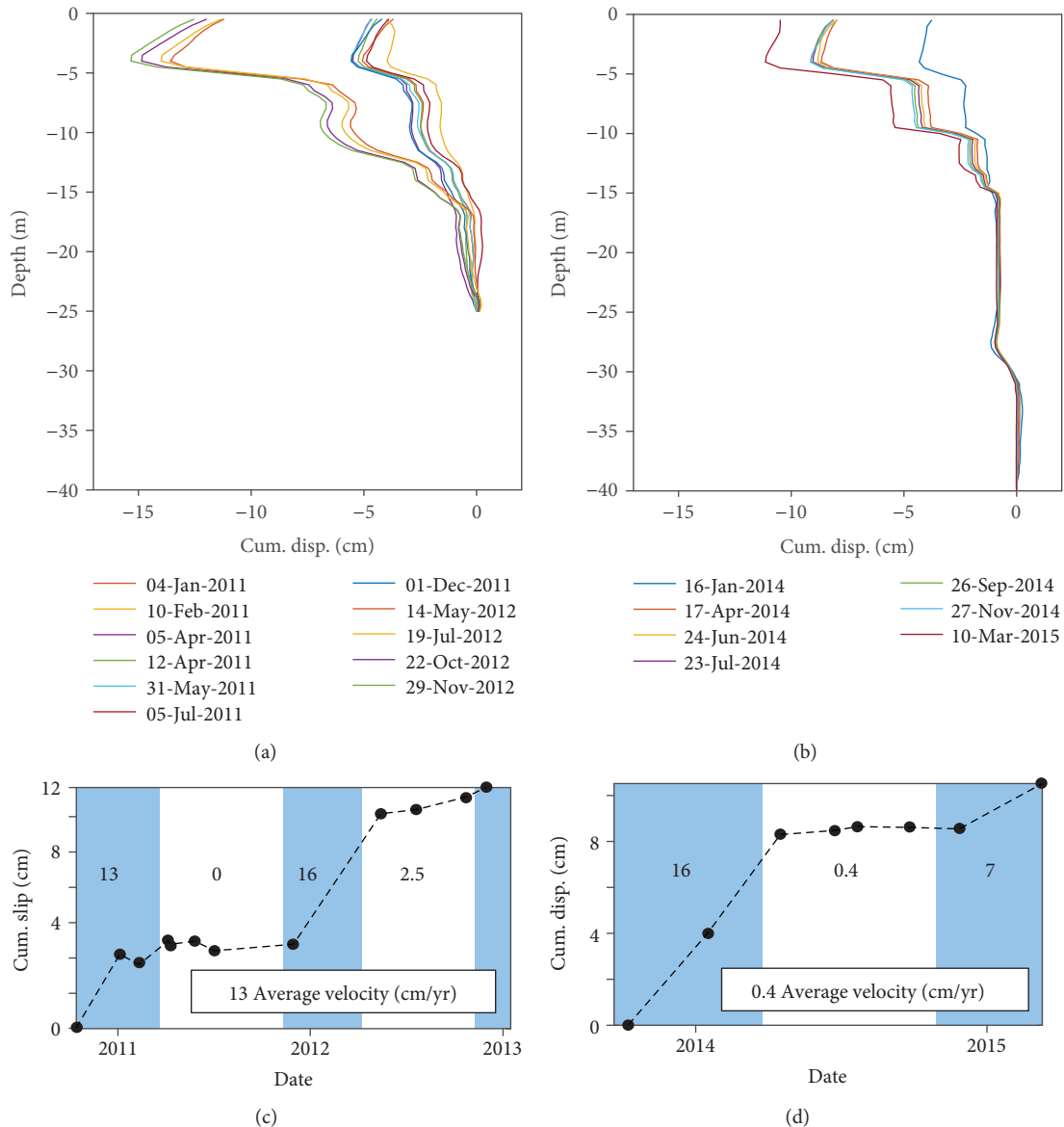
FIGURE 6: Inclinometer data for (a) i1 and (b) i2. (c) and (d) Extraction of cumulated displacements at 4 m to 5 m depth for i1 and i2, respectively. The blue and white bands correspond to the autumn-winter season (November to March) and to the spring-summer season (April to October), respectively. Values inside the graphs correspond to the average velocity, in cm/yr, for each period.

seasonal cycles between, on the one hand, a winter season from November to March (blue bars in Figures 6(c) and 6(d)) and, on the other hand, a summer season from April to October, leads to the discrimination of relatively linear, and distinct, displacement behaviours for both inclinometers. Average displacement rates were computed for each season and appear to be consistent for both inclinometers: from 7 cm/yr to 16 cm/yr during winter and 0 cm/yr to 2.5 cm/yr during summer.

4.3. Stability Calculations. The geotechnical model derived from geological and deformation results was then used to compute the slope stability and to determine a safety factor along the studied failure curve. Three geotechnical strata were taken into account (Table 2): upper moraines and

lacustrine sands from the surface down to 3–5 m (Moraines), upper glaciolacustrine clays with residual mechanical parameters (upper laminated clays) down to a depth of 8–12 m, and lower glaciolacustrine clays (lower laminated clays) with classical mechanical parameters. Geotechnical parameters (Table 2) were derived from direct shear tests on samples originating from coring s1. These parameters were compared to previously published results in the area and showed a good agreement [2–4]. Residual parameters were obtained with residual shear tests. The difference between upper and lower laminated clays originates from results on coring s1. Actually, this depth of 12 m corresponds to the location of a shear surface (Figure 6).

The geotechnical model is presented in Figure 7. Several failure curves were computed by the software. The selected

TABLE 2: Geotechnical parameters used for stability computations.

Unit	Depth range (m)	Weight (kN/m³)	Cohesion (kPa)	Friction angle (°)
Moraines	0 to 3–5	20	0	30
Upper laminated clays	3–5 to 8–12	19	2	19
Lower laminated clays	>12	19	4	20
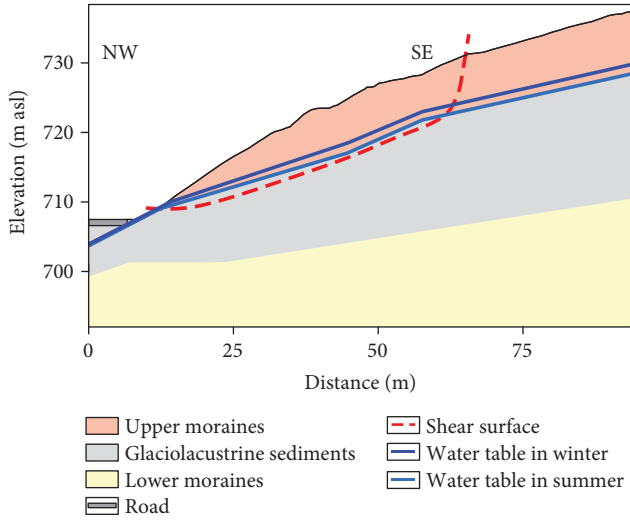
FIGURE 7: Geotechnical model and hydrogeological conditions used for stability calculations considering the shear surface at 12 m depth only.

failure curve was chosen as the one matching field observations (location of shear surface at depth in inclinometers and location of cracks in the field) but also as the one providing the lowest safety factor. The selected shear surface corresponds to the most superficial share surface observed in inclinometer i1 at a depth of 5 m (Figure 6(a)) and was considered because it is the most active (50% of the total deformation).

Then, two calculations were performed which differ only by the location of the phreatic water table (lower in summer than in winter). This water table is located immediately above the interface between the moraines and the glaciolacustrine sediments. Results indicate a safety factor of 1.23 during summer (low water table level) and of 1.15 during winter (high water table level). From a global point of view, this means that stability is not critical but is however below the 1.5 value required for long-term stability [43]. Furthermore, it indicates that an increase in the water table level decreases the global stability of the site. This decrease of the safety factor in winter is in agreement with inclinometer and D-GNSS data (Figure 6) which show an increase in kinematics and in deformation during the winter season. This could also explain the opening of cracks observed during the winter season in the field.

However, it must be stressed out that these computations were conducted for the most superficial shear surface located at 5 m depth and that at least three supplementary shear surfaces, encompassing around 50% of the total deformation, were observed on inclinometer results from i2 down to a 30 m depth (Figure 6(b)). Furthermore, the difference between those two results remains small and highlights the progressive degradation of the stability conditions in this area. This might originate from the progressive change of the geometry of the upper part of the slope (towards SE) which becomes more unfavourable. At this stage, however, it is only possible to conclude that, despite remediation works, this area of the landslide is substable but that the global stability remains tenuous. Moreover, the model and the computation have to be improved. Supplementary geotechnical data (such as mechanical parameters at different depths and additional inclinometer data located in a profile along the slope) are required. They would noticeably allow taking into account the strong anisotropy of the laminated clays [42, 76] and improving the geometry of the failure curve. In agreement with Van Asch et al. [26], there is also a more or less strong discrepancy between parameters defined at the scale of the laboratory and at the scale of the field. Finally, the global stability of the area could be computed using other calculation methods which would be able to encompass the different shear surfaces and water tables observed on inclinometer data (Figure 6) and piezometers (Figure 8), respectively.

4.4. Cross-Correlation Results. Figure 8 presents the data used for the quantitative hydrogeological study. The total amount of rainfall is depicted in Figure 8(a) under the form of daily rainfall and of the cumulated rainfall over the studied time range. Rainfall has been further separated into summer and winter rainfall, on the basis of the kinematics analysis from inclinometer data (Figure 6). The time series shows that rainfall is regularly spread along the year with average amounts of 1 m per year (0.9 m in 2016 to 1.2 m in 2013). In the same way as for total rainfall, effective rainfall is presented in Figure 8(b). The average amount of effective rainfall over the studied period is 0.19 m per year (0.12 m in 2016 to 0.26 m in 2013). From the total rainfall time series (Figure 8), it is observed that rainfall is more or less regularly spread along years. However, the effective rainfall in Figure 8(b) shows a slight discrepancy between winter and summer. In winter, effective rainfall is more important especially because of reduced evapotranspiration (no vegetation, lower temperatures) with an average amount of 0.1 m between November and the end of April. In summer, evapotranspiration is more important and induces a reduced effective rain (average amount of 0.09 m over the studied period). Furthermore, run-off is favoured in summer whereas, on
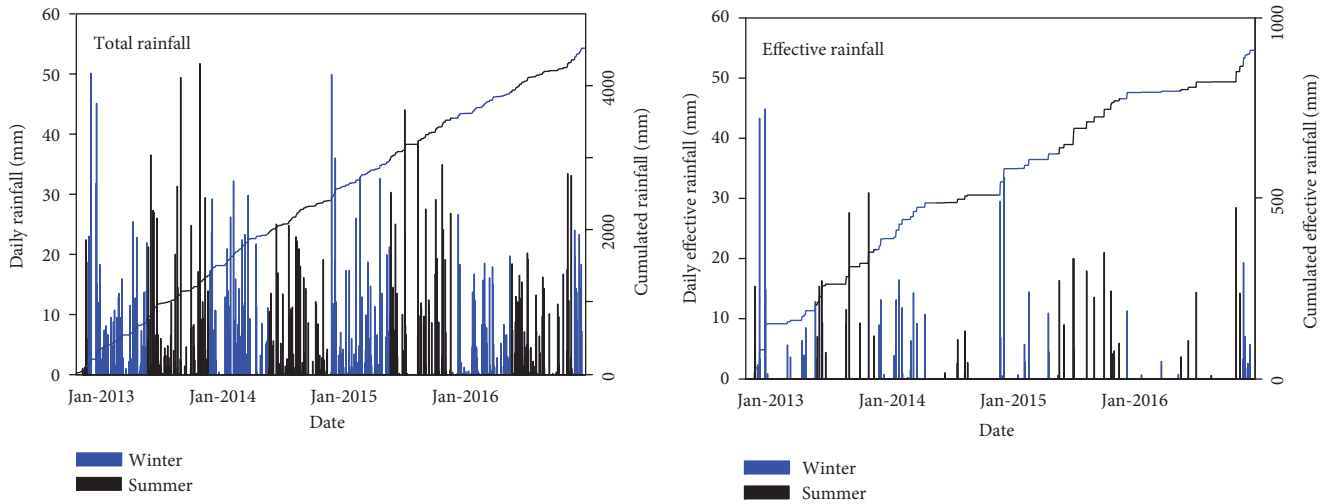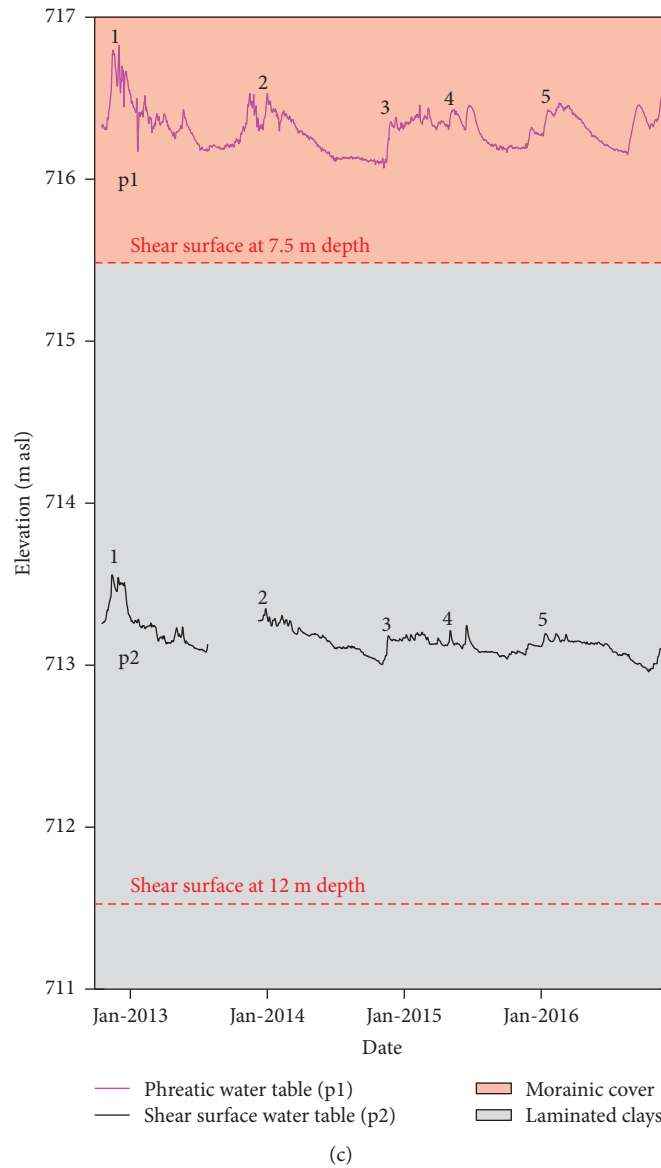
FIGURE 8: Rainfall and water table time series. (a) Total rainfall, (b) effective rainfall, and (c) water tables. Numbers: see text for details.
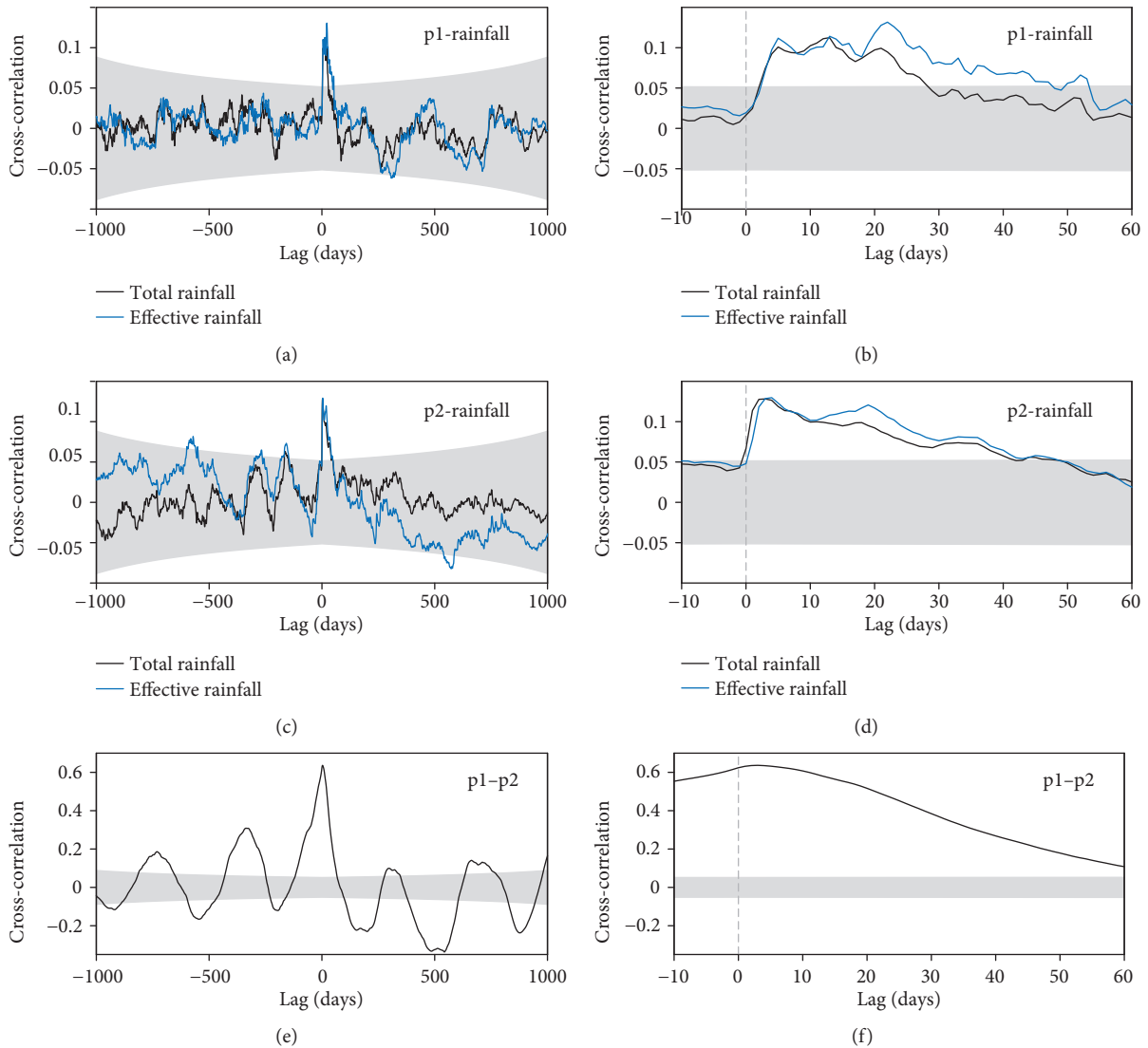
Figure 9: Cross-correlation of water tables and rainfall: (a) phreatic water table in p1, (b) shear surface water table in p2, and (c) water tables in p1 and p2. (d), (e), and (f) Close-ups from (a), (b), and (c), respectively.

the contrary, infiltration is predominant in autumn and winter. This suggests that the variation in kinematics could be related to seasonal effects related to water infiltration within the ground.

Figure 8(c) depicts the variation with time of the two studied water tables. The phreatic water table monitored by piezometer p1 is located at an elevation of around 716 m to 716.5 m asl, 2 m above the interface between the morainic cover and the laminated clays (which is also the base of the aquifer). It shows maximum annual amplitudes of around 0.3 m to 0.4 m. The water table monitored by p2 is located at an elevation of around 713.3 m asl, around 2 m above the shear surface located at 12 m depth (corresponding elevation of 711.5 m asl). It shows a lower amplitude of variation (0.15 m to 0.3 m) compared to the phreatic water table. Both water tables exhibit the same trends. The recharge occurs between mid-to-late November and early January and is relatively rapid (2 to 3 weeks). The following decrease is slow and may last up to several months. Both water tables

show similar variations (among others, labels 1 to 5 in Figure 8(c)), which suggests that they react almost simultaneously to the same meteorological events.

To evidence more quantitatively linear relationships between rainfall and water table levels, these time series were then cross-correlated and the results are presented in Figure 9. Computations were conducted for both total and effective rainfall time series. Figures 9(a) and 9(c) depict the cross-correlation over the whole time lags for p1 and p2, respectively. They reveal only one peak with a confidence greater than 95%. Both cross-correlations exhibit a positive peak (i.e., a rainfall event induces an increase of the water tables) but with different lags. Figures 9(b) and 9(d) present close-ups around these peaks. For p1, the first peak has a cross-correlation coefficient (CC) value of 0.1 for a positive lag of 5 days (Figure 9(b)), whereas, for p2, it has a CC of almost 0.13 for a positive lag of 2 days (Figure 9(d)). This first observation implies that p2 and, hence, the water table located above the shear surface at 12 m depth, reacts to a rain

event 3 days before the phreatic water table. To control this observation, p1 was cross-correlated to p2 and the results are presented in Figure 9(e) (whole cross-correlation curve) and in Figure 9(f) (close up around 0 lag). The results show several significant peaks with a one-year-long periodicity, suggesting that the two water tables are both controlled by the same environmental parameters (rainfall). The first positive peak is observed at a positive lag of 3 days with a strong CC of 0.64. This lag confirms previous observations, and the relatively strong CC once again suggests that the two water tables behave similarly. It must be stressed out that the three time series were conducted with independent devices (different recording units). The shape of the curves after the first peak also brings insight into the hydrogeological behaviour of these two reservoirs. Following the first peak at five days for the phreatic water table p1 (Figure 9(b)), CC remains stable at a value of around 0.1 until a lag of 21 days and then it decreases rapidly to a nonsignificant value for a lag of almost 30 days. This indicates that rainfall (and subsequent water infiltration) has a constant effect on the phreatic water table up to three weeks after a rain event (i.e., the water table stays at a constant level). Furthermore, the decrease in the water table after a lag of 21 days suggests that a drainage of this aquifer is initiated. Differently, the water table monitored by p2 shows a regular decrease in CC just after the first peak, and nonsignificant CC values are reached for a lag of around 42 days (Figure 9(d)). These results suggest that contrarily to the phreatic water table which behaves like a short-term reservoir, the water is drained directly after reaching the water table located above the shear surface at 12 m depth. From a general point of view, there is no discrepancy between cross-correlations conducted with total and effective rainfall time series. This suggests that, when correlating water tables with complete rainfall time series, the use of effective rainfall is of very limited added value.

To further evaluate a possible influence of the seasonal variability of water table level to rainfall, the time series were further distinguished between spring and summer (April to October, further labelled summer) and between autumn and winter (November to March, further labelled winter) seasons. The distinct time series were then cross-correlated, and the results are presented in Figure 10. Results for winter and summer using effective rainfall are presented in Figures 10(a) and 10(b), respectively. In winter, p1 (resp., p2) shows a peak with cc around 0.145 (0.14) 5 (3) days after a rain event (Figure 10(a)). The correlation coefficient for p1 (resp., p2) remains stable up to 22 (19) days after rain events and then decrease to nonsignificant levels around 33 (51) days after rainfall. These globally similar results suggest that the two water tables have a comparable behaviour in winter. On the contrary, they exhibit very contrasted evolutions in summer (Figure 10(b)). p1 shows a first peak (CC ≈ 0.1) 6 days after a rain event. The influence of rainfall on the water table level lasts around 17 days, and then the cross-correlation coefficient decreases to a nonsignificant level 27 days after rain events. p2 reveals a first peak (CC ≈ 0.12) 3 days after rainfall and a subsequent fast decrease of the correlation coefficient to nonsignificant levels 6 days after rain events.

p1 and p2 in winter and p1 in summer exhibit comparable behaviours, despite that p2 reacts always before p1 (3 days compared to 5 to 6 days). The first peak is followed by a plateau-like shape, indicating that the infiltrated rain maintains the water table at a more or less constant level for around 17 days (p1 in summer) to 19 days and 22 days (p2 in winter and in summer, resp.). This limited but effective reservoir effect exists for both water tables in winter and for the phreatic water table (p1) in summer. On the contrary, the deepest water table in p2 reacts quickly in summer (3 days after rainfall) and the water table decreases directly after the peak with CC back to nonsignificant values 3 days after the peak. It indicates that, in summer, the infiltrated water is not stored in the water table, even briefly. Instead, it is rapidly drained from the water table located above the shear surface at 12 m depth.

Seasonal cross-correlations were also conducted using total rainfall and water table time series. Results are presented in Figures 10(c) and 10(d) for winter and summer, respectively. The shapes of the correlation curves between effective and total rainfall exhibit similar trends, especially in winter (Figures 10(a) and 10(c)). They mainly differ by their correlation coefficient, especially for summer time series. Using total rainfall, the cross-correlation in summer does not show a significant peak and a further plateau-like shape for the phreatic water table (Figure 10(d)) whereas it does when using effective rainfall (Figure 10(b)). In an opposite way, the correlation curve of p2 with total rainfall in summer reveals a short-duration peak followed by a 40-day-long plateau-shaped positive correlation with a weak but significant value of 0.08 (Figure 10(d)). The consequent interpretation deeply differs since, in the case of correlations using total rainfall time series, it could be suggested that rainfall has a long-lasting influence on the water table located above the shear surface at 12 m depth. However, from the processing of these seasonal data with effective rainfall, it is evidenced that, once infiltrated, the water is rapidly drained out of this water table. These observations confirm the interest of using effective rainfall to evaluate their influence on water tables. As a matter of fact, the interpretation of the behaviour of the water tables in summer would have been opposite using total or effective rainfall.

Finally, seasonal water table time series were cross-correlated and results are presented in Figures 10(e) and 10(f) for winter and summer, respectively. In winter, a positive and strong correlation is observed for a lag of 2 days (CC ≈ 0.67), indicating that the two water tables have similar evolutions with time. On the contrary, in winter, the peak is badly defined and is observed for a lag between 0 days and 2 days with weak correlation coefficients (CC ≈ 0.112 and CC ≈ 0.11, resp.). This observation suggests that, in summer, there is no linear dependency between the two time series and that the two water tables have different behaviours.

To summarize, it has been evidenced that water infiltrates faster down to the water table located above the shear surface at 12 m depth than down to the phreatic water table located at around 7 m depth. This fast infiltration is favoured by a preferential infiltration path corresponding to a shear surface. Splitting time series between dry and wet seasons reveals
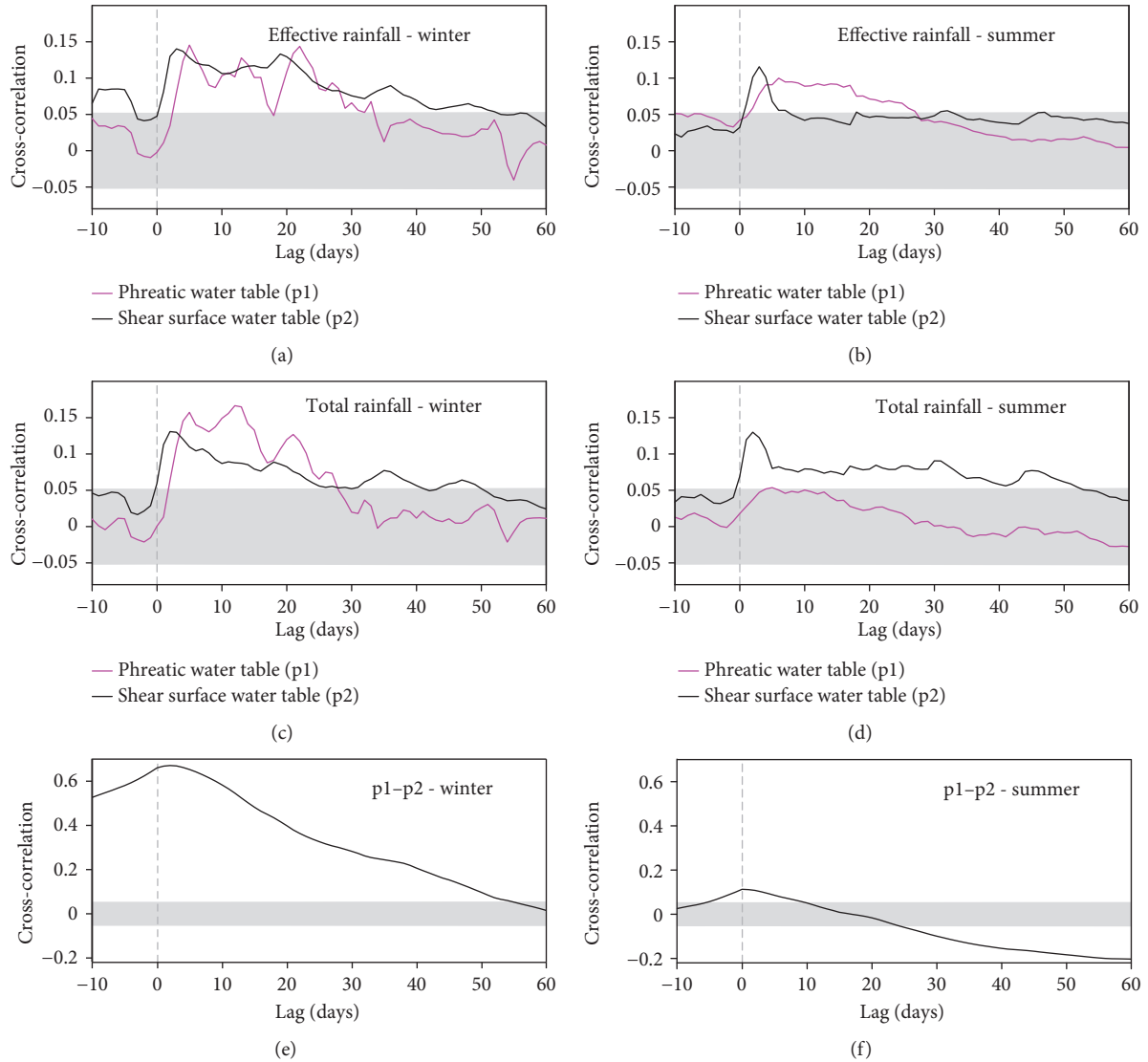
FIGURE 10: Seasonal cross-correlation of water table and rainfall. (a) and (b) Cross-correlation of water tables and effective rainfall in winter and summer, respectively. (c) and (d) Cross-correlation of water tables and total rainfall in winter and summer, respectively. (e) and (f) Cross-correlation of water table levels in winter and summer, respectively.

a comparable behaviour of the phreatic water table (both seasons) and of the deeper water table in winter. Infiltrated rainwater reaches both water tables within a few days and is stored during a few tens of days (typically around 20 days) before the water is drained. On the contrary, in summer, the water reaches the deep water table within a limited time (typically 3 days) and is immediately drained out of the water table within a comparable time delay.

4.5. Conceptual Hydrogeological Model. The synthetic hydrogeological and geotechnical conceptual model of the study site is exposed in Figure 11. The cross section is located in Figures 1(b), 3 and 5. It can be considered as representative of landslide zone 1. The geometry of the lithological units was derived from geological and geophysical prospecting, and the location of the shear surfaces was deduced from inclinometer data. Time lags deduced from cross-correlation using effective rainfall (Figures 10(c) and 10(d)) were used

to compute average infiltration rates (or, equivalently, velocities of pore pressure transmission from the surface down to the top of the water table). From the surface down to the phreatic water table, assuming a vertical distance of 7 m and a lag of 5 days in winter and 6 days in summer, the average infiltration rate is 1.48×10^{-5} m/s (1.62×10^{-5} m/s in winter and 1.35×10^{-5} m/s in summer). From the surface down to the water table above the shear surface at 12 m depth, assuming a 20 m-long path along the shear surface (Figure 11) associated to a lag of 3 days (both in winter and in summer) drives to an infiltration rate of 7.7×10^{-5} m/s.

Results from the infiltration rates and from the water infiltration tests in Figure 4 were compared to similar tests conducted on the Avignonet landslide [36, 56]. Results are synthesized in Table 3. They show that infiltration rates in the moraine and along fractures are in good agreement over the two sites. In the same way, SIR values in moraines and in the laminated clays are identical. This comparison tends to
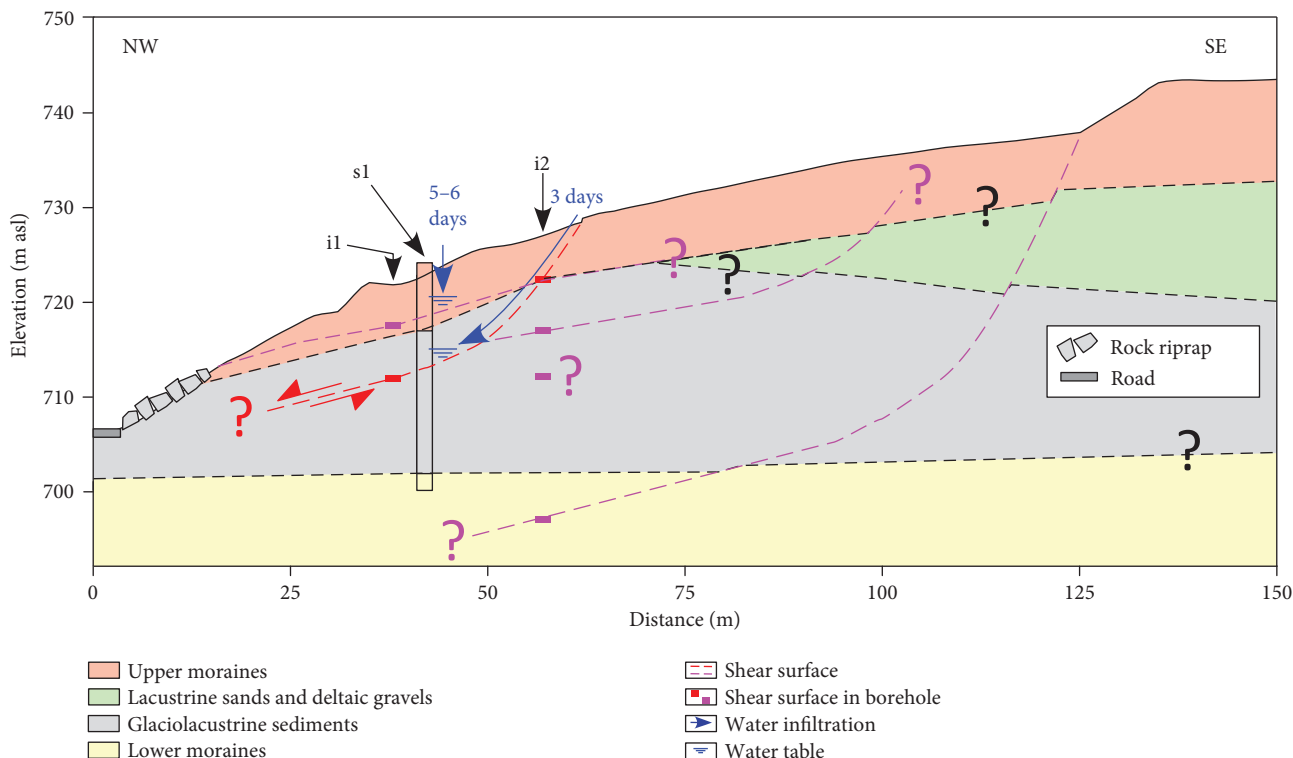
FIGURE 11: Synthetic geological and geotechnical cross section and conceptual model for water infiltration. The shear surface in red corresponds to the shear surface above which the deepest water table is studied in this work.

TABLE 3: Hydraulic properties measured on the study site and comparison with the Avignonet landslide [36, 56]. IR: infiltration rate; SIR: saturated infiltration rate after Beerkan tests.

Unit	IR ($\times 10^{-5}$ m/s)		SIR ($\times 10^{-5}$ m/s)	
	Charlaix	Avignonet	Charlaix	Avignonet
Moraines	1.48	2.7	1	1
Laminated clays			0.57	0.3
Along fractures	7.7	5		4

confirm the results obtained in this work and suggests that the established conceptual model for water infiltration is realistic.

Results from both sites show that the water infiltration rate along fissures and shear surfaces is faster than through the morainic matrix. This rate is faster by a factor of at least two and up to five at Avignonet and Charlaix landslides, respectively.

5. Synthesis and Conclusions

An extensive geophysical, geotechnical, and hydrogeological study was performed between 2010 and 2017 on the slow-moving Charlaix clayey landslide in the French western Alps. This landslide showed two main sliding zones with motions up to 10 to 15 cm/yr. Following remediation works achieved in 2009, one specific zone continued to exhibit motions of the same order of magnitude. The objective of this study was to

establish a geological and geotechnical model following numerous geotechnical and geophysical prospecting conducted on the study site and to understand the seasonal variations of displacement rates observed in situ.

Geological and geophysical results showed that the site is complex with a heterogeneous vertical and lateral arrangement of lithological layers. A thick (20 m to 30 m at least) permeable reservoir uphill, furthermore connected to the upper part of landslide zone 1, was evidenced (Figures 2–4). Geotechnical prospecting showed the presence of 4 main shear surfaces at depths of 4–5 m, 12 m, 15 m, and 30 m with more than 75% of the deformation being accommodated within the first 12 m below ground surface (Figure 6). Surface and underground kinematics (Figures 5 and 6) revealed a strong seasonality of the deformation with almost no displacements during dry seasons (April to October) and motions up to 16 cm/yr during wet seasons (November to March). Simplified stability computations taking into account the shallowest shear surface only and variable water table levels (highest in wet season) showed a decrease of the safety factor during the wet season, with a reduced global stability (Figure 7). This result is in agreement with surface and underground deformation observations which revealed higher velocity during these periods.

From geophysical and geological prospecting, it was hypothesized that a semipermeable reservoir exists uphill (Figure 2(a)) and which could feed landslide zone 1 with a significant amount of water. The drainage of water from this reservoir to the upper part of landslide zone 1 would be favoured by the presence of a permeable channel

(Figures 2(b)–4). However, no increase related to a water flux from this reservoir could be evidenced from the analysis of the time series (Figure 8).

Further hydrogeological monitoring was conducted during four years between late 2012 and late 2016 to characterize the evolution of two water tables (Figure 8). The first is the phreatic water table located at around 7 m depth, and the second is deeper (around 12 m depth) and located immediately above a shear surface. The cross-correlation of piezometer time series with effective rainfall showed that the deepest water table reacts twice faster to effective rainfall than the phreatic water table does (Figure 10). This confirms the role of fissures and shear surfaces as preferential infiltration paths for rainfall from the surface down to 12 m at least (in this work). Furthermore, the seasonal cross-correlation of the same time series reveals a globally similar behaviour of the phreatic water table in summer and in winter. Infiltrated rainwater reaches the water table within a few days (5 to 6 days) and is stored during a few tens of days (around 20 days) before the water is drained out of the aquifer. On the contrary, the second water table showed a very contrasted seasonal behaviour. In winter, it behaves similarly to the phreatic water table but, in summer, it acts as a drainage structure with no significant effect of rainfall on the water table six days after a rain event. Nevertheless, the hydrogeological analysis of the time series showed that the two water tables are both sensitive to rainfall. This implies that water infiltration within the ground affects both reservoirs even if lags are observed. These new observations and analysis bring insight into the mechanisms of water infiltration at depth within clayey landslides and confirm the role of fissures connected to shear surfaces as preferential infiltration paths.

However, despite the original observations conducted in this work, several issues remain to understand the relationships between water infiltration and landslide activity. First, the balance between run-off and infiltration is required to establish more robust correlations. It would allow to discriminate the quantity of water actually infiltrating into the ground and reaching both water tables. Second, the impact of pore pressure increase on deformation, especially at the vicinity of shear surfaces, still needs to be assessed. A joint monitoring of these two parameters would allow to quantitatively evaluate the physical phenomenon leading to landslide acceleration (dilatancy and/or fluidization). The experimental monitoring of these parameters at depths of several metres within active landslides remains challenging.

Data Availability

Time series used for this work are available at https://www.researchgate.net/project/The-Charlaix-landslide-French-western-Alps. They are also available upon request.

Conflicts of Interest

The authors declare that they have no conflicts of interest.

References

[1] R. M. Iverson and J. J. Major, "Rainfall, ground-water flow, and seasonal movement at Minor Creek landslide, northwestern California: physical interpretation of empirical relations," *Geological Society of America Bulletin*, vol. 99, no. 4, p. 579, 1987.

[2] P. B. Van Genuchten and T. W. J. Van Asch, "Factors controlling the movement of a landslide in varved clays near La Mure (French Alps)," *Bulletin de la Société Géologique de France*, vol. IV, no. 3, pp. 461–469, 1988.

[3] P. M. B. Van Genuchten, "On the temporal and spatial variance in displacement velocity of a slide in varved clays in the French Alps," *Earth Surface Processes and Landforms*, vol. 14, no. 6, pp. 565–576, 1989.

[4] P. M. B. Van Genuchten and J. D. Nieuwenhuis, "On the stability of seasonally sliding soil masses in the French Alps," *Engineering Geology*, vol. 28, no. 1-2, pp. 41–69, 1990.

[5] T. W. J. Van Asch, M. R. Hendriks, R. Hessel, and F. E. Rappange, "Hydrological triggering conditions of landslides in varved clays in the French Alps," *Engineering Geology*, vol. 42, no. 4, pp. 239–251, 1996.

[6] I. Braud, D. Condappa De, J. M. Soria et al., "Use of scaled forms of the infiltration equation for the estimation of unsaturated soil hydraulic properties (the Beerkan method)," *European Journal of Soil Science*, vol. 56, pp. 361–374, 2005.

[7] A. L. Handwerger, J. J. Roering, and D. A. Schmidt, "Controls on the seasonal deformation of slow-moving landslides," *Earth and Planetary Science Letters*, vol. 377-378, pp. 239–247, 2013.

[8] R. M. Iverson, "Regulation of landslide motion by dilatancy and pore pressure feedback," *Journal of Geophysical Research: Earth Surface*, vol. 110, no. F2, article F02015, 2005.

[9] W. H. Schulz, J. P. McKenna, J. D. Kibler, and G. Biavati, "Relations between hydrology and velocity of a continuously moving landslide: evidence of pore-pressure feedback regulating landslide motion?," *Landslides*, vol. 6, no. 3, pp. 181–190, 2009.

[10] G. Mainsant, D. Jongmans, G. Chambon, E. Larose, and L. Baillet, "Shear-wave velocity as an indicator for rheological changes in clay materials: lessons from laboratory experiments," *Geophysical Research Letters*, vol. 39, no. 19, 2012.

[11] R. M. Iverson, D. L. George, K. Allstadt et al., "Landslide mobility and hazards: implications of the 2014 Oso disaster," *Earth and Planetary Science Letters*, vol. 412, pp. 197–208, 2015.

[12] G. Mainsant, G. Chambon, D. Jongmans, E. Larose, and L. Baillet, "Shear-wave-velocity drop prior to clayey mass

movement in laboratory flume experiments," *Engineering Geology*, vol. 192, pp. 26–32, 2015.

[13] S. Carrière, D. Jongmans, G. Chambon et al., "Rheological properties of clayey soils originating from flow-like landslides," *Landslides*, vol. 15, pp. 1615–1630, 2018.

[14] P. Lacroix, G. Bièvre, E. Pathier, U. Kniess, and D. Jongmans, "Use of Sentinel-2 images for the detection of precursory motions before landslide failures," *Remote Sensing of Environment*, vol. 215, pp. 507–516, 2018.

[15] R. M. Iverson, "Landslide triggering by rain infiltration," *Water Resources Research*, vol. 36, no. 7, pp. 1897–1910, 2000.

[16] N. Caine, "The rainfall intensity-duration control of shallow landslides and debris flows," *Geografiska Annaler: Series A, Physical Geography*, vol. 62, no. 1-2, pp. 23–27, 1980.

[17] F. Guzzetti, S. Peruccacci, M. Rossi, and C. P. Stark, "Rainfall thresholds for the initiation of landslides in central and southern Europe," *Meteorology and Atmospheric Physics*, vol. 98, no. 3-4, pp. 239–267, 2007.

[18] F. Guzzetti, S. Peruccacci, M. Rossi, and C. P. Stark, "The rainfall intensity–duration control of shallow landslides and debris flows: an update," *Landslides*, vol. 5, no. 1, pp. 3–17, 2008.

[19] S. Matsuura, S. Asano, and T. Okamoto, "Relationship between rain and/or meltwater, pore-water pressure and displacement of a reactivated landslide," *Engineering Geology*, vol. 101, no. 1-2, pp. 49–59, 2008.

[20] H. Saito, D. Nakayama, and H. Matsuyama, "Relationship between the initiation of a shallow landslide and rainfall intensity—duration thresholds in Japan," *Geomorphology*, vol. 118, no. 1-2, pp. 167–175, 2010.

[21] M. T. Brunetti, M. Melillo, S. Peruccacci, L. Ciabatta, and L. Brocca, "How far are we from the use of satellite rainfall products in landslide forecasting?," *Remote Sensing of Environment*, vol. 210, pp. 65–75, 2018.

[22] T. Glade, M. Crozier, and P. Smith, "Applying probability determination to refine landslide-triggering rainfall thresholds using an empirical "antecedent daily rainfall model"," *Pure and Applied Geophysics*, vol. 157, no. 6-8, pp. 1059–1079, 2000.

[23] P. Aleotti, "A warning system for rainfall-induced shallow failures," *Engineering Geology*, vol. 73, no. 3-4, pp. 247–265, 2004.

[24] G. Martelloni, S. Segoni, R. Fanti, and F. Catani, "Rainfall thresholds for the forecasting of landslide occurrence at regional scale," *Landslides*, vol. 9, no. 4, pp. 485–495, 2012.

[25] S. L. Gariano, M. T. Brunetti, G. Iovine et al., "Calibration and validation of rainfall thresholds for shallow landslide forecasting in Sicily, southern Italy," *Geomorphology*, vol. 228, pp. 653–665, 2015.

[26] T. W. J. Van Asch, L. P. H. Van Beek, and T. A. Bogaard, "Problems in predicting the mobility of slow-moving landslides," *Engineering Geology*, vol. 91, no. 1, pp. 46–55, 2007.

[27] T. W. J. Van Asch, J.-P. Malet, and T. A. Bogaard, "The effect of groundwater fluctuations on the velocity pattern of slow-moving landslides," *Natural Hazards and Earth System Sciences*, vol. 9, no. 3, pp. 739–749, 2009.

[28] O. Hungr, S. Leroueil, and L. Picarelli, "The Varnes classification of landslide types, an update," *Landslides*, vol. 11, no. 2, pp. 167–194, 2014.

[29] L. Piccinini, M. Berti, A. Simoni, A. R. Bernardi, M. Ghirotti, and A. Gargini, "Slope stability and groundwater flow system in the area of Lizzano in Belvedere (Northern Apennines, Italy)," *Engineering Geology*, vol. 183, pp. 276–289, 2014.

[30] R. M. Iverson and D. L. George, "Modelling landslide liquefaction, mobility bifurcation and the dynamics of the 2014 Oso disaster," *Géotechnique*, vol. 66, no. 3, pp. 175–187, 2016.

[31] L. M. Highland and P. Bobrowsky, *The Landslide Handbook: a Guide to Understanding Landslides*, USGS, Reston, VA, USA, 2008.

[32] T. W. J. Van Asch, W. H. Brinkhorst, H. J. Buist, and P. V. Vessem, "The development of landslides by retrogressive failure in varved clays," *Zeitschrift für Geomorphologie Supplementband*, vol. 4, pp. 165–181, 1984.

[33] D. Jongmans, G. Bièvre, F. Renalier, S. Schwartz, N. Beaurez, and Y. Orengo, "Geophysical investigation of a large landslide in glaciolacustrine clays in the Trièves area (French Alps)," *Engineering Geology*, vol. 109, no. 1-2, pp. 45–56, 2009.

[34] E. Vuillermet, D. Cordary, and A. Giraud, "Caractéristiques hydrauliques des argiles litées du Trièves (Isère)," *Bulletin of the International Association of Engineering Geology*, vol. 49, no. 1, pp. 85–90, 1994.

[35] J. E. Van der Spek, T. A. Bogaard, and M. Bakker, "Characterization of groundwater dynamics in landslides in varved clays," *Hydrology and Earth System Sciences*, vol. 10, no. 1, pp. 295–324, 2013.

[36] G. Bièvre, D. Jongmans, T. Winiarski, and V. Zumbo, "Application of geophysical measurements for assessing the role of fissures in water infiltration within a clay landslide (Trièves area, French alps)," *Hydrological Processes*, vol. 26, no. 14, pp. 2128–2142, 2012.

[37] D. M. Krzeminska, T. A. Bogaard, T. W. J. van Asch, and L. P. H. van Beek, "A conceptual model of the hydrological influence of fissures on landslide activity," *Hydrology and Earth System Sciences*, vol. 16, no. 6, pp. 1561–1576, 2012.

[38] J. Travelletti, P. Sailhac, J.-P. Malet, G. Grandjean, and J. Ponton, "Hydrological response of weathered clay-shale slopes: water infiltration monitoring with time-lapse electrical resistivity tomography," *Hydrological Processes*, vol. 26, no. 14, pp. 2106–2119, 2012.

[39] J. Corominas, J. Moya, A. Ledesma, A. Lloret, and J. A. Gili, "Prediction of ground displacements and velocities from groundwater level changes at the Vallcebre landslide (Eastern Pyrenees, Spain)," *Landslides*, vol. 2, no. 2, pp. 83–96, 2005.

[40] G. Monjuvent, "La transfluence Durance-Isère. Essai de synthèse du Quaternaire du bassin du Drac (Alpes françaises)," *Géologie Alpine*, vol. 49, pp. 57–118, 1973.

[41] P. Antoine, A. Giraud, and G. Monjuvent, "Les argiles litées du Trièves (Isère); Conditions de gisement et exemples de propriétés géotechniques," *Bulletin de la Société Géologique de France*, vol. S7-XXIII, no. 2, pp. 117–127, 2013.

[42] A. Giraud, P. Antoine, T. W. J. Van Asch, and J. D. Nieuwenhuis, "Geotechnical problems caused by glaciolacustrine clays in the French Alps," *Engineering Geology*, vol. 31, no. 2, pp. 185–195, 1991.

[43] ECS, *Eurocode 7: Geotechnical Design. Part 1: General Rules*, European Committee for Standardization, 2004.

[44] D. Jongmans and S. Garambois, "Geophysical investigation of landslides: a review," *Bulletin de la Société Géologique de France*, vol. 178, no. 2, pp. 101–112, 2007.

[45] M. H. Loke, J. E. Chambers, D. F. Rucker, O. Kuras, and P. B. Wilkinson, "Recent developments in the direct-current geoelectrical imaging method," *Journal of Applied Geophysics*, vol. 95, pp. 135–156, 2013.

[46] T. Dahlin and B. Zhou, "Multiple-gradient array measurements for multichannel 2D resistivity imaging," *Near Surface Geophysics*, vol. 4, pp. 113–123, 2006.

[47] T. Dahlin and B. Zhou, "A numerical comparison of 2D resistivity imaging with 10 electrode arrays," *Geophysical Prospecting*, vol. 52, no. 5, pp. 379–398, 2004.

[48] T. Günther, C. Rücker, and K. Spitzer, "Three-dimensional modelling and inversion of DC resistivity data incorporating topography – II. Inversion," *Geophysical Journal International*, vol. 166, no. 2, pp. 506–517, 2006.

[49] C. Rücker, T. Günther, and K. Spitzer, "Three-dimensional modelling and inversion of DC resistivity data incorporating topography – I. Modelling," *Geophysical Journal International*, vol. 166, no. 2, pp. 495–505, 2006.

[50] W. M. Telford, L. P. Geldart, and R. E. Sheriff, *Applied Geophysics*, Cambridge University Press, Cambridge, UK, 1990.

[51] J. D. McNeill, *Electrical Terrain Conductivity Measurement at Low Induction Numbers*, Geonics Ltd, Mississauga, Canada, 1980.

[52] S. Donohue, M. Long, P. O'Connor, T. Eide Helle, A. A. Pfaffhuber, and M. Rømoen, "Multi-method geophysical mapping of quick clay," *Near Surface Geophysics*, vol. 10, no. 3, pp. 207–219, 2012.

[53] M. Schmutz, R. Guérin, P. Andrieux, and O. Maquaire, "Determination of the 3D structure of an earthflow by geophysical methods: the case of Super Sauze, in the French southern Alps," *Journal of Applied Geophysics*, vol. 68, no. 4, pp. 500–507, 2009.

[54] J. A. Coe, W. L. Ellis, J. W. Godt et al., "Seasonal movement of the Slumgullion landslide determined from Global Positioning System surveys and field instrumentation, July 1998-March 2002," *Engineering Geology*, vol. 68, pp. 67–101, 2003.

[55] L. Lassabatère, R. Angulo-Jaramillo, J. M. Soria Ugalde, R. Cuenca, I. Braud, and R. Haverkamp, "Beerkan estimation of soil transfer parameters through infiltration experiments-BEST," *Soil Science Society of America Journal*, vol. 70, no. 2, pp. 521–532, 2006.

[56] G. Bièvre, D. Jongmans, D. Goutaland, E. Pathier, and V. Zumbo, "Geophysical characterization of the lithological control on the kinematic pattern in a large clayey landslide (Avignonet, French Alps)," *Landslides*, vol. 13, no. 3, pp. 423–436, 2016.

[57] E. Brückl, F. K. Brunner, E. Lang, S. Mertl, M. Müller, and U. Stary, "The Gradenbach Observatory—monitoring deep-seated gravitational slope deformation by geodetic, hydrological, and seismological methods," *Landslides*, vol. 10, no. 6, pp. 815–829, 2013.

[58] L. Benoit, P. Briole, O. Martin, C. Thom, J.-P. Malet, and P. Ulrich, "Monitoring landslide displacements with the Geocube wireless network of low-cost GPS," *Engineering Geology*, vol. 195, pp. 111–121, 2015.

[59] S. Uhlemann, A. Smith, J. Chambers et al., "Assessment of ground-based monitoring techniques applied to landslide investigations," *Geomorphology*, vol. 253, pp. 438–451, 2016.

[60] C. R. I. Clayton, M. C. Matthews, and N. E. Simons, *Site Investigation*, Blackwell Publishing, Oxford, England, 1995.

[61] G. Gullà, D. Peduto, L. Borrelli, L. Antronico, and G. Fornaro, "Geometric and kinematic characterization of landslides affecting urban areas: the Lungro case study (Calabria, Southern Italy)," *Landslides*, vol. 14, no. 1, pp. 171–188, 2017.

[62] AFNOR, *Mesures à l'inclinomètre*, Standard NF-P-94156, French Association for Standardization, 1995.

[63] A. Vallet, C. Bertrand, O. Fabbri, and J. Mudry, "An efficient workflow to accurately compute groundwater recharge for the study of rainfall-triggered deep-seated landslides, application to the Séchilienne unstable slope (western Alps)," *Hydrology and Earth System Sciences*, vol. 19, no. 1, pp. 427–449, 2015.

[64] National French Landslide Observatory Facility and RESIF Datacenter, "French multidisciplinary observatory of versant instabilities," *Réseau Sismologique et Géodésique Français*, 2006.

[65] R. G. Allen, L. S. Pereira, D. Raes, and M. Smith, "Crop evapotranspiration-guideline for computing crop water requirements," *Irrigation and Drain*, vol. 56, p. 300, 1998.

[66] M. Berti and A. Simoni, "Observation and analysis of near-surface pore-pressure measurements in clay-shales slopes," *Hydrological Processes*, vol. 26, no. 14, pp. 2187–2205, 2012.

[67] M. Larocque, A. Mangin, M. Razack, and O. Banton, "Contribution of correlation and spectral analyses to the regional study of a large karst aquifer (Charente, France)," *Journal of Hydrology*, vol. 205, no. 3-4, pp. 217–231, 1998.

[68] J.-Y. Lee and K.-K. Lee, "Use of hydrologic time series data for identification of recharge mechanism in a fractured bedrock aquifer system," *Journal of Hydrology*, vol. 229, no. 3-4, pp. 190–201, 2000.

[69] L. J. E. Lee, D. S. L. Lawrence, and M. Price, "Analysis of water-level response to rainfall and implications for recharge pathways in the Chalk aquifer, SE England," *Journal of Hydrology*, vol. 330, no. 3-4, pp. 604–620, 2006.

[70] J. Okkonen and B. Klove, "A conceptual and statistical approach for the analysis of climate impact on ground water table fluctuation patterns in cold conditions," *Journal of Hydrology*, vol. 388, no. 1-2, pp. 1–12, 2010.

[71] A. Helmstetter and S. Garambois, "Seismic monitoring of Séchilienne rockslide (French Alps): analysis of seismic signals and their correlation with rainfalls," *Journal of Geophysical Research*, vol. 115, no. F3, article F03016, 2010.

[72] P. D. Diggle, *Time series: a biostatistical Introduction*, Oxford Science Publications, Oxford, England, 1990.

[73] C. Chatfield, *The Analysis of Time Series: An Introduction*, Chapman & Hall/CRC Press, London, England, 2003.

[74] S. Leroueil, J. Locat, G. Sève, L. Picarelli, and R. M. Faure, "Slopes and mass movements," in *Geotechnical and Geoenvironmental Engineering Handbook*, R. K. Rowe, Ed., pp. 397–428, Springer, Boston, MA, USA, 2001.

[75] GEOS, *GEOSTAB 2013 User Manual*, Paris, France, 2014, http://www.geostab.fr.

[76] T. W. J. Van Asch and P. M. B. Van Genuchten, "A comparison between theoretical and measured creep profiles of landslides," *Geomorphology*, vol. 3, no. 1, pp. 45–55, 1990.

Research Article

Effects of the Grain Size on Dynamic Capillary Pressure and the Modified Green–Ampt Model for Infiltration

Yi-Zhih Tsai [iD],[1] Yu-Tung Liu,[2] Yung-Li Wang,[1] Liang-Cheng Chang,[3] and Shao-Yiu Hsu [iD][1]

[1]*Department of Bioenvironmental Systems Engineering, National Taiwan University, Taipei 10617, Taiwan*
[2]*Department of Water Resources Engineering and Conservation, Feng Chia University, Taichung 40724, Taiwan*
[3]*Department of Civil Engineering, National Chiao Tung University, Hsinchu 30050, Taiwan*

Correspondence should be addressed to Shao-Yiu Hsu; syhsu@ntu.edu.tw

Darcy-scale capillary pressure is traditionally assumed to be constant. By contrast, a considerable gap exists between the measured and equilibrium capillary pressures when the same moisture saturation is considered with a high flow rate, and this gap is called the dynamic effect on the capillary pressure. In this study, downward infiltration experiments of sand columns are performed to measure cumulative infiltration and to calculate the wetting front depth and wetting front velocity in sands with different grain sizes. We estimate the equilibrium capillary pressure head or suction head at the wetting front using both the classical Green–Ampt (GAM) and modified Green–Ampt (MGAM) models. The results show that the performance of MGAM in simulating downward infiltration is superior to that of GAM. Moreover, because GAM neglects the dynamic effect, it systematically underestimates the equilibrium suction head in our experiments. We also find that the model parameters $\hat{\alpha}$ and β of MGAM are affected by the grain size of sands and porosity, and the dynamic effect of the capillary pressure increases with decreasing grain size and increasing porosity.

1. Introduction

Infiltration involves gas and liquid flows in porous media and occurs during precipitation or when liquid contaminants leak underground or onto the soil surface. This contributes to runoff generation, crop irrigation, and transport of nutrients and contaminants. Infiltration is a main process in subsurface hydrology and plays a crucial role in geohazards, such as landslides, flooding, and groundwater contamination. Richards' equation is the most general model to address such flows with spatially and temporally variable saturation [1, 2]. Nevertheless, computational time is an issue of numerically solving Richards' equation in a large-scale simulation. Therefore, the simple one-dimensional Green–Ampt model (GAM) [3] is an attractive alternative [4, 5]. Actually, the GAM has been widely incorporated in large-scale hydrological processes and erosion models [6] such as HEC-HMS [7], WEPP [8], SWAT [9], and ANSWERS [10] models. However, describing the transient behavior during early infiltration based on the GAM remains a challenging task.

The classical GAM for downward infiltration can be expressed as an ordinary differential equation (ODE) [3, 11]:

$$\frac{\theta_s - \theta_i}{K_s} \frac{dl_f}{dt} l_f = h_w + s_f + l_f, \tag{1}$$

where θ_s is the saturated water content, θ_i is the initial water content, K_s is the saturated hydraulic conductivity, l_f is the length of the porous medium with infiltrated liquid (the wetting front depth), $v_f = dl_f/dt$ is the wetting front velocity, $s_f = P_c/\rho g$ is the equilibrium suction head, P_c is capillary pressure, ρ is the water density, g is the gravitational acceleration, and h_w is the ponding height. In the model, a wetting front moves downward as a sharp moving boundary during downward infiltration. The porous media above and below the wetting front are assumed to have water saturated with θ_s and unsaturated with θ_i, respectively. In addition, the air pressure in the porous medium is assumed to be constant and, therefore, the viscous pressure drop due to the air

movement is neglected. The capillary pressure P_c across the moving wetting front is commonly assumed to be constant and determined from the soil water retention curve [12, 13].

Nevertheless, during the past few decades, studies conducted under nonequilibrium conditions have indicated that the soil water retention curve may depend on the dynamics of water flow [14, 15]. Water content measured under transient flow conditions has been shown to be significantly different from that measured under static and steady-state conditions [16–21]. Considering the soil water retention curve based on thermodynamics, Hassanizadeh and Gray [22], postulated the existence of a dynamic component in the unsaturated water flow. This dynamic component depends on both flow dynamics and the process of either drainage or imbibition. In addition, studies conducting column experiments have shown that during downward infiltration, the water pressure head at the gas-water or liquid-liquid interfaces changes as the flow velocity changes [11, 23–28]. The aforementioned studies suggest that the capillary pressure under dynamic conditions can be less than that under static conditions during infiltration. Therefore, infiltration can be better described by a GAM with a nonequilibrium suction head s_f.

The modified Green–Ampt model (MGAM) was first developed in Hsu and Hilpert [29]. They verified the model by the experimental data from upward infiltration [30], and downward infiltration [25]. Hsu and Hilpert [29] showed that the MGAM is better than the classical GAM at describing both transient capillary rise and downward infiltration in dry sands. For downward infiltration, the MGAM can also be expressed as an ordinary differential equation [11]:

$$\frac{\theta_s - \theta_i}{K}\frac{dl_f}{dt}l_f = h_w + s_f - \frac{\gamma}{d\rho g}\widehat{\alpha}\left(\frac{\eta}{\gamma}\frac{dl_f}{dt}\right)^{\beta} + l_f, \qquad (2)$$

where γ is the interfacial tension, d is the grain size, $\widehat{\alpha} = \alpha\varepsilon$ (ϵ, θ_i) is the lumped parameter related to a nondimensional function (ε) of porosity ϵ and θ_i, α and β are model parameters, and η is the dynamic viscosity of water. The additional term $(\gamma/d\rho g)\widehat{\alpha}[(\eta/\gamma)(dl_f/dt)]^{\beta}$ is added into GAM to consider the dynamic effect of capillary pressure.

The physical concept of the MGAM and the additional parameters $\widehat{\alpha}$ and β are based on the theory of the pore-scale dynamic contact angle. The upscaling of dynamic contact angle to the dynamic effect of capillary pressure has been derived and discussed in Hsu and Hilpert [29]. Based on the studies of dynamic contact angle, β is in the range of 1/2 to 1/3, but the value of $\widehat{\alpha}$ highly relies on the solid surface structure [31–34].

Hsu et al. and Pellichero et al. [11, 26] showed that the MGAM approach can avoid the initial unphysical infinite rate of infiltration and better describe the experimental results than can the classical GAM for downward infiltration at an early stage in both dry and prewetted sand columns with varied initial water contents. Indications are that the grain size and pore size distributions affect the dynamic effect on the soil water retention curve [20, 35–37]. DiCarlo [36] showed that when a saturation overshoot occurs during the

downward infiltration, the length of the gravitational fingering tips varies with the grain size and distribution. Hilpert [38] proposed a theory based on velocity-dependent capillary pressure that correctly predicts the degree to which the saturation overshoot depends on both the liquid contents and grain size. Hsu and Hilpert [29] pointed out that the model parameters $\widehat{\alpha}$ and β in MGAM might be related to the porosity and grain size. Based on (2), the dynamic effect on the suction head should be inversely proportional to the grain size. However, the effect of the grain size and pore size distribution of the sand column on the nonequilibrium suction head as well as the model parameters $\widehat{\alpha}$ and β in (2) of the MGAM have not yet been systematically investigated. Therefore, we performed a series of infiltration experiment to systematically investigate the effect of the grain size of the sand column on the nonequilibrium suction head as well as the model parameters $\widehat{\alpha}$ and β.

In this study, the cumulative infiltration depths were measured during a series of downward infiltration experiments in dry sand columns with different grain sizes, subject to different constant ponding heights. The remainder of this paper is organized as follows. In Section 2, we describe our experimental method and preparation of the porous materials. In Section 3, we describe the results of the experiments, and in Section 4, we compare the predictions from classical GAM and MGAM as well as the values of fitting parameters. We also discuss the effects of the grain size on the dynamic capillary pressure and the fitting of the equilibrium suction head.

2. Experimental Setup

2.1. Experimental Material Properties and Grain Size Measurement.
In this study, sands (glass beads) with four grain sizes (labeled B35, B60, B150, and B320) were used for our infiltration experiments. The sands had the same shape, with a particle density of 2.5 g/cm^3. Because glass beads after conditioning hardly aggregate, we could exclude the influence of the aggregates on the observed dynamic capillary pressure. Moreover, the grain size distribution (GSD) of the sands was determined through sieve analysis (ASTM C136) of eight different mesh screens.

2.2. Downward Infiltration Experiment.
The infiltration experiments were conducted using glass filter columns (inner diameter = 2.6 cm, depth = 60 and 30 cm, cross-section area = 5.3 cm^2). Based on Wang et al. [39], the sizes of the fingering flow for downward infiltration in sands are mostly ranged from 3 to 15 cm. The fingering flow with a width of less than 3 cm was only observed by Glass et al. [40]. In this study, our sand column with the inner diameter of 2.6 cm is small enough to avoid 2D fingering flows. All the sands were conditioned by being rinsed with deionized water to remove impurities and dried overnight in an oven at 100°C. We packed sands B35, B60, and B150 into the 60 cm column and sand B320 into the 30 cm column. To achieve uniform packing, the sands poured into the column were maintained at a constant 3 cm distance between the supply funnel and the top of the sand packing. In addition, a rubber hammer was

used to tap the top of the sand in the column to obtain an even more homogeneous packing.

Figure 1 is a schematic representation of the experiment setup. A Mariotte's bottle was connected through Tygon tubing and a valve to the sand column to maintain the hydraulic head. The bottle was placed on the top of an analytical balance (Sartorius TE1502S) to record the weight at 0.2 s intervals and automatically send the data to a computer. When the valve was opened, the water in the Mariotte's bottle flowed into the column packed with dry sand, infiltrated the sand and reached the bottom of the column. The weight change measured by the analytical balance was used to calculate the cumulative infiltration and infiltration rate. All infiltration experiments in this study were conducted in triplicate.

2.3. Saturated Hydraulic Conductivity (K_s) Measurement. Saturated hydraulic conductivity (K_s) is an important parameter of the GAM, as it determines the flow rate of water in the saturated soil. K_s in this study was determined by the constant-head method. The measurement procedure was the same as that for the infiltration experiment previously described. Following the infiltration experiments, the sand in the column was at saturation, and the flow rate gradually reached equilibrium. We measured the equilibrium infiltration rate, and K_s was estimated based on Darcy's law:

$$K_s = \frac{QL}{Ah},$$ (3)

where Q is the flow rate, L is the length of the sand column, A is the total cross-section area, and h is the constant hydraulic head. The flow rate value was obtained by calculating the weight change of water per unit time.

3. Results

3.1. Grain Size Distribution of Experimental Materials. Figure 2 shows the grain size distributions of the sands. Sand B35 was the coarsest in grain size, ranging from 2 to 7×10^{-2} cm and was followed in order by B60 (distributed between 1 and 6×10^{-2} cm), B150 (ranging from 5×10^{-3} to 2.3×10^{-2} cm), and B320 (which had the finest grain size and was distributed between 1×10^{-4} and 2×10^{-2} cm).

The curves in Figure 2 are plotted based on a grain size distribution equation provided by Fredlund et al. [41]. We used the same equation to calculate the geometric mean grain size (d_{50}). Table 1 shows the geometric mean grain sizes of sands B35 (4.51×10^{-2} cm), B60 (3.48×10^{-2} cm), B150 (1.38×10^{-2} cm), and B320 (1.3×10^{-3} cm).

The sands were uniform. Specifically, the uniformity coefficients of sands B35, B60, B150, and B320 were 1.33, 1.46, 1.55, and 3.85, respectively. In the discussion that follows, we used d_{50} to quantify the effect of grain size on the infiltration model and dynamic capillary pressure.

3.2. Results of Infiltration Experiments. Table 1 shows the measured porosity, bulk density, and saturated hydraulic conductivity. In each of the 36 infiltration replicate experiments, we controlled the bulk density and porosity of the soil column. The average bulk density of sand B35 column was
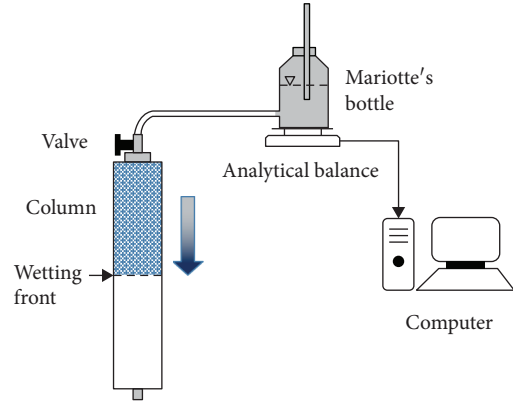
FIGURE 1: Schematic of the experimental setup for the downward infiltration experiments.
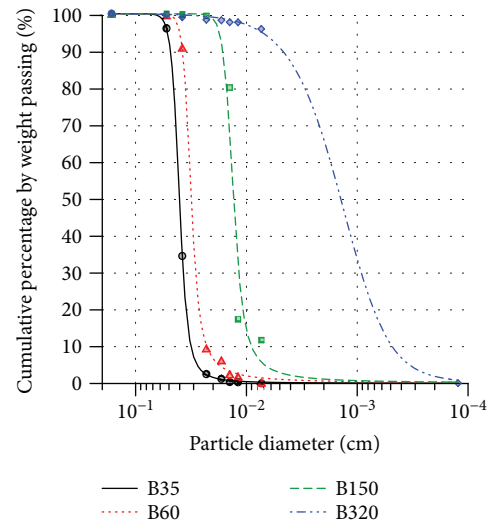
FIGURE 2: Grain size distribution curves of sands B35, B60, B150, and B320.

1.36 g/cm^3 and the average porosity was 0.46 cm^3/cm^3. The bulk density of sand B60 was 1.42–1.43 g/cm^3, B150 was 1.38–1.39 g/cm^3, and B320 was 1.33–1.36 g/cm^3. The porosity of sands B60, B150, and B320 was 0.43, 0.45, and 0.47 cm^3/cm^3, respectively.

Under the assumption of GAM, the sand has a water content $\theta = \theta_s$ behind the wetting front and an initial water content θ_i ahead of the front. Mobile water content ($\Delta\theta$) indicates the moisture change ($\theta_s - \theta_i$) at the wetting front and can be estimated from the total cumulative infiltration and total volume of the sand column, that is, $\Delta\theta = F_{total}/V_{total}$ [11]. In our study, the $\Delta\theta$ of sand B35 column was obtained from 0.42 to 0.44 cm^3/cm^3, B60 from 0.39 to 0.41 cm^3/cm^3, B150 from 0.40 to 0.42 cm^3/cm^3, and B320 from 0.39 to 0.44 cm^3/cm^3.

The results of the saturated hydraulic conductivity from additional experiments show that B35 had the largest value, followed by B60, B150, and B320, at 1.84–1.97×10^{-1}, 6.42–6.53×10^{-2}, 1.16–1.42×10^{-2}, and 0.8–1.1×10^{-3} cm/s, respectively.

TABLE 1: Geometric mean grain size, porosity, bulk density, and saturated hydraulic conductivity for column experiments with different ponding heights.

Materials	Geometric mean grain size, $d_{50} \times 10^{-4}$ (cm)	Water ponding height, h_w (cm)	Bulk density, ρ_b (g·cm^{-3})	Porosity, ϵ (cm^3·cm^{-3})	Mobile water content, $\Delta\theta$ (cm^3·cm^{-3})	Saturated hydraulic conductivity, $K_s \times 10^{-2}$ (cm·s^{-1})
B35	451	10	1.36 ± 0.006	0.46 ± 0.003	0.44 ± 0.011	19.68 ± 0.683
		20	1.36 ± 0.002	0.46 ± 0.001	0.42 ± 0.006	18.35 ± 0.132
		40	1.36 ± 0.017	0.46 ± 0.007	0.43 ± 0.006	18.37 ± 1.591
B60	348	10	1.43 ± 0.003	0.43 ± 0.001	0.41 ± 0.014	6.53 ± 0.202
		20	1.42 ± 0.005	0.43 ± 0.002	0.39 ± 0.003	6.42 ± 0.079
		40	1.42 ± 0.008	0.43 ± 0.003	0.39 ± 0.003	6.50 ± 0.393
B150	138	10	1.38 ± 0.004	0.45 ± 0.002	0.40 ± 0.001	1.21 ± 0.024
		20	1.38 ± 0.007	0.45 ± 0.003	0.40 ± 0.005	1.16 ± 0.055
		40	1.39 ± 0.000	0.45 ± 0.000	0.42 ± 0.021	1.42 ± 0.391
B320	13	10	1.36 ± 0.004	0.46 ± 0.002	0.39 ± 0.007	0.08 ± 0.003
		20	1.34 ± 0.013	0.47 ± 0.005	0.44 ± 0.040	0.11 ± 0.026
		40	1.33 ± 0.006	0.47 ± 0.002	0.42 ± 0.036	0.10 ± 0.028
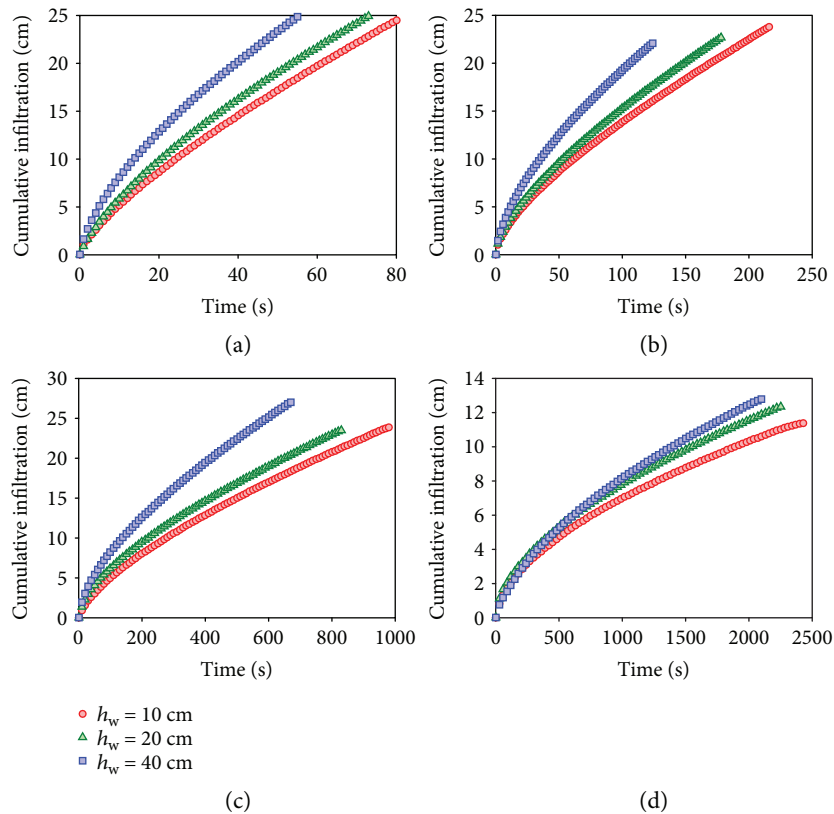
FIGURE 3: Cumulative infiltration versus time of the sands: (a) B35, (b) B60, (c) B150, and (d) B320.

We used the analytical balance to measure the mass (m_w) of water infiltrating the sand column. In addition, the cumulative infiltration (F) was calculated from the mass (m_w), water density (ρ), and soil column cross-sectional area (A), such that $F = m_w/\rho A$. We plotted the relationship between F and time (t) according to different water ponding heights and soil sizes. Figure 3 shows F versus t in our experiments. Each plotted point represents the average result of three replicate experiments. However, one of the infiltration experiments of soil B320 column at a water ponding height of 20 cm failed because of water leakage, a fact that was not mentioned in our subsequent discussion. Figures 3(a)–3(d) clearly show that F increased as the water ponding height increased.
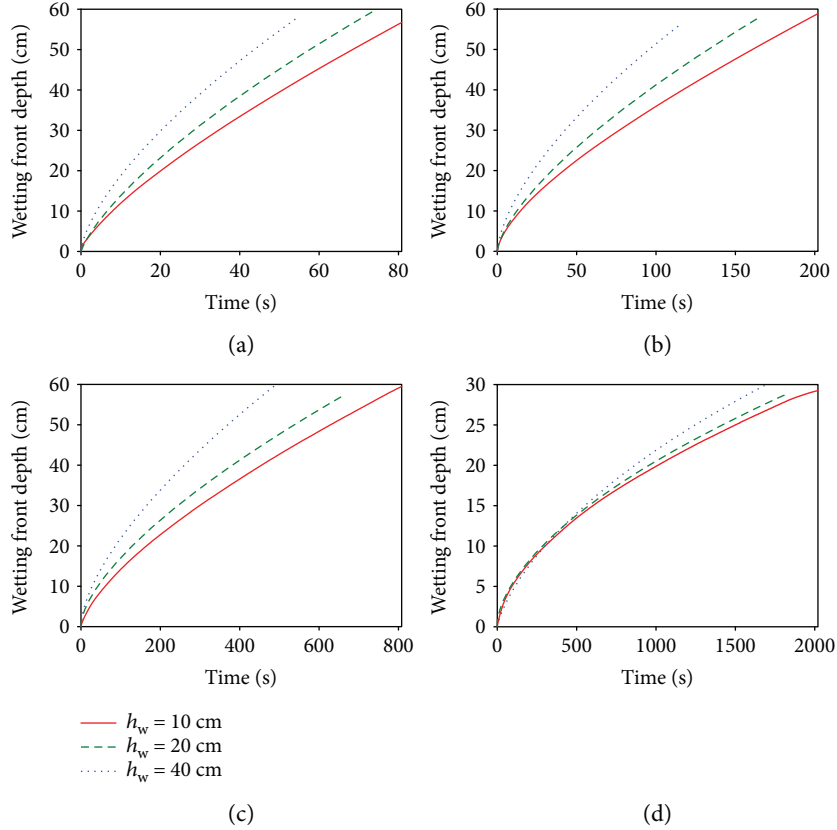
Figure 4: Wetting front depth of sand versus time: (a) B35, (b) B60, (c) B150, and (d) B320. The column length of sands B35, B60, and B150 was 60 cm and of sand B320 was 30 cm.

3.3. *Wetting Front Depth and Velocity versus Water Ponding Height and Grain Size.* Wetting front depth (l_f) can be calculated from F and $\Delta\theta$, such that $l_f = F/\Delta\theta$. Figure 4 shows l_f versus t in our experiments. In general, the l_f monotonously increased with t. In addition, water ponding height $h_w = 40$ cm had the largest l_f value at the same time, followed by $h_w = 20$ cm and $h_w = 10$ cm. For different grain sizes, the wetting front of B35 with the largest grain size and fastest infiltration rate spent 55–80.8 s to arrive $l_f = 60$ cm, B60 spent 125–217.6 s, and B150 spent 597.2–980 s. Finally, the wetting front of B320 with the smallest grain size and slowest infiltration rate spent 2040–2430 s to arrive $l_f = 30$ cm.

We divided dl_f by dt to obtain the wetting front velocity (v_f) and plotted the relationship of v_f and t in Figure 5. To compare the wetting front velocities in different experiments with t, we normalized the X axis through t divided by the infiltration end time (t_{ie}). Figure 5 shows v_f versus standardized time (t/t_{ie}). We can see that v_f was the fastest at the beginning of infiltration, gradually decreased with t, and finally approached an equilibrium value. Regardless of the water ponding height, v_f increased as the grain size increased.

The main purpose of this study is to examine the relationship between flow velocity and capillary pressure during transient infiltration. The combination of ponding depths and grain sizes can lead to a range of flow rates and front velocities for examining our hypothesis. In

addition, our experimental results shown in Figures 4 and 5 confirm that our experimental design in accord with the basic physical assumptions of infiltration theory and the GAM. It implies that the fingering flow did not occur during our experiments.

3.4. *Infiltration Simulation of GAM and MGAM.* In this study, experimental data were modeled by GAM and MGAM. We used a MATLAB implementation of ODE solvers to provide a numerical solution of GAM (1) and MGAM (2) in downward infiltration conditions. GAM required only a parameter s_f for simulation, whereas other parameters K_s and $\Delta\theta$ were inputted as fixed values (listed in Table 1). Parameters used by MGAM included $s_f, \hat{\alpha}, \beta,$ $d, K_s,$ and $\Delta\theta$, where K_s and $\Delta\theta$ were inputted as fixed values (listed in Table 1). Here, grain size (d) was represented by the geometric mean grain size (d_{50}).

The fitting parameters were inversely determined from the measured data using a MATLAB nonlinear fitting function. The nonlinear fitting function uses a Levenberg-Marquardt nonlinear least squares algorithm to solve bound-constrained optimization problems [42]. MATLAB nonlinear fitting function must specify the initial value of $s_f, \hat{\alpha}, \beta,$ and d. Based on the studies of Hsu et al. [11] and Pellichero et al. [26], we set $\hat{\alpha} = 100$ and $\beta = 0.3$ as the initial values for model fitting. The initial value of d of sands B35,
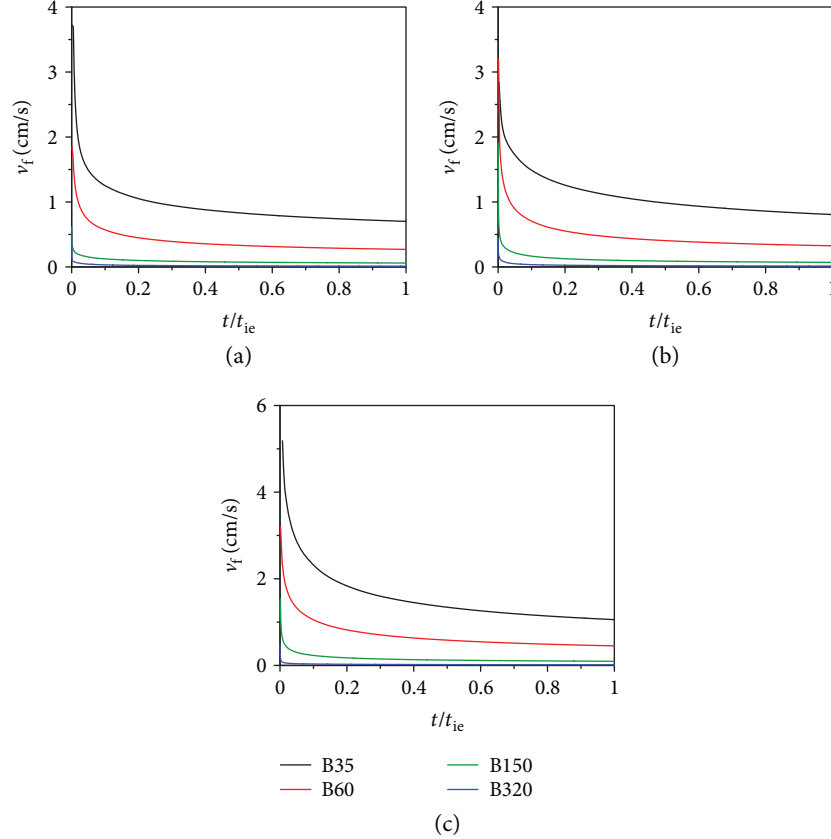
FIGURE 5: Wetting front velocity of sands B35, B60, B150, and B320 under ponding height of: (a) $h_w = 10$ cm, (b) $h_w = 20$ cm, and (c) $h_w = 40$ cm.

B60, B150, and B320 was $d_{50} = 4.51 \times 10^{-2}$, 3.48×10^{-2}, 1.38×10^{-2}, and 1.3×10^{-3} cm, respectively. The initial value of s_f was obtained by

$$s_f = \frac{2\gamma \cos \varphi}{r\rho g}, \tag{4}$$

where γ is interfacial tension (in which the surface tension of water and air is $\gamma = 7.2 \times 10^{-2}$ N/m), g is gravity acceleration ($g = 9.81$ m/s²), ρ is water density ($\rho = 1000$ kg/m³), φ is contact angle, and r is effective pore radius. In this study, the contact angle was $\varphi = 30°$; this was the static contact angle of quartz and water suggested by Friedman [43]. We used the empirical formula of Glover and Walker [44] to convert grain size (d) into effective pore size (r):

$$r = \frac{d}{2\sqrt{8/3 \times 1.5^2/8}e^{2\times1.5}}, \tag{5}$$

where ϵ is porosity. The aforementioned initial values were substituted in (1) and (2) to simulate GAM and MGAM for downward infiltration, respectively.

The results of infiltration simulation of GAM and MGAM are shown in Figure 6, and the model fitting parameters are listed in Table 2. In Figure 6, the black circles are the wetting front depths, which were calculated from measured values of m_w. The remaining four curves show

the simulation results of GAM and MGAM. The orange-dotted curve (GAM) was plotted by GAM with the calculated s_f based on (4). The yellow-dashed curve (MGAM) was simulated by MGAM with $\widehat{\alpha} = 100$, $\beta = 0.3$, s_f (which was calculated by (4)), and $d = d_{50}$. The purple-dashed curve (optimized GAM) used the nonlinear fitting method to simulate downward infiltration by GAM with s_f as a fitting parameter. Finally, the green-solid curve (optimized MGAM) was represented by MGAM with $\widehat{\alpha}$, β, s_f, and d as fitting parameters. Both the purple-dashed and green-solid curves with fitting parameters showed better simulation results; these curves could approach the black circles of the wetting front depth. The orange-dotted curve with a fixed s_f was farthest from the black circles, followed by the yellow-dashed curve with fixed $\widehat{\alpha}$, β, sf, and d in the middle. This indicates that the performance of MGAM with multiparameters for simulating downward infiltration was superior to that of the classical GAM.

Regardless of the grain size of the sand, the optimized GAM and optimized MGAM with the fitting parameters had good simulation results. For GAM and MGAM with no fitting parameters, the smaller the grain size, the more the simulation results deviated from the black circles, particularly the sand B320.

Table 2 shows that two of the fitting suction heads s_f of sand B35 based on GAM were negative. Because the grain
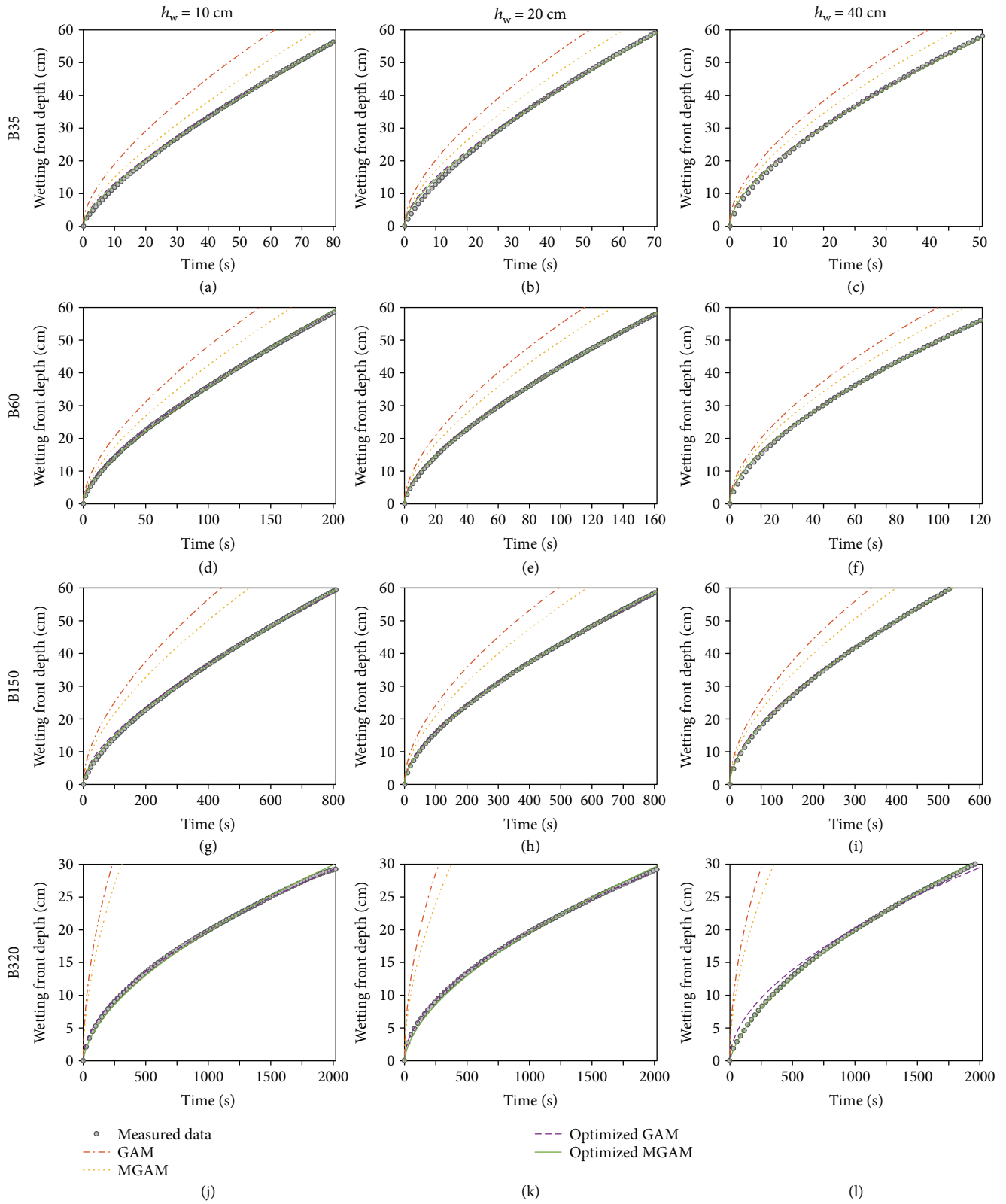
Figure 6: Infiltration simulation of GAM and MGAM of sands B35, B60, B150, and B320.

size of the B35 was larger than that of other sands, the equilibrium s_f was relatively small or even close to zero (Figure 7 and Table 2). Nevertheless, to have a negative suction head for a sand column packed with glass beads is still abnormal. It implies that the s_f was underestimated by using classical GAM during a downward infiltration with high wetting front

TABLE 2: Model parameters and RMSE of GAM and MGAM for downward infiltration simulation.

| Materials | h_w (cm) | GAM | | MGAM | | | | |
		s_f (m)	RMSE	s_f (m)	$\hat{\alpha}$	β	d ($\times 10^{-4}$ cm)	RMSE
B35	10	0.011	0.007	0.105	86.138	0.305	425	0.004
	20	−0.009	0.011	0.094	93.316	0.297	456	0.008
	40	−0.052	0.009	0.09	100.741	0.283	442	0.006
B60	10	0.053	0.002	0.112	85.391	0.339	361	0.003
	20	0.025	0.005	0.133	98.828	0.3	351	0.002
	40	0.015	0.007	0.135	93.037	0.29	361	0.004
B150	10	0.134	0.008	0.326	97.797	0.288	138	0.003
	20	0.147	0.004	0.323	98.817	0.3	138	0.001
	40	0.099	0.006	0.31	98.585	0.291	137	0.002
B320	10	0.528	0.003	1.063	95.888	0.335	16	0.003
	20	0.467	0.002	1.007	97.124	0.335	17	0.004
	40	0.279	0.009	1.496	109.98	0.305	13	0.002
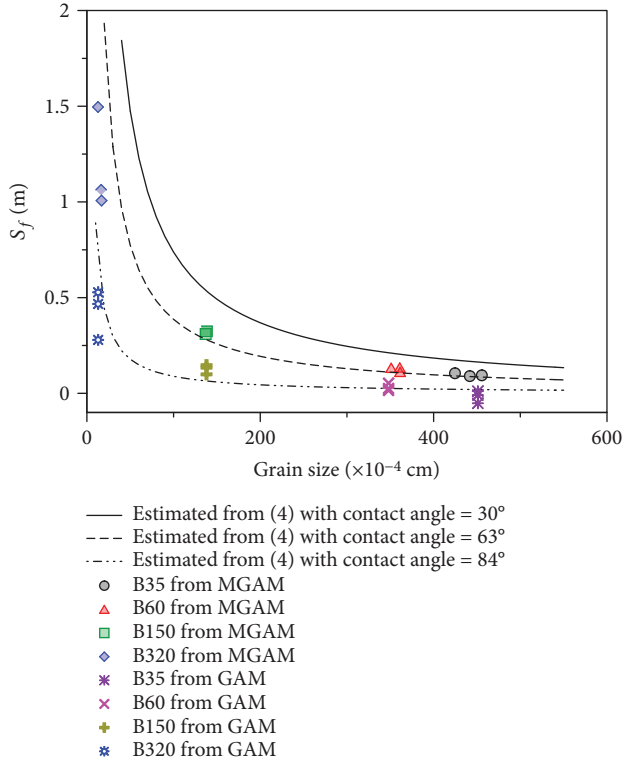
FIGURE 7: Wetting front suction head s_f versus grain size. In all sands, s_f from MGAM was larger than s_f from GAM. The solid curve estimates s_f from a static contact angle of 30°, the dotted line represents the best contact angle (63°) with s_f from MGAM, and the dashed-dotted line represents the contact angle = 84° with s_f from GAM.

velocity. According to Chow et al. [12], the s_f is distributed from 0.97 cm (0.0097 m) to 156.5 cm (1.565 m) from sand to clay. From the grain size distribution in Figure 2, the texture class of B320 can be classified as silt loam. Its s_f value

ranges from 2.92 cm (0.0292 m) to 95.39 cm (0.9539 m). However, theoretical values of sf based on (4) are over 2 m. The s_f value for sand B320 is larger than that from Chow et al. [12], but it should still be in the range of silt loam or soils slightly smaller than silt loam for practical problems.

The performances of GAM and MGAM were evaluated using root mean square error (RMSE). For each simulation, the difference between the measured wetting front depth ($l_{f(m)}$) and the calculated wetting front depth ($l_{f(p)}$) was expressed in RMSE as:

$$\text{RMSE} = \sqrt{\frac{\sum_{i=1}^{N} \left(l_{f(m)} - l_{f(p)} \right)^2}{N}}, \tag{6}$$

where N is the number of observed samples. By statistically verifying RMSE, we could evaluate the reliability of the model simulation; when the RMSE was small, the model was more reliable. The results of RMSE for infiltration simulation of GAM and MGAM are listed in Table 2. In general, the RMSEs of most MGAMs (0.001–0.008) in this study were less than those of GAMs (0.002–0.011), indicating that the simulation results of MGAM were superior to those of GAM. Except for two sets of simulation results for B60 and B320, the RMSE of GAM was smaller than that of MGAM. Fortunately, the RMSE of these two sets of results were also very small, which meant that the performance of MGAM was also good.

4. Discussion

4.1. Relationship between Wetting Front Suction Head (s_f) *and Grain Size.* The relationship between the suction head and grain size can be linked by using (4) and (5). Figure 7 shows the relationship between the grain sizes of the sand columns and the equilibrium suction heads estimated by GAM and MGAM. The solid line in Figure 7 shows the theoretical relationship based on (4) and (5) between the grain

FIGURE 8: MGAM parameter $\widehat{\alpha}$ versus (a) grain size and (b) porosity.

FIGURE 9: MGAM parameter β versus grain size. The fitted β was approximately 0.3.
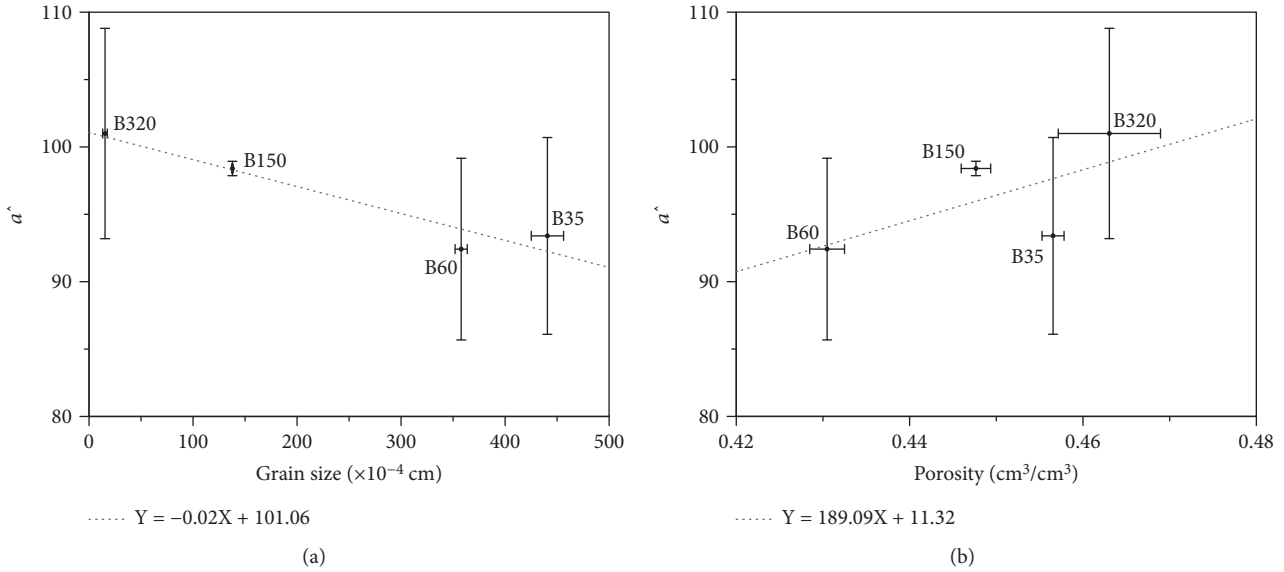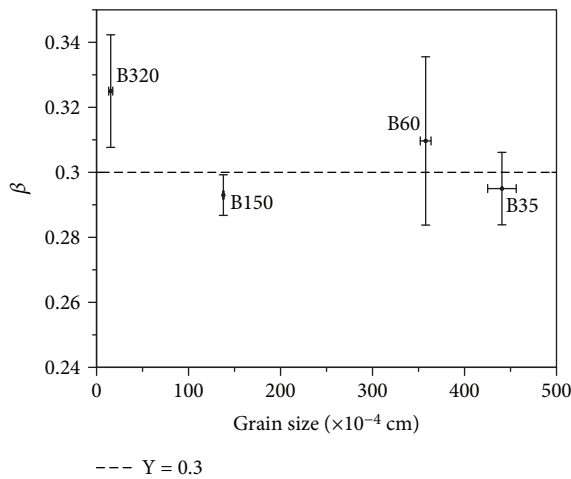
sizes of the sand columns and the equilibrium suction heads with the assumed effective contact angle between air, water, and the glass bead of 30°. Using the same equations, we determined the effective pore radius and contact angles by fitting the effective contact angle to the grain size and the determined equilibrium suction heads. The dashed lines in Figure 7 show the fitted relationship between grain sizes and the equilibrium suction heads estimated by GAM and MGAM with the fitted effective contact angle of 84° and 63°, respectively.

The equilibrium suction heads estimated by the GAM were systematically lower than those estimated by the MGAM. Consequently, the effective contact angle estimated by the GAM was also systematically greater than that by the MGAM. The overestimated effective contact angle from GAM was because we neglected the dynamic effect when

estimating the suction head. The effective contact angle estimated by GAM was the average dynamic contact angle during the infiltration process. Nevertheless, the contact angle (63°) estimated by MGAM was still greater than that (30°) measured in previous studies, even when the dynamic effect was considered. One explanation for this is related to the contact angle hysteresis: the contact angle no longer corresponds to the static equilibrium angle but is larger when the liquid is advancing and smaller when the liquid is receding [45]. In general, during the infiltration, the water advances the air in the sand. Therefore, the contact angle during the infiltration should be in the form of an advancing contact angle, which is commonly greater than the equilibrium contact angle.

4.2. MGAM Fitting Parameters for Dynamic Capillary Pressure. Hsu and Hilpert [29] pointed out that the parameters $\widehat{\alpha}$ and β in the MGAM are related to the dynamic effect on the capillary pressure, and their values might not be the same for different initial water contents, porosities, and grain sizes. Figure 8 shows two trends in which the fitted $\widehat{\alpha}$ is proportional to the porosity and inversely proportional to the grain size. From the empirical relationship proposed by Stauffer [20] relating the dynamic coefficient to measurable porous media and fluid properties, the equation suggests that the dynamic effects would be greater for fine-grained soil with high air entry pressure and high porosity. Camps-Roach eat al. [35] observed that the dynamic coefficient statistically increases as the grain size decreases. Therefore, our fitted values of the parameters were consistent with those of the aforementioned studies.

Limited numbers of Darcy-scale studies focus on determining the β values in sand. Weitz et al. [28] yielded $\beta = 0.5 \pm 0.1$ for water displacing decane in a glass bead column. Hsu and Hilpert [29] tested a range of β values from 1/5 to 1 based on the studies of pore-scale dynamic contact angles on flat surfaces and in circular capillary tubes, which can

be described by $\cos \varphi_{eq} - \cos \varphi_{dyn} = \widehat{\alpha} Ca^{\beta}$ [33, 34, 46]. The best β value was approximately 0.31 for the experiments performed by Geiger and Durnford [25]. Pellichero et al. [26] showed that $\beta = 0.3$ resulted in the best fit in downward infiltration experiments with the same sand but varying ponding heights. The same β value also worked well in similar experiments but with various initial water contents [11]. In this study, β was set as one of the fitting parameters. Figure 9 shows that the fitted β was approximately 0.3, and the error bars overlapped for most grain sizes except for those of B320, which had the highest β value (up to 0.34) with the smallest grain size. Nevertheless, the value of the fitted β in this study agreed with the values derived or determined from the aforementioned Darcy and pore-scale studies. We confirmed again that 0.3 is a universal value for β for Darcy's scale sand experiments.

5. Conclusions

We performed a series of downward infiltration experiments and compared the predictions derived from classical GAM and MGAM as well as the values of fitting parameters. In this study, cumulative infiltration monotonously increased with time, and a greater water ponding height showed more cumulative infiltration. This kind of result was also reflected in the wetting front depth. Furthermore, the sand column with smaller grain size had a lower infiltration rate and wetting front velocity, and a greater amount of time was spent on infiltration. Regarding the model simulation, the RMSEs of MGAM were less than those of GAM, indicating that the performance of MGAM with multiparameters for simulating downward infiltration was superior to that of the classical GAM.

Because the classical GAM ignores the dynamic effect on estimating the suction head, the effective contact angle estimated by GAM was systematically greater than that by MGAM, meaning that the equilibrium suction from GAM was systematically less than that from MGAM. Moreover, the contact angle is typically in the form of an advancing one during infiltration. Therefore, the equilibrium contact angle estimated by MGAM was greater than the intrinsic contact angle. In addition, the fitted $\widehat{\alpha}$ was proportional to the porosity and inversely proportional to the grain size in our study, indicating that the dynamic effect of capillary pressure increased with decreasing grain size and increasing porosity. Furthermore, the fitted β was approximately 0.3, which is consistent with the values obtained from most of Darcy's and pore-scale studies. This study confirmed that 0.3 can be the universal value of β for Darcy-scale sand experiments.

Data Availability

The data used to support the findings of this study are available from the corresponding author upon request.

Conflicts of Interest

The authors declare that there is no conflict of interest regarding the publication of this paper.

References

[1] D. A. Barry, J.-Y. Parlange, G. C. Sander, and M. Sivaplan, "A class of exact solutions for Richards' equation," *Journal of Hydrology*, vol. 142, no. 1–4, pp. 29–46, 1993.

[2] G. Sposito, "Recent advances associated with soil water in the unsaturated zone," *Reviews of Geophysics*, vol. 33, no. S2, pp. 1059–1065, 1995.

[3] W. H. Green and G. A. Ampt, "Studies on soil physics part I – the flow of air and water through soils," *Journal of Agricultural Science*, vol. 4, pp. 1–24, 1911.

[4] S. M. Hsu, C.-F. Ni, and P.-F. Hung, "Assessment of three infiltration formulas based on model fitting on Richards equation," *Journal of Hydrologic Engineering*, vol. 7, no. 5, pp. 373–379, 2002.

[5] G. Liu, J. R. Craig, and E. D. Soulis, "Applicability of the Green-Ampt infiltration model with shallow boundary conditions," *Journal of Hydrologic Engineering*, vol. 16, no. 3, pp. 266–273, 2011.

[6] A. Van den Putte, G. Govers, A. Leys, C. Langhans, W. Clymans, and J. Diels, "Estimating the parameters of the Green–Ampt infiltration equation from rainfall simulation data: why simpler is better," *Journal of Hydrology*, vol. 476, pp. 332–344, 2013.

[7] A. D. Feldman, "Hydrologic modeling system HEC-HMS: technical reference manual," in *US Army Corps of Engineers*, Hydrologic Engineering Center, 2000.

[8] J. M. Laflen, W. Elliot, D. Flanagan, C. Meyer, and M. Nearing, "WEPP-predicting water erosion using a process-based model," *Journal of Soil and Water Conservation*, vol. 52, no. 2, pp. 96–102, 1997.

[9] P. Tuppad, K. R. Douglas-Mankin, T. Lee, R. Srinivasan, and J. G. Arnold, "Soil and water assessment tool (SWAT) hydrologic/water quality model: extended capability and wider adoption," *Transactions of the ASABE*, vol. 54, no. 5, pp. 1677–1684, 2011.

[10] F. Bouraoui and T. A. Dillaha, "ANSWERS-2000: runoff and sediment transport model," *Journal of Environmental Engineering*, vol. 122, no. 6, pp. 493–502, 1996.

[11] S.-Y. Hsu, V. Huang, S. Woo Park, and M. Hilpert, "Water infiltration into prewetted porous media: dynamic capillary pressure and Green-Ampt modeling," *Advances in Water Resources*, vol. 106, pp. 60–67, 2017.

[12] V. T. Chow, D. R. Maidment, and L. W. Mays, *Applied Hydrology*, McGraw-Hill, 1988.

[13] S. P. Neuman, "Wetting front pressure head in the infiltration model of Green and Ampt," *Water Resources Research*, vol. 12, no. 3, pp. 564–566, 1976.

[14] R. S. Mokady and P. F. Low, "The tension-moisture content relationship under static and dynamic conditions1," *Soil Science Society of America Journal*, vol. 28, no. 4, 1964.

[15] G. C. Topp, A. Klute, and D. B. Peters, "Comparison of water content-pressure head data obtained by equilibrium,

steady-state, and unsteady-state methods1," *Soil Science Society of America Journal*, vol. 31, no. 3, p. 312, 1967.

[16] E. Diamantopoulos and W. Durner, "Dynamic nonequilibrium of water flow in porous media: a review," *Vadose Zone Journal*, vol. 11, no. 3, 2012.

[17] W. C. Lo, C. C. Yang, S. Y. Hsu, C. H. Chen, C. L. Yeh, and M. Hilpert, "The dynamic response of the water retention curve in unsaturated soils during drainage to acoustic excitations," *Water Resources Research*, vol. 53, no. 1, pp. 712–725, 2017.

[18] D. M. O'Carroll, T. J. Phelan, and L. M. Abriola, "Exploring dynamic effects in capillary pressure in multistep outflow experiments," *Water Resources Research*, vol. 41, no. 11, 2005.

[19] T. Sakaki, D. M. O'Carroll, and T. H. Illangasekare, "Direct quantification of dynamic effects in capillary pressure for drainage-wetting cycles," *Vadose Zone Journal*, vol. 9, no. 2, 2010.

[20] F. Stauffer, "Time dependence of the relations between capillary pressure, water content and conductivity during drainage of porous media," in *IAHR Symp. on Scale Effects in Porous Media. Thessaloniki Greece 29 Aug.-1. IAHR*, Madrid, Spain, 1978.

[21] L. Zhuang, S. M. Hassanizadeh, C. Z. Qin, and A. de Waal, "Experimental investigation of hysteretic dynamic capillarity effect in unsaturated flow," *Water Resources Research*, vol. 53, no. 11, pp. 9078–9088, 2017.

[22] S. M. Hassanizadeh and W. G. Gray, "Mechanics and thermodynamics of multiphase flow in porous media including interphase boundaries," *Advances in Water Resources*, vol. 13, no. 4, pp. 169–186, 1990.

[23] T. Annaka and S. Hanayama, "Dynamic water-entry pressure for initially dry glass beads and sea sand," *Vadose Zone Journal*, vol. 4, no. 1, pp. 127–133, 2005.

[24] D. A. DiCarlo, "Stability of gravity-driven multiphase flow in porous media: 40 years of advancements," *Water Resources Research*, vol. 49, no. 8, pp. 4531–4544, 2013.

[25] S. L. Geiger and D. S. Durnford, "Infiltration in homogeneous sands and a mechanistic model of unstable flow," *Soil Science Society of America Journal*, vol. 64, no. 2, 2000.

[26] E. Pellichero, R. Glantz, M. Burns, D. Mallick, S. Y. Hsu, and M. Hilpert, "Dynamic capillary pressure during water infiltration: experiments and Green-Ampt modeling," *Water Resources Research*, vol. 48, no. 6, 2012.

[27] N. Weisbrod, T. McGinnis, M. L. Rockhold, M. R. Niemet, and J. S. Selker, "Effective Darcy-scale contact angles in porous media imbibing solutions of various surface tensions," *Water Resources Research*, vol. 45, no. 4, 2009.

[28] D. A. Weitz, J. P. Stokes, R. C. Ball, and A. P. Kushnick, "Dynamic capillary pressure in porous media: origin of the viscous-fingering length scale," *Physical Review Letters*, vol. 59, no. 26, pp. 2967–2970, 1987.

[29] S. Y. Hsu and M. Hilpert, "Incorporation of dynamic capillary pressure into the Green-Ampt model for infiltration," *Vadose Zone Journal*, vol. 10, no. 2, 2011.

[30] T. Tabuchi, "Infiltration and capillarity in the particle packing," *Records Land Reclam Res.*, vol. 19, pp. 1–121, 1971.

[31] P. G. D. Gennes, X. Hua, and P. Levinson, "Dynamics of wetting: local contact angles," *Journal of Fluid Mechanics*, vol. 212, no. 1, p. 55, 1990.

[32] P. Joos, P. van Remoortere, and M. Bracke, "The kinetics of wetting in a capillary," *Journal of Colloid and Interface Science*, vol. 136, no. 1, pp. 189–197, 1990.

[33] T. E. Mumley, C. J. Radke, and M. C. Williams, "Kinetics of liquid/liquid capillary rise," *Journal of Colloid and Interface Science*, vol. 109, no. 2, pp. 398–412, 1986.

[34] E. Schäffer and P.-z. Wong, "Contact line dynamics near the pinning threshold: a capillary rise and fall experiment," *Physical Review E*, vol. 61, no. 5, pp. 5257–5277, 2000.

[35] G. Camps-Roach, D. M. O'Carroll, T. A. Newson, T. Sakaki, and T. H. Illangasekare, "Experimental investigation of dynamic effects in capillary pressure: grain size dependency and upscaling," *Water Resources Research*, vol. 46, no. 8, 2010.

[36] D. A. DiCarlo, "Experimental measurements of saturation overshoot on infiltration," *Water Resources Research*, vol. 40, no. 4, 2004.

[37] D. Wildenschild, J. W. Hopmans, and J. Simunek, "Flow rate dependence of soil hydraulic characteristics," *Soil Science Society of America Journal*, vol. 65, no. 1, 2001.

[38] M. Hilpert, "Velocity-dependent capillary pressure in theory for variably-saturated liquid infiltration into porous media," *Geophysical Research Letters*, vol. 39, no. 6, 2012.

[39] Z. Wang, J. Feyen, and D. E. Elrick, "Prediction of fingering in porous media," *Water Resources Research*, vol. 34, no. 9, pp. 2183–2190, 1998.

[40] R. J. Glass, J. Y. Parlange, and T. S. Steenhuis, "Immiscible displacement in porous media: stability analysis of three-dimensional, axisymmetric disturbances with application to gravity-driven wetting front instability," *Water Resources Research*, vol. 27, no. 8, pp. 1947–1956, 1991.

[41] M. D. Fredlund, D. G. Fredlund, and G. W. Wilson, "An equation to represent grain-size distribution," *Canadian Geotechnical Journal*, vol. 37, no. 4, pp. 817–827, 2000.

[42] G. A. F. Seber and C. J. Wild, *Nonlinear Regression*, Wiley-Interscience, Hoboken, N.J, 2003.

[43] S. P. Friedman, "Dynamic contact angle explanation of flow rate-dependent saturation-pressure relationships during transient liquid flow in unsaturated porous media," *Journal of Adhesion Science and Technology*, vol. 13, no. 12, pp. 1495–1518, 1999.

[44] P. W. Glover and E. Walker, "Grain-size to effective pore-size transformation derived from electrokinetic theory," *Geophysics*, vol. 74, no. 1, pp. E17–E29, 2009.

[45] L. Makkonen, "A thermodynamic model of contact angle hysteresis," *The Journal of Chemical Physics*, vol. 147, no. 6, article 64703, 2017.

[46] L. H. Tanner, "The spreading of silicone oil drops on horizontal surfaces," *Journal of Physics D*, vol. 12, no. 9, pp. 1473–1484, 1979.

Research Article

Modeling of Transient Flow in Unsaturated Geomaterials for Rainfall-Induced Landslides Using a Novel Spacetime Collocation Method

Cheng-Yu Ku [iD],[1,2] **Chih-Yu Liu,**[1] **Yan Su,**[3] **and Jing-En Xiao**[1]

[1]*Department of Harbor and River Engineering, National Taiwan Ocean University, Keelung 20224, Taiwan*
[2]*Center of Excellence for Ocean Engineering, National Taiwan Ocean University, Keelung 20224, Taiwan*
[3]*Department of Water Resource and Harbor Engineering, College of Civil Engineering, Fuzhou University, Fuzhou, China*

Correspondence should be addressed to Cheng-Yu Ku; chkst26@mail.ntou.edu.tw

The modeling of transient flow in unsaturated soils for rainfall-induced landslides using a novel spacetime collocation method is presented. A numerical solution obtained in the spacetime coordinate system is approximated by superpositioning Trefftz basis functions satisfying the linearized Richards equation for collocation points on the spacetime domain boundary. The Gardner exponential model is adopted to derive the linearized Richards equation to describe the soil-water characteristic curve in unsaturated soils. To deal with the rainfall-induced landslides, the infinite slope stability analysis coupled with the proposed meshless method with the consideration of the fluctuation of time-dependent matric suction is developed. The proposed method is validated for several test problems. Application examples of transient modeling of flow for rainfall-induced landslides in homogenous unsaturated soils are also conducted. Numerical results demonstrate that the proposed method is highly accurate to deal with transient flow in unsaturated soils for rainfall-induced landslides. In addition, it is found that the numerical method using the Richards equation with the Gardner model may provide a promising solution for different soil textures.

1. Introduction

In recent decades, global climate change impacts have increased the frequency of severe meteorological phenomena such as heavy rainfall events [1, 2]. Increased precipitation events associated with extreme weather conditions affect the stability of slopes and can lead to a variety of geoenvironmental hazards [3, 4]. Consequently, shallow landslides may often occur within the vadose zone under unsaturated soil conditions [5–7]. The prediction of flow in transient conditions is important in engineering practice while considering the stability of unsaturated soil slopes [8–12] or poromechanical coupling influence for rainfall-induced shallow landslides in unsaturated soils [13, 14].

In the past, theoretical models have been developed to deal with slope stability assuming a steady or quasi-steady water table associated with an infinite-slope stability analysis [15]. With regard to the influence of rainfall infiltration on slope stability in unsaturated soils, Iverson [16] assumed that nearly saturated soil is a simplified form of the linear diffusion equation of the Richards equation. However, the influence of matric suction of soil and the soil-water characteristic curve (SWCC) cannot be comprehensively considered during the analysis. The theory of geofluids when rainfall infiltrates vadose zones can be described using either the variably saturated flow equation or the generalized Richards equation [17, 18]. Governed by nonlinear physical relationships, the Richards equation is a highly nonlinear equation. The SWCC is a major factor that influences the nonlinear physical relationship of the hydraulic conductivity in unsaturated zones [19–22]. Since the Richards equation is highly nonlinear and an analytical solution can only be provided by some

transformations [23], numerical solutions of the Richards equation are commonly used to model the flow process in unsaturated soils.

Numerical approaches to the modeling of various unsaturated geofluid phenomena using the mesh-based methods, such as the finite difference method (FDM) or the finite element method (FEM), have been studied extensively [24, 25]. In spite of the success of using the conventional mesh-generated methods as effective numerical tools for the solution of transient flow problems in unsaturated soils, there remains growing interest in the development of novel advanced computational methods. Due to the flexibility in solving practical problems involving complex geometry and boundary conditions such as tidal fluctuation which is usually difficult for finding the analytical solution, meshless methods have attracted considerable attention recently [26, 27]. For such problems involving regions of irregular geometry, the use of numerical methods, particularly the boundary-type meshless method, to approximate numerical solutions is advantageous. In the past decades, several meshless methods have been proposed, such as the collocation Trefftz method (CTM) [28–31], the method of fundamental solutions (MFS) [32–34], smoothed particle hydrodynamics (SPH) [35], diffuse element method [36], and the boundary particle method [37]. Among these meshless methods, the CTM can be categorized into the boundary-type meshless method and provides the most accurate solutions with optimal numerical stability [38, 39]. Because the boundary-type meshless method is originally developed to deal with the boundary value problems in Euclidean space, the study of transient flow in unsaturated soils for rainfall-induced landslides using the proposed method has not been reported yet.

In this paper, a novel spacetime collocation method for modeling of transient flow in unsaturated soils for rainfall-induced landslides is presented. For the modeling of transient flow in unsaturated soils, we proposed a pioneering work based on the proposed boundary-type meshless method and utilized the spacetime coordinate system instead of that in the original Euclidean space [10]. A numerical solution obtained in the spacetime coordinate system is approximated by superpositioning Trefftz basis functions satisfying the linearized Richards equation for collocation points on the spacetime domain boundary. To deal with the rainfall-induced landslides, the infinite slope stability analysis coupled with the proposed meshless method with the consideration of the fluctuation of time-dependent matric suction is developed. The validity of the proposed method is established for several problems by comparing the results with the exact solutions. Application examples of transient modeling of flow for rainfall-induced landslides in homogenous unsaturated soils are also conducted. The formulation of the proposed method is described as follows.

2. Modeling of Transient Flow in Unsaturated Soils

2.1. The Linearized Richards Equation for the Inclined Slope. The generalized Richards equation represents the movement of water in saturated and unsaturated soils, which can be expressed as

$$K\nabla^2 H = (S_s S_w + C(h))\frac{\partial H}{\partial t}, \tag{1}$$

where H represents the total groundwater head, K represents hydraulic conductivity, S_s represents the specific storage, S_w represents effective saturation, $C(h)$ represents specific capacity, ∇ represents gradient, and t represents time. If porous media are heterogeneous and anisotropic, (1) becomes

$$\nabla K \nabla H = (S_s S_w + C(h))\frac{\partial H}{\partial t}. \tag{2}$$

This is also known as the variably saturated flow equation to describe the groundwater flow in saturated and unsaturated zones simultaneously [17, 18]. Equation (2) can be rewritten as the three-dimensional form

$$\frac{\partial}{\partial x}\left(K_x(h)\frac{\partial H}{\partial x}\right) + \frac{\partial}{\partial y}\left(K_y(h)\frac{\partial H}{\partial y}\right) + \frac{\partial}{\partial z}\left(K_z(h)\frac{\partial H}{\partial z}\right)$$
$$= S_s S_w \frac{\partial H}{\partial t} + C(h)\frac{\partial H}{\partial t}, \tag{3}$$

where x points down the ground surface, y points to the tangent of the topographic contour passing through the origin, z is the vertical coordinate, normal to the xy plane, and $K_x(h)$, $K_y(h)$, and $K_z(h)$ are the unsaturated hydraulic conductivity functions in lateral direction and the vertical direction, respectively. The original Richards equation is developed only for horizontal ground plane. To deal with the movement of water in an unsaturated inclined slope as shown in Figure 1, the Richards equation must be revised. The total head can be expressed as follows.

$$H = h + E, \tag{4}$$

where h is the pressure head and E is the elevation head. The elevation head can be presented as follows.

$$E = x \sin(\beta) + z \cos(\beta), \tag{5}$$

where β is the angle of inclination. By substituting (4) and (5) into (3), we obtained

$$\frac{\partial}{\partial x}\left(K_x(h)\left(\frac{\partial h}{\partial x} - \sin(\beta)\right)\right) + \frac{\partial}{\partial y}\left(K_y(h)\frac{\partial h}{\partial y}\right)$$
$$+ \frac{\partial}{\partial z}\left(K_z(h)\left(\frac{\partial h}{\partial z} + \cos(\beta)\right)\right) \tag{6}$$
$$= (S_s S_w + C(h))\frac{\partial h}{\partial t}.$$
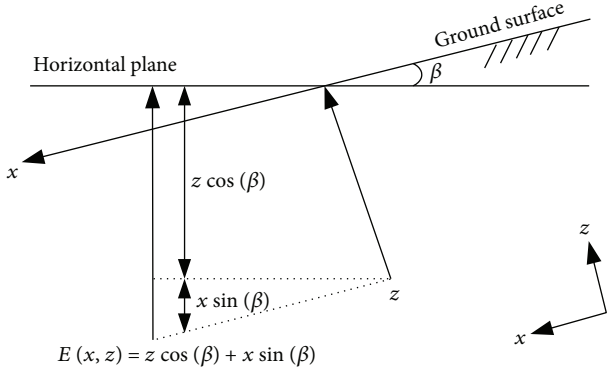
$$E(x, z) = z \cos(\beta) + x \sin(\beta)$$

Figure 1: The definition of the elevation head in an unsaturated inclined slope.

Considering only the unsaturated flow, (6) can be rewritten as

$$\frac{\partial}{\partial x}\left(K_x(h)\left(\frac{\partial h}{\partial x} - \sin(\beta)\right)\right) + \frac{\partial}{\partial y}\left(K_y(h)\frac{\partial h}{\partial y}\right)$$
$$+ \frac{\partial}{\partial z}\left(K_z(h)\left(\frac{\partial h}{\partial z} + \cos(\beta)\right)\right) \qquad (7)$$
$$= C(h)\frac{\partial h}{\partial t}.$$

The specific moisture capacity function can be defined by

$$C(h) = \frac{\partial \theta_{\mathrm{m}}}{\partial h}, \qquad (8)$$

where θ_{m} is the moisture content. Because $K_x(h)$, $K_y(h)$, and $K_z(h)$ and $C(h)$ are functions of the pressure head, the Richards equation is nonlinear. To solve (7), three characteristic functions are required including the SWCC, the unsaturated hydraulic conductivity function, and the specific moisture capacity function.

Considering an one-dimensional transient flow problem, the duration of the rainfall events is far shorter than the transmission time of pore water pressure in the x and y axes. This consideration can be realistic for the inclined slope, especially for the steep slope covered by a thin soil mantle. Besides, the numerical solution of the Richards equation is computationally expensive [40]. In this study, the Richards equation in one-dimensional vertical flow is considered as follows.

$$\frac{\partial}{\partial z}\left(K_z(h)\left(\frac{\partial h}{\partial z} + \cos(\beta)\right)\right) = \frac{\partial \theta_{\mathrm{m}}}{\partial t}. \qquad (9)$$

To normalize the hydraulic conductivity of unsaturated soils with respect to its saturated hydraulic conductivity, we obtained

$$K_{\mathrm{r}} = \frac{K_z(h)}{K_{\mathrm{s}}}, \qquad (10)$$

where K_{s} is the saturated hydraulic conductivity and K_{r} is the relative hydraulic conductivity which is a function of the

pressure head. Equation (11) can be obtained by substituting (10) into (9).

$$\frac{\partial}{\partial z}\left(K_{\mathrm{r}}\frac{\partial h}{\partial z}\right) + \frac{\partial K_{\mathrm{r}}}{\partial z}\cos(\beta) = \frac{1}{K_{\mathrm{s}}}\frac{\partial \theta_{\mathrm{m}}}{\partial t}. \qquad (11)$$

The high nonlinearity of physical behavior of unsaturated soils is rooted in the SWCC. The SWCC represents the relationship between water content and matric suction in unsaturated soils, which is important for the seepage analysis in the vadose zone. Many mathematical equations have been proposed to describe the SWCC. The Gardner and van Genuchten models of SWCC are commonly found in analytical and numerical solutions for flow problems, respectively [19, 41]. The Gardner exponential model is mostly used to derive analytical solutions of unsaturated flow problems, whereas the van Genuchten model is used in numerical implementations to simulate the physical behavior of unsaturated soils. Gardner [41] proposed a simple one-parameter exponential model as

$$S_{\mathrm{e}} = e^{\alpha_g h}, \qquad (12)$$

where α_g is the pore size distribution parameter, S_{e} is the effective saturation defined by normalizing volumetric water content with its saturated and residual values as $S_{\mathrm{e}} = (\theta_{\mathrm{m}} - \theta_{\mathrm{r}})/(\theta_{\mathrm{s}} - \theta_{\mathrm{r}})$, θ_{s} and θ_{r} denote the saturated and residual water content, respectively. The volumetric water content can be expressed as follows.

$$\theta_{\mathrm{m}} = \theta_{\mathrm{r}} + (\theta_{\mathrm{s}} - \theta_{\mathrm{r}})e^{\alpha_g h}. \qquad (13)$$

For the porous media including gilat loam and sandy loam, the Gardner model exhibits good match with the van Genuchten model [42]. The relative hydraulic conductivity is modeled by the Gardner exponential model [43, 44] as

$$K_{\mathrm{r}} = e^{\alpha_g h}. \qquad (14)$$

Adopting the Gardner exponential model, the linearized Richards equation for the one-dimensional transient Richards equation can be derived as follows [6, 10, 43, 45].

$$\frac{\partial^2 \bar{h}}{\partial z^2} + \alpha_g \cos(\beta)\frac{\partial \bar{h}}{\partial z} = c\frac{\partial \bar{h}}{\partial t}, \qquad (15)$$

where $c = [\alpha_g(\theta_{\mathrm{s}} - \theta_{\mathrm{r}})]/K_{\mathrm{s}}$, $\bar{h}$ is the pressure head of the linearized Richards equation which can be defined as $\bar{h} = e^{\alpha_g h} - e^{\alpha_g h_d}$, and h_d is the pressure head when the soil is dry.

2.2. The Novel Spacetime Collocation Method. In this study, the proposed spacetime collocation method rooted from the CTM. The Trefftz method is first proposed by the German mathematician Erich Trefftz [28]. Later, the CTM [29–31, 46] is commonly used for the numerical solution of partial differential equations. Since the CTM is a boundary-type meshless method, it approximates the solutions using the T-complete basis functions where the solutions can be expressed as a linear combination of the T-complete basis functions automatically satisfying governing equations [38]. The CTM requires the evaluation of a coefficient

(a) Conventional collocation scheme for one-dimensional transient flow problem

(b) Collocation points of one-dimensional transient flow problem in the spacetime domain
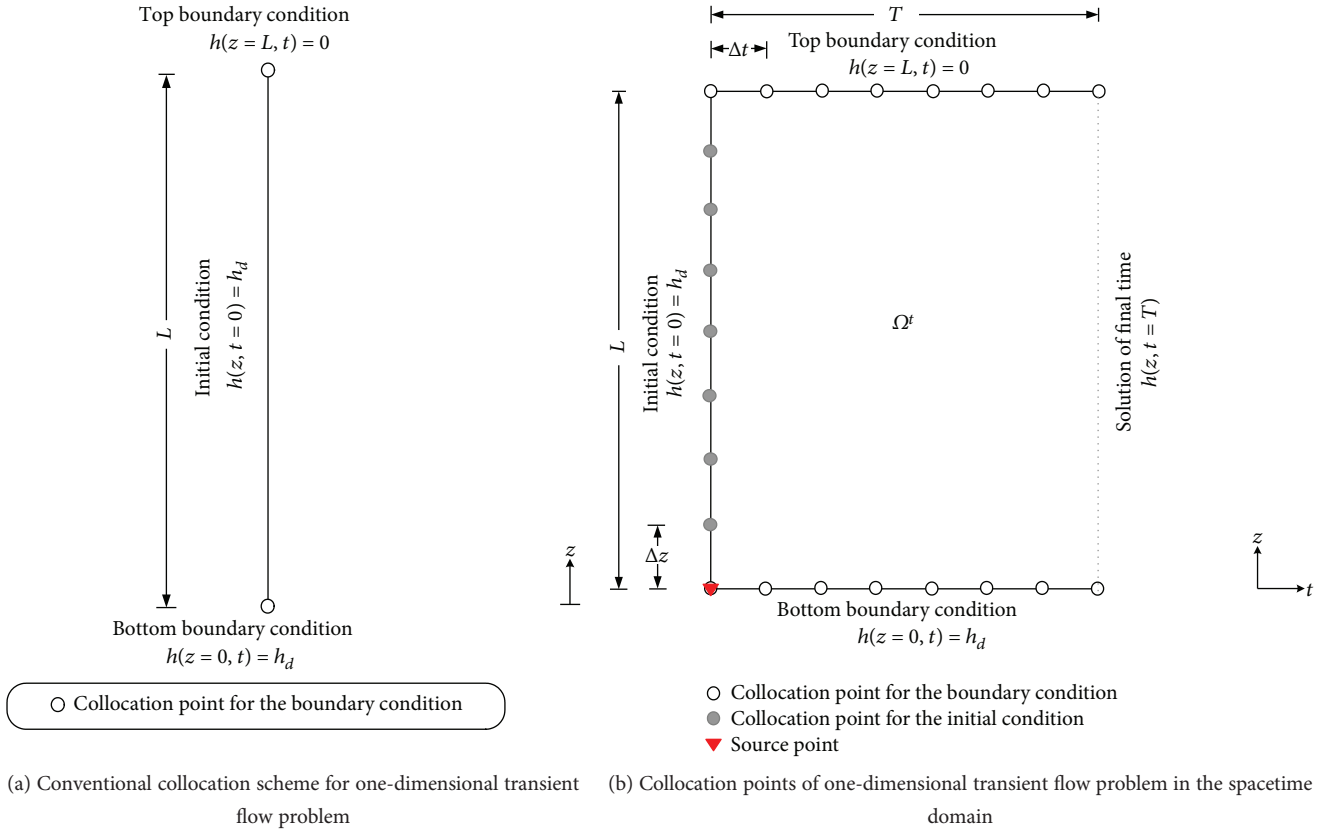
Figure 2: Illustration of the proposed collocation scheme.

for each term in the series. The determination of coefficients may be obtained by solving the unknown coefficients in the linear simultaneous equations which are accomplished by collocation imposing the boundary conditions at a number of points. The CTM used to deal with the Laplace equation in the two-dimensional cylindrical coordinate system. The numerical solution of the Laplace equation is approximated by superpositioning the T-complete basis functions satisfying the governing equation [39]. The T-complete basis functions are composed of a set of linearly independent functions which can be obtained by finding the general solutions to the Laplace equation in cylindrical coordinates. Since the CTM is originally developed to deal with the boundary value problems in the past, the application of the CTM for solving transient problems is hardly found [47].

In this paper, we proposed a novel spacetime collocation method, named the spacetime collocation method (SCM) [10]. The numerical approximation was developed by using the general solution of the one-dimensional linearized Richards equation. Different from the conventional collocation method based on a set of unstructured points in space only, a pioneering work in this study uses the SCM by collocating the boundary points in the spacetime coordinate system such that the initial and boundary conditions can both be treated as boundary conditions on the spacetime domain boundary.

We assume that time and the speed of light are absolute physical quantities that play the role of the independent variable such that the spacetime coordinate system is an

n-dimensional space and one-dimensional of time [10]. For instance, the one-dimensional linearized Richards equation is one-dimensional in space and one-dimensional in time. In the past, the collocation points of the meshless method are only applied on the boundary in Euclidean space, as shown in Figure 2(a), and the conventional time-marching scheme is also adopted for time discretization. However, in this study, the spacetime domain is a one-dimensional space and one-dimensional of time which constructs a rectangular shape, as shown in Figure 2(b). Meanwhile, we transformed the one-dimensional initial value problem, into a two-dimensional inverse boundary value problem. It should be noted that the initial and boundary conditions are both applied on the spacetime boundary. In addition, it becomes an inverse boundary value problem because the final time boundary values may not be assigned.

Considering the one-dimensional spacetime domain, Ω^t, enclosed by a spacetime boundary, Γ^t, the one-dimensional linearized Richards equation can be expressed as

$$\frac{\partial^2 \bar{h}}{\partial z^2} + \alpha_g \cos(\beta) \frac{\partial \bar{h}}{\partial z} = c \frac{\partial \bar{h}}{\partial t} \text{ in } \Omega^t. \tag{16}$$

The initial condition can be described as

$$\bar{h}(z, t = 0) = \bar{g}, \tag{17}$$

where $\bar{g}$ denotes the distribution of the pressure head in the spacetime domain, Ω^t, at time zero. To solve (16), the following boundary conditions must be given.

$$\bar{h}(z, t) = \bar{f} \text{ on } \Gamma_D^t, \tag{18}$$

$$\bar{h}_n(z, t) = \bar{w} \text{ on } \Gamma_N^t. \tag{19}$$

where Γ_D^t denotes the spacetime boundary where the Dirichlet boundary condition is given, Γ_N^t denotes the spacetime boundary where the Neumann boundary condition is given, $\bar{f}$ denotes the Dirichlet boundary condition in the spacetime domain, and $\bar{w}$ denotes the Neumann boundary condition in the spacetime domain.

The transient pressure head of the linearized Richards equation [48] can be expressed as

$$\bar{h} = \bar{h}_t + \bar{h}_s, \tag{20}$$

where $\bar{h}_s$ and $\bar{h}_t$ denote the steady-state and transient pressure head of the linearized Richards equation, respectively. The transient linearized Richards equation is determined by substituting (20) into (16), which gives

$$\frac{\partial^2 \bar{h}_t}{\partial z^2} + \alpha_g \cos(\beta) \frac{\partial \bar{h}_t}{\partial z} = c \frac{\partial \bar{h}_t}{\partial t}. \tag{21}$$

The process of the separation of variables may be used by having the transient solution as

$$\bar{h}_t(z, t) = Z(z)\varpi(t). \tag{22}$$

Substituting the above equation into (21) and dividing by $Z(z)\varpi(t)$ gives

$$\varpi(t) \frac{\partial^2 Z(z)}{\partial z^2} + \alpha_g \cos(\beta)\varpi(t) \frac{\partial Z(z)}{\partial z} = c Z(z) \frac{\partial \varpi(t)}{\partial t}, \tag{23}$$

$$\frac{1}{Z(z)} \left(\frac{\partial^2 Z(z)}{\partial z^2} + \alpha_g \cos(\beta) \frac{\partial Z(z)}{\partial z} \right) = \frac{c}{\varpi(t)} \frac{\partial \varpi(t)}{\partial t}. \tag{24}$$

Each term in the above equation must be a constant for a nonzero solution. Accordingly, we obtained the following equations.

$$\frac{1}{Z(z)} \left(\frac{\partial^2 Z(z)}{\partial z^2} + \alpha_g \cos(\beta) \frac{\partial Z(z)}{\partial z} \right) = \eta = \frac{c}{\varpi(t)} \frac{\partial \varpi(t)}{\partial t}, \tag{25}$$

$$\frac{\partial^2 Z(z)}{\partial z^2} + \alpha_g \cos(\beta) \frac{\partial Z(z)}{\partial z} - \eta Z(z) = 0, \tag{26}$$

$$c \frac{\partial \varpi(t)}{\partial t} - \eta \varpi(t) = 0, \tag{27}$$

where η is the arbitrary constant. This leads to the characteristic equations

$$m_1^2 + \alpha_g \cos(\beta) m_1 - \eta = 0, \tag{28}$$

$$c m_2 - \eta = 0, \tag{29}$$

where $m_1 = [-\alpha_g \cos(\beta) \pm \sqrt{(\alpha_g \cos(\beta))^2 + 4\eta}]/2$, and $m_2 = \eta/c$. The above equations are simple ordinary differential equations that have solutions,

$$Z(z) = A_1 e^{m_{1a}z} + A_2 e^{m_{1b}z}, \tag{30}$$

$$\varpi(t) = e^{m_2 t}, \tag{31}$$

where $m_{1a} = [-\alpha_g \cos(\beta) + \sqrt{(\alpha_g \cos(\beta))^2 + 4\eta}]/2$ and $m_{1b} = [-\alpha_g \cos(\beta) - \sqrt{(\alpha_g \cos(\beta))^2 + 4\eta}]/2$.

The general solution for $\bar{h}_t(z, t)$ becomes

$$\bar{h}_t(z, t) = Z(z)\varpi(t) = (A_1 e^{m_{1a}z} + A_2 e^{m_{1b}z})e^{m_2 t}, \tag{32}$$

where A_1 and A_2 are arbitrary constants to be determined. Rewriting the above equations in terms of sine and cosine series, we obtained the following equation:

$$\bar{h}_t(\mathbf{x}) \approx \sum_{k=1}^{M} \mathbf{p}_k \mathbf{W}_k(\mathbf{x}), \tag{33}$$

where $\mathbf{x} = (z, t)$, $\mathbf{p}_k = [p_{1k} \, p_{2k} \, p_{3k}]^T$, and $\mathbf{W}_k(\mathbf{x}) = [W_{1k} \quad W_{2k} \quad W_{3k}]$. $\mathbf{p}_k$ are unknown coefficients, $\mathbf{W}_k(\mathbf{x})$ are the Trefftz basis functions, T is the transpose of the matrix, k is the positive integer, M is the order of the basis function, $W_{1k} = e^{(-\alpha_g \cos(\beta)z)/2 - \mu_k t} \sin(\lambda_k z)$, $W_{2k} = e^{(-\alpha_g \cos(\beta)z)/2 - \mu_k t}$, $W_{3k} = e^{(-\alpha_g \cos(\beta)z)/2 - \mu_k t} \cos(\lambda_k z)$, $\lambda_k = \pi k/L$, $\mu_k = [(\alpha_g \cos(\beta))^2/4 + \lambda_k^2]/c$ and L is the characteristic length. Equation (33) can be discretized at a number of collocated points on the spacetime boundary using the initial and boundary conditions, which can be expressed as follows.

$$\bar{h}_t^i(\mathbf{x}_i) \approx \sum_{k=1}^{M} \mathbf{p}_k \mathbf{W}_k^i(\mathbf{x}_i), \tag{34}$$

where $\mathbf{x}_i = (z_i, t_i)$ and $\mathbf{W}_k^i(\mathbf{x}_i) = [W_{1k}^i \quad W_{2k}^i \quad W_{3k}^i]$.

A system of simultaneous linear equations can then be obtained as

$$\mathbf{A}\boldsymbol{\alpha} = \mathbf{B}. \tag{35}$$

where $\mathbf{A} = \begin{bmatrix} W_{11}^1 & W_{21}^1 & W_{31}^1 & \cdots & W_{3M}^1 \\ W_{11}^2 & W_{21}^2 & W_{31}^2 & \cdots & W_{3M}^2 \\ \vdots & \vdots & \vdots & \vdots & \vdots \\ W_{11}^I & W_{21}^I & W_{31}^I & \cdots & W_{3M}^I \end{bmatrix}$, $\boldsymbol{\alpha} = \begin{bmatrix} p_{11} \\ p_{21} \\ p_{31} \\ \vdots \\ p_{3M} \end{bmatrix}$,

$\mathbf{B} = \begin{bmatrix} \bar{g}_1 \\ \bar{g}_2 \\ \bar{g}_3 \\ \vdots \\ \bar{g}_I \end{bmatrix}$, $\mathbf{A}$ is a matrix of the Trefftz basis functions with the size of $I \times 3M$, $\boldsymbol{\alpha}$ with the size of $3M \times 1$ is a vector of unknown coefficients, $\mathbf{B}$ with the size of $I \times 1$ is a vector of given values from the Dirichlet boundary condition at collocation points, I is the number of collocation points, $3M$ is the number of the terms related to the order of the basis function

as depicted in (34), $p_{11}, p_{21}, p_{31}, \ldots, p_{3M}$ are unknown coefficients to be evaluated, and $\bar{g}_1, \bar{g}_2, \bar{g}_3, \ldots, \bar{g}_I$ are the values of the Dirichlet boundary condition. The boundary and source points are collocated in the spacetime domain. Solving the above simultaneous linear equations using the commercial program MATLAB backslash operator, we may obtain the set of unknown coefficients for the spacetime domain, Ω_t. To obtain the pressure head results for the spacetime domain, the inner collocation points in Ω_t must be placed. The pressure head, $\bar{h}_t(z, t)$, at inner collocation points can then be found by (35) using $\mathbf{A}$ and $\boldsymbol{\alpha}$ for the spacetime domain, Ω_t. Once we obtained the transient pressure head of the linearized Richards equation, $\bar{h}_t(z, t)$, the transient solution can be obtained using the following two equations.

$$\bar{h}(z, t) = \bar{h}_t(z, t) + \bar{h}_s(z), \tag{36}$$

$$\bar{h}_s(z) = \left(1 - e^{\alpha_g h_d}\right) \frac{1 - e^{-\alpha_g \cos(\beta)z}}{1 - e^{-\alpha_g \cos(\beta)L}}, \tag{37}$$

where $\bar{h}_s(z)$ is the steady-state pressure head of the linearized Richards equation [45]. Finally, the transient solution can be obtained as follows.

$$h(z, t) = \frac{1}{\alpha_g} \ln \left(\bar{h}(z, t) + e^{\alpha_g h_d}\right). \tag{38}$$

3. Model Verification and Comparison

3.1. Verification Example 1. The first verification example is an one-dimensional transient subsurface flow problem in homogenous unsaturated soil. The unsaturated soil is initially dry until water begins to infiltrate the soil. The ponding on the ground surface is then maintained holding the pressure head to zero. This is known as the one-dimensional Green-Ampt problem [49]. The height of the column of soil (L) is 10 (m). The saturated hydraulic conductivity (K_s), pore size distribution parameter (α_g), saturated water content (θ_s), and residual water content (θ_r) for this example are 9×10^{-5} (m/h), 10^{-4}, 0.50, and 0.11, respectively. The total simulation time (T) is ten hours (h). The governing equation can be expressed as follows.

$$\frac{\partial}{\partial z}\left(K_r \frac{\partial h}{\partial z}\right) + \frac{\partial K_r}{\partial z} = \frac{1}{K_s} \frac{\partial \theta_m}{\partial t}. \tag{39}$$

The initial condition was the soil in dry condition where $h_d = -10^5$ (m). Thus,

$$h(z, t = 0) = h_d. \tag{40}$$

The boundary conditions of the top and bottom boundaries are the pressure head-type boundary condition, which can be expressed as follows.

$$h(z = 0, t) = h_d, \tag{41}$$

$$h(z = L, t) = 0. \tag{42}$$

The analytical transient solution of this example can be found as follows [45].

$$\bar{h}_t(z, t) = \frac{2\left(1 - e^{\alpha_g h_d}\right)}{Lc} e^{\alpha_g(L-z)/2} \sum_{k=1}^{M} (-1)^k \left(\frac{\lambda_k}{\mu_k}\right) \sin(\lambda_k z) e^{-\mu_k t}. \tag{43}$$

The $\bar{h}(z, t)$ can be obtained using the following equations.

$$\bar{h}(z, t) = \bar{h}_t(z, t) + \bar{h}_s(z), \tag{44}$$

$$\bar{h}_s(z) = \left(1 - e^{\alpha_g h_d}\right) \frac{1 - e^{-\alpha_g z}}{1 - e^{-\alpha_g L}}. \tag{45}$$

Finally, the transient solution $h(z, t)$ can be obtained as follows.

$$h(z, t) = \frac{1}{\alpha_g} \ln \left(\bar{h}(z, t) + e^{\alpha_g h_d}\right). \tag{46}$$

In this example, there is one-dimensional in space and one-dimensional in time. It is clear that the spacetime domain is a rectangular shape. We adopted 600 boundary collocation points and a source point. The number of boundary points in space domain and in time domain was considered to be 200 and 400, respectively. The Dirichlet boundary values were given on boundary collocation points which collocated on three sides of the domain except the right side which is the final time solution to be found. The order of the basis function depicted in (34) and the characteristic length for the transient analysis were 60 and 10, respectively. To view the results clearly, the profiles of the computed results on different times were selected to compare with the exact solution. To examine the accuracy of the proposed method, we collocated 2496 inner points uniformly placed inside the rectangular spacetime domain. This example was solved using both the proposed method and the finite difference method (FDM). For the FDM analysis, the spatial and temporal discretization for the problem must be considered separately. The central difference approximation was adopted for the spatial discretization. On the other hand, the implicit scheme is adopted for time discretization. The space interval and time interval were 0.02 (m) and 0.01 (h), respectively.

The profiles of the computed results from the proposed method and the FDM on different times were then compared with the exact solution, as shown in Figure 3. It is found that the computed results agreed well with the exact solution. Comparing the maximum absolute error, it is found that the maximum absolute errors are in the order of 10^{-6} and 10^{-1} for the proposed meshless method and the FDM, respectively, as shown in Figure 4. In this example, we proposed an innovative concept which is based on the spacetime coordinate system. Consequently, the transient flow problems can be transformed into the inverse boundary problem in which the boundary values of the final time are unknown. The advantages of the proposed method are that the highly accurate results can be obtained and the convergence problem can be avoided since the one-dimensional transient example is solved without using the traditional time-marching scheme.
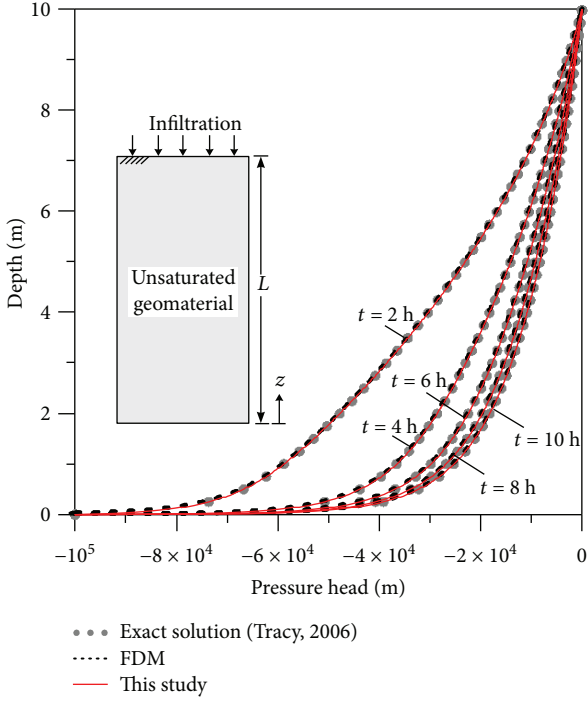
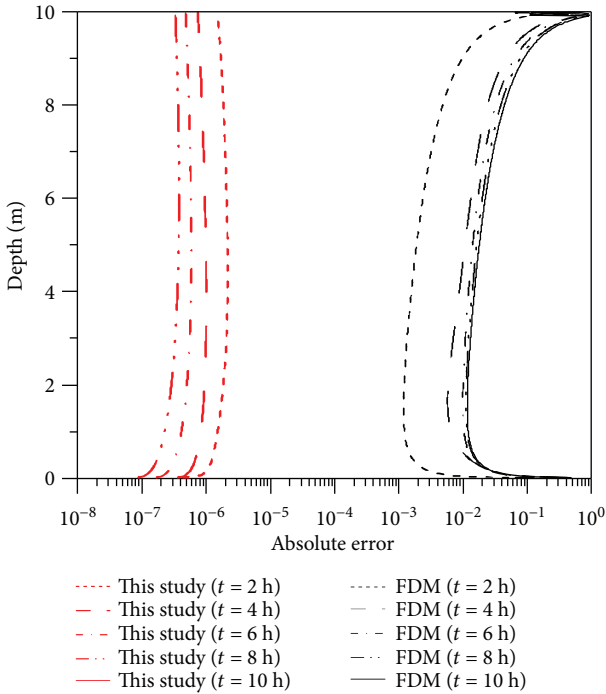FIGURE 3: Comparison of results for solving one-dimensional Green-Ampt problem.

FIGURE 4: Comparison of the absolute error of the computed results and the FDM.

3.2. Verification Example 2. The second example under investigation is the transient modeling of one-dimensional flow in a homogenous unsaturated inclined slope. A column of soil is initially dry until water begins to infiltrate the soil. A
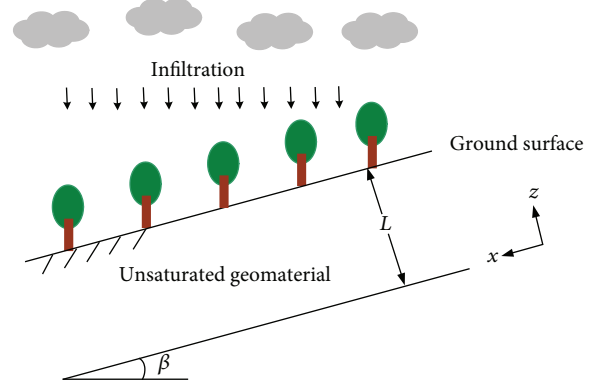

FIGURE 5: Schematic illustration of homogenous unsaturated inclined slope.

TABLE 1: Unsaturated soil parameters used in the verification example 2.

Parameters for SWCC	Soil type	
	Sandy soil	Silty loam
Saturated hydraulic conductivity (m/h)	6.00×10^{-2}	1.50×10^{-3}
Pore size distribution parameter (1/m)	1.60×10^{-2}	8.00×10^{-3}
Saturated water content	0.50	0.46
Residual water content	0.11	0.14

pool of water at ground surface is then maintained holding the pressure head to zero. The thickness of the soil is 10 (m) and the slope angle is 20 degrees, as shown in Figure 5. The total simulation time is two hours. The governing equation can be expressed as (11).

The initial condition was the soil in dry condition maintained as $h_d = -10 \text{(m)}$. The boundary conditions at the top and bottom of the soil can be expressed as follows.

$$h(z = 0, t) = h_d, \tag{47}$$

$$h(z = L, t) = 0. \tag{48}$$

The transient analytical solution can be expressed as follows [45].

$$\bar{h}_t(z, t) = \frac{2\left(1 - e^{\alpha_g h_d}\right)}{Lc} e^{\alpha_g \cos(\beta)(L-z)/2} \sum_{k=1}^{M} (-1)^k \left(\frac{\lambda_k}{\mu_k}\right) \sin(\lambda_k z) e^{-\mu_k t}. \tag{49}$$

In this study, the modeling of one-dimensional transient flow in the homogenous unsaturated inclined slope is conducted. To validate the applicability of the proposed Gardner model, we selected two different soils which are sandy soil and silty loam for this example. The data sets from Brooks and Corey [50] and Lu and Likos [51] were adopted. These data sets cover a broad range of porous media, ranging from sandy soil to silty loam. The fitted parameters including saturated hydraulic conductivity, pore size distribution parameter, saturated water content, and residual water content are listed in Table 1 [51].
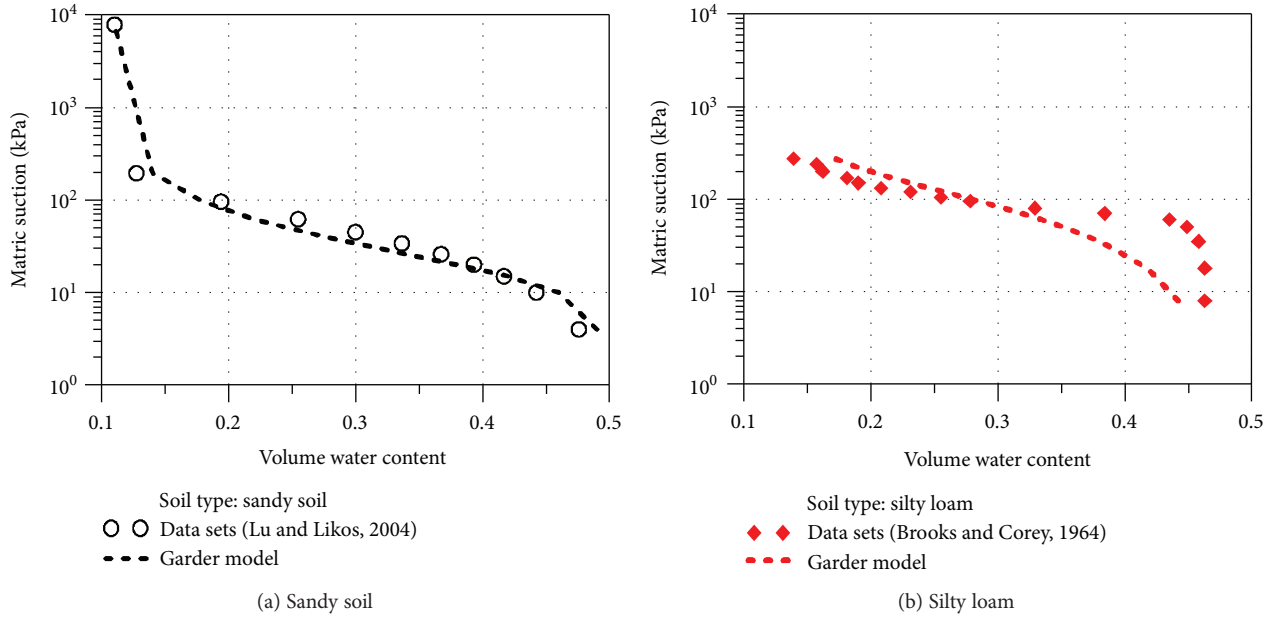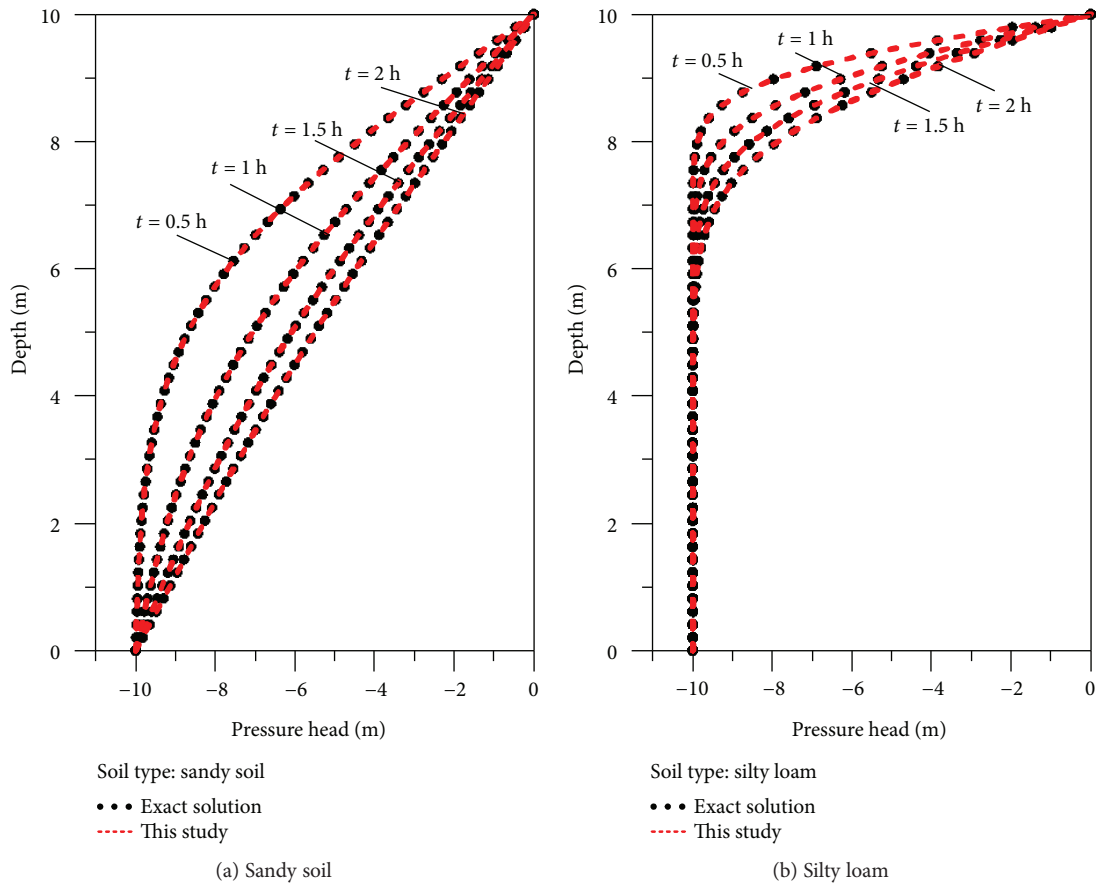
(a) Sandy soil

(b) Silty loam

Figure 6: Fitting curves of the SWCC.

(a) Sandy soil

(b) Silty loam

Figure 7: Result comparison with the exact solution for sandy soil and silty loam.
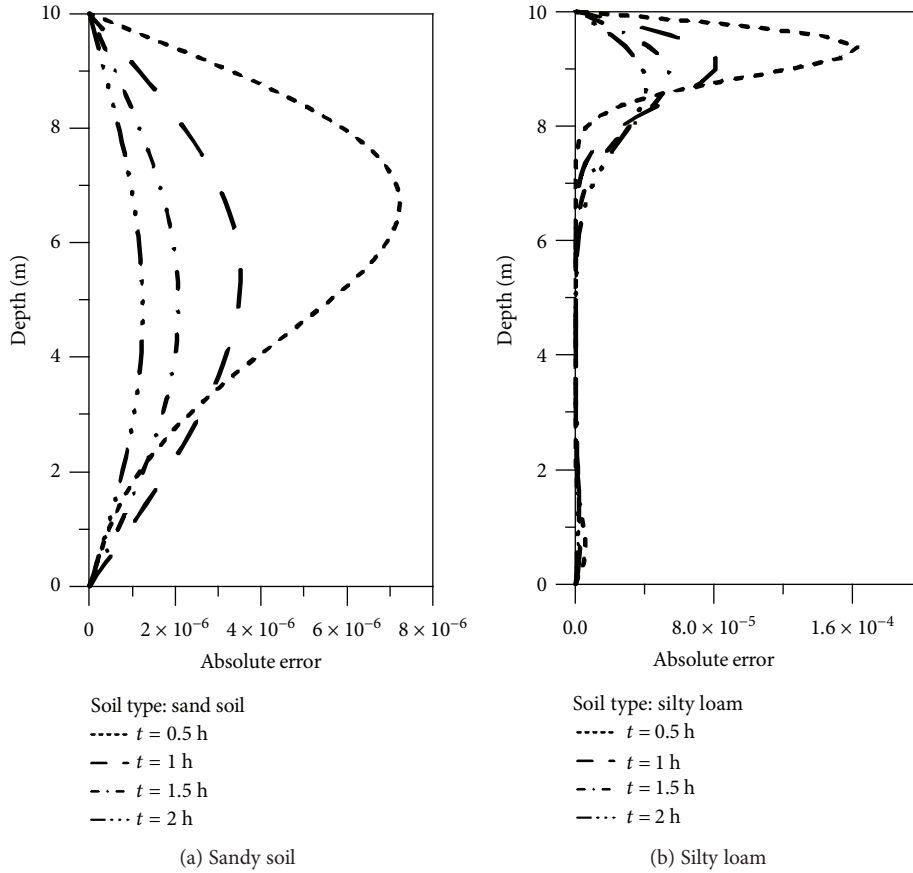
(a) Sandy soil

(b) Silty loam

FIGURE 8: The absolute error of the computed results for sandy soil and silty loam.

We adopted 375 boundary collocation points and a source point. The number of boundary points in space domain and in time domain was considered to be 125 and 250, respectively. The Dirichlet boundary values were given on boundary collocation points which collocated on three sides of the domain using the analytical solution for the problem. The order of the basis function depicted in (33) and the characteristic length for the transient analysis were 60 and 10, respectively. To obtain the computed results of the pressure head at different times, we collocated 2496 inner points uniformly placed inside the rectangular domain. The profiles of the numerical solution on different times were selected to compare with the analytical solution.

The fitting curves of the SWCC for two different types of soil are illustrated in Figure 6, and the computed results for sandy soil and silty loam in this investigation are shown in Figure 7. Figure 7 indicates that the computed results agree very well with the analytical solution. Results obtained demonstrate that the accuracy of the absolute error can be reached to the order of 10^{-6} and 10^{-4} for sandy soil and silty loam, as depicted in Figures 8(a) and 8(b), respectively.

3.3. Verification Example 3. Since the proposed spacetime collocation method is advantageous in solving problems of irregular geometry, the third verification example is the two-dimensional transient subsurface flow problem in homogenous unsaturated soil enclosed by an irregular boundary.

With a two-dimensional simply connected domain, the governing equation can be expressed as follows.

$$\frac{\partial}{\partial x}\left(K_r \frac{\partial h}{\partial x}\right) + \frac{\partial}{\partial z}\left(K_r \frac{\partial h}{\partial z}\right) + \frac{\partial K_r}{\partial z}\cos(\beta) = \frac{1}{K_s}\frac{\partial \theta_m}{\partial t}. \tag{50}$$

The unsaturated soil parameters are the same as in verification example 1. The total simulation time is two hours. The initial condition is the unsaturated soil in dry condition maintained as pressure head to be –100 (m), which can be described as follows.

$$h(x, z, t = 0) = -100. \tag{51}$$

The two-dimensional irregular boundary under consideration can be defined as the following parametric equation.

$$\Omega = \{(x, z, t)|x = \rho(\theta)\cos\theta, \quad z = \rho(\theta)\sin\theta\}. \tag{52}$$

where $\rho(\theta) = (e^{[\sin(\theta/2)\sin(2\theta)]^2} + e^{[\sin(2\theta)\cos(2\theta)]^2})/2, \quad 0 \le \theta \le 2\pi$.

The boundary conditions are assumed to be the Dirichlet boundary condition. The Dirichlet boundary data is applied using the following exact solution [10].

$$\bar{h}_t(x, z, t) = xe^{-[\alpha_g\cos(\beta)]^2 t/4c}e^{-\alpha_g\cos(\beta)z/2}. \tag{53}$$
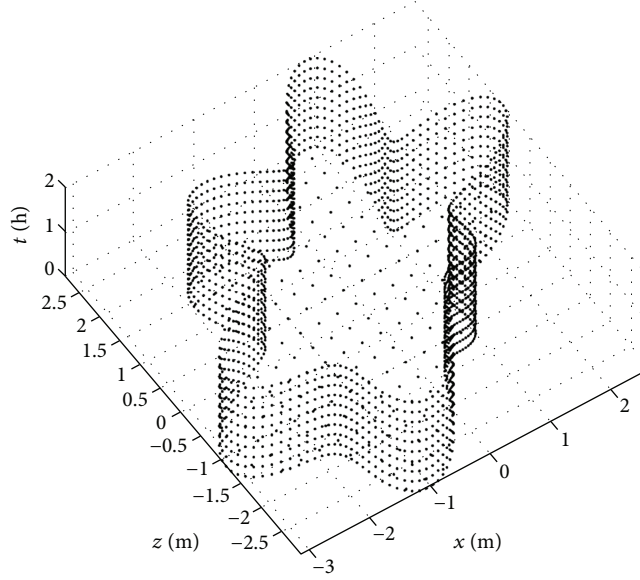
FIGURE 9: Spacetime boundary collocation points of the two-dimensional transient flow in unsaturated soils.

The transient numerical solution can be obtained using the following equations [45].

$$\bar{h}(x, z, t) = \bar{h}_t(x, z, t) + \bar{h}_s(x, z), \tag{54}$$

$$\bar{h}_s(x, z) = \left(1 - e^{\alpha_g h_d}\right) \sin\left(\frac{\pi x}{L}\right) e^{(\alpha_g \cos (\beta)/2)(L-z)} \frac{\sinh (\zeta z)}{\sinh (\zeta L)}. \tag{55}$$

where $\zeta = \sqrt{([\alpha_g \cos (\beta)]^2/4) + (\pi/L)^2}$. According to the previous study [10], the characteristic length is assumed to be 180. The CTM for the two-dimensional transient linearized Richards equation can also be composed of a set of linearly independent vectors adopting the method of the separation of variables. The solution can then be derived as follows.

$$\bar{h}_t(x, z, t) \approx \sum_{k=1}^{M} \sum_{j=1}^{M} \mathbf{s}_{jk} \mathbf{v}_{jk}(x, z, t), \tag{56}$$

where M is the order of the Trefftz basis function for approximating the solution. $\mathbf{s}_{jk}$ are the unknown coefficients, which can be expressed as $\mathbf{s}_{jk} = \begin{bmatrix} s_{1jk} & s_{2jk} & s_{3jk} & s_{4jk} \end{bmatrix}^{\mathrm{T}}$. s_{1jk}, s_{2jk}, s_{3jk}, and s_{4jk} are unknown coefficients, and $\mathbf{v}_{jk}(x, z, t)$ are the Trefftz basis functions, which can be expressed as $\mathbf{v}_{jk}(x, z, t) = \begin{bmatrix} v_{1jk} & v_{2jk} & v_{3jk} & v_{4jk} \end{bmatrix}$, $v_{1jk} = e^{(-\alpha_g \cos (\beta)z/2) - \gamma_{jk}t}$ $\sin (\lambda_j x) \sin (\lambda_k z)$, $v_{2jk} = e^{(-\alpha_g \cos (\beta)z/2) - \gamma_{jk}t} \sin (\lambda_j x) \cos (\lambda_k z)$, $v_{3jk} = e^{(-\alpha_g \cos (\beta)z/2) - \gamma_{jk}t} \cos (\lambda_j x) \cos (\lambda_k z)$, $v_{4jk} = e^{(-\alpha_g \cos (\beta)z/2) - \gamma_{jk}t} \cos (\lambda_j x) \sin (\lambda_k z)$, $\gamma_{jk} = (1/c)(\zeta_j^2 + \lambda_k^2)$, $\zeta_j = \sqrt{([\alpha_g \cos (\beta)]^2/4) + \lambda_j^2}$, and $\lambda_j = \pi j/L$.

We utilized the spacetime coordinate system to model the transient two-dimensional flow in unsaturated soil. There is two-dimensional in space and one-dimensional in time in
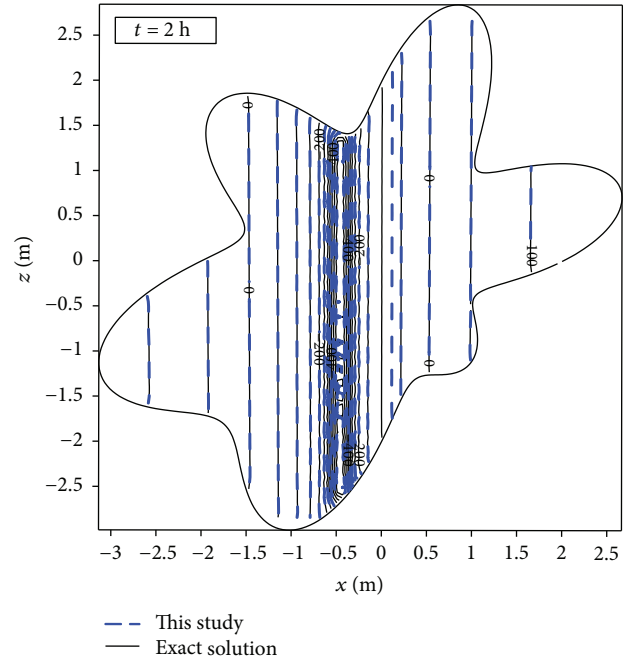
FIGURE 10: Comparison of computed results with the exact solution for the modeling of two-dimensional transient flow in unsaturated soils.

this two-dimensional transient analysis. Consequently, the spacetime domain is transformed into a three-dimensional irregular object domain, as shown in Figure 9. Since the top side boundary values of the spacetime domain were unknowns to be determined, we transformed the two-dimensional initial value problem into the three-dimensional inverse boundary value problem. The initial and boundary conditions were applied on the bottom side

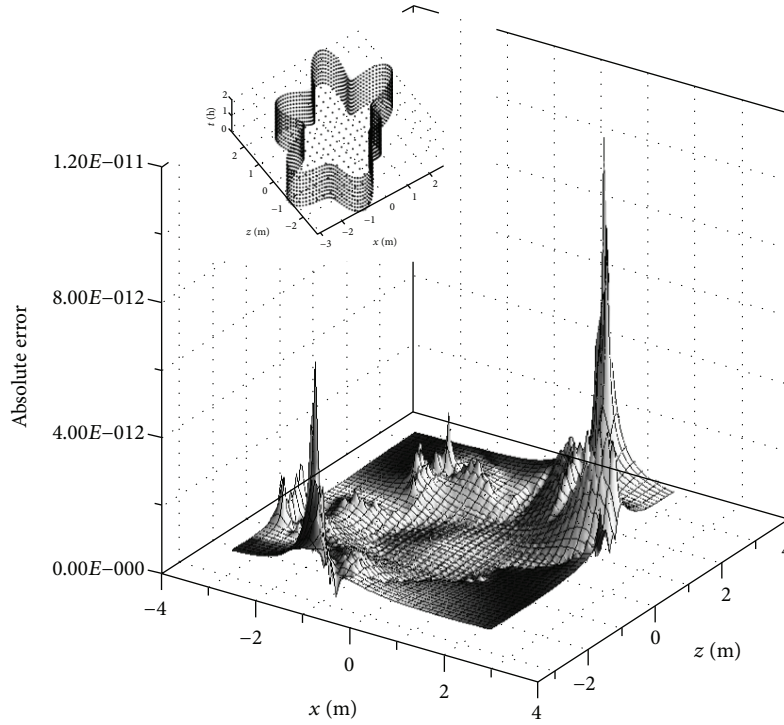FIGURE 11: The absolute error of the computed results for the modeling of two-dimensional transient flow in unsaturated soils.

TABLE 2: Unsaturated soil parameters used in the comparison example.

	This study	van Genuchten model	Iverson's model
Slope angle (degree)		33	
Soli thickness (m)		10	
Simulation time (h)		2	
Saturated hydraulic conductivity (m/h)		1.8×10^{-3}	
Other parameters	$\alpha_g = 3.2 \times 10^{-4}$ $\theta_s = 0.32$ $\theta_r = 0.03$	$\alpha_v = 2.8 \times 10^{-3}$ $n_v = 1.3$ $\theta_s = 0.32$ $\theta_r = 0.03$	$D_0 = (10 \sim 100) \times K_s$

Notation: α_v is the fitting parameter related to the modal pore size, n_v is the fitting parameter related to the pore size distribution, and D_0 is the hydraulic diffusivity.

and the circumferential irregular boundary of the spacetime domain, respectively.

The order of the basis function for this example was 10. We collocated 2162 boundary collocation points and a source point. The number of boundary points in the space domain and in the time domain was considered to be 162 and 2000, respectively. We adopted 1325 inner points uniformly placed inside the three-dimensional spacetime domain to obtain the computed results of the pressure head at different times. Figure 10 shows the comparison of the computed result with the exact solution. It is found that the computed results agreed closely with the exact solution. Figure 11 depicts the absolute error of the two-dimensional computed results. Highly accurate

numerical solutions in the order of 10^{-11} can be obtained for this two-dimensional transient analysis.

4. Application Example

4.1. Hydrological Modeling of Geofluid in Unsaturated Soils. The application example under investigation is a one-dimensional, transient, unsaturated flow problem in a homogeneous inclined slope. In this example, the thickness of the soil is assumed to be 10 (m) and the slope angle is 33 degrees. The governing equation is depicted as (11). With regard to the influence of rainfall infiltration on slope stability in unsaturated zones, Iverson [16] proposed a one-dimensional linear diffusion equation which is a simplified form of the
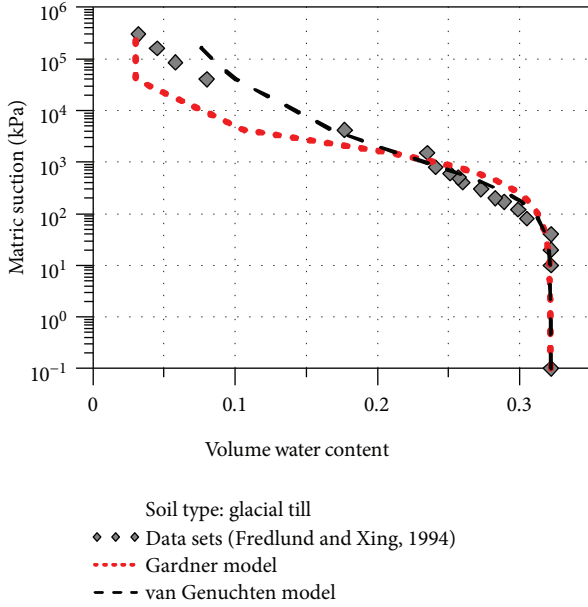
FIGURE 12: Fitting results of the SWCC using van Genuchten and Gardner models.

Richards equation. Accordingly, the influence of matric suction of soil and the SWCC cannot be comprehensively considered during the analysis using the one-dimensional linear diffusion equation. To demonstrate the difference of the result from this study and that from Iverson, we conducted a comparison example with the consideration of unsaturated flow in response to infiltration at ground surface. The total simulation time is two hours. Considering that the ponding on the ground surface is maintained holding the infiltration, the boundary conditions of the top and bottom boundaries are the pressure head-type boundary condition, which can be defined as (47) and (48). The soil was assumed to be glacial till where the following parameters are used in the example: $K_s = 1.8 \times 10^{-3}$ (m/h), $\theta_s = 0.32$, and $\theta_r = 0.03$. The effective cohesiveness, effective friction angle, and unit weight of soil are 4.6 (kPa), 30 (degrees), and 21.5 (kN/m^3), respectively. The unsaturated soil parameters used in this example are listed in Table 2 [51].

To examine the applicability of the Gardner model, we compare the Gardner model with the van Genuchten model and measured data [20]. The van Genuchten parameters of unsaturated soil were obtained by fitting the following equation to the measured data.

$$S_e = \left[\left(1 + |\alpha_v h|\right)^{n_v}\right]^{-m_v}, \qquad (57)$$

where α_v is the fitting parameter related to the modal pore size, n_v is the fitting parameter related to the pore size distribution, and $m_v = 1 - 1/n_v$. The corresponding Gardner parameters were calculated using (12).

From Figure 12, it is found that the SWCC based on the Gardner model provides acceptable agreement with the van Genuchten model. Figure 13 reveals the computed results of the pressure head from the proposed method and those from van Genuchten and Iverson's models. It is found that

the computed results agree well with those from Iverson's model, as depicted in Figures 13(a) and 13(b). However, the numerical solution from the simplified linear diffusion equation cannot obtain the appropriate pressure head when the value of the hydraulic diffusivity become smaller, as shown in Figures 13(c) and 13(d).

4.2. Rainfall-Induced Slope Stability in Unsaturated Soils. To deal with the rainfall-induced landslides, the infinite slope stability analysis coupled with the proposed meshless method with the consideration of the fluctuation of time-dependent matric suction is developed. The failure mechanism of infinite slopes mainly involves colluvium, weathered rock formations, or shallow failure and planar slides in bedrock alternations located at thin depth below the ground level. The infinite slope theory is commonly used to evaluate the slope stability while the sliding soil thickness is far less than the slope height. The factor of safety (FS) for the infinite slope theory can be expressed as follows.

$$\text{FS} = \frac{c' + \left(z\gamma_t \cos^2(\beta) - h\gamma_w \cos^2(\beta)\right) \tan \phi'}{z\gamma_t \cos(\beta) \sin(\beta)}, \qquad (58)$$

where c' represents the effective cohesiveness, ϕ' represents the effective friction angle, z represents the soil thickness, γ_t represents the unit weight of soil, and γ_w represents the unit weight of water. Fredlund and Morgenstern adopted the perspectives of continuum mechanics and demonstrated that the shear strength equation can be applied to unsaturated soils [52]. Based on the SWCC, Vanapalli et al. proposed the shear strength equation suitable for unsaturated zones [53].

$$\tau_f = c' + \sigma \tan \phi' - h\gamma_w \left(\frac{\theta_m - \theta_r}{\theta_s - \theta_r}\right) \tan \phi', \qquad (59)$$

where σ represents the total stress and τ_f represents the shear strength. The revised shear strength equation was substituted into (58), and FS for analyzing slope stability can be obtained as follows.

$$
\begin{aligned}
\text{FS} = & \frac{c'}{z\gamma_t \cos(\beta) \sin(\beta)} + \frac{\tan \phi'}{\tan(\beta)} \\
& - \frac{h\gamma_w(\theta_m - \theta_r/\theta_s - \theta_r) \tan \phi'}{z\gamma_t \cos(\beta) \sin(\beta)}.
\end{aligned} \qquad (60)
$$

Figure 14 demonstrates the computed results of FS. It is well known that Iverson's model is based on the simplified Richards equation integrated with the infinite slope stability analysis for rainfall-induced shallow landside modeling [54]. Despite the fact that Iverson's model may provide an effective tool for modeling landslides triggered by rainfall infiltration, the influence of matric suction and the high nonlinearity of physical behaviour of unsaturated soils cannot be considered comprehensively in Iverson's model. The comparison of the computed results reveals that the numerical solution of the linear diffusion equation of the Richards equation can only be applied on the problems within a certain condition and should be
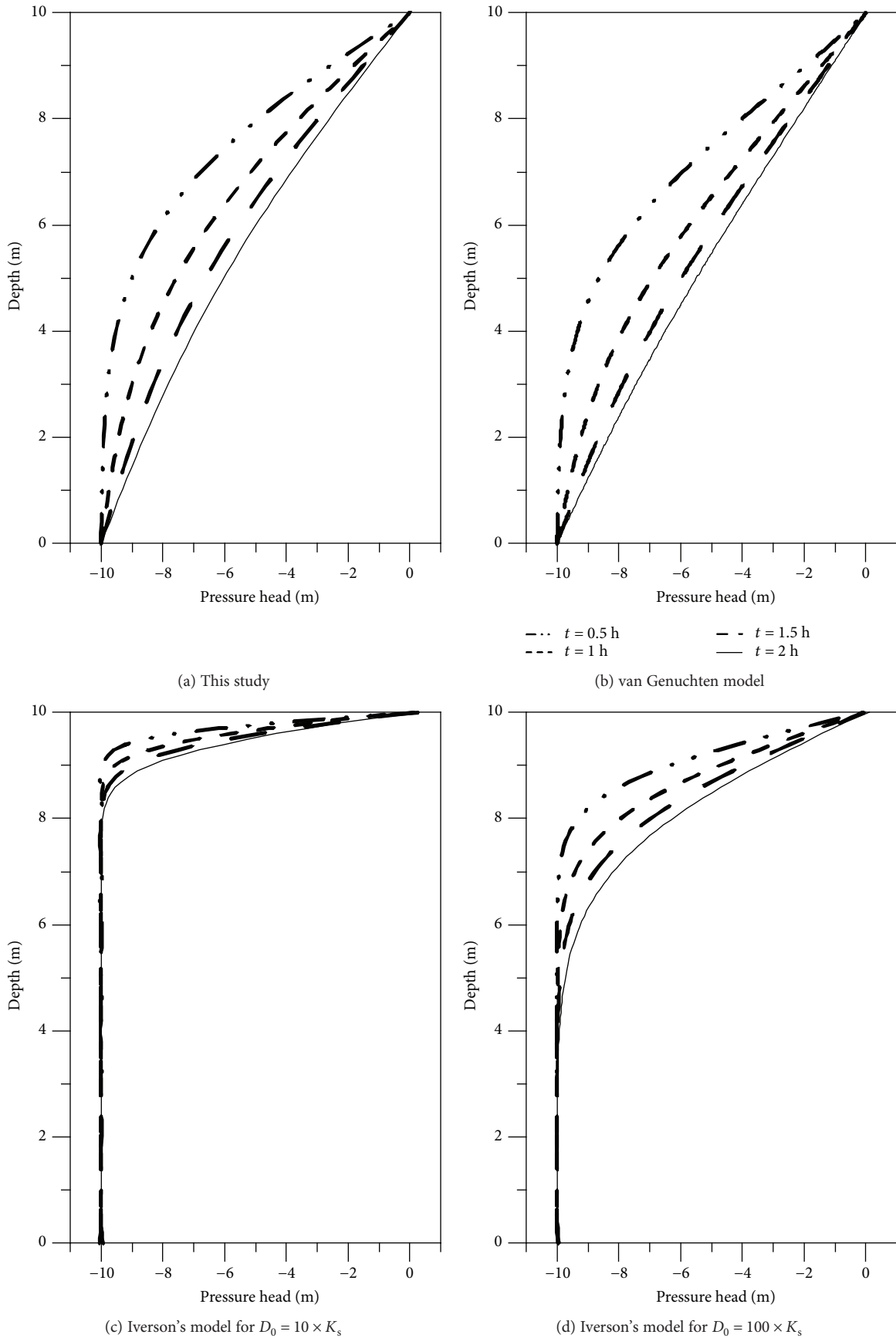
(a) This study

(b) van Genuchten model

$t = 0.5$ h $\quad$ $t = 1.5$ h
$t = 1$ h $\quad$ $t = 2$ h

(c) Iverson's model for $D_0 = 10 \times K_s$

(d) Iverson's model for $D_0 = 100 \times K_s$

FIGURE 13: Comparison of computed pressure heads.

(a) This study

(b) van Genuchten model

Legend:
- $t = 0.5$ h
- $t = 1$ h
- $t = 1.5$ h
- $t = 2$ h
- FS = 1

(c) Iverson's model for $D_0 = 10 \times K_s$

(d) Iverson model's for $D_0 = 100 \times K_s$
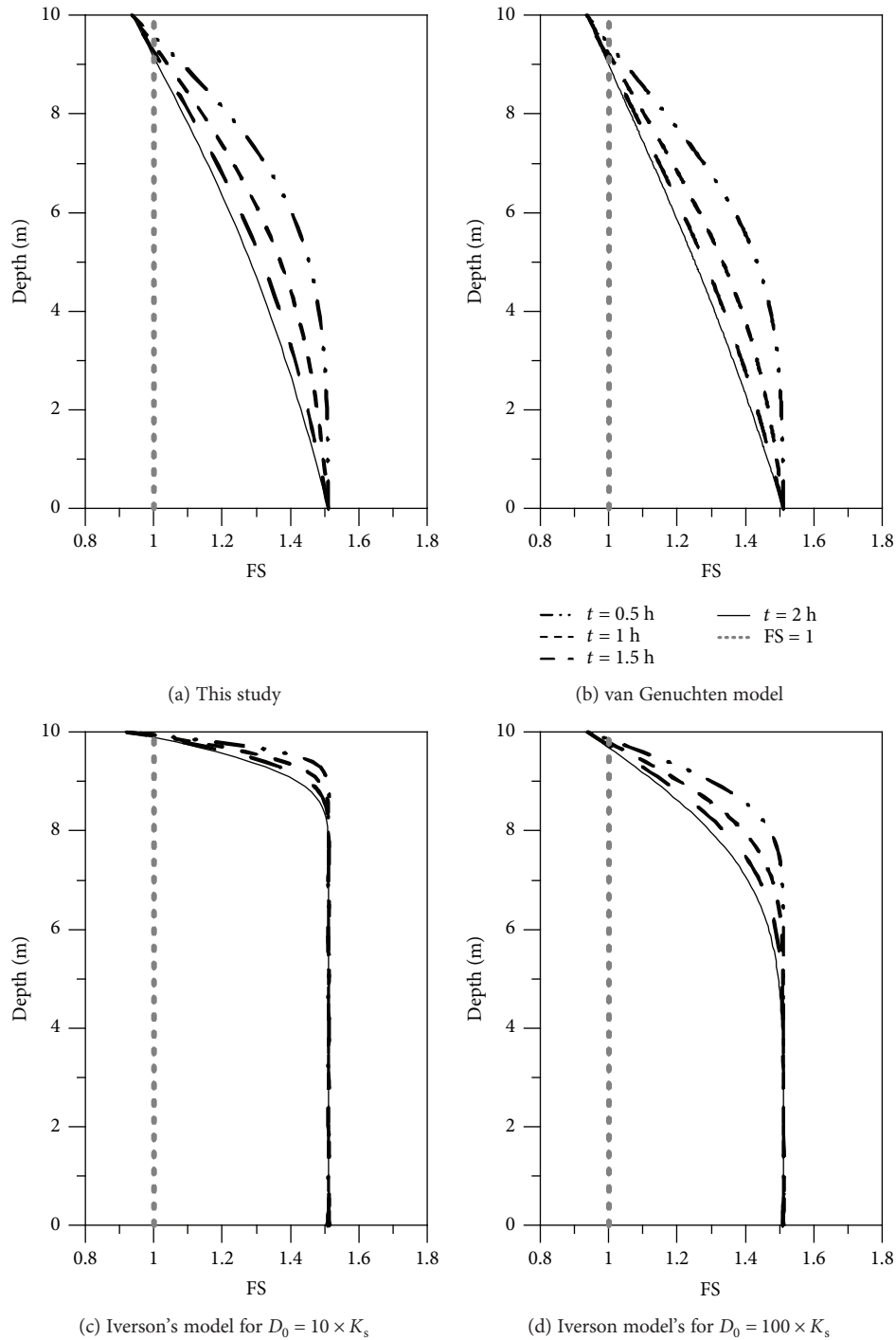
Figure 14: Comparison of the computed FS.

used with caution when the value of the hydraulic diffusivity becomes smaller.

5. Conclusion

A novel spacetime collocation method for modeling of transient flow in unsaturated soils for rainfall-triggered landslides is developed. This pioneering work is based on the boundary-type meshless method and provides a promising solution for modeling the transient flow in unsaturated soils. The validity of the proposed method is established for a number of unsaturated flow problems. The fundamental concepts and the construct of the proposed method are clearly addressed in detail. Findings from this study are drawn as follows.

(1) The pioneering work in this study is the first successful attempt to solve the transient flow in unsaturated soils for an inclined slope using the novel

spacetime collocation method. For the modeling of the transient flow in unsaturated soils, we proposed an innovative concept that one may utilize the space-time coordinate system instead of that in the original Euclidean space. Consequently, both the initial and boundary conditions can be treated as boundary conditions on the spacetime domain boundary. The unsaturated flow problems can then be transformed into the inverse boundary value problem. Therefore, the one-dimensional problems can be solved without using the traditional time-marching scheme.

(2) Since the SWCC is a major factor that influences the nonlinear physical relationship of unsaturated soils, we adopted the Gardner model to formulate the linearized Richards equation. For the numerical modeling of transient flow, we proposed a pioneering work using the proposed boundary-type meshless method in which the hydrological model coupled with the infinite slope stability analysis with the consideration of the SWCC can be used to model rainfall-induced landslides.

(3) From the results of verification examples, it is found that the computed numerical results agree well with the analytical transient solution. Results from the numerical examples demonstrate that highly accurate numerical solutions with the error in the order of 10^{-6} can be obtained. In addition, the proposed numerical scheme for the Richards equation to model one-dimensional flow in unsaturated inclined slopes is applicable for different soil textures.

Data Availability

The data used to support the findings of this study are included within the article. The data supporting Figures 6 and 9 are from previously reported studies and data sets, which have been cited. The processed data are available [from the corresponding author upon request].

Conflicts of Interest

The authors declare that they have no conflicts of interest.

Acknowledgments

References

[1] P. Pereira, M. Oliva, and E. Baltrenaite, "Modelling extreme precipitation in hazardous mountainous areas. Contribution to landscape planning and environmental management," *Journal of Environmental Engineering and Landscape Management*, vol. 18, no. 4, pp. 329–342, 2010.

[2] Y. C. Kuo, M. A. Lee, and M. M. Lu, "Association of Taiwan's rainfall patterns with large-scale oceanic and atmospheric phenomena," *Advances in Meteorology*, vol. 2016, Article ID 3102895, 11 pages, 2016.

[3] J. W. Zhou, C. Shi, and F. G. Xu, "Geotechnical characteristics and stability analysis of rock-soil aggregate slope at the Gushui Hydropower Station, Southwest China," *The Scientific World Journal*, vol. 2013, Article ID 540636, 16 pages, 2013.

[4] N. Zhao, B. Hu, Q. Yi, W. Yao, and C. Ma, "The coupling effect of rainfall and reservoir water level decline on the Baijiabao landslide in the three gorges reservoir area, China," *Geofluids*, vol. 2017, Article ID 3724867, 12 pages, 2017.

[5] N. Lu and J. Godt, "Infinite slope stability under steady unsaturated seepage conditions," *Water Resources Research*, vol. 44, no. 11, 2008.

[6] C.-Y. Liu, C.-Y. Ku, J.-E. Xiao, C.-C. Huang, and S.-M. Hsu, "Numerical modeling of unsaturated layered soil for rainfall-induced shallow landslides," *Journal of Environmental Engineering and Landscape Management*, vol. 25, no. 4, pp. 329–341, 2017.

[7] Y. Que, P. Lin, and D. Lin, "Integrative analysis of surface runoff and macropore flow for slopes under rainfall conditions," *Mathematical Problems in Engineering*, vol. 2018, Article ID 9458410, 13 pages, 2018.

[8] H.-F. Yeh and C.-H. Lee, "Soil water balance model for precipitation-induced shallow landslides," *Environmental Earth Sciences*, vol. 70, no. 6, pp. 2691–2701, 2013.

[9] G. R. Zhang, Y. J. Qian, Z. C. Wang, and B. Zhao, "Analysis of rainfall infiltration law in unsaturated soil slope," *The Scientific World Journal*, vol. 2014, Article ID 567250, 7 pages, 2014.

[10] C. Y. Ku, C. Y. Liu, J. E. Xiao, and W. Yeih, "Transient modeling of flow in unsaturated soils using a novel collocation meshless method," *Water*, vol. 9, no. 12, 2017.

[11] C.-Y. Ku, C.-Y. Liu, Y. Su, J.-E. Xiao, and C.-C. Huang, "Transient modeling of regional rainfall-triggered shallow landslides," *Environmental Earth Sciences*, vol. 76, no. 16, p. 570, 2017.

[12] J.-E. Xiao, C.-Y. Ku, C.-Y. Liu, and W.-C. Yeih, "A novel boundary-type meshless method for modeling geofluid flow in heterogeneous geological media," *Geofluids*, vol. 2018, Article ID 9804291, 13 pages, 2018.

[13] L. Z. Wu, A. P. S. Selvadurai, L. M. Zhang, R. Q. Huang, and J. Huang, "Poro-mechanical coupling influences on potential for rainfall-induced shallow landslides in unsaturated soils," *Advances in Water Resources*, vol. 98, pp. 114–121, 2016.

[14] L. Z. Wu, L. M. Zhang, and R. Q. Huang, "Analytical solution to 1D coupled water infiltration and deformation in two-layer unsaturated soils," *International Journal for Numerical and Analytical Methods in Geomechanics*, vol. 36, no. 6, pp. 798–816, 2012.

[15] B. M. Das, *Principles of Geotechnical Engineering*, Cengage Learning, USA, 7th ed edition, 2010.

[16] R. M. Iverson, "Landslide triggering by rain infiltration," *Water Resources Research*, vol. 36, no. 7, pp. 1897–1910, 2000.

[17] L. A. Richards, "Capillary conduction of liquids through porous mediums," *Physics*, vol. 1, no. 5, pp. 318–333, 1931.

[18] Z. Ye, Q. Jiang, C. Yao et al., "The parabolic variational inequalities for variably saturated water flow in heterogeneous fracture networks," *Geofluids*, vol. 2018, Article ID 9062569, 16 pages, 2018.

[19] M. T. van Genuchten, "A closed-form equation for predicting the hydraulic conductivity of unsaturated soils 1," *Soil Science Society of America Journal*, vol. 44, no. 5, p. 892, 1980.

[20] D. G. Fredlund, A. Xing, and S. Huang, "Predicting the permeability function for unsaturated soils using the soil-water characteristic curve," *Canadian Geotechnical Journal*, vol. 31, no. 4, pp. 533–546, 1994.

[21] J. Salas-García, J. Garfias, R. Martel, and L. Bibiano-Cruz, "A low-cost automated test column to estimate soil hydraulic characteristics in unsaturated porous media," *Geofluids*, vol. 2017, Article ID 6942736, 13 pages, 2017.

[22] S. Nazari, M. Hassanlourad, E. Chavoshi, and A. Mirzaii, "Experimental investigation of unsaturated silt-sand soil permeability," *Advances in Civil Engineering*, vol. 2018, Article ID 4946956, 12 pages, 2018.

[23] C. P. Liang, S. Y. Hsu, and J. S. Chen, "An analytical model for solute transport in an infiltration tracer test in soil with a shallow groundwater table," *Journal of Hydrology*, vol. 540, pp. 129–141, 2016.

[24] L. Z. Wu, A. P. S. Selvadurai, and J. Yang, "The role of surface infiltration in hydromechanical coupling effects in an unsaturated porous medium of semi-infinite extent," *Geofluids*, vol. 2017, Article ID 2918479, 10 pages, 2017.

[25] F. Huang, J. Lyu, G. Wang, and H. Liu, "One-dimensional vacuum steady seepage model of unsaturated soil and finite difference solution," *Mathematical Problems in Engineering*, vol. 2017, Article ID 9589638, 7 pages, 2017.

[26] F. K. Huang, M. H. Chuang, G. S. Wang, and H. D. Yeh, "Tide-induced groundwater level fluctuation in a U-shaped coastal aquifer," *Journal of Hydrology*, vol. 530, pp. 291–305, 2015.

[27] J. S. Chen, K. H. Lai, C. W. Liu, and C. F. Ni, "A novel method for analytically solving multi-species advective-dispersive transport equations sequentially coupled with first-order decay reactions," *Journal of Hydrology*, vol. 420-421, pp. 191–204, 2012.

[28] E. Trefftz, "Ein Gegenstück zum Ritzschen Verfahren," in *Proceedings of the 2nd International Congress of Applied Mechanics*, pp. 131–137, Orell Füssli, Zurich, Switzerland, 1926.

[29] E. Kita and N. Kamiya, "Trefftz method: an overview," *Advances in Engineering Software*, vol. 24, no. 1-3, pp. 3–12, 1995.

[30] C. S. Liu, "A modified collocation Trefftz method for the inverse Cauchy problem of Laplace equation," *Engineering Analysis with Boundary Elements*, vol. 32, no. 9, pp. 778–785, 2008.

[31] Z. C. Li, Z. Z. Lu, H. Y. Hu, and H. D. Cheng, *Trefftz and Collocation Methods*, WIT Press, Southampton, UK, 2008.

[32] V. D. Kupradze and M. A. Aleksidze, "The method of functional equations for the approximate solution of certain boundary value problems," *USSR Computational Mathematics and Mathematical Physics*, vol. 4, no. 4, pp. 82–126, 1964.

[33] J. E. Xiao, C. Y. Ku, C. Y. Liu, C. M. Fan, and W. Yeih, "On solving free surface problems in layered soil using the method of fundamental solutions," *Engineering Analysis with Boundary Elements*, vol. 83, pp. 96–106, 2017.

[34] C. S. Chen, A. Karageorghis, and Y. Li, "On choosing the location of the sources in the MFS," *Numerical Algorithms*, vol. 72, no. 1, pp. 107–130, 2016.

[35] R. A. Gingold and J. J. Monaghan, "Smoothed particle hydrodynamics: theory and application to non-spherical stars," *Monthly Notices of the Royal Astronomical Society*, vol. 181, no. 3, pp. 375–389, 1977.

[36] B. Nayroles, G. Touzot, and P. Villon, "Generalizing the finite element method: diffuse approximation and diffuse elements," *Computational Mechanics*, vol. 10, no. 5, pp. 307–318, 1992.

[37] W. Chen, "Meshfree boundary particle method applied to Helmholtz problems," *Engineering Analysis with Boundary Elements*, vol. 26, no. 7, pp. 577–581, 2002.

[38] C. Y. Ku, "On solving three-dimensional Laplacian problems in a multiply connected domain using the multiple scale Trefftz method," *Computer Modeling in Engineering and Sciences*, vol. 98, no. 5, pp. 509–541, 2014.

[39] C. Y. Ku, C. L. Kuo, C. M. Fan, C. S. Liu, and P. C. Guan, "Numerical solution of three-dimensional Laplacian problems using the multiple scale Trefftz method," *Engineering Analysis with Boundary Elements*, vol. 50, pp. 157–168, 2015.

[40] M. D. Tocci, C. T. Kelley, and C. T. Miller, "Accurate and economical solution of the pressure-head form of Richards' equation by the method of lines," *Advances in Water Resources*, vol. 20, no. 1, pp. 1–14, 1997.

[41] W. R. Gardner, "Some steady-state solutions of the unsaturated moisture flow equation with application to evaporation from a water table," *Soil Science*, vol. 85, no. 4, pp. 228–232, 1958.

[42] T. A. Ghezzehei, T. J. Kneafsey, and G. W. Su, "Correspondence of the Gardner and van Genuchten–Mualem relative permeability function parameters," *Water Resources Research*, vol. 43, no. 10, 2007.

[43] R. Srivastava and T. C. J. Yeh, "Analytical solutions for one-dimensional, transient infiltration toward the water table in homogeneous and layered soils," *Water Resources Research*, vol. 27, no. 5, pp. 753–762, 1991.

[44] G. Segol, *Classic Groundwater Simulations*, Prentice Hall, Englewood Cliffs, NJ, USA, 1994.

[45] F. T. Tracy, "Clean two- and three-dimensional analytical solutions of Richards' equation for testing numerical solvers," *Water Resources Research*, vol. 42, no. 8, 2006.

[46] Z. C. Li, M. G. Lee, J. Y. Chiang, and Y. P. Liu, "The Trefftz method using fundamental solutions for biharmonic equations," *Journal of Computational and Applied Mathematics*, vol. 235, no. 15, pp. 4350–4367, 2011.

[47] B. Movahedian, B. Boroomand, and S. Soghrati, "A Trefftz method in space and time using exponential basis functions: application to direct and inverse heat conduction problems," *Engineering Analysis with Boundary Elements*, vol. 37, no. 5, pp. 868–883, 2013.

[48] J. D. Logan, *Applied Mathematics*, John Wiley & Sons, Inc., Hoboken, NJ, USA, 1987.

[49] W. H. Green and G. A. Ampt, "Studies on soil physics I. The flow of air and water through soils," *The Journal of Agricultural Science*, vol. 4, pp. 1–24, 1911.

[50] R. H. Brooks and A. T. Corey, *Hydraulic Properties of Porous Media, Hydrol. Pap. 3*, Civ. Eng. Dep., Univ. of Colo., Boulder, Colo, 1964.

[51] N. Lu and W. J. Likos, *Unsaturated Soil Mechanics*, John Wiley and Sons, Inc., 2004.

[52] D. G. Fredlund and N. R. Morgenstern, "Stress state variables for unsaturated soils," *Journal of the Geotechnical Engineering Division*, vol. 103, pp. 447–466, 1977.

[53] S. K. Vanapalli, D. G. Fredlund, D. E. Pufahl, and A. W. Clifton, "Model for the prediction of shear strength with respect to soil suction," *Canadian Geotechnical Journal*, vol. 33, no. 3, pp. 379–392, 1996.

[54] B. D. Collins and D. Znidarcic, "Stability analyses of rainfall induced landslides," *Journal of Geotechnical and Geoenvironmental Engineering*, vol. 130, no. 4, pp. 362–372, 2004.

Research Article

Numerical Analysis of Damaged River Embankment during the 2011 Tohoku Earthquake Using a Multiphase-Coupled FEM Analysis Method

Li Chen and Sayuri Kimoto [ID]

Department of Civil and Earth Resources Engineering, Kyoto University, Kyoto 615-8540, Japan

Correspondence should be addressed to Sayuri Kimoto; kimoto.sayuri.6u@kyoto-u.ac.jp

According to the investigation and restoration report by the Ministry of Land, Infrastructure, Transport and Tourism (MLIT, 2011), 1195 river embankments were damaged in Tohoku region during the 2011 Tohoku earthquake. The failures of the river embankments were typically due to the soil liquefaction of embankment fill. In the present study, a severely damaged river embankment along Naruse River was simulated by using a three-phase coupled finite element program, namely, COMVI2D-DY, which is developed to analyze large deformation behavior of partially saturated soils. In addition, the reconsolidation process after the earthquake was simulated. To reproduce the reconsolidation behavior, a cyclic elastoplastic constitutive model based on nonlinear kinematical hardening rule was modified by considering stiffness recovery during reconsolidation. From the analysis results, it could be concluded that the numerical method is able to reproduce the key characteristics of the actual damaged pattern; the embankment is heavily damaged and deformed largely towards the land side, and the settlement at the top of the embankment is 2.5 m. In addition, realistic simulation results can be obtained from the reconsolidation analysis.

1. Introduction

A river embankment is a large-scale earth structure that mainly functions as a measure for flood prevention. Though the geological stratigraphy of the river embankment varies from location to location, a particular common feature is that the ground water table within the embankment is very shallow, hence keeping the earth embankment close to full saturation. Such feature will make the embankments susceptible to soil liquefaction, especially for those which are filled with granular soils.

In Japan, the seismic performance of the river embankment has been inspected in the last decades [1] since the significant subsidence of the Yodo River levee in Osaka was reported by the 1995 Kobe earthquake. The vulnerability of numerous river embankments, however, remains unknown until the occurrence of embankment failure due to soil liquefaction induced by large earthquakes. For instance, more than 2000 river embankments were damaged during the 2011 off-the-Pacific-Coast Tohoku earthquake. According to the investigation and restoration report by the Ministry of Land, Infrastructure, Transport and Tourism [2], 1195 river embankments were damaged in the Tohoku region with the total length of approximately 100,000 meters. Liquefaction of river embankments and the failure mechanism during the 2011 Tohoku earthquake were discussed and summarized by some researchers (e.g., [1, 3–5]). The failures of the river embankments were mainly due to the soil liquefaction of foundation soil or embankment fill. Figures 1 and 2 show heavily damaged embankments during the earthquake.

In order to prevent future losses, it is necessary to understand the failure mechanism of river embankments due to soil liquefaction. On the other hand, the restoration

FIGURE 1: Damaged river embankment in the Edano area of Abukuma River [2].

FIGURE 2: Damaged river embankment at Shimonakanome upper stream of Naruse River [2].

time for damaged river embankments is usually limited, as they are to be reinstated before the raining reason. It is hence common that the embankment was repaired without the knowledge of its stress status or hydraulic characteristics. This would result in potential risk of damage in the future. Hence, a reconsolidation mechanism after liquefaction is as important as a soil liquefaction mechanism for a river embankment.

Over the past few decades, multiphase coupled numerical analysis methods have been proposed for partially saturated soils (e.g., [6, 7]). Numerical simulations of embankment liquefaction have been conducted using various modelling methods in conjunction with a variety of constitutive models. Some (e.g., [8–10]) adopted infinitesimal strain theory to simulate seismic response of embankments. The infinitesimal strain theory is capable of capturing some important characteristics of soil liquefaction at the element level, such as the increase in pore water pressure and the loss of effective stress, but can hardly replicate the embankment deformation pattern, especially under the extreme ground motion. In addition, the behavior of partially saturated soil is not considered in most, and the embankment fill is generally treated as a dry material. To analyze the soil behavior within the embankment, however, the descriptions of partially saturated soil, such as the soil-water characteristics and the constitutive model for unsaturated soil, need to be introduced. Recently, Yoshikawa et al. [11] conducted a numerical analysis on the seismic behavior of an unsaturated embankment focusing on the effect of the groundwater level. There are, however, few numerical examples to reproduce the actual damage of river embankment.

In the present study, the dynamic behavior of a severely damaged river embankment along Naruse River during the 2011 Tohoku earthquake was simulated by using a three-phase coupled finite element program, namely, COMVI2D-DY [12, 13]. The program COMVI2D-DY was developed to analyze large deformation behavior of partially saturated soils under dynamic loading. The simulations are compared with the observed deformation pattern of the river embankment. Failure mechanisms due to liquefaction of embankment fill including but not limited to the pore water pressure distribution and the effective stress distribution can be clarified. In addition, reconsolidation analysis was carried out as a continuation of the dynamic one to understand the mechanical as well as the hydraulic characteristics of the damaged embankment before restoration. To reproduce the reconsolidation behavior, a cyclic elastoplastic constitutive model based on the nonlinear kinematical hardening rule [14] was modified by considering stiffness recovery during reconsolidation, and the behavior is discussed.

2. Governing Equations for Large Deformation Dynamic Analysis of Multiphase Geomaterials

A finite element program, namely, COMVI2D-DY [13], was developed to simulate large deformation of partially saturated soil under dynamic loading. The governing equations of dynamic analysis for multiphase geomaterials, that is, air-water-soil three-phase materials, are described within the framework of theory of porous media. In the theory, the governing equations are described for the multiphase mixture, that is, an immiscible mixture of solid and fluids [15]. The u-p formulation based on the updated Lagrangian method has been employed along with the Jaumann rate of Cauchy stress tensor for the weak form of the equilibrium equation.

An elastoplastic constitutive model [14, 16] is used to reproduce cyclic plastic behavior and liquefaction behavior, that is, the reduction of the mean effective stress of the saturated sandy soil. In the model, a nonassociativity parameter that controls the nonassociative behavior of sandy soils is incorporated. The formulation of the elastoplastic constitutive model is given in the following section. For the partially saturated sand, an extended elastoplastic model considering the effect of suction [17] is used, in which the so-called skeleton stress which provides a natural application of the two-phase mixture theory to the three-phase mixture (e.g., [18–21]) is the basic stress variable. In addition, the suction is included in the overconsolidation boundary surface and the yield surface to describe the bonding effect. An elastoviscoplastic constitutive model by Kimoto et al. [22] was used for clayey soils which can reproduce the dynamic behavior of clayey soils which exhibit plastic behavior as well as the rate-dependent behaviors. A van Genuchten-type model [23] is used as a soil-water characteristic curve.

The weak form of the continuity equation for water and gas, the conservation of momentum for the whole mixture is discretized in space by the finite element method. Assuming two-dimensional plane strain condition, an 8-node isoparametric element is used for the displacement, velocity, and acceleration of the solid skeleton, and a 4-node isoparametric element is used for pore water pressure and pore gas pressure. For the time discretization, Newmark's β method is adopted. The detailed descriptions for the dynamic finite element formulations are shown by Shahbodagh Khan [13]. Note that the pore-air pressure is assumed to be zero in the following simulations since the effect of air pressure was found to be negligible under drained conditions at the surface boundary.

3. Elastoplastic Constitutive Model

3.1. Formulation of the Model. Oka and Kimoto [14, 16] have developed a cyclic elastoplastic constitutive model based on the kinematical hardening theory by extending the previous model by Oka et al. [24]. In the new model, the yield function includes the changes in the stress ratio and the mean effective stress. A nonassociativity parameter that controls the nonassociative behavior of sandy soils, which is important for the simulation of unstable behavior such as liquefaction, is incorporated. In this section, the formulation of the model is briefly shown. The detailed explanations for the model are shown in Oka and Kimoto [14, 16].

The overconsolidation boundary which defines the boundary between the normally consolidated region and the overconsolidated region is given in

$$f_b = \overline{\eta}_\xi^* + M_m^* \ln\left(\frac{\sigma_m'}{\sigma_{mb}'}\right) = 0. \tag{1}$$

In this equation, $f_b \geq 0$ indicates a normally consolidated region, whereas $f_b < 0$ indicates an overconsolidated region. Relative stress ratio $\overline{\eta}_\xi^*$ is given in

$$\overline{\eta}_\xi^* = \left\{\left(\eta_{ij}^* - \xi_{ij}\right)\left(\eta_{ij}^* - \xi_{ij}\right)\right\}^{1/2}, \quad \eta_{ij}^* = \frac{s_{ij}}{\sigma_m'}, \tag{2}$$

where σ_m' is the mean effective stress and η_{ij}^* denotes the stress ratio tensor. The hardening parameter σ_{mb}' controls the size of the overconsolidation boundary surface. M_m^* is the value of the stress ratio at the transformation phase, at which point, the soil transforms from compression to dilation. The initial value of ξ_{ij} is equal to the stress ratio tensor after the end of consolidation, and ξ_{ij} follows and evolutional equation as

$$d\xi_{ij} = -C_d \xi_{ij} d\gamma^{p*}, \quad \gamma^{p*} = \int d\gamma^{p*} = \int \left(de_{ij}^P de_{ij}^P\right)^{1/2}, \tag{3}$$

where γ^{p*} is the accumulated plastic shear strain from the initial state, de_{ij}^P is the plastic deviatoric strain increment, and C_d is a material constant which controls the disappearance of anisotropy.
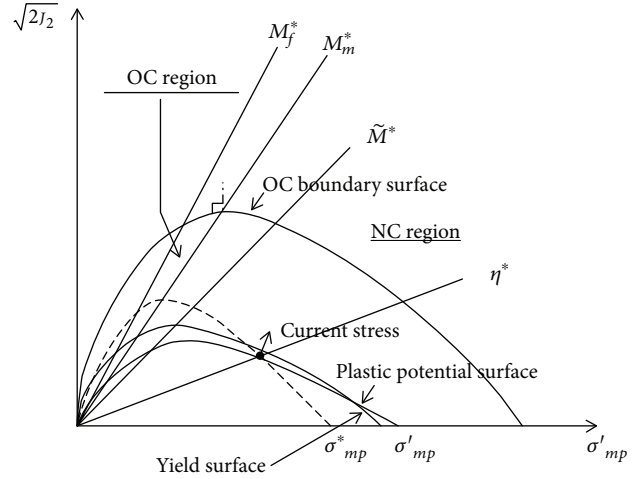

Figure 3: Overconsolidation boundary surface, yield function, and plastic potential function for an isotropically consolidated state.
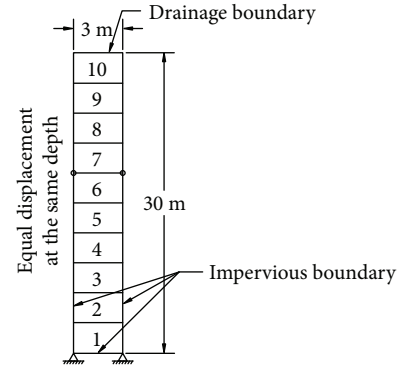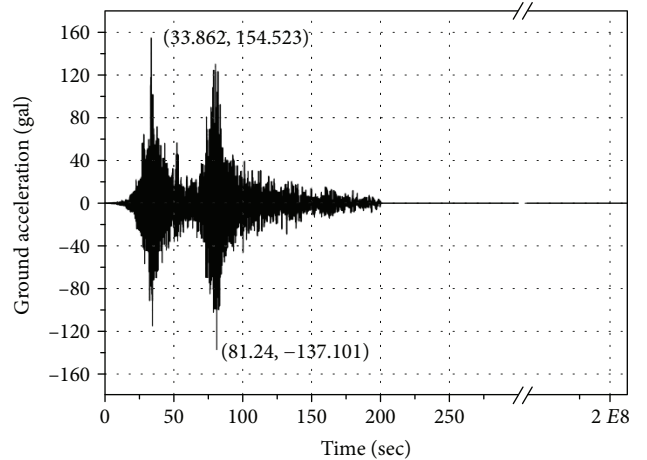

Figure 4: 1-D model for parametric study.

— MYGH06 at −80 m Tajiri station (NIED, 2011)

Figure 5: Ground acceleration input [25].

The static yield surface is given by a function of the nonlinear kinematic hardening rule of the stress ratio, mean effective stress, and plastic volumetric strain, in

$$f_y = \overline{\eta}_\chi^* + C_{ns}\tilde{M}^* \left(\ln \frac{\sigma'_{mk}}{\sigma'_{ma}} + \left| \ln \frac{\sigma'_m}{\sigma'_{mk}} - y_m^* \right| \right) = 0, \tag{4}$$

$$\overline{\eta}_\chi^* = \left\{ \left(\eta_{ij}^* - \chi_{ij}^* \right) \left(\eta_{ij}^* - \chi_{ij}^* \right) \right\}^{1/2},$$

where σ'_{mk} is in the unit of stress which is kilopascal (kPa). y_m^* is the kinematic hardening parameter that associates with the change of plastic volumetric strain. Parameter C_{ns} is the non-associativity material parameter which is ranging from zero to one; $C_{ns} = 1.0$ for associated flow rule and $C_{ns} < 1.0$ for nonassociated flow rule. It should be noted that $C_{ns} = 1.0$ is assumed before the stress ratio reaches the phase transformation line and during consolidation after liquefaction. χ_{ij}^* is the back stress parameters with the same dimension as the stress ratio η_{ij}^*. The nonlinear hardening rule, as an evolutional equation of χ_{ij}^*, is given by

$$d\chi_{ij}^* = B^* \left(A^* de_{ij}^P - \chi_{ij}^* d\gamma^{P*} \right), \tag{5}$$

where A^* and B^* are material parameters related to the stress ratio at failure, M_f^*, and the nondimensional initial plastic shear modulus, G^P, as follows:

$$A^* = M_f^*,$$
$$B^* = \frac{G^P}{M_f^*}. \tag{6}$$

In addition, B^* follows an equation as

$$B^* = (B_{max}^* - B_1^*) \exp\left(-C_f d\gamma^{P*} \right), \tag{7}$$

where B_1^* is the lower boundary of B^*. Parameter C_f controls the rate of hardening, and B_{max}^* is the maximum value of B^*, which is expressed in

$$B_{max}^* = \begin{cases} B_0^* & \text{before reaching phase transformation,} \\ 1 + \dfrac{B_0^*}{\gamma_{ap}^{p*}/\gamma_r^{p*}} & \text{after reaching phase transformation,} \end{cases} \tag{8}$$

where B_0^* is a hardening parameter before the stress ratio reaches the phase transformation stress ratio M_m^*, γ_r^{p*} is the reference plastic strain, and γ_{ap}^{p*} is accumulative plastic shear strain after phase transformation. Note that the material parameter C_f is set to zero in this research.

The kinematical hardening associated with the change in the mean effective stress is given by

$$y_m^* = y_{m1}^* + y_{m2}^*,$$
$$dy_{m1}^* = B_2^* (A_2^* d\varepsilon_v^p - y_{m1}^* |d\varepsilon_v^p|), \tag{9}$$
$$dy_{m2}^* = B_3^* d\varepsilon_v^p,$$

where A_2^*, B_2^*, and B_3^* are material constants and $d\varepsilon_v^p$ is the volumetric plastic increment.

The plastic potential function is given by

$$g = \overline{\eta}_\chi^* + \tilde{M}^* \left(\ln \frac{\sigma'_{mk}}{\sigma'_{mp}} + \left| \ln \frac{\sigma'_m}{\sigma'_{mk}} - y_m^* \right| \right) = 0, \tag{10}$$

where σ'_{mp} is a constant and $\tilde{M}^*$ is the dilatancy parameter whose definition is distinguished between the normally consolidated region and the overconsolidated region, as given in

$$\tilde{M}^* = \begin{cases} M_m^*, & f_b \geq 0 \text{(normally consolidated region and after stress ratio reached } M_m^*), \\ \left(\dfrac{\sigma_m^*}{\sigma'_{mb}} \right)^{n_2} M_m^*, & f_b < 0 \text{(overconsolidated region),} \end{cases} \tag{11}$$

where n_2 is a material parameter and σ_m^* is the mean effective stress at the intersection between the surface which passed through the current stress and has the same shape as f_b, and the anisotropic stress axis. The overconsolidated boundary surface, yield function, and plastic potential function for an isotropic overconsolidated state are illustrated in Figure 3.

Oka and Kimoto [14] used Equation (12) to account for the stress and strain dependency of the elastic shear modulus:

$$G^E = \frac{G_0^E}{1 + \alpha_e \left(\gamma_{ap}^{P*}/\gamma_r^{E*} \right)^{r_{e1}}} \left(\frac{\sigma'_m}{\sigma'_{m0}} \right)^{r_{e2}}, \tag{12}$$

where α_e, r_{e1}, and r_{e2} are material parameters and G_0^E the initial elastic shear modulus. γ_{ap}^{P*} denotes the accumulative plastic deviatoric strain after the stress ratio reaches the phase transformation M_m^*, and γ_r^{E*} is the reference strain which can be obtained by fitting to liquefaction resistance curve.

3.2. Parametric Study on C_{ns}.

The effect of nonassociativity parameter C_{ns} in the cyclic elastoplastic model under undrained simple shear conditions was presented in Oka and Kimoto [16] by simulating the behavior of loose Toyoura silica sand. They showed that the parameter C_{ns} controls the minimum mean effective stress during cyclic loading, namely, the minimum mean effective stress is smaller for the case with smaller C_{ns}. In this section, a parametric study is performed by using COMVI2D-DY with a 1-D horizontally layered model to demonstrate the effect of C_{ns} on the dynamic behavior and the reconsolidation behavior. The 1-

TABLE 1: Material parameters of Naruse sand.

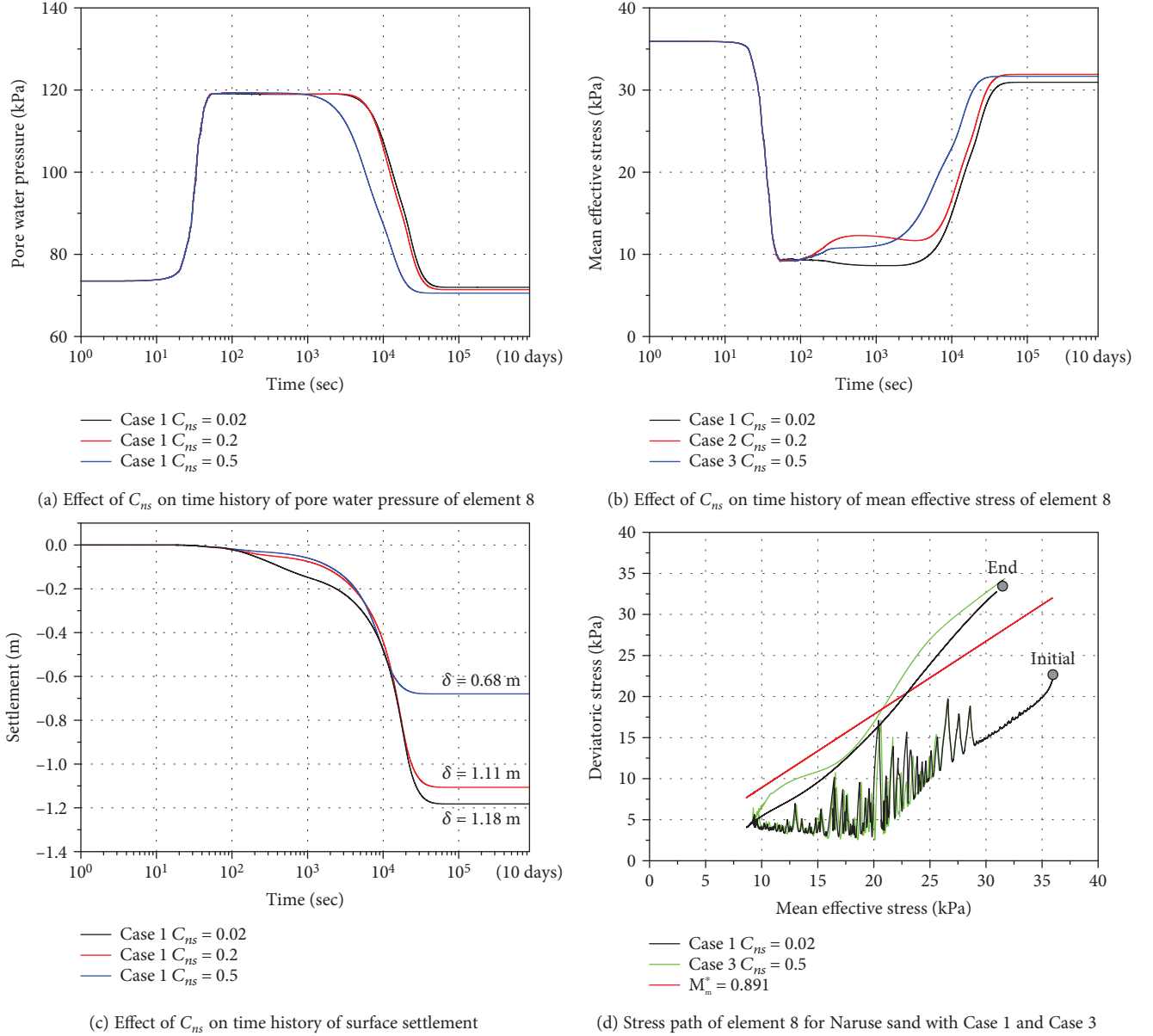| Soil parameters		Elastoplastic model [24]	Extended elastoplastic model
Initial void ratio	e_0	1.159	1.159
Density	ρ	1.73	1.73
Compression index	λ	0.0500	0.0500
Swelling index	κ	0.0057	0.0057
Normalized initial elastic shear modulus	$\dfrac{G_0}{\sigma'_{m0}}$	340	340
Water permeability (m/s)	k_{ws}	1.13×10^{-4}	1.13×10^{-4}
Quasi-overconsolidation ratio	OCR*	1.2	1.2
Stress ratio at phase transformation	M_m^*	0.891	0.891
Stress ratio at failure	M_f^*	1.229	1.229
Hardening parameter	B_0^*	5000	5000
Hardening parameter	B_1^*	100	100
Hardening parameter	C_f	0	0
Dilatancy coefficient	D_0^*	1.0	1.0
Dilatancy coefficient	n	6.0	6.0
Reference value of plastic strain	γ_r^{p*}	0.001	0.001
Reference value of elastic strain	γ_r^{E*}	0.003	0.003
Hardening parameter	A_2^*	—	0.0
Hardening parameter	B_2^*	—	0.0
Hardening parameter	B_3^*	—	40.47
Elastic shear modulus parameter	r_{e2}	—	1.0
Elastic shear modulus parameter	α_e	—	1.0
Elastic shear modulus parameter	r_{e1}	—	1.0
Anisotropy disappearance parameter	C_d	2000.0	2000.0
Nonassociativity flow rule	C_{ns}	—	Parametric study
Stiffness recovery rate	C_{cf}	—	2000*

*This parameter is not used in the parametric study.

D model consists of 10 elements with a total height of 30 m and a width of 3 m as shown in Figure 4. The bottom boundary of the model is perfectly fixed, and the equal nodal displacements on both sides are assumed at the same depth. A pervious boundary with a zero static pore water pressure is set at the top of the model while an impervious boundary is set for the other boundaries. The ground motion of the 2011 Tohoku earthquake recorded at a depth of 80 m at the Tajiri earthquake observation station in Miyagi Prefecture [25] is used. The acceleration profile is shown in Figure 5. The dynamic loading lapses after 200 seconds; the modelled soil column is then allowed to consolidate for 10 days. Material parameters used in this parametric are shown in Table 1 in the right column, which is determined for Naruse River sand in Miyagi Prefecture.

The effect of nonassociativity parameter C_{ns} is revealed by comparing analysis Case 1: $C_{ns} = 0.02$, Case 2: $C_{ns} = 0.2$, and Case 3: $C_{ns} = 0.5$. Figures 6(a) and 6(b) show the time history of the pore water pressure and the mean effective stress of element 8. It can be observed that C_{ns} has almost no effect on the excess pore water pressure generation during dynamic loading. However, a higher value of C_{ns} leads to faster dissipation of the excess pore water pressure during reconsolidation, as well as a faster recovery of the mean effective stress. The final surface settlements of case 1, case 2, and case 3 are 0.68 m, 1.11 m, and 1.18 m, respectively, as shown in Figure 6(c). It appears that the value of C_{ns} has significant influence on consolidation settlement. It is worth noting that associate flow rule ($C_{ns} = 1.0$) is assumed during consolidation analysis for all the three cases. Therefore, the difference in consolidation settlement between each case is due to the combination effect of the C_{ns} value and accumulative plastic strain during dynamic analysis.

Moreover, C_{ns} controls the reduction of mean effective stress when soil liquefies, together with the nonlinear kinematic hardening parameter y_m^*. Therefore, the minimum mean effective stress is larger in Case 3 than in Case 1 as shown in Figure 6(d). This tendency agrees with the results shown in Oka and Kimoto [16]. Besides, the response of stress due to ground acceleration is slightly smaller for larger

(a) Effect of C_{ns} on time history of pore water pressure of element 8

(b) Effect of C_{ns} on time history of mean effective stress of element 8

(c) Effect of C_{ns} on time history of surface settlement

(d) Stress path of element 8 for Naruse sand with Case 1 and Case 3

FIGURE 6: Parametric study on C_{ns}.

C_{ns}. Such a mechanism is important for not only the realistic soil behavior simulation but also the stability of numerical calculation. Furthermore, larger increase in stress ratio in Case 3 is found during consolidation than that in Case 1. This is due to the higher stiffness of soil in Case 3 which would result in a higher response stress.

From the parametric study, it was found that the parameter C_{ns} has a significant influence on consolidation settlement, that is, a larger value of C_{ns} gives smaller settlement for this set of parameters. It should be noted, however, that the model with strong nonassociativity with a small value of C_{ns} has a potential for simulating liquefaction while the model with the associated flow rule does not as mentioned in Oka and Kimoto [16]. In other words, a large value of C_{ns} may not be appropriate to simulate liquefaction behavior.

3.3. Modification of the Model considering Stiffness Recovery.
In the elastoplastic constitutive model shown in the previous section, the reduction of the elastic stiffness G^E and the plastic stiffness B^* with increasing deviatoric strain was given in (8) and (12). In the following, the elastic and plastic stiffness recovery during reconsolidation is introduced in the model.
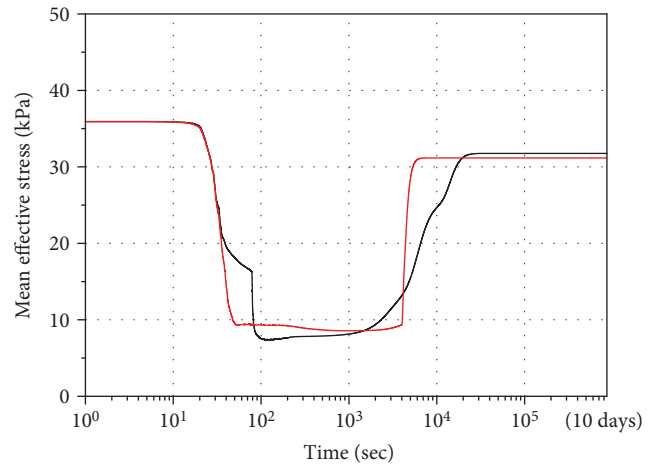
The elastic shear modulus is extended to incorporate the hardening effect of volumetric strain compression during reconsolidation in the form of

$$G^E = \frac{G_0^E}{1 + \alpha_e \left(\gamma_{ap}^{P*} / \gamma_r^{E*} \right)^{r_{e1}}} \left(\frac{\sigma_m'}{\sigma_{m0}'} \right)^{r_{e2}} + G_f^E - G_f^E \exp \left(-C_{cf} \Delta \varepsilon_v \right), \tag{13}$$
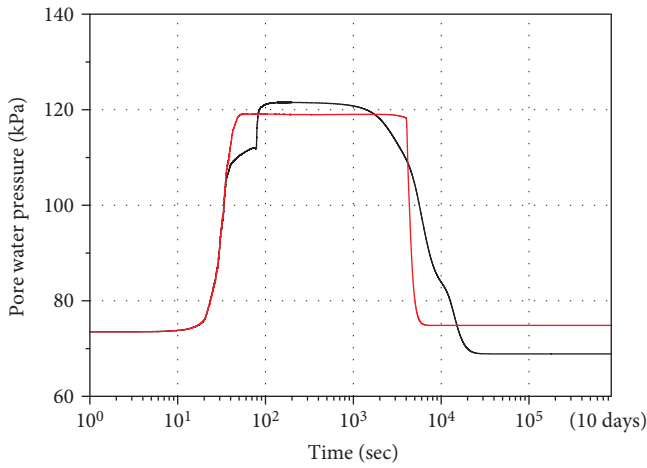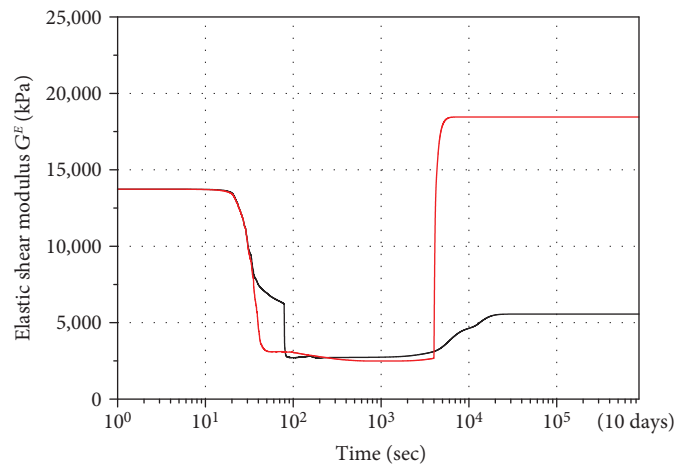
(a) Comparison of time history of pore water pressure

(b) Comparison of time history of mean effective stress

(c) Comparison of time history of elastic shear modulus G^E
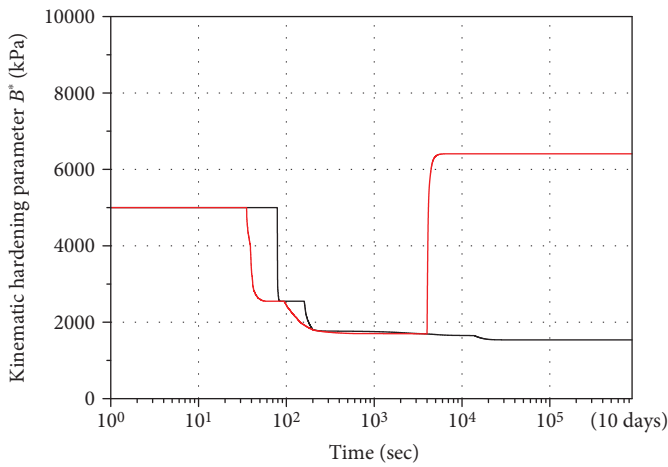
(d) Comparison of time history of kinematic hardening parameter B^*
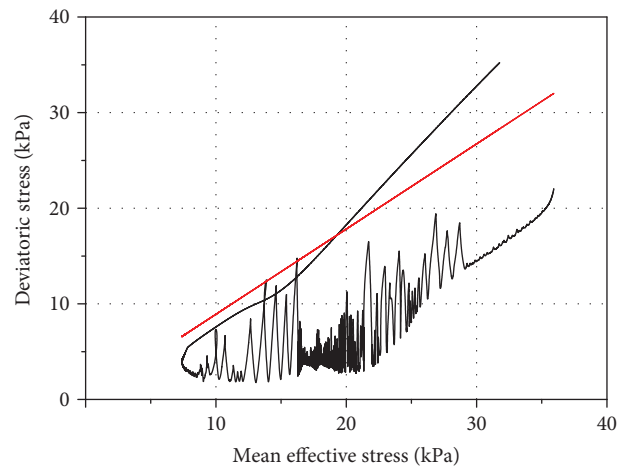
(e) Stress path of element 8 for cyclic elastoplastic model

FIGURE 7: Continued.
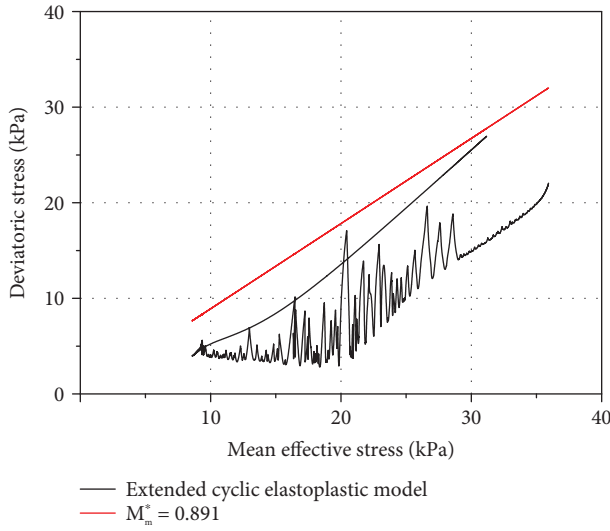
(f) Stress path of element 8 for extended cyclic elastoplastic model
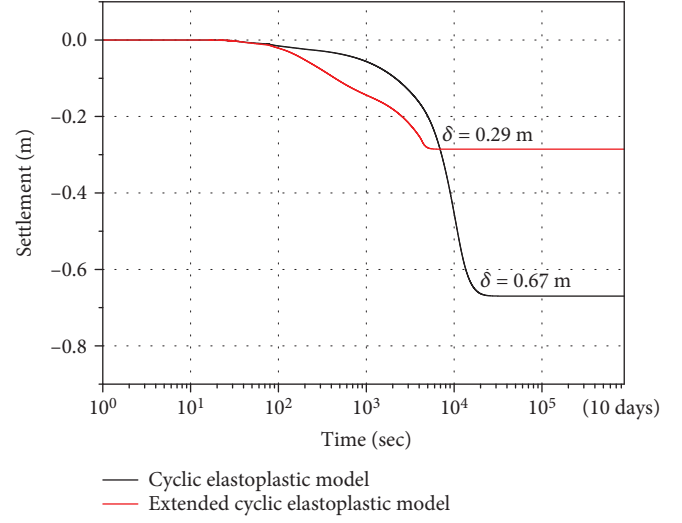
(g) Comparison of time history of settlement

FIGURE 7: Comparison between the original elastoplastic model and the modified elastoplastic model.
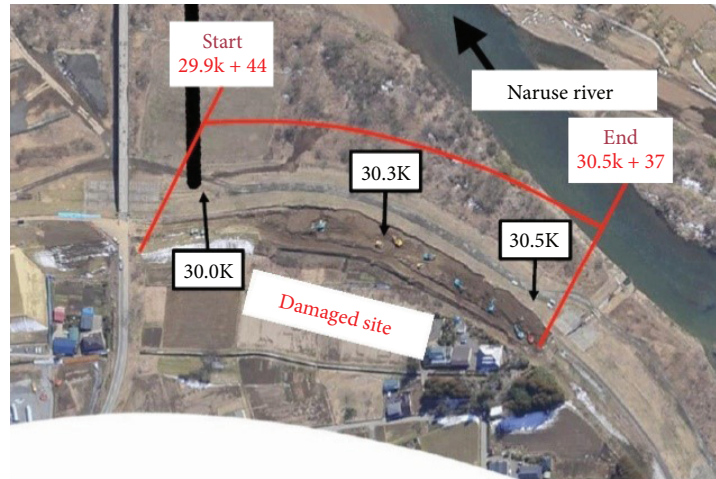

FIGURE 8: Location of the damaged site along the Naruse River [2].

in which G_f^E is a material parameter that represents the value of final elastic shear modulus at the end of consolidation and C_{cf} is a material parameter to control the recovery rate of elastic shear modulus during consolidation. The accumulative volumetric compression after dynamic loading, namely, during reconsolidation, is denoted by $\Delta\varepsilon_v$. Equation (13) separates the hardening component attained from volumetric compression, that is, consolidation, from that attained during dynamic shearing. In addition, it is assumed that G^E is not affected by the change of plastic deviatoric strain during consolidation. In other words, γ_{ap}^{P*} is constant.

Similar to the elastic shear modulus, the hardening term is considered in the plastic shear modulus B^* during consolidation which is associated with the volumetric compression:

$$B^* = 1 + \frac{B_0^*}{\gamma_{ap}^{P*}/\gamma_r^{P*}} + B_f^* - B_f^* \exp\left(-C_{cf}\Delta\varepsilon_v\right), \quad (14)$$

FIGURE 9: Sand boiling in the embankment crack [27].

where B_f^* is the material parameter and equals the value of recovery at the end of consolidation. Ye et al. [26] experimentally investigated the stiffness recovery of liquefied sandy
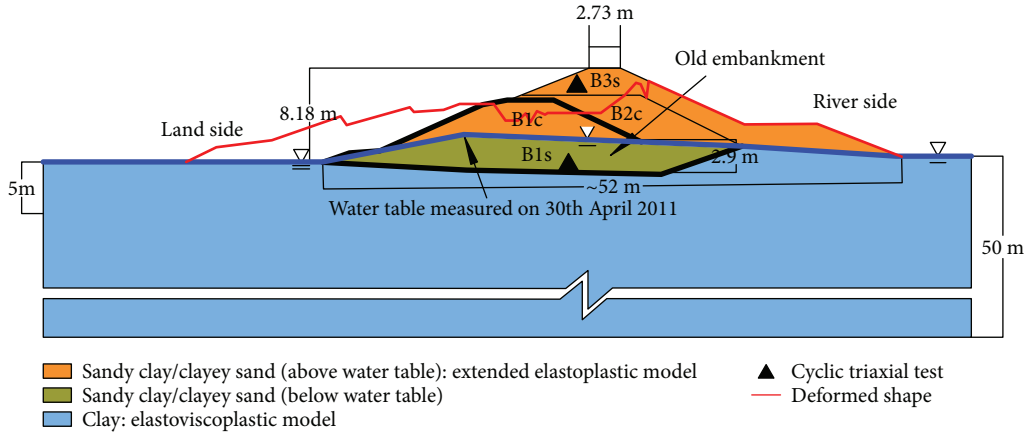
FIGURE 10: Cross section of river embankment at Shimonakanome upper stream of Naruse River (30.3 km).
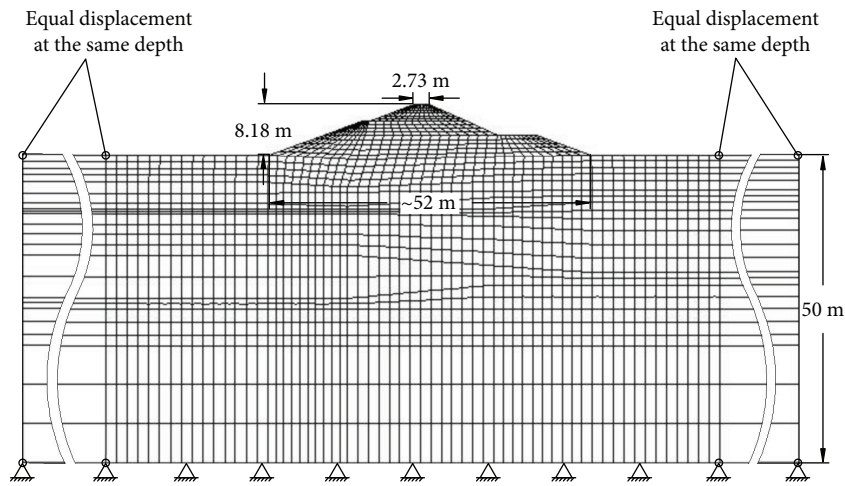
FIGURE 11: Finite element mesh and boundary conditions.
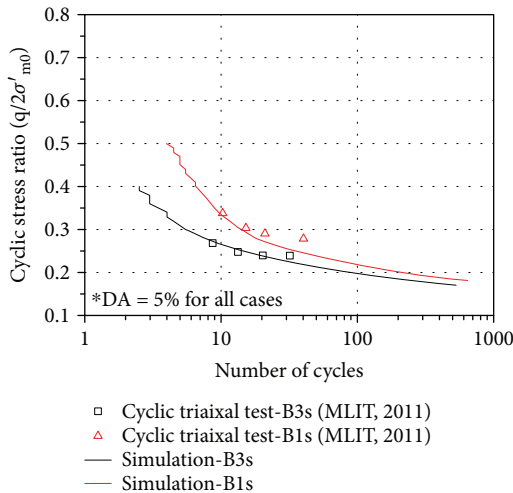
FIGURE 12: Liquefaction resistance curve for embankment fill.
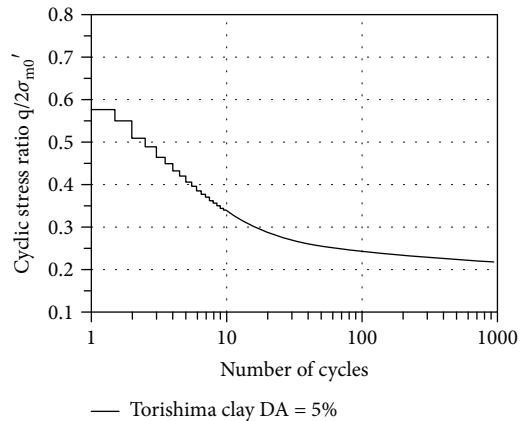
FIGURE 13: Liquefaction resistance curve for Torishima clay.

ground and showed that the stiffness after earthquake motion was the same or larger than that before the earthquake. In the present study, $G_f^E = G_0^E$ and $B_f^* = B_0^*$ are assumed.

A comparison between the original elastoplastic model [24] in which the yield function is given by the stress ratio, and the extended elastoplastic model with stiffness recovery will be presented in the following. The exercise is mainly to demonstrate the stiffness recovery ability of the modified model with modifications in the current research. The same

TABLE 2: Soil parameters for damaged river embankment.

Soil parameters		B1s/B1c	B3s/B2c	Foundation
Initial void ratio	e_0	1.159	1.100	1.456
Density	ρ	1.73	1.74	1.66
Compression index	λ	0.0500	0.0500	0.5930
Swelling index	κ	0.0057	0.0057	0.027
Normalized initial elastic shear modulus	$\dfrac{G_0}{\sigma'_{m0}}$	340	1020	255
Water permeability (m/s)	k_{ws}	1.11×10^{-6}	2.66×10^{-7}	8.10×10^{-9}
Quasi-overconsolidation ratio	OCR*	1.2	1.2	1.0
Stress ratio at phase transformation	M_m^*	0.891	0.891	0.891
Stress ratio at failure	M_f^*	1.229	1.229	0.891
Hardening parameter	B_0^*	5000	2000	100
Hardening parameter	B_1^*	100	100	40
Hardening parameter	C_f	0	0	10
Dilatancy coefficient	D_0^*	1.0	1.0	—
Dilatancy coefficient	n	6.0	6.0	—
Reference value of plastic strain	γ_r^{p*}	0.001	0.001	—
Reference value of elastic strain	γ_r^{E*}	0.003	0.003	—
Viscoplastic parameter	m'	—	—	24.68
Viscoplastic parameter (1/s)	C_1			1.00×10^{-6}
Viscoplastic parameter (1/s)	C_2			3.83×10^{-7}
Hardening parameter	A_2^*	0.0	0.0	5.9
Hardening parameter	B_2^*	0.0	0.0	1.8
Hardening parameter	B_3^*	50.11	41.6	—
Elastic shear modulus parameter	r_{e2}	1.0	1.0	—
Elastic shear modulus parameter	α_e	1.0	1.0	—
Elastic shear modulus parameter	r_{e1}	1.0	1.0	—
Anisotropy disappearance parameter	C_d	2000	2000	—
Nonassociativity flow rule	C_{ns}	0.02	0.02	—
Stiffness recovery rate*	C_{cf}	2000	2000	—

*This parameter is not used in dynamic analysis.

model configuration, drainage conditions, boundary conditions, and loading conditions as those used in the previous section are adopted. Material parameters are shown in Table 1. $C_{ns} = 0.02$ is chosen for the case of strong nonassociativity, similar to the cyclic elastoplastic model. The hardening parameter B_3^* is set to be $(1 + e_0)/(\lambda - \kappa) = 40.47$. It was widely understood that liquefied soil would experience a low-rigidity period before the stiffness recovery. Therefore, the onset of consolidation in the case of using the extended model is set to be 4000 seconds, which correspond to the time lapse before the excess pore water pressure starts to dissipate in the case of the original model.

Simulation results are shown in Figures 7(a)–7(g) for element 8. It is observed that the cyclic elastoplastic model [24] experienced higher excess pore water pressure during dynamic loading than the extended model. This is mainly due to the combination effect of C_{ns} and the kinematic hardening term. Figure 7(b) shows the comparison of the mean effective stress of element 8, in which the elastoplastic model experienced lower mean effective stress. The effect of volumetric compression hardening on stiffness recovery is depicted in Figures 7(c) and 7(d). Figure 7(c) shows the recovery of elastic shear modulus, whereas the recovery of the kinematic hardening parameter B^*, which is related to soil plastic stiffness, is shown in Figure 7(d). The stiffness recovers effectively and ends with a higher final stiffness than the initial one. Note that the amount of stiffness recovery at the end of consolidation is an input parameter and should be determined from experimental data. However, due to the lack of information, they are assumed to be equal to the initial stiffness value. Figures 7(e) and 7(f) show the effective stress path of element 8 for the original elastoplastic model

TABLE 3: Soil-water characteristic curve and hydraulic parameters.

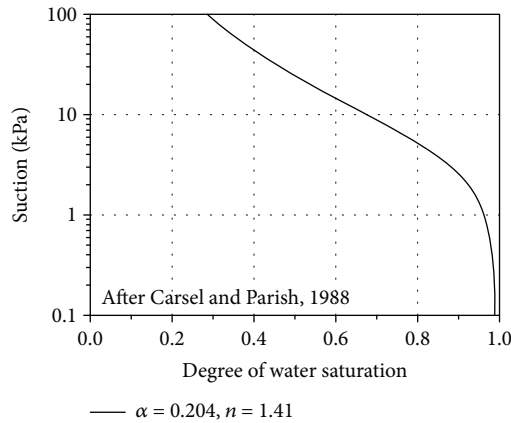| Water characteristic parameters		Embankment fill
van Genuchten parameter (1/kPa)	α	0.275
van Genuchten parameter	n'	1.23
Minimum saturation	$S_{\min}$	0.00
Maximum saturation	$S_{\max}$	0.99
Water permeability shape parameter	a	3
Gas permeability shape parameter	b	1
Suction parameter	S_I	0.2
Suction parameter	S_d	0.1
Suction parameter	S_{IB}	0.2
Suction parameter	S_{db}	0.1

FIGURE 14: Soil-water characteristic curve used for Naruse soil.

and extended elastoplastic model, respectively. The minimum mean effective stress is smaller in the original model. Significant distinction is observed in Figure 7(g)—the total settlement of the case with the elastoplastic model is 0.67 m whereas that of the case with the extended model is 0.29 m. This is due to the effect of kinematic hardening and stiffness during consolidation. Such a result is reasonable because it is not realistic for sandy soil to have much larger settlement due to consolidation than during liquefaction.

4. Numerical Analysis of River Embankment during Earthquake and Reconsolidation

4.1. Model Description. The target river embankment is located at Shimonakanome upper stream of Naruse River, 30.3 km from the river mouth. The location of the embankment is shown in Figure 8. This embankment was found heavily damaged after the 2011 Tohoku earthquake. According to the investigation report [27], boiling sand was observed in the longitudinal cracks as shown in Figure 9. In addition, the presence of ground water in the embankment was confirmed. Therefore, it was concluded by MLIT [2] that
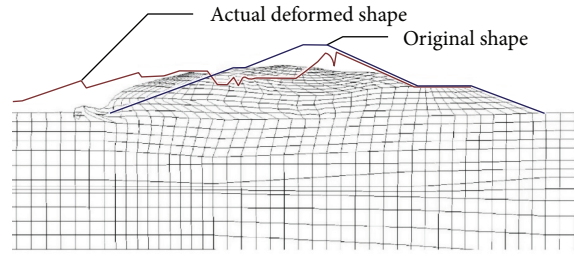

FIGURE 15: Comparison between deformed mesh, original embankment shape, and actual deformed shape.
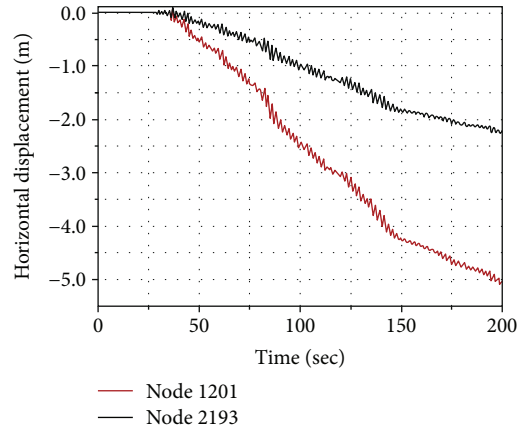
FIGURE 16: Time history of horizontal displacement for node 1201 and node 2193.
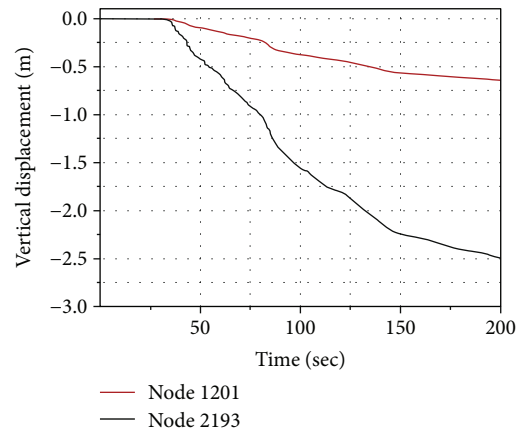
FIGURE 17: Time history of vertical displacement for node 1201 and node 2193.

the failure of river embankment is caused by liquefaction of the embankment fill.

A cross section of the river embankment including its geometry, geological stratigraphy, and the location of the water table is shown in Figure 10. The liquefied soil is identified as clayey sand (B1s) with a maximum thickness of 2.9 m. According to the geological map of Naruse River, this river embankment was a natural levee [28] which was indicated as "old embankment" in Figure 10. The old embankment was formed by sandy soil (B1c and B1s) and then enlarged twice using sand and clay material. The location

FIGURE 18: Location of focused nodes and elements.

FIGURE 19: Time history of response horizontal acceleration for node 1201.
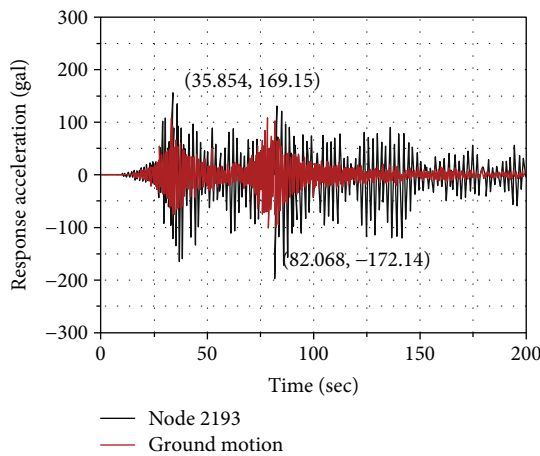
FIGURE 20: Time history of response horizontal acceleration for node 2193.

FIGURE 21: Time history of pore water pressure for element 681 and element 865 during dynamic analysis.
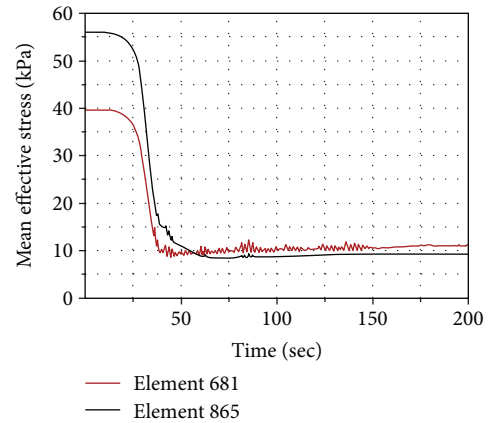
FIGURE 22: Time history of mean effective stress for element 681 and element 865 during dynamic analysis.

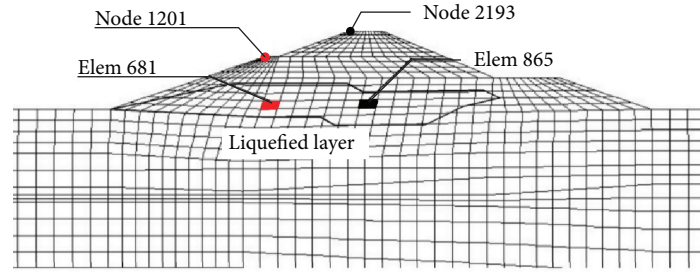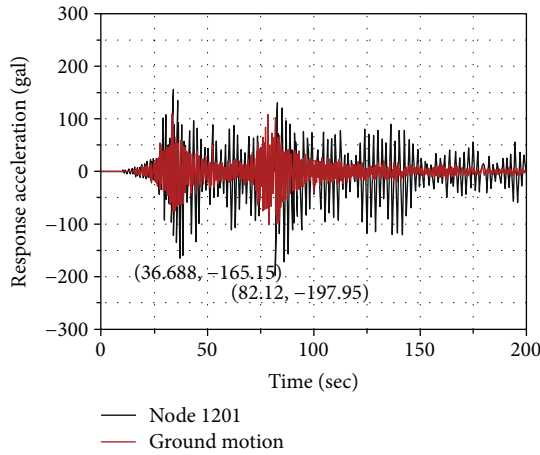of ground water table is indicated by the blue line, which was measured on site one month after the earthquake. The deformation shape is illustrated in Figure 10 as well. It could be observed that large sliding occurred towards the land side, after liquefaction.

Geometry of the finite element model, the mesh, and the boundary conditions are depicted in Figure 11. The numerical simulation was conducted under 2-D plane strain condition. A full-scale model was considered with an engineering datum of 50 m below ground level. To reduce the side boundary effects, semi-infinite elements with equidisplacement conditions were used on the left and right ends, each being 100 m long. Drainage boundary is set at ground level where the initial pore water pressure is zero. A no-water-flow boundary is prescribed along the surface of the embankment to avoid unrealistic water inflow due to suction. Regarding the mesh size in the vertical direction, it is generally determined to be 1/5 of the minimum wavelength in dynamic FEM analysis. For example, when the shear wave velocity is 100 m/s and the target maximum frequency is 10 Hz,

(a) Initial

(b) 60 s

(c) 100 s

(d) 200 s

−19.1	8.7	36.5	64.4	92.2	120.0

FIGURE 23: Distribution of pore water pressure (unit: kPa).

(a) Initial

(b) 60 s

(c) 100 s

(d) 200 s

1.9	17.5	33.1	48.7	64.4	80.0

FIGURE 24: Distribution of mean effective stress (unit: kPa).

the minimum wavelength is 10 m; thus, the required mesh size is 2 m. In the present analysis, the vertical mesh size of the embankment is determined to be around 0.5 m considering the change of the shear wave velocity and the frequency after liquefaction.

Ground acceleration of the Tohoku earthquake recorded at a depth of 80 m at Tajiri station in Miyagi Prefecture shown in Figure 5 was used during dynamic analysis, which is the same as that was used in the 1-D dynamic-reconsolidation analysis. The rigid base is used so that the bottom boundary of the model is fixed. The Tajiri earthquake motion observation station is located approximately 8.7 km away from the river embankment at Shimonakanome upper stream of Naruse River.
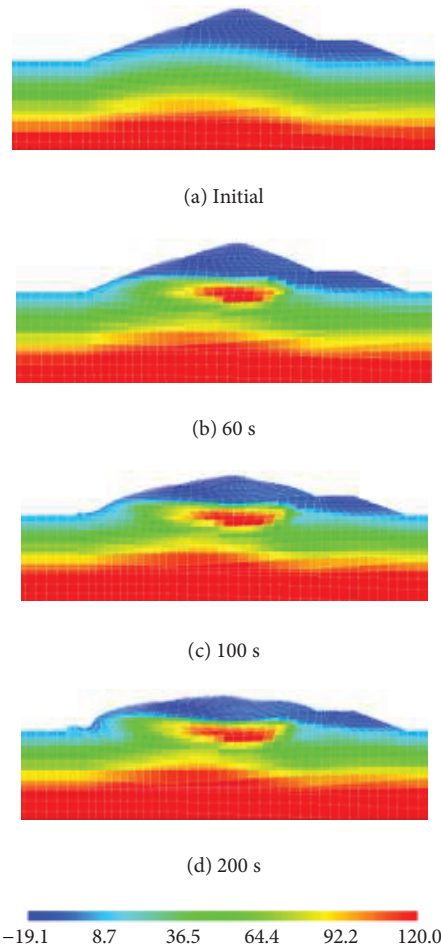
4.2. Material Parameters. In this analysis, sandy soil is modeled by the extended elastoplastic model whereas the elastoviscoplastic model is used for clayey soil. Soil physical tests were carried out and presented in the investigation report of the damaged river embankment in the Tohoku region [2]. It was found that fine content of the embankment fill is generally close to 50%; hence, the extended elastoplastic model is adopted for all the embankment fills for the sake of numerical simplicity. For the partially saturated region above the water table, namely, the B1c, B2c, and B3s

layers, an extended elastoplastic model considering the effect of suction is used, in which the skeleton stress is the basic stress variable and the suction is included in the overconsolidation boundary surface and the yield surface to describe the bonding effect. The embankment is situated on a thick layer of soft clay, which is simulated by the elastoviscoplastic model. Note that the foundation soil is assumed to be homogenous in this analysis.

The cyclic behavior of soil can be represented by a liquefaction resistance curve. Two cyclic triaxial tests were conducted for this river embankment [25]. Location of the soil samples are shown in Figure 10. Due to inadequate experimental results, cyclic behavior of soil B2c and B1c is considered as the same as that of B3s and B1s. Soil test simulation was carried out, and the material parameters are determined to reproduce the results from cyclic triaxial test. The cyclic triaxial test for B3s and B1s and their numerical behavior under cyclic load are plotted in Figure 12. Since the cyclic triaxial test was not carried out for the clayey foundation, material parameters for Torishima clay [13] are adopted since it is a soft alluvium deposit as well. The liquefaction resistance curve of Torishima clay is shown in Figure 13. Material parameters are shown in Table 2, and the suction parameters for the partially saturated region are shown in Table 3.

In COMVI2D-DY, the degree of water saturation depends on the soil-water characteristic curve (SWCC), adopting van Genuchten's [23] model. In Carsel and Parrish

(a) Initial

(b) 60 s

(c) 100 s

(d) 200 s

0.00   0.18   0.36   0.54   0.72   0.90

FIGURE 25: Distribution of skeleton stress decreasing ratio (ESDR).

(a) Initial
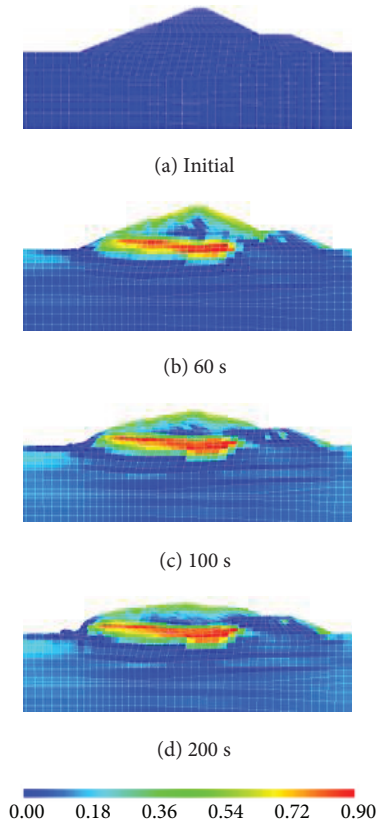
(b) 60 s

(c) 100 s

(d) 200 s

0.00   0.45   0.90   1.35   1.79   2.24

FIGURE 26: Distribution of accumulative deviatoric plastic strain (GAMP).

[29], typical values of SWCC parameters, α and n', in van Genuchten's model were proposed according to soil descriptions and their permeability. In this simulation, α and n', for silt loam, were chosen by considering the soil type and average permeability of the embankment fill. Hydraulic properties and material parameters for the effect of suction for unsaturated soil are listed in Table 3. Since the water table is located above the foundation soil, it is not necessary to consider the soil-water characteristic for soft clay. The SWCC used in the dynamic analysis is shown in Figure 14. The initial degree of saturation above the water table is assumed to be 0.6, which corresponds to an initial suction of 14.5 kPa.

In this analysis, an initial stiffness-dependent type of Rayleigh damping is adopted with an attenuation constant of 0.01. Time is discretized by Newmark's β method where β and γ are 0.3025 and 0.6, respectively. The time increment for the dynamic analysis was set to be 0.002 second.

Before conducting the dynamic analysis, the initial effective stress was generated by a static finite element analysis with an elastoperfect plastic model of which the failure surface follows the Drucker-Prager model.

4.3. Dynamic Behavior. The comparison between the original shape of the river embankment, its observed deformed shape after the earthquake, and the deformed mesh from the dynamic analysis at the end of ground acceleration, 200 sec, is shown in Figure 15. It could be observed that the embankment is heavily damaged at the end of ground shaking. The key characteristics of the damaged pattern can be reproduced by dynamic analysis. First, the embankment deformed largely towards the land side. Second, part of the embankment on the river side remains undamaged. It appears that the actual deformation on the land side is much larger than that from the simulation. This large lateral spreading of the river embankment is not only due to the collapse of earth structure but also due to the sliding of soil. Such phenomenon is difficult to simulate by finite element analysis since this would involve disconnection between elements or soil particles. In addition, the amount of the simulated deformed soil cannot be compared to that which was observed on-site, since the ground acceleration used in this analysis is not at the exact location of the river embankment.

Time history of the horizontal and the vertical displacements at node 1201 and node 2193 is shown in Figures 16 and 17, respectively. The locations of node 1201 and node 2193 are depicted in Figure 18. It could be observed that the maximum lateral movements towards the land side and settlement at the top of the embankment are 5.02 m and 2.50 m, respectively. The simulated settlement at the top of the embankment is close to the observed settlement after the earthquake which is approximately 3 m. However, a lateral displacement of 12 m was observed on site which is much larger than the simulated one. This result agrees with the previous conclusion that the sliding of earth is difficult to simulate by finite element method. In addition, it can be seen that

(a) Initial

(b) 60 s

(c) 100 s

(d) 200 s

0.00   3.82   7.64   11.47   15.29   19.11
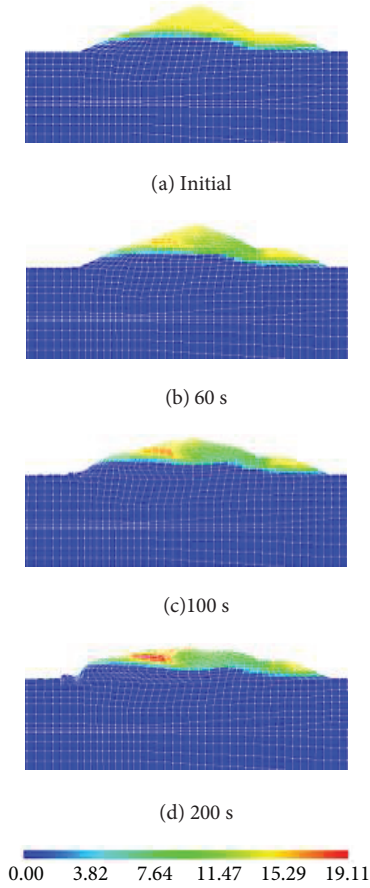
FIGURE 27: Distribution of suction (unit: kPa).

(a) Initial

(b) 60 s

(c) 100 s
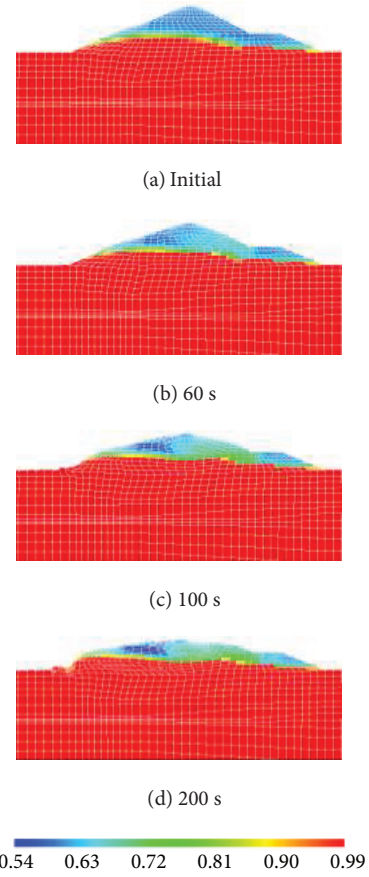
(d) 200 s

0.54   0.63   0.72   0.81   0.90   0.99

FIGURE 28: Distribution of degree of saturation.

both large horizontal and vertical displacements occurred from 30 sec to 150 sec which corresponds to the time period from the start of the first main shock till the end of the second main shock.

Figures 19 and 20 show the acceleration response for node 1201 and node 2193, respectively. Both nodes exhibit acceleration amplification. The peak ground acceleration of the Tohoku earthquake occurs at 33.9 second and 81.2 second. An average delay of 2 seconds of the peak response can be observed in both nodes. Moreover, although the shaking reduces significantly after 150 seconds, the amplification of acceleration for both nodes remains large. This might be contributed by the viscosity of the soft foundation clay.

Failure mechanism of the river embankment can be clarified by examining the change of pore water pressure, change of stress, change of strain, and so on The increase of the pore water pressure results in reduction of the effective stress, which is a direct indication of soil liquefaction. Time history of the pore water pressure and the mean effective stress of element 681 and element 865 are plotted in Figures 21 and 22, respectively. Element 681 and element 865 are located at the center of the liquefied soil layer, as shown in Figure 18. It can be seen that the excess pore water pressure generates rapidly from about 30 seconds, the first main shock, and reaches maximum even before the second main shock. The mean effective stress experienced rapid decrease as well, corresponding to the time when a large amount of the excess

pore water pressure is generated. Therefore, element 681 and element 865 are liquefied after the first main shock.

The distribution of the pore water pressure, the mean effective stress, and the skeleton stress decreasing ratio are shown in Figures 23, 24, and 25, respectively. It can be observed that the excess pore water pressure is generated within the embankment, which leads to the reduction of the mean effective stress to a minimum value of 1.9 kPa at 60 seconds. The mean skeleton stress decreasing ratio (ESDR) is defined by

$$\text{ESDR} = 1 - \frac{\sigma'_m}{\sigma'_{m0}}. \tag{15}$$

According to Figure 25, the minimum value of ESDR in the embankment is 90% at 60 seconds, indicating a complete liquefaction after the first mean shock.

Distribution of the accumulative deviatoric plastic/viscoplastic strain (GAMP) is shown in Figure 26. Although GAMP appears to be small at 60 s, the maximum GAMP is in fact 52%. As the simulation continues, a clear shear band was developed along the base of the liquefied soil layer. At the end of the dynamic analysis, the maximum value of GAMP is 224% that causes large deformation of the embankment.

The distribution of the suction and distribution of the degree of saturation are shown in Figures 27 and 28,

TABLE 4: Time steps used in consolidation analysis.

Time step Δt	Simulation time		
	Sec	Hrs	Days
0.002	210	0.06	0.002
0.005	215	0.06	0.002
0.02	235	0.07	0.003
0.05	285	0.08	0.003
0.2	485	0.13	0.006
0.5	985	0.27	0.011
1	1985	0.55	0.023
2	3985	1.11	0.046
5	8985	2.50	0.104
10	18,985	5.27	0.220
20	38,985	10.83	0.451
50	88,985	24.72	1.030
100	188,985	52.50	2.187
200	388,985	108.05	4.502
500	620,000	172.22	7.176

respectively. The initial maximum suction is set to be 14.5 kPa, as a result of assuming that the initial degree of saturation is 0.6. The maximum value of suction at the end of consolidation is 19.1 kPa. Therefore, in this analysis, the change of suction is not significant. It is observed that during the shaking, the unsaturated soil on the land side of the embankment increases whereas that on the river side decreases. This is mainly due to the deformation of the embankment. In addition, the increase in degree of saturation is also due to the shorter drainage length on the river side of the embankment that was caused by large settlement of the embankment.

4.4. Reconsolidation Behavior. Although the dynamic behavior and the reconsolidation behavior of liquefied river embankment are discussed separately, the reconsolidation analysis is a continuation of the dynamic simulation by setting ground acceleration to zero. Therefore, material parameters, boundary conditions, and numerical conditions remain unchanged from the dynamic analysis. Note that the reconsolidation analysis starts at 4000 seconds which is the same as the onset time in 1-D analysis, in order to retain the stiff low-rigidity zone of liquefied soil as well as to avoid any numerical instability. The time step for dynamic analysis was 0.002 second, which is too small for consolidation analysis. Hence, time steps are gradually increased during consolidation analysis. The time history of the time steps is shown in Table 4.

The results from reconsolidation analysis are shown in Figures 29, 30, 31, 32, 33, 34, 35, and 36. The same elements, element 681 and element 865, are chosen for illustrating the pore water pressure dissipation during reconsolidation. From Figure 29, it could be observed that the excess pore water pressure dissipates immediately after the beginning of reconsolidation, from 4000 second. Meanwhile, the mean effective stress is effective in recovering as excess pore water pressure dissipates, as shown in Figure 30. The excess pore water
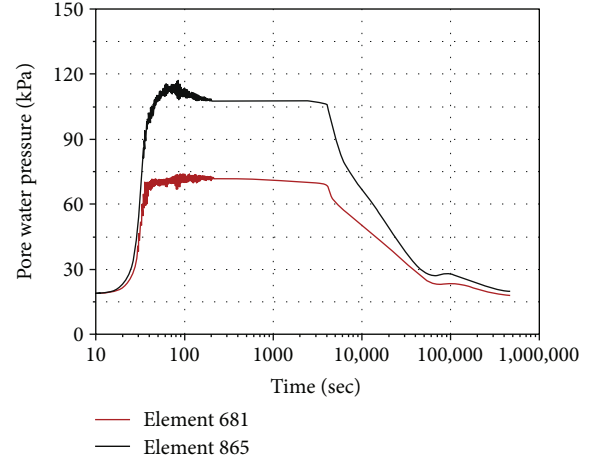
FIGURE 29: Dissipation of excess pore water pressure for element 681 and element 865 during consolidation.
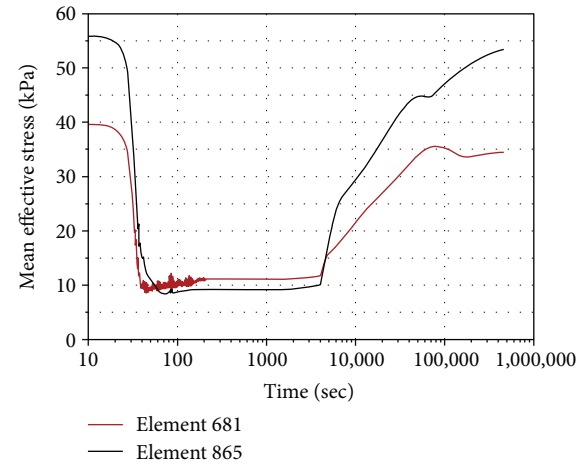
FIGURE 30: Recovery of mean effective stress for element 681 and element 865 during consolidation.

pressure is fully dissipated after approximately 400,000 seconds (110 hours). Fluctuation of pore water pressure and mean effective stress are found at about 60,000 seconds. One shall note that unlike one-dimensional analysis, the behavior of the elements is affected by global behavior of the river embankment and the interaction with other soil layers. The stress paths of element 681 and element 865 during dynamic and reconsolidation analysis are shown in Figure 31. It could be observed that the mean effective stresses for both elements are not completely reduced to zero after liquefaction. This is due to the combination effect by the nonassociativity parameter C_{ns} and the nonlinear kinematic hardening parameter y_m^*.

Figures 32, 33, and 34 depict the change of distribution of pore water pressure, mean effective stress, and ESDR. The distribution of pore water pressure was smooth at 11 hours, but the excess pore water pressure was not fully dissipated. A full dissipation can be obtained after 110 hours. The distribution of ESDR also shows that the mean effective stress is effectively recovered at 110 hours. It was also found that the

(a) Element 681

(b) Element 865
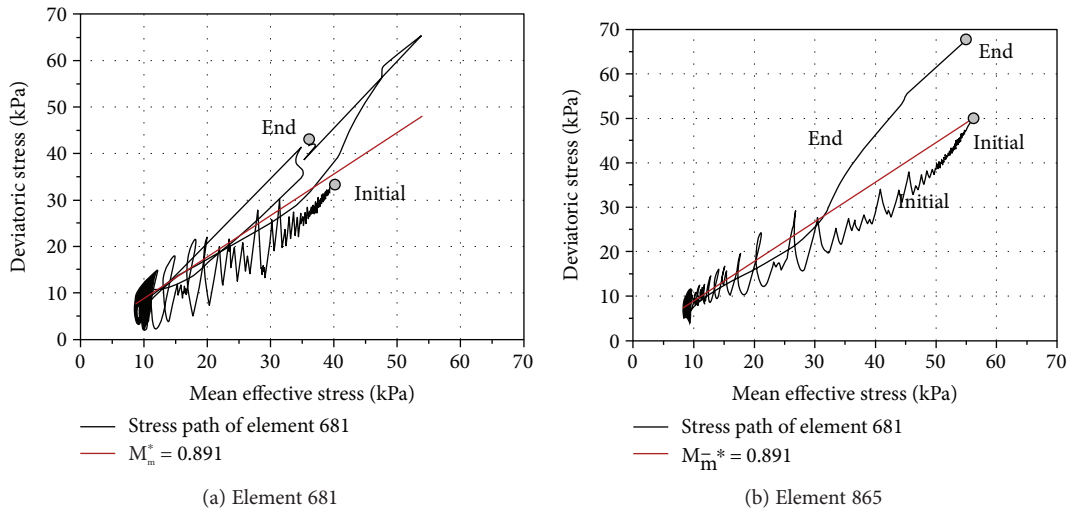
FIGURE 31: Stress paths for dynamic and reconsolidation analysis.

(a) 200 s

(b) 4,000 s (1.1 hours)

(c) 40,000 s (11 hours)

(d) 400,000 s (110 hours)
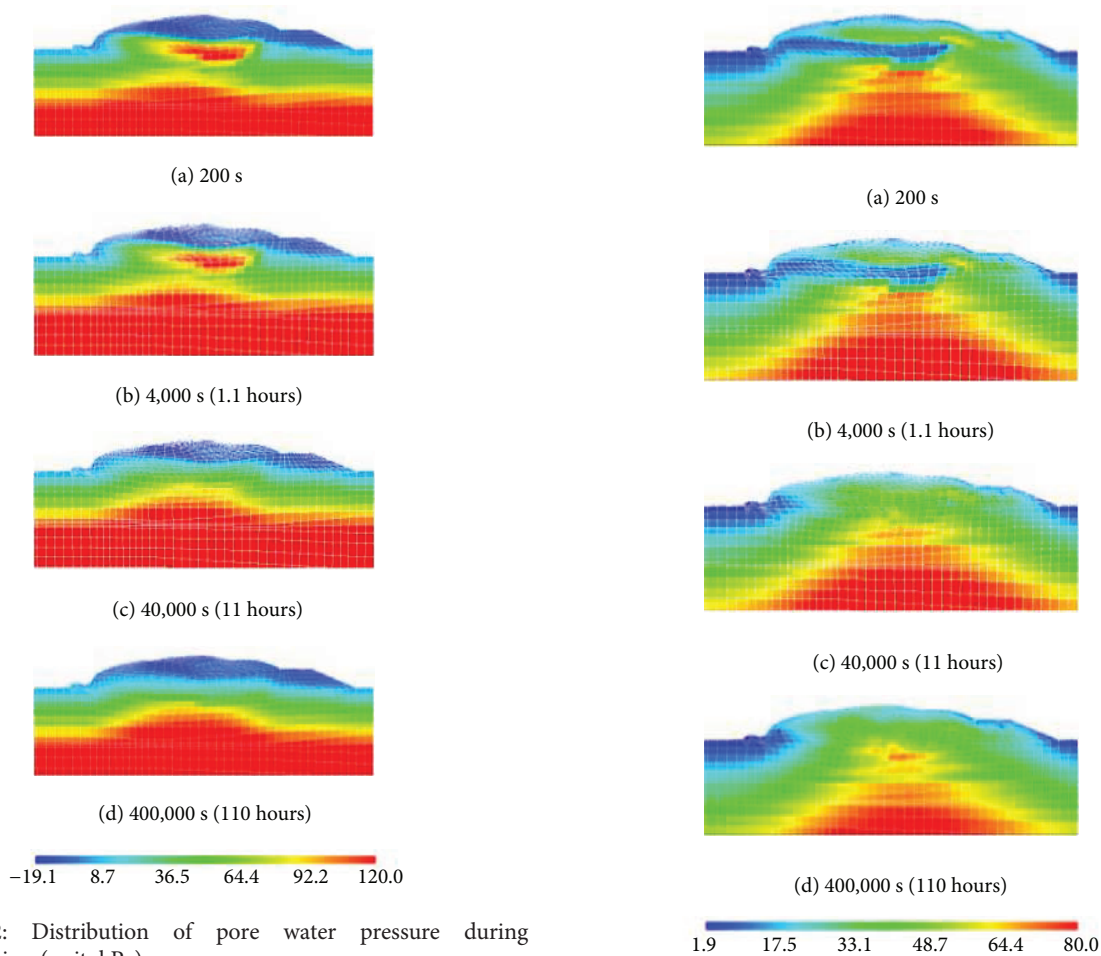
FIGURE 32: Distribution of pore water pressure during reconsolidation (unit: kPa).

(a) 200 s

(b) 4,000 s (1.1 hours)

(c) 40,000 s (11 hours)

(d) 400,000 s (110 hours)

FIGURE 33: Distribution of mean effective stress during reconsolidation (unit: kPa).

consolidation analysis has almost no effect on the distribution of suction and degree of water saturation.

As mentioned earlier, soil stiffness was described by the elastic shear modulus G^E in (8). Rapid stiffness recovery occurred almost immediately after the onset of reconsolidation, as shown in Figure 35. Note that the stiffness would not recover until the occurrence of volumetric compression during reconsolidation. In addition, the softening effect due to the increase in accumulative deviatoric strain is seized during reconsolidation. The rate of stiffness recovery is

(a) 200 s

(b) 4,000 s (1.1 hours)

(c) 40,000 s (11 hours)

(d) 400,000 s (110 hours)

| 0.00 | 0.18 | 0.36 | 0.54 | 0.72 | 0.90 |

Figure 34: Distribution of mean skeleton stress decreasing ratio (ESDR) during reconsolidation.
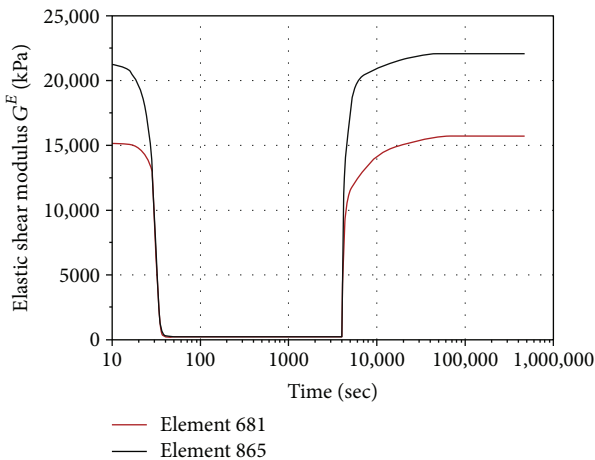
Figure 35: Recovery of elastic shear modulus for element 681 and element 865 during consolidation.

mainly governed by the input parameter C_{cf}, which should be chosen depending on experimental results. In this analysis, C_{cf} is set to be 2000.

Vertical displacement during dynamic and reconsolidation analysis is shown in Figure 36. It can be seen that the
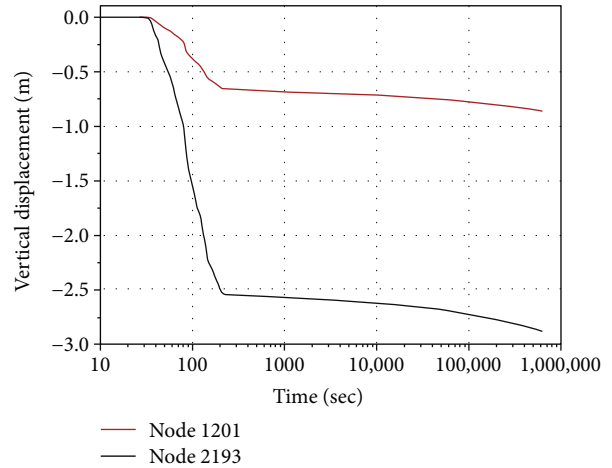
Figure 36: Time history of vertical displacement for 110 hours.

vertical displacement rate decreased drastically after 200 seconds when the shaking was stopped. Consolidation settlement continues slowly for node 1201 and node 2193, at almost the same rate. The consolidation settlement was not only contributed to by the embankment fill but also by the foundation clay.
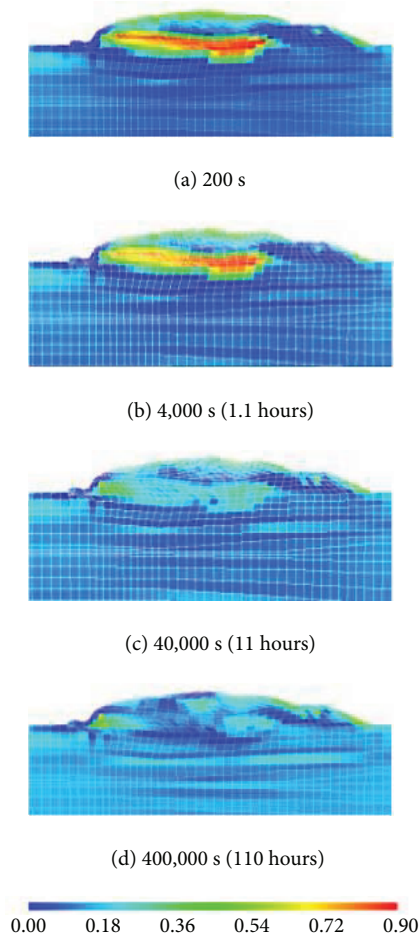
5. Conclusions

In the present study, first, an extended cyclic elastoplastic constitutive model [14] was introduced into a three-phase coupled finite element program COMVI2D-DY. This model is then modified by incorporating volumetric compression hardening during reconsolidation. The cyclic-reconsolidation behavior of the extended model is studied and examined by one-dimensional analysis. It can be concluded that stiffness recovery during consolidation is effectively reflected on the elastic and plastic shear stiffness, which results in significant reduction of the consolidation settlement. Second, a severely damaged river embankment along the Naruse River in Tohoku District during the 2011 off-the-Pacific-Coast Tohoku earthquake is simulated to validate the numerical method of COMVI2D-DY incorporating the behaviors of the cyclic elastoviscoplastic model and the extended cyclic elastoplastic model. The validation exercise is based upon comparing the monitored deformation pattern of the river embankment with that from simulation. From the simulation results, it could be concluded that the numerical method is able to reproduce the key characteristics of the actual damaged pattern.

Data Availability

The data used to support the findings of this study are available from the corresponding author upon request.

Conflicts of Interest

The authors declare that there is no conflict of interest regarding the publication of this paper.

Acknowledgments

References

[1] Y. Sasaki, I. Towhata, K. Miyamoto et al., "Reconnaissance report on damage in and around river levees caused by the 2011 off the Pacific coast of Tohoku earthquake," *Soils and Foundations*, vol. 52, no. 5, pp. 1016–1032, 2012.

[2] Tohoku Regional Development Bureau of Ministry of Land, Infrastructure, Transport and Tourism, *Report of Restoration of River Embankment along Kitakami River and etc*, 2011.

[3] F. Oka, P. Tsai, S. Kimoto, and R. Kato, "Damage patterns of river embankments due to the 2011 off the Pacific coast of Tohoku earthquake and a numerical modeling of the deformation of river embankments with a clayey subsoil layer," *Soils and Foundations*, vol. 52, no. 5, pp. 890–909, 2012.

[4] M. Okamura and S. Hayashi, "Damage to river levees by the 2011 off the Pacific coast Tohoku earthquake and prediction of liquefaction in levees," in *Geotechnics for Catastrophic Flooding Events*, pp. 57–67, 2014.

[5] A. Yamaguchi, T. Mori, M. Kazama, and N. Yoshida, "Liquefaction in Tohoku district during the 2011 off the Pacific coast of Tohoku earthquake," *Soils and Foundations*, vol. 52, no. 5, pp. 811–829, 2012.

[6] R. de Boer, *Theory of Porous Media*, Springer, 2000.

[7] B. A. Schrefler, "Mechanics and thermodynamics of saturated/unsaturated porous materials and quantitative solutions," *Applied Mechanics Reviews*, vol. 55, no. 4, pp. 351–388, 2002.

[8] Y. Huang, A. Yashima, K. Sawada, and F. Zhang, "A case study of seismic response of earth embankment foundation on liquefiable soils," *Journal of Central South University of Technology*, vol. 16, no. 6, pp. 994–1000, 2009.

[9] Y. Okochi, S. Sreng, M. Matsumoto, H. Miki, M. Tsuda, and H. Ito, "Numerical simulation of centrifuge model tests on embankment with a new liquefaction countermeasure by ground improvement considering constraint effect," in *6th International Conference on Earthquake Geotechnical Engineering*, Christchurch, New Zealand, November 2015.

[10] R. Uzuoka and K. Semba, "Numerical analysis of liquefaction in a river levee on soft cohesive ground," *Journal of Disaster Research*, vol. 7, no. 6, pp. 711–717, 2012.

[11] T. Yoshikawa, T. Noda, T. Kodaka, and T. Takaine, "Analysis of the effect of groundwater level on the seismic behavior of an unsaturated embankment on clayey ground," *Soil Dynamics and Earthquake Engineering*, vol. 85, pp. 217–230, 2016.

[12] H. Sadeghi, *Dynamic analysis of river embankments during earthquakes based on finite deformation theory considering liquefaction*, Kyoto University, 2014, Doctoral dissertation.

[13] B. Shahbodagh Khan, *Large deformation dynamic analysis method for partially saturated elasto-viscoplastic soils*, Kyoto University, 2011, Doctoral dissertation.

[14] F. Oka and S. Kimoto, "Cyclic elastoplastic constitutive model for soils based on non-linear kinematical hardening rule with volumetric and deviatoric kinematical parameters," in *Bifurcation and Degradation of Geomaterials with Engineering Applications, IWBDG 2017*, E. Papamichos, P. Papanastasiou, E. Pasternak, and A. Dyskin, Eds., pp. 81–87, Springer Series in Geomechanics and Geoengineering, 2017.

[15] F. Oka and S. Kimoto, *Computational Modeling of Multi-Phase Gematerials*, CRC Press, Taylor & Francis group, 2012.

[16] F. Oka and S. Kimoto, "A cyclic elastoplastic constitutive model and effect of non-associativity on the response of liquefiable sandy soils," *Acta Geotechnica*, pp. 1–15, 2018.

[17] R. Kato, F. Oka, and S. Kimoto, "A numerical simulation of seismic behavior of highway embankments considering seepage flow, computer methods and recent advances in geomechanics," in *Proc. of the 14th Int. Conf. Of International Association for Computer Methods and Recent Advances in Geomechanics*, pp. 755–760, Kyoto, Japan, 2014.

[18] D. Gallipoli, A. Gens, G. Chen, and F. D'Onza, "Modelling unsaturated soil behaviour during normal consolidation and at critical state," *Computers and Geotechnics*, vol. 35, no. 6, pp. 825–834, 2008.

[19] C. Jommi, "Remarks on the constitutive modelling of unsaturated soils," *Experimental Evidence and Theoretical Approaches in Unsaturated Soil*, pp. 139–153, 2000.

[20] L. Laloui and M. Nuth, "On the use of the generalised effective stress in the constitutive modelling of unsaturated soils," *Computers and Geotechnics*, vol. 36, no. 1-2, pp. 20–23, 2009.

[21] F. Oka, T. Kodaka, S. Kimoto, Y. S. Kim, and N. Yamasaki, *An Elasto-Viscoplastic Model and Multiphase Coupled FE Analysis for Unsaturated Soil. Unsaturated Soils 2006*, ASCE, 2006.

[22] S. Kimoto, B. Shahbodagh Khan, M. Mirjalili, and F. Oka, "Cyclic elastoviscoplastic constitutive model for clay considering nonlinear kinematic hardening rules and structural degradation," *International Journal of Geomechanics*, vol. 15, no. 5, article A4014005, 2015.

[23] M. T. van Genuchten, "A closed-form equation for predicting the hydraulic conductivity of unsaturated soils1," *Soil Science Society of America Journal*, vol. 44, no. 5, pp. 892–899, 1980.

[24] F. Oka, A. Yashima, A. Tateishi, Y. Taguchi, and A. Yamashita, "A cyclic elasto-plastic constitutive model for sand considering a plastic-strain dependence of the shear modulus," *Géotechnique*, vol. 49, no. 5, pp. 661–680, 1999.

[25] National Research Institute for Earth Science and Disasters Resilience (NIED), *Ground Motion Data MYGH06 (−80m) at Tajiri Station, Miyagi Prefecture*, 2011.

[26] B. Ye, H. Yokawa, T. Kondo, A. Yashima, F. Zhang, and N. Yamada, "Investigation on stiffness recovery of liquefied sandy ground after liquefaction using shaking-table tests," in *Soil and Rock Behavior and Modeling*, 2006.

[27] National Institute for Land and Infrastructure Management, "Technical Report, Prompt Report on Damage of Civil Structures Caused by the 2011 Great East Japan Earthquake (NILIM and PWRI)," 2011, Chapter 6.

[28] Geological Survey of Japan, *Online Geological Map of Japan*, 2017, https://gbank.gsj.jp/geonavi/geonavi.php#8,38.764,140.213.

[29] R. F. Carsel and R. S. Parrish, "Developing joint probability distributions of soil water retention characteristics," *Water Resources Research*, vol. 24, no. 5, pp. 755–769, 1988.

Research Article

Soil-Water Characteristic Curve of Residual Soil from a Flysch Rock Mass

Josip Peranić,[1] Željko Arbanas [ID],[1] Sabatino Cuomo,[2] and Matej Maček[3]

[1]*Faculty of Civil Engineering, University of Rijeka, Rijeka, Croatia*
[2]*Department of Civil Engineering, University of Salerno, Fisciano, Italy*
[3]*Faculty of Civil and Geodetic Engineering, University of Ljubljana, Ljubljana, Slovenia*

Correspondence should be addressed to Željko Arbanas; zeljko.arbanas@gradri.uniri.hr

Depending on the nature of the material and suction range, laboratory measurements of the soil-water characteristic curve (SWCC) can be time-consuming and expensive, especially for residual soils, in which a wide range of particle sizes and soil structures typically results in SWCCs that cover a wide range of suction. Investigations of the SWCCs of residual soil from flysch rock masses are rare, and so far, no results were presented in the literature which were obtained by performing measurements on undisturbed specimens. In this paper, a detailed examination of water retention characteristics is performed for a specific type of residual soil (CL) formed by the weathering of a flysch rock mass. Measurements performed by using different techniques and devices on intact specimens were successfully combined to obtain the SWCC during both drying and wetting processes, under different stress conditions, and from saturated to air-dried conditions. Used procedures are suitable for the determination of SWCCs of soils that undergo volume changes during the drying or the wetting process, since instantaneous volumetric water content can be determined. Results presented in this paper can be used to assess the influence of desaturation of the residual soil covering flysch slopes during dry summer periods by providing key-in material properties required to analyze the transient rainfall infiltration process.

1. Introduction

Landslides in flysch deposits frequently occur in European countries such as Italy, Slovenia, Austria, Czech Republic, and Poland and are mainly caused by heavy precipitation. Previous studies of landslides in flysch slopes have mainly focused on the increase in pore water pressure caused by long-term, heavy precipitation as a landslide triggering factor [1] and on the effects of the weathering process of flysch rock masses on the soil shear strength [2, 3]. The influence of the rainfall pattern and antecedent rainfall, coupled with the unsaturated soil property functions (USPFs) that govern the complex infiltration processes between the soil surface and the phreatic line, was not considered. The aim of this study is to assess the influence of the material behavior above the phreatic line on the infiltration process, since the pore water pressures existing in this zone are generally negative. The complex nature of this material and long periods of heavy

rainfall that precede instability phenomena on these slopes suggest that the negative pore water pressure should have an important role in slope stability.

Determination of the SWCCs of residual soils from flysch rock masses is the first step in the analysis of the unsaturated soil behavior in slopes composed of this material. Accuracy of SWCCs largely depends on used techniques and procedures used for the determination of the water retention characteristics. Various techniques use the SWCCs as input data to derive other unsaturated soil property functions, instead of collecting direct measurements. Thus, the precise measurement of SWCCs has an important role in the practical implementation of unsaturated soil mechanics in geotechnical practice. A large part of the existing SWCC database is obtained by performing measurements on specimens prepared using different remolding techniques. Considering the time needed for measuring the SWCCs, the drying process is usually preferred, while the SWCCs obtained during

the wetting process are rare. Although using reconstituted specimens has clear advantages in terms of the consistency of the test results and homogeneity of the specimens, the measured values are not representative of the material and phenomena occurring in situ. Another important feature of the soil is its hysteretic behavior during the drying and wetting processes, causing significant differences in the matric suction or hydraulic conductivity values obtained for the same soil water content.

The main goal of this paper is to present relevant soil-water retention characteristics and other material properties that are fundamental for modeling the rainfall infiltration process. Since direct measurements are time-consuming, expensive, and difficult procedures, USPFs could instead be estimated based on the data presented in this paper. The procedures used for the determination of the SWCCs in all three characteristic zones: the boundary effect, transition and residual zones [4], and the obtained results, are presented. The most frequently used equations were employed to fit the measurements of the drying and wetting path tests. The obtained parameters can be implemented in future analyses; therefore, the results are discussed and compared to those available in the literature by using comparable materials.

2. Material and Study Area

The Rječina River Valley, located in the outback of the city of Rijeka, Croatia (Figure 1), is well known to have experienced numerous historical and recent landslides on both slopes of the valley [1]. The valley is composed of Cretaceous and Paleogene limestone at the top of the slopes and Paleogene siliciclastic rocks and flysch at the lower slopes and the valley bottom, where the sliding processes have primarily developed.

The term flysch was introduced in 1827 by the Swiss geologist Bernhard Studer and originates from the German word *fliessen*, which means flow. Actually, flysch is a sequence of alternations of various clastic sedimentary rocks that were deposited as a deep marine facies during an early stage of orogenesis. Well-known flysch deposits are found in the forelands of the Pyrenees, Dinarides, northern Alps, and Carpathians and tectonically similar regions in Italy, the Balkans, and Cyprus. Flysch is characterized by rhythmic alternations of sandstone and fine-grained layers that contain siltstones, silty shales, and clayey shales. Flysch deposits may also include breccias, conglomerates, and limestone beds. From a geotechnical point of view, a flysch rock mass could be described by the following characteristics [5]: (i) heterogeneity due to alterations of competent and incompetent members; (ii) the presence of clay minerals; (iii) tectonic fatigue and sheared discontinuities, often resulting in a soil-like material; and (iv) generally low permeability and significant weakening where free drainage does not occur due to the presence of clay minerals.

A flysch rock mass, especially its incompetent members (siltstones and shales), that has been exposed to water and air is strongly affected by chemical weathering and decomposition. These processes cause changes in the physical and mechanical properties. Mechanical weathering also influences the chemical weathering of flysch components. Fine-grained fractions, such as siltstones, are the most affected by chemical weathering [2]. As a result of these processes, the flysch rock mass increases in volume over time, disintegrating to silt or clay. Through this gradual degradation, the physical and mechanical properties of the clayey siltstone materials become similar to engineering soil. A consequence of these types of geomorphological processes is a sporadic accumulation of eroded colluvial deposits on the slopes; these deposits can be susceptible to sliding [6].

Landslides in the flysch slopes occur in two typical forms: (i) deep-seated landslides through the flysch rock mass (some parts of the slip surface could cut through the superficial colluvial deposits) and (ii) shallow landslides with slip surfaces at the contact of the superficial deposits and flysch rock mass or through the superficial colluvial deposits. The type of landslides [7, 8] depends on the conditions present in the sliding slope. The main triggering factors are long periods of precipitation, snowmelt, and, rarely, earthquakes.

It was determined that most of the landslides in the Rječina River Valley occurred after long, mostly continuous periods of rain, while short periods of intense precipitation events never initiate a landslide on flysch slopes [9].

A similar scenario was identified in the flysch deposits in Europe, indicating that the main types of instability phenomena in flysch slopes were debris flows and shallow landslides (<3 m) in superficial deposits and deep-seated landslides with rupture surfaces that cut through the flysch bedrock [6]. The main triggering factors were rainfall and snow melt, while earthquakes also triggered instability phenomena in Italy [10]. The period of cumulative precipitation that caused landslide initiation on the flysch slopes varies in different countries: approximately 90 days in the Istria Peninsula in Croatia [6]; 25–45 days in the Polish Flysch Carpathians [11]; 15–60 days in the Northern Apennines in Italy [10]; 30–60 days in the Southern Apennines in Italy [12]; 25 days in the Slano Blato Landslide area in Slovenia, [13]; and "several months" in the Outer Western Carpathians in the Czech Republic [14]. A longer period, ranging between 180 and 360 days, of accumulated precipitation was associated with major landslide reactivations in the Southern Apennines, Italy [12]. The variability in these findings is due to the different regional and local conditions, but the most important condition associated with the time to landslide activation is the rate of surface water infiltration.

The infiltration process has a main role in landslide initiation, influencing the soil saturation, the behavior and strength of the soil in the unsaturated zone above the groundwater level, the changes in the soil unit weight, the groundwater level rise, and the overall relation between the active forces and soil resistance in a slope. Knowledge and understanding of soil-water characteristics are necessary conditions for the explanation of the landslide initiation on flysch slopes. Investigations of the soil-water retention characteristic of residual soil from flysch rock masses are very rare, and only a few valuable results have been presented in the literature.

The Valići Landslide occurred on 13 February 2014 at the southwestern slope of the Rječina River Valley after a long period of heavy rain [9, 15]. Undisturbed soil samples were
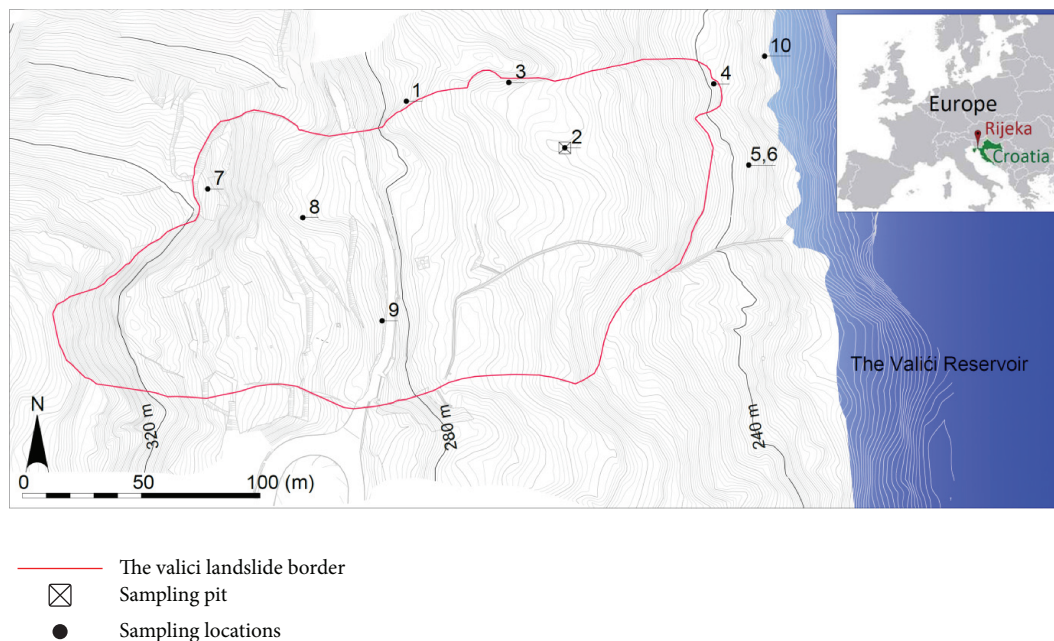
FIGURE 1: Map of the reactivated landslide on a detailed topographic map with sampling positions [9].

collected from the sample pit in the central part of the Valići Landslide (position 2 in Figure 1), and a series of tests were conducted to determine the basic index properties of the soil. Sampling was performed from the surface at a small hand-drilled pit by using hard-plastic tubes (Figure 2(a)). The sampling depths for all the samples varied from 0.5 to 1 m. After pushing the tubes into the soil, they were excavated and sealed to prevent evaporation. The natural water content ranged from 28% at the ground surface to 10% at a depth of 1 m, while the in situ density varied from 1.91 to 2.13 g/cm^3. The mean values of the basic properties of the tested material, including the specific gravity of soil solids (ASTM D854-14) [16], saturated unit weight, particle size distribution (ASTM D1140-17 [17] and ASTM D7928-17 [18]), liquid limit (w_L), plastic limit (w_P), plasticity index (PI) (ASTM D4318-17) [19], and classification of material according to the USCS (ASTM D2487-11) [20], are summarized in Table 1.

2.1. Grain Size Distribution (GSD) Analysis and Plasticity Limits. The inverse distribution of the solid particles (e.g., the distribution of the voids), for each material type, provides an insight into the possible unsaturated soil behavior and soil-water retention characteristics.

To analyze the possible GSD characteristics of the material in the landslide body, samples were taken from the landslide surface at 10 different locations, which are marked in Figure 1. Wet sieving tests, the hydrometer method, and particle sizing by using the SediGraph method were combined to obtain the GSD curves. The obtained results (Figure 3) show that fine-grained particles dominate in the tested samples with the highest average contents of silt and clay.

GSD curves show a similar grain-size composition of the material along different parts of the landslide surface,

indicating similar conditions in the material origin due to the weathering process of the bedrock siltstone. The only sample that had a slightly higher content of sand particles (28.2%) was sample number 10, which was collected outside the landslide body at the lowest position of the slope. The largest quantity of particles larger than 2 mm was found in samples collected from the central part of the landslide body (points 2, 8 and 9), and the sample from location number 9 had the highest content (9.5%) by weight.

The Atterberg limits were determined, and most of the materials could be classified as low-plasticity clay (CL). Only samples taken from locations number 8 and number 10 are plotted beneath the A-line in the plasticity chart. The obtained results cluster in the plasticity chart, indicating that the whole landslide body has uniform material properties (Figure 4).

Unlike in the case of disturbed and compacted specimens, in successive tests for different purposes, undisturbed specimens could be characterized as highly heterogeneous on the macroscale. Heterogeneity arises from the presence of macroscale voids caused by the biological activity of worms and roots in the soil close to the surface or arises from the presence of silt grains that can vary in size and weathering degrees (Figure 2(b)). Such heterogeneous results create difficulties when performing laboratory tests on small specimens. However, in the sense of the granulometric composition and plasticity limits, the material located near the ground surface seems to be very homogeneous. It is well known that granulometric composition and plasticity limits are directly connected with water retention capabilities and hydraulic conductivity features of a material. Therefore, the identification test results indicate that the superficial residual soil should have similar USPF characteristics.

(a)   (b)

FIGURE 2: (a) Sampling pit. (b) Half of the oven-dried specimen from a depth of 0.75 m.

TABLE 1: Mean values of the basic properties of the residual soil samples used in this study.

Specific gravity, G_s (/)	Sat. unit weight, γ_s (kN/m³)	Particle size distribution				Atterberg limits		Plasticity index, PI	USCS
		Clay, C (%)	Silt, M (%)	Sand, S (%)	Gravel, G (%)	Liquid limit, w_L (%)	Plastic limit, w_P (%)		
2.7	20.9	30.3	53	10.4	6.3	44	24	20	CL

FIGURE 3: GSD results for samples collected at 10 locations along the landslide body and slope.
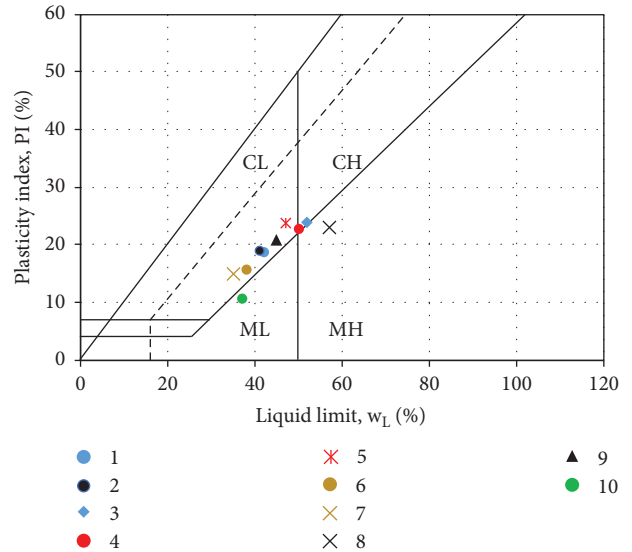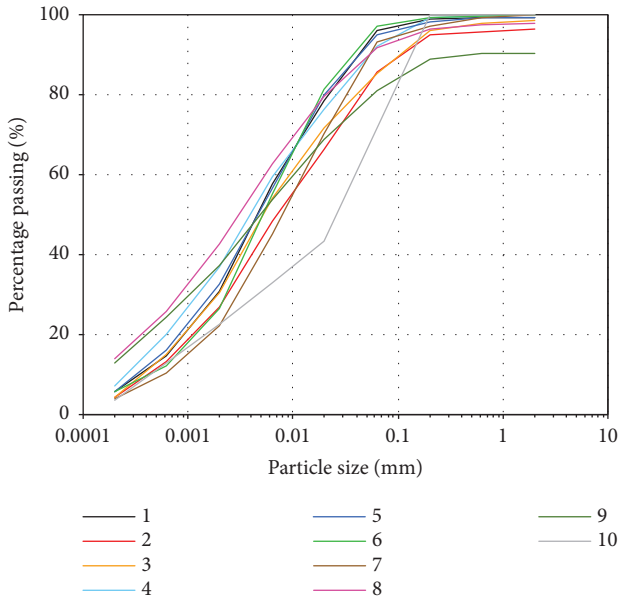
FIGURE 4: Plasticity chart of the samples.

3. Methods Used for Determination of Soil-Water Characteristic Curves

A SWCC is one of the most important features in unsaturated soil mechanics and relates to the potential energy of a liquid phase, which is usually characterized by the suction ψ, to the variations in the water content w in the soil [21]. Depending on the material behavior of the soil as the suction varies, the soil water content is commonly designated in terms of the gravimetric water content w, volumetric water content θ, or degree of saturation S. For compressible soils that undergo a change in volume with a change in the suction, both the changes in water volume change and total volume should be measured [22]. For a single type of material, the SWCC should be presented in terms that consider both phenomena (θ, S). Different approaches were developed for the accurate determination of the SWCCs of different types of soils. Different measuring techniques and devices were developed to measure the water retention characteristics at different suction ranges. The existing devices and testing procedures were often modified to adjust for different factors that affect the measurement results.

3.1. Literature Overview. Many studies were conducted to assess the influence of different factors on the water retention properties of the soil in geotechnical engineering applications.

Numerous investigations (e.g., [23–26]) noted that the void ratio, water content, and stress state of a soil have a strong influence on the SWCC. Standard laboratory equipment based on the axis translation technique, such as the pressure plate, volume extractor, suction-controlled oedometer, modified triaxial apparatuses, and standard tensiometers, are the most common devices used to control or measure matric suction. Although every type of the above-mentioned equipment has some advantages and limitations, they can be combined to measure or control matric suction up to 1500 kPa. Generally, capillary forces dominate the wet range and adsorptive surface forces dominate the dry range of the SWCC. Measurement accuracy in the dry area of the SWCC, such as those above 1 MPa of suction, has greatly benefited from the development of precise chilled hygrometers [27]. Gee et al. [27] noted that the structural changes induced by sampling should have a minimal impact on the measured water potential at low water contents. They concluded that for low water contents, SWCCs are controlled by a surface area rather than pore geometry. A dew-point potentiometer device (Decagon Devices Inc.) was used to investigate water retention characteristics of different soil types (e.g., [28–31]).

Agus and Schanz [32] compared four laboratory methods commonly used for measuring soil total suction by using two bentonite-sand mixtures: the noncontact filter paper method, the psychrometer technique, the relative humidity (RH) sensor, and the chilled-mirror hygrometer technique. They concluded that the chilled-mirror hygrometer technique was the most accurate among the four methods used in the study. Campbell et al. [33] presented a procedure for specimen preparation, suction, and water content measurements during a wetting process using the WP4-T apparatus.

In this paper, different testing devices were used to cover the wide range of suctions that this material can exhibit. All tests were performed to measure both the (matric) suction and the volumetric water contents during the drying and wetting processes in undisturbed specimens.

3.2. Testing Programme. All the undisturbed samples used to determine the SWCC were taken from the same sample pit in the central part of the Valići Landslide (position 2 in Figure 1). By using different devices and measurement techniques in their optimum measuring ranges and combining the measurement results, a SWCC was defined in all three characteristic zones of desaturation. For testing the residual soil from the flysch rock mass at a low range of matric suctions, different testing conditions were used to simulate the field conditions that can affect SWCCs. The effect of the overburden pressure on the SWCC was analyzed using different values of the net vertical stress and suction-controlled oedometer-type devices. The measurements collected during the drying and wetting processes were performed using multiple devices to identify the hysteresis and retention characteristics that material exhibits in situ during rainfall infiltration or evaporation. The influence of different initial water contents and saturation conditions was examined by measuring different scanning curves, starting from initially saturated conditions, natural water content conditions, or air-dried conditions. To identify the possible effects of the soil structure and the sample preparation method on the suction measurements using a WP4-T device, the measurements were performed on undisturbed specimens that were prepared using commonly adopted specimen preparation techniques for testing with the WP4-T device, as proposed by various authors (e.g., [30, 33]), for both the drying and the wetting paths. Due to shortcomings of the axis translation technique for measurements of soil suction at high degrees of saturation [34], minitensiometer measurements were used to determine the wet part of the SWCC more precisely.

3.3. Standard and Volumetric Pressure Plate Extractor Apparatus. A pressure plate extractor apparatus (Soilmoisture Equipment Corp.) with 1500 kPa ceramic plates was used on undisturbed samples to obtain results of the drying branch of the SWCC, for up to 700 kPa of matric suction. The tests were performed on undisturbed specimens with the diameter of 51 mm and height of 10 mm. A short specimen height was used to shorten the equilibration time. At higher water contents, caliper measurements of the total volume have shown to be inapplicable due to the soft consistency of the samples. Wax dipping and the water displacement techniques (ASTM D7263-09) [35] were used to determine the total density of a single specimen after every equilibration step. The total volume measurement, combined with the gravimetric measurement for the determination of the water content according to ASTM D6836-02 [36], enabled the use of the conventional pressure plate extractor apparatus to obtain a more advanced characterization of the soil-water retention properties than that possible with a conventional ψ-w relationship. The results obtained using this device and the adopted testing procedure enabled the evaluation of the change in the void ratio and degree of saturation due to the increase in matric suction during the drying process of the undisturbed samples, up to 700 kPa. Gravimetric water content measurements were performed on multiple specimens during the RP03 test (samples se1 to se7), starting from the natural water content w_n. To minimize evaporation from the samples during the density measurement, volume measurements were performed only on one sample (RP03-se1) after every equilibration stage.

A volumetric pressure plate (Soilmoisture Equipment Corp.) extractor with a 200 kPa ceramic plate and hysteresis attachments was used to determine the hysteresis of the soil in the low matric suction range. Test VE-1w was performed on an undisturbed specimen previously equilibrated in a standard pressure plate extractor apparatus at a matric suction of 300 kPa. The total volume change measurements were performed after every equalization step, using the previously described procedure. The water content was calculated after every equilibration step using the gravimetric or volumetric measurements of the water volume change.

3.4. Suction-Controlled Oedometer Apparatus. Two different suction-controlled oedometer-type devices were used for a

more advanced investigation of the soil-water retention properties through the control of the stress state variables (net vertical stress and matric suction) and measurements of the axial deformations of the sample and water volume variations during the test. Automated data acquisition during the test is an important advantage over the previously described null-type axis-translation devices, especially for the long-lasting wetting tests. The main advantage of the suction-controlled oedometer apparatus (SCOED) at UniSa is the advanced air-flushing system, which removes diffused air beneath the high air entry porous disc (HAEPD) and consists of two double-wall burettes coupled to a differential pressure transducer and a peristaltic pump. HAEPDs with 200 and 500 kPa AEV were used to perform different types of tests. The Hydrocon hydraulic consolidation cell for unsaturated samples (Controls S.p.A.), used at UniRi, enables sample saturation through back pressurization in a confined system. The apparatus was equipped with a 1 MPa HAEPD. These devices were used to perform multiple (main and scanning) drying and wetting tests on undisturbed specimens with different net vertical stresses. Tests UVH-1, UVH-2, and UVH-3 were performed using the Hydrocon device to obtain the main drying curves under net vertical stresses of 25, 100, and 200 kPa, respectively. Test OEUVCJ01 was performed using the SCOED apparatus and included a scanning drying and wetting test at a net vertical stress of 200 kPa, while test OEUVCJ03w was performed on an oven-dried sample during the wetting path, using a net vertical stress of 5 kPa to measure the vertical deformations during the wetting test. Following this test, the sample was consolidated at 200 kPa, and test OEUVCJ03 was performed during the drying path.

3.5. HYPROP Evaporation Method Device. The HYPROP evaporation method device (Decagon Devices Inc.) was used to determine the wet part of the SWCC more precisely. Tests were performed on three undisturbed specimens with different initial water contents, starting from the saturated water content or from the natural water content. Saturation of the specimens prior to testing was performed inside a steel cylinder either by immersion in water or by immersion in water with the application of a small vacuum. The water loss from the sample due to evaporation is automatically recorded by placing the sample on a high-precision scale, and the negative water pressures are measured directly using two minitensiometers installed in predrilled holes at different heights. No volume changes were measured due to evaporation during the suction increase; therefore, the obtained results are shown in terms of only the gravimetric water content w. However, information on the hydraulic gradient between two measuring points and the water flux can be used to calculate the unsaturated hydraulic conductivity in the measured range, according to the Darcy-Buckingham law. Due to cavitation problems when using direct tensiometer measurements, the simplified evaporation method [37] is frequently used for measuring both the SWCC and the suction permeability curve in sands and silts. By using the tensiometer-preconditioning procedure [38], the results were obtained for matric suctions up

to 130 kPa. The results obtained from the sample starting from the natural water content are denoted by HYPROP-2.

3.6. Dew-Point Potentiometer WP4-T. The WP4-T (Decagon Devices Inc.) potentiometer device was used to measure the suction in the dry area of the SWCC, extending into the midrange. A detailed description of the dew point device that measures the total suction by the vapor pressure method is provided by Leong et al. [29] and Campbell et al. [33]. The device was used to obtain the soil-water characteristics of undisturbed and remolded specimens undergoing drying and wetting processes. Testing procedures were conducted according to ASTM D 6836-02, in combination with density measurements after each suction measurement, by using the wax dipping and water displacement technique (ASTM D7263-09) [35]. The measurements were extended into the midrange of the SWCC for undisturbed and remolded soil specimens to compare the measurement results. In the first test (WP4-T-1), a total of 8 completely remolded specimens were prepared and equilibrated at different water contents, using the specimen preparation procedure similar to that described by Campbell et al. [33]. Test WP4-T-2 was performed during the wetting process on 11 completely remolded samples prepared using the specimen preparation procedure proposed by Campbell et al. [33]. In this test, only the water content was measured during the wetting process. Another test (WP4-T-3) was performed on 9 undisturbed specimens prepared at a natural water content. The first three specimens (WP4-T-3se1, WP4-T-3se2, and WP4-T-3se3) were submerged in water and left to saturate for 24 h. The measurements of the next three specimens were performed starting from the natural water content and were slowly air-dried (WP4-T-3se4, WP4-T-3se5, and WP4-T-3se6). The last three specimens (WP4-T-3se7, WP4-T-3se8, and WP4-T-3se9) were used to perform measurements during the wetting process, starting from the air-dried condition. Air-dried specimens were wetted with a small amount of water and rested for approximately 24 hours in small sealed plastic bags. After each step of the equilibration, the suction and weight of the specimen were measured. Then, the total density of the specimens was measured, and the procedure was repeated until the suction values became too low during the wetting process or until the air-dried conditions were achieved during the drying process. During both the drying and the wetting processes, multiple measurements of the suction and density were performed. Suction values as low as 230 kPa and higher than 90 MPa were measured using the WP4-T device.

4. Test Results

The matric suction and total suction measurements were combined to define the soil-water characteristics from the capillary saturation zone to the zone of residual saturation. All the results were obtained from undisturbed specimens, except for the drying test WP4-T-1 and wetting test WP4-T-2. Different colors are used to highlight different specimen conditions at the start of the test, in terms of the saturation and preparation technique. Markers with solid fill indicate

that disturbed specimens were used in the test. Red and blue colors indicate that the drying path started from saturated conditions or natural water content conditions, respectively, while the green color is used to represent the measurements obtained from specimens undergoing wetting.

The results obtained from air-dried samples prior to the wetting path are used for hydraulic characterization of the soil in the wetting process, and results obtained from only undisturbed soil specimens were used for the development of the SWCC. By comparing the results obtained from the disturbed and undisturbed specimens using the same device or technique, the influence of the specimen preparation method and soil structure on the measured values could also be evaluated.

The measurement results used to obtain the suction ψ versus the water content w SWCC (SWCC-w) are presented in Figure 5(a). Some of the results obtained using the standard and volumetric pressure plate extractor devices, suction-controlled oedometer devices, HYPROP and WP4-T devices are included. The suction ψ versus the volumetric water content θ (SWCC-θ) results are presented in Figure 5(b), for the measurements that show changes in both the water volume and the total volume (or density) due to the suction change during the test. For the suction-controlled oedometer devices, the total volume was calculated using the measured axial deformations, assuming no specimen sidewall detachments.

The slope of the drying branch in the SWCC before reaching the AEV of the material is visible for both the SWCC-w and the SWCC-θ, indicating that the material undergoes a volume change when the suction is increased, due to the increase in the stress state of the soil. Many studies (e.g., [39, 40]) have concluded that the rate of the volume change in the saturated part of the SWCC depends on the stress history of a soil. However, the total volume change should not affect the degree of saturation of deformable soil before the AEV of the soil is reached. The degree of saturation remains equal to unity, and the SWCC-S plot should remain horizontal until the AEV of the material is reached. After this point, desaturation starts at a rate that depends on the features of the material being tested. By plotting a large number of experimental data on a log-log plot of the suction ψ versus the effective degree of saturation Se, Brooks and Corey [41] found that the rate of desaturation exhibits a linear shape for the unsaturated part of the SWCC. This approach was used to avoid the usual difficulties in the determination of the true AEV due to the volume changes in the saturated part of SWCC ([39, 42]).

The SWCC results are shown in the SWCC-S form in Figure 6. A semi-log plot is shown in Figure 6(a) for tests in which the degree of saturation could be calculated. For the remolded specimens, the density measurements were combined with the standard WP4-T suction and water content measurements for only the drying test WP4-T-1, and the WP4-T-2 results are not included. In Figure 6(b), the SWCC-S results are presented in a log-log plot. Using the plot and results from the unsaturated linear part of the SWCC, the AEV of 210 kPa and air expulsion value (AExV) of 56 kPa were determined for the drying and wetting paths.

The regression lines for the drying and wetting processes are parallel, and the value of the pore-size distribution index λ [41] is 0.26, which seems to not be affected by the ongoing process type. However, the results obtained from the remolded specimens along the drying path (WP4-T-1) show a deviation from the abovementioned values, with a higher AEV (450 kPa) and higher desaturation rate ($\lambda = 0.33$).

Hysteresis between the drying and the wetting processes is observed for all the SWCC plots. The shape of the SWCC, saturated water contents, and other soil properties associated with the drying and wetting SWCC paths [43] suggest that the tested material is more similar to silty soil than clayey soil [44]. Another important observation from the wetting tests is that the specimens did not reach full saturation. Similar results are obtained for drying tests performed on samples that were saturated prior to testing by submerging into water. The obtained volumetric water contents typically corresponded to 80–95% of the saturated water content values. Similar observations were noted by other researchers. Chiu and Shackelford [45] obtained maximum volumetric water contents θ_m from 0.84 to 0.90 of the saturated value θ_s during the wetting process of compacted sand-kaolin mixtures. After several days of soaking, Perera et al. [46] determined that the degree of saturation was 87%–100% for the clayey samples.

The influence of the sample preparation technique on the measurement results obtained using the WP4-T device is highlighted in Figure 5(a) (SWCC-w), for both the drying and the wetting paths. For the drying path, the measured results from the remolded specimens plot higher than the results obtained from the undisturbed specimens, especially for suction values below 1000 kPa. The effects of the sample preparation method and the soil structure on the measurements start to wane above a suction of 1000 kPa for the drying branch. The influence of the specimen preparation method is even more emphasized in the case of the results obtained during the wetting process (WP4-T-2). The results start to deviate from those obtained from the undisturbed samples when the suction values become lower than 6000 kPa.

In contrast, the measurements obtained from the undisturbed specimens using the WP4-T device seem to be in good agreement with the measurements obtained using the axis translation technique, even for the suction values well below 1000 kPa. This could indicate that the soil structure does have an important effect on the results obtained using the WP4-T device in the part of the SWCC with lower suction values and that the measurements from the undisturbed specimens should be preferred when using the WP4-T device and when the suction values of interest are lower than 1 MPa.

The results obtained on undisturbed specimens underline the smooth and gradual transition between the saturated and unsaturated parts of the SWCC. This feature of the soil is closely related to the water retention and permeability characteristics and should thus have a direct influence on the rainfall infiltration process occurring in the slopes in situ. For sands and slits, the transition zone of the SWCC is generally steep, indicating higher rates at which the material can be saturated during the infiltration process
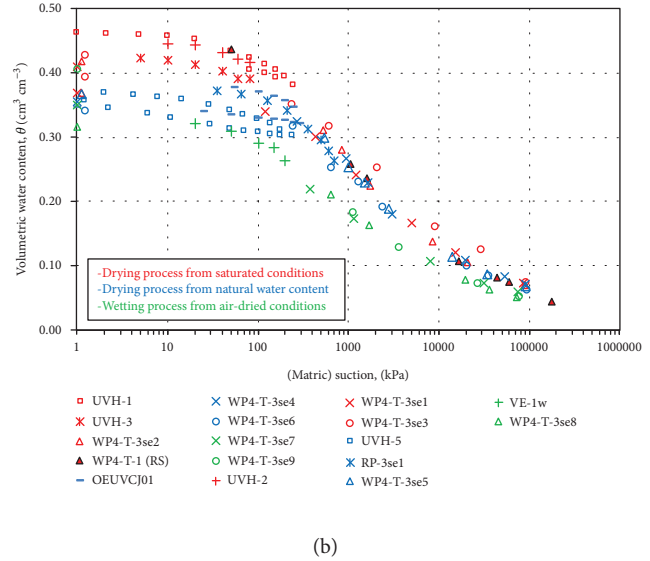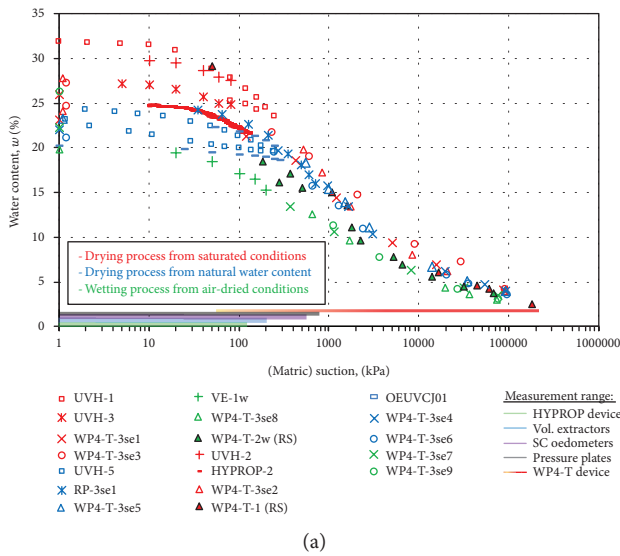
(a)

(b)

FIGURE 5: SWCC in terms of (a) gravimetric water content and (b) volumetric water content for the drying and wetting processes. Symbol (RS) indicates remolded samples; all other samples are undisturbed.
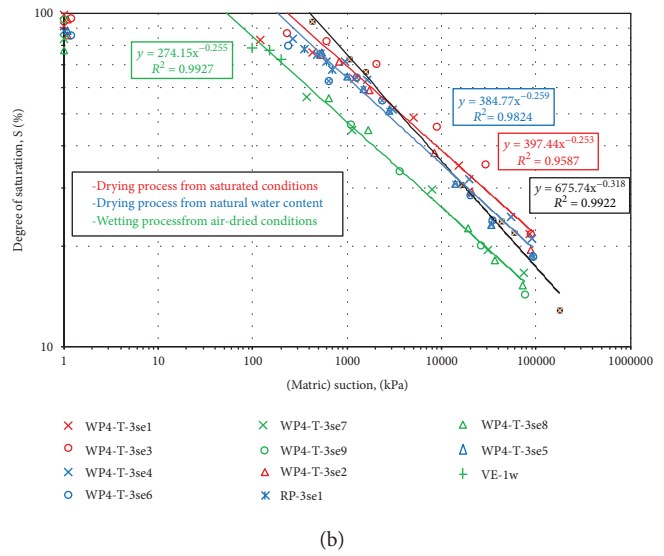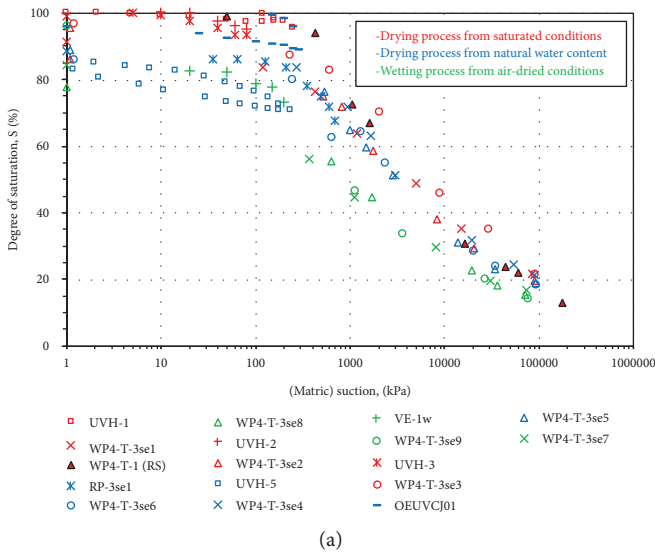

(a)

(b)

FIGURE 6: Drying and wetting paths of the SWCC-S at (a) semilog and (b) log-log scale.

or desaturated during evapotranspiration. Consequently, short-duration precipitation with higher intensities is the common triggering factor for landslides occurring in these types of material ([47–49]). In contrast, the SWCCs with gentle slopes in the transition zone imply low rates of change in the water content in the soil. Long evaporation periods are required to significantly dry these types of soils, and long infiltration periods are required for water to saturate these types of soils.

The density measurements combined with the standard ψ-w measurements from the pressure plate and WP4-T devices, and the measurements by the suction-controlled oedometer devices can provide an insight into the volume changes affected by the change in suction. Figure 7 presents the e-S-ψ relationship for the specimens that underwent zero

total stress and total density measurements after every measurement of the (total) suction or equalization step. The results obtained using the standard pressure plate apparatus and WP4-T device are included here.

The results obtained using the standard and suction-controlled oedometer apparatuses are shown in terms of the effective stress σ' versus the void ratio e in Figure 8(a). The effective stress is defined using the Bishop's effective stress formulation [50] and the Khalili and Khabbaz [51] expression for the effective stress parameter. Since the suction stress is not in the main focus of this paper, more recent papers on this topic can be found elsewhere (e.g., see [52–55] and [56]). The results show that the effective stress approach works well for the results obtained on the undisturbed specimens in the range of the effective stress considered
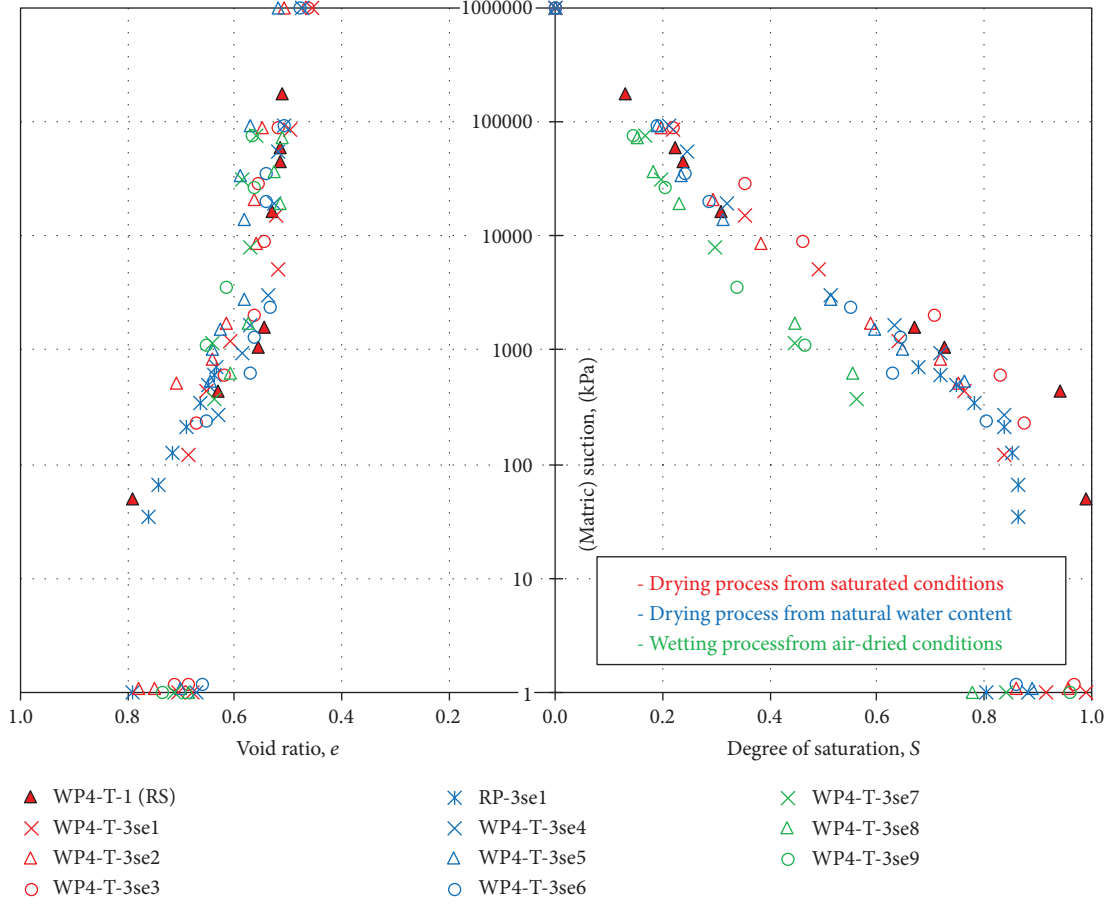
FIGURE 7: S-ψ-e measurements obtained using the WP4-T and pressure plate extractor apparatus.

(a)

(b)
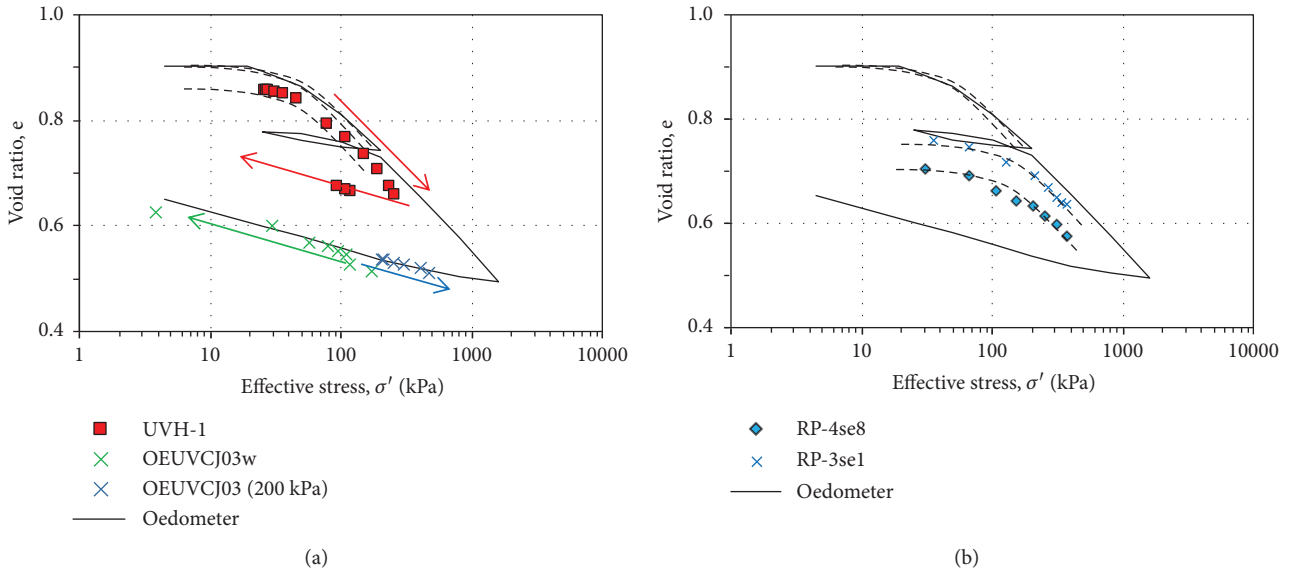
FIGURE 8: Results in terms of σ'-e compared with the conventional oedometer test results for the (a) UVH-1, OEUVCJ03w, and OEUVCJ03 and (b) RP-3se1 and RP4-se8 tests.

in these tests, during both the drying and the wetting processes. The undisturbed specimen in the UVH-1 test was saturated using the incremental back-pressurization procedure and consolidated at 25 kPa of net vertical stress. Next, the material was dried, increasing the matric suction up to 250 kPa, and then wetted to 80 kPa of matric suction. The

specimen in the UVH-1 test behaves as an over-consolidated material until the increase in suction causes the effective stress to increase beyond the preconsolidation pressure of 50 kPa (determined in the standard oedometer test). From this point, the results follow the slope of the virgin compression line ($C_c = 0.262$). Due to a decrease in the matric suction, the results along the wetting path follow the slope of the swelling curve ($C_s = 0.065$), suggesting a suction-over-consolidated material. A similar behavior is observed for the suction-over-consolidated specimen OEUVCJ03. The oven-dried sample for this test was equilibrated at 490 kPa of matric suction and incrementally wetted to 0 kPa of suction. During the wetting process, the specimen follows the swelling line obtained from the standard oedometer test. After absorbing water and reaching equilibration at atmospheric pressure, the specimen was consolidated at an effective stress of 200 kPa. Finally, the matric suction was increased to 350 kPa under a constant net vertical stress. Again, the specimen behaves as a preconsolidated material, following the slope of the swelling curve in the log (σ')-e plane. The results obtained using the standard pressure plate extractor on the samples that start the drying process from the natural water content, the RP-3se1 and RP-4se8 tests, are shown together with the results obtained using the conventional oedometer apparatus in Figure 8(b). Using the same formulation to determine σ', the preconsolidation pressure due to the suction seems to be slightly higher for this specimen.

Using the same formulation for the effective stress, the results obtained using the WP4-T device in the WP4-T-1 and WP4-T-3se1, WP4-T-3se2, WP4-T-3se3, WP4-T-3se4, WP4-T-3se5, and WP4-T-3se6 tests are shown in Figure 9. Depending on the achieved suction during the drying process, the undisturbed specimens from the WP4-T-3 test follow the same behavior pattern as seen in the results from the suction-controlled oedometer devices. A completely different behavior pattern is observed in the case of the remolded specimens in the WP4-T-1 test, in which the specimens behave as a normally consolidated material, undergoing a large reduction in the void ratio from the beginning of the drying process.

The Khalili and Khabbaz's effective stress parameter [51] seems to reasonably predict the effective stress for suctions up to 8000 kPa. However, using a fixed value for the fitting parameter (-0.55) seems to overestimate the increase in effective stress due to the increase in suction for suctions higher than 8000 kPa, according to the standard oedometer results.

5. Interpretation and Discussion

For modeling, comparison, and characterization purposes, it is useful to present the fragmented SWCC laboratory measurements in the form of a mathematical equation. Consequently, a continuous function is obtained for a wide range of suctions. A nonlinear regression analysis was performed using the "solver" add-in in Microsoft Excel on the results obtained during the drying and wetting process. The best-fit equation parameters were obtained by minimizing the
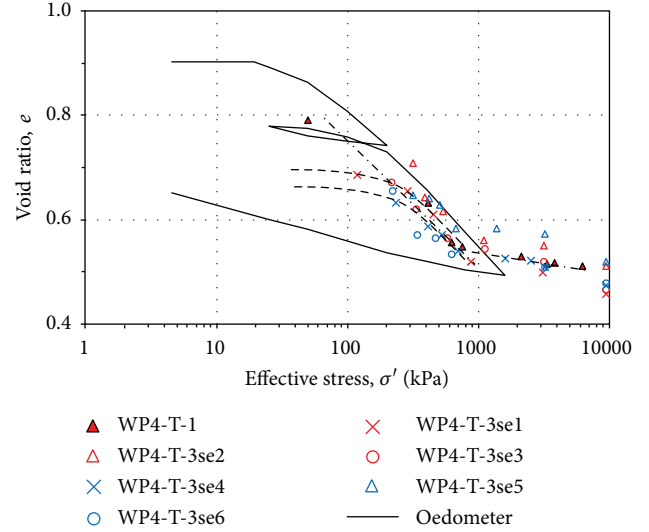

FIGURE 9: Results in terms of σ'-e compared with the conventional oedometer test results for the WP4-T-1 and WP4-T-3se1, WP4-T-3se2, WP4-T-3se3, WP4-T-3se4, WP4-T-3se5, and WP4-T-3se6 tests.

objective function with respect to the sum of the squared residuals (SSR). Smaller values of the SSR imply a better fit between the measured and the calculated values using the different SWCC equations. Three of the most frequently used equations were used to fit the obtained measurements: Brooks and Corey (BC) [41], van Genuchten (VG) [57], and Fredlund and Xing [58].

Brooks and Corey's SWCC equation [41] is given by

$$\theta = \theta_s,$$
$$\theta = \theta_s \left(\frac{\psi_b}{\psi} \right)^{\lambda}, \quad \psi \leq \psi_b, \psi > \psi_b, \tag{1}$$

where θ is the volumetric water content, θ_s is the saturated volumetric water content, ψ is the matric suction, ψ_b is the AEV of the soil, and λ is a constant.

Van Genuchten's SWCC equation [57] is given by

$$\theta = \theta_s \left[\frac{1}{1 + (\alpha\psi)^n} \right]^m, \tag{2}$$

where α, n, and m are constants.

Fredlund and Xing's SWCC equation [58] is given by

$$\theta = C(\psi) \frac{\theta_s}{\{\ln [e + (\psi/a)^n]\}^m}, \tag{3}$$

where a, n, and m are constants and $C(\psi)$ is a correction function defined as $C(\psi) = (-\ln (1 + (\psi/\psi_r))/\ln [1 + (1,000,000/\psi_r)]) + 1$.

Although a sharp discontinuity near saturation in the BC equation very often limits its practical application for modeling purposes, it is one of the oldest equations and is valuable for comparing the soil-water characteristics of different soils using the existing databases. As it is expected from the

obtained SWCC shape, the sigmoidal equations (VG and FX) performed better than the nonsigmodal (BC) equation, while the FX equation performed slightly better than the VG equation. A higher number of fitting parameters provided a stronger correlation, in all the considered cases.

5.1. Interpretation for the Drying Branch of the SWCC. The UVH-1 test results were used for the fitting in the initial part of the desorption branch of the SWCC and the determination of the saturated water content θ_s. Starting from the saturated conditions and using the results from only those tests with a net vertical stress of 25 kPa, the UVH-1 test results represent the upper bounding curve. The WP4-T-3 test measurements on initially saturated specimens were used to extend the SWCC in the region of higher suction values. The results obtained from the WP4-T-3se3 test plot higher than the rest of the results obtained starting from the saturated conditions. Although this is probably due to the specimen inhomogeneity, the exclusion of the WP4-T-3se3 resulted in a significant decrease in the SSR value, from 0.00270 to 0.00039 in the case of the FX equation and from 0.00283 to 0.00054 in the case of the VG equation. In the case of the BC equation, only a slight decrease in the SSR value, from 0.00702 to 0.00428, was obtained by omitting the WP4-T-3se3 results.

Using the three-parameter form of the FX equation ("correction" factor $C(\psi) = 1$ [58]) causes an increase in the SSR value, from 0.00039 to 0.00058. Leaving the m and n parameters with no fixed relationship provides a slightly lower value of the SSR (0.00049) than that obtained when fixing these parameters using the relation $m = 1 - 1/n$ (0.00054), as used in van Genuchten [57] when trying to obtain a closed-form expression for hydraulic conductivity.

Considering that suctions as low as 2.1 and 1 kPa were used in the fitting procedure for the drying branch, the saturated volumetric water content did not affect the result significantly if kept as a constant value ($\theta_s = 0.4625$) or used as another fitting parameter for the VG and FX equations. However, due to the limitation of the BC equation to predict the water contents of soils that exhibit volume changes below the AEV, the best fit was obtained for a slightly lower value, $\theta_s = 0.450$.

The curves and best-fit parameters obtained by using the nonlinear regression procedure on measurements performed on undisturbed specimens in the (main) drying and wetting processes are presented in Tables 2 and 3 and Figure 10.

5.2. Interpretation for the Wetting Branch of the SWCC. The results obtained from the VE-1w and WP4-T-3se7, WP4-T-3se8, and WP4-T-3se9 tests were used to fit the parameters of all three equations in the case of the adsorption branch of the SWCC. Only the last measurement from the WP4-T-3se7 test, at a total suction of 370 kPa, was excluded from the nonlinear regression procedure, since it plots slightly lower in the ψ-θ plane, causing a slight increase in the SSR value from 0.00025 to 0.00047 for the FX equation. The results obtained from air-dried samples represent the lower bounding curve of the SWCC.

The highest volumetric water content of 0.335 did not change significantly if it was used as a fitting parameter for the FX and VG equations. Again, for the BC equation, the best fit was obtained for a slightly lower value (0.307).

5.3. Prediction Models. Two correlation models that predict the SWCC for plastic materials were tested on the obtained results along the drying and wetting paths. The FX equation parameters were obtained by using the correlation models proposed by Zapata [59] and Perera et al. [46]. Both models use only two basic material properties: the percent passing through number 200 sieve (P_{200}) and PI. The SSR values indicate the level of convergence between the measured and the model-predicted values. The obtained curves are shown in Figure 11, together with the previously derived best-fit FX curve. Table 4 presents the calculated parameters. During both the drying and the wetting process, the Zapata [59] model seems to perform reasonably well. On the other hand, the model proposed by Perera et al. [46] was unable to accurately predict the SWCC, especially for the drying process (SSR = 0.103). However, it was noted that this model performed much better if the clay percentage (30.3%) was used instead of P_{200} (Figure 11).

The hydromechanical features of the tested soil are compared with Guadalix Red silty clay [60], which is 48% silt and has $w_L = 33\%$ and PI = 13.6%. According to the SWCC parameters $\psi_r = 19.6$ MPa, $a = 242.1$, $n = 0.81$, and $m = 0.79$ [61], two materials closely match. If the obtained retention model parameters are compared with the average values for different soil textural groups [62], it is clear that the complex origin process generates interesting hydromechanical features in this soil. The saturated and residual volumetric water contents correspond to the silts, while $\alpha = 0.005$ and $n = 1.332$ are characteristic values for the silty clay and clay loam textures, respectively. On the other hand, the saturated shear strength parameters determined in the previous studies [2] are commonly obtained in materials with a significant portion of sandy particles.

6. Conclusions

The soil-water characteristic curves (SWCCs) of residual soil formed by the weathering process of a flysch rock mass have been presented in this paper. A wide range of pore sizes present in the material results in gentle slopes of the SWCC, covering a wide range of suctions. The measurements performed on air-dried specimens indicated suction values higher than 90 MPa for undisturbed specimens and 175 MPa for remolded specimens. Six different devices were used to perform measurements on the undisturbed specimens in all three characteristic zones of the SWCC. The water retention characteristics were determined using intact specimens undergoing the drying and wetting processes, from different initial water contents. Due to the volumetric changes that the material undergoes during the change in suction, all the tests were performed in a way that allowed both the total volume and the water volume to be measured. The effects of the overburden pressure on the soil-water characteristics were analyzed using the suction-controlled oedometers during the drying and wetting processes. The density measurements collected by using the wax dipping and water displacement

TABLE 2: Best-fit parameters and SSR values for the two- and three-parameter equations: the Brooks and Corey [41], van Genuchten [57], and Fredlund and Xing [58] equations.

| | | | | | Three-parameter equations | | | |
| | Brooks and Corey eq. [41] | | | | van Genuchten [57]; m* = 1 − 1/n | | | |
$\theta_{sd} = 0.4625$; $\theta_{sw} = 0.335$	SSR (r^2)	θ_r	ψ_b	λ	SSR (r^2)	θ_r	α	n	m^*
Bounding drying curve	0.00428	0	99.491	0.260	0.00054	0.013	0.005	1.332	0.249
Bounding wetting curve	0.00203	0	72.567	0.246	0.00033	0.000	0.008	1.280	0.219

TABLE 3: Best-fit parameters and SSR values for the four-parameter equations: the van Genuchten [57] and Fredlund and Xing [58] equations.

| | | | | | Four-parameter equations | | | |
| | van Genuchten [57]; m free | | | | Fredlund and Xing [58] | | | |
$\theta_{sd} = 0.4625$; $\theta_{sw} = 0.335$	SSR (r^2)	θ_r	α	n	m	SSR (r^2)	ψ_r	a	n	m
Bounding drying curve	0.00049	0.028	0.004	1.186	0.323	0.00039	177720.9	299.753	1.073	0.907
Bounding wetting curve	0.00021	0.011	0.005	0.973	0.348	0.00022	254164.3	284.117	0.859	1.053

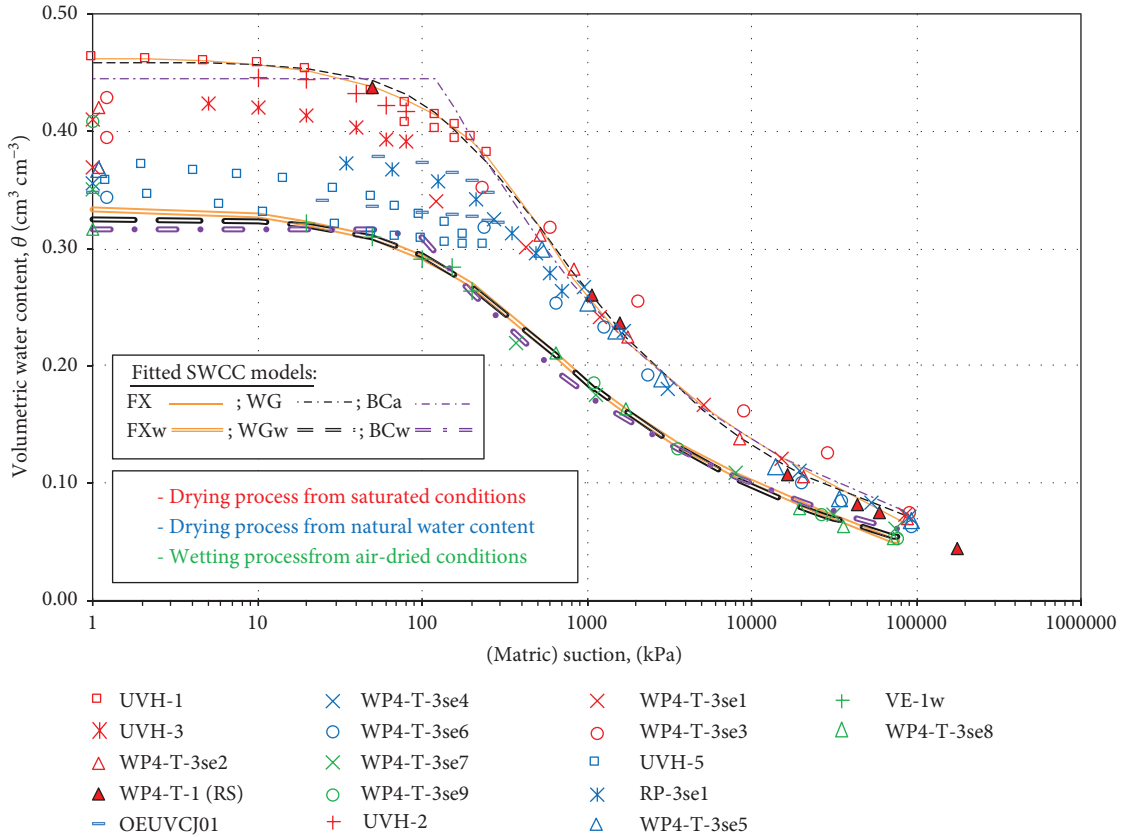FIGURE 10: Best-fit Brooks and Corey [41], van Genuchten [57], and Fredlund and Xing [58] equations plotted with the measurements in ψ-θ plane.

technique and standard null-type pressure plate devices provided the SWCC-θ measurements for the undisturbed specimens undergoing drying, for up to 700 kPa of matric suction. The density measurements combined with the WP4-T device provided the water retention characteristics of the undisturbed specimens undergoing the drying or wetting process for suction values lower than 1 MPa and higher than 175 MPa. The obtained results showed a good agreement with the measurements performed by using the axis translation technique for suction values as low as 300 kPa, suggesting that the use of undisturbed specimens should be preferred in this case. The measurements performed with the WP4-T device from the remolded specimens converge with the measurements obtained from the undisturbed specimens at suction values higher than 1 MPa during the drying process and 6 MPa during the wetting process. A nonlinear regression
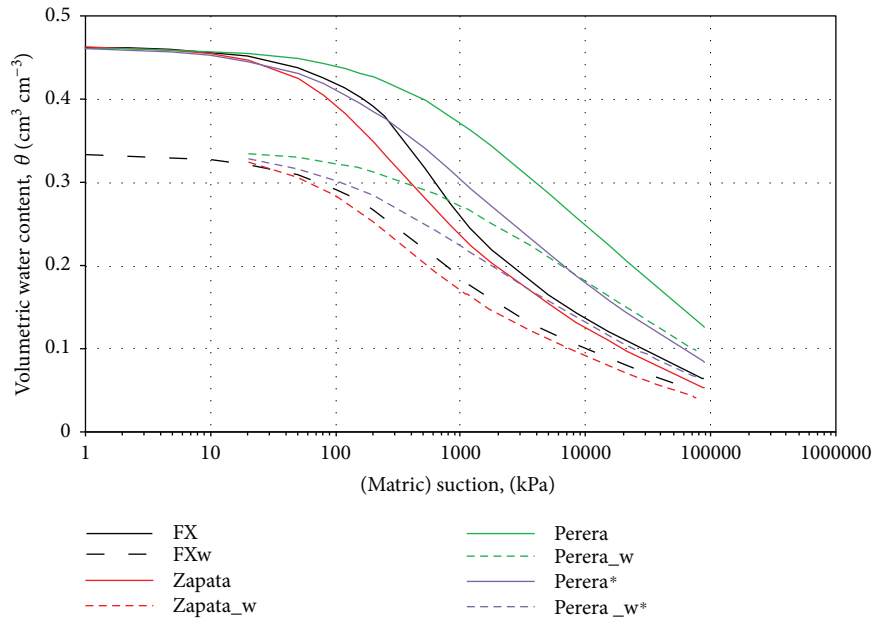
FIGURE 11: Performance of the two prediction models compared with the Fredlund and Xing [58] equation obtained by using the nonlinear regression procedure on the measured data.

TABLE 4: Fredlund and Xing [58] equation parameters and SSR values obtained using the Zapata [59] and Perera et al. [46] correlation models for the SWCC.

	Fredlund and Xing [58] equation					
$\theta_{sd} = 0.4625$; $\theta_{sw} = 0.335$	SSR_d	SSR_w	ψ_{rf}	a_f	n_f	m_f
Zapata correlation [59]	0.01109	0.00227	5385.4	121.911	1.085	0.690
Perera et al. correlation [46]	0.10287	0.07522	500.0	123.599	0.587	0.116
Perera correlation [46]*	0.01526	0.01237	500.0	91.597	0.801	0.326

*Clay percentage, C (%) instead of P_{200}

analysis was performed on the results obtained during the drying and wetting processes to obtain the best-fit equation and parameters of three of the most commonly used SWCC equations: Brooks and Corey [41], van Genuchten [57], and Fredlund and Xing [58]. Obtained results are valuable for further research of rainfall-induced landslides in flysch slopes. Rainfall infiltration through initially unsaturated residual soil can be simulated as a transient process in order to investigate the influence of different initial conditions (moisture contents) of the geotechnical cross-section and rainfall characteristics on the pore water pressure changes and, consequently, changes in slope stability state in time.

Data Availability

All the data obtained in this study are included in the article. Graphically presented data are available in text form from the corresponding author upon request.

Conflicts of Interest

The authors declare that there are no conflicts of interest regarding the publication of this paper.

Acknowledgments

References

[1] Ž. Arbanas, S. Dugonjić Jovančević, M. Vivoda, and S. Mihalić Arbanas, "Study of landslides in flysch deposits of North Istria,

Croatia: landslide data collection and recent landslide occurrences," in *Proceedings of the WLF 3, Landslide Science for a Safer Geoenvironment, Volume 1: The International Programme on Landslides (IPL)*, K. Sassa, P. Canuti, and Y. Yin, Eds., pp. 89–94, Springer, Switzerland, 2014.

[2] M. Vivoda Prodan, M. Mileusnić, S. Mihalić Arbanas, and Ž. Arbanas, "Influence of weathering processes on the shear strength of siltstones from a flysch rock mass along the northern Adriatic coast of Croatia," *Bulletin of Engineering Geology and the Environment*, vol. 76, no. 2, pp. 695–711, 2017.

[3] M. Vivoda Prodan and Ž. Arbanas, "Weathering influence on properties of siltstones from Istria, Croatia," *Advances in Materials Science and Engineering*, vol. 2016, Article ID 3073202, 15 pages, 2016.

[4] S. Vanapalli, "Simple test procedures and their interpretation in evaluating the shear strength of an unsaturated soil," PhD thesis, University of Sasatchewan, Canada, 1994.

[5] P. Marinos and E. Hoek, "Estimating the geotechnical properties of heterogeneous rock masses such as flysch," *Bulletin of Engineering Geology and the Environment*, vol. 60, no. 2, pp. 85–92, 2001.

[6] S. Dugonjić Jovančević and Ž. Arbanas, "Recent landslides on the Istrian Peninsula, Croatia," *Natural Hazards*, vol. 62, no. 3, pp. 1323–1338, 2012.

[7] D. M. Cruden and D. J. Varnes, "Landslide types and processes," *Landslides: Investigation and Mitigation (Special Report)*, A. K. Turner and R. L. Schuster, Eds., National Research Council, Transportation and Research Board Special Report 247, Washington, DC, USA, 1996.

[8] O. Hungr, S. Leroueil, and L. Picarelli, "The Varnes classification of landslide types, an update," *Landslides*, vol. 11, no. 2, pp. 167–194, 2014.

[9] S. Mihalić Arbanas, M. Sečanj, S. Bernat Gazibara, M. Krkač, and Ž. Arbanas, "Identification and mapping of the Valići Lake Landslide (Primorsko-Goranska County, Croatia)," *Proceedings of the 2nd Regional Symposium on Landslides*, 2017, pp. 197–202, Belgrade, May 2015.

[10] G. Tosatti, D. Castaldini, M. Barbieri et al., "Additional causes of seismical related landslides in the Northern Apennines, Italy," *Revista de Geomorfologie*, vol. 10, pp. 5–21, 2008.

[11] E. Gil and M. Dlugosz, "Threshold values of rainfalls triggering selected deep-seated landslides in the polish flysch Carpathians," *Studia Geomorphologica Carpatho-Balcanica*, vol. 40, pp. 21–43, 2006.

[12] M. Polemio, "Rainfall and Senerchia Landslides, Southern Italy," in *ABMS-ISSMFE, 2nd Panamerican Symposium on Landslides*, pp. 175–184, Rio De Janeiro, Brasil, January 1997.

[13] J. Logar, K. Fifer Bizjak, M. Kočevar, M. Mikoš, M. Ribičič, and B. Majes, "History and present state of the Slano Blato Landslide," *Natural Hazards and Earth System Sciences*, vol. 5, no. 3, pp. 447–457, 2005.

[14] J. Klimeš, I. Baron, T. Panek et al., "Investigation of recent catastrophic landslides in the flysch belt of Outer Western Carpathians (Czech Republic): progress towards better hazard assessment," *Natural Hazards and Earth System Sciences*, vol. 9, no. 1, pp. 119–128, 2009.

[15] Ž. Arbanas, S. Mihalić Arbanas, M. Vivoda Prodan et al., "Preliminary investigations and numerical simulations of a landslide reactivation," in *Advancing Culture of Living with Landslides. WLF 2017*, M. Mikos, B. Tiwari, Y. Yin, and K. Sassa, Eds., pp. 649–657, Springer, Cham, 2017.

[16] ASTM D854-14, *Standard Test Methods for Specific Gravity of Soil Solids by Water Pycnometer*, ASTM International, West Conshohocken, PA, USA, 2014.

[17] ASTM D1140-17, *Standard Test Methods for Determining the Amount of Material Finer than 75-μm (No. 200) Sieve in Soils by Washing*, ASTM International, West Conshohocken, PA, USA, 2017.

[18] ASTM D7928-17, *Standard Test Method for Particle-Size Distribution (Gradation) of Fine-Grained Soils Using the Sedimentation Analysis*, ASTM International, West Conshohocken, PA, USA, 2017.

[19] ASTM D4318-17, *Standard Test Methods for Liquid Limit, Plastic Limit, and Plasticity Index of Soils*, ASTM International, West Conshohocken, PA, USA, 2017.

[20] ASTM D2487-11, *Standard Practice for Classification of Soils for Engineering Purposes (Unified Soil Classification System)*, ASTM International, West Conshohocken, PA, USA, 2011.

[21] S. Salager, M. S. el Youssoufi, and C. Saix, "Definition and experimental determination of a soil-water retention surface," *Canadian Geotechnical Journal*, vol. 47, no. 6, pp. 609–622, 2010.

[22] D. Fredlund and S. L. Houston, *Interpretation of Soil-Water Characteristic Curves When Volume Change Occurs as Soil Suction Is Changed*, Taylor & Francis Group, Cartagena de Indias, Colombia, 2013.

[23] C. W. W. Ng and Y. W. Pang, "Influence of stress state on soil-water characteristics and slope stability," *Journal of Geotechnical and Geoenvironmental Engineering*, vol. 126, no. 2, pp. 157–166, 2000.

[24] A. Tarantino, "A water retention model for deformable soils," *Geotechnique*, vol. 59, no. 9, pp. 751–762, 2009.

[25] S. K. Vanapalli, D. G. Fredlund, and D. E. Pufahl, "The influence of soil structure and stress history on the soil-water characteristics of a compacted till," *Geotechnique*, vol. 49, no. 2, pp. 143–159, 1999.

[26] X. Zhang, M. Mavroulidou, and M. J. Gunn, "A study of the water retention curve of lime-treated London Clay," *Acta Geotechnica*, vol. 12, no. 1, pp. 23–45, 2017.

[27] G. W. Gee, M. D. Campbell, G. S. Campbell, and J. H. Campbell, "Rapid measurement of low soil water potentials using a water activity meter," *Soil Science Society of America Journal*, vol. 56, no. 4, pp. 1068–1070, 1992.

[28] R. Cardoso, E. Romero, A. Lima, and A. Ferrari, "A comparative study of soil suction measurement using two different high-range psychrometers," in *Experimental Unsaturated Soil Mechanics. Springer Proceedings in Physics, vol 112*, T. Schanz, Ed., pp. 79–93, Springer, Berlin, Heidelberg, 2007.

[29] E.-C. Leong, S. Tripathy, and H. Rahardjo, "Total suction measurement of unsaturated soils with a device using the chilled-mirror dew-point technique," *Geotechnique*, vol. 53, no. 2, pp. 173–182, 2003.

[30] V. K. S. Thakur, S. Sreedeep, and D. N. Singh, "Laboratory investigations on extremely high suction measurements for fine-grained soils," *Geotechnical and Geological Engineering*, vol. 24, no. 3, pp. 565–578, 2006.

[31] M. Tuller and D. Or, "Water films and scaling of soil characteristic curves at low water contents," *Water Resources Research*, vol. 41, no. 9, pp. 1–6, 2005.

[32] S. S. Agus and T. Schanz, "Comparison of four methods for measuring total suction," *Vadose Zone Journal*, vol. 4, no. 4, pp. 1087–1095, 2005.

[33] G. S. Campbell, D. M. Smith, and B. L. Teare, "Application of a dew point method to obtain the soil-water characteristics," in *Experimental Unsaturated Soil Mechanics. Springer Proceedings in Physics, vol 112*, T. Schanz, Ed., pp. 71–77, Springer, Berlin, Heidelberg, 2007.

[34] K. A. Bocking and D. Fredlund, "Limitations of the axis translation technique," *Fourth International Conference on Expansive Soils*, 1980, pp. 117–135, Denver, CO, USA, June 1980.

[35] ASTM D7263-09, *Standard Test Methods for Laboratory Determination of Density (Unit Weight) of Soil Specimens*, ASTM International, West Conshohocken, PA, USA, 2009.

[36] ASTM D6836-02, *Standard Test Methods for Determination of the Soil Water Characteristic Curve for Desorption Using a Hanging Column, Pressure Extractor, Chilled Mirror Hygrometer, and/or Centrifuge*, ASTM International, West Conshohocken, PA, USA, 2002.

[37] U. Schindler, "Ein schnellverfahren zur messung der wasserleitfähigkeit im teilgesättigten boden an stechzylinderproben. s.l.," *Archiv für Acker- und Pflanzenbau und Bodenkunde*, vol. 24, pp. 1–7, 1980.

[38] U. Schindler, W. Durner, G. von Unold, L. Mueller, and R. Wieland, "The evaporation method: extending the measurement range of soil hydraulic properties using the air-entry pressure of the ceramic cup," *Journal of Plant Nutrition and Soil Science*, vol. 173, no. 4, pp. 563–572, 2010.

[39] A. Pasha, A. Khoshghalb, and N. Khalili, *Common Mistakes in Determination of Air Entry Value from Gravimetric Water Content Based Soil-Water Characteristic Curve*, CRC Press, Guilin, China, 2015.

[40] H. Q. Pham and D. G. Fredlund, *A Volume-Mass Constitutive Model for Unsaturated Soils*, College of Graduate and Postdoctoral Studies, Saskatoon, 2005.

[41] R. Brooks and A. Corey, *Hydraulic Properties of Porous Media*, Hydrology Papers, Colorado State University, 1964.

[42] M. Wijaya, E. C. Leong, and H. Rahardjo, "Effect of shrinkage on air-entry value of soils," *Soils and Foundations*, vol. 55, no. 1, pp. 166–180, 2015.

[43] D. G. Fredlund, H. Rahardjo, and M. D. Fredlund, *Unsaturated Soil Mechanics in Engineering Practice*, John Wiley & Sons, Inc., New Jersey, Hoboken, 2012.

[44] D. G. Fredlund, D. Sheng, and J. Zhao, "Estimation of soil suction from the soil-water characteristic curve," *Canadian Geotechnical Journal*, vol. 48, no. 2, pp. 186–198, 2011.

[45] T.-F. Chiu and C. D. Shackelford, "Unsaturated hydraulic conductivity of compacted sand-kaolin mixtures," *Journal of Geotechnical and Geoenvironmental Engineering*, vol. 124, no. 2, pp. 160–170, 1998.

[46] Y. Perera, C. Zapata, W. Houston, and S. Houston, "Prediction of the soil-water characteristic curve based on grain-size-distribution and index properties," in *Geotechnical Special Publications 130–142 & GRI-18; Proceedings of the Geo-Frontiers 2005 Congress*, pp. 49–60, Austin, TX, USA, October 2005.

[47] M. Clarizia, G. Gulla, and G. Sorbino, "Sui meccanismi di innesco dei soil slip," in *Proceeding of Convegno Internazionale "La prevenzione delle catastrofi idrogeologiche: il contributo della ricerca scientifica" ALBA 96*, pp. 585–597, Alba, Italia, November 1996.

[48] G. B. Crosta and P. Fratini, "Rainfall thresholds for triggering soil slips and debris flow," in *Proceedings of the 2nd EGS Plinius Conference on Mediterranean Storms: Publication CNR GNDCI*, pp. 463–487, Siena, 2001.

[49] F. Guzzetti, S. Peruccacci, M. Rossi, and C. P. Stark, "The rainfall intensity–duration control of shallow landslides and debris flows: an update," *Landslides*, vol. 5, no. 1, pp. 3–17, 2008.

[50] A. W. Bishop, "The principle of effective stress," *Teknisk Ukeblad*, vol. 106, no. 39, pp. 859–863, 1959.

[51] N. Khalili and M. H. Khabbaz, "A unique relationship for χ for the determination of the shear strength of unsaturated soils," *Geotechnique*, vol. 48, no. 5, pp. 681–687, 1998.

[52] S. Oh, N. Lu, Y. K. Kim, S. J. Lee, and S. R. Lee, "Relationship between the soil-water characteristic curve and the suction stress characteristic curve: experimental evidence from residual soils," *Geotechnical and Geological Engineering*, vol. 138, no. 1, pp. 47–57, 2012.

[53] P. Chen, C. Wei, J. Liu, and T. Ma, "Strength theory model of unsaturated soils with suction stress concept," *Journal of Applied Mathematics*, vol. 2013, Article ID 756854, 10 pages, 2013.

[54] E. Nikooee, G. Habibagahi, S. M. Hassanizadeh, and A. Ghahramani, "Effective stress in unsaturated soils: a thermodynamic approach based on the interfacial energy and hydromechanical coupling," *Transport in Porous Media*, vol. 96, no. 2, pp. 369–396, 2013.

[55] W. J. Likos, "Effective stress in unsaturated soil: accounting for surface tension and interfacial area," *Vadose Zone Journal*, vol. 13, no. 5, article vzj2013.05.0095, 2014.

[56] R. Greco and R. Gargano, "A novel equation for determining the suction stress of unsaturated soils from the water retention curve based on wetted surface area in pores," *Water Resources Research*, vol. 51, no. 8, pp. 6143–6155, 2015.

[57] M. T. van Genuchten, "A closed-form equation for predicting the hydraulic conductivity of unsaturated soils," *Soil Science Society of America Journal*, vol. 44, no. 5, pp. 892–898, 1980.

[58] D. G. Fredlund and A. Xing, "Equations for the soil-water characteristic curve," *Canadian Geotechnical Journal*, vol. 31, no. 4, pp. 521–532, 1994.

[59] C. E. Zapata, *Uncertainty in Soil-Water-Characteristic Curve and Impacts on Unsaturated Shear Strength Predictions*, PhD Dissertation, Arizona State University, Tempe, AZ, USA, 1999.

[60] V. Escario and J. Juca, "Strength and deformation of partly saturated soils," in *Proceedings of the 12th International Conference on Soil Mechanics and Foundation Engineering*, pp. 43–46, Rio de Janeiro, August 1989.

[61] S. Vanapalli, W. Sillers, and M. Fredlund, "The meaning and relevance of residual state to unsaturated soils," in *51st Canadian Geotechnical Conference*, Edmonton, Alberta, October 1988.

[62] R. F. Carsel and R. S. Parrish, "Developing joint probability distributions of soil water retention characteristics," *Water Resources Research*, vol. 24, no. 5, pp. 755–769, 1988.

Research Article

Seepage Behavior of an Inclined Wall Earth Dam under Fluctuating Drought and Flood Conditions

Wei Ye,[1] **Fuheng Ma** ⓘ**,**[1,2] **Jiang Hu** ⓘ**,**[1] **and Ziyang Li** ⓘ[1]

[1]*Nanjing Hydraulic Research Institute, Nanjing 210029, China*
[2]*State Key Laboratory of Hydrology-Water Resources and Hydraulic Engineering, Nanjing 210029, China*

Correspondence should be addressed to Jiang Hu; huj@nhri.cn

Most dam seepage safety analyses evaluate a stable seepage field, infiltration line, and seepage flow. However, under fluctuating drought-flood conditions, the soil surface becomes cracked, making it too complicated to conduct a routine seepage analysis. In this paper, the seepage characteristics of an inclined wall dam under fluctuating drought-flood conditions were studied using a large-scale physical model. The results show that after drought, the permeability coefficient of clay with low crack development was smaller than that of the saturated permeability, but for cracked areas, with high permeability, permeability coefficients were much larger than those of the saturated permeability. As the water level rose, cracks could heal themselves, but this healing was superficial, and the soil could no longer return to its predrought state. After crack healing, the integrity of the dam slope was much less than its original state. In addition, the formation of cracks increased the porosity of the soil and changed the soil permeability, which permanently weakened the antiseepage performance of the clay soil. This study evaluated the seepage flow behavior of an inclined wall dam under fluctuating drought-flood conditions, and results can be used to monitor and protect the weak parts of seepage dams in practical engineering projects.

1. Introduction

Influenced by global climate change, the frequency of extreme events like droughts and floods is increasing [1, 2], and the cycle is getting shorter and shorter [3, 4]. These extreme events bring great challenges for water conservancy facilities, especially for earth dams. By analyzing climate status charts and comparing the highest and the lowest dam failure rates in Shanxi and Hunan Province, China, respectively, it was found that a large amount of precipitation after a long dry period will increase the risk of reservoir failure accidents [5, 6]. Therefore, a study on the effects of fluctuating drought-flood conditions on the safety of dams is crucial.

In general, extreme events can be divided into two processes. The first is drought, and the second is heavy rainfall, causing flooding. Different processes have different influences on an earth dam, but the main effect of the whole sequence is the seepage problem, which is a very important factor leading to dam failure [7]. When suffering drought,

the water level drops, and the reservoir is exhausted. Then, the low water level and drying of the reservoir cause cracks in the clay of the inclined wall and horizontal blanket structures. Development of cracks damages the continuity and integrity of the impermeable structures and weakens its antiseepage performance. So, a seepage analysis with the presence of cracks is of widespread concern.

For several decades, researchers have studied seepage through cracks and made fruitful advances. The occurrence of cracks changes the boundary conditions of the soil, thus affecting the infiltration of water flow. Based on this, seepage of water in cracked soil can be divided into two types: (a) vertical infiltration through the soil surface and (b) transverse seepage through cracks [8]. Moreover, the appearance of a crack breaks the integrity of the soil, so a discrete crack model was established based on the concept of discrete cracks to carry out seepage calculations [9]. This model elaborates the basic principle of two-phase seepage flow, and a finite element format of the model was established based on the Galerkin weighted residual method. When water flows into
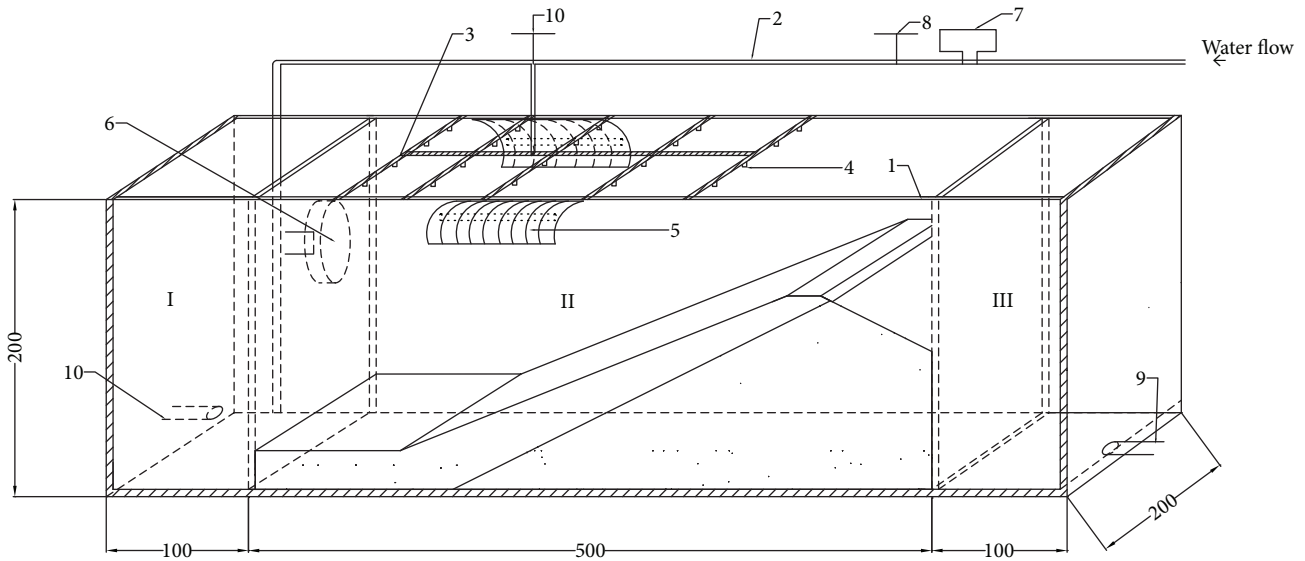
FIGURE 1: Model system (unit: cm). 1: tempered glass cover, 2: water pipe, 3: rain line, 4: atomization nozzle, 5: long arc xenon lamp, 6: fan, 7: booster lamp, 8: flow meter, 9: drain hole, and 10: rainfall/impound valve.

a crack, the infiltration capacity in the cracks is controlled by several factors. To describe this phenomenon, the concept of critical rate of water-level rise was put forward by model tests, which illustrated that when the rate of water-level rise is faster than the critical value, fissure water flow rate increases, and the relationship between the water flow and the water level is not positive [10]. For different forms of cracks, to find out what factors affect infiltration, and considering the impact of crack parameters on water flow, a single crack test model was conducted using test equipment designed by Fan [11]. By changing the depth of the crack and the height of the water level, the relationships among infiltration volume, crack height, permeability coefficient, and crack depth were obtained. Water infiltration changes the moisture content of cracked soil, and this change determines the development of cracks, which influences seepage behavior. This is an interactive process [12]. Therefore, to accurately reflect the influence of crack position and size on seepage flow, Liu [13] calculated the permeability pressure and infiltration line and leakage of an inclined wall, from the perspective of a single crack, taking crack location and crack width as parameters. Using the method of superposition, he obtained the pressure distribution and seepage flow of multiple different positions and widths. Additionally, to investigate the influence of crack depth on the hydrodynamic characteristics of soil under flood conditions, Khandelwal et al. [14] proposed a two-dimensional numerical model to analyze the change in seepage for random crack depths. However, moisture contents increased linearly with depth and then sharply decreased at what was interpreted to be the bottom of the crack, and longitudinal tension cracks at or near the crest of a slope or earth embankment did not appear to relate to the development of a Rankine failure state in the underlying soil [15]. When they develop past a certain degree, cracks in a clay blanket can damage its impermeable barrier. The penetrating cracks may lead to an increase of

seepage pressure and leakage, causing the hazard of seepage failure. Therefore, the formation of cracks changes the method of water infiltration, and the crack morphology affects the method of water infiltration. Combined with a continuous change in external water level, seepage analysis of cracked soil becomes very complex.

Current research on seepage in cracked soil mainly has focused on crack development, calculations of crack seepage, and the effect of crack parameters on seepage flow [16–19], and the occurrence of heavy rainfall immediately after a drought and comparisons of seepage flow during different periods under these conditions have rarely been considered. Therefore, taking an inclined wall dam as an example, this study simulated fluctuating drought-flood conditions and evaluated the seepage behavior of the impermeable structure.

2. Materials and Methods

2.1. Testing System. The test compartment, as shown in Figure 1, was divided into two systems to simulate the fluctuating drought-flood conditions: the drying system, which consists of a long arc xenon lamp and fan to simulate drought, and the rainfall system, which contains a booster pump, flow meter, and rainfall pipeline to simulate heavy rainfall. The test compartment has external dimensions of $700 \, \text{cm} \times 200 \, \text{cm} \times 200 \, \text{cm}$ (length × width × height), divided into three sections. Section I is 100 cm in length, and it can accommodate direct water injection when the water level is required to rise rapidly. Section II is 500 cm in length, where instruments are installed and the model operates. Section III is 100 cm in length, and it is used to discharge the water infiltrated from upstream to downstream. The outer walls of the test compartment are made of tempered glass to facilitate the observation of internal model filling and to control the water level. To avoid the direct erosion of soil by rainwater, atomization nozzles were adopted. Instruments

used in the test included osmometers, soil pressure gauges, and matric suction sensors. Parameters of each instrument are shown in Table 1.

2.2. Testing Model

2.2.1. Similarity of the Model. The production of this test model is based on the first, second, and third similarity theorems in geometry. Model parameters that needed to be considered include density ρ, cohesion c, internal friction angle ϕ, permeability coefficient k, dimension L, side pressure p, and time t. After calculation, the similarity ratios of ϕ, c, and ρ are 1, which are in line with those in the practical engineering site at Zhaopingtai Reservoir in He'nan Province, China. The similarity ratio of t and k was $\sqrt{n}$. To satisfy the geometric similarity, the size of the model was reduced by $1:28$ during the design phase. The clay soil used in the test was selected from the actual project site, and therefore the density of the soil samples was consistent with the site to ensure that the model had the same degree of compaction as the original soil. The water level in the test corresponds to the measured water level in the actual reservoir, at a ratio of $1:28$. Additionally, sensors were installed as far as possible from the boundary so that the measurement results would be less affected by the boundary.

2.2.2. Model Production. The soil samples used in the test were excavated from the upstream dam slope of Zhaopingtai Reservoir in He'nan Province, China, and they mainly consisted of clay (23%) and silt (46.8%), with some sand (18.5%) and gravel (11.7%). The particle size distribution of soil is shown in Table 2 and Figure 2. The liquid limit and plasticity index of the soil were 30.8% and 17.1%, respectively, and the optimum moisture content and the maximum dry density were 19.2% and $1.4 \, \text{g/cm}^3$, respectively. The nonuniform coefficient was 17.5 (bigger than 5), and the curvature coefficient was 0.914 (close to 1), indicating that the soil body was easily compacted. The basic parameters of the soil are presented in Table 3.

The whole model was 165 cm in height, and the clay blanket was 40 cm thick and 110 cm long. Upstream and downstream slope gradients of the inclined wall were $1:2.5$ and $1:2$, respectively (Figure 3). The dam model was constructed by layers. To control the height of each layer, the elevation was marked on the outside wall of the tempered glass for reference. After the completion of the sand filling at the back end of the model, considering the difference in permeability coefficients between sand and clay, a mixed transition layer, about 10 cm thick, was added over the fine sand soil. After that, the clay blanket was added to the transitional material, and the slope gradient of the upstream side was $1:2.5$. However, because of the layered filling, it was difficult to control the slope of each layer, so after the whole construction was completed, slope shaping was carried out. Due to concern that burial of instruments would affect the quality of filling, the installation of instruments was carried out after the model filling was completed. All sensors embedded in the clay blanket and sand soil were at the same height,

TABLE 1: Test instrument parameters.

Sensor	Type	Range (kPa)	Precision
Osmometer	BWMK-0.015	0~40	±0.05%F·S
Earth pressure gauge	BW-0.2	0~600	±0.05%F·S
Matric suction sensor	FTC-100	1~1500	±5%F·S

located 10 cm up from the bottom of the model. Osmometers were buried downstream of the matric suction sensors, as shown in Figures 4 and 5 (S: osmometer, Z: matric suction sensor, and T: soil pressure gauge). All instruments were connected to an automatic data acquisition system.

3. Results and Discussion

The test was carried out in three steps. The first was to impound water to form a stable seepage field in the dam body. The second was to simulate drought conditions to promote the development of cracks in the soil, and the third step was to simulate rainfall to create fluctuating drought-flood conditions. When the first step was finished, the test was suspended due to the Chinese traditional Spring Festival holiday and all instruments were powered off. The length of the holiday was 13 days (from January 23, 2017, to February 4, 2017). The other two processes were conducted after the holidays.

3.1. Impoundment Period. In the impoundment period, the water level in the upper reach was 1.2 m (Figure 6). Changes of pore water pressure, soil pressure, and matric suction in the dam are shown in Figure 7.

The impoundment process started with the water injection in section I, and then the water level rose to the same height as the front end of the clay blanket, so the pore water pressure at the front of the blanket changed first and then increased at a fast rate. Then, 6 hours later, except for the front of the clay blanket and middle of the inclined wall, pore water pressure at all parts changed simultaneously. This is mainly because the water level in the upper reach had already submerged the clay blanket 6 hours earlier, so some water was infiltrating into the blanket and the bottom of the inclined wall but was not yet penetrating the impermeable body into the sand layer. At this time, the water level had not reached the middle of the inclined wall, but the water had begun to penetrate the impermeable body to the sand layer. Subsequently, the water level remained unchanged for about 12 hours and then increased again, and values of pore water pressure remained steady for a while, after which they underwent a sharp increase. In this process, the water level rose to the design value of 1.2 m, so in addition to the middle of the inclined wall, pore water pressure at all parts showed a dramatic upward trend and water seeped from the downstream end of the dam. Because of the high potential, no matter the change rate or amplitude, the pore water pressure in the middle of the inclined wall was smaller than that in other parts. The last stage of the test lasted for 50 hours, and then water in section I was drained, causing the water

TABLE 2: Particle composition of soil.

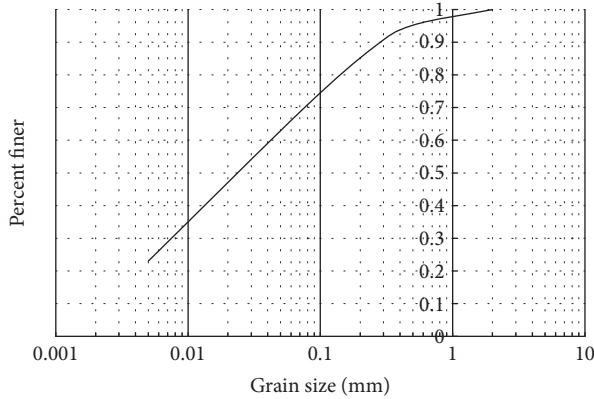| | Particle composition (%) | | | | | Boundary size (mm) | | | |
	Gravel (>2 mm)	Coarse sand (2 mm~0.50 mm)	Medium sand (0.50 mm~0.25 mm)	Fine sand (0.25 mm~0.075 mm)	Silt (0.075 mm~0.005 mm)	Clay (<0.005 mm)	Effective particle size (d10)	Intermediate particle size (d30)	Average particle size (d50)	Restricted particle size (d60)
	0.0	4.8	6.9	18.5	46.8	23.0	0.002	0.008	0.021	0.035

Figure 2: Particle size distribution.

Table 3: Physical properties of the soil.

Moisture content w (%)	Wet density ρ (g/cm^3)	Dry density ρ_d (g/cm^3)	Saturation permeability coefficient k (cm/s)
18.1	1.65	1.40	1.69×10^{-6}

level to drop rapidly, which resulted in a drop in pore water pressure.

For soil pressure, because the water content of the soil in upper part of the inclined wall did not change significantly after the impoundment, the soil weight did not change much as well, and the value of soil pressure basically remained steady. After the impoundment, due to the saturation and settling of sand in the lower layer, the clay layer was loosened and some settlement joints were formed in the middle of the dam. The widest settlement joint was located near the middle of the dam slope, from slightly above to slightly below the midpoint, and there were some transverse cracks near the vertical distribution of the main settlement joint. Formation of settlement joints resulted in large changes in soil pressure in the middle part of the inclined wall. As time went on, stress between the upper and lower parts of the settlement joints got smaller and smaller, and the pressure value in the middle decreased. Unlike the middle and upper parts, because of the increase in water content adding to the soil weight, the soil pressure at the lower part of the inclined wall increased. Thereafter, water in the dam body flowed out through the sand, and the weight of soil decreased, leading to the drop of soil pressure.

In many previous studies, it was mentioned that the matric suction in soil was affected by factors such as moisture content, confining pressure, and temperature. In this test, it took much time to make the dam model, so the moisture content of all parts could not be guaranteed the same. Affected by the filling quality and instrument embedment, the porosity was not uniform throughout the model. Also, the confining pressure at different locations was also slightly different. All of these factors have resulted in differences in initial matric suction across the dam model. Besides, the range of the FTC-100 sensor for measuring matric suction was 1 to 1500 kPa. The maximum difference of initial matric

suction (except the crest) was about 20 kPa, which accounted for about 1.3% of the measuring range, while the sensor measurement accuracy was ±5%. Therefore, the difference of initial suction could be considered acceptable. In order to measure the matric suction more accurately, it was necessary to ensure a certain thickness of soil around the sensor. However, the thickness of the soil at the crest was thin, and the size of the sensor was relatively big (the thickness of the crest was 10 cm, and the diameter of the instrument probe was about 6 cm). Therefore, the measured data was uncertain at the crest. In this period, the initial impoundment process increased the moisture content of the soil and caused a decrease in matric suction everywhere. Specifically, for the clay blanket, affected by the front water level in the upper reach, the variation in matric suction was not very large, with an amplitude of around 10 kPa. For the inclined wall, the moisture content of the clay soil increased as the water level rose, and the amplitude of matric suction was around 20–30 kPa. Finally, for the dam crest, it could be found from the measurement results that the initial matric suction at the crest differed greatly from other parts, so that the matric suction at the crest could not be compared with the rest at other parts directly. In the process of testing, the researchers had to step on the soil mass to carry out related work at the top of the dam, which caused a decrease in the volume of soil, and as a result, the water content at the dam crest was relatively large and the suction became small.

3.2. Drought Period.

The drought process and crack development are shown in Figure 8, and the results during this period are shown in Figure 9.

In the drought period, pore water pressure was roughly 0, except at the front of the clay blanket and in the sand layer. Due to the limitation of the drain equipment, the water could not be completely drained out of sections I and III, and vaporized water liquefied on the insulating film and then fell back into sections I and III, so some water remained in those sections, although the water level was very low. Additionally, according to the osmometer data, the water stayed in a stable state, while in the dry soil, due to the limited precision of the instrument, measurements showed microfluctuations.

Compared with the soil pressure in the impoundment period, the soil pressure in the middle of the inclined wall changed from 0 to 5 kPa after the saturation settling, and the measurements in the other parts basically maintained a stable state. As the test went on, soil pressure decreased, which resulted from the evaporation of water. After 4 days, the water content of the dam slope was measured, and this operation required test personnel to walk on the dam body, leading to a fluctuation in the soil pressure.

After the instruments were powered on in this period, a large change in the matric suction at the dam crest was found, confirming the uncertainty of the data measurement at the crest mentioned in Section 3.1. At the beginning of the drought, the suction value at the crest was close to that at other parts, but it was unreliable. The suction at the dam crest was only suitable for the observation of changes in the same process and could not be used to compare with each other across multiple periods. During this period, because water
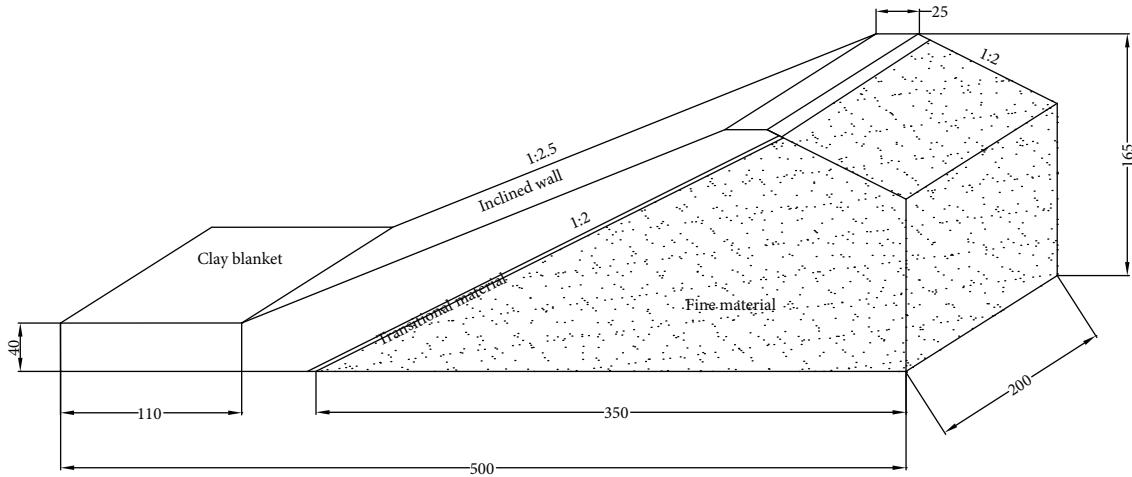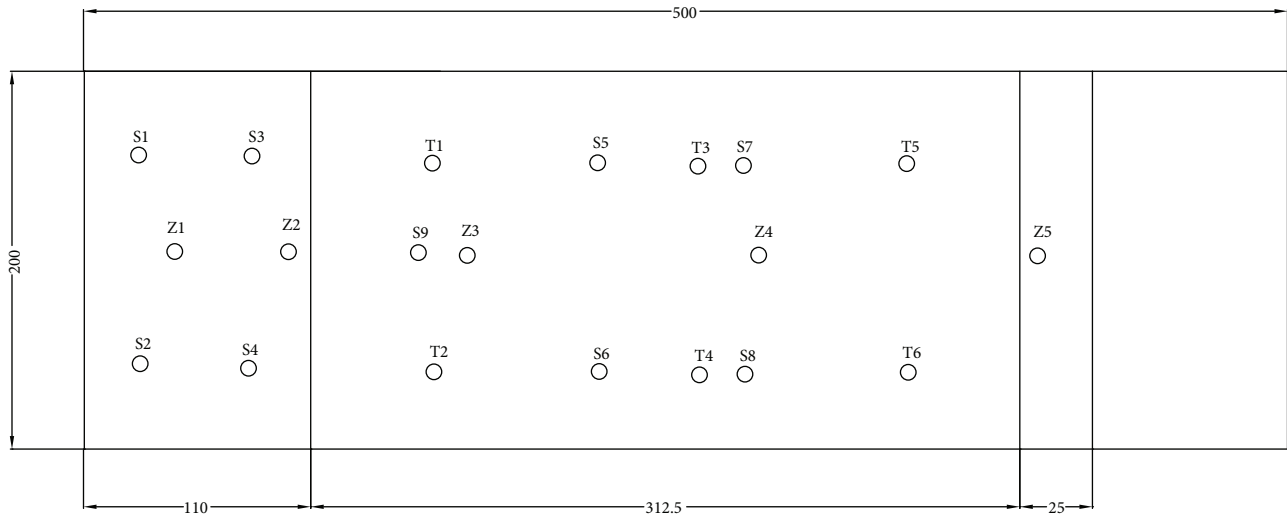
FIGURE 3: Test model (unit: cm).

FIGURE 4: Top view of sensor embedding (unit: cm). S: osmometer, Z: matric suction sensor, and T: soil pressure gauge.
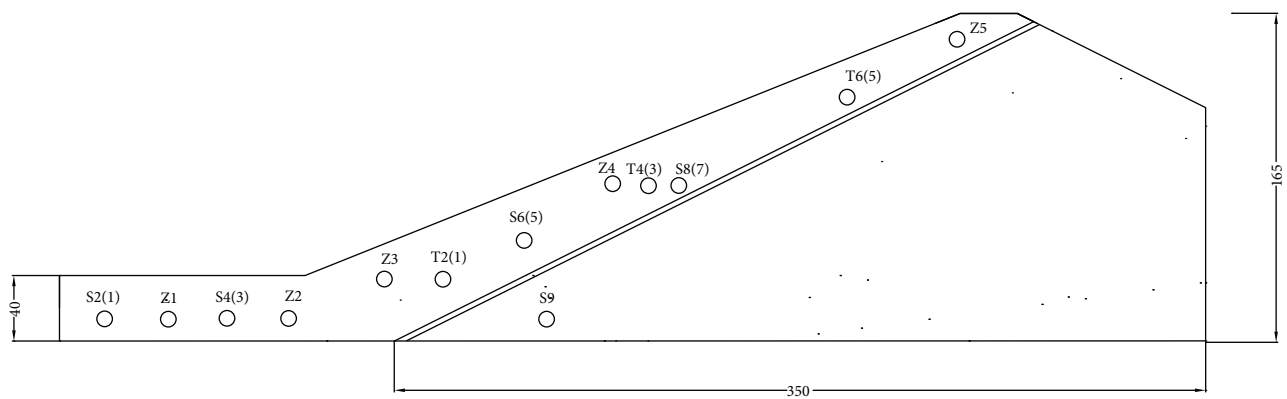

FIGURE 5: Front view of sensor embedding (unit: cm). S: osmometer, Z: matric suction sensor, and T: soil pressure gauge.

content at the front of the clay blanket was always high, the suction there increased at a low and steady rate. In the drying process, cracks formed at the connection between the front blanket and the inclined wall, so water content at the back end of the blanket decreased at a high rate of speed, resulting in an increase in suction at the back of the blanket at the

Figure 6: Initial water level.

beginning. As drying continued, due to the water supply in section I, water content at the front of the clay blanket did not decrease much more, so the matric suction remained at a relatively stable level. The lower part of the inclined wall was affected by the crack development. These cracks caused the suction to increase initially, but as they ceased widening, water content stabilized and the matric suction increased slowly. Because there were few cracks at the beginning of drying, the increase in matric suction at the middle part of the inclined wall was slow. As the cracks developed along the inclined wall, suction there increased rapidly. Above the five locations where most cracks developed, suction at the dam crest was the most stable. There was no direct lamplight over the dam crest when drying, so water content at this part changed slowly, leading to insignificant change in suction. During the later stage of drying, small cracks appeared in the dam crest. Considering that the clay layer at the dam crest was thin and the sensor was buried shallower, these small cracks also influenced the matric suction, so a slight increase in suction at the dam crest appeared.

3.3. Fluctuating Drought-Flood Period. The initial rainfall intensity was $1.5\,m^3/h$ during the fluctuating drought-flood period. However, after 5 minutes of rain, it was found that the rain was falling along the outer wall of the compartment, and there was a severe scour around the model. So, the rainfall intensity was reduced to $0.8\,m^3/h$, and the average rainfall was about 1000 mm/h per square meter, as shown in Figure 10. The results during this period are shown in Figure 11.

In this period, the soil was unsaturated, and the appearance of cracks led the water to flow through cracks first and then infiltrate into the soil. In the front of the clay blanket, because the water could infiltrate into the soil from the front and top of the blanket, pore water pressure changed significantly along with the water level, and the pressure was relatively large. At the back of the blanket, due to the development of cracks at the connection between the blanket and inclined wall, the water could seep into the model quickly along cracks. However, in this case, the soil was unsaturated, and the permeability coefficient of the soil was very small, so it was difficult for the water to flow in cracks to enter into the soil. That led to low pore water pressure. The lower part of

the inclined wall was also located near the connection between the blanket and inclined wall, so that the change was similar to that at the back of the blanket. Nonetheless, because of the placement of the instrument sensors, the pressure value was smaller than that at the back of the blanket. Additionally, in the middle of the inclined wall, cracks were more developed, and compared with pore water pressure at other parts, the pressure there was the first to decrease and was significantly affected by water level. Generally, due to the effect of drought, all soil was unsaturated, so it was difficult for the water to run through the model. However, from Figure 11(a), the pore water pressure at the bottom of the sand soil layer increased at the beginning of the rainfall process. This was surprising, but during the rainfall process, the rain fell directly to the lower sand soil layer, and because of the large permeability coefficient of the sand soil, the water flow could quickly converge at the bottom of the sand layer, which made the pore water pressure at the bottom increase. As the rain continued, the water level in section III rose gradually, but after it reached a certain height, it was lowered by artificial drainage. Repetition of this process resulted in the fluctuation of pore water pressure in the sandy soil layer.

After the rainfall process, soil pressure at the lower, middle, and upper parts of the inclined wall increased to varying degrees. Among these three areas, soil pressure at the lower part of the inclined wall had the largest growth, and the pressure value was also the largest. In the dam structure, the lower part withstood most of the weight of the slope, and the smallest gravitational force was on the upper part. Therefore, the lower part showed the largest soil pressure. However, for the middle part of the inclined wall, due to the wide cracks there, an unloading phenomenon occurred around the soil pressure gauge that led to the smallest pressure value. Even after cracks had been healed to some degree after the rainfall, the integrity of the soil did not return to its original state. Therefore, the soil pressure at the middle part remained the smallest during the whole process.

During the fluctuating drought-flood period, the matric suction decreased everywhere. Because few cracks developed in the blanket, the suction variation there was small. In contrast, cracks in the inclined wall were wider and more developed than those in other parts of the model dam, so changes of suction at the lower and middle parts of the inclined wall were relatively more obvious than those at other parts. Combined with the variable trend in seepage at this time, pore water pressure was not much changed as the matric suction changed modestly. However, for the middle of the inclined wall, pore water pressure was larger than that during the impoundment period, and both matric suction and pore water pressure changed greatly. Combining related studies with the results of the test, it could be found that the variation of matric suction reflected the change of the permeability coefficient. Therefore, there was a mutual reaction between the matric suction and the permeability coefficient. It was difficult to directly measure the permeability coefficient of each part of the model, but the measurement of the matric suction of the corresponding
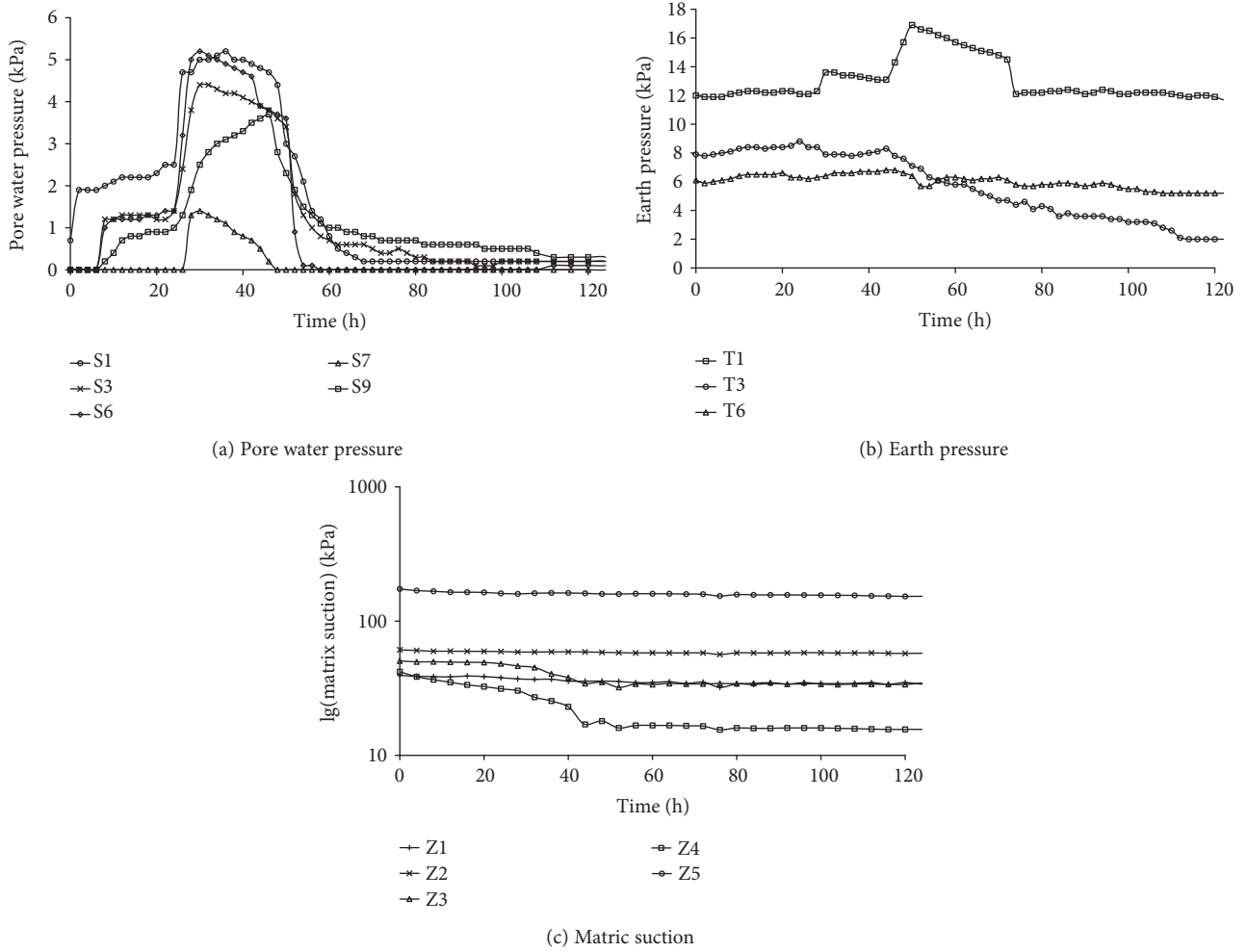
(a) Pore water pressure

(b) Earth pressure

(c) Matric suction

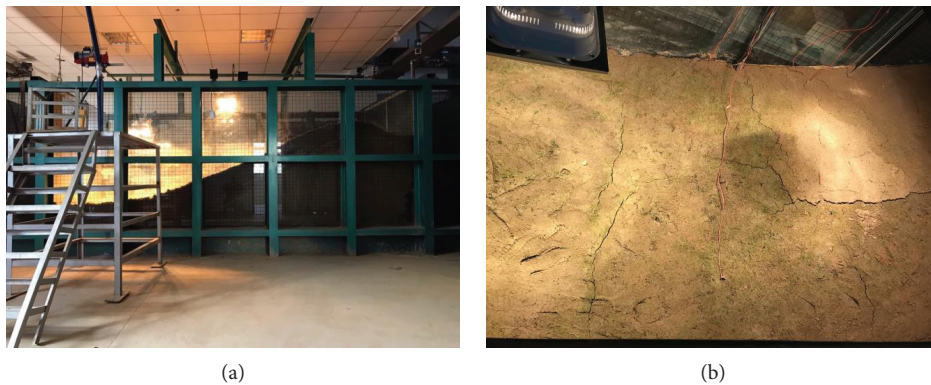Figure 7: Results during the impoundment period.

(a)

(b)

Figure 8: Simulated drought and crack development.

part was possible. The change of the permeability coefficient caused the water infiltration rate to change and affected the change rate of the moisture content, which influenced the variation trend and speed of the matric suction. According to the matric suction, the permeability coefficients at

different parts of the dam at different times could be inverted. When the permeability coefficient of the soil was low, it was hard for the water to penetrate into the soil and the pore water pressure increased slowly. At this time, the matric suction value was large. On the contrary, when

(a) Pore water pressure

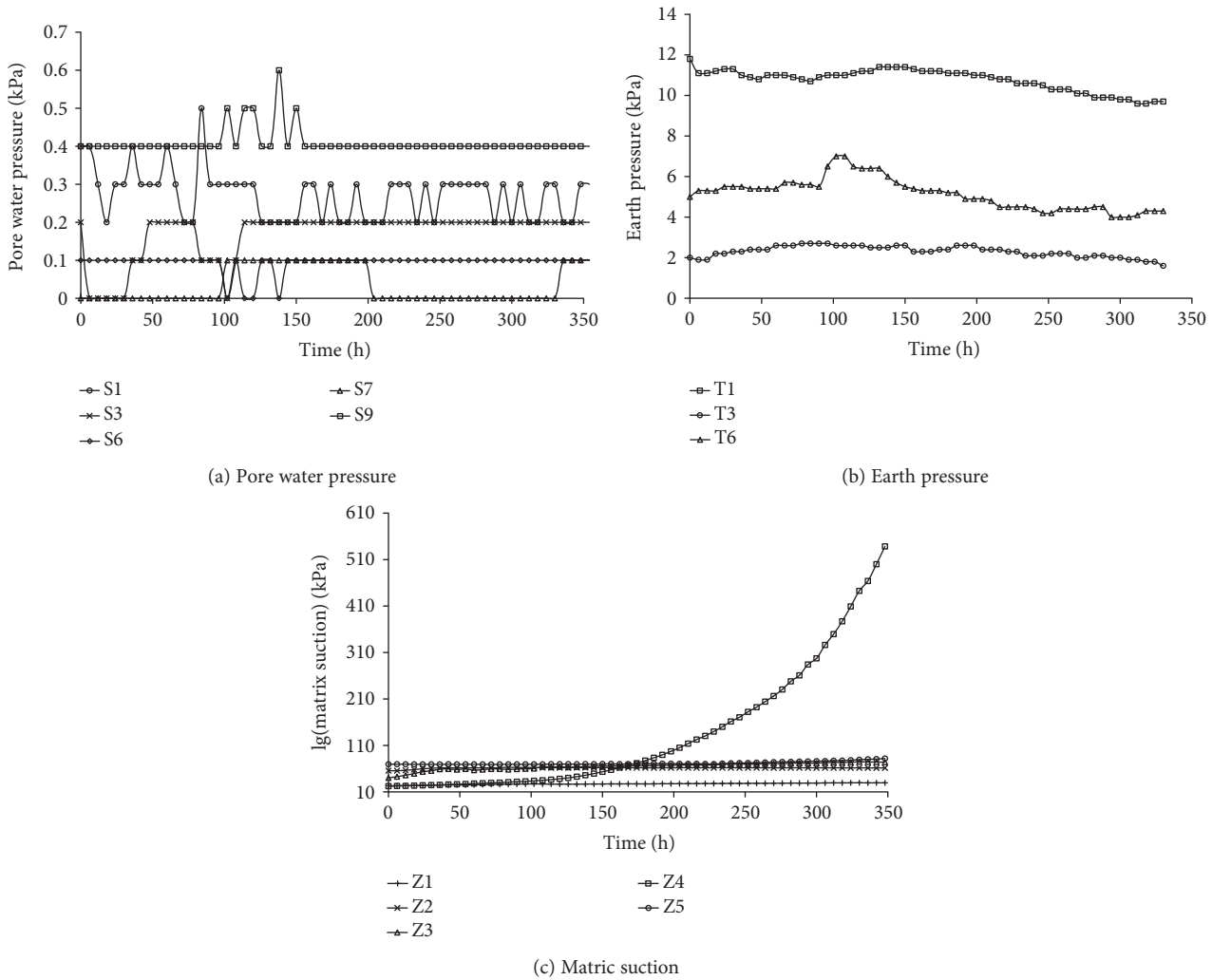
(b) Earth pressure

(c) Matric suction

FIGURE 9: Results during the drought period.

FIGURE 10: Rainfall and flooding process.

the permeability coefficient of the soil was high, it was easy for the water to penetrate into the soil, which showed that there were a rapid change rate and big amplitude of the pore water pressure. At this time, the matric suction was small.

4. Conclusion

Based on a physical model test, the behavior of seepage in an inclined wall dam under fluctuating drought-flood conditions was studied. The main conclusions are as follows:

(1) Cracks developed to different degrees over the surface of the clay soil after drought. Afterwards, the water filled cracks first and then seeped into the surrounding soil during the rainfall process. For areas with shallow or no cracks, the permeability coefficient of the clay layer decreased substantially. For the same water level and duration time, pore water pressure was smaller than that before the drought. However, in the region with cracks, the pore water pressure changed greatly and was much larger than that before the drought.

(2) Cracks could be healed during the rainfall process, but the integrity of the soil was no longer as good as it was in its original state. Therefore, the soil pressure

(a) Pore water pressure

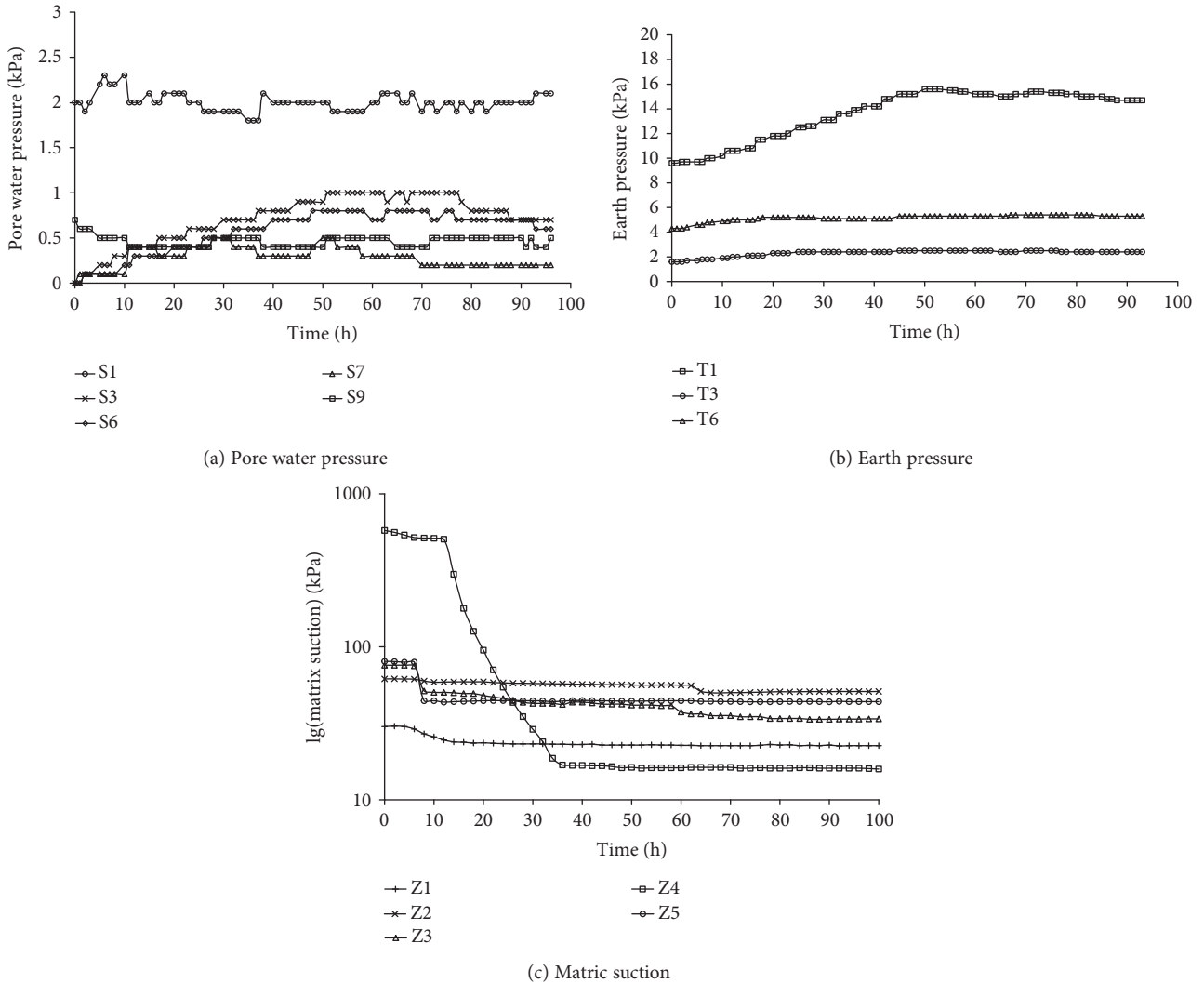(b) Earth pressure

(c) Matric suction

FIGURE 11: Results during the rainfall and flooding period.

in the inclined wall was incoherent, and the upper pressure could not be transferred to the bottom. In this situation, if the weight of the upper soil kept increasing, a landslide would occur.

(3) Changes in matric suction in the region with low development of cracks were relatively small. However, for areas with high crack development, matric suction decreased abruptly during the rainfall. Moreover, the decrease of suction increased the soil permeability in this region, and the weak seepage turned into saturated seepage. In general, this rapid transition in seepage would be detrimental to dam safety.

The results of this study will be useful in monitoring practical engineering projects, such as the Zhaopingtai Reservoir in He'nan Province, China, and other water conservancy dams with inclined earthen walls, and mitigating possible dam failures due to seepage problems.

Data Availability

The data used to support the findings of this study are available from the corresponding author upon request.

Conflicts of Interest

The authors declare that there is no conflict of interests regarding the publication of this article.

Acknowledgments

References

[1] A. Ahmed and M. Maddaus, "Understanding the impact of climate change on water resources sustainability—AWWA's Climate Change Committee report," in *World Environmental and Water Resources Congress 2011*, pp. 1347–1356, Palm Springs, CA, USA, 2011.

[2] J. C. Huang and P. Makar, "Reclamation's research on climate change impact on reservoir capacity," in *World Environmental and Water Resources Congress 2013*, pp. 1202–1212, Cincinnati, OH, USA, 2013.

[3] Y.-I. Moon, T.-S. Oh, M.-S. Kim, and S.-S. Kim, "A drought frequency analysis for Palmer Drought Severity Index using boundary kernel function," in *World Environmental and Water Resources Congress 2010*, pp. 2708–2716, Providence, RI, USA, 2010.

[4] J. Feng, D. Yan, C. Li, Y. Gao, and J. Liu, "Regional frequency analysis of extreme precipitation after drought events in the Heihe River Basin, Northwest China," *Journal of Hydrologic Engineering*, vol. 19, no. 6, pp. 1101–1112, 2014.

[5] X. Y. He, Z. Y. Wang, J. C. Huang, and L. Q. Ding, "Statistics and preliminary analysis of the dam crash of China reservoir," in *Proceedings of the 2005 Academic Annual Conference of China Water Conservancy Association-Risk Management of Water and Drought Disasters*, pp. 321–329, Qing Dao, China, 2005.

[6] X. Y. He, Z. Y. Wang, and J. C. Huang, "Analysis on the spatial distribution of dam-failure in China," *Journal of Catastrophology*, vol. 23, pp. 1–4, 2008.

[7] I. Sasanakul, S. L. Gassman, C. E. Pierce et al., "Dam failures from a 1000-year rainfall event in South Carolina," in *Geotechnical Frontiers 2017*, pp. 114–124, Orlando, FL, USA, 2017.

[8] V. Novák, J. Šimåunek, and M. T. van Genuchten, "Infiltration of water into soil with cracks," *Journal of Irrigation and Drainage Engineering*, vol. 126, no. 1, pp. 41–47, 2000.

[9] Z. Q. Huang, J. Yao, Y. Y. Wang, and K. Tao, "Numerical study on two-phase flow through fractured porous media," *Science China Technological Sciences*, vol. 54, no. 9, pp. 2412–2420, 2011.

[10] Z. H. Ge, B. H. Fan, Q. Y. Fen, and Y. H. Wang, "The study of water-flow in a clay fracture," *Journal of Geological*, vol. 67, pp. 159–167, 1993.

[11] J. L. Fan, *The Test Research on Soil Landslide's Stability Influenced by Crack Water*, Chengdu Univerisity of Technology, 2008.

[12] S. Kakuturu and L. N. Reddi, "Mechanistic model for self-healing of core cracks in earth dams," *Journal of Geotechnical and Geoenvironmental Engineering*, vol. 132, no. 7, pp. 890–901, 2006.

[13] Z. F. Liu, "Seepage calculation of pavement cracks," *Journal of Jiang Xi Water Technology*, vol. 22, pp. 7–22, 1986.

[14] S. Khandelwal, M. Sanchez, and Z. Medina-Cetina, "Effect of depth of desiccation cracks on earth embankments," in *Geo-Congress 2013*, pp. 800–803, San Diego, CA, USA, 2012.

[15] R. L. Handy and M. Lustig, "Tension cracks in a compacted clay embankment," *Journal of Geotechnical and Geoenvironmental Engineering*, vol. 143, no. 7, article 06017006, 2017.

[16] Z. L. Ge, "Leaking and warping through cracks of earth dam blanket," *Hydro-Science and Engineering*, vol. 41, pp. 36–44, 1982.

[17] H.-J. Vogel, H. Hoffmann, A. Leopold, and K. Roth, "Studies of crack dynamics in clay soil: II. A physically based model for crack formation," *Geoderma*, vol. 125, no. 3-4, pp. 213–223, 2005.

[18] J. H. Li and L. M. Zhang, "Study of desiccation crack initiation and development at ground surface," *Engineering Geology*, vol. 123, no. 4, pp. 347–358, 2011.

[19] H. Hoang, D. Hoxha, N. Belayachi, and D. P. Do, "On the impact of cracking on unsaturated hydrous properties of porous materials," in *Fifth Biot Conference on Poromechanics*, pp. 1560–1569, Vienna, Austria, 2013.